Computational modelling of non-simple and anisotropic materials

von der Fakultät Maschinenbau
der Technischen Universität Dortmund
zur Erlangung des akademischen Grades

Doktor-Ingenieur (Dr.-Ing.)

genehmigte Dissertation

von

Tobias Kaiser

aus Castrop-Rauxel

Vorsitz:	Prof. Dr.-Ing. A. Brümmer
Hauptreferent:	Prof. Dr.-Ing. habil. A. Menzel
Korreferenten:	Prof. Dr.-Ing. habil. S. Forest
	Prof. Dr.-Ing. Dipl.-Wirt.Ing. W. Tillmann
Tag der Einreichung:	05.03.2019
Tag der mündlichen Prüfung:	25.07.2019

"One, remember to look up at the stars and not down at your feet. Two, never give up work. Work gives you meaning and purpose and life is empty without it. Three, if you are lucky enough to find love, remember it is there and don't throw it away."

Stephen William Hawking (1942–2018)

Acknowledgements

Zusammenfassung

Die vorliegende Arbeit behandelt die Modellierung *generalisierter* sowie *anisotroper Materialien* und lässt sich in drei Abschnitte gliedern. Im ersten Abschnitt wird eine *gradientenerweiterte Elastizitätstheorie* zur Modellierung von faserverstärkten Verbundwerkstoffen, mit Fasern die eine Biegesteifigkeit aufweisen, untersucht. Der verwendete Ansatz basiert auf einer Erweiterung der Energiefunktion um Beiträge die höhere Gradienten der Deformationsabbildung, welche durch den Gradienten des räumlichen Faser-Richtungsfeldes definiert sind, beinhalten und kann als eine Erweiterung des klassischen *Strukturtensoransatzes* aufgefasst werden. Der zweite Abschnitt der vorliegenden Arbeit befasst sich mit der Entwicklung physikalisch wohl-motivierter *gradientenerweiterter (Kristall-)Plastizitätstheorien* basierend auf einer generalisierten Form der Clausius-Duhem Ungleichung. Insbesondere werden inkompatible plastische Deformationen im Rahmen von Versetzungsdichtetensoren interpretiert und energetisch in der Formulierung berücksichtigt. Der letzte Abschnitt der Arbeit beschäftigt sich mit der Modellierung sich *entwickelnder materieller Symmetriegruppen.* Hierbei liegt der Fokus insbesondere auf der Entwicklung eines konstitutiven Modells, welches eine Anisotropieentwicklung, die durch finite plastische Deformationsprozesse induziert ist, abbilden kann.

Abstract

This work focuses on the modelling and simulation of *non-simple* and *anisotropic materials*, and consists of three primary parts. In the first part, a *gradient elasticity* approach for the modelling of fibre-reinforced composites with fibres possessing fibre-bending stiffness is studied. The particular approach is based on the incorporation of higher-gradient contributions of the deformation map in terms of the gradient of the spatial fibre direction field in the energy density function and can be regarded as an extension of the classic *structural tensor approach.* The second part of the contribution deals with the development of physically well-motivated *gradient (crystal) plasticity formulations* which rely on an extended form of the Clausius-Duhem inequality. In particular, incompatible plastic deformations are interpreted in terms of dislocation density tensors which are energetically accounted for in the formulations. The final part of the contribution addresses the modelling of *evolving material symmetry groups.* To be specific, a constitutive model for the simulation of deformation-induced anisotropy evolution in finite plasticity is elaborated.

Publications

This thesis is based on the following peer-reviewed journal articles which were either published or submitted during the preparation of the thesis. Modifications of the original articles were made whenever considered meaningful, e.g. to avoid repetitions and to enhance clarity of the presentation.

Chapter 2: T. Asmanoglo and A. Menzel. A multi-field finite element approach for the modelling of fibre-reinforced composites with fibre-bending stiffness. *Computer Methods in Applied Mechanics and Engineering*, 317:1037–1067, 2017, [13].

T. Asmanoglo and A. Menzel. Fibre-reinforced composites with fibre-bending stiffness under azimuthal shear – Comparison of simulation results with analytical solutions. *International Journal of Non-Linear Mechanics*, 91:128–139, 2017, [12].

T. Asmanoglo and A. Menzel. A finite deformation continuum modelling framework for curvature effects in fibre-reinforced nanocomposites. *Journal of the Mechanics and Physics of Solids*, 107:411–432, 2017, [11].

Chapter 3: T. Kaiser and A. Menzel. An incompatibility tensor-based gradient plasticity formulation – Theory and numerics. *Computer Methods in Applied Mechanics and Engineering*, 345:671–700, 2019, [63].

T. Kaiser and A. Menzel. A dislocation density tensor-based crystal plasticity framework. *Journal of the Mechanics and Physics of Solids*, 131:276–302, 2019, [62].

Chapter 4: T. Kaiser, J. Lu, A. Menzel and P. Papadopoulos. A covariant formulation of finite plasticity with plasticity-induced evolution of anisotropy: Modeling, algorithmics, simulation, and comparison to experiments. *International Journal of Solids and Structures*, 2019, doi:10.1016/j.ijsolstr.2019.08.005, [64].

For the journal articles mentioned above, which were prepared in collaboration with one or more co-authors, the author of this thesis contributed fundamental aspects with regard to the outline of the theory, carried out the numerical implementations, evaluated the simulations and prepared the articles.

Contents

3 Dislocation density tensor-based gradient plasticity — 95

Notation

For the reader's convenience the notation used within this contribution is briefly summarised. In most parts of the thesis the co- or contravariant nature of tensors is not of primary interest for the derivations or the presented results and will hence not explicitly be indicated. Likewise, the respective metric tensors will be omitted in (most of) the contractions. This will, however, be different in Chapter 4 were we resort to a more stringent notation, the details of which are presented in Section 4.1.1.

Tensors   Let e_i with $i \in \{1, 2, 3\}$ represent the Cartesian base vectors spanning the three-dimensional Euclidean space $\mathbb{R}^3$. We express tensors of first, second and fourth order in terms of their coefficients using index notation, specifically

$$\boldsymbol{a} = a_i \, \boldsymbol{e}_i \quad ,$$
$$\boldsymbol{A} = A_{ij} \, \boldsymbol{e}_i \otimes \boldsymbol{e}_j \quad ,$$
$$\mathsf{A} = \mathsf{A}_{ijkl} \, \boldsymbol{e}_i \otimes \boldsymbol{e}_j \otimes \boldsymbol{e}_k \otimes \boldsymbol{e}_l \quad ,$$

and apply the Einstein summation convention if not stated differently to shorten the notation. In general, we denote scalar valued quantities by non-bold letters, first- and second order tensors by bold-face italic letters and fourth order tensors by bold-face sans-serif letters.

Inner tensor products   Inner tensor products are indicated by dots, with the number of dots indicating the number of contractions. With $\boldsymbol{\mathcal{A}}$ and $\boldsymbol{\mathcal{B}}$ denoting tensors of arbitrary order, the single tensor product is introduced as

$$\boldsymbol{\mathcal{A}} \cdot \boldsymbol{\mathcal{B}} = [\mathcal{A}_{ij...kl} \, \boldsymbol{e}_i \otimes \boldsymbol{e}_j \ldots \boldsymbol{e}_k \otimes \boldsymbol{e}_l] \cdot [\mathcal{B}_{mn...op} \, \boldsymbol{e}_m \otimes \boldsymbol{e}_n \ldots \boldsymbol{e}_o \otimes \boldsymbol{e}_p]$$
$$= \mathcal{A}_{ij...kl} \, B_{ln...op} \, \boldsymbol{e}_i \otimes \boldsymbol{e}_j \ldots \boldsymbol{e}_k \otimes \boldsymbol{e}_n \ldots \boldsymbol{e}_o \otimes \boldsymbol{e}_p \quad .$$

Furthermore, if $\boldsymbol{\mathcal{A}}$ and $\boldsymbol{\mathcal{B}}$ are at least of second order, the double tensor product is understood in the sense

$$\boldsymbol{\mathcal{A}} : \boldsymbol{\mathcal{B}} = [\mathcal{A}_{ij\ldots kl}\, \boldsymbol{e}_i \otimes \boldsymbol{e}_j \ldots \boldsymbol{e}_k \otimes \boldsymbol{e}_l] : [\mathcal{B}_{mn\ldots op}\, \boldsymbol{e}_m \otimes \boldsymbol{e}_n \ldots \boldsymbol{e}_o \otimes \boldsymbol{e}_p]$$
$$= \mathcal{A}_{ij\ldots kl}\, \mathcal{B}_{kl\ldots op}\, \boldsymbol{e}_i \otimes \boldsymbol{e}_j \ldots \boldsymbol{e}_o \otimes \boldsymbol{e}_p \quad .$$

For second order tensors the double tensor product gives rise to the norm

$$\|\boldsymbol{A}\| = \sqrt{\boldsymbol{A} : \boldsymbol{A}} \quad .$$

Outer tensor products   In addition to the classic outer product $\otimes$, the non-standard outer products $\underline{\otimes}$ and $\overline{\otimes}$ will frequently be used to allow for a compact notation. With $\boldsymbol{\mathcal{A}}$ and $\boldsymbol{\mathcal{B}}$ denoting again tensors of suitable order, these are defined as

$$\boldsymbol{\mathcal{A}} \otimes \boldsymbol{\mathcal{B}} = [\mathcal{A}_{ij\ldots kl}\, \boldsymbol{e}_i \otimes \boldsymbol{e}_j \ldots \boldsymbol{e}_k \otimes \boldsymbol{e}_l] \otimes [\mathcal{B}_{mn\ldots op}\, \boldsymbol{e}_m \otimes \boldsymbol{e}_n \ldots \boldsymbol{e}_o \otimes \boldsymbol{e}_p]$$
$$= \mathcal{A}_{ij\ldots kl}\, \mathcal{B}_{mn\ldots op}\, \boldsymbol{e}_i \otimes \boldsymbol{e}_j \ldots \boldsymbol{e}_k \otimes \boldsymbol{e}_l \otimes \boldsymbol{e}_m \otimes \boldsymbol{e}_n \ldots \boldsymbol{e}_o \otimes \boldsymbol{e}_p \quad ,$$
$$\boldsymbol{\mathcal{A}} \overline{\otimes} \boldsymbol{\mathcal{B}} = [\mathcal{A}_{ij\ldots kl}\, \boldsymbol{e}_i \otimes \boldsymbol{e}_j \ldots \boldsymbol{e}_k \otimes \boldsymbol{e}_l] \overline{\otimes} [\mathcal{B}_{mn\ldots op}\, \boldsymbol{e}_m \otimes \boldsymbol{e}_n \ldots \boldsymbol{e}_o \otimes \boldsymbol{e}_p]$$
$$= \mathcal{A}_{ij\ldots kl}\, \mathcal{B}_{mn\ldots op}\, \boldsymbol{e}_i \otimes \boldsymbol{e}_j \ldots \boldsymbol{e}_k \otimes \boldsymbol{e}_m \otimes \boldsymbol{e}_l \otimes \boldsymbol{e}_n \ldots \boldsymbol{e}_o \otimes \boldsymbol{e}_p \quad ,$$
$$\boldsymbol{\mathcal{A}} \underline{\otimes} \boldsymbol{\mathcal{B}} = [\mathcal{A}_{ij\ldots kl}\, \boldsymbol{e}_i \otimes \boldsymbol{e}_j \ldots \boldsymbol{e}_k \otimes \boldsymbol{e}_l] \underline{\otimes} [\mathcal{B}_{mn\ldots op}\, \boldsymbol{e}_m \otimes \boldsymbol{e}_n \ldots \boldsymbol{e}_o \otimes \boldsymbol{e}_p]$$
$$= \mathcal{A}_{ij\ldots kl}\, \mathcal{B}_{mn\ldots op}\, \boldsymbol{e}_i \otimes \boldsymbol{e}_j \ldots \boldsymbol{e}_k \otimes \boldsymbol{e}_m \otimes \boldsymbol{e}_n \otimes \boldsymbol{e}_l \ldots \boldsymbol{e}_o \otimes \boldsymbol{e}_p \quad .$$

Identity tensors   Based on the definition of the second order identity tensor $\boldsymbol{I}$ in terms of the Kronecker delta symbol δ_{ij},

$$\boldsymbol{I} = \delta_{ij}\, \boldsymbol{e}_i \otimes \boldsymbol{e}_j \quad , \quad \delta_{ij} = \begin{cases} 1 \,, & \text{if } i = j \\ 0 \,, & \text{if } i \neq j \end{cases} \quad ,$$

fourth order identity tensors or rather projection operators are introduced, namely,

$$\mathsf{I} = \boldsymbol{I} \overline{\otimes} \boldsymbol{I} \quad ,$$
$$\mathsf{I}^{\text{dev}} = \boldsymbol{I} \overline{\otimes} \boldsymbol{I} - \frac{1}{3} \boldsymbol{I} \otimes \boldsymbol{I} \quad ,$$
$$\mathsf{I}^{\text{sym}} = \frac{1}{2} [\boldsymbol{I} \overline{\otimes} \boldsymbol{I} + \boldsymbol{I} \underline{\otimes} \boldsymbol{I}] \quad ,$$
$$\mathsf{I}^{\text{skw}} = \frac{1}{2} [\boldsymbol{I} \overline{\otimes} \boldsymbol{I} - \boldsymbol{I} \underline{\otimes} \boldsymbol{I}] \quad .$$

Permutation tensors Permutation tensors with regard to the reference configuration and to the spatial configuration are defined with respect to a Cartesian basis as

$$
\begin{aligned}
\boldsymbol{\epsilon}_0 &= \epsilon_{ijk}\,\boldsymbol{e}_i \otimes \boldsymbol{e}_j \otimes \boldsymbol{e}_k \\
\boldsymbol{\epsilon}_t &= \epsilon_{ijk}\,\boldsymbol{e}_i \otimes \boldsymbol{e}_j \otimes \boldsymbol{e}_k
\end{aligned}
\quad , \quad
\epsilon_{ijk} =
\begin{cases}
1\,, & \text{if } (ijk) \text{ an even permutation of } (123) \\
-1\,, & \text{if } (ijk) \text{ an odd permutation of } (123) \\
0\,, & \text{if at least two indices are identical}
\end{cases}
\quad .
$$

Vector product Making use of the definition of the permutation symbol, the vector product of two (spatial) first order tensors in $\mathbb{R}^3$ is defined as

$$
\boldsymbol{a} \times \boldsymbol{b} = \boldsymbol{\epsilon}_t : [\boldsymbol{a} \otimes \boldsymbol{b}] \quad .
$$

Operators Gradient and divergence operations are denoted in terms of the Nabla operator $\nabla_{\bullet}$ with the subscript referring to the respective configuration. Being understood in the sense of a right-gradient and a right-divergence they can be represented in index notation (e.g. with respect to referential coordinates) as

$$
\nabla_{\boldsymbol{X}}\boldsymbol{\mathcal{A}} = \frac{\partial}{\partial X_m}\,[\mathcal{A}_{ij\ldots kl}\,\boldsymbol{e}_i \otimes \boldsymbol{e}_j \ldots \boldsymbol{e}_k \otimes \boldsymbol{e}_l] \otimes \boldsymbol{e}_m = \frac{\partial \mathcal{A}_{ij\ldots kl}}{\partial X_m}\,\boldsymbol{e}_i \otimes \boldsymbol{e}_j \ldots \boldsymbol{e}_k \otimes \boldsymbol{e}_l \otimes \boldsymbol{e}_m
$$

and

$$
\nabla_{\boldsymbol{X}} \cdot \boldsymbol{\mathcal{A}} = \nabla_{\boldsymbol{X}}\boldsymbol{\mathcal{A}} : \boldsymbol{I} = \frac{\partial \mathcal{A}_{ij\ldots kl}}{\partial X_l}\,\boldsymbol{e}_i \otimes \boldsymbol{e}_j \ldots \boldsymbol{e}_k \quad .
$$

With these definitions at hand, the referential and spatial curl operators are introduced as

$$
\mathrm{Curl}^{\mathrm{t}}\,(\boldsymbol{\mathcal{A}}) = -\,[\nabla_{\boldsymbol{X}}\boldsymbol{\mathcal{A}}] : \boldsymbol{\epsilon}_0 \quad , \qquad \mathrm{curl}^{\mathrm{t}}\,(\boldsymbol{\mathcal{A}}) = -\,[\nabla_{\boldsymbol{x}}\boldsymbol{\mathcal{A}}] : \boldsymbol{\epsilon}_t \quad .
$$

In addition, (referential and spatial) spin operators, relating an axial vector to the corresponding skew-symmetric second order tensor, are introduced as

$$
\mathrm{Spn}\,(\boldsymbol{a}) = -\boldsymbol{\epsilon}_0 \cdot \boldsymbol{a} \qquad , \qquad \mathrm{spn}\,(\boldsymbol{a}) = -\boldsymbol{\epsilon}_t \cdot \boldsymbol{a} \quad .
$$

Finally, the material time derivative of tensor $\boldsymbol{\mathcal{A}}$ will be denoted by $\dot{\boldsymbol{\mathcal{A}}}$, respectively $\mathrm{d}\boldsymbol{\mathcal{A}}/\mathrm{d}t$.

1 Introduction

1.1 Motivation and state of the art

The present contribution focuses on the modelling and simulation of non-simple and anisotropic materials. In particular, a gradient elasticity theory for the modelling of fibre-reinforced composites with fibres possessing fibre-bending stiffness is presented in Chapter 2, gradient (crystal) plasticity formulations which are based on the incorporation of dislocation density tensors are elaborated in Chapter 3, and the deformation-induced evolution of material symmetry groups is studied in Chapter 4. Setting the stage and against this background, Section 1.1.1, Section 1.1.2 and Section 1.1.3 briefly introduce the particular materials to be studied as well as their possible areas of application, summarise important experimental findings and present approaches which are currently used to simulate these materials.

1.1.1 Fibre-reinforced composites with fibre-bending stiffness

Fibre-reinforced composites Progress in materials science and manufacturing technologies drives the development of new, innovative materials with improved mechanical properties. With regard to the latter, especially the usage of (fibre-reinforced) composite materials is a promising approach since *"the combination of high-strength, high-stiffness structural fibres with low-cost, lightweight, environmentally resistant polymers results in composite materials with mechanical properties and durability better than either of the constituents alone"*, [15]. However, the production of such advanced composites used to be too expensive except for high-performance applications, [15], like the aerospace industry where lightweight construction and composites are frequently used. The price of composites has nevertheless dropped over the last years such that the aerospace market accounted only for 20% of all productions with regard to carbon fibres in 2005, [128]. Apart from the aerospace industry, other areas of application can thus be found for example in bio- and environmental engineering applications or in the automotive and construction industries, [15, 25, 50, 95].

1
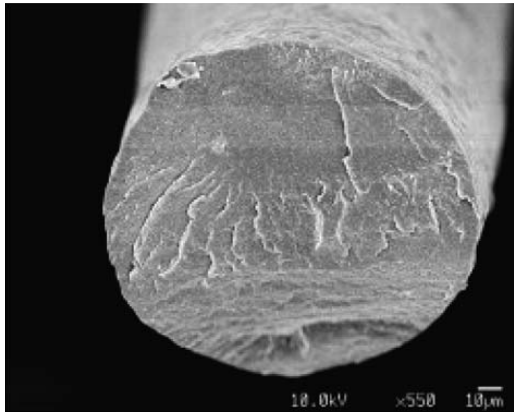
(a) Scanning electron microscopy image of a nanocomposite fibre.
Reprinted from J.K.W. Sandler et al., Polymer 45 (2004), 2001-2015, Copyright (2004), with permission from Elsevier.
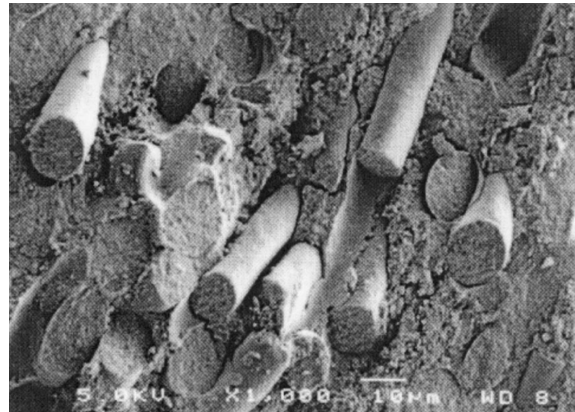
(b) Scanning electron microscopy image of a fibre-reinforced ceramic-matrix composite.
Reprinted from H. Suemasu et al., Composite Science and Technology 61 (2001), 281-288, Copyright (2001), with permission from Elsevier.

Figure 1.1: Scanning electron microscopy images of a composite fibre consisting of a polyamide-12 matrix that is reinforced with carbon nanofibres, [114], and of a random short fibre-reinforced ceramic matrix composite, [136].

The importance of fibre-reinforced composites is further underlined by the ongoing research on advanced composite materials. A property which has been receiving increasing interest over the past years is for example the self-healing functionality of damaged composites. This property is especially interesting for the aerospace industry and discussed in, e.g., [72] and [143]. With the development of composite materials with enhanced properties it becomes increasingly important to provide material models which allow for an accurate simulation of the latter in order to predict the mechanical behaviour of materials such as those shown in Figure 1.1, [128].

Nanocomposites Because of their exceptional mechanical and physical properties, especially the usage of carbon nanotube-based high-performance composites is considered a natural starting point for the development of new materials, e.g. for microactuators, [67, 112, 119, 139]. Since carbon and glass fibres which are frequently used as reinforcements for composites on the macroscale exhibit diameters ranging from 3 to 20 µm, [7], they are not suited as reinforcements for nanocomposites. On the other hand, the typical diameter of one-dimensional nanomaterials ranges from 1 to 100 nm, [7]. A review of micromechanics models, frequently applied to predict the average elastic properties especially of (short) fibre-reinforced composites, is given in [140]. These are for example models which employ Eshelby's equivalent inclusion approach, bounding or shear lag models. Attempts to apply these theories to the modelling of carbon nanotube-reinforced composites have been reported recently, see e.g. [7] and [138]. Specifically

speaking, the stiffness of aligned and perfectly random polymer-matrix nanocomposites is analysed in [7] using the Eshelby-Mori-Tanaka theory, and the longitudinal wave velocity of the composite is approximated by means of an Euler-Bernoulli beam theory. In doing so, the required force for the deformation as well as the response time of microactuators is simulated and the suitability of nanocomposites as structural materials for microelectromechanical systems pointed out. In [138], it is moreover aspired to gain a basic understanding of the influence of the structure and size of the nanotubes on the overall properties of the nanocomposite. To this end, a detailed study is carried out for a nanocomposite consisting of a polystyrene matrix which is reinforced with aligned multi-walled carbon nanotubes, and a micromechanical modelling approach is proposed.

Experimental findings A size-dependent deformation behaviour for different material classes is observed for structural components on the micro- and nanoscale, [70, 79, 81, 142], and reliable experimental data is required for the development of sophisticated material models which allow for a simulation of the latter effect. However, experiments on these small scales are difficult to conduct due to the required precision of the testing devices and the difficulties arising in the manipulation of micro- or even nano-sized objects,[3, 26, 111, 144]. For these reasons, a variety of (new) experimental approaches has been developed over the past years to measure the (mechanical) material properties on the nanoscale [111, 144], e.g. to determine material parameters akin to the Young's modulus. These include, amongst others, methods which are based on the atomic force microscopy (AFM) and methods which make use of the (high-resolution) transmission electron microscopy (TEM), like the electric-field-induced resonance method or the thermal vibration analysis.

A variety of experimental results for fibre-like materials on the micro- and nanoscale has recently been published, which motivates the developments to be presented as this work proceeds. In [70], experimental investigations in terms of bending and tension tests are carried out for epoxy-polymeric beams with the beam height ranging from $20\,\mu m$ to $115\,\mu m$. The Young's modulus obtained by means of uni-axial tension tests is found to be independent of the beam height. However, when investigating the bending behaviour of the cantilever-like microbeams using a nanoindenter, the ratio between the experimentally observed bending rigidity and the bending rigidity predicted by a classic beam theory is found to significantly increase with decreasing beam height.

Regarding wire-like materials on the nanoscale, the mechanical properties of silver nanowires have been analysed by means of three-point bending tests using the atomic force microscopy – in [24] for samples with a diameter ranging from $65\,nm$ to $140\,nm$ and in [59] for a fibre diameter ranging from $20\,nm$ to $140\,nm$. A scanning electron microscopy image of the experiments carried out in [59] is depicted in Figure 1.2(a) and the experimental results in terms of the Young's modulus, determined by means of the classic Euler-Bernoulli beam theory, are presented in Figure 1.2(b). These experiments suggest a significant increase in the elastic stiffness for a decreasing fibre diameter,
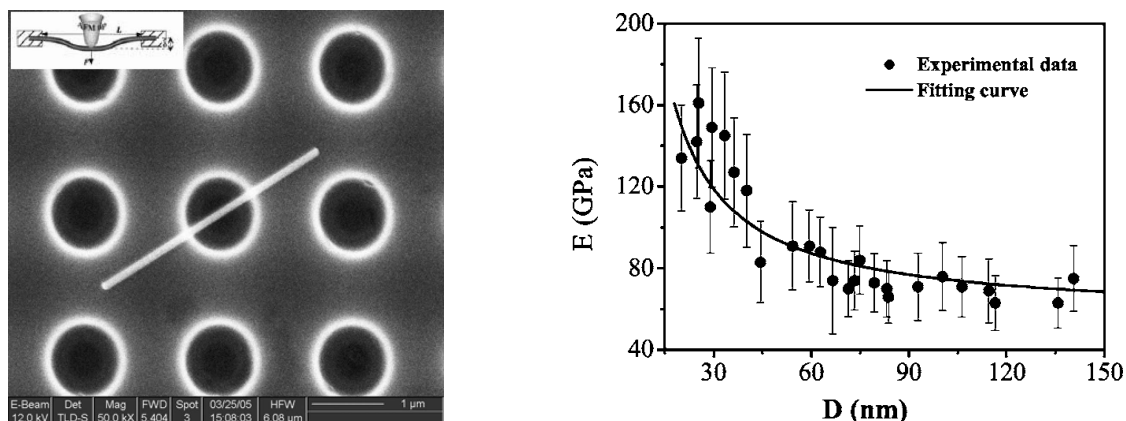
(a) Scanning electron microscopy image of a silver nanowire (diameter 79 nm) which is suspended over etched holes in a silicon wafer. Inset: Schematic diagram of a nanowire which is deformed by an atomic force microscopy tip. Reprinted figure with permission from G. Y. Jing et al., Physical Review B, 73, 235409, 2006. Copyright 2006 by the American Physical Society.

(b) Experimentally determined Young's modulus (E) as a function of the diameter (D) of silver nanowires. A significant increase in the Young's modulus is observed for a decreasing diameter. Reprinted figure with permission from G. Y. Jing et al., Physical Review B, 73, 235409, 2006. Copyright 2006 by the American Physical Society.

Figure 1.2: Experimental setup and measured elastic stiffness of silver nanowires by means of nanoscale three-point bending tests based on the contact atomic force microscopy.

especially for nanowires with diameters smaller than approximately 70 nm. The classic Euler-Bernoulli beam theory is also applied in [24] to predict the Young's modulus of silver nanowires based on experimental data. However, no pronounced size effect is reported in [24], which may be explained by the comparatively large diameters (> 65 nm) of the fibres which are analysed. Note that we will, in accordance with [107], refer to the Young's modulus which is calculated based on experimental data with the help of a beam theory as the bending modulus hereafter.

An experimental approach to determine the bending modulus for ZnO nanowires using the electric-field-induced resonance method, cf. [107], is presented in [23]. In these experiments free-standing ZnO nanowires are vertically grown from the substrate and a frequency tunable ac voltage is applied across the nanowire and a countering tip. A scanning electron microscope is then used to analyse the natural frequencies of the nanowires, and the bending modulus is approximated based on natural frequencies in a second step, [23]. With this method, ZnO nanowires with a diameter of between 17 nm-550 nm are analysed, and a significant increase in the bending modulus is observed for nanowires with a diameter smaller than approximately 120 nm, reflecting again the qualitative relation observed in Figure 1.2(b).

Various experiments to characterise the (mechanical) properties of single-walled carbon nanotubes (SWNTs), e.g. [67], carbon nanotube ropes, e.g. [112], and multi-walled

carbon nanotubes (MWNTs), e.g. [107, 113, 139, 144], by means of different experimental approaches have been reported in the literature. In [139], MWNTs with an outer diameter of between 5.6 nm-24.8 nm and a corresponding inner diameter of between 1.0 nm-6.6 nm are analysed by measuring the amplitude of their intrinsic thermal vibrations in the transmission electron microscope, with the highest bending modulus being on average reported for thinner nanotubes. Using the atomic force microscopy, the bending modulus of MWNTs with an outer diameter of between 26 nm-76 nm is experimentally analysed in [144], and the one of nanotubes with an outer diameter of between 4.8 nm-10.0 nm and an assumed inner diameter of 2 nm is measured in [113]. In both experiments no significant dependence of the bending modulus on the tube diameter is observed. Using the electric-field-induced resonance method, the bending modulus of MWNTs with an outer diameter of between 4 nm-40 nm is analysed in [107]. In these experiments the MWNTs are attached to a fine gold wire and assumed to deform like cantilever beams such that the bending modulus can be deduced using the classic Euler-Bernoulli beam theory, with a pronounced dependence of the bending modulus on the tube diameter being revealed which is found to be similar to the qualitative relation depicted in Figure 1.2(b).

It further is remarked that, with regard to other materials, different relations between the bending modulus and the fibre diameter than the one indicated in Figure 1.2(b), can be observed in experiments. To give an example, it is shown in [96] by using the atomic force microscopy that the bending moduli of chromium cantilevers, with a height of 50 nm-83 nm, decrease as the cantilevers become thinner. Moreover, the bending modulus of each of the analysed nano-sized chromium beams is found to be smaller than that of bulk chromium.

One-dimensional nanomaterials are ideally suited as reinforcements for composites on the nanoscale, [7], which motivates the development of continuum composite models that allow us to account for the size-dependent mechanical behaviour of the fibres as has been observed in experiments. Nevertheless, further experiments on the deformation behaviour of nano-sized (beam-like) composite structures for different sample dimensions and fibres of different diameters are required in order to analyse in detail the size-dependent material response, as experimentally observed for structurally isolated fibres.

Modelling of micro and nanoscale devices Over the past 20 years there has been an increasing interest in the development of micro- and nanoscale devices such as microactuators and microsensors, micromechanical testing instruments, biochemical analysis systems as well as micro- and nanoelectromechanical systems, see e.g. [7, 79, 81, 142] and Figure 1.3. Since experiments at these scales are expensive and difficult to conduct [3, 111, 144], the need arises for (material) models which allow for predictive simulations. However, for micro- and nanoscale devices, size effects are observed, cf. [70, 79, 81] which cannot be captured using models based on the classic continuum theory as these do not feature an internal length scale. On the other hand, atomic and molecular models which
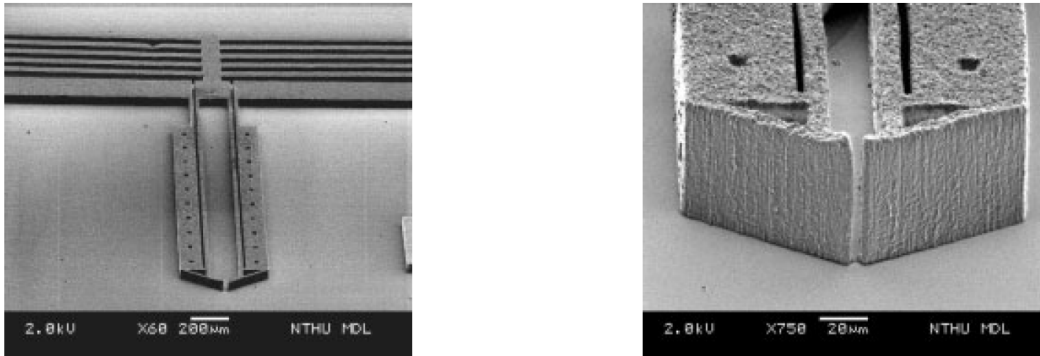
Figure 1.3: Scanning electron microscopy image of a polymer-reinforced multi-walled nanotube micro-gripper and of its gripper front, [44]. Reprinted from W. Fang et al., Advanced Materials 17 (2005), 2987-2992, Copyright (2005), with permission from John Wiley & Sons, Inc..

are conceptually valid for such small length scales are limited by the computational capacities and require long computation times, [3, 14, 79, 127]. This motivates the use of extended continuum approaches which introduce a natural length scale into the models and henceforth allow, in principle, for the simulation of a size-dependent material behaviour. Driven by the progress in nano-technologies, there has thus been extensive research on the application of extended continuum approaches to the modelling of nano-sized devices over the past years.

Due to the beam or plate-like structure of many components used in micro- and nanoscale devices, classic beam and plate theories are often considered as a starting point for the development of more sophisticated theories and combined with extended continuum approaches. In this contribution, we will focus on so-called one-dimensional nanomaterials, [24], like nanowires, nanotubes and nanorods, for which various extended beams theories have been elaborated in the literature.

One frequently used approach to account for the underlying microstructural effects is offered by the theory of nonlocal elasticity proposed in [39, 40], which assumes the stress state at a reference point to be a functional of the strain state at every point of the continuum, respectively within a chosen neighbourhood. An extended Euler-Bernoulli beam model which relies on the latter theory is, for example, proposed in [104] in order to study the influence of the nonlocal effect for different length scales, and a critical review of nonlocal Euler-Bernoulli and nonlocal Timoshenko beam models with emphasis on the consistent use of the nonlocal constitutive relations and appropriate boundary conditions is given in [79]. Accounting for the possible influence of a matrix material the axial vibrations of carbon nanotubes which are embedded in an elastic medium are furthermore analysed in [14] using a rod model in combination with the theory of nonlocal elasticity.

A different approach to account for the size-dependent material behaviour of beam-like structures which is based on the theory of micropolar elasticity, cf. [41], is pursued in [108] to analyse the tip deflection of cantilever beams. The predictions of the extended beam theory, which reduces to the classic Timoshenko beam theory for a specific choice of the material parameters, are furthermore compared to those of the classic Euler-Bernoulli- and the Timoshenko beam theory as well as to the finite element-based simulation results for micropolar elastic beams provided in [57].

In addition, extended beam models which are based on the couple stress theory are proposed in, e.g., [5] and [103]. Being more specific, the principle of minimum potential energy is employed in [103] to derive a size-dependent Euler-Bernoulli beam theory which is based on the couple stress theory proposed in [149]. On the other hand, the classic (linear) couple stress theory, cf. [94], is used in [5] to derive an analytical solution for the bending dominated deformation of a beam with a circular cross section.

It is moreover suggested in [53] to use the Young–Laplace equation to extend the classic Euler-Bernoulli beam theory such that surface effects are accounted for. With the extended beam theory at hand, bending tests are analysed especially with regard to the size effect, and the predicted stiffness as a function of the beam diameter is compared with the experimental findings presented in [24] and [59].

An approach to account for fibre-bending stiffness and for size effects Besides taking the gradient of the deformation into account, the classic approach for the modelling of fibre-reinforced composites presented in [129] considers the fibre direction as an additional argument of the energy function. By doing so, the energy function which was originally an anisotropic function of the deformation can be rewritten as an isotropic function in the extended list of arguments, enabling a representation by means of invariants. The classic modelling approach therefore has close connections to the representation theories of anisotropic tensor functions by means of structural tensors, see e.g. [20, 89, 92, 153]. Nevertheless, as pointed out in [130], models which are based on the classic modelling approach by means of structural tensors assume that the fibres are perfectly flexible – i.e. they do not exhibit any resistance against bending. This theoretically allows for deformation patterns in which the fibres exhibit slope-discontinuities since the preferred material direction is allowed to change arbitrarily from one point of the continuum to another without considering any related energy contribution, as discussed in [125]. Moreover, no natural length scale is included in the models so that the resulting theory is size-independent and can for example not account for such effects related to different fibre diameters.

Moving away from the assumption of perfectly flexible fibres and relying on the generalised continuum approach presented in [94], an enhanced theory for the modelling of fibre-reinforced composites is proposed in [130]. By accounting for higher gradients of the motion map, a natural length scale is introduced into the model. Assuming a general dependence on the higher gradients, it is then shown that the energy function may, in

general, depend on 33 independent invariants. Dealing with fibre-reinforced composites, however, it can be motivated from a physical point of view to restrict the dependence on higher gradients to their directional derivative into the direction of the fibre, i.e. the fibre curvature and the gradient of the fibre stretch are taken into account, [130]. Under this assumption, the most general form of the strain energy function may be expressed in terms of eleven independent invariants. Assuming a plane strain state, the theory is further specified for two-dimensional problems and a linearised version is derived in [130].

Analytical solutions   To gain a basic understanding of the modelling of fibre-reinforced composites with fibre-bending stiffness, simplified versions of the general finite strain theory proposed in [130] have been analysed over the past years, cf. [30, 31, 124, 125]. These investigations often imposed further assumptions to allow for analytical solutions of the respective boundary value problems. These comprise assumptions on the fibre-extensibility, the compressibility of the bulk or the restriction to small deformations.

The first attempt to provide an analytical solution to a boundary value problem with the fibre-bending stiffness being explicitly accounted for in accordance with the derivations presented in [130] is documented in [125]. Therein, the analysis focuses on the bending of a block and on the finite azimuthal shear deformation of a tube-like structure for a plane strain deformation state, subject to the assumption of inextensible fibres and of an incompressible matrix material. Motivated by the results presented in [125], the analysis of the azimuthal shear deformation of the tube-like structure is continued in [30]. To simplify the derivation of an analytical solution, the investigations are restricted to linearised kinematics, and different combinations of constraints are imposed, e.g. incompressibility of the matrix material or inextensibility of the fibres. Finally, a detailed analysis of the azimuthal shear deformation of the tube is presented for two different sets of boundary conditions with regard to the support of the fibres. To be specific, the fibres are assumed to be either clamped or free to rotate such that different restrictions on the fibre slope are imposed. Another approach to a more general solution of the azimuthal shear deformation problem of the tube-like structure is presented in [31]. Therein, the matrix material is assumed to be incompressible and the simulation accounts for finite deformations. The results which are achieved under these assumptions, for fibres which are assumed to be clamped at the inner boundary, are then compared to the ones presented in [30] for the corresponding small strain theory.

1.1.2 Dislocation density tensor-based gradient plasticity

A notion of incompatible deformations and dislocations densities   While the motion of dislocations on the one hand allows a metal to deform plastically, the presence of dislocations, on the other hand, increases the resistance to dislocation motion and hence results in an increase in the (macroscopically observable) yield limit. There are two primary types of dislocations to be considered. Statistically stored dislocations are

the result of a statistical trapping of dislocations inside the body. Geometrically necessary dislocations, on the other hand, are required to preserve lattice compatibility in inhomogeneous plastic deformation processes. From a modelling point of view geometrically necessary dislocations are thus closely related to the incompatible part of the plastic deformation and can be measured in terms of dislocation density tensors. The fundamental concepts of incompatibilities and their interpretation in terms of dislocation density tensors are meanwhile well-established and date, amongst others, back to the works [19, 49, 66, 68, 69, 99]. Extending purely phenomenological gradient plasticity approaches where gradients of (scalar valued) internal variables are often used as means to regularise formulations, the introduction of higher-gradient contributions in terms of dislocation density tensors is thus well-motivated by physical considerations.

On mesh dependent results and regularised approaches Classic (local) plasticity formulations lead to mesh dependent results when they are used for the finite element simulation of localised plastic deformation processes in softening materials. When simulating the formation of shear bands for example, the calculated width of the bands decreases with a refinement of the finite element mesh such that the simulation is not capable of reproducing experimentally observed shear bands of finite width and that no convergence upon mesh refinement is achieved, [32, 87, 106]. To remedy this problem various regularisation schemes have been proposed in the literature, e.g. the usage of nonlocal plasticity theories or gradient plasticity formulations. In nonlocal plasticity theories the regularisation of the formulation is achieved by the weighted integration of a quantity that characterises the plastic deformation over a certain influence volume, see e.g. [35, 37, 38, 135]. Gradient plasticity formulations, on the other hand, provide an alternative regularisation approach and can be regarded as a reduced form of the nonlocal theory, [84, 106]. These theories rely on the introduction of higher gradients of quantities that characterise the plastic deformation process as additional arguments of the energy function or of the yield function, as for example discussed in [18, 85, 86, 100, 148]. Motivated, among other things, by the objective to incorporate the underlying physics of crystallographic slip, especially gradient crystal plasticity formulations have been in the focus of intense research over the past years, see e.g. [22, 36, 146–148].

Accounting for the crystallographic structure: crystal plasticity Inelastic processes in the class of materials we are focusing on are the result of the motion of large numbers of dislocations. Although this motion is not resolved for each individual dislocation in crystal plasticity, the underlying physical process of crystallografic slip is taken into account on the macroscale. To this end, typical crystallografic systems, e.g. face-centred cubic (fcc) or body-centred cubic (bcc), are studied to define the planes on which, and the directions in which plastic slip is likely to occur. From a physical point of view atomic bonds need to be broken and re-established in the plastic slip process. Thus, plastic slip tends to occur between planes of greatest atomic density and closest-packed

(a) tension tests

(b) torsion tests
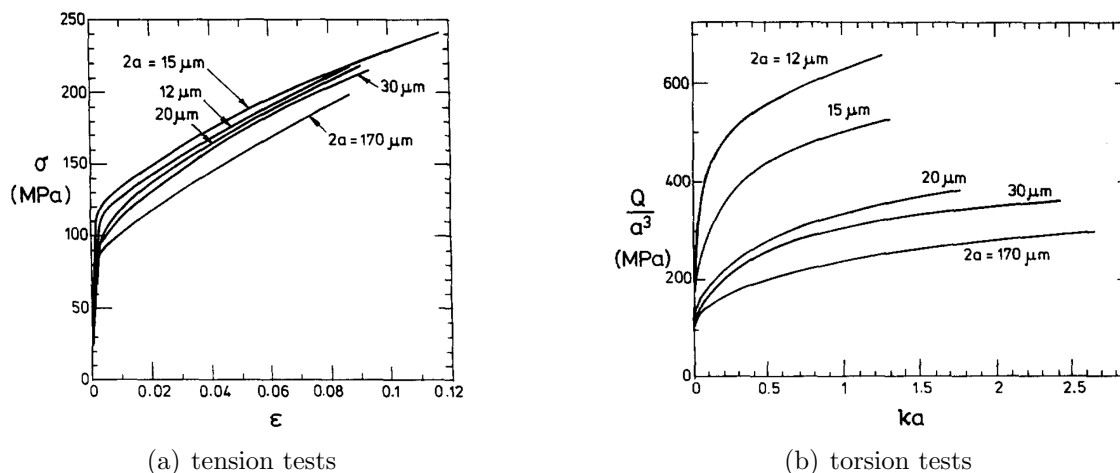
Figure 1.4: Experimental results for polycrystalline copper wires (99.99% purity) of diameter $2\,a$. The tension test results are presented in terms of the Cauchy stress σ and the logarithmic strain ε with the influence of the wire diameter on the resulting curves being small, i.e. no distinct size effect is observable. In contrast, the torsion test results which are given in terms of the normalised torque Q/a^3 and with κ denoting the twist per unit length show a significant size dependence. Reprinted from N.A. Fleck et al., Acta Metallurgica et Materialia 42(2) (1994), 475–487, Copyright (1994), with permission from Elsevier.

directions are identified with the slip directions, [33]. The slip process itself is assumed to be driven by the Schmid resolved shear stress, i.e. by the stress acting on the slip plane into the slip direction. Note is taken of the fact that slip mode uniqueness can generally not be expected in rate-independent crystal plasticity, see e.g. [6, 33, 54, 115] for a detailed discussion. This results in the problem that neither the set of active slip systems nor the slip rates on the individual slip systems can in general be determined in a unique manner and that numerical tools, such as generalised or pseudo-inverses, must be used to determine a solution, [4, 21, 93]. Alternatively, rate-dependent viscoplasticity approaches can be applied, where the slip rates are uniquely determined by the stress state and possibly by some internal variables, [115]. Approaching the rate-independent limit, however, the governing system of differential equations becomes considerably stiff and special numerical schemes are required to stabilise the solution process, [134].

Experimental findings and size effects   In the experiments presented in [48], polycrystalline, cold-drawn copper wires (99.99% purity) with diameters $2\,a$ ranging from $12\,\mu\text{m}$ to $170\,\mu\text{m}$ were analysed in uni-axial tension and torsion tests. The tension test results, given in terms of the Cauchy stress σ and the logarithmic strain ε, are reproduced in Figure 1.4(a). The experimental results of the torsion tests are depicted in Figure 1.4(b) with Q/a^3 denoting the normalised torque and with κ representing the twist per unit length. As pointed out in [48], the influence of the diameter on the tension test results is small, while a significant size dependence is found in the torsion tests. This observation
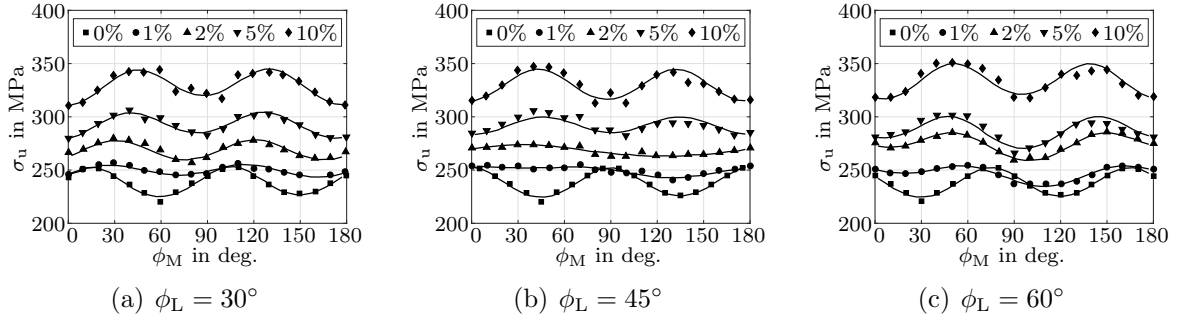
Figure 1.5: Experimental findings by Kim and Yin reproduced from [65] and discussed in detail in Section 4.3.1.

is attributed to the inhomogeneous deformation state, i.e. to the occurrence of strain gradients which are not observable in the (homogeneous) uni-axial tension tests. Moreover, it is argued on the basis of a dimensional analysis that a material model which does not contain an internal length scale is not capable of reproducing the results shown in Figure 1.4(b), as the curves would coincide. This observation will be exemplified by (normalised) moment-rotation curves in Section 3.3.4.3.

1.1.3 Deformation induced anisotropy evolution in finite plasticity

Experimental findings Kim and Yin, [65], analysed the yielding behaviour of cold-rolled steel sheets by means of tension tests with the focus being on the (evolution of the directional dependency of the) uni-axial yield limit. In particular, their experimental observations suggest that the principle structure of the macroscopically observable uni-axial yield limit distribution and hence the material symmetry group of the deduced yield function is maintained during a finite plastic deformation process. However, a rotation of the yield function's symmetry group was observed. For the sake of motivation the experimentally determined uni-axial yield limit σ_{u} as a function of the angle ϕ_{M} relative to the loading direction is depicted in Figure 1.5. Specifically speaking, the distribution of σ_{u} is provided for various load states in terms of the Hencky strain in loading direction, i.e. $\{0\%, 1\%, 2\%, 5\%, 10\%\}$, and for samples which were prepared at various angles ϕ_{L} relative to the rolling direction of the sheet metal. These experiments will be discussed in detail in Section 4.3.1 and motivate the specific evolution equation for the material symmetry group that is elaborated in Chapter 4.

On finite plasticity and the modelling of texture (evolution) Over the past years intense research has been focusing on the modelling of (anisotropic) finite plasticity, e.g. [22, 36]. With dislocation motion being a main carrier of plastic deformation in metals, recent trends in discrete dislocation dynamics focus on resolving the motion and interaction of individual dislocations to predict the overall macroscopic response, [151, 152].

11

However, these approaches are still limited by the available computational capacities such that continuum theories are proposed which do not resolve individual dislocations but may take into account the associated kinematics of slip and the crystallographic structure in each grain in an averaged manner on the mesoscale, as is done in crystal plasticity. Approaching the modelling of finite plasticity on the macroscale, modelling approaches are used in which the constitutive equations are functions of internal state variables that characterise e.g. the material symmetry group and the state of plastic deformation in order to account for the deformation history.

A natural approach to account for experimentally observed anisotropic features is offered by the incorporation of structural tensors which characterise the respective material symmetry group into the constitutive equations, as broadly advocated in [88, 153]. The evolution of the symmetry group may thus be described in terms of appropriate evolution equations for the structural tensors, as was done in [52, 60, 61, 88] for example. Assuming that the anisotropic features are induced by the crystalline symmetry and that the plastic deformation leaves the lattice structure and hence the material symmetry unaltered, motivates the definition of the structural tensors in the intermediate configuration. However, as is well-established within the theory of finite plasticity, the intermediate configuration is only determined except for a rotation. The structural tensors, being introduced as quantities of the intermediate configuration, are thus subject to the same rotational indeterminacy which is closely related to the notion of the plastic spin which is discussed in detail in [29] and which merits special attention.

In this regard, Lu and Papadopoulos, [77], proposed a theoretical framework for the modelling of evolving plastic anisotropies where the rotational consistency condition is enforced through the more general covariance condition. Aspiring a purely referential approach and recalling Noll's rule, [97, 98], it is shown that the symmetry group, which is a subgroup of the Euclidean orthogonal group in the intermediate configuration, is characterised by generalised orthogonal transformations with respect to the plastic right Cauchy-Green tensor in the reference configuration. In particular, it is elaborated that the rate equation for the structural tensor consists of two contributions termed convected- and residual-type evolution. Whereas the convected-type evolution varies with the plastic right Cauchy-Green tensor, the residual-type evolution allows the structural tensor to evolve independently from the latter. When interpreted in the context of the multiplicative split and especially with regard to [29], the residual-type evolution may be thought of in the sense that the structural tensors are allowed to spin at a rate different from the one of the intermediate configuration which resembles the plastic spin.

1.2 Scope and outline

To familiarise the reader with the structure and with the scope of the present work, a brief summary of each chapter is given. We like to stress that each chapter is self-

consistent such that the thesis does not need to be read in a chronological order but that each chapter may be studied independently of the others.

Chapter 2 *(Fibre-reinforced composites with fibre-bending stiffness)* focuses on the elaboration and validation of a computational framework for the modelling of fibre-reinforced composites with fibres possessing fibre-bending stiffness, as well as on its application to the modelling of nanocomposites.

After a brief summary of the essential kinematics and of the balance equations of the couple stress continuum, the main findings presented in [130] regarding a generalised theory for the description of fibre-reinforced materials with fibres possessing bending stiffness are outlined – i.e. higher gradients of the deformation map in terms of the gradient of the spatial fibre orientation field are incorporated as additional arguments of the energy function. Based on the presented theory, a mixed-type multi-field finite element formulation for the numerical solution of the underlying system of coupled partial differential equations is discussed. Subsequently, a specific prototype model is proposed where the focus lies especially on the consistency of the energy function and on the deduced constitutive equations for the symmetric part of the Cauchy stresses and the couple stresses with their corresponding counterparts from the small strain theory which have been used in [30]. With the specific choice of the energy function at hand, we focus in detail on the comparison of the analytical solution for the azimuthal shear deformation of a fibre-reinforced tube, derived in [30] under the assumption of small deformations, with the one calculated by means of the proposed finite element approach, which takes finite deformations into account. In particular, the general deformation pattern as well as the stress- and the couple stress fields are taken into account. Thereafter, homogeneous and inhomogeneous stretch dominated deformation fields are analysed, and the three-dimensional bending of a plate with a hole is investigated to further study the model properties with regard to the chosen gradient-enhanced form of the stored energy function. Motivated by these investigations and by the experimental findings on one-dimensional nanomaterials, in particular on carbon nanotubes and silver nanowires, the focus finally lies on the design and physical interpretation of the stored energy function. To be specific, it will be assumed that the nanofibres exhibit non-negligible resistance against bending, in contrast to the classic structural tensor-based modelling approach, which assumes the fibres to be perfectly flexible – the underlying idea is that the fibres behave like nanobeams, similar to the size-dependent beam theories summarised before. The bending resistance is then accounted for in an energetic manner via a certain combination of invariants which is associated with the fibre curvature. Likewise it is shown that fibre stretch gradient contributions can be separately addressed in terms of further combinations of invariants. This chapter is supplemented by **Appendix A**.

Chapter 3 *(Dislocation density tensor-based gradient plasticity)* addresses the theoretical foundations and the numerics of a gradient plasticity formulation in which the

incorporation of higher-gradient contributions to the free energy density function is micromechanically motivated and gives rise to the occurrence of microstresses that take the interpretation of back stress tensors in the respective yield function.

At the outset of our developments we will resort to the fundamental theoretical foundations of a thermodynamic consistent formulation of gradient plasticity presented in [106]. The proposed theory is based on the extension of the Clausius-Duhem inequality by an additional term, the so-called nonlocality residual, which is introduced to account for energy exchanges between particles at the microscale and, as the name already suggests, induces a nonlocal character to the inequality. On the basis of the extended form of the Clausius-Duhem inequality, we show that taking into account dislocation density tensors as additional arguments of the free energy density function, in the present framework, gives rise to the field equation of a generalised stress tensor that drives the plastic evolution. After a detailed analysis of a specific quadratic energy contribution in terms of the dislocation density tensor and the resulting microstress contribution, we first focus on the implementation of a specific model within the framework of phenomenological associated-type plasticity. In particular, the solution of the governing system of partial differential equations by means of a multi-field finite element scheme that makes use of a global Fischer-Burmeister approach to fulfil the plastic consistency conditions on a global level is discussed. We then focus on the simulation of representative boundary value problems, like the plastic evolution at material interfaces or the shear band formation that is induced by geometric imperfections, to study basic model properties.

Taking into account the physics of plastic deformations in crystalline materials a natural extension of the proposed formulation to gradient crystal plasticity is addressed in a next step. Specifically speaking, it is shown that the assumption of a crystal plasticity framework gives rise to the same set of balance equations. However, in order to maintain the structure of the stabilisation algorithm that is used in the underlying viscoplastic crystal plasticity model to approach the rate-independent limit, a different interpretation (of the balance equation of the generalised stress tensor) is taken, which is closely related to the choice of the primary field variable in the proposed finite element formulation. After studying the constitutive response at material point level and the principal model properties in a two-dimensional setting, the focus is eventually on experimentally motivated torsion tests on micro wires in a three-dimensional setting and on the modelling of experimentally observed size effects. This chapter is supplemented by **Appendix B**.

Chapter 4 *(Deformation-induced anisotropy evolution in finite plasticity)* is motivated by the experimental findings on the yielding behaviour of cold-rolled sheet metal presented in [65], and studies as to whether a model which is solely based on a convected-type evolution is capable of reproducing the experimentally observed evolution of the material symmetry group or if a residual-type evolution needs additionally to be taken into account. To this end, we especially focus on the evaluation of the dissipation inequality and on the derivation of a well-interpretable form of the plastic spin tensor.

Regarding real materials and the application to metal plasticity, the anisotropic properties of the elastic response and those of the yielding behaviour may be different. For the specific model at hand, we will assume that the elastic response may be treated as isotropic, while the yielding behaviour exhibits appreciable directional dependence. With regard to [65], finite element-based simulations of tension tests in two- and three-dimensional settings are then carried out. In particular, we focus on the general evolution of the plastic deformation, on the rotation of the material symmetry group and on the global response in terms of load-displacement curves. Overall, the simulation results and the experimental findings are found to be in good accordance and suggest that invoking the residual-type evolution of the yield function's symmetry group allows us to capture the experimental findings, while a purely convected evolution-based modelling approach does not seem to be sufficient. By studying basic model properties for shear dominated deformation states, we finally focus on the simulation of in-plane torsion tests. This chapter is supplemented by **Appendix C**.

2 Fibre-reinforced composites with fibre-bending stiffness

This chapter focuses on the elaboration of a higher gradient-based modelling approach for fibre-reinforced composites with fibres possessing fibre-bending stiffness and is structured as follows:

Section 2.1 *(Theoretical foundations and multi-field finite element approach)* gives a brief summary of the fundamental equations of the underlying extended continuum theory and presents the theoretical foundations of the theory proposed in [130] to account for the fibre-bending stiffness by taking into account higher-order gradients of the deformation map as additional arguments of the stored energy function. Moreover, the multi-field finite element formulation proposed in [10] to address the solution of the resulting system of coupled partial differential equations is recapitulated.

Section 2.2 *(Comparison with analytical solutions and study of basic model properties)* focuses on the comparison of simulation results with analytical solutions based on the azimuthal shear deformation problem of a tube-like structure to validate the proposed formulation. Furthermore, basic model properties are studied in two- and three-dimensional settings.

Section 2.3 *(Modelling of curvature effects in fibre-reinforced nanocomposites)* addresses the development of a more elaborated form of the gradient energy contribution that is well-interpretable from a physical point of view and motivated by the experimental findings on one-dimensional nanomaterials presented in Section 1.1.1.
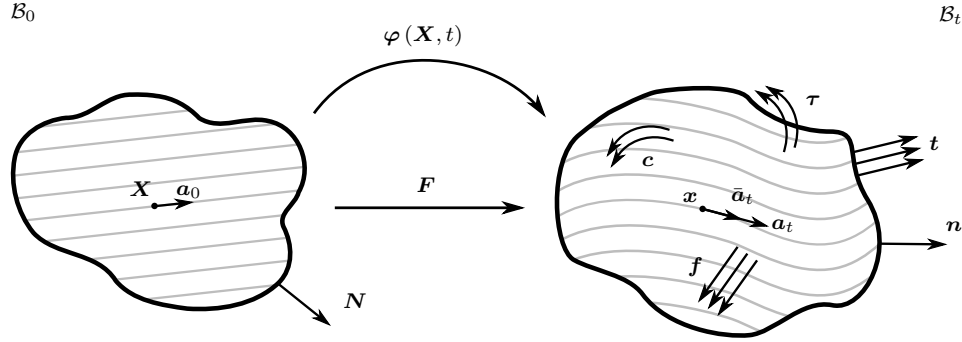
Figure 2.1: Essential kinematics.

2.1 Theoretical foundations and multi-field finite element approach

After introducing basic kinematic quantities and the balance equations of the underlying extended continuum theory, the fundamentals of the modelling approach for fibre-reinforced composites with fibres possessing fibre-bending stiffness as derived in [130] are briefly summarised in Section 2.1.2. The theoretical framework relies on the introduction of higher gradients of the deformation map as additional arguments of the energy function – in particular, energy contributions which are based on the gradient of the spatial fibre direction field, projected onto the fibre direction are taken into account. In this thesis, the solution of the resulting system of coupled partial differential equations is addressed by means of a multi-field finite element formulation. Specifically speaking, we will make use of the finite element formulation proposed in [10], the fundamentals of which are briefly recapitulated in Section 2.1.3.

2.1.1 Balance equations and essential kinematics

Let $\mathcal{B}_0 \subset \mathbb{R}^3$ denote the region occupied by the body under consideration and let $\boldsymbol{X} \in \mathcal{B}_0$ denote the position of a material point at some reference time $t_0 \in \mathbb{R}$. We then introduce the deformation map $\boldsymbol{\varphi} : \mathcal{B}_0 \times \mathbb{R} \to \mathcal{B}_t \subset \mathbb{R}^3$ as the function which maps positions in the reference configuration to their spatial positions $\boldsymbol{x} = \boldsymbol{\varphi}(\boldsymbol{X}, t) = \boldsymbol{X} + \boldsymbol{u}$ at time $t \geq t_0$, with $\boldsymbol{u}$ denoting the displacement of a material point. The deformation gradient is denoted by $\boldsymbol{F} = \nabla_{\boldsymbol{X}} \boldsymbol{\varphi}$, with Jacobian $J_{\boldsymbol{F}} = \det(\boldsymbol{F}) > 0$ and its cofactor $\mathrm{cof}(\boldsymbol{F}) = J_{\boldsymbol{F}} \boldsymbol{F}^{-\mathrm{t}}$. The deformation gradient is understood as the linear mapping which correlates line elements $\mathrm{d}\boldsymbol{X}$ of the reference configuration and their spatial counterparts $\mathrm{d}\boldsymbol{x}$, i.e.

$$\mathrm{d}\boldsymbol{x} = \boldsymbol{F} \cdot \mathrm{d}\boldsymbol{X} \quad . \tag{2.1}$$

Moreover, the cofactor tensor of the deformation gradient is related to the change of differential area elements such that, with the definition of the outward surface normal of the reference configuration $\boldsymbol{N}$ and the corresponding area element $\mathrm{d}A$, the spatial representations are given according to

$$\boldsymbol{n}\,\mathrm{d}a = \mathrm{cof}\,(\boldsymbol{F}) \cdot \boldsymbol{N}\,\mathrm{d}A \quad . \tag{2.2}$$

In addition, differential volume elements $\mathrm{d}V$ of the reference configuration are related to their spatial counterpart $\mathrm{d}v$ by use of the Jacobian $J_{\boldsymbol{F}}$, to be specific

$$\mathrm{d}v = J_{\boldsymbol{F}}\,\mathrm{d}V \quad . \tag{2.3}$$

The velocity of a particle is $\dot{\boldsymbol{\varphi}}\,(\boldsymbol{X},t)$ and, accordingly, the spatial velocity gradient $\boldsymbol{l}$ is introduced as

$$\nabla_{\boldsymbol{x}}\dot{\boldsymbol{\varphi}} = \boldsymbol{l} = \frac{1}{2}\left[\boldsymbol{l} + \boldsymbol{l}^{\mathrm{t}}\right] + \frac{1}{2}\left[\boldsymbol{l} - \boldsymbol{l}^{\mathrm{t}}\right] = \boldsymbol{l}^{\mathrm{sym}} + \boldsymbol{l}^{\mathrm{skw}} = \boldsymbol{d} + \boldsymbol{\varpi} \quad , \tag{2.4}$$

with the rate of deformation tensor $\boldsymbol{d} = \boldsymbol{l}^{\mathrm{sym}}$ and spin tensor $\boldsymbol{\varpi} = \boldsymbol{l}^{\mathrm{skw}}$ given by the symmetric and by the skew part of $\boldsymbol{l}$ as indicated by the respective superscripts. With the introduction of the third-order permutation tensor $\boldsymbol{\epsilon}_t$ the associated spin vector is then defined as

$$\boldsymbol{\omega} = -\frac{1}{2}\boldsymbol{\epsilon}_t : \boldsymbol{\varpi} \quad . \tag{2.5}$$

Aiming at the modelling of fibre-reinforced composites, we further introduce the fibres as material curves, termed a-curves in accordance with [125]. The direction of the a-curves at each point of the continuum can be characterised by a unit vector field which will be denoted by $\boldsymbol{a}_0$ for the reference- and by $\bar{\boldsymbol{a}}_t$ for the deformed configuration. Since the fibres are assumed to be convected with the material, relation

$$\boldsymbol{a}_t = \lambda_{\mathrm{A}}\,\bar{\boldsymbol{a}}_t = \boldsymbol{F} \cdot \boldsymbol{a}_0 \quad , \quad \|\boldsymbol{a}_0\| = \|\bar{\boldsymbol{a}}_t\| = 1 \tag{2.6}$$

holds, so that λ_{A} is identified with the fibre stretch. In addition to the latter, the enhanced modelling approach which is to be discussed in detail in Section 2.1.2 takes into account higher-order energy contributions including the fibre curvature. To this end, the referential gradient of the spatial fibre direction vector

$$\boldsymbol{G} = \nabla_{\boldsymbol{X}}\,\boldsymbol{a}_t = \nabla_{\boldsymbol{X}}\left[\boldsymbol{F} \cdot \boldsymbol{a}_0\right] = \boldsymbol{a}_0 \cdot \nabla_{\boldsymbol{X}}\left[\boldsymbol{F}^{\mathrm{t}}\right] + \boldsymbol{F} \cdot \nabla_{\boldsymbol{X}}\boldsymbol{a}_0 \tag{2.7}$$

is considered and its purely referential representation,

$$\boldsymbol{\Lambda} = \boldsymbol{F}^{\mathrm{t}} \cdot \boldsymbol{G} \quad , \tag{2.8}$$

is introduced as suggested in [130].

Due to the occurrence of second-order gradients of the deformation map in (2.7) and, in consequence, as arguments of the energy function, the classic Boltzmann continuum theory is not suitable. Instead, it is proposed in [130] to base the model on a Mindlin theory from which the governing equations are derived in, e.g., [94] and which are briefly summarised as this work proceeds.

2.1.1.1 Balance of mass

The body under consideration represents a closed system such that the total mass is preserved. Assuming the existence of a mass density ρ_t thus results in

$$\frac{\mathrm{d}}{\mathrm{d}t} \int_{\mathcal{B}_t} \rho_t \, \mathrm{d}v = \int_{\mathcal{B}_0} \frac{\mathrm{d}}{\mathrm{d}t} \left(\rho_t \, J_{\boldsymbol{F}} \right) \mathrm{d}V = \int_{\mathcal{B}_0} \dot{\rho}_0 \, \mathrm{d}V = 0 \quad , \tag{2.9}$$

with the mass density per unit volume of the reference configuration $\rho_0 = \rho_t \, J_{\boldsymbol{F}}$ being introduced. Performing the localisation of (2.9) and using $\mathrm{d}J_{\boldsymbol{F}}/\mathrm{d}t = J_{\boldsymbol{F}} \, \nabla_{\boldsymbol{x}} \cdot \dot{\boldsymbol{\varphi}}$ the local form of the balance equation of mass can be derived as

$$\dot{\rho}_t + \rho_t \, \nabla_{\boldsymbol{x}} \cdot \dot{\boldsymbol{\varphi}} = 0 \quad . \tag{2.10}$$

2.1.1.2 Balance of linear momentum

Regarding the balance equation of linear momentum, the rate of change of linear momentum equals the sum of all forces resulting from volume distributed loads $\boldsymbol{f}$ and tractions $\boldsymbol{t}$. The integral form of the balance equation of linear momentum reads

$$\frac{\mathrm{d}}{\mathrm{d}t} \int_{\mathcal{B}_t} \rho_t \, \dot{\boldsymbol{\varphi}} \, \mathrm{d}v = \int_{\mathcal{B}_t} \rho_t \, \boldsymbol{f} \, \mathrm{d}v + \int_{\partial \mathcal{B}_t} \boldsymbol{t} \, \mathrm{d}a \quad . \tag{2.11}$$

Before localising (2.11) the surface integral is rewritten as a volume integral using Cauchy's theorem, i.e.

$$\boldsymbol{\sigma}^{\mathrm{t}} \cdot \boldsymbol{n} = \boldsymbol{t} \quad , \tag{2.12}$$

including the Cauchy-type stress tensor $\boldsymbol{\sigma}$ and the outward surface normal $\boldsymbol{n}$ along with the divergence theorem, to be specific

$$\int_{\partial \mathcal{B}_t} \boldsymbol{t} \, \mathrm{d}a = \int_{\mathcal{B}_t} \nabla_{\boldsymbol{x}} \cdot \boldsymbol{\sigma}^{\mathrm{t}} \, \mathrm{d}v \quad . \tag{2.13}$$

Additionally making use of (2.10), the local form of the balance equation is given by

$$\rho_t \, \ddot{\boldsymbol{\varphi}} = \rho_t \, \boldsymbol{f} + \nabla_{\boldsymbol{x}} \cdot \boldsymbol{\sigma}^{\mathrm{t}} = \rho_t \, \boldsymbol{f} + \nabla_{\boldsymbol{x}} \cdot \left[\boldsymbol{\sigma}^{\mathrm{sym}} + \boldsymbol{\sigma}^{\mathrm{skw}} \right]^{\mathrm{t}} \quad . \tag{2.14}$$

2.1.1.3 Balance of angular momentum

Let $\boldsymbol{r} = \boldsymbol{x} - \boldsymbol{x}_{\mathrm{ref}}$ denote the difference vector of the current position of a particle and a fixed, but otherwise arbitrary reference point $\boldsymbol{x}_{\mathrm{ref}}$. The balance of angular momentum of the Mindlin theory considered then states that the rate of change of angular momentum with respect to $\boldsymbol{x}_{\mathrm{ref}}$ equals the sum of all couples acting on the body. The related integral form results in

$$\frac{\mathrm{d}}{\mathrm{d}t} \int_{\mathcal{B}_t} \rho_t \, \boldsymbol{r} \times \dot{\boldsymbol{\varphi}} \, \mathrm{d}v = \int_{\mathcal{B}_t} \rho_t \, [\boldsymbol{r} \times \boldsymbol{f} + \boldsymbol{c}] \, \mathrm{d}v + \int_{\partial \mathcal{B}_t} \boldsymbol{r} \times \boldsymbol{t} + \boldsymbol{\tau} \, \mathrm{d}a \quad . \tag{2.15}$$

In contrast to the Boltzmann continuum theory, the Mindlin theory does not only account for the action of couples resulting from body distributed forces and tractions, but further takes into account volume distributed couples $\boldsymbol{c}$ in $\mathcal{B}_t$ and surface couples $\boldsymbol{\tau}$ acting on $\partial \mathcal{B}_t$.
In analogy to the stress tensor (2.12), the couple stress tensor $\boldsymbol{m}$ is introduced via its relation with $\boldsymbol{\tau}$, namely

$$\boldsymbol{m}^{\mathrm{t}} \cdot \boldsymbol{n} = \boldsymbol{\tau} \quad , \tag{2.16}$$

and the surface integral in (2.15) is rewritten as a volume integral using the divergence theorem, to be specific

$$\int_{\partial \mathcal{B}_t} \boldsymbol{r} \times \boldsymbol{t} + \boldsymbol{\tau} \, \mathrm{d}a = \int_{\mathcal{B}_t} \boldsymbol{r} \times \left[\nabla_{\boldsymbol{x}} \cdot \boldsymbol{\sigma}^{\mathrm{t}} \right] + \boldsymbol{\epsilon}_t : \boldsymbol{\sigma} + \nabla_{\boldsymbol{x}} \cdot \boldsymbol{m}^{\mathrm{t}} \, \mathrm{d}v \quad . \tag{2.17}$$

Noting that $\dot{\boldsymbol{\varphi}} \times \dot{\boldsymbol{\varphi}} = \boldsymbol{0}$ and making use of (2.10) and (2.14) renders the local form of the balance of angular momentum as

$$\boldsymbol{0} = \nabla_{\boldsymbol{x}} \cdot \boldsymbol{m}^{\mathrm{t}} + \rho_t \, \boldsymbol{c} + \boldsymbol{\epsilon}_t : \boldsymbol{\sigma} \tag{2.18a}$$

$$= \nabla_{\boldsymbol{x}} \cdot \boldsymbol{m}^{\mathrm{t}} + \rho_t \, \boldsymbol{c} + \boldsymbol{\epsilon}_t : \boldsymbol{\sigma}^{\mathrm{skw}} \quad . \tag{2.18b}$$

2.1.1.4 Balance of energy

Neglecting temperature effects, the integral form of the balance of energy reads

$$\frac{\mathrm{d}}{\mathrm{d}t} \int_{\mathcal{B}_t} \rho_t \left[\frac{1}{2} \| \dot{\boldsymbol{\varphi}} \|^2 + e \right] \mathrm{d}v = \int_{\mathcal{B}_t} \rho_t \, [\boldsymbol{f} \cdot \dot{\boldsymbol{\varphi}} + \boldsymbol{c} \cdot \boldsymbol{\omega}] \, \mathrm{d}v + \int_{\partial \mathcal{B}_t} \boldsymbol{t} \cdot \dot{\boldsymbol{\varphi}} + \boldsymbol{\tau} \cdot \boldsymbol{\omega} \, \mathrm{d}a \quad , \tag{2.19}$$

with e denoting the specific internal energy of the continuum. Evaluating the integral on the left-hand side by making use of the balance of mass (2.10), and rewriting the surface integral on the right-hand side as a volume integral one arrives at

$$\int_{\mathcal{B}_t} \rho_t\, \dot{e} = \int_{\mathcal{B}_t} \dot{\boldsymbol{\varphi}} \cdot \left[-\rho_t\, \ddot{\boldsymbol{\varphi}} + \rho_t\, \boldsymbol{f} + \nabla_{\boldsymbol{x}} \cdot \boldsymbol{\sigma}^{\mathrm{t}} \right]\, \mathrm{d}v$$
$$+ \int_{\mathcal{B}_t} \boldsymbol{\omega} \cdot \left[\nabla_{\boldsymbol{x}} \cdot \boldsymbol{m}^{\mathrm{t}} + \rho_t \boldsymbol{c} \right]\, \mathrm{d}v \tag{2.20}$$
$$+ \int_{\mathcal{B}_t} \boldsymbol{\sigma}^{\mathrm{t}} : \nabla_{\boldsymbol{x}} \dot{\boldsymbol{\varphi}} + \boldsymbol{m}^{\mathrm{t}} : \nabla_{\boldsymbol{x}} \boldsymbol{\omega}\, \mathrm{d}v \quad .$$

Moreover, taking into account the balance of linear momentum (2.14), the balance of angular momentum (2.18) and noting that by using the $\boldsymbol{\epsilon}$-$\boldsymbol{\delta}$-identity $\boldsymbol{\epsilon}_t \cdot \boldsymbol{\epsilon}_t = 2\,\mathsf{I}^{\mathrm{skw}}$ together with (2.5),

$$\boldsymbol{\omega} \cdot \boldsymbol{\epsilon}_t : \boldsymbol{\sigma} = \boldsymbol{\varpi} : \boldsymbol{\sigma}^{\mathrm{t}} \quad , \tag{2.21}$$

holds, one finally obtains

$$\rho_t\, \dot{e} = \boldsymbol{\sigma}^{\mathrm{t}} : \boldsymbol{d} + \boldsymbol{m}^{\mathrm{t}} : \nabla_{\boldsymbol{x}} \boldsymbol{\omega} \quad . \tag{2.22}$$

2.1.2 Incorporation of fibre-bending stiffness

Assuming the existence of an elastic potential W, the classic modelling approach for anisotropic materials accounts for anisotropic material properties that are induced by the fibres by introducing structural tensors $\boldsymbol{A}_0$ as additional arguments of the energy function. If the anisotropic material behaviour is induced by a single family of fibres, $\boldsymbol{A}_0$ can be specified based on the local referential fibre orientation according to

$$\boldsymbol{A}_0 = \boldsymbol{a}_0 \otimes \boldsymbol{a}_0 \tag{2.23}$$

and the energy function, accounting for invariance with respect to rigid body motions, can be written in terms of

$$W\left(\boldsymbol{C}, \boldsymbol{A}_0\right) \quad , \tag{2.24}$$

where $\boldsymbol{C} = \boldsymbol{F}^{\mathrm{t}} \cdot \boldsymbol{F}$ denotes the right Cauchy-Green tensor, see e.g. [20, 129, 153]. With this approach, the fibre stretch can be accounted for – nevertheless, effects due to fibre twist and fibre bending are not considered. In order to capture the latter effects, it is proposed in [130] to take into account the gradient of the deformed fibre vector $\boldsymbol{G}$ as an additional argument of the energy function which, in its most general form, can then be introduced as

$$W\left(\boldsymbol{F}, \boldsymbol{G}, \boldsymbol{a}_0\right) \quad . \tag{2.25}$$

By assuming a quasi-static system and by neglecting temperature effects, body forces and body couples, constitutive functions for the symmetric part of the stress tensor

$$\boldsymbol{\sigma}^{\mathrm{sym}} = J_{\boldsymbol{F}}^{-1} \left[\frac{\partial W}{\partial \boldsymbol{F}} \cdot \boldsymbol{F}^{\mathrm{t}} + \frac{\partial W}{\partial \boldsymbol{G}} \cdot \boldsymbol{G}^{\mathrm{t}} \right] \tag{2.26}$$

and for the deviatoric part of the couple stress tensor

$$\left[\boldsymbol{m}^{\mathrm{dev}} \right]^{\mathrm{t}} = -\frac{2}{3} J_{\boldsymbol{F}}^{-1} \, \boldsymbol{\epsilon}_t : \left[\frac{\partial W}{\partial \boldsymbol{G}} \cdot \left[\boldsymbol{F}^{\mathrm{t}} \, \overline{\otimes} \, \boldsymbol{a}_t + \boldsymbol{F}^{\mathrm{t}} \otimes \boldsymbol{a}_t \right] \right] \tag{2.27}$$

are then derived in [130] based on (2.22). The volumetric part of the couple stress tensor remains undetermined from energetic considerations, which is a general result of the couple stress theory; see, e.g., [94, 130]. It is then shown that an energy function which fulfils the postulate of invariance with respect to rigid body motions a priori is given in terms of

$$W \left(\boldsymbol{C}, \boldsymbol{\Lambda}, \boldsymbol{a}_0 \right) \quad . \tag{2.28}$$

With (2.28) at hand, the constitutive function for the symmetric part of the stress tensor (2.26) is recast in the form

$$\boldsymbol{\sigma}^{\mathrm{sym}} = J_{\boldsymbol{F}}^{-1} \left[2 \, \boldsymbol{F} \cdot \frac{\partial W}{\partial \boldsymbol{C}} \cdot \boldsymbol{F}^{\mathrm{t}} + \boldsymbol{G} \cdot \left[\frac{\partial W}{\partial \boldsymbol{\Lambda}} \right]^{\mathrm{t}} \cdot \boldsymbol{F}^{\mathrm{t}} + \boldsymbol{F} \cdot \frac{\partial W}{\partial \boldsymbol{\Lambda}} \cdot \boldsymbol{G}^{\mathrm{t}} \right] \tag{2.29}$$

and the deviatoric part of the couple stress tensor (2.27) is specified as

$$\left[\boldsymbol{m}^{\mathrm{dev}} \right]^{\mathrm{t}} = -\frac{2}{3} J_{\boldsymbol{F}}^{-1} \, \boldsymbol{\epsilon}_t : \left[\boldsymbol{F} \cdot \frac{\partial W}{\partial \boldsymbol{\Lambda}} \cdot \left[\boldsymbol{F}^{\mathrm{t}} \, \overline{\otimes} \, \boldsymbol{a}_t + \boldsymbol{F}^{\mathrm{t}} \otimes \boldsymbol{a}_t \right] \right] \quad , \tag{2.30}$$

see [130].

Neglecting fibre twist, the dependence of the energy function on the gradient of the deformed fibre vector can further be restricted to its normal projection onto the direction of the fibre, i.e. only the vector

$$\boldsymbol{\kappa} = \boldsymbol{G} \cdot \boldsymbol{a}_0 \tag{2.31a}$$

$$= \left[\boldsymbol{a}_0 \cdot \nabla_{\boldsymbol{X}} \boldsymbol{F}^{\mathrm{t}} + \boldsymbol{F} \cdot \nabla_{\boldsymbol{X}} \boldsymbol{a}_0 \right] \cdot \boldsymbol{a}_0 \tag{2.31b}$$

$$= \frac{\partial \lambda_{\mathrm{A}}}{\partial \boldsymbol{X}} \cdot \boldsymbol{a}_0 \, \bar{\boldsymbol{a}}_t + \lambda_{\mathrm{A}} \frac{\partial \bar{\boldsymbol{a}}_t}{\partial \boldsymbol{X}} \cdot \boldsymbol{a}_0 \tag{2.31c}$$

is additionally accounted for as an argument of the energy function which takes the form

$$W \left(\boldsymbol{F}, \boldsymbol{\kappa}, \boldsymbol{a}_0 \right) \quad . \tag{2.32}$$

With regard to (2.31b) it is first observed that $\boldsymbol{\kappa}$ includes contributions which are due to higher gradients of the placement field $\boldsymbol{\varphi}$, i.e. $\nabla_{\boldsymbol{X}} \boldsymbol{F}$, as well as contributions which are associated with the fibre curvature in the reference configuration. Secondly, when analysing (2.31c) it is revealed that $\boldsymbol{\kappa}$ includes contributions resulting from both the fibre stretch gradient and the fibre curvature. The latter observations will be of particular importance for the design and analysis of the energy function to be presented in Section 2.3.

In view of invariance with respect to rigid body motions one furthermore finds that the energy function (2.32) can equivalently be expressed in terms of

$$W\left(\boldsymbol{C}, \boldsymbol{\kappa}_0, \boldsymbol{\kappa} \cdot \boldsymbol{\kappa}, \boldsymbol{a}_0\right) \quad , \tag{2.33}$$

with

$$\boldsymbol{\kappa}_0 = \boldsymbol{F}^{\mathrm{t}} \cdot \boldsymbol{\kappa} = \boldsymbol{\Lambda} \cdot \boldsymbol{a}_0 \tag{2.34}$$

being a referential representation of $\boldsymbol{\kappa}$ that was introduced in [130] and which merits special attention as outlined in Remark 2.1. Employing a specific form of the energy function based on (2.33) generally allows the capturing of fibre bending in an energetic manner while effects like fibre twist are not taken into account, [130]. Moreover, specifying (2.33) as an isotropic tensor function results in

$$W\left(I_i\left(\boldsymbol{C}, \boldsymbol{\Lambda}, \boldsymbol{a}_0\right)\right), \quad i \in \{1, \ldots, 11\} \quad , \tag{2.35}$$

with the eleven invariants given by

$$\begin{aligned}
&I_1 = \boldsymbol{C} : \boldsymbol{I} &&I_2 = \operatorname{cof}\left(\boldsymbol{C}\right) : \boldsymbol{I} &&I_3 = \det\left(\boldsymbol{C}\right) \\
& &&I_4 = \boldsymbol{a}_0 \cdot \boldsymbol{C} \cdot \boldsymbol{a}_0 &&I_5 = \boldsymbol{a}_0 \cdot \boldsymbol{C}^2 \cdot \boldsymbol{a}_0 \\
&I_6 = \boldsymbol{\kappa}_0 \cdot \boldsymbol{\kappa}_0 &&I_7 = \boldsymbol{\kappa}_0 \cdot \boldsymbol{C} \cdot \boldsymbol{\kappa}_0 &&I_8 = \boldsymbol{\kappa}_0 \cdot \boldsymbol{C}^2 \cdot \boldsymbol{\kappa}_0 \\
&I_9 = \boldsymbol{a}_0 \cdot \boldsymbol{\kappa}_0 &&I_{10} = \boldsymbol{a}_0 \cdot \boldsymbol{C} \cdot \boldsymbol{\kappa}_0 &&I_{11} = \boldsymbol{a}_0 \cdot \boldsymbol{C}^2 \cdot \boldsymbol{\kappa}_0
\end{aligned} \tag{2.36}$$

cf. [130, 153]. If it is furthermore assumed that the sense of the fibre orientation may not influence the constitutive relations, W must be even in both $\boldsymbol{a}_0$ and $\boldsymbol{\Lambda}$ such that the invariants I_9, I_{10} and I_{11} may enter the energy function only in terms of their powers of even order and products in pairs, [130].

The latter invariant-based representation of the energy function together with the constitutive relations for the stresses (2.29) and couple stresses (2.30) shall serve as a basis for the constitutive framework of the finite element formulation to be presented in Section 2.1.3.

Remark 2.1 (Tensor spaces) *In order to fulfil the requirement of invariance with respect to rigid body motions the referential vector $\boldsymbol{\kappa}_0 = \boldsymbol{F}^{\mathrm{t}} \cdot \boldsymbol{\kappa}$ is introduced in [130] as an argument of the energy function. In this remark it is briefly outlined that this format of $\boldsymbol{\kappa}_0$ is not the (contravariant) referential representation of the (contravariant) spatial*

vector $\boldsymbol{\kappa}$, but rather the pullback of the dual vector $\boldsymbol{\kappa}^\flat$ which is an element of the spatial cotangent space.

Using convected coordinates, the contravariant spatial vector $\boldsymbol{\kappa}$ can be represented as

$$\boldsymbol{\kappa} = \frac{\partial \boldsymbol{a}_t}{\partial \boldsymbol{X}} \cdot \boldsymbol{a}_0 = \frac{\partial a_t^i}{\partial X^p} \, a_0^p \, \boldsymbol{g}_i = \kappa^i \, \boldsymbol{g}_i = \boldsymbol{\kappa}^\sharp \quad . \tag{2.37}$$

The related dual vector is given by

$$\boldsymbol{\kappa}^\flat = \boldsymbol{g}^\flat \cdot \boldsymbol{\kappa}^\sharp = g_{ij} \, \kappa^j \, \boldsymbol{g}^i = \kappa_i \, \boldsymbol{g}^i \tag{2.38}$$

where the spatial co- and contravariant base vectors $\boldsymbol{g}_i$, respectively $\boldsymbol{g}^i$ and the covariant metric tensor $\boldsymbol{g}^\flat = g_{ij} \, \boldsymbol{g}^i \otimes \boldsymbol{g}^j$ of the curvilinear coordinate system are introduced. Since the deformation gradient tensor using convected coordinates is given in terms of $\boldsymbol{F} = \boldsymbol{g}_i \otimes \boldsymbol{G}^i$, we find

$$\boldsymbol{\kappa}_0 = \left[\boldsymbol{G}^i \otimes \boldsymbol{g}_i \right] \cdot \left[\kappa^j \, \boldsymbol{g}_j \right] = \left[\boldsymbol{G}^i \otimes \boldsymbol{g}_i \right] \cdot \left[g_{kl} \, \boldsymbol{g}^k \otimes \boldsymbol{g}^l \right] \cdot \left[\kappa^j \, \boldsymbol{g}_j \right] = \left[\boldsymbol{G}^i \otimes \boldsymbol{g}_i \right] \cdot \left[\kappa_k \, \boldsymbol{g}^k \right] = \kappa_i \, \boldsymbol{G}^i$$
$$= \boldsymbol{F}^{\mathrm{t}} \cdot \boldsymbol{g}^\flat \cdot \boldsymbol{\kappa} \qquad\qquad = \boldsymbol{F}^{\mathrm{t}} \cdot \boldsymbol{\kappa}^\flat \qquad\qquad = \boldsymbol{\kappa}_0^\flat \, . \tag{2.39}$$

Hence, $\boldsymbol{\kappa}_0$ turns out to be the covariant referential representation of the contravariant spatial vector $\boldsymbol{\kappa}$. Note that $\boldsymbol{G}^i \otimes \boldsymbol{g}_i$ formally represents the dual of the transpose of $\boldsymbol{F}$ which is not indicated due to simplification of the notation. The contravariant referential representation of $\boldsymbol{\kappa} = \boldsymbol{\kappa}^\sharp$ results from the pullback via $\boldsymbol{F}^{-1}$, that is

$$\boldsymbol{\kappa}_0^\sharp = \boldsymbol{F}^{-1} \cdot \boldsymbol{\kappa} = \left[\boldsymbol{G}_i \otimes \boldsymbol{g}^i \right] \cdot \left[\kappa^j \, \boldsymbol{g}_j \right] = \kappa^i \, \boldsymbol{G}_i \quad , \tag{2.40}$$

and can be related to the representation in the dual-space according to

$$\boldsymbol{\kappa}_0 = \boldsymbol{\kappa}_0^\flat = \kappa_i \, \boldsymbol{G}^i = \left[g_{ij} \, \boldsymbol{G}^i \otimes \boldsymbol{G}^j \right] \cdot \left[\kappa^k \, \boldsymbol{G}_k \right] = \boldsymbol{C} \cdot \boldsymbol{\kappa}_0^\sharp \quad , \tag{2.41}$$

with the right Cauchy-Green tensor being expressed in terms of $\boldsymbol{C} = \boldsymbol{F}^{\mathrm{t}} \cdot \boldsymbol{g}^\flat \cdot \boldsymbol{F}$.

The interpretation of $\boldsymbol{\kappa}_0$ as a covariant vector is important for the physical interpretation of the invariants and the definition of length-type measures. As an example, consider the squared norm of the spatial vector $\boldsymbol{\kappa}$ which is given according to

$$\|\boldsymbol{\kappa}\|^2 = \|\boldsymbol{\kappa}^\sharp\|^2 = \boldsymbol{\kappa}^\sharp \cdot \boldsymbol{g}^\flat \cdot \boldsymbol{\kappa}^\sharp \quad . \tag{2.42}$$

This measure can be expressed in terms of referential quantities via

$$\|\boldsymbol{\kappa}^\sharp\|^2 = \boldsymbol{\kappa}_0^\sharp \cdot \boldsymbol{C} \cdot \boldsymbol{\kappa}_0^\sharp \quad , \tag{2.43}$$

respectively

$$\|\boldsymbol{\kappa}^{\sharp}\|^2 = \boldsymbol{\kappa}_0^{\flat} \cdot \boldsymbol{C}^{-1} \cdot \boldsymbol{\kappa}_0^{\flat} \quad , \tag{2.44}$$

such that, with the introduction of $\boldsymbol{\kappa}_0 = \boldsymbol{\kappa}_0^{\flat}$ as a covariant quantity, the inverse right Cauchy-Green deformation tensor $\boldsymbol{C}^{-1} = \boldsymbol{F}^{-1} \cdot \boldsymbol{g}^{\sharp} \cdot \boldsymbol{F}^{-t}$ has to be employed for the calculation of the norm of the spatial vector $\boldsymbol{\kappa}$ in referential representation. In contrast, the right Cauchy-Green tensor would need to be used if the referential representation of $\boldsymbol{\kappa}$ was introduced as a contravariant quantity.

2.1.3 Numerics and finite element formulation

With the general form of the energy function (2.35) and the constitutive relations for the stresses (2.29) and couple stresses (2.30) at hand, (2.14) and (2.18) yield a system of two coupled non-linear partial differential equations for the determination of the unknown field variables $\boldsymbol{\varphi}$ and $\boldsymbol{\sigma}^{\mathrm{skw}}$. First, regarding (2.29) and (2.30) together with (2.35), the stresses $\boldsymbol{\sigma}^{\mathrm{sym}}$ and $\boldsymbol{m}^{\mathrm{dev}}$, in general, are non-linear functions including the argument

$$\begin{aligned}
\boldsymbol{\Lambda} &= \boldsymbol{F}^{\mathrm{t}} \cdot \boldsymbol{G} \\
&= \boldsymbol{F}^{\mathrm{t}} \cdot \left[\boldsymbol{a}_0 \cdot \nabla_{\boldsymbol{X}} \left[\boldsymbol{F}^{\mathrm{t}} \right] + \boldsymbol{F} \cdot \nabla_{\boldsymbol{X}} \boldsymbol{a}_0 \right] \\
&= \boldsymbol{F}^{\mathrm{t}} \cdot \left[\boldsymbol{a}_0 \cdot \nabla_{\boldsymbol{X}} \left[\nabla_{\boldsymbol{X}} \boldsymbol{\varphi} \right]^{\mathrm{t}} + \boldsymbol{F} \cdot \nabla_{\boldsymbol{X}} \boldsymbol{a}_0 \right] \quad .
\end{aligned} \tag{2.45}$$

Thus, inserting the constitutive equations for the stresses and couple stresses into balance equations (2.14) and (2.18) results in a system of partial differential equations, each of which includes up to third-order derivatives in $\boldsymbol{x}$, see Section 2.1.3.1 and Section 2.1.3.2. Alternatively, the balance equation of angular momentum can be regarded as the definition of the skew-symmetric part of the stress tensor and inserted into the balance equation of linear momentum which would result in one partial differential equation of fourth-order as elaborated in, e.g., [126] and as briefly discussed in Remark 2.2 and the related Appendix A.4.

After multiplication with test functions and integration by parts, the weak form of the system of coupled partial differential equations includes second-order gradients of the deformation map. From a mathematical point of view, this implies that a $\mathcal{C}^0$-continuous approximation of the placement field $\boldsymbol{\varphi}$ is generally not sufficient, but that a higher degree of continuity is required for the approximation of the field variables, cf. [47, 120, 154]. Although certain Hermitian finite elements which fulfil the continuity requirement in a strong sense are available in the literature, see e.g. [105] for a two- and [102] for a three-dimensional element formulation, there is still a lack of robust and efficient $\mathcal{C}^1$-continuous elements, [120]. Another novel approach to fulfil higher-order continuity requirements is the framework of isogeometric analysis which is presented in [58] and applied to gradient elasticity problems in, e.g., [46] and [110].

An alternative to the usage of $\mathcal{C}^1$-continuous element formulations offers the fulfilment of the continuity requirement in weak sense only, using a mixed-type finite element approach, [8, 132, 141]. To this end, an additional field variable is introduced and coupled to the deformation gradient, respectively the gradient of the spatial placement field. Examples of this procedure for the linear elastic strain gradient theory can be found in [120] for a two-dimensional or [155] for a three-dimensional setting. In these works, so-called relaxed displacement gradients are introduced as additional field variables and coupled with the displacement gradients using Lagrange multipliers. Hence, by following this procedure only first gradients of field variables occur in the weak formulation of the balance equations to be solved.

In this contribution we will follow a similar procedure to approximate the higher gradients of the spatial placement field which enter the balance equations via the constitutive equations for the stress and couple stress tensor. Being more specific, the additional field variable $\boldsymbol{\Theta}$ is introduced and coupled to the deformation gradient in the spirit of an L_2-projection, which results in the additional field equation

$$p\left[\boldsymbol{F} - \boldsymbol{\Theta}\right] = \boldsymbol{0} \quad , \tag{2.46}$$

with $p \neq 0$ being an arbitrary but constant parameter used for the scaling of the constraint. In line with [120], $\boldsymbol{\Theta}$ will further be referred to as the relaxed deformation gradient.

Since the relaxed deformation gradient is treated as an independent field variable and approximated by means of $\mathcal{C}^0$-continuous functions, the first derivative of $\boldsymbol{\Theta}$ with respect to the referential coordinates is still $\mathcal{C}^{-1}$-continuous. Accordingly, second gradients of the spatial placement field which are still $\mathcal{C}^{-1}$-continuous, can be approximated in terms of

$$\nabla_{\boldsymbol{X}}\left[\nabla_{\boldsymbol{X}}\boldsymbol{\varphi}\right] = \nabla_{\boldsymbol{X}}\boldsymbol{F} \approx \nabla_{\boldsymbol{X}}\boldsymbol{\Theta} = \boldsymbol{\Upsilon} \quad . \tag{2.47}$$

2.1.3.1 Field equations

For a quasi-static system subject to the assumption that no temperature effects occur and that body forces as well as body couples are negligible, the coupled system of partial differential equations takes the form

balance of linear momentum	$\nabla_{\boldsymbol{x}} \cdot \left[\boldsymbol{\sigma}^{\mathrm{sym}} + \boldsymbol{\sigma}^{\mathrm{skw}}\right]^{\mathrm{t}}$	$= \boldsymbol{0}$		(2.48a)
balance of angular momentum	$\nabla_{\boldsymbol{x}} \cdot \boldsymbol{m}^{\mathrm{t}} + \boldsymbol{\epsilon}_t : \boldsymbol{\sigma}^{\mathrm{skw}}$	$= \boldsymbol{0}$		(2.48b)
constraint	$p\left[\boldsymbol{F} - \boldsymbol{\Theta}\right]$	$= \boldsymbol{0}$		(2.48c)
boundary conditions	$\boldsymbol{\varphi}$	$= \bar{\boldsymbol{\varphi}}$	on $\partial\mathcal{B}_t^{\varphi}$	(2.48d)
	$\boldsymbol{\sigma}^{\mathrm{t}} \cdot \boldsymbol{n}$	$= \bar{\boldsymbol{t}}$	on $\partial\mathcal{B}_t^{\boldsymbol{t}}$	(2.48e)
	$\boldsymbol{m}^{\mathrm{t}} \cdot \boldsymbol{n}$	$= \bar{\boldsymbol{\tau}}$	on $\partial\mathcal{B}_t$	(2.48f)

with the symmetric part of the stress tensor and the couple stress tensor being defined by the constitutive relations (2.29) and (2.30). Moreover, the volumetric part of the couple stress tensor is assumed to remain undetermined, i.e. it is assumed that

$$\mathrm{tr}\,(\boldsymbol{m}) = 0 \quad \Leftrightarrow \quad \boldsymbol{m} = \boldsymbol{m}^{\mathrm{dev}} \quad . \tag{2.49}$$

The system of equations is subject to certain boundary conditions which are applied in terms of placements

$$\boldsymbol{\varphi} = \bar{\boldsymbol{\varphi}} \quad \text{on} \quad \partial \mathcal{B}_t^{\varphi} \tag{2.50}$$

and tractions

$$\boldsymbol{\sigma}^{\mathrm{t}} \cdot \boldsymbol{n} = \boldsymbol{t} = \bar{\boldsymbol{t}} \quad \text{on} \quad \partial \mathcal{B}_t^{\boldsymbol{t}} \quad , \tag{2.51}$$

with prescribed quantities being denoted by an overbar. We shall further assume homogeneous Neumann boundary conditions of the couple stresses,

$$\boldsymbol{m}^{\mathrm{t}} \cdot \boldsymbol{n} = \boldsymbol{\tau} = \bar{\boldsymbol{\tau}} = \boldsymbol{0} \quad \text{on} \quad \partial \mathcal{B}_t \quad . \tag{2.52}$$

For a more detailed discussion on appropriate representations of boundary conditions for the couple stress continuum theory the reader is referred to [94, 120, 132] and Remark 2.2, respectively Appendix A.4.

2.1.3.2 Weak form of field equations

In the context of the finite element method the partial differential equations are multiplied with test functions and integrated over the domain $\mathcal{B}_t$. For the balance equation of linear momentum (2.48a), using the test function $\boldsymbol{\eta}^{\varphi}$, this procedure along with the usage of the divergence theorem results in

$$0 = \int_{\mathcal{B}_t} \boldsymbol{\eta}^{\varphi} \cdot \left[\nabla_{\boldsymbol{x}} \cdot \boldsymbol{\sigma}^{\mathrm{t}} \right] \mathrm{d}v \tag{2.53a}$$

$$= - \int_{\mathcal{B}_0} \nabla_{\boldsymbol{X}} \boldsymbol{\eta}^{\varphi} : \left[\boldsymbol{\sigma}^{\mathrm{t}} \cdot \mathrm{cof}\,(\boldsymbol{F}) \right] \mathrm{d}V + \int_{\partial \mathcal{B}_t} \boldsymbol{\eta}^{\varphi} \cdot \boldsymbol{t}\, \mathrm{d}a \quad , \tag{2.53b}$$

wherein the first part in (2.53b) contributes to the internal force vector $\boldsymbol{f}_{\mathrm{int}}^{\varphi}$, whereas the second part is related to the external forces $\boldsymbol{f}_{\mathrm{ext}}^{\varphi}$. By applying the same procedure to the balance equation of angular momentum (2.48b), using a test function $\boldsymbol{\eta}^{\sigma}$, a weak form representation is given by

$$0 = \int_{\mathcal{B}_t} \boldsymbol{\eta}^{\sigma} \cdot \left[\nabla_{\boldsymbol{x}} \cdot \boldsymbol{m}^{\mathrm{t}} + \boldsymbol{\epsilon}_t : \boldsymbol{\sigma}^{\mathrm{skw}} \right] \mathrm{d}v \tag{2.54a}$$

$$= -\int_{\mathcal{B}_0} \nabla_{\boldsymbol{X}} \boldsymbol{\eta}^{\boldsymbol{\sigma}} : \left[\boldsymbol{m}^{\mathrm{t}} \cdot \mathrm{cof}\left(\boldsymbol{F} \right) \right] - \boldsymbol{\eta}^{\boldsymbol{\sigma}} \cdot \boldsymbol{\epsilon}_t : \boldsymbol{\sigma}^{\mathrm{skw}} \, J_{\boldsymbol{F}} \, \mathrm{d}V + \int_{\partial \mathcal{B}_t} \boldsymbol{\eta}^{\boldsymbol{\sigma}} \cdot \boldsymbol{\tau} \, \mathrm{d}a \quad . \tag{2.54b}$$

In (2.54b), the volume integrals contribute to the vector of internal forces $\boldsymbol{f}_{\mathrm{int}}^{\sigma}$, whereas the surface integral contributes to the external force vector $\boldsymbol{f}_{\mathrm{ext}}^{\sigma}$. Moreover, by using (2.52) we find that the vector of external forces $\boldsymbol{f}_{\mathrm{ext}}^{\sigma}$ is assumed to be identically zero. Finally, by multiplying the constraint (2.48c) with the test function $\boldsymbol{\eta}^{\boldsymbol{\Theta}}$ one arrives at

$$0 = \int_{\mathcal{B}_0} p \, \boldsymbol{\eta}^{\boldsymbol{\Theta}} : \left[\boldsymbol{F} - \boldsymbol{\Theta} \right] \, J_{\boldsymbol{F}} \, \mathrm{d}V \quad , \tag{2.55}$$

which can be interpreted as the L_2-projection of the deformation gradient field onto the $\boldsymbol{\Theta}$-field.

2.1.3.3 Discretisation of the weak form

The element-wise discretisation of the weak forms of the balance equations and of the constraint is performed by using Lagrange polynomials

$$\boldsymbol{\varphi}^{\mathrm{h}} = \sum_{A=1}^{\mathrm{n}_{\mathrm{en},\boldsymbol{\varphi}}} N_A^{\boldsymbol{\varphi}} \, \boldsymbol{\varphi}_A \qquad\qquad \boldsymbol{\eta}^{\boldsymbol{\varphi}\,\mathrm{h}} = \sum_{D=1}^{\mathrm{n}_{\mathrm{en},\boldsymbol{\varphi}}} N_D^{\boldsymbol{\varphi}} \, \boldsymbol{\eta}_D^{\boldsymbol{\varphi}} \tag{2.56}$$

$$\boldsymbol{\sigma}^{\mathrm{skw}\,\mathrm{h}} = \sum_{B=1}^{\mathrm{n}_{\mathrm{en},\boldsymbol{\sigma}}} N_B^{\boldsymbol{\sigma}} \, \boldsymbol{\sigma}_B^{\mathrm{skw}} \qquad\qquad \boldsymbol{\eta}^{\boldsymbol{\sigma}\,\mathrm{h}} = \sum_{E=1}^{\mathrm{n}_{\mathrm{en},\boldsymbol{\sigma}}} N_E^{\boldsymbol{\sigma}} \, \boldsymbol{\eta}_E^{\boldsymbol{\sigma}} \tag{2.57}$$

$$\boldsymbol{\Theta}^{\mathrm{h}} = \sum_{C=1}^{\mathrm{n}_{\mathrm{en},\boldsymbol{\Theta}}} N_C^{\boldsymbol{\Theta}} \, \boldsymbol{\Theta}_C \qquad\qquad \boldsymbol{\eta}^{\boldsymbol{\Theta}\,\mathrm{h}} = \sum_{F=1}^{\mathrm{n}_{\mathrm{en},\boldsymbol{\Theta}}} N_F^{\boldsymbol{\Theta}} \, \boldsymbol{\eta}_F^{\boldsymbol{\Theta}} \tag{2.58}$$

and by allowing for a different polynomial order for each field. Shape functions used for the approximation of the field quantities and of the test functions are denoted by $N^{\bullet}$ with the superscript referring to the corresponding field, and with $\mathrm{n}_{\mathrm{en}\bullet}$ denoting the number of element nodes used for the approximation of the respective field. Furthermore, an isoparametric approximation in the sense that identical shape functions are used for the discretisation of the geometry and for the discretisation of the spatial placement field, is used.

With the assembly operator $\mathbf{A}$ and the total number of elements being denoted by n_{el}, the discrete vector of internal forces of the balance equation of linear momentum is given by

$$\boldsymbol{f}_{\mathrm{int}}^{\boldsymbol{\varphi}\mathrm{h}} = \mathop{\mathbf{A}}_{e=1}^{\mathrm{n}_{\mathrm{el}}} \int_{\mathcal{B}_0^e} \left[\boldsymbol{\sigma}^{\mathrm{sym}} + \boldsymbol{\sigma}^{\mathrm{skw}} \right]^{\mathrm{t}} \cdot \mathrm{cof}\left(\boldsymbol{F} \right) \cdot \nabla_{\boldsymbol{X}} N_A^{\boldsymbol{\varphi}} \, \mathrm{d}V_e \tag{2.59}$$

while the discrete version of (2.54b) reads

$$
\boldsymbol{f}_{\text{int}}^{\boldsymbol{\sigma}\text{h}} = \mathop{\mathbf{A}}_{e=1}^{n_{\text{el}}} \int_{\mathcal{B}_0^e} \boldsymbol{m}^{\text{t}} \cdot \text{cof}\,(\boldsymbol{F}) \cdot \nabla_{\boldsymbol{X}} N_B^{\boldsymbol{\sigma}} - \boldsymbol{\epsilon}_t : \boldsymbol{\sigma}^{\text{skw}}\, J_{\boldsymbol{F}}\, N_B^{\boldsymbol{\sigma}}\, \mathrm{d}V_e
\tag{2.60}
$$

and (2.55) results in

$$
\boldsymbol{f}_{\text{int}}^{\boldsymbol{\Theta}\text{h}} = \mathop{\mathbf{A}}_{e=1}^{n_{\text{el}}} \int_{\mathcal{B}_0^e} p\,[\boldsymbol{F} - \boldsymbol{\Theta}]\, J_{\boldsymbol{F}}\, N_C^{\boldsymbol{\Theta}}\, \mathrm{d}V_e \quad .
\tag{2.61}
$$

2.1.3.4 Linearisation

The solution of the discrete system of equations is performed in an iterative manner with the residuum

$$
\boldsymbol{r}^{\bullet\,\text{h}} = \boldsymbol{f}_{\text{int}}^{\bullet\,\text{h}} - \boldsymbol{f}_{\text{ext}}^{\bullet\,\text{h}}
\tag{2.62}
$$

and its linearisation at some iteration step q,

$$
\boldsymbol{r}_{q+1}^{\bullet\,\text{h}} = \boldsymbol{r}_{q}^{\bullet\,\text{h}} + \Delta \boldsymbol{r}^{\bullet\,\text{h}} \quad .
\tag{2.63}
$$

The linear part of the residuum can further be specified as

$$
\Delta \boldsymbol{r}^{\bullet\,h} = \frac{\mathrm{d}\boldsymbol{r}^{\bullet\,\text{h}}}{\mathrm{d}\widehat{\boldsymbol{\varphi}}} \cdot \Delta\widehat{\boldsymbol{\varphi}} + \frac{\mathrm{d}\boldsymbol{r}^{\bullet\,\text{h}}}{\mathrm{d}\widehat{\boldsymbol{\sigma}}^{\,\text{skw}}} \cdot \Delta\widehat{\boldsymbol{\sigma}}^{\,\text{skw}} + \frac{\mathrm{d}\boldsymbol{r}^{\bullet\,\text{h}}}{\mathrm{d}\widehat{\boldsymbol{\Theta}}} \cdot \Delta\widehat{\boldsymbol{\Theta}} \quad ,
\tag{2.64}
$$

such that the overall global system to be solved for the increments of the field variables takes the form

$$
\begin{bmatrix} \mathbf{K}^{\varphi\varphi} & \mathbf{K}^{\varphi\sigma} & \mathbf{K}^{\varphi\Theta} \\ \mathbf{K}^{\sigma\varphi} & \mathbf{K}^{\sigma\sigma} & \mathbf{K}^{\sigma\Theta} \\ \mathbf{K}^{\Theta\varphi} & \mathbf{K}^{\Theta\sigma} & \mathbf{K}^{\Theta\Theta} \end{bmatrix}_q \cdot \begin{bmatrix} \Delta\widehat{\boldsymbol{\varphi}} \\ \Delta\widehat{\boldsymbol{\sigma}}^{\,\text{skw}} \\ \Delta\widehat{\boldsymbol{\Theta}} \end{bmatrix}_q = - \begin{bmatrix} \boldsymbol{r}^{\varphi\,\text{h}} \\ \boldsymbol{r}^{\sigma\,\text{h}} \\ \boldsymbol{r}^{\Theta\,\text{h}} \end{bmatrix}_q \quad ,
\tag{2.65}
$$

with $\widehat{\boldsymbol{\varphi}}$, $\widehat{\boldsymbol{\sigma}}^{\,\text{skw}}$ and $\widehat{\boldsymbol{\Theta}}$ denoting the global lists of degrees of freedom. The various contributions to the overall stiffness matrix are summarised in Appendix A.1. Note, that the evaluation of (2.124)–(2.132) requires the calculation of the sensitivities of the stress tensor (2.29) and of the couple stress tensor (2.30) with respect to the field variables, which are given in Appendix A.2 in their most general form. With these derivatives at hand, the global stiffness matrix can be set based on the specification of the energy function (2.35) together with the first and second derivatives of the energy function with respect to $\boldsymbol{C}$ and $\boldsymbol{\Lambda}$. To facilitate the derivation of the latter, the derivatives of the invariants with respect to $\boldsymbol{C}$ and $\boldsymbol{\Lambda}$ are provided in Appendix A.3.

Remark 2.2 (Boundary conditions) *In [94] it is shown that an alternative represen-*
tation of the boundary conditions, (2.48e) and (2.48f), of the couple stress theory is
possible. In this alternative form, it turns out that the normal component of the cou-
ple stress vector $\boldsymbol{\tau}$ enters the surface integrals only in combination with the force stress
vector $\boldsymbol{t}$, cf. [94], reducing the number of effectively applied boundary conditions by one.
This derivation of the alternative form of the boundary conditions relies on the relation
between the velocity and the spin vector.

Different from the weak form representation discussed in Section 2.1.3.2 an alternative
form is derived in Appendix A.4, which makes use of the relation $\boldsymbol{\eta}^{\boldsymbol{\sigma}} = \frac{1}{2}\operatorname{curl}^{\mathrm{t}}(\boldsymbol{\eta}^{\boldsymbol{\varphi}})$.
This alternative representation of the balance relations and boundary conditions results,
in accordance with [94], in

$$
\begin{aligned}
0 = &- \int_{\mathcal{B}_t} \nabla_{\boldsymbol{x}}\boldsymbol{\eta}^{\boldsymbol{\varphi}} : \boldsymbol{\sigma}^{\mathrm{sym}} + \nabla_{\boldsymbol{x}}\boldsymbol{\eta}^{\boldsymbol{\varphi}} : \left[\boldsymbol{\sigma}^{\mathrm{skw}}\right]^{\mathrm{t}} \, \mathrm{d}v + \int_{\partial\mathcal{B}_t} \left[\boldsymbol{n} \cdot \boldsymbol{\sigma} - \frac{1}{2}\,\boldsymbol{n} \times \nabla_{\boldsymbol{x}} m_{\mathrm{nn}}\right] \cdot \boldsymbol{\eta}^{\boldsymbol{\varphi}} \, \mathrm{d}a \\
&- \int_{\mathcal{B}_t} \nabla_{\boldsymbol{x}}\boldsymbol{\eta}^{\boldsymbol{\sigma}} : \boldsymbol{m}^{\mathrm{t}} \;\; - \boldsymbol{\eta}^{\boldsymbol{\sigma}} \cdot \boldsymbol{\epsilon}_t : \boldsymbol{\sigma}^{\mathrm{skw}} \quad \mathrm{d}v + \int_{\partial\mathcal{B}_t} \boldsymbol{n} \cdot \boldsymbol{m} \cdot \left[\boldsymbol{I} - \boldsymbol{n} \otimes \boldsymbol{n}\right] \cdot \boldsymbol{\eta}^{\boldsymbol{\sigma}} \qquad \mathrm{d}a \quad .
\end{aligned}
\tag{2.66}
$$

Note, that in contrast to the approach presented in Appendix A.4, the balance equations
will be regarded as separate equations in this contribution with no relation between the
test functions being assumed.

2.1.4 Summary

Based on the fundamental theory for the modelling of fibre-reinforced composites with
fibres possessing non-negligible bending stiffness presented in [130], the solution of the
resulting system of partial differential equations by means of a mixed- and multi-field
finite element approach was presented. To this end, a relaxed deformation gradient field
was introduced as an additional field variable and coupled to the deformation gradient
by means of an L_2-projection. Thus, higher gradients of the placement function could
be approximated without using a truly $\mathcal{C}^1$-continuous element formulation but rather by
fulfilling the necessary continuity requirement only in a weak sense. Taking into account
the proposed formulation, a weak form of the balance equations and of the constraint
was derived and the corresponding discrete contributions to the global force and tangent
stiffness matrix were provided.

2.2 Comparison with analytical solutions and study of basic model properties

The scope of this section is threefold: firstly, a specific form of the energy function is proposed in Section 2.2.1 and shown to be consistent with the small strain version of the theory employed in [30] to derive an analytical solution. Secondly, a comparison of the numerical solution by means of the multi-field finite element approach with the analytical solution for the azimuthal shear deformation of a tube-like structure is carried out in Section 2.2.2 in order to validate the proposed formulation. Thirdly, the fundamental model properties for the specific form of the stored energy function chosen are studied further and boundary value problems in a three-dimensional setting are analysed in Section 2.2.3.

2.2.1 Specification of the constitutive model

In this section a specific form of the energy function is proposed and the specific constitutive equations for the symmetric part of the stress and the couple stress tensor are presented. It is then shown that this form of the energy function is consistent with the small strain version of the theory employed in [30] to derive an analytical solution for the azimuthal shear deformation of a tube-like structure which serves as the basis for the comparison of the proposed finite element formulation with analytical solutions in Section 2.2.2.

2.2.1.1 A specific form of the energy function

Before the gradient-enhanced modelling approach for fibre-reinforced composites can be applied to the simulation of boundary value problems, the energy function (2.35) needs to be specified. In particular, we propose an additive split of the energy function according to

$$W\left(I_i\right) = W^{\text{iso}}\left(I_1, \ldots, I_3\right) + W^{\lambda_{\text{A}}}\left(I_1, \ldots, I_5\right) + W^{\kappa_0}\left(I_1, \ldots, I_{11}\right), \, i \in \{1, \ldots, 11\} \, , \tag{2.67}$$

with the different contributions being motivated from a physical point of view. The first contribution in (2.67) reflects the isotropic part of the material response which is defined by the properties of the matrix material without considering the influence of the fibres. Hence, it is assumed to be a function of the deformation only, such that solely the first three invariants or combinations thereof are taken into account.

On the contrary, both the second and the third part are related to the action of the fibres. To be more specific, $W^{\lambda_{\text{A}}}$ is associated with transversely-isotropic properties induced by a single family of fibres. This energy contribution is based on the classic structural tensor approach and is well-discussed in the literature, e.g. [20, 129, 153]. In

particular, a detailed analysis of the mathematical properties of W^{λ_A} has recently been presented in [116, 117, 131], where different combinations of the first five invariants have been analysed and their physical interpretations given. The last summand in (2.67), W^{κ_0}, induces a different kind of anisotropy which is due to the assumption that the fibres exhibit a certain resistance to bending. This property essentially manifests the enhanced character of the presented modelling approach. In addition to the deformation measure and the fibre direction field which characterises the preferred material direction, $W^{\kappa_0}(I_1, \ldots, I_{11})$ therefore additionally takes into account invariants which are based on the gradient of the spatial fibre orientation vector. Since higher gradients of the deformation map enter the energy function via the invariants $I_6 - I_{11}$, cf. (2.36), it is further evident that, by employing the energy contribution W^{κ_0}, a natural length scale is introduced into the model. Accordingly the modelling of size effects becomes possible.

As the modelling of the fibre-bending stiffness is the main subject of this section, and since the anisotropic part W^{λ_A} is still extensively being discussed in the literature,

$$W^{\lambda_A} = \text{const} \tag{2.68}$$

shall be assumed. Thus, the only fibre contributions considered within the subsequent analysis are included in the energy contribution W^{κ_0}. In view of model calibration based on experimental findings, the contribution $W^{\lambda_A} \neq \text{const}$ can generally not be neglected and will be accounted for in an enhanced model to be discussed in Section 2.3.

For the isotropic part of the energy function a simple Neo-Hookean-type ansatz is adopted,

$$W^{\text{iso}} = W^{\text{neo}}(I_1, I_3) = \lambda \frac{I_3 - 1}{4} - \left[\frac{\lambda}{2} + \mu\right] \ln\left(\sqrt{I_3}\right) + \frac{\mu}{2}[I_1 - 3] \quad , \tag{2.69}$$

including the two material parameters λ and μ. What remains is the specification of the higher-order energy part W^{κ_0}. Focusing on invariant I_6 we notice that

$$I_6 = \boldsymbol{\kappa}_0 \cdot \boldsymbol{\kappa}_0 = \left[\boldsymbol{F}^{\text{t}} \cdot \boldsymbol{\kappa}\right] \cdot \left[\boldsymbol{F}^{\text{t}} \cdot \boldsymbol{\kappa}\right] = \boldsymbol{\kappa} \cdot \boldsymbol{b} \cdot \boldsymbol{\kappa} \tag{2.70}$$

represents a quadratic measure which includes the fibre curvature, with $\boldsymbol{b} = \boldsymbol{F} \cdot \boldsymbol{F}^{\text{t}}$ the left Cauchy-Green tensor. In accordance with [31] and [125], a possible ansatz for W^{κ_0} which accounts for the fibre-bending contributions is therefore given by

$$W^{\kappa_0}(I_6) = c\, I_6, \quad c \in \mathbb{R}^+ \quad . \tag{2.71}$$

Since the material parameter c introduced in (2.71) directly weights the higher-order energy contribution associated with the fibres, it can further be interpreted as a kind of fibre-bending stiffness.

In the case that the undeformed fibres are not oriented straight one obtains

$$\boldsymbol{\kappa}_0 = \boldsymbol{F}^{\mathrm{t}} \cdot \left[\boldsymbol{a}_0 \cdot \nabla_{\boldsymbol{X}} \left[\nabla_{\boldsymbol{X}} \boldsymbol{\varphi} \right]^{\mathrm{t}} + \boldsymbol{F} \cdot \nabla_{\boldsymbol{X}} \boldsymbol{a}_0 \right] \cdot \boldsymbol{a}_0 \neq \boldsymbol{0} \quad \text{for} \quad \boldsymbol{F} = \boldsymbol{I} \tag{2.72}$$

so that neither the related energy

$$W_{t_0}^{\boldsymbol{\kappa}_0} \left(I_6 \right) = c \, I_6 = c \left[\boldsymbol{\Lambda} \cdot \boldsymbol{a}_0 \right] \cdot \left[\boldsymbol{\Lambda} \cdot \boldsymbol{a}_0 \right] \neq 0 \tag{2.73}$$

nor the related stress contributions vanish identically. The underlying physical assumption would be that the fibres are straight in their reference configuration, i.e. after the fibre production process, and that any deviation from this state within the composite the fibres are embedded into requires the supply of energy. Further simple forms of the stored energy function which rely on a different physical interpretation have been discussed in [10] and are briefly recapitulated in Appendix A.5.

Within the scope of this contribution, we will focus on fibres the reference configurations of which are straight so that $\nabla_{\boldsymbol{X}} \boldsymbol{a}_0 \cdot \boldsymbol{a}_0 = \boldsymbol{0}$. Thus taking into account (2.69) and (2.71), the energy function is assumed to take the form

$$W \left(I_1, \, I_3, \, I_6; \, \lambda, \, \mu, \, c \right) = \lambda \, \frac{I_3 - 1}{4} - \left[\frac{\lambda}{2} + \mu \right] \ln \left(\sqrt{I_3} \right) + \frac{\mu}{2} \left[I_1 - 3 \right] + c \, I_6 \quad . \tag{2.74}$$

It is further noted that the structure of the energy function (2.74) is comparable to the one proposed in [31] for the modelling of incompressible fibre-reinforced tube-like structures when accounting for finite deformations. Essentially note that such an energy function is consistent with the strain energy function met when assuming small deformations, cf. [31] and Section 2.2.1.3. This is an important observation which allows us to compare the analytical results presented in [30], subject to the assumption of small deformations, with the ones calculated by means of the finite element approach analysed in this contribution, which accounts for finite deformations.

2.2.1.2 Specification of the stress and couple stress tensor

Based on the specific form of the energy function (2.74) the (symmetric part of the) stress tensor and the (deviatoric part of the) couple stress tensor can be specified.

According to (2.29) and with the use of Table 2.5 the specific form of the (symmetric part of the) stress tensor reads

$$\begin{aligned}
\boldsymbol{\sigma}^{\mathrm{sym}} = {}& J_{\boldsymbol{F}}^{-1} \boldsymbol{F} \cdot \left[\frac{\lambda}{2} \left[I_3 - 1 \right] \boldsymbol{C}^{-1} + \mu \left[\boldsymbol{I} - \boldsymbol{C}^{-1} \right] \right] \cdot \boldsymbol{F}^{\mathrm{t}} \\
& + 2 \, c \, J_{\boldsymbol{F}}^{-1} \left[\boldsymbol{G} \cdot \left[\boldsymbol{a}_0 \otimes \boldsymbol{\Lambda} \cdot \boldsymbol{a}_0 \right] \cdot \boldsymbol{F}^{\mathrm{t}} + \boldsymbol{F} \cdot \left[\boldsymbol{\Lambda} \cdot \boldsymbol{a}_0 \otimes \boldsymbol{a}_0 \right] \cdot \boldsymbol{G}^{\mathrm{t}} \right] \quad .
\end{aligned} \tag{2.75}$$

The first part of (2.75) represents the isotropic Neo-Hookean part, whereas the second part results from the assumption that the fibres exhibit significant resistance against bending. Further specifying the latter we find

$$
\left[\boldsymbol{G} \cdot [\boldsymbol{a}_0 \otimes \boldsymbol{\Lambda} \cdot \boldsymbol{a}_0] \cdot \boldsymbol{F}^{\mathrm{t}} + \boldsymbol{F} \cdot [\boldsymbol{\Lambda} \cdot \boldsymbol{a}_0 \otimes \boldsymbol{a}_0] \cdot \boldsymbol{G}^{\mathrm{t}} \right] \tag{2.76a}
$$

$$
= [\boldsymbol{G} \cdot \boldsymbol{a}_0] \otimes [\boldsymbol{F} \cdot \boldsymbol{\Lambda} \cdot \boldsymbol{a}_0] + [\boldsymbol{F} \cdot \boldsymbol{\Lambda} \cdot \boldsymbol{a}_0] \otimes [\boldsymbol{G} \cdot \boldsymbol{a}_0] \tag{2.76b}
$$

$$
= \boldsymbol{\kappa} \otimes \boldsymbol{b} \cdot \boldsymbol{\kappa} + \boldsymbol{\kappa} \cdot \boldsymbol{b} \otimes \boldsymbol{\kappa} \tag{2.76c}
$$

$$
= \boldsymbol{F}^{-\mathrm{t}} \cdot \boldsymbol{\kappa}_0 \otimes \boldsymbol{\kappa}_0 \cdot \boldsymbol{F}^{\mathrm{t}} + \boldsymbol{F} \cdot \boldsymbol{\kappa}_0 \otimes \boldsymbol{\kappa}_0 \cdot \boldsymbol{F}^{-1} \quad . \tag{2.76d}
$$

It is apparent that this part is based on $\boldsymbol{\kappa}$, respectively $\boldsymbol{\kappa}_0$, so that gradients in the fibre deformation field result into a stress response. In particular we find that the symmetric part of the stress tensor is influenced by the first gradient of the deformation map, e.g. in terms of $\boldsymbol{F}$ and $\boldsymbol{C}$, and by the projection of the second gradient of the deformation map onto the direction of the fibres, e.g. in terms of $\boldsymbol{\kappa}$ and $\boldsymbol{\kappa}_0$.

Furthermore, by applying the constitutive relation (2.30) and by using Table 2.5, the specific form of the couple stress tensor is given by

$$
\left[\boldsymbol{m}^{\mathrm{dev}} \right]^{\mathrm{t}} = -\frac{4}{3} \, J_{\boldsymbol{F}}^{-1} \, \boldsymbol{\epsilon}_t \, : \, \left[\boldsymbol{F} \cdot c \, [\boldsymbol{\Lambda} \cdot \boldsymbol{a}_0 \otimes \boldsymbol{a}_0] \cdot \left[\boldsymbol{F}^{\mathrm{t}} \, \overline{\otimes} \, \boldsymbol{a}_t + \boldsymbol{F}^{\mathrm{t}} \otimes \boldsymbol{a}_t \right] \right] \tag{2.77a}
$$

$$
= \quad \frac{8}{3} \, c \, J_{\boldsymbol{F}}^{-1} \, \boldsymbol{\epsilon}_t \, : \, [\boldsymbol{F} \cdot \boldsymbol{a}_0 \otimes \boldsymbol{F} \cdot \boldsymbol{\kappa}_0 \otimes \boldsymbol{F} \cdot \boldsymbol{a}_0] \tag{2.77b}
$$

$$
= \quad \frac{8}{3} \, c \, J_{\boldsymbol{F}}^{-1} \, \boldsymbol{\epsilon}_t \, : \, [\boldsymbol{a}_t \otimes \boldsymbol{b} \cdot \boldsymbol{\kappa} \otimes \boldsymbol{a}_t] \quad . \tag{2.77c}
$$

Regarding (2.77) it is revealed that the couple stress tensor is influenced by the first gradient of the deformation map via its dependence on $\boldsymbol{F}$, respectively on $\boldsymbol{b}$, and the second gradient of the deformation which enters (2.77) via $\boldsymbol{\kappa}_0$, respectively $\boldsymbol{\kappa}$. Based on this observation it is concluded that the skew symmetric part of the stress tensor, in general, is also influenced by both the first and second gradient of the deformation field, since $\boldsymbol{\sigma}^{\mathrm{skw}}$ is directly linked to the divergence of $\boldsymbol{m}$ via (2.48b).

2.2.1.3 Consistency of the linearised and the finite strain theory

The modelling approach for fibre-reinforced composites with fibres possessing fibre-bending stiffness is presented in [130] for a finite strain setting, and a corresponding small strain theory is deduced. To derive an analytical solution for the azimuthal shear deformation of a fibre-reinforced tube-like structure, the small strain version of the theory is employed in [30]. Nevertheless, a comparison with the results calculated by means of the corresponding finite strain theory by using the finite element-based solution procedure proposed in Section 2.1 is generally meaningful due to the consistency of the two modelling approaches, which will be outlined in this section.

To start with, the model proposed in [30] assumes in accordance with [130] the symmetric part of the linearised stress tensor $\boldsymbol{\Sigma}^{\mathrm{sym}}$, expressed in polar coordinates (with r, φ and z indicating the radial, azimuthal and height direction) and represented in Voigt notation, to take the form

$$
\begin{bmatrix} \Sigma_{rr}^{\mathrm{sym}} \\ \Sigma_{\varphi\varphi}^{\mathrm{sym}} \\ \Sigma_{r\varphi}^{\mathrm{sym}} \end{bmatrix} = \begin{bmatrix} \mathsf{E}_{rrrr} & \mathsf{E}_{rr\varphi\varphi} & 0 \\ \mathsf{E}_{\varphi\varphi rr} & \mathsf{E}_{\varphi\varphi\varphi\varphi} & 0 \\ 0 & 0 & \mathsf{E}_{r\varphi r\varphi} \end{bmatrix} \cdot \begin{bmatrix} \varepsilon_{rr} \\ \varepsilon_{\varphi\varphi} \\ 2\,\varepsilon_{r\varphi} \end{bmatrix} \quad , \tag{2.78}
$$

with the linearised strain tensor $\boldsymbol{\varepsilon} = [\boldsymbol{F} - \boldsymbol{I}]^{\mathrm{sym}}$ and material constants $\mathsf{E}_\bullet$ with $\mathsf{E}_{rr\varphi\varphi} = \mathsf{E}_{\varphi\varphi rr}$. Furthermore, the constitutive relation for the only non-vanishing coefficient of the (deviatoric part of the) linearised couple stress tensor $\boldsymbol{\upsilon}$, which features the additional material parameter d^f, is given by

$$
\upsilon_{rz} = d^f \frac{\partial^2 u_\varphi}{\partial r^2} \tag{2.79}
$$

and implicitly defines the skew symmetric part of the couple stress tensor via the balance equation of angular momentum, cf. [30, 31], to be specific,

$$
\Sigma_{\varphi r}^{\mathrm{skw}} = -\,\Sigma_{r\varphi}^{\mathrm{skw}} = \frac{1}{2}\,d^f \left[\frac{\partial^3 u_\varphi}{\partial r^3} + \frac{1}{r}\frac{\partial^2 u_\varphi}{\partial r^2} \right] \quad . \tag{2.80}
$$

In view of the energy function (2.74), however, the symmetric part of the (finite deformation) Cauchy stress tensor takes the form (2.75). The second summand, which results from the derivative $\partial W/\partial \boldsymbol{\Lambda}$, induces higher-order terms in the partial derivatives of $\boldsymbol{\varphi}$ so that these contributions are neglected in the linearised theory, cf. [31] and [130]. With this consideration, the linearisation of (2.75) yields

$$
\boldsymbol{\sigma}^{\mathrm{sym,lin}} = 2\,\mu\,\boldsymbol{\varepsilon} + \lambda\,\mathrm{tr}\,(\boldsymbol{\varepsilon})\,\boldsymbol{I} \tag{2.81}
$$

which can be represented in Voigt notation according to

$$
\begin{bmatrix} \sigma_{rr}^{\mathrm{sym,lin}} \\ \sigma_{\varphi\varphi}^{\mathrm{sym,lin}} \\ \sigma_{r\varphi}^{\mathrm{sym,lin}} \end{bmatrix} = \begin{bmatrix} 2\,\mu + \lambda & \lambda & 0 \\ \lambda & 2\,\mu + \lambda & 0 \\ 0 & 0 & \mu \end{bmatrix} \cdot \begin{bmatrix} \varepsilon_{rr} \\ \varepsilon_{\varphi\varphi} \\ 2\,\varepsilon_{r\varphi} \end{bmatrix} \quad . \tag{2.82}
$$

As mentioned in Section 2.2.1.1, the finite strain model does not account for an energy contribution W^{λ_A} such that a material described with the help of (2.82) is isotropic in contrast to the transverse isotropic material model implied in (2.78). However, since the material parameters E_{rrrr}, $\mathsf{E}_{\varphi\varphi\varphi\varphi}$, $\mathsf{E}_{rr\varphi\varphi}$ and $\mathsf{E}_{\varphi\varphi rr}$ do not enter the differential equation for the azimuthal displacement, they are not relevant for the comparison to be carried out in this contribution, see also [30].

Further analysing the couple stress tensor, respectively the skew-symmetric part of the stress tensor, the consistency of a bending energy contribution of the form (2.71) with the definition of the couple stress tensor (2.79) is shown in [31] for a pure azimuthal shear deformation with the relation

$$c = \frac{3}{8}\, d^f \tag{2.83}$$

between the two material parameters. For the boundary value problem to be studied in Section 2.2.2, we observe a maximal change of the outer radius of less than -0.65% for all values of the fibre-bending stiffness parameter and loading states analysed. In consequence, the condition of pure azimuthal shear is approximately met, cf. Section 2.2.2.2, Figure 2.4(a). It is further pointed out in [31], that the summand $d^f\,[2r]^{-1}\,\partial^2 u_\varphi/\partial r^2$ presented in (2.80) is missing in the derivation of the skew-symmetric part of the stress tensor in [30]. Nevertheless, the results presented in [30] are considered to be very accurate and are used for the sake of comparison in [31].

2.2.2 Comparison of finite element simulations with analytical solutions

An azimuthal shear deformation of a cylindrical tube under plane strain conditions is analysed in detail in [30], whereby the composites considered are assumed to be reinforced either with perfectly flexible fibres or with fibres exhibiting bending stiffness. For the special case of straight fibres which are oriented along the radial direction of the tube in the reference configuration, it is shown that the coupled system of differential equations for the displacement in radial and azimuthal direction becomes uncoupled, [30]. This result is achieved regardless of the constraints with respect to the extensibility of the fibres and the compressibility of the matrix material. Interestingly, the resulting differential equation for the azimuthal displacement is identical for each of the latter cases if the fibres are assumed to be perfectly flexible. This means that, in the case of a radial fibre orientation, the differential equation which is to be solved for the azimuthal displacement is not influenced by the fibres which does not meet physical expectations. In contrast, it is shown that by dropping the assumption of perfectly flexible fibres, i.e. by accounting for the fibre-bending stiffness, the differential equation for the displacement in azimuthal direction is influenced by the fibres, cf. [30]. However, the system of differential equations for the displacement in radial and azimuthal direction remains uncoupled.

Focusing on the azimuthal shear deformation, the resulting differential equation can be rewritten in a non-dimensional form and subsequently solved analytically by means of a power series method or numerically by using the successive step approximation method (SAM), cf. [123], with both schemes leading to the same results, [30]. With the aforementioned solution procedures for the azimuthal displacement at hand, the

deformation of the cylindrical tube is analysed in [30], subject to two different sets of boundary conditions:

1. The displacement in azimuthal direction u_φ is fixed at the inner radius and prescribed at the outer radius. Furthermore, the fibres are assumed to be clamped at the inner radius and are free to rotate at the outer radius, such that $m_{rz} = 0$ at the outer radius holds.

2. The displacement in azimuthal direction u_φ is fixed at the inner radius and prescribed at the outer radius. However, the fibres are assumed to be free to rotate at the inner and outer radius, such that $m_{rz} = 0$ at both the inner and the outer radius holds.

In the following, we will focus on the second set of boundary conditions and compare results obtained based on the finite element solution scheme proposed in Section 2.1 with analytical results presented in [30]. Note that the applied finite element formulation accounts for finite deformations in contrast to the linearised version which is employed in [30]. However, due to the consistency of the underlying energy functions, see Section 2.2.1.3 and [31], the comparison is generally meaningful.

2.2.2.1 Specification of the boundary value problem

The comparison to the analytical solutions provided in [30] will be made on the basis of the finite element model of the cylindrical tube sketched in Figure 2.2. Note that the investigations presented in [30] are based on dimensionless quantities. The respective formulas used in [30] to convert the dimensional into dimensionless quantities are outlined in Appendix A.6, and may be taken into account to obtain a first idea of the quantitative agreement of the simulation results with the analytical solution.

To start with, let the inner radius of the tube take a value $B_0 = 40$ and let the outer radius be $B_1 = 100$ such that the same ratio $\beta = B_1/B_0 = 2.5$ as in [30] is used in the upcoming analysis. In accordance with the second set of boundary conditions, as introduced above, the fibre slope at the boundary is not prescribed and $m_{rz} = 0$ is assumed to hold at the inner and outer radius. Moreover, the displacement in azimuthal direction at the inner boundary will be fixed, and the load shall be prescribed at the outer radius in terms of follower forces $\boldsymbol{t}_{\mathrm{tang}}$, see e.g. [118] and [145], which act in tangential direction. Thus, the finite element-based simulation results presented in this contribution are based on force-controlled simulations in contrast to the findings presented in [30] where the displacement at the outer boundary is prescribed. Since the load is prescribed, the (azimuthal-) displacement at the boundary depends on the values of the fibre(-bending) stiffness parameter. Nevertheless, this effect turns out to be small which becomes evident when considering the shear stress coefficient of the analytical solution provided in Figure 2.6(a), which clearly indicates that the difference in the shear stress distribution at the outer boundary obtained for different values of the fibre(-bending)
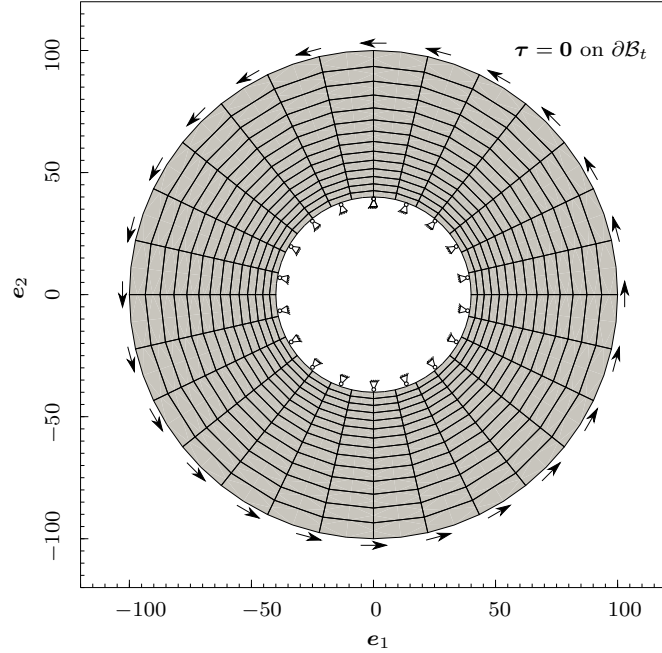
Figure 2.2: Discretised cross section of the cylindrical tube under investigation with the inner radius subject to homogeneous Dirichlet boundary conditions, while Neumann boundary conditions are applied at the outer radius. Moreover, m_{rz} is assumed to be zero at the inner and outer radius, which represents a simple support without restrictions on the fibre slope imposed at the boundaries.

stiffness and for prescribed displacements is negligible. Note that we will focus on the load state $\|\boldsymbol{t}_{\text{tang}}\|/\|\boldsymbol{t}_{\text{tang}}^{\max}\| = 0.1$ as this work proceeds, with $\|\boldsymbol{t}_{\text{tang}}^{\max}\| = 6000$ denoting the maximal applied traction load to be analysed. However, the qualitative results for the stress and couple stress tensor turn out to be quasi-independent of the load level which is shown in Appendix A.7, where the simulation results for the loads $\|\boldsymbol{t}_{\text{tang}}\|/\|\boldsymbol{t}_{\text{tang}}^{\max}\| = 0.5$ and $\|\boldsymbol{t}_{\text{tang}}\|/\|\boldsymbol{t}_{\text{tang}}^{\max}\| = 1.0$ are additionally provided. Since the general coupled system of partial differential equations is solved using the finite element solution scheme presented in Section 2.1.3, boundary conditions for the radial direction also need to be prescribed. To this end, homogeneous Dirichlet boundary conditions for the radial direction are assumed at the inner radius, while homogeneous Neumann boundary conditions in radial direction are applied at the outer radius.

The material parameters which characterise the isotropic part of the elastic energy function are assumed to take the values $\lambda = 1.037 \times 10^5$ and $\mu = 4.4444 \times 10^4$. Moreover, the fibre(-bending) stiffness c will be varied within the interval $c \in [0.0, \ 2.5 \times 10^8]$ in the upcoming analysis, where use was made of (2.163) and (2.165) to approximate the material parameter c based on its dimensionless counterpart d^{f*} which is used in [30], see also Table 2.1 and Table 2.2.

From a numerical point of view, bi-quadratic serendipity-type shape functions are used for the approximation of the $\boldsymbol{\varphi}$-field, while both the skew-symmetric stress field
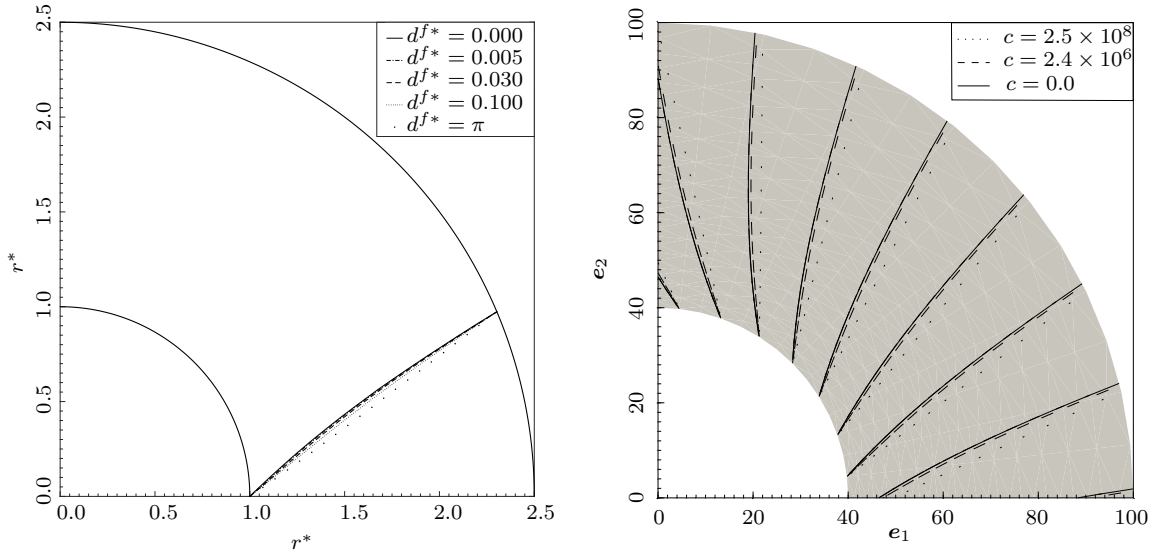
(a) Analytical solution based on the small strain theory, reproduced from [30].

(b) Finite element solution based on the finite strain theory for the applied load of $\|\boldsymbol{t}_{\text{tang}}\|/\|\boldsymbol{t}_{\text{tang}}^{\max}\| = 1.0$.

Figure 2.3: General deformation pattern of a tube-like structure subject to the assumption of a plane strain deformation state for different values of the fibre(-bending) stiffness.

$\boldsymbol{\sigma}^{\text{skw}}$ as well as the relaxed deformation gradient field $\boldsymbol{\Theta}$ are approximated by means of bi-linear Lagrangian shape functions. Being more specific, the tube is discretised by means of 14 elements in radial- and 28 elements in azimuthal direction, as depicted in Figure 2.2. Occurring integrals are evaluated in a standard manner using a Gaussian quadrature scheme which employs nine sampling points.

2.2.2.2 Deformation pattern and fibre slope

In a first step, we will study the general deformation pattern which is predicted by the analytical solution of the linearised theory presented in [30] and the one simulated with the finite element scheme proposed in Section 2.1 for a general finite strain setting. We are especially interested in the qualitative response in dependence of the fibre(-bending) stiffness which is given in terms of the dimensionless material parameter d^{f*} for the analytical, respectively the material parameter c for the finite element-based solution scheme.

In order to assess the qualitative agreement of the deformation patterns, the spatial configurations of the tube cross sections are provided in Figure 2.3, with fibres of different bending stiffness parameters being indicated by dashed and dotted lines. Note that the deformed fibres generally exhibit a curved shape along the radial direction with a decrease in the curvature value encountered for increasing values of the fibre(-bending) stiffness parameter. In fact, the fibres remain nearly straight for high values of the

Table 2.1: Analytical solution for the non-dimensional fibre slope $\partial u_\varphi^* / \partial r^*$ at the inner boundary $(r^* = 1)$ in dependence of the non-dimensional fibre(-bending) stiffness parameter d^{f*}, taken from [30].

d^{f*}	0.000	0.005	0.030	0.100	π
$\left.\dfrac{\partial u_\varphi^*}{\partial r^*}\right|_{r^*=1}$	0.952	0.887	0.825	0.771	0.674

fibre(-bending) stiffness such that they are rather rotated and stretched than bent for the highest values of the fibre(-bending) stiffness parameters which have been taken into account in the analysis. Overall, a similar deformation pattern is observed for the analytical solution which is based on the small strain theory, Figure 2.3(a), and the finite element-based solution of the finite strain theory, Figure 2.3(b).

Since the plate is assumed to be simply supported at the inner boundary, i.e. no restrictions on the fibre slope are imposed, a different fibre slope is noted for each value of the fibre(-bending) stiffness parameter. To quantify the latter, the dimensionless fibre slope at the inner boundary which is calculated based on the analytical solution scheme, cf. [30], is provided in dependence of the dimensionless fibre(-bending) stiffness parameter, see Table 2.1. On the other hand, the fibre slope which is predicted by the finite element-based solution scheme is provided in Table 2.2 for the values of the fibre(-bending) stiffness parameter c which were approximated based on its non-dimensional counterpart d^{f*}, cf. Section 2.2.2.1. To allow for a convenient comparison with the dimensionless fibre slope predicted by the analytical solution scheme, the fibre slope scaled by conversion factor $f_4 \approx 11.29$, cf. Appendix A.6, is additionally provided. Since the fibre orientation field is not a primary field variable, it is only available at the sampling points if no additional projection scheme is used. For this reason, the fibre slope at the inner boundary is approximated as the average fibre slope predicted at the three sampling points nearest to the boundary of the first element near the inner bound-

Table 2.2: Finite element-based solution for the fibre slope at the inner boundary $(r \approx B_0)$ in dependence of the material parameter c, given for the load state $\|\boldsymbol{t}_{\text{tang}}\| / \|\boldsymbol{t}_{\text{tang}}^{\max}\| = 0.1$. The conversion factor $f_4 = 11.29$ is calculated as shown in Appendix A.6 to allow for a comparison with the dimensionless fibre slope presented in Table 2.1.

c	0.0000	0.4×10^6	2.4×10^6	8.0×10^6	2.5×10^8
$\left.\dfrac{\bar{\boldsymbol{a}}_t \cdot \boldsymbol{e}_\varphi}{\bar{\boldsymbol{a}}_t \cdot \boldsymbol{e}_r}\right|_{r \approx B_0}$	0.0838	0.0785	0.0730	0.0680	0.0597
$f_4 \left.\dfrac{\bar{\boldsymbol{a}}_t \cdot \boldsymbol{e}_\varphi}{\bar{\boldsymbol{a}}_t \cdot \boldsymbol{e}_r}\right|_{r \approx B_0}$	0.9459	0.8865	0.8238	0.7682	0.6741
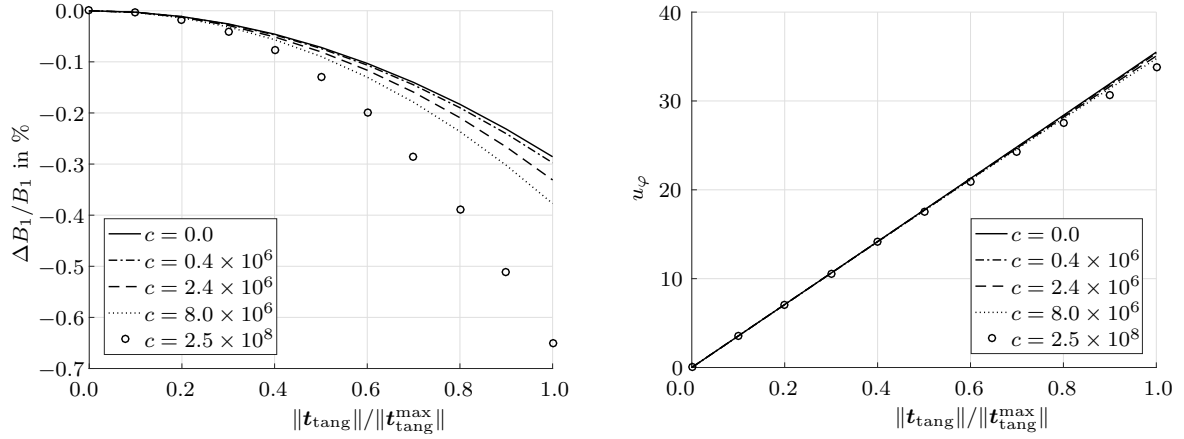
(a) Relative change of the outer tube radius $\Delta B_1/B_1$ in % as a function of the relative tangential load $\|\boldsymbol{t}_{\text{tang}}\|/\|\boldsymbol{t}_{\text{tang}}^{\text{max}}\|$.

(b) Approximated azimuthal displacement u_φ at the outer boundary in dependence of relative tangential load $\|\boldsymbol{t}_{\text{tang}}\|/\|\boldsymbol{t}_{\text{tang}}^{\text{max}}\|$.

Figure 2.4: Detailed analysis of the deformation pattern predicted by the finite element-based solution procedure.

ary. Comparing the results presented in Table 2.1 and Table 2.2, both the analytical and the finite element based-solution scheme predict that the fibre slope at the inner boundary decreases with increasing values of the fibre(-bending) stiffness parameter. Furthermore, the predicted values of the fibre slope are found to be in good accordance with the analytical results.

Concluding the analysis of the deformation pattern we will focus on the influence of the boundary conditions which are applied at the outer boundary. For the analytical solution scheme it is shown in [30] that the system of differential equations to be solved for the radial and azimuthal displacement becomes uncoupled, such that no boundary conditions in radial direction need to be specified to calculate the azimuthal displacement response. However, the finite element-based solution scheme requires the specification of boundary conditions for the radial direction. These are chosen to be of homogeneous Neumann-type so that the outer tube radius is free to extend or contract. In Figure 2.4(a), the relative change of the outer tube radius $\Delta B_1/B_1$ is shown in dependence of the relative load state for various values of the material parameter c. For the load state $\|\boldsymbol{t}_{\text{tang}}\|/\|\boldsymbol{t}_{\text{tang}}^{\text{max}}\| = 0.1$ we observe a contraction of the outer tube radius of between -0.0028% for a non-reinforced tube and -0.0040% for a fibre-reinforced tube with $c = 2.5 \times 10^8$. The contraction increases with increasing load such that a relative reduction of the outer tube radius of -0.28% for a non-reinforced-, respectively -0.65% for a fibre-reinforced tube with $c = 2.5 \times 10^8$ is observable for an applied load of $\|\boldsymbol{t}_{\text{tang}}\|/\|\boldsymbol{t}_{\text{tang}}^{\text{max}}\| = 1.0$. Hence, the outer tube radius is found to remain nearly constant which is important for the findings presented in Appendix 2.2.1.3.
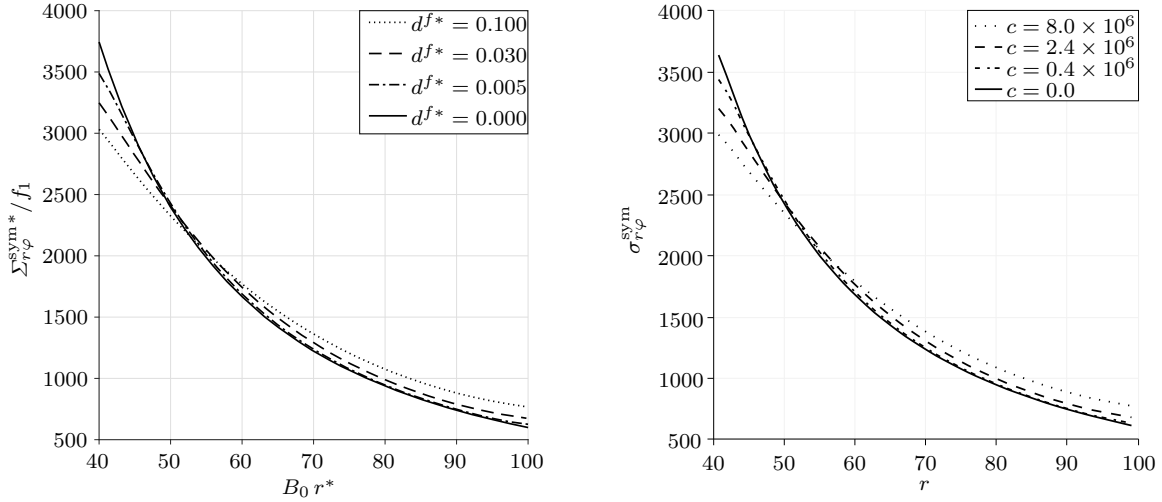
(a) Analytical solution based on the small strain theory, reproduced from [30] and scaled by $f_1 = 5.34 \times 10^{-4}$ as derived in Appendix A.6.

(b) Finite element solution based on the finite strain theory for the applied load of $\|\boldsymbol{t}_{\text{tang}}\|/\|\boldsymbol{t}_{\text{tang}}^{\max}\| = 0.1$.

Figure 2.5: Symmetric contribution to the dimensionless linearised stress tensor $\boldsymbol{\Sigma}^*$ and the Cauchy stress tensor $\boldsymbol{\sigma}$ of the finite strain theory along the radial direction of the tube.

Considering the observation that the outer tube radius remains nearly constant for the deformation states considered, i.e. $B_1 \approx 100$, the azimuthal displacement u_φ of material points which are positioned at the outer radius may be approximated according to $u_\varphi \approx B_1 \arctan \left(x_2/x_1 \right)|_{\boldsymbol{X} = B_1 \boldsymbol{e}_1}$. The azimuthal displacement for various values of the material parameter c is depicted in Figure 2.4(b) as a function of the relative load state. We find a slight decrease in the azimuthal displacement for increasing values of the material parameter c since the boundary conditions in azimuthal direction have been applied in terms of tractions rather than displacements.

2.2.2.3 Stress distribution

Next, the resulting stress fields in terms of the dimensionless linearised stress tensor $\boldsymbol{\Sigma}^*$ and the Cauchy stress tensor $\boldsymbol{\sigma}$ are investigated, with an emphasis on the assessment of the influence of the fibre(-bending) stiffness and the consistency of the analytical and finite element-based solution. Since the azimuthal displacement for the axisymmetric tube-like structure is mainly determined by the shear stress, and since the fibre-bending theory generally implies an unsymmetry of the linearised stresses as well as of the finite deformation Cauchy-type stress tensor, we will focus on the analyses of the in-plane shear-stress coefficients as this work proceeds.

To this end, the symmetric shear stress contributions which result immediately from the evaluation of the constitutive models (2.75), (2.76) and (2.78) are provided in Figure 2.5. Firstly, regarding the inner boundary of the tube at $r^* = 1$, respectively $r = 40$,
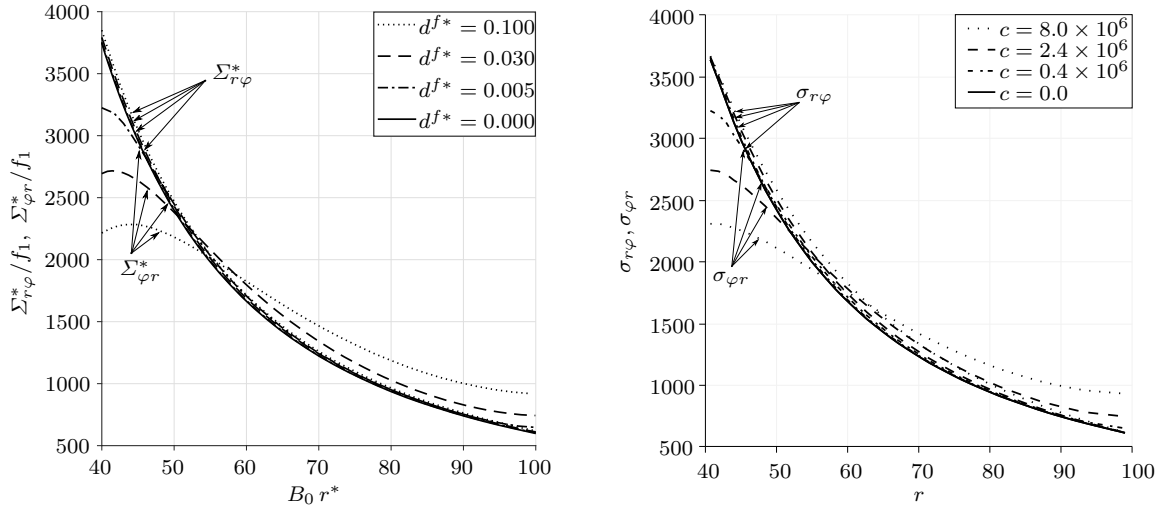
(a) Analytical solution based on the small strain theory, reproduced from [30] and scaled by $f_1 = 5.34 \times 10^{-4}$ as derived in Appendix A.6.

(b) Finite element solution based on the finite strain theory for the applied load of $\|\boldsymbol{t}_{\text{tang}}\| / \|\boldsymbol{t}_{\text{tang}}^{\max}\| = 0.1$.

Figure 2.6: In-plane shear stress coefficient of the dimensionless linearised stress tensor $\boldsymbol{\Sigma}^*$ and the Cauchy stress tensor $\boldsymbol{\sigma}$ of the finite strain theory along the radius of the tube.

we find that, for the analytical as well as the finite element-based solution, the $r\varphi$-coefficients of the respective stress tensors take their maximal values in the case of a non-reinforced material, with a decreasing shear stress coefficient being observed for increasing values of the fibre(-bending) stiffness parameter. In contrast, the latter observation is reversed at the outer boundary, where the maximal symmetric shear stress contribution is observed for the fibre-reinforced composite with the highest bending stiffness parameter. Moreover, the intersection point of the curves is found at approximately 15% of the tube's wall thickness for both the analytical and the numerical solution procedure, resulting in remarkably similar simulation results.

The modelling of the fibre-bending stiffness which is based on the introduction of higher-order energy contributions as additional arguments of the energy function, requires an extended continuum approach, [130], which implies the action of a couple stress tensor such that the linearised stress tensor and the Cauchy stress tensor become unsymmetric. Thus, in Figure 2.6 the distribution of both the $r\varphi$- as well as the φr-coefficients of the respective stress tensor are provided along the radial direction. At first glance, a significant difference in the $r\varphi$- and the φr-coefficient is observed for composites with an assumed non-negligible fibre(-bending) stiffness. This shows that the higher-gradient mode is activated in the azimuthal shear deformation of the tube, such that a pronounced skew-symmetric stress contribution is present due to the action of the couple stress tensor, which implicitly defines the latter based on (2.48b).

In view of the stress distribution, we find that the $r\varphi$-coefficients of the stress tensors take higher values, compared with the φr-coefficients, at the inner boundary. For different values of the fibre(-bending) stiffness parameter, the $r\varphi$-coefficients of the stress tensors are further observed to be nearly identical at the inner boundary for the analytical solution of the displacement-controlled shear deformation, Figure 2.6(a), and identical for the force-controlled finite element-based solution, Figure 2.6(b), due to the overall balance of linear momentum. Regarding the stress distribution along the radial direction, it can be observed that the fibre-reinforced composites with fibres possessing bending stiffness, in general, take higher shear stress values compared to a composite with negligible bending stiffness. This effect reduces in the vicinity of the outer boundary where the stress state for different values of the fibre(-bending) stiffness is similar. The slight difference in the $r\varphi$-coefficient of the linearised stress tensors at the outer boundary results from the fact that the displacement at the outer boundary, and not the traction, is prescribed. Note that both solution approaches, i.e. the displacement-controlled analytical framework and the force-controlled finite element formulation, can be well compared, since the coefficients $\Sigma_{r\varphi}^*$ at the outer boundary turn out to be quasi-independent of the fibre-stiffness parameter d^{f*}, see Figure 2.6(a).

Studying the distribution of the φr-stress coefficients, we find an interesting characteristic at the inner boundary layer: whereas the φr-stress coefficients monotonically decrease along the radius for the assumption of perfectly flexible fibres, i.e. $c = 0$ and $d^{f*} = 0$, a parabolic shape is observed for fibres possessing fibre(-bending) stiffness which becomes more pronounced for increasing values of the fibre stiffness parameter. Moreover, the maximal value of the parabola decreases with an increasing fibre(-bending) stiffness. The parabolic structure close to the boundary is not perfectly represented for the finite element-based solutions due to the limited resolution arising from the discrete character of the method and the number of elements near the boundary, cf. Figure 2.2. It can also be observed that, in contrast to the inner boundary, the φr-stress coefficient takes higher values than the $r\varphi$-coefficient at the outer boundary for both solution schemes. The resulting crossing points of the lines resembling the φr- and $r\varphi$-stress coefficient for a specific value of c , respectively d^{f*}, gradually move into the direction of the outer boundary for increasing values of the fibre(-bending) stiffness.

Overall, the analytical solution by means of the small strain theory and the finite element-based solution which accounts for finite deformations are observed to be in accordance.

2.2.2.4 Couple stress distribution

Finally, we will focus on the couple stress tensor in terms of the rz-coefficient defined by (2.79) for the small strain formulation, respectively (2.30) for the finite strain theory and depicted in Figure 2.7. First, we notice that υ_{rz}^* takes zero values at the boundaries due to the assumed simple support at the inner radius which goes along with the assumption that the fibre slope is not restrained at the boundary. Same holds for the outer radius
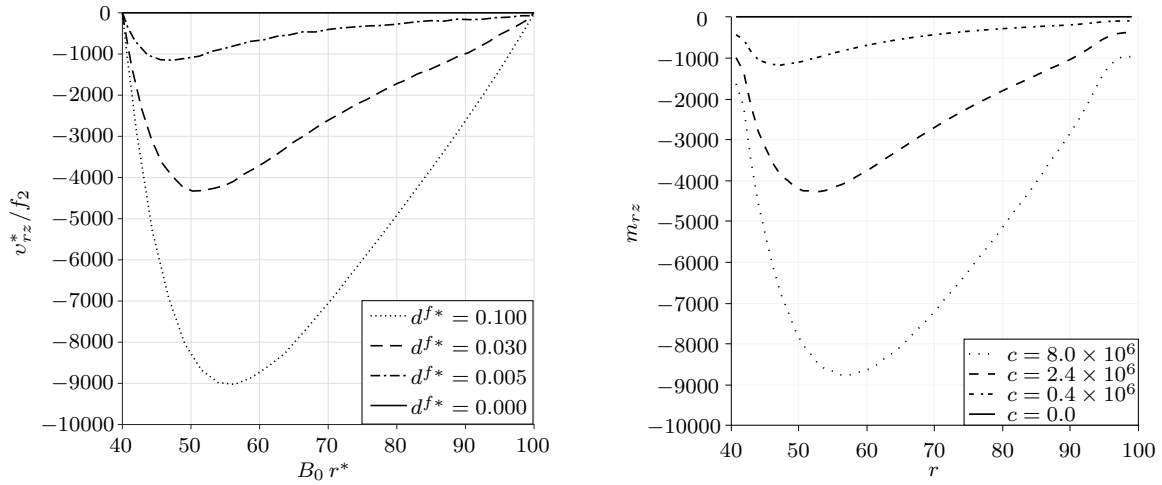
(a) Analytical solution based on the small strain theory, reproduced from [30] and scaled by $f_2 = 1.33 \times 10^{-5}$ as derived in Appendix A.6.

(b) Finite element solution based on the finite strain theory for the applied load of $\|\boldsymbol{t}_{\text{tang}}\|/\|\boldsymbol{t}_{\text{tang}}^{\max}\| = 0.1$.

Figure 2.7: Distribution of the rz-coefficient of the dimensionless couple stress tensor of the linearised theory $\boldsymbol{v}^*$ and the couple stress tensor of the finite strain theory $\boldsymbol{m}$ along the radial direction of the tube.

where the fibre slope is not restrained either. With increasing distance to the inner boundary, v_{rz}^* gradually takes smaller values until the minimal value is reached. Note that the absolute value of the minimum increases with increasing values of the fibre(-bending) stiffness and that the position of the minimum is shifted towards the outer radius but generally remains near the inner boundary layer. Moreover, it is observed that for the case of perfectly flexible fibres, i.e. $d^{f*} = 0$, the couple stress tensor is equal to zero, since the proposed model reduces in the limiting case to the classic structural tensor approach.

The same tendency observed for the analytical solution of the small strain approach, Figure 2.7(a), is also captured by the numerical solution of the finite strain problem, Figure 2.7(b). Regarding Figure 2.7(b) we further find that the homogeneous boundary condition is not reflected accurately. This inaccuracy can be explained by the fact that the couple stress tensor is only available at the sampling points and is mapped to the nodes using an L_2-projection, cf. [56, 137]. With the nodal data at hand, the dependent field variables can then be approximated in each point in the same way as was done with the primary field variables. Note that the inaccuracy in the representation at the boundaries can further be reduced by using a finer triangulation (at the boundaries) than the one shown in Figure 2.2. Overall, the distributions of the couple stress tensor for the analytical and the numerical solution by means of the finite element method match very well.
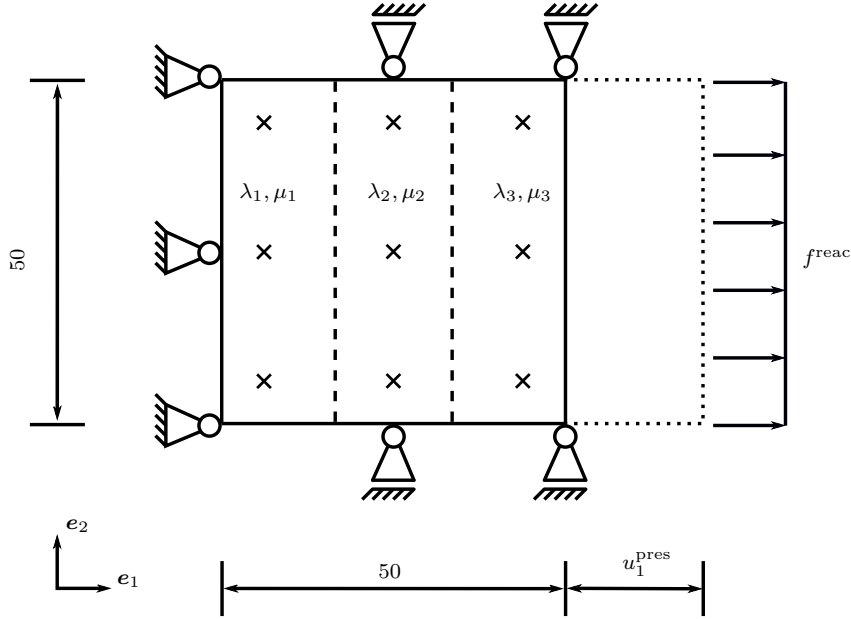
Figure 2.8: Dimensions and boundary conditions for the simulation of homogeneous and inhomogeneous uni-axial deformation states.

2.2.3 Representative simulation results

In Section 2.2.2 it was shown that the simulation results of the proposed finite element scheme compare well with analytical solutions which validates the proposed formulation to a certain extent. Based on this study, the properties of the gradient-extended modelling approach with regard to the chosen form of the gradient energy contribution will further be investigated in this section. In particular, homogeneous and inhomogeneous uni-axial deformation states are analysed, and the influence of the fibre stretch gradient on the load displacement curves is discussed in Section 2.2.3.1. By extending the analysis to boundary value problems in a three-dimensional setting, the bending dominated deformation of a plate with a hole is studied in Section 2.2.3.2 with the emphasis being on the anisotropic material properties that are induced by the higher-gradient energy contribution.

2.2.3.1 Homogeneous and inhomogeneous deformation states

In this section the influence of the stretch contribution of the higher-gradient part of the energy function, cf. (2.67) and (2.71), on the constitutive response for homogeneous and inhomogeneous uni-axial deformation states is investigated in detail. To this end we will focus on the block-like structure with edge length 50 depicted in Figure 2.8. As indicated by the supports, homogeneous Dirichlet boundary conditions are enforced in both e_1- and e_2-direction on the left boundary and in e_2-direction on the upper and lower boundary. On the right boundary, the displacement in e_2-direction is enforced

Table 2.3: Material parameters at different sections of the block depicted in Figure 2.8.

	$\lambda_\bullet$	$\mu_\bullet$
Position 1	5.185×10^4	2.222×10^4
Position 2	1.037×10^5	4.444×10^4
Position 3	2.074×10^5	8.888×10^4

to be zero while the displacement in $\boldsymbol{e}_1$-direction, denoted by u_1^{pres}, will be linearly increased up to a maximum of $u_1^{\text{pres}} = 10$ which is equal to an average strain of 20%. As the analysis proceeds, we are further interested in the resulting reaction force (in horizontal direction) which is required for the elongation of the block and which will be denoted by f^{reac}. In accordance with Section 2.1.3, $\boldsymbol{\tau} = \boldsymbol{0}$ will furthermore be assumed to hold on $\partial \mathcal{B}_t$.

The block is discretised with one two-dimensional mixed-type element. Specifically speaking, eight-node serendipity-type elements are used for the approximation of the placement field, while both the skew-symmetric stress field as well as the relaxed deformation gradient field are approximated by using bi-linear Lagrangian-type elements. The integration is performed by means of a Gaussian quadrature scheme which employs nine sampling points.

For the boundary value problem at hand both homogeneous and inhomogeneous deformation states can be obtained for an initial uniform field of fibre orientation $\boldsymbol{a}_0 = \boldsymbol{e}_1$ by choosing the material parameters λ and μ either uniform or non-uniform in the domain. For a homogeneous deformation to take place we choose the material parameters at the sampling points, which are indicated in Figure 2.8 by the black-coloured crosses, according to $\lambda_1 = \lambda_2 = \lambda_3 = 1.037 \times 10^5$ and $\mu_1 = \mu_2 = \mu_3 = 4.444 \times 10^5$. In view of the reaction force f^{reac}, which is depicted in Figure 2.9(a) in dependence of the prescribed displacement u_1^{pres} for different values of the fibre(-bending) stiffness parameter c, we find that f^{reac} takes the same value independent of c which essentially means that the higher-gradient part of the energy function is not activated.

Choosing spatially non-uniform material parameters according to Table 2.3 results in an inhomogeneous deformation of the block, since the initial material stiffness increases from left to right. For the latter simulation the reaction force f^{reac} in dependence of the prescribed displacement u_1^{pres} for various values of the material parameter c is provided in Figure 2.9(b). It can be observed that an influence of the additionally introduced part of the energy function $W^{\boldsymbol{\kappa}_0}$ becomes noticeable for $c \approx 10^6$ with a stiffer material response being observed for increasing values of the material parameter c. Note that the fibres remain straight, since the displacement in vertical direction is enforced to be zero within the entire domain, so that no fibre bending is activated and only contributions which result from referential gradients of the fibre stretch take influence on the constitutive

(a) homogeneous deformation   (b) inhomogeneous deformation
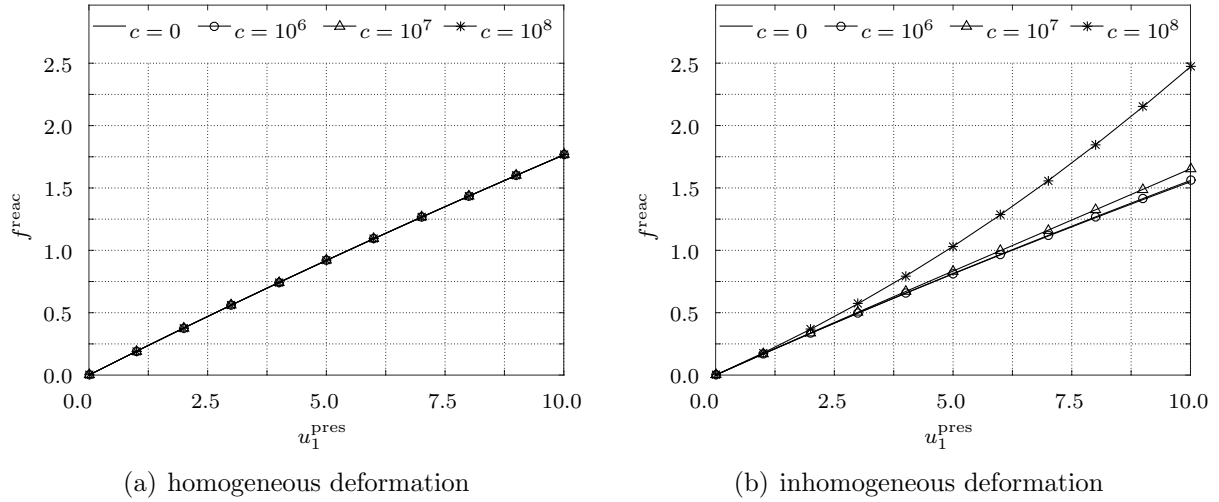
Figure 2.9: Reaction force f^{reac} in dependence of the prescribed displacement u_1^{pres} and the material parameter c for calculations based on (a) uniform material parameters $\lambda_1 = \lambda_2 = \lambda_3 = 1.037 \times 10^5$ and $\mu_1 = \mu_2 = \mu_3 = 4.444 \times 10^5$ and (b) non-uniform material parameters λ and μ according to Table 2.3.

response via I_6. It is further noted that this example usually requires a discretisation with more than one element to approximate the field quantities accurately. However, a discretisation based on one element is sufficient to demonstrate the influence of the modelling approach, respectively of the gradient of the fibre stretch, on homogeneous and inhomogeneous uni-axial dominated deformation states.

Thus, the simulation results exemplify that, in contrast to the classic structural tensor approach which energetically accounts for the fibre stretch via the invariant I_4, the extended modelling approach allows to account for changes in the fibre stretch, resembling higher-order energy contributions via the invariant I_6. Moreover, taking into account the process of parameter identification, the knowledge that the additionally introduced higher-order part of the energy function is not activated in the case of initially straight fibres in combination with homogeneous stretch deformations is helpful. This would for example allow to use tension tests, where the deformation field is assumed to be homogeneous, to identify material parameters which, e.g., correlate to the tension stiffness modulus independent of the fibre(-bending) stiffness.

Finally, it is interesting to note that, although the higher-order energy contribution is activated for the inhomogeneous deformation state, the couple stress tensor turns out to be zero for the boundary value problem at hand and, accordingly, the Cauchy-type stress tensor remains symmetric. To further emphasise this, we focus next on the resulting state of deformation in more detail, in particular on the deformation of the fibres. For each boundary node of the block depicted in Figure 2.8, the displacement in $\boldsymbol{e}_2$-direction is enforced to be zero and the displacement in $\boldsymbol{e}_1$-direction at the left and right boundary

Table 2.4: Material parameters for the simulation of the plate with a hole subjected to bending load.

λ	μ	c
1.037×10^5	4.4444×10^4	5.0×10^5

is prescribed. Furthermore, a uni-axial strain state is enforced such that the deformation gradient takes the form

$$\boldsymbol{F} = [\lambda_{\mathrm{A}}(X_1, t) - 1]\, \boldsymbol{e}_1 \otimes \boldsymbol{e}_1 + \boldsymbol{I} \quad , \tag{2.84}$$

and the left Cauchy-Green tensor is given by

$$\boldsymbol{b} = \left[[\lambda_{\mathrm{A}}(X_1, t)]^2 - 1\right] \boldsymbol{e}_1 \otimes \boldsymbol{e}_1 + \boldsymbol{I} \quad . \tag{2.85}$$

Since the fibres are initially aligned with the $\boldsymbol{e}_1$-coordinate axis, i.e. $\boldsymbol{a}_0 = \boldsymbol{e}_1$, using (2.6) and (2.84) the spatial fibre orientation vector can further be specified as

$$\boldsymbol{a}_t = \lambda_{\mathrm{A}}(X_1, t)\, \boldsymbol{e}_1 \quad . \tag{2.86}$$

Making use of (2.86) and applying the definitions (2.7) and (2.31a), $\boldsymbol{\kappa}$ can be specified according to

$$\boldsymbol{\kappa} = \frac{\partial \lambda_{\mathrm{A}}(X_1, t)}{\partial X_1}\, \boldsymbol{e}_1 \quad . \tag{2.87}$$

With the kinematic considerations (2.85)–(2.87) at hand, the evaluation of (2.77c) finally yields

$$\left[\boldsymbol{m}^{\mathrm{dev}}\right]^{\mathrm{t}} = \frac{8}{3}\, c\, J_{\boldsymbol{F}}^{-1}\, \boldsymbol{\epsilon} : [\boldsymbol{a}_t \otimes \boldsymbol{b} \cdot \boldsymbol{\kappa} \otimes \boldsymbol{a}_t] = \boldsymbol{0} \quad , \tag{2.88}$$

since $[\boldsymbol{a}_t \otimes \boldsymbol{b} \cdot \boldsymbol{\kappa}]$ turns out to be a symmetric tensor of rank one proportional to $\boldsymbol{e}_1 \otimes \boldsymbol{e}_1$. Taking the balance equation of angular momentum, (2.48b), into account which serves as the definition for the skew-symmetric part of the Cauchy-type stress tensor, we find $\boldsymbol{\sigma}^{\mathrm{skw}} = \boldsymbol{0}$. Regarding the specific form of the symmetric part of the Cauchy-type stress tensor, the contribution highlighted in (2.76) turns out to be different from zero such that higher-order energy contributions in terms of the gradient of the fibre stretch influence the stress state.

2.2.3.2 Bending of a plate with a hole

A detailed analysis of bending dominated deformations of a plate with a hole in a three-dimensional setting was presented in [10]. Here, we will briefly recapitulate some of the
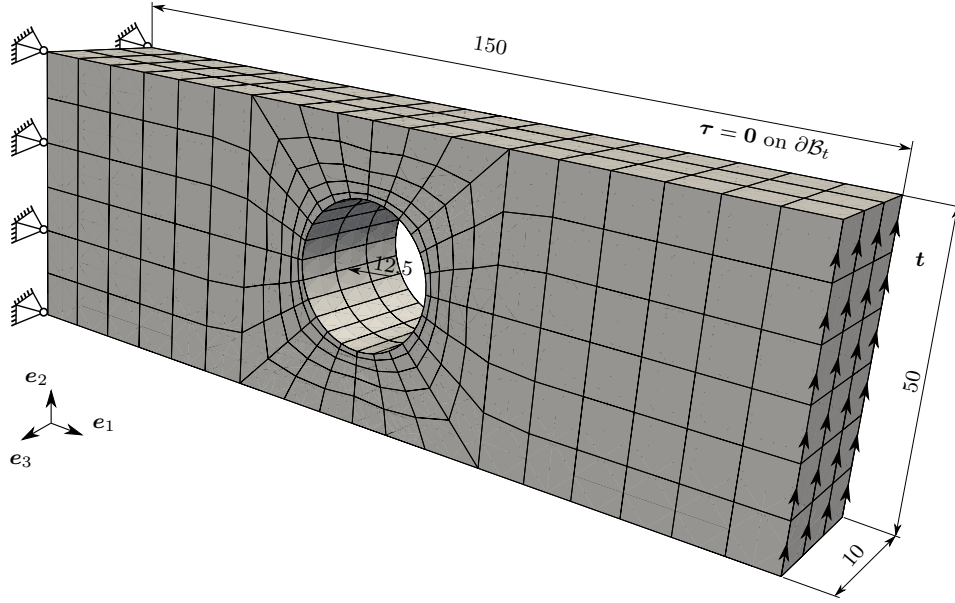
Figure 2.10: Dimensions and boundary conditions for the three-dimensional simulation of a plate with a hole subject to bending-type load.

findings with regard to the resulting deformation pattern and shall extend the analysis for the case that the fibres are not aligned with the $\boldsymbol{e}_1$-direction which yields some interesting insights with regard to the induced anisotropies.

To this end, the focus lies on the plate with a hole depicted in Figure 2.10 and the material parameters, summarised in Table 2.4, are chosen in accordance with Section 2.2.3.1. Moreover, we shall focus on three different combinations of the fibre(-bending) stiffness and the fibre orientation, namely:

1. the plate material is isotropic, no fibres are present

2. the plate is reinforced with fibres acting along the $\boldsymbol{e}_1$-direction with $c = 5 \times 10^5$

3. the plate is reinforced with fibres acting along the $\frac{1}{\sqrt{3}} \left[\boldsymbol{e}_1 + \boldsymbol{e}_2 + \boldsymbol{e}_3 \right]$ direction with $c = 5 \times 10^5$

The displacement of the nodes which are located at the left boundary is fixed in all three spatial dimensions, while tractions in terms of dead-loads acting in positive $\boldsymbol{e}_2$-direction are applied at the nodes of the right surface, resulting in a total force of 5.11×10^6, see Figure 2.10. By analogy with Section 2.2.3.1, it is further assumed that $\boldsymbol{\tau} = \boldsymbol{0}$ on $\partial \mathcal{B}_t$ holds.

From a numerical point of view, 20-node serendipity-type elements are used for the discretisation of the spatial placement field, while both the relaxed deformation gradient field as well as the skew-symmetric stress field are approximated using eight-node
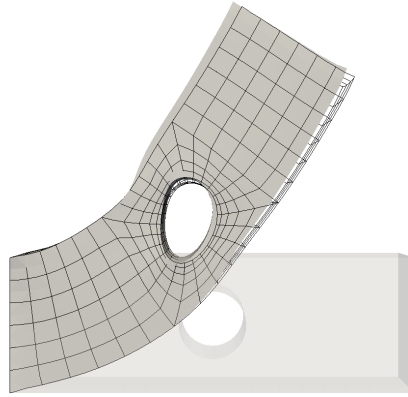
Figure 2.11: Deformation pattern of a fibre-reinforced plate with $\boldsymbol{a}_0 = \boldsymbol{e}_1$, $c = 5 \times 10^5$ and of a non-reinforced plate for the final load state. The spatial configuration of the fibre-reinforced plate is illustrated by the black-coloured mesh, whereas the spatial configuration of the non-reinforced plate is represented by the grey-coloured surface. In addition, the reference configuration is shown as a transparent surface.

Lagrangian-type elements. The occurring integrals are evaluated numerically by means of a Gaussian quadrature scheme with 27 quadrature points.

For the three different combinations of the fibre orientation and the fibre(-bending) stiffness parameter as introduced above, the resulting deformation behaviour will be compared. Focusing on the influence of the fibre(-bending) stiffness on the deformation for fibres being initially aligned with the $\boldsymbol{e}_1$-axis, the deformed configuration of the reinforced plate is illustrated in Figure 2.11 by means of its mesh, along with the deformed configuration of the non-reinforced plate which is shown by the grey-coloured surface. It is interesting to notice that, although the principle deformation patterns seem similar at a first glance, cf. Figure 2.12(a) and Figure 2.12(d), Figure 2.11 reveals that noticeable differences in the deformation occur in the region around the hole. Especially the difference between the nearly constant curvature of the upper surface in the case of the reinforced material and the change of curvature in the case of a non-reinforced material is revealed. This leads to the conclusion that configurations with high values of the fibre curvature are suppressed, see also the detailed discussion in [10].

Focusing on the anisotropic properties induced by the higher-gradient energy contribution, the resulting spatial configurations for the final load state and for the different combinations of the material parameter c with the fibre orientation are provided in Figure 2.12, together with the reference configuration which is visualised in terms of the transparent surface. When comparing the deformation behaviour it becomes evident that both the non-reinforced as well as the reinforced plate with $\boldsymbol{a}_0 = \boldsymbol{e}_1$ show the expected symmetric deformation pattern. In contrast, one finds that the deformation pattern of the reinforced plate with an initial fibre orientation along the $[\boldsymbol{e}_1 + \boldsymbol{e}_2 + \boldsymbol{e}_3]/\sqrt{3}$ direction does not exhibit the formerly observed symmetry pattern. This shows that accounting for the fibre(-bending) stiffness induces an anisotropic material behaviour in

addition to the anisotropic properties which are already accounted for within the classic structural tensor approach.

2.2.4 Summary

This section focused on the comparison of the simulation results which can be achieved by means of the finite element-based solution procedure presented in Section 2.1 with the analytical solution presented in [30]. To this end, the azimuthal shear deformation of a tube-like structure, analysed in [30] under the assumption of linearised kinematics, was simulated with the finite element-based solution procedure presented in Section 2.1, within a finite deformation setting. To allow for the comparability of the results, the constitutive relations chosen for the symmetric part of the Cauchy stress tensor and the couple stress tensor were shown to be consistent with their corresponding linearised counterparts, provided specific ratios of the material parameters were accounted for.

In order to assess the conformity of the results, the general deformation patterns for varying values of the fibre(-bending) stiffness were then analysed for the analytical and the numerical solution procedure. In both cases, a stiffer constitutive response was observed for increasing values of the fibre(-bending) stiffness which was accompanied by a decreasing maximal fibre curvature. In particular, it was shown that the fibres remained nearly straight for high values of the fibre(-bending) stiffness parameter.

With the general deformation patterns being in good accordance, the comparison focused on the dependent field variables in a next step. First, regarding the symmetric contributions to the shear coefficients of stress tensors, which result directly from the evaluation of the constitutive models, a gradually decreasing shear stress contribution from the inner to the outer radius with a characteristic crossing point of the curves corresponding to different values of the fibre(-bending) stiffness was noticed. This characteristic was found to be comparable for both the analytical as well as the finite element-based solution. Furthermore, taking into account the skew-symmetric stress contributions, which are implicitly defined based on the balance equation of angular momentum, it was subsequently observed that the distribution of the shear stress along the radius once more exhibited a characteristic shape with a crossing point of the curves representing the $r\varphi$- and the φr-stress coefficients. Specifically speaking, it was noted that the radial distribution of the φr-stress coefficient showed a parabolic shape near the inner boundary layer with the peak value and its distance from the inner radius highly depending on the assumed fibre(-bending) stiffness.

The comparison of the non-zero coefficient of the couple stress tensor once more revealed similar results for both solution procedures, with an at first monotonically decreasing $r\varphi$-couple stress coefficient along the radius, which showed a minimum at the end of the inner boundary layer and then gradually increased again such that the homogeneous Neumann boundary condition was met at the outer radius. The peak value and the shift of the peak value's position in the direction of the outer radius was observed to depend on the fibre(-bending) stiffness.

(a) $c = 0$

(b) $c = 0$

(c) $c = 0$

(d) $c = 5 \times 10^5$, $\boldsymbol{a}_0 = \boldsymbol{e}_1$

(e) $c = 5 \times 10^5$, $\boldsymbol{a}_0 = \boldsymbol{e}_1$

(f) $c = 5 \times 10^5$, $\boldsymbol{a}_0 = \boldsymbol{e}_1$

(g) $c = 5 \times 10^5$, $\boldsymbol{a}_0 = \frac{1}{\sqrt{3}} [\boldsymbol{e}_1 + \boldsymbol{e}_2 + \boldsymbol{e}_3]$

(h) $c = 5 \times 10^5$, $\boldsymbol{a}_0 = \frac{1}{\sqrt{3}} [\boldsymbol{e}_1 + \boldsymbol{e}_2 + \boldsymbol{e}_3]$

(i) $c = 5 \times 10^5$, $\boldsymbol{a}_0 = \frac{1}{\sqrt{3}} [\boldsymbol{e}_1 + \boldsymbol{e}_2 + \boldsymbol{e}_3]$
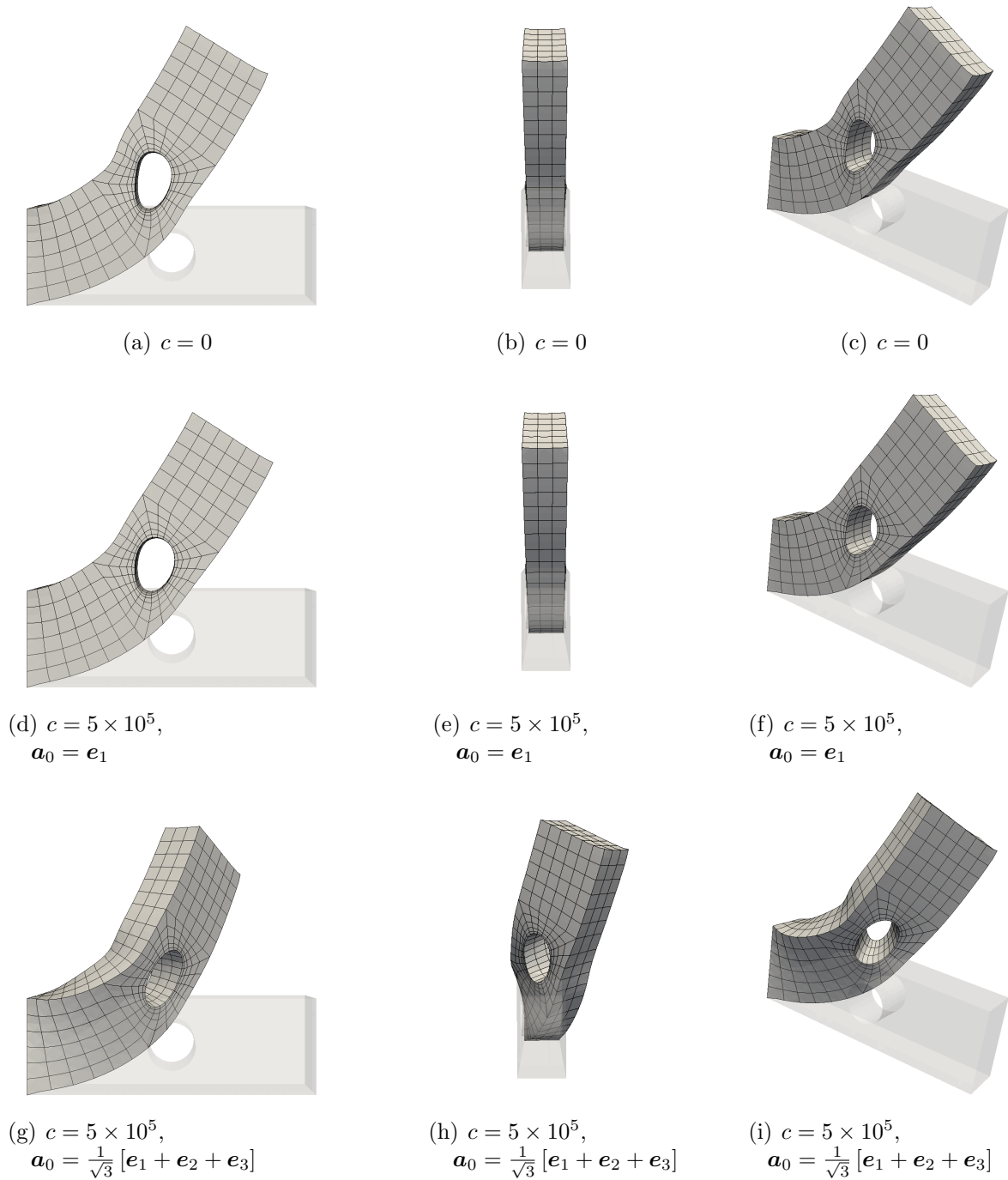
Figure 2.12: Deformation pattern of the three-dimensional plate subject to bending load for different parameters of the fibre(-bending) stiffness c and different initial fields of fibre orientation. The spatial configurations of the plate are given by the respective meshes, whereas the reference configuration is represented by the transparent surface.

Overall, the analytical solution which could be derived for the linearised theory and the finite element simulation results which were based on the corresponding finite strain theory were found to be in good accordance for the azimuthal shear deformation of the tube-like structure, which verifies the applicability and accuracy of the established finite element formulation.

In a next step, homogeneous and inhomogeneous uni-axial deformation states of a block-like structure were analysed for different values of the fibre(-bending) stiffness parameter, and the resulting forces related to the elongations of the blocks were compared. It was observed that the higher-order part of the energy function was not activated in the case of the homogeneous deformation field in combination with the initially straight fibre orientation considered. For the inhomogeneous deformation field, however, the influence of the additionally introduced higher-order energy part was pronounced. Thus, the chosen form of the strain energy function, although being well-suited for the comparison with the analytical solution, is also activated by deformation modes which do not include fibre bending. In particular it was shown that the gradient of the fibre stretch contributes to the chosen form of the energy function. This important observation motivates the development of a more elaborated higher-gradient energy contribution solely relying on the fibre curvature and to be discussed in detail in Section 2.3.

Finally, the investigation was extended to a more complex three-dimensional boundary value problem – a plate with a hole subject to bending load – for three different combinations of the fibre orientation and the fibre(-bending) stiffness parameter. Analogously to the previous example a stiffer response was observed for fibres exhibiting fibre(-bending) stiffness, resulting especially in a different deformation behaviour in the area around the hole. Furthermore, a non-symmetric deformation behaviour was observed for a specific fibre orientation – here the space diagonal with respect to the chosen Cartesian frame – so that the presented modelling approach introduces an anisotropic material behaviour in addition to the anisotropic properties which are already accounted for when employing the classic structural tensor approach.

2.3 Modelling of curvature effects in fibre-reinforced nanocomposites

This section focuses on the elaboration of a specific form of the higher-gradient contribution to the stored energy function which is solely based on the fibre curvature and motivated by the experimental findings on one-dimensional nanomaterials presented in Section 1.1.1. In particular it is shown that the higher-gradient contribution proposed in Section 2.2, though well-suited for the comparison with analytical solutions, is less straightforward to interpret, and a scalar valued measure of the fibre curvature is extracted from the list of invariants that allows for a direct physical interpretation. A particular form of the stored energy function which relies on a quadratic measure in the fibre curvature is then proposed and found to result into well-interpretable contributions to the stress tensor and to the couple stress tensor. Motivated by the experimental findings, bending dominated boundary value problems are eventually analysed with the focus being on the resulting size effect and on the influence of the fibre curvature energy contribution on the deformation pattern.

2.3.1 Specification of the constitutive model

In accordance with Section 2.2 an additive split of the energy function into three contributions according to

$$
\begin{aligned}
W\left(I_1, \ldots, I_{11}\right) = {} & \left[1 - \eta_{\mathrm{vol}}\right] W^{\mathrm{iso}}\left(I_1, \ldots, I_3\right) \\
& + \eta_{\mathrm{vol}}\, W^{\lambda_{\mathrm{A}}}\left(I_1, \ldots, I_5\right) \\
& + \eta_{\mathrm{vol}}\, W^{\boldsymbol{\kappa}_{\mathrm{tru}}}\left(I_1, \ldots, I_{11}\right)
\end{aligned}
\tag{2.89}
$$

will be assumed. The first contribution W^{iso} is again related to the deformation of the matrix material and accordingly weighted by the matrix volume fraction $\left[1 - \eta_{\mathrm{vol}}\right]$. The matrix contribution is assumed to be of isotropic type and to solely depend on the invariants which are related to the deformation, i.e. $I_{1,2,3}$. A suitable form of the energy function which employs the two material parameters λ and μ corresponding to the Lamé parameters of the small strain theory is given by the St.Venant-Kirchhoff-type model

$$
W^{\mathrm{iso}} = W^{\mathrm{svk}} = \frac{1}{2}\,\lambda\, \mathrm{tr}^2\left(\boldsymbol{E}\right) + \mu\, \mathrm{tr}\left(\boldsymbol{E}^2\right) \quad ,
\tag{2.90}
$$

with the Green-Lagrangian strain tensor $\boldsymbol{E} = \left[\boldsymbol{C} - \boldsymbol{I}\right]/2$. Considering the influence of the fibres, the two contributions $W^{\lambda_{\mathrm{A}}}$ and $W^{\boldsymbol{\kappa}_{\mathrm{tru}}}$ will be distinguished which are both weighted by the fibre volume fraction η_{vol}. The energy contribution $W^{\lambda_{\mathrm{A}}}$ is related to the fibre stretch and is based on the classic structural tensor approach which is discussed in detail in, for example, [16, 116, 117, 131]. Thus, invariants I_4 and I_5 which include

information on the fibre direction field are additionally accounted for with I_4 taking the physical interpretation of the squared fibre stretch, i.e.

$$I_4 = \boldsymbol{a}_0 \cdot \boldsymbol{C} \cdot \boldsymbol{a}_0 = [\boldsymbol{F} \cdot \boldsymbol{a}_0] \cdot [\boldsymbol{F} \cdot \boldsymbol{a}_0] = \lambda_{\mathrm{A}} \, \bar{\boldsymbol{a}}_t \cdot \bar{\boldsymbol{a}}_t \, \lambda_{\mathrm{A}} = \lambda_{\mathrm{A}}^2 \quad . \tag{2.91}$$

To be more specific, we will assume an energy contribution $W^{\lambda_{\mathrm{A}}}$ of the form

$$W^{\lambda_{\mathrm{A}}} (I_4) = \frac{1}{2} \, E_{\mathrm{fib}} \, \ln^2 \left(\sqrt{I_4} \right) \tag{2.92}$$

in this contribution which employs material parameter E_{fib} that can be associated with the fibres' Young's modulus, as becomes apparent when performing the linearisation of the corresponding contribution to the stress tensor given in Section 2.3.1.2. It is observed that the energy contribution (2.92) tends towards infinity when the fibre stretch approaches zero. However, we also note that an energy contribution of the form (2.92) is not polyconvex. In addition to the fibre stretch which corresponds to the first derivative of the fibre deformation field, the extended modelling approach allows us to take into account energy contributions which are based on higher-order gradients of the fibre deformation field. These include for example the fibre curvature and will be discussed in detail in Section 2.3.1.1

Remark 2.3 (Volume and mass fractions) *The contributions W^{iso}, $W^{\lambda_{\mathrm{A}}}$ and $W^{\boldsymbol{\kappa}_{\mathrm{tru}}}$ to the elastic energy function (2.89) are weighted by the corresponding volume fraction of the bulk, respectively the volume fraction of the fibres. However, from an experimental point of view it may turn out to be more convenient to work with the respective mass fractions instead. The overall density of the composite can be expressed in terms of the density of the fibres ρ_{fib} and the density of the matrix material ρ_{mat} according to, [138],*

$$\rho = [1 - \eta_{\mathrm{vol}}] \, \rho_{\mathrm{mat}} + \eta_{\mathrm{vol}} \, \rho_{\mathrm{fib}} \quad . \tag{2.93}$$

Further observing that the relation

$$\eta_{\mathrm{vol}} = \frac{\rho}{\rho_{\mathrm{fib}}} \, \eta_{\mathrm{mas}} \tag{2.94}$$

between the fibre volume fraction η_{vol} and the fibre mass fraction η_{mas} holds, allows us to calculate the fibre volume fraction based on the densities of the two constituents and the fibre mass fraction, cf. [138], specifically

$$\eta_{\mathrm{vol}} = \frac{\eta_{\mathrm{mas}}}{\dfrac{\rho_{\mathrm{fib}}}{\rho_{\mathrm{mat}}} + \left[1 - \dfrac{\rho_{\mathrm{fib}}}{\rho_{\mathrm{mat}}}\right] \eta_{\mathrm{mas}}} \quad . \tag{2.95}$$

For carbon nanotube-reinforced composites, the fibres are of tube-like structure which complicates the specification of the density, as it is a function of the tube inner diameter

d_i and outer diameter d_o. To approximate the density of a multi-walled carbon nanotube it is assumed in [138] that each graphitic layer of a multi-walled carbon nanotube has the density of dense graphite $\rho_{gra} = 2.25\,\mathrm{g\,cm^{-3}}$ such that a first approximation of the density of a multi-walled carbon nanotube is given by

$$\rho_{MWNT} \approx \rho_{gra} \frac{d_o^2 - d_i^2}{d_o^2} \quad . \tag{2.96}$$

2.3.1.1 Fibre curvature-based higher-order energy contribution

A specific form of the higher-order energy contribution $W^{\boldsymbol{\kappa}_{tru}}$ which is solely based on invariant I_6 has been used in Section 2.2 to validate the proposed finite element framework and to study basic model properties. For reasons to be discussed hereafter, however, this section focuses on the elaboration of a more sophisticated form of the energy function which is solely based on the fibre curvature. To this end, rewriting invariant I_6, we find that

$$I_6 = \boldsymbol{\kappa}_0 \cdot \boldsymbol{\kappa}_0 = \boldsymbol{\kappa} \cdot \boldsymbol{b} \cdot \boldsymbol{\kappa} = \left[\underbrace{\lambda_A \frac{\partial \bar{\boldsymbol{a}}_t}{\partial \boldsymbol{X}} \cdot \boldsymbol{a}_0}_{①} + \underbrace{\frac{\partial \lambda_A}{\partial \boldsymbol{X}} \cdot \boldsymbol{a}_0 \, \bar{\boldsymbol{a}}_t}_{②} \right] \cdot \boldsymbol{b} \cdot \left[\underbrace{\lambda_A \frac{\partial \bar{\boldsymbol{a}}_t}{\partial \boldsymbol{X}} \cdot \boldsymbol{a}_0}_{①} + \underbrace{\frac{\partial \lambda_A}{\partial \boldsymbol{X}} \cdot \boldsymbol{a}_0 \, \bar{\boldsymbol{a}}_t}_{②} \right], \tag{2.97}$$

where use was made of (2.31c) and (2.34). Noting that the fibre curvature vector $\boldsymbol{\kappa}_{tru}$ can be expressed as

$$\boldsymbol{\kappa}_{tru} = \frac{\partial \bar{\boldsymbol{a}}_t}{\partial \boldsymbol{x}} \cdot \bar{\boldsymbol{a}}_t = \frac{1}{\lambda_A} \frac{\partial \bar{\boldsymbol{a}}_t}{\partial \boldsymbol{X}} \cdot \boldsymbol{a}_0 \quad , \tag{2.98}$$

see e.g. [122] for the general definition of the curvature of three-dimensional curves, it is observed from (2.97) that I_6 is influenced by the fibre curvature vector scaled with λ_A^2 via ① and by the gradient of the fibre stretch along the fibre direction via ②. The form of the higher-order energy contribution, (2.71), though suitable for a comparison with analytical solutions, is less straightforward to interpret as it combines both the fibre curvature and the gradient of the fibre stretch in a coupled form. From a modelling point of view it seems thus reasonable to separate these two contributions, motivating the derivation of a higher-order energy contribution which is solely based on the fibre curvature.

In doing so, we first observe that the squared norm of the directional derivative of the spatial fibre orientation vector into the direction of the fibres, i.e. $\boldsymbol{\kappa} \cdot \boldsymbol{\kappa}$, can be expressed as a combination of the invariants I_1, I_2, I_3, I_4, I_6, I_7, I_8, I_9 by means of the Cayley-

Hamilton theorem and is hence found to be an invariant. To be specific, $\hat{I} = \boldsymbol{\kappa} \cdot \boldsymbol{\kappa}$ can be rewritten as

$$\hat{I} = \boldsymbol{\kappa} \cdot \boldsymbol{\kappa} = \boldsymbol{\kappa}_0 \cdot \boldsymbol{C}^{-1} \cdot \boldsymbol{\kappa}_0 = \boldsymbol{\kappa}_0 \cdot \left[\alpha \, \boldsymbol{I} + \beta \, \boldsymbol{C} + \gamma \, \boldsymbol{C}^2 \right] \cdot \boldsymbol{\kappa}_0 = \alpha \, I_6 + \beta \, I_7 + \gamma \, I_8 \quad (2.99)$$

with $\alpha = I_2/I_3$, $\beta = -I_1/I_3$, $\gamma = 1/I_3$. Expanding $\hat{I}$ by making use of (2.31c) and the orthogonality relation

$$\bar{\boldsymbol{a}}_t \cdot \boldsymbol{\kappa}_{\text{tru}} = 0 \tag{2.100}$$

we find that

$$\hat{I} = \left[\frac{\partial \lambda_A}{\partial \boldsymbol{X}} \cdot \boldsymbol{a}_0 \, \bar{\boldsymbol{a}}_t + \lambda_A \, \frac{\partial \bar{\boldsymbol{a}}_t}{\partial \boldsymbol{X}} \cdot \boldsymbol{a}_0 \right] \cdot \left[\frac{\partial \lambda_A}{\partial \boldsymbol{X}} \cdot \boldsymbol{a}_0 \, \bar{\boldsymbol{a}}_t + \lambda_A \, \frac{\partial \bar{\boldsymbol{a}}_t}{\partial \boldsymbol{X}} \cdot \boldsymbol{a}_0 \right] \tag{2.101a}$$

$$= \left[\frac{\partial \lambda_A}{\partial \boldsymbol{X}} \cdot \boldsymbol{a}_0 \right]^2 \bar{\boldsymbol{a}}_t \cdot \bar{\boldsymbol{a}}_t + 2 \, \lambda_A \left[\frac{\partial \lambda_A}{\partial \boldsymbol{X}} \cdot \boldsymbol{a}_0 \right] \left[\bar{\boldsymbol{a}}_t \cdot \frac{\partial \bar{\boldsymbol{a}}_t}{\partial \boldsymbol{X}} \cdot \boldsymbol{a}_0 \right]$$

$$+ \lambda_A^2 \left[\frac{\partial \bar{\boldsymbol{a}}_t}{\partial \boldsymbol{X}} \cdot \boldsymbol{a}_0 \right] \cdot \left[\frac{\partial \bar{\boldsymbol{a}}_t}{\partial \boldsymbol{X}} \cdot \boldsymbol{a}_0 \right] \tag{2.101b}$$

$$= \left[\frac{\partial \lambda_A}{\partial \boldsymbol{X}} \cdot \boldsymbol{a}_0 \right]^2 + \lambda_A^4 \, \boldsymbol{\kappa}_{\text{tru}} \cdot \boldsymbol{\kappa}_{\text{tru}} \quad . \tag{2.101c}$$

Accordingly, $\hat{I}$ includes the fibre stretch and both the directional derivative of the fibre stretch into the fibre direction as well as the fibre curvature. Considering invariant I_9 which can be rewritten according to

$$I_9 = \boldsymbol{a}_0 \cdot \boldsymbol{\kappa}_0 = \boldsymbol{a}_t \cdot \boldsymbol{\kappa} = \frac{\partial \lambda_A}{\partial \boldsymbol{X}} \cdot \boldsymbol{a}_0 \otimes \boldsymbol{a}_t \cdot \bar{\boldsymbol{a}}_t + \lambda_A \, \boldsymbol{a}_t \cdot \frac{\partial \bar{\boldsymbol{a}}_t}{\partial \boldsymbol{X}} \cdot \boldsymbol{a}_0 = \lambda_A \, \frac{\partial \lambda_A}{\partial \boldsymbol{X}} \cdot \boldsymbol{a}_0 \quad (2.102)$$

where use was again made of (2.6), (2.31c), (2.34) and (2.100), we find that, by using (2.91) and (2.98), the squared norm of the fibre curvature vector can be expressed in terms of the invariants I_4, I_9 and $\hat{I}$ according to

$$\boldsymbol{\kappa}_{\text{tru}} \cdot \boldsymbol{\kappa}_{\text{tru}} = \frac{1}{\lambda_A^2} \left[\frac{\partial \bar{\boldsymbol{a}}_t}{\partial \boldsymbol{X}} \cdot \boldsymbol{a}_0 \right]^2 = \frac{1}{I_4^2} \left[\hat{I} - \frac{I_9^2}{I_4} \right] \tag{2.103}$$

or, alternatively, making use of (2.99) in terms of the invariants presented in (2.36) as

$$\boldsymbol{\kappa}_{\text{tru}} \cdot \boldsymbol{\kappa}_{\text{tru}} = \frac{1}{I_4^2} \left[\frac{I_2}{I_3} I_6 - \frac{I_1}{I_3} I_7 + \frac{1}{I_3} I_8 - \frac{I_9^2}{I_4} \right] \quad . \tag{2.104}$$

Introducing the material parameter $c_{\boldsymbol{\kappa}_{\text{tru}}}$ we thus propose the fibre curvature-based higher-order energy contribution

$$
\begin{aligned}
W^{\boldsymbol{\kappa}_{\mathrm{tru}}}\left(I_1,\, I_2,\, I_3,\, I_4,\, I_6,\, I_7,\, I_8,\, I_9\right) &= \frac{c_{\boldsymbol{\kappa}_{\mathrm{tru}}}}{I_4^2}\left[\frac{I_2}{I_3}\,I_6 - \frac{I_1}{I_3}\,I_7 + \frac{1}{I_3}\,I_8 - \frac{I_9^2}{I_4}\right] \\
&= \frac{c_{\boldsymbol{\kappa}_{\mathrm{tru}}}}{I_4^2}\left[\hat{I} - \frac{I_9^2}{I_4}\right] \\
&= W^{\boldsymbol{\kappa}_{\mathrm{tru}}}\left(I_4,\, I_9,\, \hat{I}\right)
\end{aligned}
\tag{2.105}
$$

for the modelling of fibre-reinforced composites with non-negligible bending stiffness as this work proceeds. Moreover, the derivatives of the non-standard invariant $\hat{I}$ with respect to $\boldsymbol{C}$ and $\boldsymbol{\Lambda}$, which are required for the derivation of the respective stress and couple stress contributions, are summarised in Appendix A.8.

2.3.1.2 Specification of the stress and couple stress tensor

Based on the additive split of the energy function into three parts, we may distinguish between three different contributions to the symmetric part of the stress tensor $\boldsymbol{\sigma}^{\mathrm{sym}}$ and the deviatoric part of the couple stress tensor $\boldsymbol{m}^{\mathrm{dev}}$ which result from the evaluation of the constitutive equations (2.29) and (2.30).

Since W^{iso} and $W^{\lambda_{\mathrm{A}}}$ do not feature higher-gradient contributions, the corresponding derivatives with respect to $\boldsymbol{\Lambda}$ are found to vanish identically as do the respective contributions to the couple stress tensor. Thus, those energy contributions only influence the symmetric part of the stresses. The specific contribution of (2.90) to the stress tensor is given by

$$
\boldsymbol{\sigma}_{\mathrm{iso}}^{\mathrm{sym}} = \frac{[1 - \eta_{\mathrm{vol}}]}{J_{\boldsymbol{F}}}\left[\lambda\,\mathrm{tr}\left(\boldsymbol{E}\right)\boldsymbol{b} + \mu\left[\boldsymbol{b}^2 - \boldsymbol{b}\right]\right]
\tag{2.106}
$$

and the contribution of (2.92) reads

$$
\boldsymbol{\sigma}_{\lambda_{\mathrm{A}}}^{\mathrm{sym}} = \frac{\eta_{\mathrm{vol}}\,E_{\mathrm{fib}}}{J_{\boldsymbol{F}}}\ln\left(\sqrt{I_4}\right)\bar{\boldsymbol{a}}_t \otimes \bar{\boldsymbol{a}}_t\quad .
\tag{2.107}
$$

We take note of the fact that the energy contribution $W^{\lambda_{\mathrm{A}}}$ yields, in the spirit of the classic structural tensor approach, a rank-one stress contribution which increases in the natural logarithm of the fibre stretch.

In contrast to W^{iso} and $W^{\lambda_{\mathrm{A}}}$, the energy contribution $W^{\boldsymbol{\kappa}_{\mathrm{tru}}}$ accounts for higher-gradient contributions and thus manifests the extended character of the presented approach. For the sake of brevity, the details of the ensuing derivations of the specific contributions to the stress and to the couple stress tensor are not given in this section but presented in Appendix A.9. Evaluating (2.29) by using the derivatives of the in-

variants I_4, I_9 and $\hat{I}$ provided in Table 2.5, respectively in Appendix A.8, $\boldsymbol{\sigma}^{\mathrm{sym}}_{\boldsymbol{\kappa}_{\mathrm{tru}}}$ can be specified according to

$$\boldsymbol{\sigma}^{\mathrm{sym}}_{\boldsymbol{\kappa}_{\mathrm{tru}}} = \frac{\eta_{\mathrm{vol}}\, c_{\boldsymbol{\kappa}_{\mathrm{tru}}}}{J_{\boldsymbol{F}}} \left[\left[6\, \frac{I_9^2}{I_4^4} - 4\, \frac{\hat{I}}{I_4^3} \right]\, \boldsymbol{a}_t \otimes \boldsymbol{a}_t + \frac{2}{I_4^2}\, \boldsymbol{\kappa} \otimes \boldsymbol{\kappa} - 2\, \frac{I_9}{I_4^3}\, [\boldsymbol{\kappa} \otimes \boldsymbol{a}_t + \boldsymbol{a}_t \otimes \boldsymbol{\kappa}] \right] \quad . \tag{2.108}$$

Noting that $\boldsymbol{\kappa} \otimes \boldsymbol{\kappa}$ can be rewritten as

$$\boldsymbol{\kappa} \otimes \boldsymbol{\kappa} = \left[\frac{\partial \lambda_{\mathrm{A}}}{\partial \boldsymbol{X}} \cdot \boldsymbol{a}_0 \right]^2\, \bar{\boldsymbol{a}}_t \otimes \bar{\boldsymbol{a}}_t + \left[\frac{\partial \lambda_{\mathrm{A}}}{\partial \boldsymbol{X}} \cdot \boldsymbol{a}_0 \right]\, \lambda_{\mathrm{A}}^2\, [\boldsymbol{\kappa}_{\mathrm{tru}} \otimes \bar{\boldsymbol{a}}_t + \bar{\boldsymbol{a}}_t \otimes \boldsymbol{\kappa}_{\mathrm{tru}}] + \lambda_{\mathrm{A}}^4\, \boldsymbol{\kappa}_{\mathrm{tru}} \otimes \boldsymbol{\kappa}_{\mathrm{tru}}\,, \tag{2.109}$$

and that a representation of $\boldsymbol{\kappa} \otimes \boldsymbol{a}_t + \boldsymbol{a}_t \otimes \boldsymbol{\kappa}$ is given by

$$\boldsymbol{\kappa} \otimes \boldsymbol{a}_t + \boldsymbol{a}_t \otimes \boldsymbol{\kappa} = 2\, \left[\lambda_{\mathrm{A}}\, \frac{\partial \lambda_{\mathrm{A}}}{\partial \boldsymbol{X}} \cdot \boldsymbol{a}_0 \right]\, \bar{\boldsymbol{a}}_t \otimes \bar{\boldsymbol{a}}_t + \lambda_{\mathrm{A}}^3\, [\boldsymbol{\kappa}_{\mathrm{tru}} \otimes \bar{\boldsymbol{a}}_t + \bar{\boldsymbol{a}}_t \otimes \boldsymbol{\kappa}_{\mathrm{tru}}]\,, \tag{2.110}$$

see Appendix A.9, (2.108) may further be simplified. To this end, after inserting (2.109) and (2.110) into (2.108), after reordering terms and using relations (2.91), (2.101c) and (2.102) we finally arrive at

$$\boldsymbol{\sigma}^{\mathrm{sym}}_{\boldsymbol{\kappa}_{\mathrm{tru}}} = \frac{\eta_{\mathrm{vol}}\, c_{\boldsymbol{\kappa}_{\mathrm{tru}}}}{J_{\boldsymbol{F}}} \left[-4\, \boldsymbol{\kappa}_{\mathrm{tru}} \cdot \boldsymbol{\kappa}_{\mathrm{tru}}\, \bar{\boldsymbol{a}}_t \otimes \bar{\boldsymbol{a}}_t + 2\, \boldsymbol{\kappa}_{\mathrm{tru}} \otimes \boldsymbol{\kappa}_{\mathrm{tru}} \right] \quad . \tag{2.111}$$

Regarding the contribution of $W^{\boldsymbol{\kappa}_{\mathrm{tru}}}$ to the couple stress tensor, the evaluation of (2.30) yields

$$\left[\boldsymbol{m}^{\mathrm{dev}}_{\boldsymbol{\kappa}_{\mathrm{tru}}} \right]^{\mathrm{t}} = \frac{8}{3}\, \frac{\eta_{\mathrm{vol}}\, c_{\boldsymbol{\kappa}_{\mathrm{tru}}}}{J_{\boldsymbol{F}}}\, \frac{1}{I_4^2}\, \boldsymbol{\epsilon}_t : [\boldsymbol{a}_t \otimes \boldsymbol{\kappa} \otimes \boldsymbol{a}_t] \quad , \tag{2.112}$$

where (2.31a), (2.169) and Table 2.5 were used along with the skew-symmetry of the Levi-Civita tensor with respect to the last two indices. By using (2.31c) and (2.98), (2.112) may further be simplified as

$$\boldsymbol{m}^{\mathrm{dev}}_{\boldsymbol{\kappa}_{\mathrm{tru}}} = \frac{8}{3}\, \frac{\eta_{\mathrm{vol}}\, c_{\boldsymbol{\kappa}_{\mathrm{tru}}}}{J_{\boldsymbol{F}}}\, \bar{\boldsymbol{a}}_t \otimes [\bar{\boldsymbol{a}}_t \times \boldsymbol{\kappa}_{\mathrm{tru}}] \quad . \tag{2.113}$$

With regard to (2.111) we observe that, for a non-vanishing fibre curvature, the stress contribution $\boldsymbol{\sigma}^{\mathrm{sym}}_{\boldsymbol{\kappa}_{\mathrm{tru}}}$ is a rank-two tensor with its principal axes being aligned with the fibre direction vector $\bar{\boldsymbol{a}}_t$ and the normalised fibre curvature vector $\bar{\boldsymbol{\kappa}}_{\mathrm{tru}} = \boldsymbol{\kappa}_{\mathrm{tru}}/\|\boldsymbol{\kappa}_{\mathrm{tru}}\|$ which is perpendicular to $\bar{\boldsymbol{a}}_t$. For $c_{\boldsymbol{\kappa}_{\mathrm{tru}}} > 0$, the corresponding eigenvalue in $\bar{\boldsymbol{a}}_t$-direction turns out to be negative, whereas the one in $\bar{\boldsymbol{\kappa}}_{\mathrm{tru}}$-direction is found to be positive. This indicates a compressive load state in the direction of the fibre while tensile stresses are observed
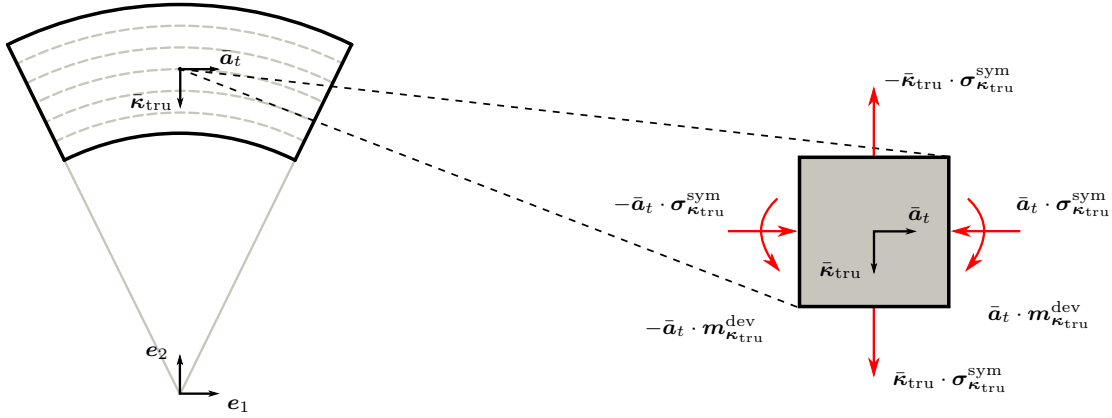
Figure 2.13: Contributions $\boldsymbol{\sigma}_{\boldsymbol{\kappa}_{\text{tru}}}^{\text{sym}}$ and $\boldsymbol{m}_{\boldsymbol{\kappa}_{\text{tru}}}^{\text{dev}}$ to the symmetric part of the stresses, respectively the deviatoric part of the couple stresses, depicted with respect to the local coordinate system spanned by the normalised fibre direction vector $\bar{\boldsymbol{a}}_t$ and the normalised fibre curvature vector $\bar{\boldsymbol{\kappa}}_{\text{tru}} = \boldsymbol{\kappa}_{\text{tru}}/\|\boldsymbol{\kappa}_{\text{tru}}\|$.

in the direction of $\bar{\boldsymbol{\kappa}}_{\text{tru}}$. However, both the tensile as well as the compressive stresses are determined by the quadratic fibre curvature measure $\|\boldsymbol{\kappa}_{\text{tru}}\|^2$ and by the inverse determinant of the deformation gradient. When analysing (2.113), the couple stress tensor $\boldsymbol{m}_{\boldsymbol{\kappa}_{\text{tru}}}^{\text{dev}}$ is found to be a rank-one tensor based on the dyadic product of the fibre direction $\bar{\boldsymbol{a}}_t$ and of the vector perpendicular to the plane spanned by the fibre direction $\bar{\boldsymbol{a}}_t$ and by the curvature vector $\bar{\boldsymbol{\kappa}}_{\text{tru}}$. Thus, a couple around the axis $\bar{\boldsymbol{a}}_t \times \bar{\boldsymbol{\kappa}}_{\text{tru}}$ acts on the material surface transverse to $\bar{\boldsymbol{a}}_t$ which is, in addition to the material parameter, scaled by the fibre curvature and by the determinant of the deformation gradient. Furthermore, the couple stress vector vanishes identically on the surfaces with outward normal $\bar{\boldsymbol{\kappa}}_{\text{tru}}$, respectively $\bar{\boldsymbol{a}}_t \times \bar{\boldsymbol{\kappa}}_{\text{tru}}$. Thus, an energy contribution of the form (2.105) results into well-interpretable contributions to the stress and couple stress tensor which are further illustrated in Figure 2.13 for an infinitesimal volume element.

Remark 2.4 (Energy contribution based on the fibre stretch gradient) *The presented framework for the modelling of fibre-reinforced composites with fibres possessing fibre-bending stiffness is based on the additional energy contribution (2.105) which can be associated with the fibre curvature. However, it is also possible to express the spatial and the referential gradient of the fibre stretch in terms of invariants. To this end, making use of (2.91) and (2.102) we observe that*

$$\frac{I_9^2}{I_4^2} = \frac{\left[\lambda_{\text{A}} \dfrac{\partial \lambda_{\text{A}}}{\partial \boldsymbol{X}} \cdot \boldsymbol{a}_0\right]^2}{\lambda_{\text{A}}^4} = \left[\frac{\partial \lambda_{\text{A}}}{\partial \boldsymbol{x}} \cdot \bar{\boldsymbol{a}}_t\right]^2 \tag{2.114}$$

is a quadratic measure in the spatial gradient of the fibre stretch. Similarly, a quadratic measure in the referential gradient of the fibre stretch is given by

$$\frac{I_9^2}{I_4} = \frac{\left[\lambda_A \dfrac{\partial \lambda_A}{\partial \boldsymbol{X}} \cdot \boldsymbol{a}_0\right]^2}{\lambda_A^2} = \left[\frac{\partial \lambda_A}{\partial \boldsymbol{X}} \cdot \boldsymbol{a}_0\right]^2 \quad . \tag{2.115}$$

The relations (2.114) and (2.115) motivate contributions to the stored energy function of the form

$$W^{\partial_{\boldsymbol{x}} \lambda_A} = c_{\partial_{\boldsymbol{x}} \lambda_A} \, \frac{I_9^2}{I_4^2} \quad , \tag{2.116} \qquad\qquad W^{\partial_{\boldsymbol{X}} \lambda_A} = c_{\partial_{\boldsymbol{X}} \lambda_A} \, \frac{I_9^2}{I_4} \quad , \tag{2.117}$$

with material parameters $c_{\partial_{\boldsymbol{x}} \lambda_A}$ and $c_{\partial_{\boldsymbol{X}} \lambda_A}$. Evaluating the constitutive equations (2.29) and (2.30) by using (2.31a), (2.91), (2.102), (2.110) and Table 2.5 yields the contributions to the symmetric part of the stresses

$$\boldsymbol{\sigma}_{\partial_{\boldsymbol{x}} \lambda_A}^{\mathrm{sym}} = \frac{\eta_{\mathrm{vol}} \, c_{\partial_{\boldsymbol{x}} \lambda_A}}{J_{\boldsymbol{F}}} \left[2\,\lambda_A \left[\frac{\partial \lambda_A}{\partial \boldsymbol{x}} \cdot \bar{\boldsymbol{a}}_t\right] \left[\boldsymbol{\kappa}_{\mathrm{tru}} \otimes \bar{\boldsymbol{a}}_t + \bar{\boldsymbol{a}}_t \otimes \boldsymbol{\kappa}_{\mathrm{tru}}\right] \right] \tag{2.118a}$$

$$= \frac{\eta_{\mathrm{vol}} \, c_{\partial_{\boldsymbol{x}} \lambda_A}}{J_{\boldsymbol{F}}} \left[\quad 2 \left[\frac{\partial \lambda_A}{\partial \boldsymbol{X}} \cdot \boldsymbol{a}_0\right] \left[\boldsymbol{\kappa}_{\mathrm{tru}} \otimes \bar{\boldsymbol{a}}_t + \bar{\boldsymbol{a}}_t \otimes \boldsymbol{\kappa}_{\mathrm{tru}}\right] \right] \tag{2.118b}$$

$$\boldsymbol{\sigma}_{\partial_{\boldsymbol{X}} \lambda_A}^{\mathrm{sym}} = \frac{\eta_{\mathrm{vol}} \, c_{\partial_{\boldsymbol{X}} \lambda_A}}{J_{\boldsymbol{F}}} \left[2\,\lambda_A^2 \left[\frac{\partial \lambda_A}{\partial \boldsymbol{X}} \cdot \boldsymbol{a}_0\right] \left[\boldsymbol{\kappa}_{\mathrm{tru}} \otimes \bar{\boldsymbol{a}}_t + \bar{\boldsymbol{a}}_t \otimes \boldsymbol{\kappa}_{\mathrm{tru}}\right] + 2 \left[\frac{\partial \lambda_A}{\partial \boldsymbol{X}} \cdot \boldsymbol{a}_0\right]^2 \bar{\boldsymbol{a}}_t \otimes \bar{\boldsymbol{a}}_t \right]$$
$$\tag{2.119}$$

and the ones to the deviatoric part of the couple stresses

$$\left[\boldsymbol{m}_{\partial_{\boldsymbol{x}} \lambda_A}^{\mathrm{dev}}\right]^{\mathrm{t}} = \boldsymbol{0} \quad , \tag{2.120}$$

$$\left[\boldsymbol{m}_{\partial_{\boldsymbol{X}} \lambda_A}^{\mathrm{dev}}\right]^{\mathrm{t}} = \boldsymbol{0} \quad , \tag{2.121}$$

see Appendix A.9 for details of the derivations. Furthermore note that, in accordance with (2.89), the energy contributions (2.116) and (2.117) are weighted by the fibre volume fraction η_{vol}.

With regard to (2.118a) it is observed that an energy contribution of the form (2.116) results into a symmetrised rank-one stress contribution which is influenced by the fibre stretch, the spatial gradient of the fibre stretch as well as the fibre curvature. In addition, taking into account (2.100), it is noted that the resulting stress state, expressed in a local coordinate system defined by the spatial fibre direction vector $\bar{\boldsymbol{a}}_t$ and normalised fibre curvature vector $\bar{\boldsymbol{\kappa}}_{\mathrm{tru}}$, is of pure shear type. Furthermore, we find that the energy
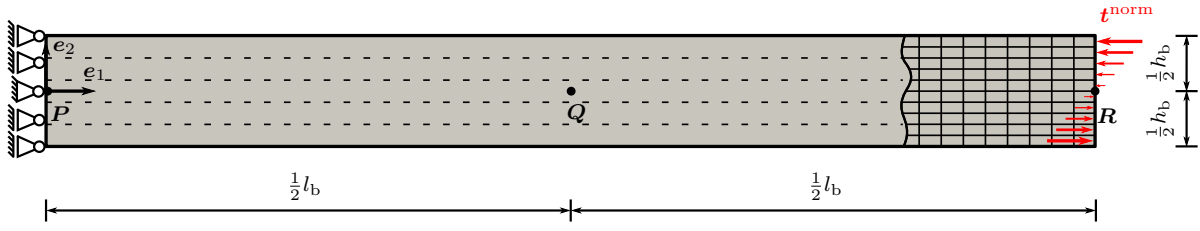
Figure 2.14: Bending of a fibre-reinforced beam of length l_b and height h_b. The fibres, indicated by the dashed lines, are assumed to be aligned with the beam's axis in the reference configuration. The load is applied in terms of follower forces at the right boundary which act normal to the beam's surface and result into a moment.

contribution (2.117) *on the one hand results into the same symmetrised rank-one stress contribution as already observed for the energy contribution* (2.116), *except for a factor of λ_A^2. On the other hand, an additional rank-one stress contribution is observed which scales in the squared referential fibre stretch gradient.*

2.3.2 Representative simulation results

Although real composites have misoriented fibres of varying shape and size, the modelling of composites with aligned fibres is usually taken into account as a starting point for the modelling of more realistic situations, [140]. This further motivates models which assume uniform fibre properties [140], an assumption which will also be applied in this contribution, though the extension to spatially non-uniform material parameters and a spatially varying fibre orientation is possible in the proposed framework without any major adjustments.

To start with, we will focus on the bending problem of a beam with length l_b, height h_b and unit width $w_\mathrm{b} = 1\,\mu m$ as schematically depicted in Figure 2.14. The composite beam is assumed to consist of an isotropic nickel matrix which is reinforced with $\eta_\mathrm{vol} = 10\%$ of multi-walled carbon nanotubes that are aligned with the beam's axis in the reference configuration as indicated by the dashed lines. With the Young's modulus and the Poisson's ratio of the matrix, respectively the Young's modulus of the fibres taking values of $E_\mathrm{mat} \approx 180\,\mathrm{mN/\mu m^2}$, $\nu_\mathrm{mat} \approx 0.3$ and $E_\mathrm{fib} \approx 800\,\mathrm{mN/\mu m^2}$, [7], the Lamé-type parameters used in (2.90) are approximated according to $\lambda_\mathrm{mat} = \nu_\mathrm{mat}\,E_\mathrm{mat}/\left[\left[1 + \nu_\mathrm{mat}\right]\left[1 - 2\,\nu_\mathrm{mat}\right]\right] \approx 103.85\,\mathrm{mN/\mu m^2}$ and $\mu_\mathrm{mat} = E_\mathrm{mat}/\left[2\left[1 + \nu_\mathrm{mat}\right]\right] \approx 69.23\,\mathrm{mN/\mu m^2}$, such that the Young's modulus and the Poisson's ratio may be reproduced for infinitesimal deformations. It is stated here that we do not intend to precisely reproduce either the load-displacement behaviour of nickel or of multi-walled carbon nanotubes with the simple form of the energy function given in (2.89). Rather, the objective of the upcoming analysis is a basic understanding of the properties of the fibre curvature-based energy contribution W^{κ_tru}. The aim is also to show that the presented higher-gradient modelling approach allows us to incorporate the experimentally observed size-dependent bending behaviour presented in

64

Section 1.1.1. It is moreover pointed out that the simulation results to be presented are calculated subject to the assumption of a plane strain deformation state.

Regarding the boundary conditions, the horizontal displacement of all nodes on the left boundary will be fixed while the vertical displacement is only prescribed to be zero for the central node of the left boundary. Furthermore, the load will be applied at the right boundary in terms of follower forces $\boldsymbol{t}^{\text{norm},0}$ which act normal to the beam's surface and are defined per unit area of the reference configuration, see also Appendix A.10. The load is chosen to linearly increase from the bottom to the top of the beam with $\|\boldsymbol{t}^{\text{norm},0}\left(X_1 = l_{\text{b}}, X_2 = -0.5\,h_{\text{b}}\right)\| = \|\boldsymbol{t}^{\text{norm},0}\left(X_1 = l_{\text{b}}, X_2 = 0.5\,h_{\text{b}}\right)\|$, resembling the stress distribution which is predicted by the classic Euler-Bernoulli beam theory for pure bending of an idealised beam, see Figure 2.14. From a numerical point of view, eight-node serendipity-type elements are used for the discretisation of the displacement field, while linear Lagrangian-type elements are used for both the relaxed deformation gradient field as well as the skew-symmetric stress field.

2.3.2.1 Influence of the material parameter $c_{\boldsymbol{\kappa}_{\text{tru}}}$

To analyse the influence of the material parameter $c_{\boldsymbol{\kappa}_{\text{tru}}}$, we will focus on a beam with length $l_{\text{b}} = 40\,\mu\text{m}$ and height $h_{\text{b}} = 1\,\mu\text{m}$ which is discretised by means of 60 elements in length and 10 elements in height direction. The load is linearly increased over 13 time steps with a maximal value of $\|\boldsymbol{t}_{\max}^{\text{norm},0}\| = 13\,\text{mN}/\mu\text{m}^2$ prescribed on the top and bottom element of the right boundary, a load value of $0.8\,\|\boldsymbol{t}_{\max}^{\text{norm},0}\|$ on the second element from the top respectively the second element from the bottom and so forth, see Figure 2.14.

To assess the influence of the bending energy contribution $W^{\boldsymbol{\kappa}_{\text{tru}}}$ on the deformation, we will make use of an equivalent process and approximate the overall bending modulus. In [121] the exact solution for the pure (finite) bending of a cantilever beam is given by a circular curve of radius $r_{\text{ben}} = EI/M_{\text{ben}}$, with EI being the bending stiffness and M_{ben} denoting a concentrated end moment. Making use of the latter equation, an equivalent bending modulus may be defined as

$$E_{\text{eq}} = \frac{r_{\text{ben}}\,M_{\text{ben}}}{I} \quad . \tag{2.122}$$

To approximate the bending radius r_{ben}, a circle is fitted through three nodes which are positioned at the middle of the left boundary, the middle of the right boundary and at the centre of the beam. These nodes are highlighted in Figure 2.14 by black-coloured dots, and the corresponding formulas for the centre and the radius of the circle are provided in Appendix A.11. Moreover, the deformed configurations of the beams which are reinforced with fibres of varying bending stiffness are provided in Figure 2.21 alongside the circles which are used for the approximation of the bending radius. It is observed that the circular deformation pattern is matched well at the load levels investigated, however, we take note of the fact that no perfect circular deformation pattern is observable for significantly higher loadings. One reason for the latter observation is given

(a) Deformation of fibre-reinforced beams in dependence of the fibre-bending stiffness parameter $c_{\kappa_{\mathrm{tru}}}$.

(b) Effective bending modulus in dependence of the fibre-bending stiffness parameter $c_{\kappa_{\mathrm{tru}}}$.

(c) Horizontal displacement u_1 as a function of the applied moment.

(d) Vertical displacement u_2 as a function of the applied moment.
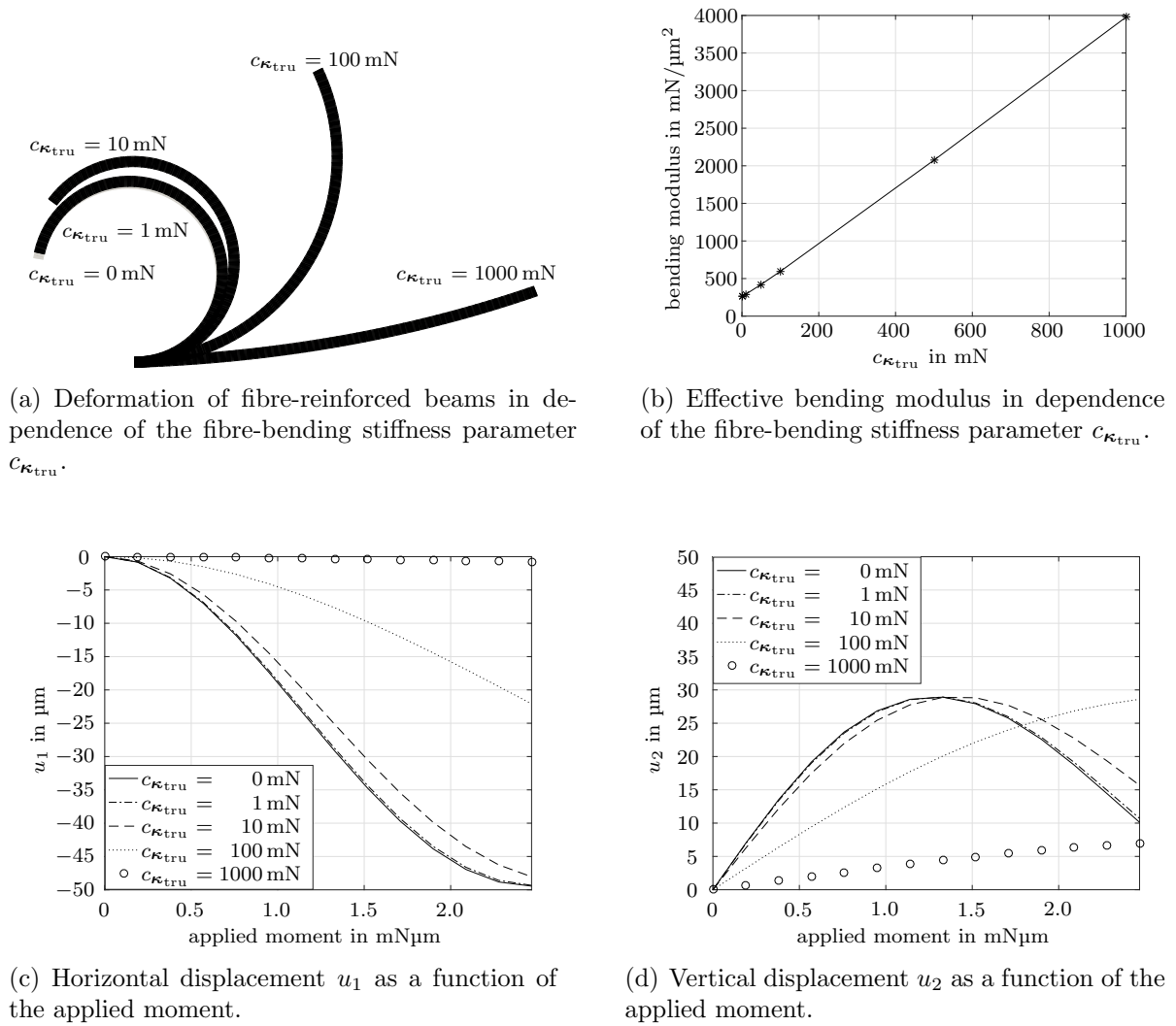
Figure 2.15: Analysis of the deformation of fibre-reinforced beams of length $l_{\mathrm{b}} = 40\,\mu\mathrm{m}$ and height $h_{\mathrm{b}} = 1\,\mu\mathrm{m}$ in dependence of the fibre-bending stiffness parameter $c_{\kappa_{\mathrm{tru}}}$. In addition, the load-displacement-diagrams for the node which is centred on the right surface (cf. Figure 2.14) are provided as a function of the applied moment.

by the tension-compression asymmetry of the energy contributions (2.90) and (2.92). The concentrated end moment M_{ben} is approximated based on the discrete nodal forces and the distance of the respective nodes, positioned at the right boundary, to the node positioned at the middle of the right boundary. We note that the distance is measured in the deformed configuration of the beam. Furthermore, the area moment of inertia is approximated by the area moment of inertia in the reference configuration according to

$$
I \approx \frac{w_{\mathrm{b}}\,h_{\mathrm{b}}^3}{12} = \frac{1}{12}\,\mathrm{\mu m}^4 \quad , \tag{2.123}
$$

neglecting a change of the beam height with the deformation and thus assuming the area moment of inertia to be constant along the beam axis.

In Figure 2.15(a), the deformed configurations of fibre-reinforced beams are provided for various values of material parameter $c_{\boldsymbol{\kappa}_{\mathrm{tru}}}$ in terms of their meshed spatial configurations. In addition, the spatial configuration of a fibre-reinforced beam with negligible bending stiffness is provided in terms of the grey-coloured surface, serving as a reference. It is revealed that the bending radius increases with increasing values of material parameter $c_{\boldsymbol{\kappa}_{\mathrm{tru}}}$ – in other words, the curvature of the fibres which is inversely proportional to the bending radius is reduced. However, the circular shape of the deformed configuration is well maintained, cf. Figure 2.21. The equivalent bending modulus calculated by using (2.122) is provided in Figure 2.15(b) as a function of $c_{\boldsymbol{\kappa}_{\mathrm{tru}}}$ with a, in good approximation, linear relation being revealed. In addition, the corresponding moment-displacement curves for the node which is positioned at the centre of the right boundary are provided in Figures 2.15(c) and 2.15(d).

Adjusting material parameter $c_{\boldsymbol{\kappa}_{\mathrm{tru}}}$ may thus allow us to account for fibres of different bending stiffness which, however, may show the same properties with regard to tension and compression tests, cf. Remark 2.5. With regard to the experimental findings discussed in Section 1.1.1 it seems furthermore reasonable to assume that $c_{\boldsymbol{\kappa}_{\mathrm{tru}}}$ should, apart from the fibre material, also depend on the fibre geometry, e.g. in terms of the fibre diameter, cf. Figure 1.2.

2.3.2.2 Size effects

This section addresses the size-dependent constitutive response which is induced into the model by taking into account higher gradients of the placement function as additional arguments of the energy function. To this end, we will concentrate on the boundary value problem previously discussed in Section 2.3.2.1. However, material parameter $c_{\boldsymbol{\kappa}_{\mathrm{tru}}} = 1000\,\mathrm{mN}$ will be kept constant in the upcoming analysis and the geometrical dimensions in terms of the beam height will be varied. To be specific, beams of length $40\,\mathrm{\mu m}$, width $1\,\mathrm{\mu m}$ and height $1\,\mathrm{\mu m}$, $2\,\mathrm{\mu m}$ and $4\,\mathrm{\mu m}$ are taken into account which are discretised by 60×10 elements in length and height direction respectively. The displacement of the beams is constrained at the left boundary and the load is applied on the right boundary in terms of follower forces acting normal to the beam's surface. The

(a) Deformation of fibre-reinforced beams for $c_{\kappa_{\mathrm{tru}}} = 0\,\mathrm{mN}$.

(b) Deformation of fibre-reinforced beams for $c_{\kappa_{\mathrm{tru}}} = 1000\,\mathrm{mN}$.

(c) Bending modulus as a function of the beam height.

(d) Beam of height $h_{\mathrm{b}} = 1\,\mathrm{\mu m}$.

(e) Beam of height $h_{\mathrm{b}} = 2\,\mathrm{\mu m}$.

(f) Beam of height $h_{\mathrm{b}} = 4\,\mathrm{\mu m}$.
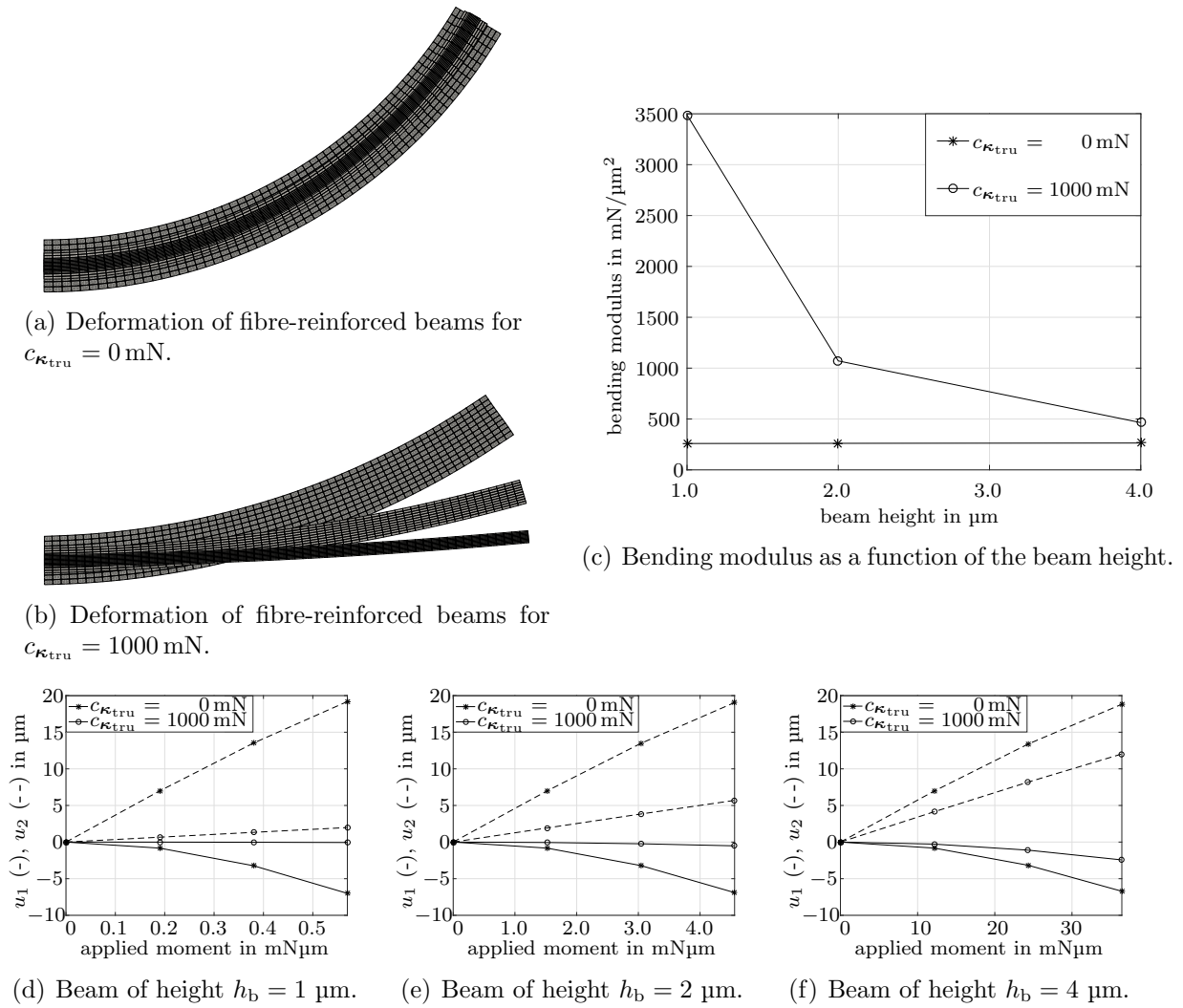
Figure 2.16: Analysis of the deformation and the bending modulus of composite beams which are reinforced with perfectly flexible fibres and fibres resisting bending, in dependence of the beam heights. In addition, the load-displacement-diagrams for the node which is centred on the right surface (cf. Figure 2.14) are provided in terms of the horizontal displacement u_1 and vertical displacement u_2 as a function of the applied moment.

maximal load to be prescribed at the top and the bottom element of the beam of height $1\,\mu\mathrm{m}$ is chosen to take a value of $\|\boldsymbol{t}_{\max}^{\mathrm{norm},0}\| = 3\,\mathrm{mN/\mu m^2}$. Using (2.122) and (2.123) it is observed that, for the resulting bending radius to be approximately the same for the beams of different heights, $\|\boldsymbol{t}_{\max}^{\mathrm{norm},0}\|$ is to be chosen proportional to h_{b}. For this reason, the maximal loadings of $\|\boldsymbol{t}_{\max}^{\mathrm{norm},0}\| = 6\,\mathrm{mN/\mu m^2}$ and $\|\boldsymbol{t}_{\max}^{\mathrm{norm},0}\| = 12\,\mathrm{mN/\mu m^2}$ are applied to the beams of heights $2\,\mu\mathrm{m}$, respectively $4\,\mu\mathrm{m}$.

The spatial configurations of fibre-reinforced beams of different heights assuming negligible fibre-bending stiffness are provided in Figure 2.16(a), those of fibre-reinforced beams with fibres resistant in bending are depicted in Figure 2.16(b). First, it is observed that the bending radius is nearly the same for the beams which are reinforced with perfectly flexible fibres, as the load is chosen as described before. On the contrary, a considerable difference in the bending radius is observable for the beams reinforced with fibres which are assumed to resist bending. Comparing the bending radius of two beams of the same height, it is revealed that the influence of the fibre-bending stiffness on the deformation is pronounced for the thinnest beam but noticeably decreases with increasing beam height. Since the observed deformation pattern is nearly circular, as shown in Figure 2.21, (2.122) may be used again to approximate the equivalent bending modulus. For the beams which are reinforced with perfectly flexible fibres, the bending modulus thus calculated is almost independent of the beam height ($E_{\mathrm{eq}} \approx 261\,\mathrm{mN/\mu m^2}$), Figure 2.16(c), and only slightly higher than the expected Young's modulus in the direction of the fibres predicted by the linearised theory, i.e. $E_{\mathrm{com}} \approx [1 - \eta_{\mathrm{vol}}]\,E_{\mathrm{mat}} + \eta_{\mathrm{vol}}\,E_{\mathrm{fib}} \approx 242\,\mathrm{mN/\mu m^2}$. It is further noted that the results provided in Figure 2.16(c) only slightly change for the different loadings analysed. Thus, the influence of the non-linear material model is limited for the loadings analysed and found to be significantly smaller than the influence of the bending energy contribution. As becomes evident, the equivalent bending modulus significantly increases when accounting for the fibre-bending stiffness. This effect, however, turns out to depend on the size of the beam and becomes more pronounced with decreasing beam height. The latter observation is further underlined by the (differences in the) moment-displacement curves for the node which is positioned at the centre of the right boundary provided in Figures 2.16(d-f).

The results presented in this section indicate that the observable influence of the fibre-bending stiffness may depend on the problem dimensions. When keeping the fibre properties, i.e. the material and the geometry of the fibres as well as the fibre volume fraction constant, a more considerable influence is to be expected for smaller problem dimensions. If, and to which extent this effect can be observed in real materials requires further experimental analysis.

2.3.2.3 Convergence behaviour on mesh refinement

With regard to bending dominated boundary value problems, the analysis of the influence of the finite element discretisation is of particular importance. In this section we will
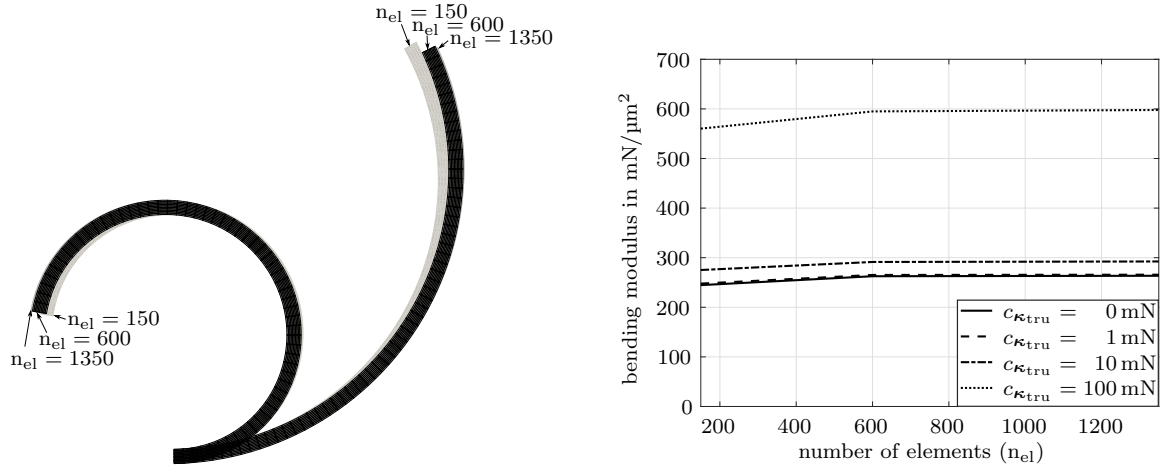
(a) Deformation behaviour of fibre-reinforced beams with $c_{\kappa_{\mathrm{tru}}} = 0\,\mathrm{mN}$ and $c_{\kappa_{\mathrm{tru}}} = 100\,\mathrm{mN}$ for different mesh sizes.

(b) Predicted bending modulus of fibre-reinforced beams in dependence of the finite element mesh size and the material parameter.

Figure 2.17: Analysis of the deformation and bending modulus for fibre-reinforced composite beams for varying values of the material parameter $c_{\kappa_{\mathrm{tru}}}$ with regard to the finite element mesh size. For the beam with length $40\,\mu\mathrm{m}$ and height $1\,\mu\mathrm{m}$, finite element meshes with $30/60/90$ elements in the length direction and $5/10/15$ elements over the beam height are considered. The respective curve for $c_{\kappa_{\mathrm{tru}}} = 1000\,\mathrm{mN}$ is not depicted in Figure 2.17(b) for the sake of clarity, however the same tendency is observed.

exemplarily focus again on the boundary value problem presented in Section 2.3.2.1 and study the equivalent bending modulus for three different mesh densities. In particular, the beam of length $l_{\mathrm{b}} = 40\,\mu\mathrm{m}$ and height $h_{\mathrm{b}} = 1\,\mu\mathrm{m}$ is discretised by 30×5, 60×10 and 90×15 elements in length, respectively height direction, resulting in a total number of $\mathrm{n_{el}} = 150$, $\mathrm{n_{el}} = 600$ and $\mathrm{n_{el}} = 1350$ elements. The load is applied at the right boundary in terms of follower forces acting normal to the beam's surface, cf. Figure 2.14. Regarding the coarse mesh ($\mathrm{n_{el}} = 150$), a maximal load value of $\|\boldsymbol{t}_{\max}^{\mathrm{norm},0}\| = 12.35\,\mathrm{mN}/\mu\mathrm{m}^2$ is prescribed at the top and bottom element of the right boundary, while a maximal load value of $0.5\,\|\boldsymbol{t}_{\max}^{\mathrm{norm},0}\|$ is applied to the second element from the top and bottom. For the applied load to be comparable for the different discretisations, the same traction load is applied to the same area of the beam, resulting in a load value of $\|\boldsymbol{t}_{\max}^{\mathrm{norm},0}\|$ to be applied to the first two, respectively the first three elements, from the top and bottom for the standard ($\mathrm{n_{el}} = 600$), and for the fine discretisation ($\mathrm{n_{el}} = 1350$) respectively.

In Figure 2.17(a), the spatial configurations for the final load step are exemplarily depicted for a fibre-reinforced beam with $c_{\kappa_{\mathrm{tru}}} = 0\,\mathrm{mN}$ and a fibre-reinforced beam with $c_{\kappa_{\mathrm{tru}}} = 100\,\mathrm{mN}$ for the three different mesh densities. For both the reference material model which assumes perfectly flexible fibres and the enhanced approach which accounts for the fibre-bending stiffness, the same tendency is observable: the overall stiffness of the cantilever beam increases with an increase in the number of elements in a saturation-

type manner such that convergence is indicated. Whereas the observed difference in the stiffness is noticeable when comparing the coarse and the standard discretisation, it is found to be comparably small for the standard and the fine discretisation. Making use of (2.122), subject to the assumptions stated in Section 2.3.2.1, the equivalent bending stiffness E_{eq} is provided in Figure 2.17(b) as a function of the mesh density for different values of the material parameter $c_{\boldsymbol{\kappa}_{\text{tru}}}$. In accordance with the observations described before, it turns out that the difference in the predicted bending modulus is small when comparing the standard and the fine discretisation. Finally, we take note of the fact that the influence of the mesh density on the deformation, respectively on the bending modulus, is small compared with the influence of the material parameter $c_{\boldsymbol{\kappa}_{\text{tru}}}$. The results presented in Section 2.3.2.1 and Section 2.3.2.2 are based on a finite element mesh with $n_{\text{el}} = 600$, since the deviation of the results compared with a finer discretisation with $n_{\text{el}} = 1350$ seems sufficiently small.

Remark 2.5 (Inhomogeneous tension tests) *In Section 2.3.1.2, the constitutive equations for the stress and couple stress tensor have been specified. We are especially interested in the contributions which correspond to the higher-order energy part, i.e. (2.111) and (2.113), in the following analysis. These are found to vanish for homogeneous tension tests and for inhomogeneous tension tests with the fibres being aligned with the elongation direction, since the fibre curvature vector $\boldsymbol{\kappa}_{\text{tru}}$ is zero for both deformation states. This is of special interest from a modelling point of view since it allows us to identify the material parameters of the presented model which are related to the tension and the compression stiffness of the composite in a first step, neglecting a possible influence of the fibre-bending stiffness. The fibre-bending stiffness may then be adjusted in a second step by carrying out bending tests for example.*

In the experiments reviewed in Section 1.1.1, the Young's modulus or rather the bending modulus is measured implicitly making use of beam theories, with a size effect being reported in some of the experiments. On the other hand, experimental data from both tension and bending tests is used in [70], and it is found that the Young's modulus which is calculated based on the tension tests is independent of the beam dimensions. However, a size effect which is attributed to the action of strain gradient effects is observed for the Young's modulus calculated based on the bending tests. These observations raise the question as to whether effects which may be related to some higher-gradient effects, e.g. the curvature of the fibre-like structures, become important in the experiments mentioned in Section 1.1.1 and certainly require further investigation.

2.3.3 Summary

Motivated by the various extended beam theories which have been presented in the literature for the simulation of beam-like structural components on the nanoscale and the experimental observations on one-dimensional nanomaterials, Section 2.3 focused on

the elaboration of a fibre curvature-based, higher-gradient energy contribution for the modelling of fibre-reinforced (nano-)composites.

The non-standard invariants in the form presented in [130] partly include combinations of the fibre orientation, the fibre stretch, the fibre stretch gradient, the fibre curvature and the deformation in terms of the left, respectively right Cauchy-Green tensor. Aspiring to separate pure bending and stretch gradient contributions, the derivation of suitable (combinations of) invariants which allow for a direct physical interpretation was pursued. It was shown that one combination of the original invariants may be interpreted as the fibre curvature. The evaluation of the constitutive equations for an energy function based on this combination of invariants and one additional material parameter, was furthermore found to be particularly useful since it results, after some algebraic manipulations, into well-interpretable contributions to the stress- and the couple stress tensor respectively. It was furthermore revealed that these contributions vanish for homogeneous tension tests and for inhomogeneous tension tests with the fibres being aligned with the elongation direction. This observation is of special interest with regard to the process of parameter identification and raised some questions on the interpretation of the experiments discussed in Section 1.1.1.

Assuming an additive split of the energy function into three contributions which correspond to the deformation of the bulk, the elongation of the fibres and the fibre curvature, representative boundary value problems were analysed in a next step, with a focus on the influence of the fibre curvature energy contribution. To be specific, the bending of a cantilever beam was analysed and an equivalent bending modulus was calculated based on the solution for the pure (finite) bending of cantilever beams provided in [121]. For this boundary value problem, the material parameter $c_{\kappa_{\mathrm{tru}}}$ which may take the interpretation of the fibre-bending stiffness was varied in a first step, with a stiffer overall response being observed for increasing values of the material parameter. Although the activation of the fibre curvature energy part resulted in a pronounced stiffening of the beam, the resulting deformation pattern was still found to be circular. Bearing the experiments on fibre-like structures on the nanoscale in mind, the material parameter $c_{\kappa_{\mathrm{tru}}}$ may thus be used to account for a possible influence of different fibre diameters – especially if the material parameters which govern the elastic response under extension and compression are assumed to be invariant of the problem dimensions. In a second step, the fibre-bending stiffness was assumed to be constant and the dimensions of the composite beam were varied. Evaluating the deformation and the overall equivalent bending modulus, it was shown that the influence of the fibre-bending energy contribution increases with decreasing problem dimensions.

On the whole, the findings suggest that the (size-dependent) properties of one-dimensional nanomaterials when used as reinforcements in nanocomposites may be modelled by taking into account the fibre curvature. With regard to future research, experiments on nanocomposites are now required in order to analyse whether the size-dependent material behaviour which can be observed for individual nanotubes and nanorods can also be observed for micro- and nanoscale devices made up of nanocompos-

ites. Regarding the latter, it would especially be of interest to compare the mechanical response of composites reinforced with nanotubes, respectively nanorods, of different diameters. If it is assumed that the additionally introduced fibre-bending energy contribution is related to the fibre diameter, these experiments could serve as a first step towards the identification of the material parameters and finally allow for a more accurate simulation of composites on the nanoscale.

A Appendix

A.1 Derivation of the algorithmic tangent stiffness

In this appendix, the contributions to the tangent stiffness matrix (2.65), which result from the linearisation of the discretised system of the coupled partial differential equations, (2.59)–(2.61), and which are required for the iterative (gradient-based) solution procedure presented in Section 2.1.3.4, as derived in [10], are given. Note that the derivatives of the (symmetric part of the) stress tensor and those of the (deviatoric part of the) couple stress tensor which are required for the evaluation of the tangent stiffness contributions are not inserted in the ensuing equations for the sake of brevity but are provided in Appendix A.2.

Balance of linear momentum

$$
\begin{aligned}
\mathbf{K}^{\varphi\varphi} = \overset{n_{\mathrm{el}}}{\underset{e=1}{\mathbf{A}}} \int_{\mathcal{B}_0^e} & \nabla_{\boldsymbol{X}} N_A^{\varphi} \cdot \boldsymbol{F}^{-1} \cdot \frac{\partial \boldsymbol{\sigma}^{\mathrm{sym}}}{\partial \boldsymbol{F}} \cdot \quad \nabla_{\boldsymbol{X}} N_D^{\varphi} \, J_{\boldsymbol{F}} \\
& -\nabla_{\boldsymbol{X}} N_D^{\varphi} \cdot \boldsymbol{F}^{-1} \cdot \boldsymbol{\sigma} \otimes \boldsymbol{F}^{-\mathrm{t}} \cdot \quad \nabla_{\boldsymbol{X}} N_A^{\varphi} \, J_{\boldsymbol{F}} \\
& +\nabla_{\boldsymbol{X}} N_A^{\varphi} \cdot \boldsymbol{F}^{-1} \cdot \boldsymbol{\sigma} \otimes \boldsymbol{F}^{-\mathrm{t}} \cdot \quad \nabla_{\boldsymbol{X}} N_D^{\varphi} \, J_{\boldsymbol{F}} \, \mathrm{d}V_e
\end{aligned}
\tag{2.124}
$$

$$
\mathbf{K}^{\varphi\sigma} = \overset{n_{\mathrm{el}}}{\underset{e=1}{\mathbf{A}}} \int_{\mathcal{B}_0^e} \nabla_{\boldsymbol{X}} N_A^{\varphi} \cdot \boldsymbol{F}^{-1} \cdot \mathbf{I} \, J_{\boldsymbol{F}} \, N_E^{\sigma} \, \mathrm{d}V_e
\tag{2.125}
$$

$$
\mathbf{K}^{\varphi\Theta} = \overset{n_{\mathrm{el}}}{\underset{e=1}{\mathbf{A}}} \int_{\mathcal{B}_0^e} \nabla_{\boldsymbol{X}} N_A^{\varphi} \cdot \boldsymbol{F}^{-1} \cdot \frac{\partial \boldsymbol{\sigma}^{\mathrm{sym}}}{\partial \boldsymbol{\Upsilon}} \cdot \nabla_{\boldsymbol{X}} N_F^{\Theta} \, J_{\boldsymbol{F}} \, \mathrm{d}V_e
\tag{2.126}
$$

Balance of angular momentum

$$
\begin{aligned}
\mathbf{K}^{\sigma\varphi} = \overset{n_{\mathrm{el}}}{\underset{e=1}{\mathbf{A}}} \int_{\mathcal{B}_0^e} & -\nabla_{\boldsymbol{X}} N_D^{\varphi} \cdot \boldsymbol{F}^{-1} \cdot \boldsymbol{m} \otimes \boldsymbol{F}^{-\mathrm{t}} \cdot \quad \nabla_{\boldsymbol{X}} N_B^{\sigma} J_{\boldsymbol{F}} \\
& +\nabla_{\boldsymbol{X}} N_B^{\sigma} \cdot \boldsymbol{F}^{-1} \cdot \frac{\partial \boldsymbol{m}}{\partial \boldsymbol{F}} \cdot \quad \nabla_{\boldsymbol{X}} N_D^{\varphi} \, J_{\boldsymbol{F}} \\
& +\nabla_{\boldsymbol{X}} N_B^{\sigma} \cdot \boldsymbol{F}^{-1} \cdot \boldsymbol{m} \otimes \boldsymbol{F}^{-\mathrm{t}} \cdot \quad \nabla_{\boldsymbol{X}} N_D^{\varphi} \, J_{\boldsymbol{F}} \\
& - \quad N_B^{\sigma} \, \boldsymbol{\epsilon}_t : \boldsymbol{\sigma} \otimes \boldsymbol{F}^{-\mathrm{t}} \cdot \quad \nabla_{\boldsymbol{X}} N_D^{\varphi} \, J_{\boldsymbol{F}} \, \mathrm{d}V_e
\end{aligned}
\tag{2.127}
$$

$$
\mathbf{K}^{\sigma\sigma} = \overset{n_{\mathrm{el}}}{\underset{e=1}{\mathbf{A}}} \int_{\mathcal{B}_0^e} - \, N_B^{\sigma} \, \boldsymbol{\epsilon}_t : \mathbf{I} \, N_E^{\sigma} \, J_{\boldsymbol{F}} \, \mathrm{d}V_e
\tag{2.128}
$$

$$
\mathbf{K}^{\sigma\Theta} = \overset{n_{\mathrm{el}}}{\underset{e=1}{\mathbf{A}}} \int_{\mathcal{B}_0^e} \nabla_{\boldsymbol{X}} N_B^{\sigma} \cdot \boldsymbol{F}^{-1} \cdot \frac{\partial \boldsymbol{m}}{\partial \boldsymbol{\Upsilon}} \cdot \nabla_{\boldsymbol{X}} N_F^{\Theta} \, J_{\boldsymbol{F}} \, \mathrm{d}V_e
\tag{2.129}
$$

Constraint

$$\mathbf{K}^{\Theta\varphi} = \mathop{\mathbf{A}}_{e=1}^{n_{el}} \int_{\mathcal{B}_0^e} \quad N_C^{\Theta}\, \boldsymbol{I}\,\overline{\otimes}\,\boldsymbol{I}\cdot \qquad\qquad \nabla_{\boldsymbol{X}} N_D^{\varphi}\, J_{\boldsymbol{F}}$$

$$+ N_C^{\Theta}\, [\boldsymbol{F} - \boldsymbol{\Theta}] \otimes \boldsymbol{F}^{-\mathrm{t}}\cdot \;\; \nabla_{\boldsymbol{X}} N_D^{\varphi}\, J_{\boldsymbol{F}}\, \mathrm{d}V_e \tag{2.130}$$

$$\mathbf{K}^{\Theta\sigma} = \mathop{\mathbf{A}}_{e=1}^{n_{el}} \quad \boldsymbol{0} \tag{2.131}$$

$$\mathbf{K}^{\Theta\Theta} = \mathop{\mathbf{A}}_{e=1}^{n_{el}} \int_{\mathcal{B}_0^e} \; -N_C^{\Theta}\, \boldsymbol{I}\,\overline{\otimes}\,\boldsymbol{I}\, N_F^{\Theta}\, J_{\boldsymbol{F}}\, \mathrm{d}V_e \tag{2.132}$$

A.2 Sensitivities of the stress and couple stress tensor

In this appendix the general form of the derivatives of the (symmetric part of the) stress tensor (2.29) and of the (deviatoric part of the) couple stress tensor (2.30) with respect to the strain measure $\boldsymbol{C}$ and the higher-gradient deformation measure $\boldsymbol{\Lambda}$, as derived in [10], are provided. These can be related to the derivatives with respect to the (gradients of the) primary field variables used in the finite element formulation by invoking the chain rule and making use of

$$\frac{\partial \boldsymbol{C}}{\partial \boldsymbol{F}} = \boldsymbol{F}^{\mathrm{t}}\,\underline{\otimes}\,\boldsymbol{I} + [\boldsymbol{I}\,\underline{\otimes}\,\boldsymbol{F}] : [\boldsymbol{I}\otimes\boldsymbol{I}] \tag{2.133}$$

$$\frac{\partial \boldsymbol{C}}{\partial \boldsymbol{\Upsilon}} = \boldsymbol{0} \tag{2.134}$$

$$\begin{aligned}
\frac{\partial \boldsymbol{\Lambda}}{\partial \boldsymbol{F}} =\;\; & [\boldsymbol{I}\,\underline{\otimes}\,[\boldsymbol{a}_0 \cdot [\boldsymbol{I}\,\underline{\otimes}\,\boldsymbol{I}] : \boldsymbol{\Upsilon}]] : [\boldsymbol{I}\,\underline{\otimes}\,\boldsymbol{I}] \\
& + [\boldsymbol{I}\,\underline{\otimes}\,\boldsymbol{F}\cdot\nabla_{\boldsymbol{X}}\boldsymbol{a}_0] : [\boldsymbol{I}\,\underline{\otimes}\,\boldsymbol{I}] \\
& + \boldsymbol{F}^{\mathrm{t}}\,\underline{\otimes}\,\nabla_{\boldsymbol{X}}\boldsymbol{a}_0
\end{aligned} \tag{2.135}$$

$$\frac{\partial \boldsymbol{\Lambda}}{\partial \boldsymbol{\Upsilon}} = \boldsymbol{F}^{\mathrm{t}}\,\underline{\otimes}\,[\boldsymbol{a}_0\otimes\boldsymbol{I}] \tag{2.136}$$

Furthermore, the derivatives of the invariants with respect to $\boldsymbol{C}$ and $\boldsymbol{\Lambda}$ that occur when evaluating contributions related to the specific form of the stored energy function are provided in Appendix A.3.

Sensitivity of the (symmetric part of the) Cauchy stress tensor

$$
\frac{\partial \boldsymbol{\sigma}^{\mathrm{sym}}}{\partial \boldsymbol{F}} = - \boldsymbol{\sigma}^{\mathrm{sym}} \otimes \boldsymbol{F}^{-t}
$$

$$
+ J_{\boldsymbol{F}}^{-1} \, \boldsymbol{I} \,\overline{\otimes}\left[2\, \boldsymbol{F} \cdot \frac{\partial W}{\partial \boldsymbol{C}} + \boldsymbol{G} \cdot \left[\frac{\partial W}{\partial \boldsymbol{\Lambda}}\right]^{\mathrm{t}} + \boldsymbol{F} \cdot \frac{\partial W}{\partial \boldsymbol{\Lambda}} \cdot [\nabla_{\boldsymbol{X}} \boldsymbol{a}_0]^{\mathrm{t}} \right]
$$

$$
+ J_{\boldsymbol{F}}^{-1} \left[\left[2\, \boldsymbol{F} \cdot \frac{\partial W}{\partial \boldsymbol{C}} + \boldsymbol{G} \cdot \left[\frac{\partial W}{\partial \boldsymbol{\Lambda}}\right]^{\mathrm{t}} + \boldsymbol{F} \cdot \frac{\partial W}{\partial \boldsymbol{\Lambda}} \cdot [\nabla_{\boldsymbol{X}} \boldsymbol{a}_0]^{\mathrm{t}} \right] \overline{\otimes} \boldsymbol{I} \right] : [\boldsymbol{I} \underline{\otimes} \boldsymbol{I}]
$$

$$
+ J_{\boldsymbol{F}}^{-1} \left[2\, \boldsymbol{F} \,\overline{\otimes}\, \boldsymbol{F} \right] : \qquad\qquad \left[\frac{\partial^2 W}{\partial \boldsymbol{C}\, \partial \boldsymbol{C}} : \frac{\partial \boldsymbol{C}}{\partial \boldsymbol{F}} + \frac{\partial^2 W}{\partial \boldsymbol{C}\, \partial \boldsymbol{\Lambda}} : \frac{\partial \boldsymbol{\Lambda}}{\partial \boldsymbol{F}} \right]
$$

$$
+ J_{\boldsymbol{F}}^{-1} \left[[\boldsymbol{G}\,\overline{\otimes}\,\boldsymbol{F}] : [\boldsymbol{I} \underline{\otimes} \boldsymbol{I}] + \boldsymbol{F}\,\overline{\otimes}\,\boldsymbol{G} \right] : \quad \left[\frac{\partial^2 W}{\partial \boldsymbol{\Lambda}\, \partial \boldsymbol{C}} : \frac{\partial \boldsymbol{C}}{\partial \boldsymbol{F}} + \frac{\partial^2 W}{\partial \boldsymbol{\Lambda}\, \partial \boldsymbol{\Lambda}} : \frac{\partial \boldsymbol{\Lambda}}{\partial \boldsymbol{F}} \right]
$$

$$\tag{2.137}$$

$$
\frac{\partial \boldsymbol{\sigma}^{\mathrm{sym}}}{\partial \boldsymbol{\Upsilon}} = \; J_{\boldsymbol{F}}^{-1} \left[\left[\boldsymbol{I} \,\overline{\otimes}\, \left[\boldsymbol{F} \cdot \frac{\partial W}{\partial \boldsymbol{\Lambda}} \right] + \left[\left[\boldsymbol{F} \cdot \frac{\partial W}{\partial \boldsymbol{\Lambda}} \right] \overline{\otimes}\, \boldsymbol{I} \right] : [\boldsymbol{I} \underline{\otimes} \boldsymbol{I}] \right] \otimes \boldsymbol{a}_0 \right] : [\boldsymbol{I} \underline{\otimes} \boldsymbol{I}]
$$

$$
+ J_{\boldsymbol{F}}^{-1} \left[\boldsymbol{F}\,\overline{\otimes}\,\boldsymbol{G} + [\boldsymbol{G}\,\overline{\otimes}\,\boldsymbol{F}] : [\boldsymbol{I} \underline{\otimes} \boldsymbol{I}] \right] : \frac{\partial^2 W}{\partial \boldsymbol{\Lambda}\, \partial \boldsymbol{\Lambda}} : \frac{\partial \boldsymbol{\Lambda}}{\partial \boldsymbol{\Upsilon}}
$$

$$\tag{2.138}$$

$$
+ J_{\boldsymbol{F}}^{-1} \left[2\, \boldsymbol{F}\,\overline{\otimes}\,\boldsymbol{F} \right] : \frac{\partial^2 W}{\partial \boldsymbol{C}\, \partial \boldsymbol{\Lambda}} : \frac{\partial \boldsymbol{\Lambda}}{\partial \boldsymbol{\Upsilon}}
$$

Sensitivity of the (deviatoric part of the) couple stress tensor

$$
\frac{3}{2}\, J_{\boldsymbol{F}} \, \frac{\partial \left[\boldsymbol{m}^{\mathrm{dev}}\right]^{\mathrm{t}}}{\partial \boldsymbol{F}} = -\frac{3}{2}\, J_{\boldsymbol{F}} \left[\boldsymbol{m}^{\mathrm{dev}}\right]^{\mathrm{t}} \otimes \boldsymbol{F}^{-\mathrm{t}}
$$

$$
+ \boldsymbol{\epsilon}_t : \quad \left[\boldsymbol{a}_t \otimes \quad \left[\boldsymbol{I} \,\overline{\otimes}\, \left[\boldsymbol{F} \cdot \left[\frac{\partial W}{\partial \boldsymbol{\Lambda}}\right]^{\mathrm{t}} \right] + \boldsymbol{F} \cdot \left[\frac{\partial W}{\partial \boldsymbol{\Lambda}} \,\overline{\otimes}\, \boldsymbol{I} \right] : [\boldsymbol{I} \underline{\otimes} \boldsymbol{I}] \right] \right]
$$

$$
+ [\boldsymbol{I} \underline{\otimes} \boldsymbol{I}] : [\boldsymbol{a}_t \otimes \boldsymbol{\epsilon}_t] : \left[\boldsymbol{I} \,\overline{\otimes}\, \left[\boldsymbol{F} \cdot \frac{\partial W}{\partial \boldsymbol{\Lambda}} \right] + \boldsymbol{F} \cdot \left[\left[\frac{\partial W}{\partial \boldsymbol{\Lambda}}\right]^{\mathrm{t}} \,\overline{\otimes}\, \boldsymbol{I} \right] : [\boldsymbol{I} \underline{\otimes} \boldsymbol{I}] \right]
$$

$$
+ \left[\boldsymbol{\epsilon}_t : \left[\boldsymbol{F} \cdot \frac{\partial W}{\partial \boldsymbol{\Lambda}}^{\mathrm{t}} \cdot \boldsymbol{F}^{\mathrm{t}} \right] \otimes \boldsymbol{I} + \left[\boldsymbol{\epsilon}_t \cdot \boldsymbol{F} \cdot \frac{\partial W}{\partial \boldsymbol{\Lambda}} \cdot \boldsymbol{F}^{\mathrm{t}} \right] : [\boldsymbol{I} \underline{\otimes} \boldsymbol{I}] \right] \otimes \boldsymbol{a}_0
$$

$$
+ [\boldsymbol{I} \underline{\otimes} \boldsymbol{I}] : [\boldsymbol{a}_t \otimes \boldsymbol{\epsilon}_t] : [\boldsymbol{F}\,\overline{\otimes}\,\boldsymbol{F}] : [\boldsymbol{I} \underline{\otimes} \boldsymbol{I}] : \left[\frac{\partial^2 W}{\partial \boldsymbol{\Lambda}\, \partial \boldsymbol{C}} : \frac{\partial \boldsymbol{C}}{\partial \boldsymbol{F}} + \frac{\partial^2 W}{\partial \boldsymbol{\Lambda}\, \partial \boldsymbol{\Lambda}} : \frac{\partial \boldsymbol{\Lambda}}{\partial \boldsymbol{F}} \right]
$$

$$
+ \boldsymbol{\epsilon}_t : [\boldsymbol{a}_t \otimes [\boldsymbol{F}\,\overline{\otimes}\,\boldsymbol{F}]] : \quad\left[\frac{\partial^2 W}{\partial \boldsymbol{\Lambda}\, \partial \boldsymbol{C}} : \frac{\partial \boldsymbol{C}}{\partial \boldsymbol{F}} + \frac{\partial^2 W}{\partial \boldsymbol{\Lambda}\, \partial \boldsymbol{\Lambda}} : \frac{\partial \boldsymbol{\Lambda}}{\partial \boldsymbol{F}} \right]
$$

$$\tag{2.139}$$

76

$$\frac{3}{2}J_{\boldsymbol{F}}\frac{\partial\left[\boldsymbol{m}^{\mathrm{dev}}\right]^{\mathrm{t}}}{\partial\boldsymbol{\Upsilon}}=\boldsymbol{\epsilon}_t:[\boldsymbol{a}_t\otimes\boldsymbol{F}\,\overline{\otimes}\,\boldsymbol{F}]:\qquad\frac{\partial^2W}{\partial\boldsymbol{\Lambda}\,\partial\boldsymbol{\Lambda}}:\frac{\partial\boldsymbol{\Lambda}}{\partial\boldsymbol{\Upsilon}}$$
$$+\,[\boldsymbol{I}\,\underline{\otimes}\,\boldsymbol{I}]:[\boldsymbol{a}_t\otimes\boldsymbol{\epsilon}_t:[[\boldsymbol{F}\,\overline{\otimes}\,\boldsymbol{F}]:[\boldsymbol{I}\,\underline{\otimes}\,\boldsymbol{I}]]]:\quad\frac{\partial^2W}{\partial\boldsymbol{\Lambda}\,\partial\boldsymbol{\Lambda}}:\frac{\partial\boldsymbol{\Lambda}}{\partial\boldsymbol{\Upsilon}}\tag{2.140}$$

A.3 Derivatives of invariants

The first and second derivatives of the invariants given in (2.36) with respect to $\boldsymbol{C}$ and $\boldsymbol{\Lambda}$ which are required for the specification of the stress and couple stress tensor as well as for the specification of the respective tangent stiffness contributions, as derived in [10, 130], are provided in Table 2.5 and Table 2.6.

Table 2.5: First derivatives of invariants with respect to $\boldsymbol{C}$ and $\boldsymbol{\Lambda}$.

	$\dfrac{\partial I_\bullet}{\partial\boldsymbol{C}}$	$\dfrac{\partial I_\bullet}{\partial\boldsymbol{\Lambda}}$
I_1	$\boldsymbol{I}$	$\boldsymbol{0}$
I_2	$I_1\,\boldsymbol{I}+\boldsymbol{C}$	$\boldsymbol{0}$
I_3	$I_2\,\boldsymbol{I}-I_1\boldsymbol{C}+\boldsymbol{C}^2$	$\boldsymbol{0}$
I_4	$\boldsymbol{a}_0\otimes\boldsymbol{a}_0$	$\boldsymbol{0}$
I_5	$\boldsymbol{a}_0\otimes[\boldsymbol{C}\cdot\boldsymbol{a}_0]+[\boldsymbol{a}_0\cdot\boldsymbol{C}]\otimes\boldsymbol{a}_0$	$\boldsymbol{0}$
I_6	$\boldsymbol{0}$	$2\,\boldsymbol{\Lambda}\cdot\boldsymbol{a}_0\otimes\boldsymbol{a}_0$
I_7	$[\boldsymbol{\Lambda}\cdot\boldsymbol{a}_0]\otimes[\boldsymbol{\Lambda}\cdot\boldsymbol{a}_0]$	$2\,\boldsymbol{C}\cdot\boldsymbol{\Lambda}\cdot\boldsymbol{a}_0\otimes\boldsymbol{a}_0$
I_8	$\left[\boldsymbol{a}_0\cdot\boldsymbol{\Lambda}^{\mathrm{t}}\right]\otimes[\boldsymbol{C}\cdot\boldsymbol{\Lambda}\cdot\boldsymbol{a}_0]+\left[\boldsymbol{a}_0\cdot\boldsymbol{\Lambda}^{\mathrm{t}}\cdot\boldsymbol{C}\right]\otimes[\boldsymbol{\Lambda}\cdot\boldsymbol{a}_0]$	$2\,\boldsymbol{C}^2\cdot\boldsymbol{\Lambda}\cdot\boldsymbol{a}_0\otimes\boldsymbol{a}_0$
I_9	$\boldsymbol{0}$	$\boldsymbol{a}_0\otimes\boldsymbol{a}_0$
I_{10}	$\frac{1}{2}\left[\boldsymbol{a}_0\otimes\boldsymbol{\Lambda}\cdot\boldsymbol{a}_0+\boldsymbol{\Lambda}\cdot\boldsymbol{a}_0\otimes\boldsymbol{a}_0\right]$	$\boldsymbol{C}\cdot\boldsymbol{a}_0\otimes\boldsymbol{a}_0$
I_{11}	$\begin{aligned}\frac{1}{2}\big[\;&\boldsymbol{a}_0\otimes\boldsymbol{C}\cdot\boldsymbol{\Lambda}\cdot\boldsymbol{a}_0+\boldsymbol{C}\cdot\boldsymbol{\Lambda}\cdot\boldsymbol{a}_0\otimes\boldsymbol{a}_0\\&+\boldsymbol{a}_0\cdot\boldsymbol{C}\otimes\boldsymbol{\Lambda}\cdot\boldsymbol{a}_0+\boldsymbol{\Lambda}\cdot\boldsymbol{a}_0\otimes\boldsymbol{a}_0\cdot\boldsymbol{C}\big]\end{aligned}$	$\boldsymbol{C}^2\cdot\boldsymbol{a}_0\otimes\boldsymbol{a}_0$

Table 2.6: Second derivatives of invariants with respect to C and Λ.

	$\dfrac{\partial^2 I_\bullet}{\partial C \partial C}$	$\dfrac{\partial^2 I_\bullet}{\partial C \partial \Lambda}$	$\dfrac{\partial^2 I_\bullet}{\partial \Lambda \partial C}$	$\dfrac{\partial^2 I_\bullet}{\partial \Lambda \partial \Lambda}$
I_1	0	0	0	0
I_2	$I \otimes I + I^{\text{sym}}$	0	0	0
I_3	$I \otimes [I_1 I + C] - C \otimes I - I_1 I^{\text{sym}} + \frac{1}{2}[I\overline{\otimes}C + I\underline{\otimes}C + C\overline{\otimes}I + C\underline{\otimes}I]$	0	0	0
I_4	0	0	0	0
I_5	$\frac{1}{2}\big[a_0 \otimes I \otimes a_0 + a_0 \otimes I\overline{\otimes}a_0 + a_0\overline{\otimes}I \otimes a_0 + a_0\overline{\otimes}I\overline{\otimes}a_0 \big]$	0	0	0
I_6	0	$I\overline{\otimes}[\Lambda \cdot a_0] \otimes a_0 + [\Lambda \cdot a_0]\otimes I \otimes a_0$	0	$2\,a_0 \overline{\otimes} I \otimes a_0$
I_7	$[\Lambda \cdot a_0] \otimes [a_0 \cdot \Lambda^t \cdot I^{\text{sym}}] + [\Lambda \cdot a_0]\overline{\otimes}[a_0 \cdot \Lambda^t \cdot I^{\text{sym}}]$	$[C \cdot \Lambda \cdot a_0] \otimes I \otimes a_0 + [C \cdot \Lambda \cdot a_0]\overline{\otimes}I \otimes a_0 + [\Lambda \cdot a_0] \otimes C \otimes a_0 + [\Lambda \cdot a_0]\overline{\otimes}C \otimes a_0$	$2\,a_0 \overline{\otimes} \big[a_0 \cdot \Lambda^t \cdot I^{\text{sym}}\big]$	$2\,a_0 \overline{\otimes} C \otimes a_0$
I_8	0	0	$a_0 \overline{\otimes}\big[a_0 \cdot \Lambda^t \cdot [\, I\overline{\otimes}C + I\underline{\otimes}C + C\overline{\otimes}I + C\underline{\otimes}I\,]\big]$	$2\,a_0 \overline{\otimes} C^2 \otimes a_0$
I_9	0	0	0	0
I_{10}	0	$\frac{1}{2}\big[a_0 \otimes I \otimes a_0 + a_0\overline{\otimes}I \otimes a_0 \big]$	$\frac{1}{2}\big[a_0\overline{\otimes}I \otimes a_0 + a_0 \otimes I\overline{\otimes}a_0\big]$	0
I_{11}	$\frac{1}{4}\big[a_0 \otimes I \otimes \Lambda \cdot a_0 + a_0 \otimes I\overline{\otimes}\Lambda \cdot a_0 + a_0\overline{\otimes}I \otimes \Lambda \cdot a_0 + a_0\overline{\otimes}I\overline{\otimes}\Lambda \cdot a_0 + [\Lambda \cdot a_0]\otimes I \otimes a_0 + [\Lambda \cdot a_0]\otimes I\overline{\otimes}a_0 + [\Lambda \cdot a_0]\overline{\otimes}I \otimes a_0 + [\Lambda \cdot a_0]\overline{\otimes}I\overline{\otimes}a_0 \big]$	$\frac{1}{2}\big[a_0 \otimes C \otimes a_0 + a_0\overline{\otimes}C \otimes a_0 + a_0 \cdot C \otimes I \otimes a_0 + a_0 \cdot C\overline{\otimes}I \otimes a_0 \big]$	$\frac{1}{2}a_0\overline{\otimes}\big[a_0 \cdot [\, I\overline{\otimes}C + I\underline{\otimes}C + C\overline{\otimes}I + C\underline{\otimes}I\,]\big]$	0

A.4 Interpretation of the boundary conditions

The application and interpretation of suitable boundary conditions for the couple stress theory shall be briefly discussed. To this end, a different derivation of the weak form of the balance equations as the one presented in Section 2.1.3.2 is pursued, which is similar to the derivation presented in [109] and motivates a direct relation between the test functions $\boldsymbol{\eta}^\varphi$ and $\boldsymbol{\eta}^\sigma$.

Multiplying the balance equation of linear momentum, (2.48a), with a testfunction $\boldsymbol{\eta}^\varphi$, which may be interpreted as a virtual velocity field with regard to the principle of virtual work, integrating over the volume $\mathcal{B}_t$ and applying the divergence theorem yields

$$0 = -\int_{\mathcal{B}_t} \nabla_{\boldsymbol{x}}\boldsymbol{\eta}^\varphi : \boldsymbol{\sigma}^{\mathrm{sym}}\,\mathrm{d}v + \int_{\partial\mathcal{B}_t} \boldsymbol{n}\cdot\boldsymbol{\sigma}\cdot\boldsymbol{\eta}^\varphi\,\mathrm{d}a - \int_{\mathcal{B}_t} \nabla_{\boldsymbol{x}}\boldsymbol{\eta}^\varphi : \left[\boldsymbol{\sigma}^{\mathrm{skw}}\right]^{\mathrm{t}}\,\mathrm{d}v \quad. \quad (2.141)$$

Next, the balance equation of angular momentum, (2.48b), is weighted by the third-order Levi-Civita tensor such that

$$\boldsymbol{0} = \boldsymbol{\epsilon}_t \cdot \left[\nabla_{\boldsymbol{x}}\cdot\boldsymbol{m}^{\mathrm{t}}\right] + \boldsymbol{\epsilon}_t\cdot\boldsymbol{\epsilon}_t : \boldsymbol{\sigma}^{\mathrm{skw}} = \boldsymbol{\epsilon}_t \cdot \left[\nabla_{\boldsymbol{x}}\cdot\boldsymbol{m}^{\mathrm{t}}\right] + 2\,\boldsymbol{\sigma}^{\mathrm{skw}} \quad, \quad (2.142)$$

which, for the problem at hand, defines the skew-symmetric part of the Cauchy-type stress tensor. Using (2.142) renders the third term in (2.141) to take the representation

$$-\int_{\mathcal{B}_t} \nabla_{\boldsymbol{x}}\boldsymbol{\eta}^\varphi : \left[\boldsymbol{\sigma}^{\mathrm{skw}}\right]^{\mathrm{t}}\,\mathrm{d}v = -\int_{\mathcal{B}_t} \nabla_{\boldsymbol{x}}\boldsymbol{\eta}^\varphi : \frac{1}{2}\,\boldsymbol{\epsilon}_t \cdot \left[\nabla_{\boldsymbol{x}}\cdot\boldsymbol{m}^{\mathrm{t}}\right]\,\mathrm{d}v \qquad (2.143a)$$

$$= \int_{\mathcal{B}_t} \frac{1}{2}\,\mathrm{curl}^{\mathrm{t}}\left(\boldsymbol{\eta}^\varphi\right)\cdot\left[\nabla_{\boldsymbol{x}}\cdot\boldsymbol{m}^{\mathrm{t}}\right]\,\mathrm{d}v \qquad (2.143b)$$

$$= \int_{\mathcal{B}_t} \boldsymbol{\eta}^\sigma \cdot \left[\nabla_{\boldsymbol{x}}\cdot\boldsymbol{m}^{\mathrm{t}}\right]\,\mathrm{d}v \quad, \qquad (2.143c)$$

with $\boldsymbol{\eta}^\sigma$ introduced as

$$\boldsymbol{\eta}^\sigma = \frac{1}{2}\,\mathrm{curl}^{\mathrm{t}}\left(\boldsymbol{\eta}^\varphi\right) \quad. \qquad (2.144)$$

In the case that $\boldsymbol{\eta}^\varphi$ is interpreted as a virtual velocity, $\boldsymbol{\eta}^\sigma$ corresponds to the virtual spin vector. Making use of (2.143), (2.141) can be rewritten as

$$0 = -\int_{\mathcal{B}_t} \nabla_{\boldsymbol{x}}\boldsymbol{\eta}^\varphi : \boldsymbol{\sigma}^{\mathrm{sym}}\,\mathrm{d}v + \int_{\partial\mathcal{B}_t} \boldsymbol{n}\cdot\boldsymbol{\sigma}\cdot\boldsymbol{\eta}^\varphi\,\mathrm{d}a + \int_{\mathcal{B}_t} \boldsymbol{\eta}^\sigma\cdot\left[\nabla_{\boldsymbol{x}}\cdot\boldsymbol{m}^{\mathrm{t}}\right]\,\mathrm{d}v \quad. \quad (2.145)$$

Furthermore, applying the identity

$$\boldsymbol{\eta}^{\sigma} \cdot \boldsymbol{\epsilon}_t : \boldsymbol{\sigma}^{\mathrm{skw}} = \left[\frac{1}{2} \operatorname{curl}^{\mathrm{t}} (\boldsymbol{\eta}^{\varphi}) \right] \cdot \boldsymbol{\epsilon}_t : \quad \boldsymbol{\sigma}^{\mathrm{skw}} \tag{2.146a}$$

$$= -\frac{1}{2} \nabla_{\boldsymbol{x}} \boldsymbol{\eta}^{\varphi} : \boldsymbol{\epsilon}_t \cdot \boldsymbol{\epsilon}_t : \quad \boldsymbol{\sigma}^{\mathrm{skw}} \tag{2.146b}$$

$$= \nabla_{\boldsymbol{x}} \boldsymbol{\eta}^{\varphi} \qquad : \left[\boldsymbol{\sigma}^{\mathrm{skw}} \right]^{\mathrm{t}} \quad , \tag{2.146c}$$

and adding the vanishing volume integrated term

$$0 = \int_{\mathcal{B}_t} \boldsymbol{\eta}^{\sigma} \cdot \boldsymbol{\epsilon}_t : \boldsymbol{\sigma}^{\mathrm{skw}} \, \mathrm{d}v - \int_{\mathcal{B}_t} \nabla_{\boldsymbol{x}} \boldsymbol{\eta}^{\varphi} : \left[\boldsymbol{\sigma}^{\mathrm{skw}} \right]^{\mathrm{t}} \, \mathrm{d}v \tag{2.147}$$

to (2.145) results in

$$0 = -\int_{\mathcal{B}_t} \nabla_{\boldsymbol{x}} \boldsymbol{\eta}^{\varphi} : \boldsymbol{\sigma}^{\mathrm{sym}} \, \mathrm{d}v \quad - \int_{\mathcal{B}_t} \nabla_{\boldsymbol{x}} \boldsymbol{\eta}^{\varphi} : \left[\boldsymbol{\sigma}^{\mathrm{skw}} \right]^{\mathrm{t}} \, \mathrm{d}v \quad + \int_{\partial \mathcal{B}_t} \boldsymbol{n} \cdot \boldsymbol{\sigma} \cdot \boldsymbol{\eta}^{\varphi} \, \mathrm{d}a$$
$$+ \int_{\mathcal{B}_t} \boldsymbol{\eta}^{\sigma} \cdot \left[\nabla_{\boldsymbol{x}} \cdot \boldsymbol{m}^{\mathrm{t}} \right] \, \mathrm{d}v \quad + \int_{\mathcal{B}_t} \boldsymbol{\eta}^{\sigma} \cdot \boldsymbol{\epsilon}_t : \boldsymbol{\sigma}^{\mathrm{skw}} \, \mathrm{d}v \quad . \tag{2.148}$$

By using the divergence theorem, the term containing the divergence of $\boldsymbol{m}^{\mathrm{t}}$ in (2.148) can be rewritten, to be specific

$$0 = -\int_{\mathcal{B}_t} \nabla_{\boldsymbol{x}} \boldsymbol{\eta}^{\varphi} : \boldsymbol{\sigma}^{\mathrm{sym}} \, \mathrm{d}v \quad - \int_{\mathcal{B}_t} \nabla_{\boldsymbol{x}} \boldsymbol{\eta}^{\varphi} : \left[\boldsymbol{\sigma}^{\mathrm{skw}} \right]^{\mathrm{t}} \, \mathrm{d}v \quad + \int_{\partial \mathcal{B}_t} \boldsymbol{n} \cdot \boldsymbol{\sigma} \cdot \boldsymbol{\eta}^{\varphi} \, \mathrm{d}a$$
$$- \int_{\mathcal{B}_t} \nabla_{\boldsymbol{x}} \boldsymbol{\eta}^{\sigma} : \boldsymbol{m}^{\mathrm{t}} \, \mathrm{d}v \quad + \int_{\mathcal{B}_t} \boldsymbol{\eta}^{\sigma} \cdot \boldsymbol{\epsilon}_t : \boldsymbol{\sigma}^{\mathrm{skw}} \, \mathrm{d}v \quad + \int_{\partial \mathcal{B}_t} \boldsymbol{n} \cdot \boldsymbol{m} \cdot \boldsymbol{\eta}^{\sigma} \, \mathrm{d}a \quad . \tag{2.149}$$

It is observed that the first and second line in (2.149) are comparable to the spatial representations of the weak forms of the balance equations (2.53b) and (2.54b), which were derived in Section 2.1.3.2. However, $\boldsymbol{\eta}^{\varphi}$ and $\boldsymbol{\eta}^{\sigma}$ were treated as independent test functions in Section 2.1.3.2, whereas the relation (2.144) directly results from the derivations presented in this appendix.

With (2.144) at hand, the surface integral in (2.149) may take a different representation based on a split into a normal and tangential part, cf. [94]. The normal part is then further rewritten making use of (2.144) and the chain rule, to be specific

$$\int_{\partial \mathcal{B}_t} \boldsymbol{n} \cdot \boldsymbol{m} \cdot \boldsymbol{\eta}^{\sigma} \, \mathrm{d}a = \int_{\partial \mathcal{B}_t} \boldsymbol{n} \cdot \boldsymbol{m} \cdot [\boldsymbol{n} \otimes \boldsymbol{n}] \cdot \boldsymbol{\eta}^{\sigma} \, \mathrm{d}a \quad + \int_{\partial \mathcal{B}_t} \boldsymbol{n} \cdot \boldsymbol{m} \cdot [\boldsymbol{I} - \boldsymbol{n} \otimes \boldsymbol{n}] \cdot \boldsymbol{\eta}^{\varphi} \, \mathrm{d}a$$

$$= \int_{\partial \mathcal{B}_t} \frac{1}{2} m_{\mathrm{nn}} \, \boldsymbol{n} \cdot \mathrm{curl}^{\mathrm{t}} (\boldsymbol{\eta}^{\boldsymbol{\varphi}}) \quad \mathrm{d}a \; + \int_{\partial \mathcal{B}_t} \boldsymbol{n} \cdot \boldsymbol{m} \cdot [\boldsymbol{I} - \boldsymbol{n} \otimes \boldsymbol{n}] \cdot \boldsymbol{\eta}^{\boldsymbol{\sigma}} \, \mathrm{d}a$$

$$= \int_{\partial \mathcal{B}_t} \frac{1}{2} \, \boldsymbol{n} \cdot \mathrm{curl}^{\mathrm{t}} (m_{\mathrm{nn}} \, \boldsymbol{\eta}^{\boldsymbol{\varphi}}) \quad \mathrm{d}a \; + \int_{\partial \mathcal{B}_t} \boldsymbol{n} \cdot \boldsymbol{m} \cdot [\boldsymbol{I} - \boldsymbol{n} \otimes \boldsymbol{n}] \cdot \boldsymbol{\eta}^{\boldsymbol{\sigma}} \, \mathrm{d}a$$

$$- \int_{\partial \mathcal{B}_t} \frac{1}{2} \, \boldsymbol{n} \times \nabla_{\boldsymbol{x}} m_{\mathrm{nn}} \cdot \boldsymbol{\eta}^{\boldsymbol{\varphi}} \qquad \mathrm{d}a \tag{2.150}$$

with $m_{\mathrm{nn}} = \boldsymbol{n} \cdot \boldsymbol{m} \cdot \boldsymbol{n}$. Applying Stokes' theorem and assuming the surface to be smooth renders

$$\int_{\partial \mathcal{B}_t} \frac{1}{2} \, \boldsymbol{n} \cdot \mathrm{curl}^{\mathrm{t}} (m_{\mathrm{nn}} \, \boldsymbol{\eta}^{\boldsymbol{\varphi}}) \, \mathrm{d}a = 0 \quad . \tag{2.151}$$

By making use of (2.150) and (2.151), an alternative representation of (2.149) is finally given by

$$0 = \int_{\mathcal{B}_t} \nabla_{\boldsymbol{x}} \boldsymbol{\eta}^{\boldsymbol{\varphi}} : \boldsymbol{\sigma}^{\mathrm{sym}} \, \mathrm{d}v + \int_{\mathcal{B}_t} \nabla_{\boldsymbol{x}} \boldsymbol{\eta}^{\boldsymbol{\varphi}} : \left[\boldsymbol{\sigma}^{\mathrm{skw}} \right]^{\mathrm{t}} \mathrm{d}v - \int_{\partial \mathcal{B}_t} \left[\boldsymbol{n} \cdot \boldsymbol{\sigma} - \frac{1}{2} \, \boldsymbol{n} \times \nabla_{\boldsymbol{x}} m_{\mathrm{nn}} \right] \cdot \boldsymbol{\eta}^{\boldsymbol{\varphi}} \, \mathrm{d}a \tag{2.152a}$$

$$+ \int_{\mathcal{B}_t} \nabla_{\boldsymbol{x}} \boldsymbol{\eta}^{\boldsymbol{\sigma}} : \boldsymbol{m}^{\mathrm{t}} \, \mathrm{d}v \; - \int_{\mathcal{B}_t} \boldsymbol{\eta}^{\boldsymbol{\sigma}} \cdot \boldsymbol{\epsilon}_t : \boldsymbol{\sigma}^{\mathrm{skw}} \, \mathrm{d}v \; - \int_{\partial \mathcal{B}_t} \boldsymbol{n} \cdot \boldsymbol{m} \cdot [\boldsymbol{I} - \boldsymbol{n} \otimes \boldsymbol{n}] \cdot \boldsymbol{\eta}^{\boldsymbol{\sigma}} \, \mathrm{d}a \tag{2.152b}$$

respectively,

$$0 = \int_{\mathcal{B}_t} \nabla_{\boldsymbol{x}} \boldsymbol{\eta}^{\boldsymbol{\varphi}} : \boldsymbol{\sigma}^{\mathrm{sym}} \, \mathrm{d}v + \int_{\mathcal{B}_t} \nabla_{\boldsymbol{x}} \boldsymbol{\eta}^{\boldsymbol{\varphi}} : \left[\boldsymbol{\sigma}^{\mathrm{skw}} \right]^{\mathrm{t}} \mathrm{d}v - \int_{\partial \mathcal{B}_t} \left[\boldsymbol{n} \cdot \boldsymbol{\sigma} - \frac{1}{2} \, \boldsymbol{n} \times \nabla_{\boldsymbol{x}}^{s} m_{\mathrm{nn}} \right] \cdot \boldsymbol{\eta}^{\boldsymbol{\varphi}} \, \mathrm{d}a \tag{2.153a}$$

$$+ \int_{\mathcal{B}_t} \nabla_{\boldsymbol{x}} \boldsymbol{\eta}^{\boldsymbol{\sigma}} : \boldsymbol{m}^{\mathrm{t}} \, \mathrm{d}v \; - \int_{\mathcal{B}_t} \boldsymbol{\eta}^{\boldsymbol{\sigma}} \cdot \boldsymbol{\epsilon}_t : \boldsymbol{\sigma}^{\mathrm{skw}} \, \mathrm{d}v \; - \int_{\partial \mathcal{B}_t} \boldsymbol{n} \cdot \boldsymbol{m} \cdot [\boldsymbol{I} - \boldsymbol{n} \otimes \boldsymbol{n}] \cdot \boldsymbol{\eta}^{\boldsymbol{\sigma}} \, \mathrm{d}a \tag{2.153b}$$

using the surface gradient operator $\nabla_{\boldsymbol{x}}^{s} (\bullet) = \nabla_{\boldsymbol{x}} (\bullet) \cdot [\boldsymbol{I} - \boldsymbol{n} \otimes \boldsymbol{n}]$.

Comparing (2.152a) and (2.152b) with their counterparts (2.53b) and (2.54b), derived in Section 2.1.3.1, we observe that the vectors of external forces take different forms, respectively interpretations, if the test functions are assumed to be related in accordance with (2.144). To be specific, we find that the part of the vector of external forces which corresponds to the balance equation of linear momentum is influenced by the distribution of m_{nn}, cf. (2.152a). In addition, the boundary conditions for the balance equation of angular momentum may be specified in terms of the tangential component of the couple stress vector, cf. (2.152b).

A.5 Different types of the energy function

In Section 2.2.1.1 it was stated that, by using the energy function (2.74), a reference configuration with curved fibres is neither energy nor stress free. Concerning the specific ansatz for W^{κ_0}, two further options which have been elaborated in [10] and which would both ensure that a reference configuration with curved fibres is a natural state shall be briefly recapitulated for the sake of completeness.

The first option results from including the initial value of the invariant I_6 in the energy function. Thus, with

$$I_6^0 = [\boldsymbol{\Lambda} \cdot \boldsymbol{a}_0] \cdot [\boldsymbol{\Lambda} \cdot \boldsymbol{a}_0] \quad , \qquad t = t_0 \tag{2.154}$$

we propose that energy needs to be provided to the system for any deviation from this initial state. Hence, a different ansatz for the higher-order energy part is given by

$$W_2^{\kappa_0} = c_2 \left[I_6 - I_6^0 \right]^2 \quad , \quad c_2 \in \mathbb{R}^+ \quad . \tag{2.155}$$

Since $I_6 = I_6^0$ for $t = t_0$, the energy contribution $W_2^{\kappa_0}$ vanishes identically for an undeformed state. Moreover, $W_2^{\kappa_0}$ enters the constitutive equations only in terms of its derivative with respect to $\boldsymbol{\Lambda}$, i.e.

$$\frac{\partial W_2^{\kappa_0}}{\partial \boldsymbol{\Lambda}} = c_2 \left[I_6 - I_6^0 \right] \frac{\partial I_6}{\partial \boldsymbol{\Lambda}} \tag{2.156}$$

which turns out to be identically zero for an undeformed state so that the contributions to the stress and couple stress tensor vanish identically at $t = t_0$. Nevertheless, due to the quadratic form in (2.155), $\boldsymbol{\Lambda}$ and therefore also the second gradient of the deformation function enter $W_2^{\kappa_0}$ to the fourth power. Accordingly, the stress and the couple stress tensor have cubic contributions in the first and second gradient of the deformation function.

The second alternative approach to be discussed additionally takes into account the invariant $I_7 = \boldsymbol{\kappa}_0 \cdot \boldsymbol{C} \cdot \boldsymbol{\kappa}_0$ which couples the referential representation of the projected gradient of the deformed fibre vector to the deformation in terms of the right Cauchy-Green tensor. Specifically speaking,

$$W_3^{\kappa_0} = c_3 \left[I_7 - I_6 \right]^2 \quad , \quad c_3 \in \mathbb{R}^+ \tag{2.157}$$

can be assumed. Using the definitions of the invariants (2.36), (2.157) can be rewritten in the form

$$W_3^{\kappa_0} = c_3 \left[\boldsymbol{\kappa}_0 \cdot [\boldsymbol{C} - \boldsymbol{I}] \cdot \boldsymbol{\kappa}_0 \right]^2 \quad . \tag{2.158}$$

For an undeformed state $\boldsymbol{C} = \boldsymbol{I}$ holds so that $W_3^{\boldsymbol{\kappa}_0}$ vanishes in that case independent of $\boldsymbol{\kappa}_0$. Same holds for the contributions to the stress and couple stress tensor, for the derivatives with respect to $\boldsymbol{C}$ and $\boldsymbol{\Lambda}$ are given by

$$\frac{\partial W_3^{\boldsymbol{\kappa}_0}}{\partial \boldsymbol{C}} = c_3 \left[\boldsymbol{\kappa}_0 \cdot [\boldsymbol{C} - \boldsymbol{I}] \cdot \boldsymbol{\kappa}_0\right] [\boldsymbol{\Lambda} \cdot \boldsymbol{a}_0] \otimes [\boldsymbol{\Lambda} \cdot \boldsymbol{a}_0] \tag{2.159}$$

and

$$\frac{\partial W_3^{\boldsymbol{\kappa}_0}}{\partial \boldsymbol{\Lambda}} = c_3 \left[\boldsymbol{\kappa}_0 \cdot [\boldsymbol{C} - \boldsymbol{I}] \cdot \boldsymbol{\kappa}_0\right] [2\,\boldsymbol{C} \cdot \boldsymbol{\Lambda} \cdot \boldsymbol{a}_0 \otimes \boldsymbol{a}_0 - 2\,\boldsymbol{\Lambda} \cdot \boldsymbol{a}_0 \otimes \boldsymbol{a}_0] \quad . \tag{2.160}$$

Apart from the higher powers in $\boldsymbol{F}$ and $\boldsymbol{\Lambda}$, which were already observed for the energy function $W_2^{\boldsymbol{\kappa}_0}$, the use of $W_3^{\boldsymbol{\kappa}_0}$ results in a strong coupling between the strain measure $\boldsymbol{C} - \boldsymbol{I}$ and the higher-gradient measure $\boldsymbol{\kappa}_0$.

A.6 Dimensionless quantities

The analytical simulation results presented in [30] are given in terms of dimensionless quantities. To study the quantitative match of the analytical solutions with simulation results, one can approximate the corresponding conversion factors for the coefficients of the stress and the couple stress tensor as well as the ones of the fibre(-bending) stiffness parameter and the fibre slope.

In [30], the dimensionless stress tensor $\boldsymbol{\Sigma}^*$ and couple stress tensor $\boldsymbol{v}^*$ are introduced according to

$$\boldsymbol{\Sigma}^* = f_1 \,\boldsymbol{\Sigma} \quad , \qquad f_1 = \frac{B_0}{\Psi\, \mathsf{E}_{r\varphi r\varphi}} \frac{\beta^2 - 1}{\beta} \quad , \tag{2.161}$$

respectively

$$\boldsymbol{v}^* = f_2 \,\boldsymbol{v} \quad , \qquad f_2 = \frac{1}{\Psi\, \mathsf{E}_{r\varphi r\varphi}} \frac{\beta^2 - 1}{\beta} \quad . \tag{2.162}$$

Furthermore, the dimensionless fibre(-bending) stiffness parameter d^{f*} is given by

$$d^{f*} = f_3 \,d^f \quad , \qquad f_3 = \frac{1}{2\, \mathsf{E}_{r\varphi r\varphi}\, B_0\, [B_1 - B_0]} \quad . \tag{2.163}$$

Based on the dimensionless azimuthal displacement $u_\varphi^* = u_\varphi/\Psi$ and the dimensionless radius $r^* = r/B_0$, the dimensionless fibre slope can be specified according to

$$\frac{\partial u_\varphi^*}{\partial r^*} = f_4 \frac{\partial u_\varphi}{\partial r} \quad , \qquad f_4 = \frac{B_0}{\Psi} \quad . \tag{2.164}$$

In (2.163), quantity d^f represents the fibre(-bending) stiffness parameter of the proposed small strain model which can be approximated as, cf. Section 2.2.1.3 and [31],

$$d^f = \frac{8}{3} c \quad . \tag{2.165}$$

The same holds for material parameter $\mathsf{E}_{r\varphi r\varphi}$ in (2.161), (2.162) and (2.163) which is the shear modulus of the small strain theory and comparable to parameter μ used in the corresponding finite strain theory such that we approximate the parameter according to

$$\mathsf{E}_{r\varphi r\varphi} = \mu \quad . \tag{2.166}$$

The maximal azimuthal displacement Ψ is approximated based on the results presented in Figure 2.4 in terms of the averaged azimuthal displacement at the outer boundary for the different values of material parameter c. For the load step $\|\boldsymbol{t}_{\text{tang}}\|/\|\boldsymbol{t}_{\text{tang}}^{\text{max}}\| = 0.1$, Ψ thus takes a value of

$$\Psi \approx \arctan\left(x_2/x_1\right)\big|_{\boldsymbol{X}=B_1 \boldsymbol{e}_1} B_1 \approx 3.5431 \quad . \tag{2.167}$$

With $\beta = B_1/B_0 = 100/40 = 2.5$, $\mu = 4.444 \times 10^4$ and $\Psi \approx 3.5431$ at hand, the conversion factors (2.161)-(2.164) can be estimated for the load step $\|\boldsymbol{t}_{\text{tang}}\|/\|\boldsymbol{t}_{\text{tang}}^{\text{max}}\| = 0.1$ as

$$f_1 \approx 5.34 \times 10^{-4} \tag{2.168a}$$
$$f_2 \approx 1.33 \times 10^{-5} \tag{2.168b}$$

$$f_3 \approx 4.69 \times 10^{-9} \tag{2.168c}$$
$$f_4 \approx 11.29 \tag{2.168d}$$

Note that f_1, f_2 and f_4 depend on the deformation state via the inverse maximal azimuthal displacement $1/\Psi$, whereas f_3 is completely determined by the problem dimensions and the material parameter μ. With regard to the simulation results for load states other than $\|\boldsymbol{t}_{\text{tang}}\|/\|\boldsymbol{t}_{\text{tang}}^{\text{max}}\| = 0.1$, see Appendix A.7, the conversion factors are additionally depicted as a function of the relative load state in Figure 2.18.

(a) conversion factor f_1

(b) conversion factor f_2

(c) conversion factor f_3

(d) conversion factor f_4
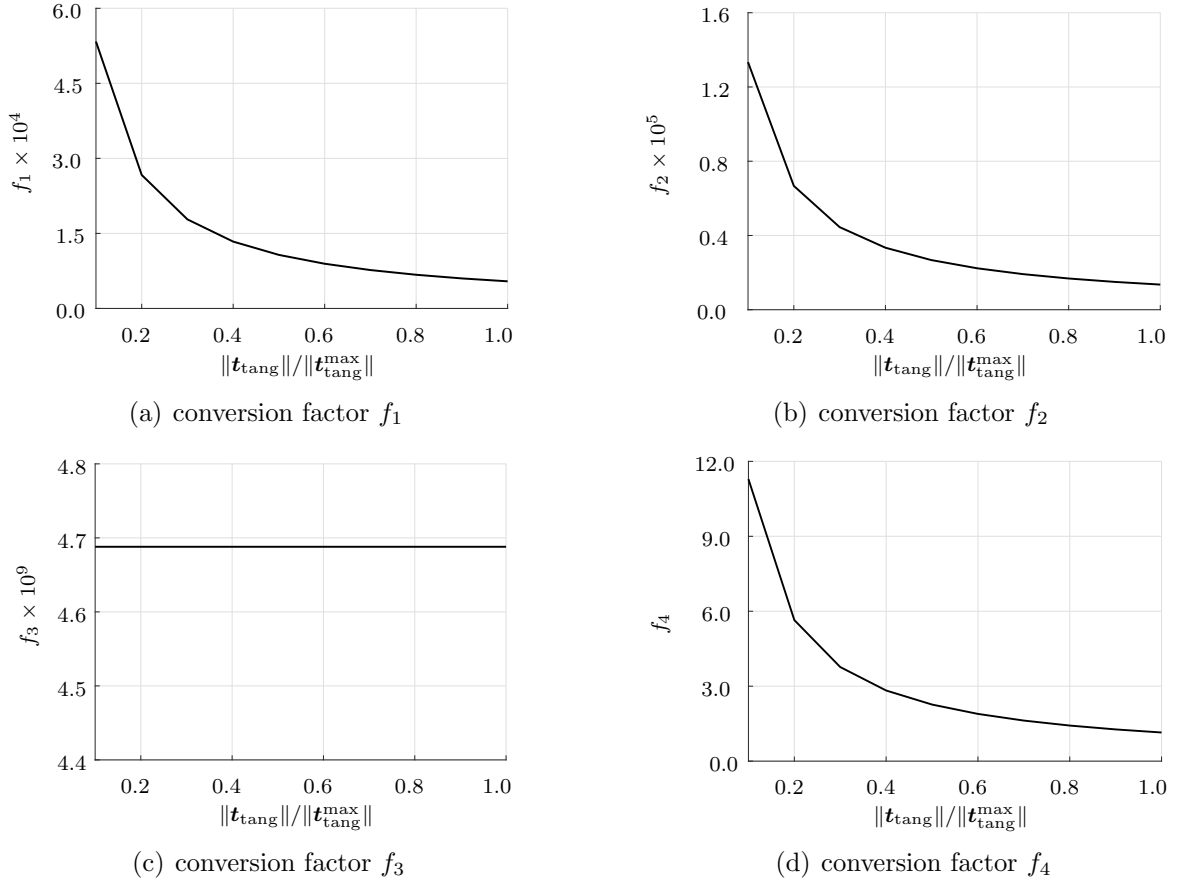
Figure 2.18: Conversion factors as a function of the relative applied load $\|\boldsymbol{t}_{\text{tang}}\|/\|\boldsymbol{t}_{\text{tang}}^{\text{max}}\|$.

A.7 Additional simulation results for different load states

In this appendix additional simulation results are presented for higher load states than those discussed in Section 2.2.2. To be specific, the radial distributions of $\sigma_{r\varphi}^{\text{sym}}$, $\sigma_{r\varphi}$, $\sigma_{\varphi r}$ as well as of m_{rz} for $\|\boldsymbol{t}_{\text{tang}}\|/\|\boldsymbol{t}_{\text{tang}}^{\text{max}}\| = 0.5$, respectively $\|\boldsymbol{t}_{\text{tang}}\|/\|\boldsymbol{t}_{\text{tang}}^{\text{max}}\| = 1.0$, are depicted in Figure 2.19. It can be observed that the absolute values of the studied coefficients of the stress and couple stress tensor increase with increasing load. However, the qualitative distribution along the radial direction remains identical within the analysed loading range.
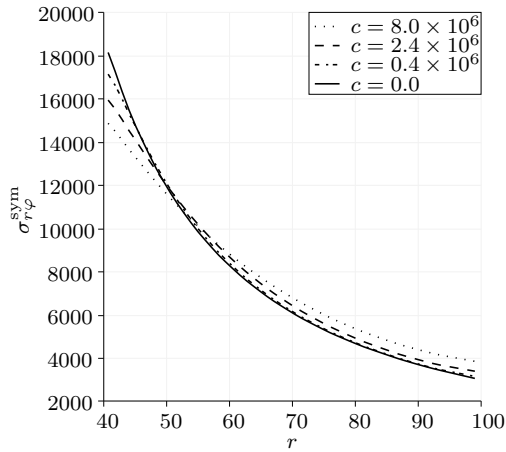
(a) $\sigma_{r\varphi}^{\mathrm{sym}}$ for $\|\boldsymbol{t}_{\mathrm{tang}}\|/\|\boldsymbol{t}_{\mathrm{tang}}^{\mathrm{max}}\| = 0.5$
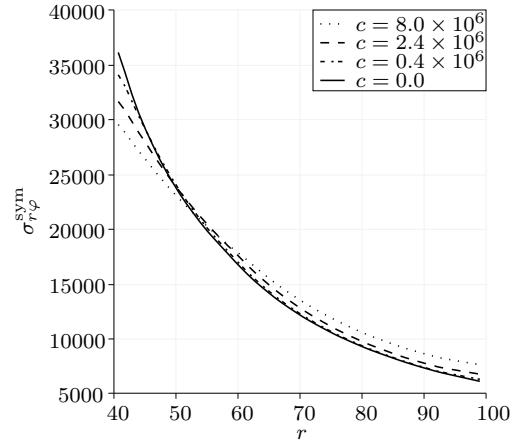
(b) $\sigma_{r\varphi}^{\mathrm{sym}}$ for $\|\boldsymbol{t}_{\mathrm{tang}}\|/\|\boldsymbol{t}_{\mathrm{tang}}^{\mathrm{max}}\| = 1.0$
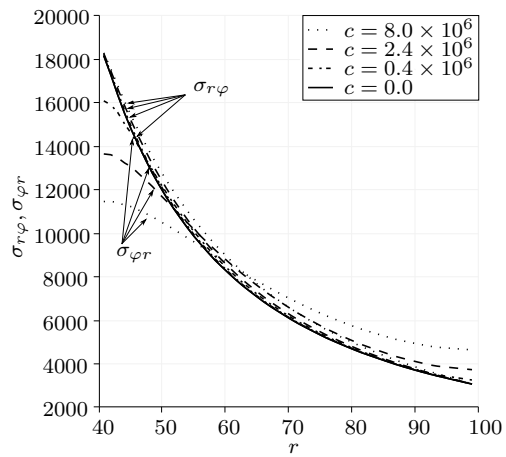
(c) $\sigma_{r\varphi}$ and $\sigma_{\varphi r}$ for $\|\boldsymbol{t}_{\mathrm{tang}}\|/\|\boldsymbol{t}_{\mathrm{tang}}^{\mathrm{max}}\| = 0.5$
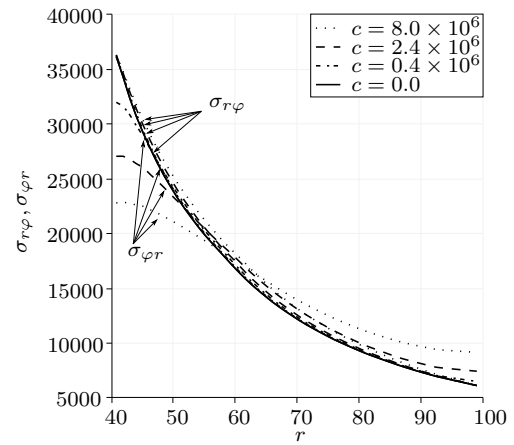
(d) $\sigma_{r\varphi}$ and $\sigma_{\varphi r}$ for $\|\boldsymbol{t}_{\mathrm{tang}}\|/\|\boldsymbol{t}_{\mathrm{tang}}^{\mathrm{max}}\| = 1.0$
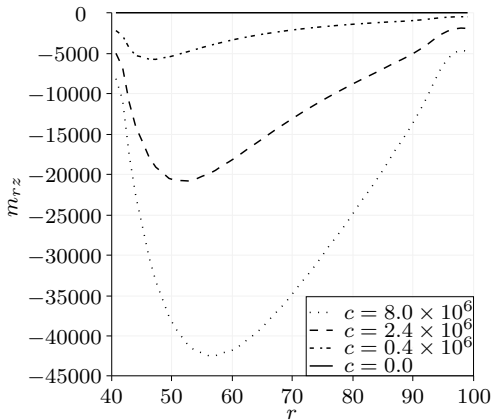
(e) m_{rz} for $\|\boldsymbol{t}_{\mathrm{tang}}\|/\|\boldsymbol{t}_{\mathrm{tang}}^{\mathrm{max}}\| = 0.5$
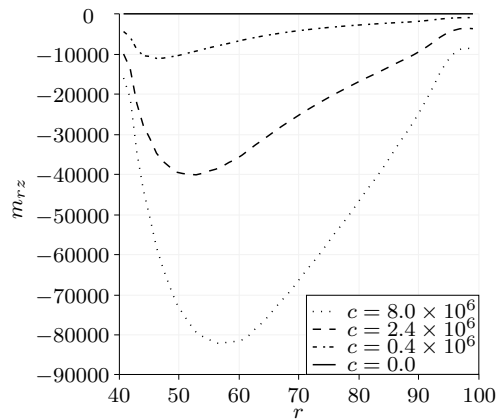
(f) m_{rz} for $\|\boldsymbol{t}_{\mathrm{tang}}\|/\|\boldsymbol{t}_{\mathrm{tang}}^{\mathrm{max}}\| = 1.0$

Figure 2.19: Analysis of the radial distribution of the stresses, the symmetric part of the stresses as well as the couple stresses for the loading states $\|\boldsymbol{t}_{\mathrm{tang}}\|/\|\boldsymbol{t}_{\mathrm{tang}}^{\mathrm{max}}\| = 0.5$ and $\|\boldsymbol{t}_{\mathrm{tang}}\|/\|\boldsymbol{t}_{\mathrm{tang}}^{\mathrm{max}}\| = 1.0$.

A.8 Derivatives of $\hat{I}$

This appendix presents the first and second derivatives of the invariant $\hat{I}$ with respect to the right Cauchy-Green tensor $\boldsymbol{C}$ and with respect to the gradient of the deformed fibre vector $\boldsymbol{\Lambda}$. These are required for the specification of the stress and couple stress tensor and of the corresponding tangent stiffness contributions.

$$\frac{\partial \hat{I}}{\partial \boldsymbol{C}} = -\frac{1}{2} \left[\boldsymbol{\kappa}_0 \otimes \boldsymbol{\kappa}_0 \right] : \left[\boldsymbol{C}^{-1} \overline{\otimes} \, \boldsymbol{C}^{-1} + \boldsymbol{C}^{-1} \underline{\otimes} \, \boldsymbol{C}^{-1} \right] \tag{2.169a}$$

$$\frac{\partial \hat{I}}{\partial \boldsymbol{\Lambda}} = 2 \, \boldsymbol{C}^{-1} \cdot \boldsymbol{\kappa}_0 \otimes \boldsymbol{a}_0 \tag{2.169b}$$

$$\frac{\partial^2 \hat{I}}{\partial \boldsymbol{C} \, \partial \boldsymbol{C}} = \left[\boldsymbol{\kappa}_0 \otimes \boldsymbol{\kappa}_0 \right] : \frac{\partial^2 \boldsymbol{C}^{-1}}{\partial \boldsymbol{C} \, \partial \boldsymbol{C}} \tag{2.170a}$$

$$\frac{\partial^2 \hat{I}}{\partial \boldsymbol{C} \, \partial \boldsymbol{\Lambda}} = - \left[\boldsymbol{C}^{-1} \cdot \boldsymbol{\kappa}_0 \right] \otimes \boldsymbol{C}^{-1} \otimes \boldsymbol{a}_0 - \boldsymbol{C}^{-1} \overline{\otimes} \left[\boldsymbol{\kappa}_0 \cdot \boldsymbol{C}^{-1} \otimes \boldsymbol{a}_0 \right] \tag{2.170b}$$

$$\frac{\partial^2 \hat{I}}{\partial \boldsymbol{\Lambda} \, \partial \boldsymbol{C}} = - \boldsymbol{C}^{-1} \overline{\otimes} \left[\boldsymbol{a}_0 \otimes \boldsymbol{\kappa}_0 \cdot \boldsymbol{C}^{-1} \right] - \boldsymbol{C}^{-1} \underline{\otimes} \left[\boldsymbol{a}_0 \otimes \boldsymbol{\kappa}_0 \cdot \boldsymbol{C}^{-1} \right] \tag{2.170c}$$

$$\frac{\partial^2 \hat{I}}{\partial \boldsymbol{\Lambda} \, \partial \boldsymbol{\Lambda}} = 2 \, \boldsymbol{C}^{-1} \overline{\otimes} \left[\boldsymbol{a}_0 \otimes \boldsymbol{a}_0 \right] \tag{2.170d}$$

A.9 Specification of the stress and couple stress tensor

The symmetric part of the stress tensor and the deviatoric part of the couple stress tensor have been specified in Section 2.3.1.2, respectively Remark 2.4 for different higher-gradient-based contributions to the stored energy function. In this appendix, the derivation of these tensors is presented in more detail. To this end, the particular useful relations (2.109) and (2.110) which result from

$$\boldsymbol{\kappa} \otimes \boldsymbol{\kappa} = \left[\bar{\boldsymbol{a}}_t \frac{\partial \lambda_\mathrm{A}}{\partial \boldsymbol{X}} \cdot \boldsymbol{a}_0 + \lambda_\mathrm{A} \frac{\partial \bar{\boldsymbol{a}}_t}{\partial \boldsymbol{X}} \cdot \boldsymbol{a}_0 \right] \otimes \left[\bar{\boldsymbol{a}}_t \frac{\partial \lambda_\mathrm{A}}{\partial \boldsymbol{X}} \cdot \boldsymbol{a}_0 + \lambda_\mathrm{A} \frac{\partial \bar{\boldsymbol{a}}_t}{\partial \boldsymbol{X}} \cdot \boldsymbol{a}_0 \right] \tag{2.171a}$$

$$= \left[\frac{\partial \lambda_\mathrm{A}}{\partial \boldsymbol{X}} \cdot \boldsymbol{a}_0 \right]^2 \bar{\boldsymbol{a}}_t \otimes \bar{\boldsymbol{a}}_t + \lambda_\mathrm{A} \left[\frac{\partial \lambda_\mathrm{A}}{\partial \boldsymbol{X}} \cdot \boldsymbol{a}_0 \right] \left[\frac{\partial \bar{\boldsymbol{a}}_t}{\partial \boldsymbol{X}} \cdot \boldsymbol{a}_0 \otimes \bar{\boldsymbol{a}}_t + \bar{\boldsymbol{a}}_t \otimes \frac{\partial \bar{\boldsymbol{a}}_t}{\partial \boldsymbol{X}} \cdot \boldsymbol{a}_0 \right]$$

$$+ \lambda_\mathrm{A}^2 \left[\frac{\partial \bar{\boldsymbol{a}}_t}{\partial \boldsymbol{X}} \cdot \boldsymbol{a}_0 \right] \otimes \left[\frac{\partial \bar{\boldsymbol{a}}_t}{\partial \boldsymbol{X}} \cdot \boldsymbol{a}_0 \right] \tag{2.171b}$$

$$= \left[\frac{\partial \lambda_\mathrm{A}}{\partial \boldsymbol{X}} \cdot \boldsymbol{a}_0 \right]^2 \bar{\boldsymbol{a}}_t \otimes \bar{\boldsymbol{a}}_t + \lambda_\mathrm{A}^2 \left[\frac{\partial \lambda_\mathrm{A}}{\partial \boldsymbol{X}} \cdot \boldsymbol{a}_0 \right] \left[\boldsymbol{\kappa}_\mathrm{tru} \otimes \bar{\boldsymbol{a}}_t + \bar{\boldsymbol{a}}_t \otimes \boldsymbol{\kappa}_\mathrm{tru} \right]$$

$$+ \lambda_\mathrm{A}^4 \, \boldsymbol{\kappa}_\mathrm{tru} \otimes \boldsymbol{\kappa}_\mathrm{tru} \quad , \tag{2.171c}$$

and

$$
\begin{aligned}
\boldsymbol{a}_t \otimes \boldsymbol{\kappa} + \boldsymbol{\kappa} \otimes \boldsymbol{a}_t =\ &\boldsymbol{a}_t \otimes \left[\bar{\boldsymbol{a}}_t \frac{\partial \lambda_\mathrm{A}}{\partial \boldsymbol{X}} \cdot \boldsymbol{a}_0 + \lambda_\mathrm{A} \frac{\partial \bar{\boldsymbol{a}}_t}{\partial \boldsymbol{X}} \cdot \boldsymbol{a}_0 \right] \\
&+ \left[\bar{\boldsymbol{a}}_t \frac{\partial \lambda_\mathrm{A}}{\partial \boldsymbol{X}} \cdot \boldsymbol{a}_0 + \lambda_\mathrm{A} \frac{\partial \bar{\boldsymbol{a}}_t}{\partial \boldsymbol{X}} \cdot \boldsymbol{a}_0 \right] \otimes \boldsymbol{a}_t
\end{aligned}
\tag{2.172a}
$$

$$
\begin{aligned}
=\ &2 \left[\lambda_\mathrm{A} \frac{\partial \lambda_\mathrm{A}}{\partial \boldsymbol{X}} \cdot \boldsymbol{a}_0 \right] \bar{\boldsymbol{a}}_t \otimes \bar{\boldsymbol{a}}_t \\
&+ \lambda_\mathrm{A}^2 \left[\left[\frac{\partial \bar{\boldsymbol{a}}_t}{\partial \boldsymbol{X}} \cdot \boldsymbol{a}_0 \right] \otimes \bar{\boldsymbol{a}}_t + \bar{\boldsymbol{a}}_t \otimes \left[\frac{\partial \bar{\boldsymbol{a}}_t}{\partial \boldsymbol{X}} \cdot \boldsymbol{a}_0 \right] \right]
\end{aligned}
\tag{2.172b}
$$

$$
=\ 2 \left[\lambda_\mathrm{A} \frac{\partial \lambda_\mathrm{A}}{\partial \boldsymbol{X}} \cdot \boldsymbol{a}_0 \right] \bar{\boldsymbol{a}}_t \otimes \bar{\boldsymbol{a}}_t + \lambda_\mathrm{A}^3 \left[\boldsymbol{\kappa}_\mathrm{tru} \otimes \bar{\boldsymbol{a}}_t + \bar{\boldsymbol{a}}_t \otimes \boldsymbol{\kappa}_\mathrm{tru} \right] \quad, \tag{2.172c}
$$

by making use of (2.6), (2.31c) and (2.98) will be taken into account in the ensuing derivations.

Regarding the contribution to the symmetric part of the stress tensor which results from the curvature-based energy contribution (2.105), one arrives at

$$
\boldsymbol{\sigma}_{\boldsymbol{\kappa}_\mathrm{tru}}^{\mathrm{sym}} = \eta_\mathrm{vol}\, J_{\boldsymbol{F}}^{-1} \left[2\,\boldsymbol{F} \cdot \frac{\partial W^{\boldsymbol{\kappa}_\mathrm{tru}}}{\partial \boldsymbol{C}} \cdot \boldsymbol{F}^\mathrm{t} + \boldsymbol{G} \cdot \left[\frac{\partial W^{\boldsymbol{\kappa}_\mathrm{tru}}}{\partial \boldsymbol{\Lambda}} \right]^\mathrm{t} \cdot \boldsymbol{F}^\mathrm{t} + \boldsymbol{F} \cdot \frac{\partial W^{\boldsymbol{\kappa}_\mathrm{tru}}}{\partial \boldsymbol{\Lambda}} \cdot \boldsymbol{G}^\mathrm{t} \right] \tag{2.173a}
$$

$$
\begin{aligned}
=\ &\frac{\eta_\mathrm{vol}\, c_{\boldsymbol{\kappa}_\mathrm{tru}}}{J_{\boldsymbol{F}}} \left[2\,\boldsymbol{F} \cdot \left[\left[3\,\frac{I_9^2}{I_4^4} - 2\,\frac{\hat{I}}{I_4^3} \right] \frac{\partial I_4}{\partial \boldsymbol{C}} + \frac{1}{I_4^2} \frac{\partial \hat{I}}{\partial \boldsymbol{C}} \right] \cdot \boldsymbol{F}^\mathrm{t} \right. \\
&+ \boldsymbol{G} \cdot \left[\frac{1}{I_4^2} \frac{\partial \hat{I}}{\partial \boldsymbol{\Lambda}} - 2\,\frac{I_9}{I_4^3} \frac{\partial I_9}{\partial \boldsymbol{\Lambda}} \right]^\mathrm{t} \cdot \boldsymbol{F}^\mathrm{t} \\
&\left. + \boldsymbol{F} \cdot \left[\frac{1}{I_4^2} \frac{\partial \hat{I}}{\partial \boldsymbol{\Lambda}} - 2\,\frac{I_9}{I_4^3} \frac{\partial I_9}{\partial \boldsymbol{\Lambda}} \right] \cdot \boldsymbol{G}^\mathrm{t} \right]
\end{aligned}
\tag{2.173b}
$$

$$
\begin{aligned}
=\ &\frac{\eta_\mathrm{vol}\, c_{\boldsymbol{\kappa}_\mathrm{tru}}}{J_{\boldsymbol{F}}} \left[2\,\boldsymbol{F} \cdot \left[\left[3\,\frac{I_9^2}{I_4^4} - 2\,\frac{\hat{I}}{I_4^3} \right] \boldsymbol{a}_0 \otimes \boldsymbol{a}_0 \right] \cdot \boldsymbol{F}^\mathrm{t} \right. \\
&2\,\boldsymbol{F} \cdot \left[-\frac{1}{2\,I_4^2} \left[\boldsymbol{\kappa}_0 \otimes \boldsymbol{\kappa}_0 \right] : \left[\boldsymbol{C}^{-1} \overline{\otimes} \boldsymbol{C}^{-1} + \boldsymbol{C}^{-1} \underline{\otimes} \boldsymbol{C}^{-1} \right] \right] \cdot \boldsymbol{F}^\mathrm{t} \\
&+ \boldsymbol{G} \cdot \left[\frac{2}{I_4^2} \boldsymbol{C}^{-1} \cdot \boldsymbol{\kappa}_0 \otimes \boldsymbol{a}_0 - 2\,\frac{I_9}{I_4^3} \boldsymbol{a}_0 \otimes \boldsymbol{a}_0 \right]^\mathrm{t} \cdot \boldsymbol{F}^\mathrm{t} \\
&\left. + \boldsymbol{F} \cdot \left[\frac{2}{I_4^2} \boldsymbol{C}^{-1} \cdot \boldsymbol{\kappa}_0 \otimes \boldsymbol{a}_0 - 2\,\frac{I_9}{I_4^3} \boldsymbol{a}_0 \otimes \boldsymbol{a}_0 \right] \cdot \boldsymbol{G}^\mathrm{t} \right]
\end{aligned}
\tag{2.173c}
$$

$$
= \frac{\eta_{\text{vol}}\, c_{\boldsymbol{\kappa}_{\text{tru}}}}{J_{\boldsymbol{F}}} \left[\left[6\,\frac{I_9^2}{I_4^4} - 4\,\frac{\hat{I}}{I_4^3} \right] \boldsymbol{a}_t \otimes \boldsymbol{a}_t - \frac{2}{I_4^2}\,\boldsymbol{\kappa} \otimes \boldsymbol{\kappa} \right.
$$
$$
\left. + \left[\frac{2}{I_4^2}\,\boldsymbol{\kappa} \otimes \boldsymbol{\kappa} - 2\,\frac{I_9}{I_4^3}\,\boldsymbol{\kappa} \otimes \boldsymbol{a}_t \right] + \left[\frac{2}{I_4^2}\,\boldsymbol{\kappa} \otimes \boldsymbol{\kappa} - 2\,\frac{I_9}{I_4^3}\,\boldsymbol{a}_t \otimes \boldsymbol{\kappa} \right] \right]
\tag{2.173d}
$$
$$
= \frac{\eta_{\text{vol}}\, c_{\boldsymbol{\kappa}_{\text{tru}}}}{J_{\boldsymbol{F}}} \left[\left[6\,\frac{I_9^2}{I_4^4} - 4\,\frac{\hat{I}}{I_4^3} \right] \boldsymbol{a}_t \otimes \boldsymbol{a}_t + \frac{2}{I_4^2}\,\boldsymbol{\kappa} \otimes \boldsymbol{\kappa} - 2\,\frac{I_9}{I_4^3}\,[\boldsymbol{\kappa} \otimes \boldsymbol{a}_t + \boldsymbol{a}_t \otimes \boldsymbol{\kappa}] \right]
\tag{2.173e}
$$

by making use of Table 2.5 and Appendix A.8. This representation of $\boldsymbol{\sigma}_{\boldsymbol{\kappa}_{\text{tru}}}^{\text{sym}}$ can further be simplified using (2.91), (2.101c) and (2.102) together with (2.171) and (2.172) such that

$$
\boldsymbol{\sigma}_{\boldsymbol{\kappa}_{\text{tru}}}^{\text{sym}} = \frac{\eta_{\text{vol}}\, c_{\boldsymbol{\kappa}_{\text{tru}}}}{J_{\boldsymbol{F}}} \left[\quad \left[\left[6\,\frac{I_9^2}{I_4^4} - 4\,\frac{\hat{I}}{I_4^3} \right] \lambda_{\text{A}}^2 + \frac{2}{I_4^2} \left[\frac{\partial \lambda_{\text{A}}}{\partial \boldsymbol{X}} \cdot \boldsymbol{a}_0 \right]^2 - 4\,\frac{I_9}{I_4^3} \left[\lambda_{\text{A}}\,\frac{\partial \lambda_{\text{A}}}{\partial \boldsymbol{X}} \cdot \boldsymbol{a}_0 \right] \right] \bar{\boldsymbol{a}}_t \otimes \bar{\boldsymbol{a}}_t \right.
$$
$$
+ \left[\frac{2}{I_4^2} \left[\frac{\partial \lambda_{\text{A}}}{\partial \boldsymbol{X}} \cdot \boldsymbol{a}_0 \right] \lambda_{\text{A}}^2 - 2\,\frac{I_9}{I_4^3}\,\lambda_{\text{A}}^3 \right] [\boldsymbol{\kappa}_{\text{tru}} \otimes \bar{\boldsymbol{a}}_t + \bar{\boldsymbol{a}}_t \otimes \boldsymbol{\kappa}_{\text{tru}}]
$$
$$
\left. + \quad \frac{2}{I_4^2}\,\lambda_{\text{A}}^4\,\boldsymbol{\kappa}_{\text{tru}} \otimes \boldsymbol{\kappa}_{\text{tru}} \right]
\tag{2.174a}
$$
$$
= \frac{\eta_{\text{vol}}\, c_{\boldsymbol{\kappa}_{\text{tru}}}}{J_{\boldsymbol{F}}} \left[-4\,\boldsymbol{\kappa}_{\text{tru}} \cdot \boldsymbol{\kappa}_{\text{tru}}\,\bar{\boldsymbol{a}}_t \otimes \bar{\boldsymbol{a}}_t + 2\,\boldsymbol{\kappa}_{\text{tru}} \otimes \boldsymbol{\kappa}_{\text{tru}} \right] \quad .
\tag{2.174b}
$$

The corresponding contribution of $W^{\boldsymbol{\kappa}_{\text{tru}}}$ to the deviatoric part of the couple stress tensor results from the evaluation of (2.30) by making use of (2.6), (2.169), Table 2.5 and by taking into account the skew-symmetry of the Levi-Civita tensor, specifically speaking

$$
\left[\boldsymbol{m}_{\boldsymbol{\kappa}_{\text{tru}}}^{\text{dev}} \right]^{\text{t}} = -\frac{2}{3}\,\eta_{\text{vol}}\,J_{\boldsymbol{F}}^{-1}\,\boldsymbol{\epsilon}_t : \left[\boldsymbol{F} \cdot \frac{\partial W^{\boldsymbol{\kappa}_{\text{tru}}}}{\partial \boldsymbol{\Lambda}} \cdot \left[\boldsymbol{F}^{\text{t}}\,\overline{\otimes}\,\boldsymbol{a}_t + \boldsymbol{F}^{\text{t}} \otimes \boldsymbol{a}_t \right] \right]
\tag{2.175a}
$$
$$
= -\frac{2}{3}\,\frac{\eta_{\text{vol}}\, c_{\boldsymbol{\kappa}_{\text{tru}}}}{J_{\boldsymbol{F}}}\,\boldsymbol{\epsilon}_t : \left[\boldsymbol{F} \cdot \left[\frac{2}{I_4^2}\,\boldsymbol{C}^{-1} \cdot \boldsymbol{\kappa}_0 \otimes \boldsymbol{a}_0 - 2\,\frac{I_9}{I_4^3}\,\boldsymbol{a}_0 \otimes \boldsymbol{a}_0 \right] \cdot \left[\boldsymbol{F}^{\text{t}}\,\overline{\otimes}\,\boldsymbol{a}_t + \boldsymbol{F}^{\text{t}} \otimes \boldsymbol{a}_t \right] \right]
\tag{2.175b}
$$
$$
= \frac{4}{3}\,\frac{\eta_{\text{vol}}\, c_{\boldsymbol{\kappa}_{\text{tru}}}}{J_{\boldsymbol{F}}}\,\boldsymbol{\epsilon}_t : \left[\frac{2}{I_4^2}\,\boldsymbol{a}_t \otimes \boldsymbol{\kappa} \otimes \boldsymbol{a}_t - 2\,\frac{I_9}{I_4^3}\,\boldsymbol{a}_t \otimes \boldsymbol{a}_t \otimes \boldsymbol{a}_t \right]
\tag{2.175c}
$$
$$
= \frac{4}{3}\,\frac{\eta_{\text{vol}}\, c_{\boldsymbol{\kappa}_{\text{tru}}}}{J_{\boldsymbol{F}}}\,\boldsymbol{\epsilon}_t : \left[\frac{2}{I_4^2}\,\boldsymbol{a}_t \otimes \boldsymbol{\kappa} \otimes \boldsymbol{a}_t \right] \quad .
\tag{2.175d}
$$

With the help of (2.31c) and (2.98), the latter representation of the couple stress contribution $\boldsymbol{m}_{\boldsymbol{\kappa}_{\text{tru}}}^{\text{dev}}$ may further be rewritten in the well-interpretable form

$$
\boldsymbol{m}_{\boldsymbol{\kappa}_{\text{tru}}}^{\text{dev}} = \frac{8}{3}\,\frac{\eta_{\text{vol}}\, c_{\boldsymbol{\kappa}_{\text{tru}}}}{J_{\boldsymbol{F}}}\,\frac{1}{I_4}\,\bar{\boldsymbol{a}}_t \otimes \left[\bar{\boldsymbol{a}}_t \times \left[\frac{\partial \lambda_{\text{A}}}{\partial \boldsymbol{X}} \cdot \boldsymbol{a}_0\,\bar{\boldsymbol{a}}_t + \lambda_{\text{A}}\,\frac{\partial \bar{\boldsymbol{a}}_t}{\partial \boldsymbol{X}} \cdot \boldsymbol{a}_0 \right] \right]
\tag{2.176a}
$$

$$= \frac{8}{3} \frac{\eta_{\mathrm{vol}} \, c_{\boldsymbol{\kappa}_{\mathrm{tru}}}}{J_{\boldsymbol{F}}} \, \bar{\boldsymbol{a}}_t \otimes [\bar{\boldsymbol{a}}_t \times \boldsymbol{\kappa}_{\mathrm{tru}}] \quad . \tag{2.176b}$$

Regarding the fibre stretch gradient-based contributions (2.116) and (2.117), the evaluation of the constitutive relation (2.29) results in

$$\boldsymbol{\sigma}^{\mathrm{sym}}_{\partial_{\boldsymbol{x}} \lambda_{\mathrm{A}}} = \eta_{\mathrm{vol}} \, J_{\boldsymbol{F}}^{-1} \left[2 \, \boldsymbol{F} \cdot \frac{\partial W^{\partial_{\boldsymbol{x}} \lambda_{\mathrm{A}}}}{\partial \boldsymbol{C}} \cdot \boldsymbol{F}^{\mathrm{t}} + \boldsymbol{G} \cdot \left[\frac{\partial W^{\partial_{\boldsymbol{x}} \lambda_{\mathrm{A}}}}{\partial \boldsymbol{\Lambda}} \right]^{\mathrm{t}} \cdot \boldsymbol{F}^{\mathrm{t}} + \boldsymbol{F} \cdot \frac{\partial W^{\partial_{\boldsymbol{x}} \lambda_{\mathrm{A}}}}{\partial \boldsymbol{\Lambda}} \cdot \boldsymbol{G}^{\mathrm{t}} \right]$$

$$= \frac{\eta_{\mathrm{vol}} \, c_{\partial_{\boldsymbol{x}} \lambda_{\mathrm{A}}}}{J_{\boldsymbol{F}}} \left[2 \, \boldsymbol{F} \cdot \left[-2 \frac{I_9^2}{I_4^3} \, \boldsymbol{a}_0 \otimes \boldsymbol{a}_0 \right] \cdot \boldsymbol{F}^{\mathrm{t}} \right.$$

$$\left. + \boldsymbol{G} \cdot \left[2 \frac{I_9}{I_4^2} \, \boldsymbol{a}_0 \otimes \boldsymbol{a}_0 \right] \cdot \boldsymbol{F}^{\mathrm{t}} \right. \tag{2.177a}$$

$$\left. + \boldsymbol{F} \cdot \left[2 \frac{I_9}{I_4^2} \, \boldsymbol{a}_0 \otimes \boldsymbol{a}_0 \right] \cdot \boldsymbol{G}^{\mathrm{t}} \right]$$

$$= \frac{\eta_{\mathrm{vol}} \, c_{\partial_{\boldsymbol{x}} \lambda_{\mathrm{A}}}}{J_{\boldsymbol{F}}} \left[-4 \frac{I_9^2}{I_4^3} \, \boldsymbol{a}_t \otimes \boldsymbol{a}_t + 2 \frac{I_9}{I_4^2} \, [\boldsymbol{\kappa} \otimes \boldsymbol{a}_t + \boldsymbol{a}_t \otimes \boldsymbol{\kappa}] \right] \tag{2.177b}$$

$$= \frac{\eta_{\mathrm{vol}} \, c_{\partial_{\boldsymbol{x}} \lambda_{\mathrm{A}}}}{J_{\boldsymbol{F}}} \left[\; 2 \frac{I_9}{I_4^2} \, \lambda_{\mathrm{A}}^3 \, [\boldsymbol{\kappa}_{\mathrm{tru}} \otimes \bar{\boldsymbol{a}}_t + \bar{\boldsymbol{a}}_t \otimes \boldsymbol{\kappa}_{\mathrm{tru}}] \right] \tag{2.177c}$$

$$= \frac{\eta_{\mathrm{vol}} \, c_{\partial_{\boldsymbol{x}} \lambda_{\mathrm{A}}}}{J_{\boldsymbol{F}}} \left[\; 2 \, \lambda_{\mathrm{A}} \left[\frac{\partial \lambda_{\mathrm{A}}}{\partial \boldsymbol{x}} \cdot \bar{\boldsymbol{a}}_t \right] [\boldsymbol{\kappa}_{\mathrm{tru}} \otimes \bar{\boldsymbol{a}}_t + \bar{\boldsymbol{a}}_t \otimes \boldsymbol{\kappa}_{\mathrm{tru}}] \right] \quad , \tag{2.177d}$$

respectively

$$\boldsymbol{\sigma}^{\mathrm{sym}}_{\partial_{\boldsymbol{X}} \lambda_{\mathrm{A}}} = \eta_{\mathrm{vol}} \, J_{\boldsymbol{F}}^{-1} \left[2 \, \boldsymbol{F} \cdot \frac{\partial W^{\partial_{\boldsymbol{X}} \lambda_{\mathrm{A}}}}{\partial \boldsymbol{C}} \cdot \boldsymbol{F}^{\mathrm{t}} + \boldsymbol{G} \cdot \left[\frac{\partial W^{\partial_{\boldsymbol{X}} \lambda_{\mathrm{A}}}}{\partial \boldsymbol{\Lambda}} \right]^{\mathrm{t}} \cdot \boldsymbol{F}^{\mathrm{t}} + \boldsymbol{F} \cdot \frac{\partial W^{\partial_{\boldsymbol{X}} \lambda_{\mathrm{A}}}}{\partial \boldsymbol{\Lambda}} \cdot \boldsymbol{G}^{\mathrm{t}} \right]$$

$$= \frac{\eta_{\mathrm{vol}} \, c_{\partial_{\boldsymbol{X}} \lambda_{\mathrm{A}}}}{J_{\boldsymbol{F}}} \left[2 \, \boldsymbol{F} \cdot \left[-\frac{I_9^2}{I_4^2} \, \boldsymbol{a}_0 \otimes \boldsymbol{a}_0 \right] \cdot \boldsymbol{F}^{\mathrm{t}} \right.$$

$$\left. + \boldsymbol{G} \cdot \left[2 \frac{I_9}{I_4} \, \boldsymbol{a}_0 \otimes \boldsymbol{a}_0 \right]^{\mathrm{t}} \cdot \boldsymbol{F}^{\mathrm{t}} \right. \tag{2.178a}$$

$$\left. + \boldsymbol{F} \cdot \left[2 \frac{I_9}{I_4} \, \boldsymbol{a}_0 \otimes \boldsymbol{a}_0 \right] \cdot \boldsymbol{G}^{\mathrm{t}} \right]$$

$$= \frac{\eta_{\mathrm{vol}} \, c_{\partial_{\boldsymbol{X}} \lambda_{\mathrm{A}}}}{J_{\boldsymbol{F}}} \left[-2 \frac{I_9^2}{I_4^2} \, \boldsymbol{a}_t \otimes \boldsymbol{a}_t + 2 \frac{I_9}{I_4} \, [\boldsymbol{\kappa} \otimes \boldsymbol{a}_t + \boldsymbol{a}_t \otimes \boldsymbol{\kappa}] \right] \tag{2.178b}$$

$$= \frac{\eta_{\mathrm{vol}} \, c_{\partial_{\boldsymbol{X}} \lambda_{\mathrm{A}}}}{J_{\boldsymbol{F}}} \left[\; 2 \frac{I_9^2}{I_4} \, \bar{\boldsymbol{a}}_t \otimes \bar{\boldsymbol{a}}_t + 2 \frac{I_9}{I_4} \, \lambda_{\mathrm{A}}^3 \, [\boldsymbol{\kappa}_{\mathrm{tru}} \otimes \bar{\boldsymbol{a}}_t + \bar{\boldsymbol{a}}_t \otimes \boldsymbol{\kappa}_{\mathrm{tru}}] \right] \tag{2.178c}$$

$$= \frac{\eta_{\mathrm{vol}}\, c_{\partial_{\boldsymbol{X}}\lambda_{\mathrm{A}}}}{J_{\boldsymbol{F}}} \left[\quad 2\left[\frac{\partial\lambda_{\mathrm{A}}}{\partial\boldsymbol{X}}\cdot\boldsymbol{a}_0\right]^2\bar{\boldsymbol{a}}_t\otimes\bar{\boldsymbol{a}}_t + 2\,\lambda_{\mathrm{A}}^2\left[\frac{\partial\lambda_{\mathrm{A}}}{\partial\boldsymbol{X}}\cdot\boldsymbol{a}_0\right]\left[\boldsymbol{\kappa}_{\mathrm{tru}}\otimes\bar{\boldsymbol{a}}_t + \bar{\boldsymbol{a}}_t\otimes\boldsymbol{\kappa}_{\mathrm{tru}}\right]\right]$$

$$(2.178\mathrm{d})$$

where use was made of (2.31a), (2.91), (2.102), (2.110), and Table 2.5. Evaluating (2.30) finally results in the contributions

$$\left[\boldsymbol{m}^{\mathrm{dev}}_{\partial_{\boldsymbol{x}}\lambda_{\mathrm{A}}}\right]^{\mathrm{t}} = -\frac{2}{3}\frac{\eta_{\mathrm{vol}}}{J_{\boldsymbol{F}}} \qquad \boldsymbol{\epsilon}_t : \left[\boldsymbol{F}\cdot\frac{\partial W^{\partial_{\boldsymbol{x}}\lambda_{\mathrm{A}}}}{\partial\boldsymbol{\Lambda}}\cdot\left[\boldsymbol{F}^{\mathrm{t}}\,\overline{\otimes}\,\boldsymbol{a}_t + \boldsymbol{F}^{\mathrm{t}}\otimes\boldsymbol{a}_t\right]\right] \qquad (2.179\mathrm{a})$$

$$= -\frac{2}{3}\frac{\eta_{\mathrm{vol}}\, c_{\partial_{\boldsymbol{x}}\lambda_{\mathrm{A}}}}{J_{\boldsymbol{F}}} \quad \boldsymbol{\epsilon}_t : \left[\boldsymbol{F}\cdot\left[2\frac{I_9}{I_4^2}\boldsymbol{a}_0\otimes\boldsymbol{a}_0\right]\cdot\left[\boldsymbol{F}^{\mathrm{t}}\,\overline{\otimes}\,\boldsymbol{a}_t + \boldsymbol{F}^{\mathrm{t}}\otimes\boldsymbol{a}_t\right]\right] \quad (2.179\mathrm{b})$$

$$= -\frac{8}{3}\frac{\eta_{\mathrm{vol}}\, c_{\partial_{\boldsymbol{x}}\lambda_{\mathrm{A}}}}{J_{\boldsymbol{F}}}\frac{I_9}{I_4^2}\,\boldsymbol{\epsilon}_t : \left[\boldsymbol{a}_t\otimes\boldsymbol{a}_t\otimes\boldsymbol{a}_t\right] \qquad (2.179\mathrm{c})$$

$$= \quad\boldsymbol{0} \qquad (2.179\mathrm{d})$$

and

$$\left[\boldsymbol{m}^{\mathrm{dev}}_{\partial_{\boldsymbol{X}}\lambda_{\mathrm{A}}}\right]^{\mathrm{t}} = -\frac{2}{3}\frac{\eta_{\mathrm{vol}}}{J_{\boldsymbol{F}}} \qquad \boldsymbol{\epsilon}_t : \left[\boldsymbol{F}\cdot\frac{\partial W^{\partial_{\boldsymbol{X}}\lambda_{\mathrm{A}}}}{\partial\boldsymbol{\Lambda}}\cdot\left[\boldsymbol{F}^{\mathrm{t}}\,\overline{\otimes}\,\boldsymbol{a}_t + \boldsymbol{F}^{\mathrm{t}}\otimes\boldsymbol{a}_t\right]\right] \qquad (2.180\mathrm{a})$$

$$= -\frac{2}{3}\frac{\eta_{\mathrm{vol}}\, c_{\partial_{\boldsymbol{X}}\lambda_{\mathrm{A}}}}{J_{\boldsymbol{F}}} \quad \boldsymbol{\epsilon}_t : \left[\boldsymbol{F}\cdot\left[2\frac{I_9}{I_4}\boldsymbol{a}_0\otimes\boldsymbol{a}_0\right]\cdot\left[\boldsymbol{F}^{\mathrm{t}}\,\overline{\otimes}\,\boldsymbol{a}_t + \boldsymbol{F}^{\mathrm{t}}\otimes\boldsymbol{a}_t\right]\right] \quad (2.180\mathrm{b})$$

$$= -\frac{8}{3}\frac{\eta_{\mathrm{vol}}\, c_{\partial_{\boldsymbol{X}}\lambda_{\mathrm{A}}}}{J_{\boldsymbol{F}}}\frac{I_9}{I_4}\,\boldsymbol{\epsilon}_t : \left[\boldsymbol{a}_t\otimes\boldsymbol{a}_t\otimes\boldsymbol{a}_t\right] \qquad (2.180\mathrm{c})$$

$$= \quad\boldsymbol{0} \qquad (2.180\mathrm{d})$$

to the deviatoric part of the couple stress tensor.

A.10 Follower forces

In Section 2.3.2.1, Section 2.3.2.2 and Section 2.3.2.3 the load has been applied in terms of follower forces which act normal to the beam's surface and which are defined per unit area of the reference configuration. The amplitude of the follower forces may alternatively be defined per unit area related to the current configuration. This, however, leads to an unwanted deformation of the beam as shown in Figure 2.20(a) – the deformed shape of the beam is not circular. When evaluating the resulting force $\boldsymbol{f}^{\mathrm{pre}}$ which acts at the right boundary, it turns out that the component in vertical direction $[\boldsymbol{f}^{\mathrm{pre}}\cdot\boldsymbol{e}_2]\,\boldsymbol{e}_2$ monotonically decreases over the first 25 load steps, Figure 2.20(b). Although the overall resulting force is small compared with the nodal forces, its influence on the deformation is striking. However, for the boundary value problem at hand, this non-zero resulting force takes a noticeably smaller absolute value if the traction load is defined per unit area of the reference configuration, resulting in a different deformation.
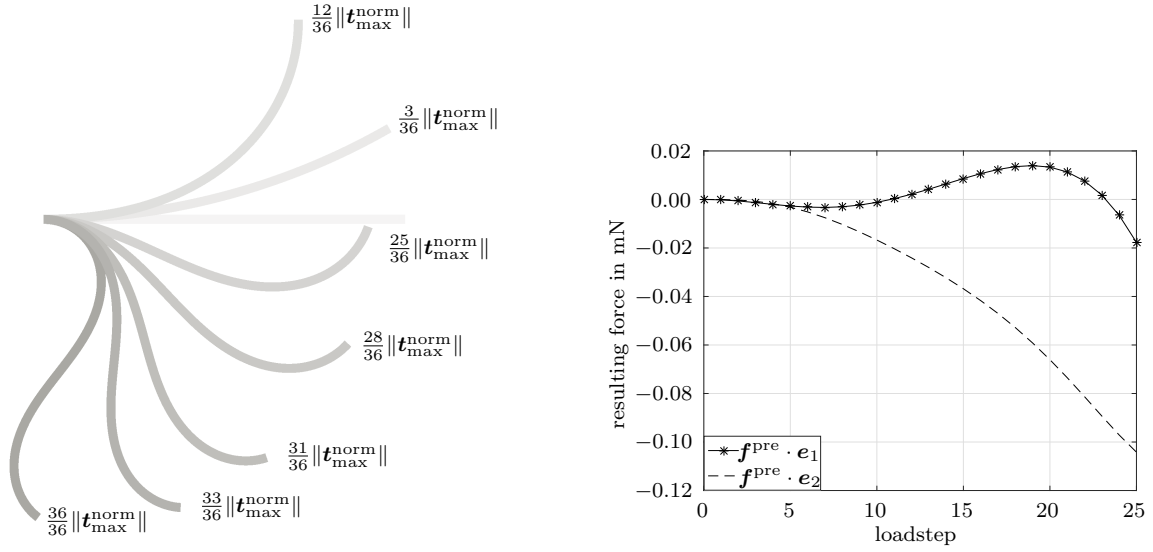
(a) Deformation of the beam for the first 36 load steps.

(b) Resulting prescribed force $\boldsymbol{f}^{\mathrm{pre}}$, acting on the right boundary, for the first 25 load steps.

Figure 2.20: Analysis of the deformation and the resulting force which is applied at the right boundary of a fibre-reinforced beam with negligible bending stiffness. The traction load is prescribed in terms of follower forces acting normal to the surface with the load magnitude being defined per unit area of the current configuration.

In the following, the governing equations are given for the follower forces as they have been used in this contribution. The implementation of follower loads defined per unit area of the current configuration is presented in, e.g. [145]. The corresponding integral expression which contributes to the vector of external forces is given by

$$\int_{\partial \mathcal{B}_t} \boldsymbol{\eta}^{\varphi} \cdot \boldsymbol{n} \, \|\boldsymbol{t}^{\mathrm{norm}}\| \, \mathrm{d}a \quad , \tag{2.181}$$

with the test function of the balance equation of linear momentum denoted by $\boldsymbol{\eta}^{\varphi}$ and the integration to be performed on the body's surface. For the two-dimensional case we introduce the area measures $J_{\square}^0 = \|\boldsymbol{e}_3 \times \partial \boldsymbol{X}/\partial \xi\|$ and $J_{\square}^t = \|\boldsymbol{e}_3 \times \partial \boldsymbol{x}/\partial \xi\|$, with the derivative to be performed with respect to the convective coordinate ξ. With these definitions at hand, the integral expression analogous to (2.181) with the amplitude of the follower load defined per unit area of the reference configuration reads

$$\int_{\partial \mathcal{B}_t} \boldsymbol{\eta}^{\varphi} \cdot \boldsymbol{n} \, \|\boldsymbol{t}^{\mathrm{norm},0}\| \, \frac{J_{\square}^0}{J_{\square}^t} \, \mathrm{d}a \quad . \tag{2.182}$$
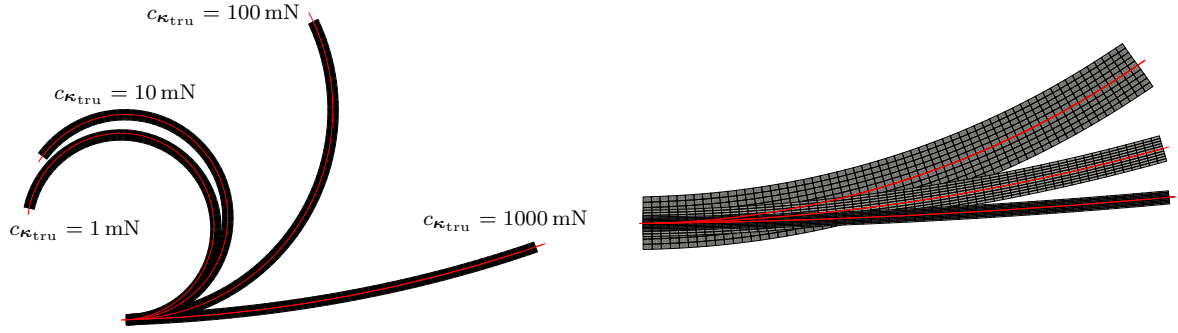
(a) Analysis of circular deformation patterns in dependence of the fibre-bending stiffness parameter $c_{\boldsymbol{\kappa}_{\mathrm{tru}}}$.

(b) Analysis of circular deformation patterns for fibre-reinforced beams with $c_{\boldsymbol{\kappa}_{\mathrm{tru}}} = 1000\,\mathrm{mN}$ of different sizes.

Figure 2.21: Analysis of the circular deformation pattern for fibre-reinforced beams for varying values of material parameter $c_{\boldsymbol{\kappa}_{\mathrm{tru}}}$ and for varying problem dimensions. The deformed configurations of the beams are provided by means of the respective finite element mesh. The circle which is used for the approximation of the overall equivalent bending stiffness, see (2.122), and which is fitted through three nodes of the beam is given as a red-coloured line.

A.11 Approximation of the bending radius

For the approximation of the bending radius r_{ben}, a circle is fitted through three nodes which are positioned at the middle of the left surface, the middle of the right surface and at the centre of the beam. These nodes are highlighted in Figure 2.14 by black-coloured dots, and the coefficients of their position vectors with respect to a Cartesian base system are denoted by P_1, P_2, Q_1, Q_2 and R_1, R_2. With these definitions at hand, the closed form solutions for the coefficients of the position vector of the centre of the circle are given by

$$C_1 = \frac{[P_1^2 + P_2^2]\,[Q_2 - R_2] + [Q_1^2 + Q_2^2]\,[R_2 - P_2] + [R_1^2 + R_2^2]\,[P_2 - Q_2]}{2\,[P_1\,[Q_2 - R_2] - P_2\,[Q_1 - R_1] + Q_1\,R_2 - R_1\,Q_2]} \quad , \tag{2.183a}$$

$$C_2 = \frac{[P_1^2 + P_2^2]\,[R_1 - Q_1] + [Q_1^2 + Q_2^2]\,[P_1 - R_1] + [R_1^2 + R_2^2]\,[Q_1 - P_1]}{2\,[P_1\,[Q_2 - R_2] - P_2\,[Q_1 - R_1] + Q_1\,R_2 - R_1\,Q_2]} \quad , \tag{2.183b}$$

and the bending radius can be specified according to

$$r_{\mathrm{ben}} = \sqrt{[C_1 - P_1]^2 + [C_2 - P_2]^2} \quad . \tag{2.184}$$

3 Dislocation density tensor-based gradient plasticity

In this chapter, a physically well-motived gradient plasticity theory is developed which is based on an extended nonlocal form of the Clausius-Duhem inequality and which relies on the interpretation of incompatibilities in terms of dislocation densities. In particular:

Section 3.1 *(Constitutive framework)* briefly recapitulates the geometrical foundations of incompatibilities and their interpretation in terms of dislocation densities. Setting the stage, the fundamentals of the gradient plasticity theory proposed in [106] are summarised. It is then shown that accounting for the dislocation density tensor in an energetic manner gives rise to the field equation of a generalised stress tensor that is energetically conjugated to the plastic deformation.

Section 3.2 *(An associated-type gradient plasticity formulation)* focuses on the elaboration of a specific associated-type plasticity model within the framework of the proposed gradient plasticity theory. In particular, a specific form of the gradient energy contribution which results into well-interpretable contributions to the generalised stress tensor is proposed, and the numerical solution of the underlying coupled system of partial differential equations, with the plastic consistency condition being accounted for by means of Fischer-Burmeister complementary functions on a global level, is discussed. Moreover, representative boundary value problems are studied in two- and three-dimensional settings.

Section 3.3 *(A gradient crystal plasticity formulation)* extends the formulation to gradient crystal plasticity. After proposing a specific crystal (visco-)plasticity model and after a detailed discussion of the related stabilisation algorithms which are used to approach the rate-independent limit, a different interpretation of the field equations is taken to derive a suitable finite element formulation. With the latter at hand and motivated by the experimental findings presented in Section 1.1.2, the focus lies especially on the analysis of micro torsion tests and on the observed size effects.

3.1 Constitutive framework

For the convenience of the reader some kinematic basics of dislocation density tensors and their interpretation in the context of multiplicative finite plasticity are briefly summarised in Section 3.1.1. Furthermore, the fundamentals of the gradient plasticity theory used are introduced in Section 3.1.2.

3.1.1 Kinematics and dislocation density tensors

In this chapter we set forth to develop a constitutive theory for the modelling of finite strain plasticity which is based on additional kinematic quantities that measure the incompatibility of the related mappings and that can be interpreted as dislocation density tensors from a physics point of view. Setting the stage, let the reference configuration of the body under consideration at reference time $t_0 \in \mathbb{R}$ be denoted by $\mathcal{B}_0 \subset \mathbb{R}^3$ and the (current) configuration at time $t \geq t_0$ be given by $\mathcal{B}_t \subset \mathbb{R}^3$. We identify the position of a material point in the reference configuration by $\boldsymbol{X} \in \mathcal{B}_0$ and relate the current position $\boldsymbol{x} \in \mathcal{B}_t$ via the point mapping $\boldsymbol{\varphi}\left(\boldsymbol{X}, t\right) : \mathcal{B}_0 \times \mathbb{R} \to \mathcal{B}_t \subset \mathbb{R}^3$. The deformation gradient tensor $\boldsymbol{F} = \partial \boldsymbol{\varphi}\left(\boldsymbol{X}, t\right) / \partial \boldsymbol{X}$ with $J_{\boldsymbol{F}} = \det\left(\boldsymbol{F}\right) > 0$ is defined as the associated tangent map and can be shown to be curl-free

$$\mathrm{Curl}^{\mathrm{t}}\left(\boldsymbol{F}\right) = -\frac{\partial \boldsymbol{F}}{\partial \boldsymbol{X}} : \boldsymbol{\epsilon}_0 = \boldsymbol{0} \quad , \tag{3.1}$$

see e.g. [133] for a more general representation in terms of curvilinear coordinates. Essentially, (3.1) implies that the (spatial) closure failure of a (referential) line integral of $\mathrm{d}\boldsymbol{x}$ over an arbitrary closed path $\partial\mathscr{A}_0$ bounding the area $\mathscr{A}_0$ with unit normal $\boldsymbol{N}$ vanishes, which becomes apparent when applying Stokes' theorem

$$\oint_{\partial\mathscr{A}_0} \mathrm{d}\boldsymbol{x} = \oint_{\partial\mathscr{A}_0} \boldsymbol{F} \cdot \mathrm{d}\boldsymbol{X} = \int_{\mathscr{A}_0} \mathrm{Curl}^{\mathrm{t}} \boldsymbol{F} \cdot \boldsymbol{N} \, \mathrm{d}A = \boldsymbol{0} \quad , \tag{3.2}$$

i.e. the deformation map $\boldsymbol{\varphi}$ is compatible. In the spirit of multiplicative finite plasticity the (incompatible) intermediate configuration $\overline{\mathcal{B}}$ is introduced which is generally only defined locally in terms of the tangent maps that result from the multiplicative decomposition of the deformation gradient into a plastic part $\boldsymbol{F}_{\mathrm{p}}$ and into an elastic part $\boldsymbol{F}_{\mathrm{e}}$ according to, [71],

$$\boldsymbol{F} = \boldsymbol{F}_{\mathrm{e}} \cdot \boldsymbol{F}_{\mathrm{p}} \quad . \tag{3.3}$$

The incompatibility of the deformations $\boldsymbol{F}_{\mathrm{e}}$ and $\boldsymbol{F}_{\mathrm{p}}$ can be associated with the presence of defects, in particular with the presence of geometrically necessary dislocations (GND), in crystalline materials, see e.g. [2, 19, 49, 66, 69, 99, 133] for materials science and differential geometric approaches. In this regard, a measure of incompatibility is given

by Burgers vector $\boldsymbol{\beta}$ (in the intermediate configuration) that can either be defined in terms of the Burgers circuit relative to the current configuration

$$\boldsymbol{\beta} = \int_{\partial\mathscr{A}_t} \boldsymbol{F}_{\mathrm{e}}^{-1} \cdot \mathrm{d}\boldsymbol{x} = \int_{\mathscr{A}_t} \mathrm{curl}^{\mathrm{t}}\left(\boldsymbol{F}_{\mathrm{e}}^{-1}\right) \cdot \boldsymbol{n}\,\mathrm{d}a = \int_{\mathscr{A}_t} \boldsymbol{d} \cdot \boldsymbol{n}\,\mathrm{d}a \tag{3.4}$$

or, alternatively and equivalently, in terms of the Burgers circuit relative to the reference configuration

$$\boldsymbol{\beta} = \int_{\partial\mathscr{A}_0} \boldsymbol{F}_{\mathrm{p}} \cdot \mathrm{d}\boldsymbol{X} = \int_{\mathscr{A}_0} \mathrm{Curl}^{\mathrm{t}}\left(\boldsymbol{F}_{\mathrm{p}}\right) \cdot \boldsymbol{N}\,\mathrm{d}A = \int_{\mathscr{A}_0} \boldsymbol{D} \cdot \boldsymbol{N}\,\mathrm{d}A \quad . \tag{3.5}$$

Moreover, (3.4) and (3.5) give rise to the definition of the (unsymmetrical, two-point) dislocation density tensors

$$\boldsymbol{d} = \mathrm{curl}^{\mathrm{t}}\left(\boldsymbol{F}_{\mathrm{e}}^{-1}\right) \tag{3.6}$$

and

$$\boldsymbol{D} = \mathrm{Curl}^{\mathrm{t}}\left(\boldsymbol{F}_{\mathrm{p}}\right) \tag{3.7}$$

that are related via Nanson's formula $J_{\boldsymbol{F}}\,\boldsymbol{d} \cdot \boldsymbol{F}^{-\mathrm{t}} = \boldsymbol{D}$, see [75, 87, 90, 133] for more details. Adhering to a continuum point of view, we neither resolve individual dislocation lines nor their corresponding Burgers vectors. Rather, a continuous distribution of dislocations is assumed such that $\boldsymbol{\beta}$ is to be interpreted as the cumulative Burgers vector of all dislocation lines piercing the area element $\mathscr{A}_t$, respectively $\mathscr{A}_0$. Following the same argument, the dislocation density tensors $\boldsymbol{D}$ and $\boldsymbol{d}$ represent measures of the dislocation line density per unit area reference, respectively per unit area current configuration. Based on these kinematic observations, the main idea of the theory to be presented in Section 3.1.2 is to take into account the information on the GND-density in the stored energy function which naturally gives rise to a kinematic-type hardening relation, as will be shown as this work proceeds.

3.1.2 Fundamentals of the gradient plasticity approach

The theory to be presented in this section is based on the fundamental developments by Polizzotto and Borino [106], as well as on the works [73–75] in which the theory of Polizzotto and Borino is applied to the modelling of damage and plasticity.

At the outset, it is assumed that the material response may be characterised by the free energy density function

$$W = \widetilde{W}\left(\boldsymbol{F}_{\mathrm{e}}, \boldsymbol{D}, \kappa\right) = \widetilde{W}\left(\boldsymbol{F}, \boldsymbol{F}_{\mathrm{p}}, \boldsymbol{D}, \kappa\right) \tag{3.8}$$
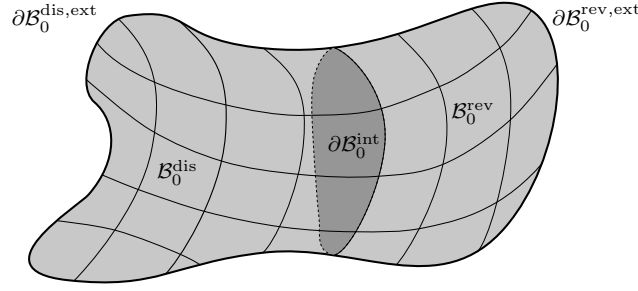
Figure 3.1: Elastic-plastic domain decomposition in the reference configuration. The reference configuration $\mathcal{B}_0$ is decomposed into an elastically deforming region $\mathcal{B}_0^{\mathrm{rev}}$ and a region $\mathcal{B}_0^{\mathrm{dis}}$ where irreversible (elasto-plastic) deformation processes take place. Note, that the decomposition is subjected to the constraints $\mathcal{B}_0 = \mathcal{B}_0^{\mathrm{rev}} \bigcup \mathcal{B}_0^{\mathrm{dis}}$ and $\mathcal{B}_0^{\mathrm{rev}} \bigcap \mathcal{B}_0^{\mathrm{dis}} = \emptyset$.

which, in addition to the deformation gradient and the plastic part of the deformation gradient, takes into account information on the geometrically necessary dislocation density via $\boldsymbol{D}$ and features an internal scalar valued variable κ which may be used to account for isotropic hardening effects that are related to statistically stored dislocations. In the spirit of [106], an extended nonlocal form of the classic dissipation inequality, namely

$$\widetilde{\mathcal{D}} = \boldsymbol{P} : \dot{\boldsymbol{F}} - \dot{\widetilde{W}} + \mathscr{P}_0 \tag{3.9a}$$

$$= \boldsymbol{P} : \dot{\boldsymbol{F}} - \left[\frac{\partial \widetilde{W}}{\partial \boldsymbol{F}} : \dot{\boldsymbol{F}} + \frac{\partial \widetilde{W}}{\partial \boldsymbol{F}_{\mathrm{p}}} : \dot{\boldsymbol{F}}_{\mathrm{p}} + \frac{\partial \widetilde{W}}{\partial \boldsymbol{D}} : \dot{\boldsymbol{D}} + \frac{\partial \widetilde{W}}{\partial \kappa} \dot{\kappa} \right] + \mathscr{P}_0 \geq 0 \tag{3.9b}$$

is proposed. This approach features the nonlocality residual $\mathscr{P}_0$ that allows for an energy exchange between particles at the microstructural level in some diffusion domain which is assumed to coincide with the region where the irreversible deformation processes take place, $\mathcal{B}_0^{\mathrm{dis}} \subseteq \mathcal{B}_0$, see also Figure 3.1. We take note of the fact that

$$\int_{\mathcal{B}_0^*} \mathscr{P}_0 \, \mathrm{d}V = 0 \quad \forall \mathcal{B}_0^* : \ \mathcal{B}_0^{\mathrm{dis}} \subseteq \mathcal{B}_0^* \subseteq \mathcal{B}_0 \tag{3.10}$$

holds for any part of the body $\mathcal{B}_0^*$ that contains the region where the dissipative process occurs. This, in turn, yields the so-called insulation condition

$$\int_{\mathcal{B}_0^{\mathrm{dis}}} \mathscr{P}_0 \, \mathrm{d}V = 0 \quad , \tag{3.11}$$

for $\mathscr{P}_0$, see [75, 106]. Note, that the insulation condition implies that no energy exchange between particles in $\mathcal{B}_0^{\mathrm{dis}}$ and those outside of $\mathcal{B}_0^{\mathrm{dis}}$ occurs. Furthermore, the nonlocality residual has to vanish identically in the elastic region, i.e.

$$\mathscr{P}_0 = 0 \quad \text{in} \quad \mathcal{B}_0^{\mathrm{rev}} \tag{3.12}$$

holds, such that (3.9) is still valid in its classic form for the elastic region. With regard to (3.9), the use of standard arguments results in the definition of the Piola stress tensor

$$\boldsymbol{P} = \frac{\partial \widetilde{W}}{\partial \boldsymbol{F}} \tag{3.13}$$

and yields the reduced (nonlocal) dissipation inequality

$$\widetilde{\mathcal{D}}^{\mathrm{red}} = -\frac{\partial \widetilde{W}}{\partial \boldsymbol{F}_{\mathrm{p}}} : \dot{\boldsymbol{F}}_{\mathrm{p}} - \frac{\partial \widetilde{W}}{\partial \boldsymbol{D}} : \dot{\boldsymbol{D}} - \frac{\partial \widetilde{W}}{\partial \kappa}\, \dot{\kappa} + \mathscr{P}_0 \tag{3.14}$$

$$= \quad \overline{\boldsymbol{M}} \ : \overline{\boldsymbol{L}}_{\mathrm{p}} + \quad \boldsymbol{\Xi} \ : \dot{\boldsymbol{D}} + \quad q\ \dot{\kappa} + \mathscr{P}_0 \geq 0 \tag{3.15}$$

with the Mandel stress tensor of the intermediate configuration and the (classic) plastic velocity gradient

$$\overline{\boldsymbol{M}} = \boldsymbol{F}_{\mathrm{e}}^{\mathrm{t}} \cdot \boldsymbol{P} \cdot \boldsymbol{F}_{\mathrm{p}}^{\mathrm{t}} \quad , \tag{3.16} \qquad\qquad \overline{\boldsymbol{L}}_{\mathrm{p}} = \dot{\boldsymbol{F}}_{\mathrm{p}} \cdot \boldsymbol{F}_{\mathrm{p}}^{-1} \quad . \tag{3.17}$$

Moreover, the work conjugated thermodynamic forces to the dislocation density tensor $\boldsymbol{D}$ and to the hardening variable κ, i.e.

$$\boldsymbol{\Xi} = -\frac{\partial \widetilde{W}}{\partial \boldsymbol{D}} \quad , \tag{3.18} \qquad\qquad q = -\frac{\partial \widetilde{W}}{\partial \kappa} \quad , \tag{3.19}$$

have been introduced to allow for a compact notation. In accordance with [75, 106], the dissipation power is assumed to be of the form

$$\widetilde{\mathcal{D}}^{\mathrm{red}} = \widetilde{\overline{\boldsymbol{M}}} : \overline{\boldsymbol{L}}_{\mathrm{p}} + q\,\dot{\kappa} \quad , \tag{3.20}$$

with $\widetilde{\overline{\boldsymbol{M}}}$ denoting the (unknown) generalised Mandel-type stress tensor settled in the intermediate configuration which is energetically conjugated to the plastic velocity gradient and can hence be interpreted as the driving force for the plastic evolution. In order to determine (the field equation for) $\widetilde{\overline{\boldsymbol{M}}}$, we will make use of the nonlocality residual. To this end, comparing (3.15) with (3.20) renders

$$\mathscr{P}_0 = \widetilde{\overline{\boldsymbol{M}}} : \overline{\boldsymbol{L}}_{\mathrm{p}} - \overline{\boldsymbol{M}} : \overline{\boldsymbol{L}}_{\mathrm{p}} - \boldsymbol{\Xi} : \dot{\boldsymbol{D}} \quad . \tag{3.21}$$

Inserting (3.21) into the insulation condition (3.11), making use of the identity

$$\boldsymbol{\Xi} : \mathrm{Curl}^{\mathrm{t}}\left(\dot{\boldsymbol{F}}_{\mathrm{p}}\right) = \mathrm{Curl}^{\mathrm{t}}\left(\boldsymbol{\Xi}^{\mathrm{t}} \cdot \dot{\boldsymbol{F}}_{\mathrm{p}}\right) : \boldsymbol{I} + \left[\mathrm{Curl}^{\mathrm{t}}\left(\boldsymbol{\Xi}\right) \cdot \boldsymbol{F}_{\mathrm{p}}^{\mathrm{t}}\right] : \overline{\boldsymbol{L}}_{\mathrm{p}} \tag{3.22}$$

and applying Gauss's theorem finally results in

$$
0 = \int_{\mathcal{B}_0^{\mathrm{dis}}} \mathscr{P}_0 \, \mathrm{d}V \tag{3.23a}
$$

$$
= \int_{\mathcal{B}_0^{\mathrm{dis}}} \left[\widetilde{\overline{M}} - \overline{M} - \mathrm{Curl}^{\mathrm{t}}\left(\boldsymbol{\Xi}\right) \cdot \boldsymbol{F}_{\mathrm{p}}^{\mathrm{t}} \right] : \overline{\boldsymbol{L}}_{\mathrm{p}} \, \mathrm{d}V - \int_{\mathcal{B}_0^{\mathrm{dis}}} \mathrm{Curl}^{\mathrm{t}}\left(\boldsymbol{\Xi}^{\mathrm{t}} \cdot \dot{\boldsymbol{F}}_{\mathrm{p}}\right) : \boldsymbol{I} \, \mathrm{d}V \tag{3.23b}
$$

$$
= \int_{\mathcal{B}_0^{\mathrm{dis}}} \left[\widetilde{\overline{M}} - \overline{M} - \mathrm{Curl}^{\mathrm{t}}\left(\boldsymbol{\Xi}\right) \cdot \boldsymbol{F}_{\mathrm{p}}^{\mathrm{t}} \right] : \overline{\boldsymbol{L}}_{\mathrm{p}} \, \mathrm{d}V - \int_{\partial\mathcal{B}_0^{\mathrm{dis}}} \left[\boldsymbol{\Xi} \cdot \mathrm{Spn}\left(\boldsymbol{N}\right)\right] : \dot{\boldsymbol{F}}_{\mathrm{p}} \, \mathrm{d}A \tag{3.23c}
$$

$$
= \int_{\mathcal{B}_0^{\mathrm{dis}}} \left[\widetilde{\overline{M}} - \overline{M} - \mathrm{Curl}^{\mathrm{t}}\left(\boldsymbol{\Xi}\right) \cdot \boldsymbol{F}_{\mathrm{p}}^{\mathrm{t}} \right] : \overline{\boldsymbol{L}}_{\mathrm{p}} \, \mathrm{d}V - \int_{\partial\mathcal{B}_0^{\mathrm{dis}}} \left[\boldsymbol{\Xi} \cdot \mathrm{Spn}\left(\boldsymbol{N}\right) \cdot \boldsymbol{F}_{\mathrm{p}}^{\mathrm{t}}\right] : \overline{\boldsymbol{L}}_{\mathrm{p}} \, \mathrm{d}A \tag{3.23d}
$$

see also [75]. Since (3.23) needs to be fulfilled for any deformation process, we require

$$
\widetilde{\overline{M}} = \overline{M} + \mathrm{Curl}^{\mathrm{t}}\left(\boldsymbol{\Xi}\right) \cdot \boldsymbol{F}_{\mathrm{p}}^{\mathrm{t}} \quad \text{in} \quad \mathcal{B}_0^{\mathrm{dis}} \quad . \tag{3.24}
$$

As this work proceeds, (3.24) will be regarded as the definition or rather as the local form of the field equation for the generalised stress field $\widetilde{\overline{M}}$. This field equation is subjected to so-called constitutive boundary conditions which will be chosen differently on the internal boundary $\partial\mathcal{B}_0^{\mathrm{int}}$ and on the external boundary $\partial\mathcal{B}_0^{\mathrm{dis,ext}}$ of the plastic domain, see Figure 3.1. Following the same argument as before, the value of $\overline{\boldsymbol{L}}_{\mathrm{p}}$ is not restricted on the external boundary of the plastic domain if (3.23) is to hold for any deformation process such that we require

$$
\boldsymbol{\Xi} \cdot \mathrm{Spn}\left(\boldsymbol{N}\right) \cdot \boldsymbol{F}_{\mathrm{p}}^{\mathrm{t}} = \boldsymbol{0} \quad \text{on} \quad \partial\mathcal{B}_0^{\mathrm{dis,ext}} \quad . \tag{3.25}
$$

Internal plastic boundaries are found between elastically and plastically deforming regions of the body under consideration. Noting that, by definition, $\overline{\boldsymbol{L}}_{\mathrm{p}} = \boldsymbol{0}$ holds for material points in $\mathcal{B}_0^{\mathrm{rev}}$ leads to the so-called continuity boundary condition on internal boundaries,

$$
\overline{\boldsymbol{L}}_{\mathrm{p}} = \boldsymbol{0} \quad \text{on} \quad \partial\mathcal{B}_0^{\mathrm{int}} \quad , \tag{3.26}
$$

see [106] for a detailed elaboration. From a physics point of view, (3.26) implies that no energy exchange between the elastic and the plastic region of the body is induced by the nonlocality residual. Likewise, no energy is exchanged at the external plastic boundary due to (3.25).

Remark 3.1 (Expansion to the domain $\mathcal{B}_0$) *The field equation (3.24) and the corresponding boundary conditions for the generalised stress field were derived in Section 3.1.2 based on the dissipation inequality for the domain $\mathcal{B}_0^{\mathrm{dis}}$, where the irreversible deformation process takes place. For the finite element implementation which will be proposed in Section 3.2.2 and Section 3.2.3, however, it is advantageous to formulate the field*

equation for the complete domain $\mathcal{B}_0$. To this end, taking into account (3.12) and (3.21) we find that

$$\mathscr{P}_0 = \widetilde{\overline{\boldsymbol{M}}} : \overline{\boldsymbol{L}}_{\mathrm{p}} - \overline{\boldsymbol{M}} : \overline{\boldsymbol{L}}_{\mathrm{p}} - \boldsymbol{\Xi} : \dot{\boldsymbol{D}} = 0 \quad in \quad \mathcal{B}_0^{\mathrm{rev}} \tag{3.27}$$

holds locally in $\mathcal{B}_0^{\mathrm{rev}}$ as no plastic evolution occurs. Furthermore, this implies

$$\int_{\mathcal{B}_0^{\mathrm{rev}}} \mathscr{P}_0 \, \mathrm{d}V = 0 \quad . \tag{3.28}$$

Following the same lines as in Section 3.1.2, we find

$$
\begin{aligned}
\int_{\mathcal{B}_0^{\mathrm{rev}}} \mathscr{P}_0 \, \mathrm{d}V = \quad & \int_{\mathcal{B}_0^{\mathrm{rev}}} \left[\widetilde{\overline{\boldsymbol{M}}} - \overline{\boldsymbol{M}} - \mathrm{Curl}^{\mathrm{t}}(\boldsymbol{\Xi}) \cdot \boldsymbol{F}_{\mathrm{p}}^{\mathrm{t}} \right] : \overline{\boldsymbol{L}}_{\mathrm{p}} \, \mathrm{d}V \\
& - \int_{\partial\mathcal{B}_0^{\mathrm{rev}}} \left[\boldsymbol{\Xi} \cdot \mathrm{Spn}(\boldsymbol{N}) \cdot \boldsymbol{F}_{\mathrm{p}}^{\mathrm{t}} \right] : \overline{\boldsymbol{L}}_{\mathrm{p}} \, \mathrm{d}A \qquad = 0 \quad .
\end{aligned}
\tag{3.29}
$$

As expected, (3.29) is trivially fulfilled for $\overline{\boldsymbol{L}}_{\mathrm{p}} = \boldsymbol{0}$ in the elastic domain and on the respective boundaries. In contrast to the plastic domain there is thus no need to require

$$\widetilde{\overline{\boldsymbol{M}}} = \overline{\boldsymbol{M}} + \mathrm{Curl}^{\mathrm{t}}(\boldsymbol{\Xi}) \cdot \boldsymbol{F}_{\mathrm{p}}^{\mathrm{t}} \quad in \quad \mathcal{B}_0^{\mathrm{rev}} \tag{3.30}$$

and

$$\boldsymbol{\Xi} \cdot \mathrm{Spn}(\boldsymbol{N}) \cdot \boldsymbol{F}_{\mathrm{p}}^{\mathrm{t}} = \boldsymbol{0} \quad on \quad \partial\mathcal{B}_0^{\mathrm{rev,ext}} \tag{3.31}$$

to hold for the elastic domain; however, we also do not induce inconsistencies in the formulation by doing so. For this reason (3.30) needs to be rather interpreted as a restrictive assumption for the $\widetilde{\overline{\boldsymbol{M}}}$-field than a constitutive necessity. In fact, it will be shown in Section 3.2.2 and Section 3.2.3 that $\widetilde{\overline{\boldsymbol{M}}}$ only enters the constitutive model in the case of plastic loading as the effective stress tensor, with $\mathrm{Curl}^{\mathrm{t}}(\boldsymbol{\Xi}) \cdot \boldsymbol{F}_{\mathrm{p}}^{\mathrm{t}}$ in (3.24) taking the interpretation of a back stress-type tensor. For elastic deformation states, $\widetilde{\overline{\boldsymbol{M}}}$ merely turns out to represent the L_2-projection of the local stress state $\overline{\boldsymbol{M}} + \mathrm{Curl}^{\mathrm{t}}(\boldsymbol{\Xi}) \cdot \boldsymbol{F}_{\mathrm{p}}^{\mathrm{t}}$ at the quadrature points onto the global field $\widetilde{\overline{\boldsymbol{M}}}$.

3.1.3 Summary

The geometrical foundations of incompatibilities and their interpretation in terms of dislocation density tensors presented in Section 3.1.1 give rise to the physically well-motivated gradient plasticity theory presented in Section 3.1.2. These fundamentals serve as the basis for the development of specific gradient (crystal) plasticity formulations in Section 3.2 and Section 3.3.

3.2 An associated-type gradient plasticity formulation

As a first step towards the application of the general gradient plasticity framework presented in Section 3.1, a specific implementation within the framework of (phenomenological) associated-type finite plasticity will be studied in this section. To this end, we focus on the evaluation of the nonlocal form of the dissipation inequality in Section 3.2.1 and propose a specific prototype model in Section 3.2.2. We then analyse the solution of the underlying coupled system of partial differential equations in Section 3.2.3 and study basic model properties in Section 3.2.4.

3.2.1 Consequences for the dissipation inequality

The constitutive equations for the plastic evolution need to be chosen in accordance with the restrictions that are posed by the second law of thermodynamics in its generalised, i.e. nonlocal form

$$\widetilde{\mathcal{D}}^{\mathrm{red}} = \widetilde{\overline{\boldsymbol{M}}} : \overline{\boldsymbol{L}}_{\mathrm{p}} + q\,\dot{\kappa} \geq 0 \quad , \tag{3.32}$$

which immediately follows from the definition of the dissipation power (3.20). To fulfil the dissipation inequality a priori for every possible load path, a (convex) plastic potential Φ is introduced in the spirit of generalised standard materials from which both the plastic velocity gradient and the rate of internal variable κ are derived, i.e.

$$\overline{\boldsymbol{L}}_{\mathrm{p}} = \lambda_{\mathrm{p}}\,\frac{\partial \Phi}{\partial \widetilde{\overline{\boldsymbol{M}}}} \quad , \tag{3.33} \qquad \dot{\kappa} = \lambda_{\mathrm{p}}\,\frac{\partial \Phi}{\partial q} \quad . \tag{3.34}$$

Note, that the plastic multiplier λ_{p} is zero in the case of elastic loading and that $\lambda_{\mathrm{p}} > 0$ holds for plastic loading – essentially, the plastic multiplier is related to the yield function f in a classic sense via the Karush-Kuhn-Tucker conditions, namely

$$\lambda_{\mathrm{p}} \geq 0 \quad , \quad f \leq 0 \quad , \quad \lambda_{\mathrm{p}}\,f = 0 \quad . \tag{3.35}$$

In this section, the plastic potential Φ is chosen to coincide with a yield function of the form

$$f = \widetilde{f}\left(\widetilde{\overline{\boldsymbol{M}}},\, q\right) = \widetilde{\overline{M}}_{\mathrm{eq}} - [q_0 - q] \quad , \tag{3.36}$$

in terms of the scalar valued equivalent stress measure $\widetilde{\overline{M}}_{\mathrm{eq}}$ and the initial yield limit q_0, resulting in an associated-type flow rule. In the case of plastic loading, evaluating (3.33)

and (3.34) for (3.36), inserting the ensuing equations into (3.32) and assuming that $\widetilde{f}$ is a convex function in $\widetilde{\overline{M}}$ with $\widetilde{f}(\mathbf{0}, 0) \leq 0$, results in

$$\widetilde{\mathcal{D}}^{\mathrm{red}} = \widetilde{\overline{M}} : \lambda_{\mathrm{p}} \frac{\partial \widetilde{f}}{\partial \widetilde{\overline{M}}} + q \, \lambda_{\mathrm{p}} \frac{\partial \widetilde{f}}{\partial q} = \lambda_{\mathrm{p}} \left[\frac{\partial \widetilde{\overline{M}}_{\mathrm{eq}}}{\partial \widetilde{\overline{M}}} : \widetilde{\overline{M}} + q \right] \geq \lambda_{\mathrm{p}} \left[q_0 - q + q \right] = \lambda_{\mathrm{p}} \, q_0 > 0 \quad .$$

(3.37)

3.2.2 Specification of the constitutive model

In the scope of this section we will take into account two material models which show the same elastic material response but exhibit a different (elasto-)plastic response. To be specific, we will analyse a gradient plasticity model that is based on the theoretical foundations presented in Section 3.1.2 and will use a classic (local) von Mises-type plasticity model as a reference. Since the gradient plasticity model represents an extension of the reference model, the fundamental constitutive relations for the reference model will briefly be recapitulated, first, in Section 3.2.2.1. Extending the specific form of the energy function used in Section 3.2.2.1 by an energy contribution that may be attributed to the presence of geometrically necessary dislocations, the focus lies on the gradient plasticity formulation in Section 3.2.2.2, with the specific form of the gradient energy contribution being studied in detail in Section 3.2.2.3.

3.2.2.1 Reference model

The reference model is characterised by a (volume specific) Helmholtz free energy density function that is assumed to be additively composed of an elastic part $\widetilde{W}^{\mathrm{e}}$ and a hardening part $\widetilde{W}^{\mathrm{p}}$, representing energy storage due to cold plastic work, according to

$$\widetilde{W}^{\mathrm{ref}}(\mathbf{F}, \mathbf{F}_{\mathrm{p}}, \kappa) = \widetilde{W}^{\mathrm{e}}(\mathbf{F}, \mathbf{F}_{\mathrm{p}}) + \widetilde{W}^{\mathrm{p}}(\kappa) \qquad .$$

(3.38)

The elastic part of the Helmholtz free energy function is chosen to be of Neo-Hookean-type

$$\widetilde{W}^{\mathrm{e}} = \lambda \, \frac{J_{\mathrm{e}}^2 - 1}{4} - \left[\frac{\lambda}{2} + \mu \right] \ln(J_{\mathrm{e}}) + \frac{1}{2} \, \mu \, [\mathrm{tr}(\mathbf{C}_{\mathrm{e}}) - 3]$$

(3.39)

with the elastic and the plastic right Cauchy-Green tensor

$$\mathbf{C}_{\mathrm{e}} = \mathbf{F}_{\mathrm{e}}^{\mathrm{t}} \cdot \mathbf{F}_{\mathrm{e}} \quad , \qquad\qquad (3.40) \qquad\qquad \mathbf{C}_{\mathrm{p}} = \mathbf{F}_{\mathrm{p}}^{\mathrm{t}} \cdot \mathbf{F}_{\mathrm{p}} \quad , \qquad\qquad (3.41)$$

the volumetric deformation measure

$$J_{\mathrm{e}} = \sqrt{\det(\mathbf{C}_{\mathrm{e}})} \quad ,$$

(3.42)

and the Lamé-type material parameters λ and μ. The hardening part employs material parameter H_κ and is assumed to take the specific form

$$\widetilde{W}^{\mathrm{p}} = \frac{1}{2} H_\kappa \, \kappa^2 \tag{3.43}$$

which results in conjunction with the form of the yield function (3.36) and the definition of q in a linear isotropic hardening relation. Evaluating the constitutive relations (3.13), (3.16) and (3.19) for the specific energy contributions (3.39) and (3.43) yields the Piola stress tensor

$$\boldsymbol{P} = \frac{\lambda}{2} \left[J_{\mathrm{e}}^2 - 1 \right] \boldsymbol{F}^{-\mathrm{t}} + \mu \left[\boldsymbol{F} \cdot \boldsymbol{C}_{\mathrm{p}}^{-1} - \boldsymbol{F}^{-\mathrm{t}} \right] \quad , \tag{3.44}$$

the (local) Mandel stress tensor settled in the intermediate configuration

$$\overline{\boldsymbol{M}} = \frac{\lambda}{2} \left[J_{\mathrm{e}}^2 - 1 \right] \boldsymbol{I} + \mu \left[\boldsymbol{C}_{\mathrm{e}} - \boldsymbol{I} \right] \tag{3.45}$$

and the energetic dual to κ

$$q = -H_\kappa \, \kappa \quad . \tag{3.46}$$

The elastic and the plastic domains of the reference model are characterised by a von Mises-type yield function in terms of the deviatoric part of the Mandel stress tensor

$$\overline{\boldsymbol{M}}_{\mathrm{dev}} = \mathsf{I}^{\mathrm{dev}} : \overline{\boldsymbol{M}} = \overline{\boldsymbol{M}} - \frac{1}{3} \mathrm{tr}\left(\overline{\boldsymbol{M}}\right) \boldsymbol{I} \quad . \tag{3.47}$$

Specifically the form

$$f^{\,\mathrm{ref}}\left(\overline{\boldsymbol{M}}, q\right) = \left\| \overline{\boldsymbol{M}}_{\mathrm{dev}} \right\| - [q_0 - q] \tag{3.48}$$

is assumed which, according to (3.33) and (3.34), yields the associated-type rate equations

$$\overline{\boldsymbol{L}}_{\mathrm{p}}^{\mathrm{ref}} = \lambda_{\mathrm{p}} \frac{\overline{\boldsymbol{M}}_{\mathrm{dev}}}{\left\| \overline{\boldsymbol{M}}_{\mathrm{dev}} \right\|} \quad , \qquad (3.49) \qquad \dot{\kappa} = \lambda_{\mathrm{p}} \quad . \tag{3.50}$$

Applying an implicit Euler scheme to discretise (3.49) and (3.50) in time, with Δt denoting the time increment and superscripts n and $n+1$ referring to the respective time step, finally results in

$$\boldsymbol{F}_{\mathrm{p}}^{n+1} \approx \boldsymbol{F}_{\mathrm{p}}^{n} + \Delta t \, \lambda_{\mathrm{p}} \frac{\overline{\boldsymbol{M}}_{\mathrm{dev}}^{n+1}}{\left\| \overline{\boldsymbol{M}}_{\mathrm{dev}}^{n+1} \right\|} \cdot \boldsymbol{F}_{\mathrm{p}}^{n+1} \quad , \tag{3.51}$$

and

$$\kappa^{n+1} \approx \kappa^n + \Delta t \, \lambda_{\mathrm{p}} \quad . \tag{3.52}$$

3.2.2.2 Gradient plasticity model

The Helmholtz free energy density function of the gradient plasticity model is assumed to be a direct extension of (3.38) in terms of a gradient energy contribution $\widetilde{W}^{\mathrm{g}}(\boldsymbol{D})$ which is based on the dislocation density tensor $\boldsymbol{D}$, i.e.

$$\widetilde{W}(\boldsymbol{F}, \boldsymbol{F}_{\mathrm{p}}, \boldsymbol{D}, \kappa) = \widetilde{W}^{\mathrm{ref}}(\boldsymbol{F}, \boldsymbol{F}_{\mathrm{p}}, \kappa) + \widetilde{W}^{\mathrm{g}}(\boldsymbol{D}) \quad . \tag{3.53}$$

Due to the assumed additive nature of the energy contributions in (3.53), the elastic- and the hardening part remain unmodified by the extension such that evaluating (3.13), (3.16) and (3.19) yields the same constitutive relations for the Piola stress tensor $\boldsymbol{P}$, the Mandel stress tensor $\overline{\boldsymbol{M}}$ and the energetic dual to κ as for the reference model presented in (3.44)-(3.46). Likewise, the yield function of the gradient plasticity model is chosen to be of von Mises-type. However, since the generalised Mandel stress tensor was identified as the driving force of the plastic evolution, the yield function is assumed to take the form

$$\widetilde{f}\left(\widetilde{\overline{\boldsymbol{M}}}, q\right) = \left\|\widetilde{\overline{\boldsymbol{M}}}_{\mathrm{dev}}\right\| - [q_0 - q] = \left\| \mathsf{I}^{\mathrm{dev}} : \left[\overline{\boldsymbol{M}} + \mathrm{Curl}^{\mathrm{t}}\left(\boldsymbol{\Xi}\right) \cdot \boldsymbol{F}_{\mathrm{p}}^{\mathrm{t}}\right]\right\| - [q_0 - q] \quad , \tag{3.54}$$

which indicates that the higher-gradient part takes the interpretation of a back stress tensor and with the deviatoric part of the generalised Mandel stress given by

$$\widetilde{\overline{\boldsymbol{M}}}_{\mathrm{dev}} = \mathsf{I}^{\mathrm{dev}} : \widetilde{\overline{\boldsymbol{M}}} = \widetilde{\overline{\boldsymbol{M}}} - \frac{1}{3}\mathrm{tr}\left(\widetilde{\overline{\boldsymbol{M}}}\right)\boldsymbol{I} \quad . \tag{3.55}$$

Evaluating (3.33) and (3.34), the corresponding rate equation for the plastic flow is given by

$$\overline{\boldsymbol{L}}_{\mathrm{p}} = \lambda_{\mathrm{p}} \frac{\widetilde{\overline{\boldsymbol{M}}}_{\mathrm{dev}}}{\left\|\widetilde{\overline{\boldsymbol{M}}}_{\mathrm{dev}}\right\|} \tag{3.56}$$

and we find the same evolution equation for internal variable κ as for the reference model, cf. (3.50). Discretising (3.56) in time by means of an implicit Euler scheme according to

$$\boldsymbol{F}_{\mathrm{p}}^{n+1} \approx \boldsymbol{F}_{\mathrm{p}}^n + \Delta t \, \lambda_{\mathrm{p}} \frac{\widetilde{\overline{\boldsymbol{M}}}_{\mathrm{dev}}^{n+1}}{\left\|\widetilde{\overline{\boldsymbol{M}}}_{\mathrm{dev}}^{n+1}\right\|} \cdot \boldsymbol{F}_{\mathrm{p}}^{n+1} \tag{3.57}$$

and making use of (3.52) yields the update relation for the plastic part of the velocity gradient

$$
\boldsymbol{F}_{\mathrm{p}}^{n+1} = \left[\boldsymbol{I} - \left[\kappa^{n+1} - \kappa^n \right] \frac{\widetilde{\overline{\boldsymbol{M}}}_{\mathrm{dev}}^{n+1}}{\left\| \widetilde{\overline{\boldsymbol{M}}}_{\mathrm{dev}}^{n+1} \right\|} \right]^{-1} \cdot \boldsymbol{F}_{\mathrm{p}}^n \quad .
\tag{3.58}
$$

We like to stress that (3.58) resembles an explicit update of the plastic part of the deformation gradient because $\widetilde{\overline{\boldsymbol{M}}}$ and κ will be introduced as global field variables in Section 3.2.3. Thus, for the present implementation no (local) iteration at the quadrature point level is required.

3.2.2.3 Energy related to geometrically necessary dislocations

Gradient effects are introduced in the formulation via the energy contribution $\widetilde{W}^{\mathrm{g}}$ which is a function of dislocation density tensor $\boldsymbol{D}$. As outlined in Section 3.1.1, $\boldsymbol{D}$ can be interpreted as a measure of dislocation lines per unit area reference configuration based on geometrical considerations.

Assuming a quadratic form in $\boldsymbol{D}$, a possible choice of the energy function is given by

$$
\widetilde{W}^{\mathrm{g}}\left(\boldsymbol{D}\right) = H_{\boldsymbol{D}} \, \boldsymbol{D} : \boldsymbol{D} = H_{\boldsymbol{D}} \operatorname{tr}\left(\boldsymbol{D} \cdot \boldsymbol{D}^{\mathrm{t}}\right)
\tag{3.59}
$$

which by evaluating (3.18) results in

$$
\boldsymbol{\Xi} = -2 \, H_{\boldsymbol{D}} \operatorname{Curl}^{\mathrm{t}}\left(\boldsymbol{F}_{\mathrm{p}}\right) \quad .
\tag{3.60}
$$

Inserting (3.60) into (3.24) yields

$$
\widetilde{\overline{\boldsymbol{M}}} = \overline{\boldsymbol{M}} - 2 \, H_{\boldsymbol{D}} \operatorname{Curl}^{\mathrm{t}}\left(\operatorname{Curl}^{\mathrm{t}}\left(\boldsymbol{F}_{\mathrm{p}}\right)\right) \cdot \boldsymbol{F}_{\mathrm{p}}^{\mathrm{t}}
\tag{3.61}
$$

and by rewriting the coefficients of the Curl-Curl summand in matrix notation with respect to a Cartesian base system we find the representation

$$
\left[\operatorname{Curl}^{\mathrm{t}}\left(\operatorname{Curl}^{\mathrm{t}}\left(\boldsymbol{F}_{\mathrm{p}}\right)\right)\right]_{ij} = \begin{bmatrix} F_{\mathrm{P}12,12} + F_{\mathrm{P}13,13} & F_{\mathrm{P}11,21} + F_{\mathrm{P}13,23} & F_{\mathrm{P}11,31} + F_{\mathrm{P}12,32} \\ F_{\mathrm{P}22,12} + F_{\mathrm{P}23,13} & F_{\mathrm{P}21,21} + F_{\mathrm{P}23,23} & F_{\mathrm{P}21,31} + F_{\mathrm{P}22,32} \\ F_{\mathrm{P}32,12} + F_{\mathrm{P}33,13} & F_{\mathrm{P}31,21} + F_{\mathrm{P}33,23} & F_{\mathrm{P}31,31} + F_{\mathrm{P}32,32} \end{bmatrix}
$$
$$
- \begin{bmatrix} F_{\mathrm{P}11,22} + F_{\mathrm{P}11,33} & F_{\mathrm{P}12,11} + F_{\mathrm{P}12,33} & F_{\mathrm{P}13,11} + F_{\mathrm{P}13,22} \\ F_{\mathrm{P}21,22} + F_{\mathrm{P}21,33} & F_{\mathrm{P}22,11} + F_{\mathrm{P}22,33} & F_{\mathrm{P}23,11} + F_{\mathrm{P}23,22} \\ F_{\mathrm{P}31,22} + F_{\mathrm{P}31,33} & F_{\mathrm{P}32,11} + F_{\mathrm{P}32,33} & F_{\mathrm{P}33,11} + F_{\mathrm{P}33,22} \end{bmatrix}
\tag{3.62}
$$

(a) Geometry of the sample consisting of two different materials.

(b) Profile of $F_{\mathrm{p}11}(--)$, $F_{\mathrm{p}22} \approx F_{\mathrm{p}33}(\cdot\cdot)$ along the e_1-axis.
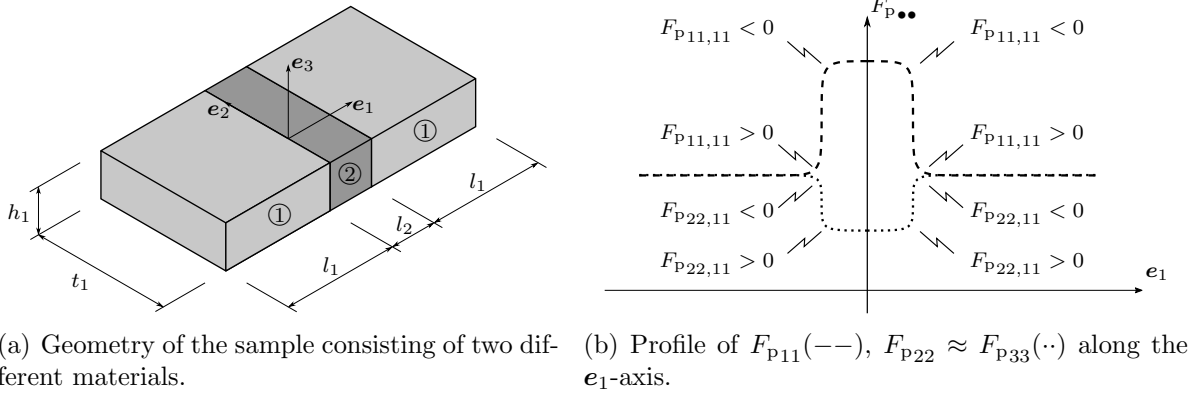
Figure 3.2: Sketch of a sample consisting of two different materials and distribution of $\boldsymbol{F}_{\mathrm{p}}$ along the e_1-axis which is normal to the material interfaces.

with the notation $\bullet_{,\nabla\triangle}$ denoting the respective partial derivatives with respect to the coefficients of $\boldsymbol{X}$. The second summand in (3.62) represents an (incomplete) coefficient-wise application of the Laplacian to the plastic part of the deformation gradient. Thus, it measures the deviation of the respective component, e.g. of $F_{\mathrm{p}11}$, from the mean value in a plane, containing the respective point, e.g. the 22-33-plane for the $F_{\mathrm{p}11}$ component. If the respective component is larger/smaller than the surrounding values in the respective plane, the corresponding coefficient, e.g. $F_{\mathrm{p}11,22} + F_{\mathrm{p}11,33}$, takes a negative/positive value. This is similar to the one-dimensional case where the application of the Laplacian reduces to the second derivative, see [75].

To emphasise the physical significance of the interpretation of (3.62), assume that the plate in Figure 3.2(a), which consists of two plastically incompressible materials with different initial yield limits, i.e. $q_0^1 > q_0^2$, is uni-axially loaded in e_1-direction. Due to plastic incompressibility, the $F_{\mathrm{p}11}$, $F_{\mathrm{p}22}$ and $F_{\mathrm{p}33}$ profiles along the e_1-axis take the form sketched in Figure 3.2(b) for moderate loadings and if the jump at the interfaces is approximated by a $\mathcal{C}^2$-continuous function such that the second derivatives are well-defined. Assume for now that $\boldsymbol{F}_{\mathrm{p}}$ is close to the identity but that the first and second gradients of $\boldsymbol{F}_{\mathrm{p}}$ take significant values due to the material inhomogeneity, and choose a material parameter $H_{\boldsymbol{D}} > 0\,\mathrm{GPa\,mm^2}$. In this case, the multiplication of the second term on the right-hand side of (3.61) with $\boldsymbol{F}_{\mathrm{p}}^{\mathrm{t}}$ is negligible and we find a decrease/increase in the 22- and 33- nonlocal stress component in the outer/inner region of the sample such that the norm of the deviatoric part of the generalised Mandel stress tensor increases/decreases.

The first summand in (3.62) is difficult to interpret due to the mixed second-order derivatives that occur. However, it seems that this contribution may take significant values at points where, e.g., material inhomogeneities in two spatial directions are present at the same time.

3.2.3 Numerics and finite element formulation

In this section, the finite element-based implementation of the theory proposed in Section 3.1.2 will be discussed subject to the assumption of quasi-statics and neglecting temperature effects as well as body forces.

3.2.3.1 Field equations

The system of coupled partial differential equations to be solved consists of the balance equation of linear momentum that is complemented by suitable boundary conditions in terms of tractions $\bar{\boldsymbol{t}}$ and placements $\bar{\boldsymbol{\varphi}}$ on mutually disjoint parts of the boundary

$$
\nabla_{\boldsymbol{X}} \cdot \boldsymbol{P} = \boldsymbol{0} \quad \text{in } \mathcal{B}_0, \qquad \boldsymbol{P} \cdot \boldsymbol{N} = \bar{\boldsymbol{t}} \quad \text{on } \partial\mathcal{B}_0^t, \qquad \boldsymbol{\varphi} = \bar{\boldsymbol{\varphi}} \quad \text{on } \partial\mathcal{B}_0^\varphi,
$$
$$
\partial\mathcal{B}_0^t \cup \partial\mathcal{B}_0^\varphi = \partial\mathcal{B}_0, \qquad \partial\mathcal{B}_0^t \cap \partial\mathcal{B}_0^\varphi = \emptyset,
$$

(3.63)

and of the balance equation for the generalised Mandel stress tensor that is subjected to homogeneous constitutive boundary conditions

$$
\widetilde{\overline{\boldsymbol{M}}} - \overline{\boldsymbol{M}} - \operatorname{Curl}^{\mathrm{t}}(\boldsymbol{\Xi}) \cdot \boldsymbol{F}_{\mathrm{p}}^{\mathrm{t}} = \boldsymbol{0} \quad \text{in } \mathcal{B}_0, \quad \boldsymbol{\Xi} \cdot \operatorname{Spn}(\boldsymbol{N}) \cdot \boldsymbol{F}_{\mathrm{p}}^{\mathrm{t}} = \boldsymbol{0} \quad \text{on } \partial\mathcal{B}_0 \quad , \quad (3.64)
$$

see also Remark 3.2. Similar to [75], the Karush-Kuhn-Tucker conditions will be solved globally. However, we will not make use of a global active set search as proposed therein, but shall reformulate (3.35) as an equality constraint by means of the Fischer-Burmeister complementary function

$$
\sqrt{\widetilde{f}^2 + \lambda_{\mathrm{p}}^2} + \widetilde{f} - \lambda_{\mathrm{p}} = 0 \quad ,
$$

(3.65)

see [17, 45, 115].

3.2.3.2 Weak form of field equations

In the spirit of the finite element method, field equations (3.63) and (3.64) are multiplied with test functions $\boldsymbol{\eta}^\varphi$ and $\boldsymbol{\eta}^{\widetilde{\overline{M}}}$ and integrated over the domain $\mathcal{B}_0$ resulting, after the application of Gauss's theorem, in the weak form of the balance equation of linear momentum

$$
0 = \int_{\mathcal{B}_0} \nabla_{\boldsymbol{X}} \boldsymbol{\eta}^\varphi : \boldsymbol{P} \, \mathrm{d}V - \int_{\partial\mathcal{B}_0} \boldsymbol{\eta}^\varphi \cdot \boldsymbol{P} \cdot \boldsymbol{N} \, \mathrm{d}A
$$

(3.66)

and the weak form of the balance equation for the generalised Mandel stress tensor

$$
0 = \int_{\mathcal{B}_0} \boldsymbol{\eta}^{\widetilde{\overline{M}}} : \left[\widetilde{\overline{\boldsymbol{M}}} - \overline{\boldsymbol{M}} - \operatorname{Curl}^{\mathrm{t}}(\boldsymbol{\Xi}) \cdot \boldsymbol{F}_{\mathrm{p}}^{\mathrm{t}} \right] \, \mathrm{d}V
$$

(3.67a)

$$= \int_{\mathcal{B}_0} \boldsymbol{\eta}^{\widetilde{\overline{M}}} : \left[\widetilde{\overline{M}} - \overline{M}\right] - \boldsymbol{\Xi} : \mathrm{Curl}^{\mathrm{t}}\left(\boldsymbol{\eta}^{\widetilde{\overline{M}}} \cdot \boldsymbol{F}_{\mathrm{p}}\right) + \mathrm{Curl}^{\mathrm{t}}\left(\boldsymbol{\Xi}^{\mathrm{t}} \cdot \boldsymbol{\eta}^{\widetilde{\overline{M}}} \cdot \boldsymbol{F}_{\mathrm{p}}\right) : \boldsymbol{I} \, \mathrm{d}V \quad \text{(3.67b)}$$

$$= \int_{\mathcal{B}_0} \boldsymbol{\eta}^{\widetilde{\overline{M}}} : \left[\widetilde{\overline{M}} - \overline{M}\right] - \boldsymbol{\Xi} : \mathrm{Curl}^{\mathrm{t}}\left(\boldsymbol{\eta}^{\widetilde{\overline{M}}} \cdot \boldsymbol{F}_{\mathrm{p}}\right) \mathrm{d}V + \int_{\partial\mathcal{B}_0} \left[\boldsymbol{\Xi} \cdot \mathrm{Spn}\left(\boldsymbol{N}\right) \cdot \boldsymbol{F}_{\mathrm{p}}^{\mathrm{t}}\right] : \boldsymbol{\eta}^{\widetilde{\overline{M}}} \, \mathrm{d}A \,.$$
$$\text{(3.67c)}$$

In general, second-order derivatives of $\boldsymbol{F}_{\mathrm{p}}$ enter (3.64) via $\mathrm{Curl}^{\mathrm{t}}\left(\boldsymbol{\Xi}\right)$ and first-order derivatives are present in the associated weak form (3.67c). In order to approximate the gradient and hence the curl of $\boldsymbol{F}_{\mathrm{p}}$, we introduce the global field variable $\boldsymbol{\Theta}_{\mathrm{p}}$ that is coupled to $\boldsymbol{F}_{\mathrm{p}}$ in terms of an L_2-projection using the test function $\boldsymbol{\eta}^{\boldsymbol{\Theta}_{\mathrm{p}}}$

$$0 = \int_{\mathcal{B}_0} \boldsymbol{\eta}^{\boldsymbol{\Theta}_{\mathrm{p}}} : \left[\boldsymbol{F}_{\mathrm{p}} - \boldsymbol{\Theta}_{\mathrm{p}}\right] \mathrm{d}V \quad , \tag{3.68}$$

see also [13, 132]. To derive a weak form of the Fischer-Burmeister equation (3.65), the yield function and the plastic multiplier are multiplied with test functions and integrated over $\mathcal{B}_0$ resulting in

$$\int_{\mathcal{B}_0} \eta^{\widetilde{f}} \, \widetilde{f} \, \mathrm{d}V \quad , \quad \eta^{\widetilde{f}} > 0 \ \text{ in } \ \mathcal{B}_0 \tag{3.69}$$

and

$$\int_{\mathcal{B}_0} \eta^{\lambda_{\mathrm{p}}} \, \lambda_{\mathrm{p}} \, \mathrm{d}V \quad , \quad \eta^{\lambda_{\mathrm{p}}} > 0 \ \text{ in } \ \mathcal{B}_0 \quad . \tag{3.70}$$

The corresponding nodal residual values that result from the discretisation and assembly procedure will then be used to determine the node-wise Fischer-Burmeister residual, see Section 3.2.3.3. Note, that this approach is in accordance with [73, 75, 91], where a global active set search instead of the Fischer-Burmeister equation was used to fulfil the Karush-Kuhn-Tucker conditions on a global level.

3.2.3.3 Discretisation and Fischer-Burmeister functions

The fields and the geometry are discretised by means of Lagrange polynomials

$$\boldsymbol{\varphi}^{\mathrm{h}} = \sum_{A=1}^{\mathrm{n}_{\mathrm{en},\boldsymbol{\varphi}}} N_A^{\boldsymbol{\varphi}} \, \boldsymbol{\varphi}_A \tag{3.71a} \qquad\qquad \boldsymbol{\eta}^{\boldsymbol{\varphi}\,\mathrm{h}} = \sum_{E=1}^{\mathrm{n}_{\mathrm{en},\boldsymbol{\varphi}}} N_E^{\boldsymbol{\varphi}} \, \boldsymbol{\eta}_E^{\boldsymbol{\varphi}} \tag{3.71b}$$

$$\widetilde{\overline{M}}^{\mathrm{h}} = \sum_{B=1}^{\mathrm{n}_{\mathrm{en},\widetilde{\overline{M}}}} N_B^{\widetilde{\overline{M}}} \, \widetilde{\overline{M}}_B \tag{3.71c} \qquad\qquad \boldsymbol{\eta}^{\widetilde{\overline{M}}\,\mathrm{h}} = \sum_{F=1}^{\mathrm{n}_{\mathrm{en},\widetilde{\overline{M}}}} N_F^{\widetilde{\overline{M}}} \, \boldsymbol{\eta}_F^{\widetilde{\overline{M}}} \tag{3.71d}$$

$$\boldsymbol{\Theta}_{\mathrm{p}}^{\mathrm{h}} = \sum_{C=1}^{\mathrm{n}_{\mathrm{en},\boldsymbol{\Theta}_{\mathrm{p}}}} N_C^{\boldsymbol{\Theta}_{\mathrm{p}}} \, \boldsymbol{\Theta}_{\mathrm{p}C} \qquad (3.71\mathrm{e}) \qquad \boldsymbol{\eta}^{\boldsymbol{\Theta}_{\mathrm{p}}\,\mathrm{h}} = \sum_{G=1}^{\mathrm{n}_{\mathrm{en},\boldsymbol{\Theta}_{\mathrm{p}}}} N_G^{\boldsymbol{\Theta}_{\mathrm{p}}} \, \boldsymbol{\eta}_G^{\boldsymbol{\Theta}_{\mathrm{p}}} \qquad (3.71\mathrm{f})$$

$$\kappa^{\mathrm{h}} = \sum_{D=1}^{\mathrm{n}_{\mathrm{en},\kappa}} N_D^{\kappa} \, \kappa_D \ (3.71\mathrm{g}) \qquad \eta^{\widetilde{f}\,\mathrm{h}} = \sum_{H=1}^{\mathrm{n}_{\mathrm{en},\kappa}} N_H^{\kappa} \, \eta_H^{\widetilde{f}} \ (3.71\mathrm{h}) \qquad \eta^{\lambda_{\mathrm{p}}\,\mathrm{h}} = \sum_{I=1}^{\mathrm{n}_{\mathrm{en},\kappa}} N_I^{\kappa} \, \eta_I^{\lambda_{\mathrm{p}}} \ (3.71\mathrm{i})$$

with $\mathrm{n}_{\mathrm{en}\bullet}$ being the number of element nodes that are used for the approximation of the respective field, $N^{\bullet}$ designating the corresponding shape function and $\bullet_A, \dots, \bullet_I$ representing the nodal field values. Denoting the assembly operator by $\mathbf{A}$ and noting that the integration is performed with respect to the element domains $\mathcal{B}_0^e$, the global vector of internal forces of the balance equation of linear momentum (3.66) takes the classic form

$$\boldsymbol{f}_{\mathrm{int}}^{\varphi\mathrm{h}} = \mathop{\mathbf{A}}_{e=1}^{\mathrm{n}_{\mathrm{el}}} \int_{\mathcal{B}_0^e} \boldsymbol{P} \cdot \nabla_{\boldsymbol{X}} N_E^{\varphi} \, \mathrm{d}V_e \quad, \tag{3.72}$$

the vector of internal forces for the balance equation of the generalised Mandel stress tensor results in

$$\boldsymbol{f}_{\mathrm{int}}^{\widetilde{\overline{M}}\mathrm{h}} = \mathop{\mathbf{A}}_{e=1}^{\mathrm{n}_{\mathrm{el}}} \int_{\mathcal{B}_0^e} N_F^{\widetilde{\overline{M}}} \left[\widetilde{\overline{\boldsymbol{M}}} - \overline{\boldsymbol{M}} \right] + \boldsymbol{\Xi} \cdot \left[N_F^{\widetilde{\overline{M}}} \nabla_{\boldsymbol{X}} \boldsymbol{\Theta}_{\mathrm{p}} : \boldsymbol{\epsilon}_0 - \boldsymbol{F}_{\mathrm{p}} \cdot \boldsymbol{\epsilon}_0 \cdot \nabla_{\boldsymbol{X}} N_F^{\widetilde{\overline{M}}} \right]^{\mathrm{t}} \mathrm{d}V_e \tag{3.73}$$

and the one corresponding to the constraint (3.68) is given by

$$\boldsymbol{f}_{\mathrm{int}}^{\boldsymbol{\Theta}_{\mathrm{p}}\mathrm{h}} = \mathop{\mathbf{A}}_{e=1}^{\mathrm{n}_{\mathrm{el}}} \int_{\mathcal{B}_0^e} N_G^{\boldsymbol{\Theta}_{\mathrm{p}}} \left[\boldsymbol{F}_{\mathrm{p}} - \boldsymbol{\Theta}_{\mathrm{p}} \right] \mathrm{d}V_e \quad. \tag{3.74}$$

To calculate the discrete version of the Fischer-Burmeister function (3.65) the generalised internal force vector for yield function (3.69)

$$\boldsymbol{f}_{\mathrm{int}}^{\widetilde{f}\,\mathrm{h}} = \mathop{\mathbf{A}}_{e=1}^{\mathrm{n}_{\mathrm{el}}} \int_{\mathcal{B}_0^e} N_H^{\kappa} \, \widetilde{f} \, \mathrm{d}V_e \tag{3.75}$$

and the generalised internal force vector for plastic multiplier (3.70)

$$\boldsymbol{f}_{\mathrm{int}}^{\lambda_{\mathrm{p}}\mathrm{h}} = \mathop{\mathbf{A}}_{e=1}^{\mathrm{n}_{\mathrm{el}}} \int_{\mathcal{B}_0^e} N_I^{\kappa} \left[\kappa^{n+1} - \kappa^n \right] \mathrm{d}V_e \tag{3.76}$$

are assembled in a first step. To this end, (3.70) is discretised in time using the approximation

$$\Delta t\, \lambda_{\mathrm{p}} \approx \kappa^{n+1} - \kappa^{n} \quad , \tag{3.77}$$

cf. (3.34) and (3.52). Based on (3.75) and (3.76), the generalised internal force vector that corresponds to the Fischer Burmeister function is then evaluated in a second step

$$\left[\boldsymbol{f}_{\mathrm{int}}^{\kappa\mathrm{h}}\right]_i = \sqrt{\left[\boldsymbol{f}_{\mathrm{int}}^{\widetilde{f}\,\mathrm{h}}\right]_i^2 + \left[\boldsymbol{f}_{\mathrm{int}}^{\lambda_{\mathrm{p}}\mathrm{h}}\right]_i^2} + \left[\boldsymbol{f}_{\mathrm{int}}^{\widetilde{f}\,\mathrm{h}}\right]_i - \left[\boldsymbol{f}_{\mathrm{int}}^{\lambda_{\mathrm{p}}\mathrm{h}}\right]_i \quad , \tag{3.78}$$

with $[\bullet]_i$ denoting the i-th coefficient of the vector $\bullet$. The resulting system of non-linear equations takes the form

$$\begin{bmatrix} \boldsymbol{f}_{\mathrm{int}}^{\boldsymbol{\varphi}\mathrm{h}} \\ \boldsymbol{f}_{\mathrm{int}}^{\widetilde{\overline{\boldsymbol{M}}}\mathrm{h}} \\ \boldsymbol{f}_{\mathrm{int}}^{\boldsymbol{\Theta}_{\mathrm{p}}\mathrm{h}} \\ \boldsymbol{f}_{\mathrm{int}}^{\kappa\mathrm{h}} \end{bmatrix} \left(\widehat{\boldsymbol{\varphi}}, \widehat{\widetilde{\overline{\boldsymbol{M}}}}, \widehat{\boldsymbol{\Theta}}_{\mathrm{p}}, \widehat{\kappa} \right) = \begin{bmatrix} \boldsymbol{f}_{\mathrm{ext}}^{\boldsymbol{\varphi}\mathrm{h}} \\ \boldsymbol{0} \\ \boldsymbol{0} \\ \boldsymbol{0} \end{bmatrix} \tag{3.79}$$

and needs to be solved for the global lists of degrees of freedom that are indicated by $\widehat{\bullet}$ with the external force vector of the balance equation of linear momentum $\boldsymbol{f}_{\mathrm{ext}}^{\boldsymbol{\varphi}\mathrm{h}}$ that results from the boundary conditions in the usual manner subject to the assumption of dead loads. Note, that due to the introduction of $\widetilde{\overline{\boldsymbol{M}}}$ and κ as global fields, the material model needs to be evaluated only – in other words, no local iteration at the integration point level is required. Furthermore, the contributions to the consistent algorithmic tangent stiffness matrix, which are required for the global iteration scheme, are provided in a general form in Appendix B.1. The derivatives of $\boldsymbol{F}_{\mathrm{p}}$, $\boldsymbol{P}$, $\overline{\boldsymbol{M}}$, $\boldsymbol{\Xi}$ and $\widetilde{f}$ with respect to the primary field variables are moreover summarised in Appendix B.1 for the specific material model proposed in Section 3.2.2.

Remark 3.2 (Interface condition) *The interface condition at internal boundaries (3.26) is implicitly included in the formulation. To illustrate this, consider two neighbouring quadrature points, one deforming plastically while the state at the other one remains elastic for the particular load step. Accordingly, an elastic-plastic interface is located somewhere between these two material points, the position of which is unknown. However, by definition $\overline{\boldsymbol{L}}_{\mathrm{p}} = \boldsymbol{0}$ holds in the elastic region. Assuming a certain continuity in the plastic flow, it is concluded that (3.26) is intrinsically fulfilled.*

Remark 3.3 (Discrete weak form of the Karush-Kuhn-Tucker conditions) *The ansatz to fulfil the Karush-Kuhn-Tucker conditions in a weak sense according to [73–75] yields decent results if (bi-)linear shape functions are chosen for the approximation of the test functions $\eta^{\widetilde{f}}$ and $\eta^{\lambda_{\mathrm{p}}}$. However, inconsistencies may occur if the test functions are*

approximated by using, e.g., (bi-)quadratic serendipity-type shape functions which, for the two-dimensional case, read

$$N_1^\kappa = -\frac{1}{4}\left[1-\xi_1\right]\left[1-\xi_2\right]\left[1+\xi_1+\xi_2\right] \tag{3.80a}$$

$$N_2^\kappa = -\frac{1}{4}\left[1+\xi_1\right]\left[1-\xi_2\right]\left[1-\xi_1+\xi_2\right] \tag{3.80b}$$

$$N_3^\kappa = -\frac{1}{4}\left[1+\xi_1\right]\left[1+\xi_2\right]\left[1-\xi_1-\xi_2\right] \tag{3.80c}$$

$$N_4^\kappa = -\frac{1}{4}\left[1-\xi_1\right]\left[1+\xi_2\right]\left[1+\xi_1-\xi_2\right] \tag{3.80d}$$

$$N_5^\kappa = \frac{1}{2}\left[1-\xi_1\right]\left[1+\xi_1\right]\left[1-\xi_2\right] \tag{3.80e}$$

$$N_6^\kappa = \frac{1}{2}\left[1+\xi_1\right]\left[1+\xi_2\right]\left[1-\xi_2\right] \tag{3.80f}$$

$$N_7^\kappa = \frac{1}{2}\left[1-\xi_1\right]\left[1+\xi_1\right]\left[1+\xi_2\right] \tag{3.80g}$$

$$N_8^\kappa = \frac{1}{2}\left[1-\xi_1\right]\left[1+\xi_2\right]\left[1-\xi_2\right] \tag{3.80h}$$

with ξ_1 and ξ_2 denoting the natural element coordinates. To illustrate these inconsistencies, assume a stress free, undeformed state, i.e. $\widetilde{f} = -q_0$, and the domain $\mathcal{B}_0 = [-1,1]\times[-1,1]$ to be discretised with a single element. Furthermore, choose $\eta_H^{\widetilde{f}} = 1$, $H \in \{1,...,8\}$ such that $\eta^{\widetilde{f}} = 1$ in $\mathcal{B}_0$ and such that particularly condition $\eta^{\widetilde{f}} > 0$ stated in [73, 74] is fulfilled. For this case, the analytical solution for the integral (3.75) is given by

$$\int_{\mathcal{B}_0^e} N_H^\kappa \, \widetilde{f}\,\mathrm{d}V_e = \left\{ \begin{array}{ll} \frac{1}{3}q_0 &, \quad H \in \{1,...,4\} \\ -\frac{4}{3}q_0 &, \quad H \in \{5,...,8\} \end{array} \right. \quad, \quad \sum_{H=1}^{8}\int_{\mathcal{B}_0^e} N_H^\kappa \, \widetilde{f}\,\mathrm{d}V_e = -4\,q_0 \tag{3.81}$$

which indicates that the mid-side nodes, $H \in \{5,...,8\}$, should stay elastic, while plastic evolution should occur at the edge nodes, $H \in \{1,...,4\}$, which is inconsistent with the assumed stress free, undeformed state.

3.2.4 Representative simulation results

Making use of the model presented in Section 3.2.2, the properties of the proposed gradient plasticity approach, in particular for the specific form of the gradient energy contribution (3.59), will be analysed in detail. Focusing in a first step on a two-dimensional setting, we analyse the plastic evolution at a material interface with the two materials exhibiting different initial yield limits in Section 3.2.4.1, study the shear band formation in a geometrically imperfect sample in Section 3.2.4.2 and discuss the (experimentally
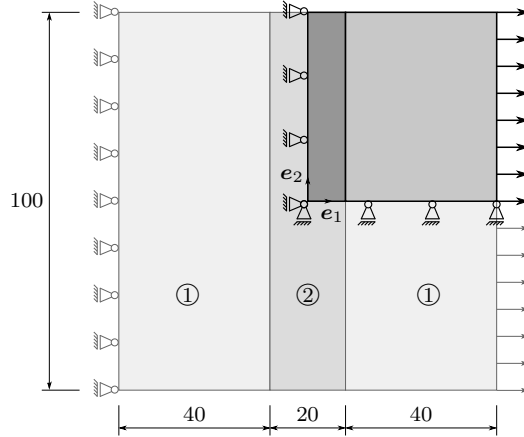
Figure 3.3: Sketch of a sample (in mm) consisting of two materials with different initial yield limits but the same elastic material parameters and hardening coefficients.

motivated) finite deformation of a plate with two round notches in Section 3.2.4.3. Extending the formulation to a three-dimensional setting, the shear band formation in a geometrically imperfect sample is again studied in Section 3.2.4.4.

The two-dimensional simulation results to be presented in the following sections are subjected to the assumption of a plane strain deformation state. For the calculation of the reference solutions, standard eight-node serendipity elements are used to discretise both the placement field as well as the geometry. As discussed in detail in Section 3.2.3.2, the gradient plasticity formulation results in a coupled system of partial differential equations, the solution of which is addressed in terms of a multi-field finite element formulation. To be precise, placement field $\boldsymbol{\varphi}$ and plastic deformation gradient-type field $\boldsymbol{\Theta}_{\mathrm{p}}$ will be discretised by means of eight-node serendipity elements, while linear Lagrangian elements are used for the discretisation of the generalised stress field $\widetilde{\overline{\boldsymbol{M}}}$ and of the κ-field. Integrals are evaluated numerically using a Gaussian quadrature scheme with nine sampling points for both the reference as well as for the gradient plasticity formulation.

3.2.4.1 Plastic evolution at material interfaces

In this section we focus on the simulation of a specimen that consists of two different materials, as depicted in Figure 3.3, and that is subjected to tensile loads. Both materials are assumed to exhibit the same elastic properties and to show the same hardening behaviour, see Table 3.1. However, the initial yield limit of material ② is chosen to be 10% smaller than that of material ①. We thus expect the reference formulation to exhibit jumps in the plastic variables at the respective material interfaces. In contrast, the curl of the plastic deformation field enters the gradient plasticity formulation due to the energy contribution (3.59) such that, as will be shown, the jumps in the plastic variables are smoothed.
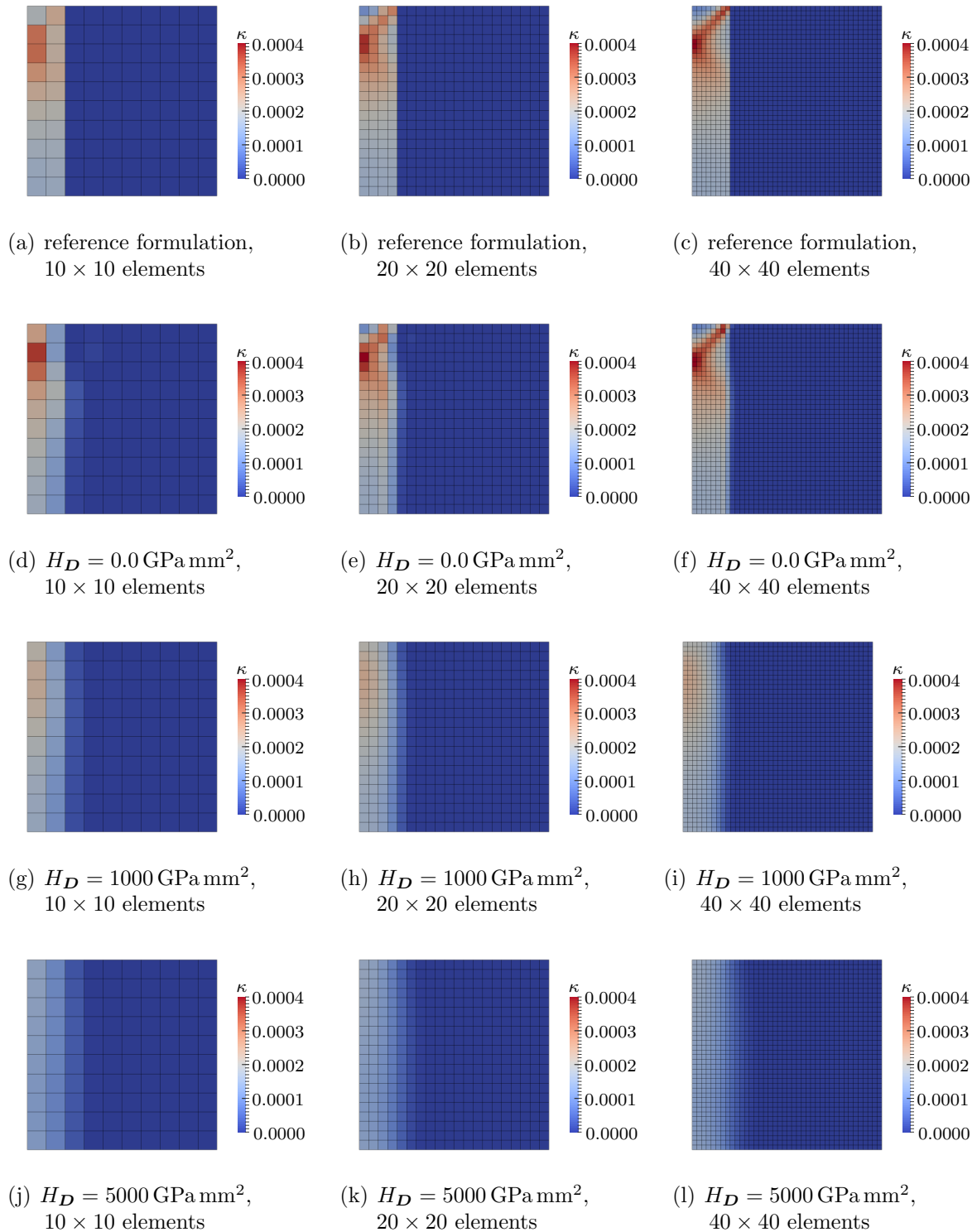
Figure 3.4: Analysis of the accumulated plastic strain κ for an elongation of 0.068 mm with respect to the 50 mm sample. The deformation state is chosen such that the domain with the smaller initial yield limit shows plastic deformation, while the deformation in the remaining part of the sample is purely elastic for the reference, i.e. the classic (local) plasticity formulation.

114

Table 3.1: Material parameters for the simulation of the boundary value problem depicted in Figure 3.3.

λ	μ	$q_0^{①}$	$q_0^{②}$	H_κ	$H_{\boldsymbol{D}}$
100 GPa	69 GPa	200 MPa	180 MPa	2000 MPa	0-5000 GPa mm^2

From a simulation point of view we will make use of symmetries and simulate only a quarter of the plate by taking into account the respective symmetry boundary conditions. Moreover, the load will be applied in terms of displacements at the right boundary, see Figure 3.3. For the reference formulation, the application of a displacement of approx. 0.068 mm to the 50 mm sample, which equals an overall strain of 1.36 ‰, results in the evolution of plasticity in material region ② while material region ① remains elastic, as is revealed by analysing the distribution of the accumulated plastic strain-like variable κ in Figures 3.4(a-c). The resulting jump in the plastic variables is furthermore exemplified in Figure 3.5 where the distribution of the accumulated plastic strain along the $\boldsymbol{e}_1$-axis is provided. In contrast, regarding the gradient plasticity formulation, the jump at the material interface is smoothed with increasing values of the material parameter $H_{\boldsymbol{D}}$ as shown in Figure 3.4. This finding is furthermore underpinned by the results presented in Figure 3.5(b) which clearly indicate an expansion of the plastic zone into the material region ① as well as an overall decrease of the accumulated plastic strain with increasing values of $H_{\boldsymbol{D}}$. Expressed differently, the plastic zone is smeared. Furthermore, note that in the limit $H_{\boldsymbol{D}} \to 0$ the gradient plasticity formulation closely reproduces the results that are achieved by means of the standard plasticity formulation except for the jump at the material interface which is not perfectly reproduced owing to the continuity requirement that is enforced on the κ- and on the $\boldsymbol{\Theta}_{\mathrm{p}}$-field by the choice of shape functions, see Figure 3.5(b) and also Remark 3.4. Analysing the influence of the difference in the initial yield limits $q_0^{①}$ and $q_0^{②}$ one observes that the plastically deforming zone of material ① significantly decreases with increasing values of $q_0^{①}$ and that the value of κ at the interface ($X_1 = 10$ mm) approaches zero. Moreover, one finds that the shape of the κ profile is in principle maintained, Figure 3.5(c). In addition to the presented results, the convergence behaviour upon mesh refinement of the gradient plasticity formulation is shown in Figure 3.5(a).

Remark 3.4 (Oscillations for $H_{\boldsymbol{D}} \to 0$) *Comparing Figures 3.4(a-c) and Figures 3.4(d-f) we note that the gradient plasticity formulation closely approximates the reference solution that was achieved with the standard formulation. However, as shown in Figure 3.5(b), oscillations in the κ-field are induced at the interface, where the solution exhibits a jump due to material discontinuity. The mixed-type formulation is, of course, not capable of reproducing the jump in the solution since $\mathcal{C}^0$-continuous functions are chosen for the approximation of the plastic field variables. Note, that the same ef-*
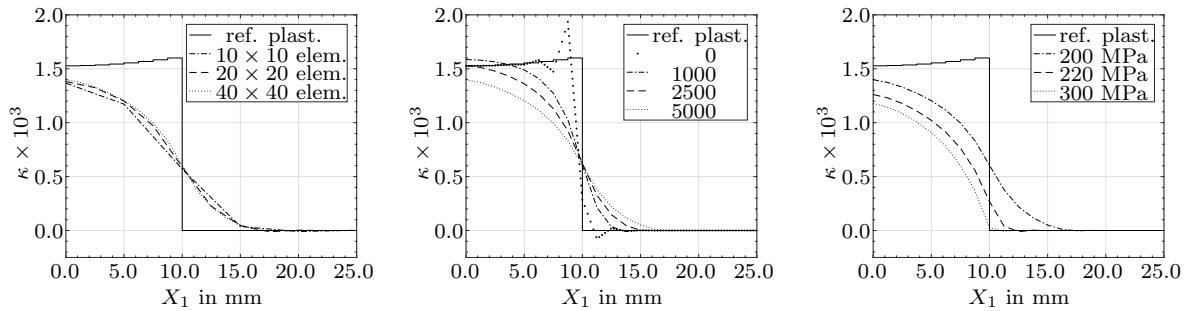
(a) Solution based on the reference formulation and convergence behaviour on mesh refinement for the multi-field gradient plasticity formulation with $H_D = 5000\,\mathrm{GPa\,mm^2}$.

(b) Solution based on the reference formulation and influence of the material parameter H_D (in $\mathrm{GPa\,mm^2}$) on the evolution of the plastic domain within the multi-field gradient plasticity formulation.

(c) Solution based on the reference formulation and influence of the initial yield limit $q_0^{\textcircled{1}}$ on the evolution of the plastic domain within the multi-field gradient plasticity formulation with $H_D = 5000\,\mathrm{GPa\,mm^2}$.

Figure 3.5: Analysis of the accumulated plastic strain κ along the $\boldsymbol{e}_1$-axis for an elongation of $0.068\,\mathrm{mm}$ with respect to the $50\,\mathrm{mm}$ sample. The deformation state is chosen such that the domain with the lower initial yield limit shows plastic deformation while the deformation in the remaining part of the sample is purely elastic for the reference, i.e. the classic (local) plasticity formulation.

fects were observed in [73, 75] where the gradient effect was restricted to a scalar valued internal variable.

3.2.4.2 Shear band formation induced by geometric imperfection

The computation of localised plastic deformations, e.g. the formation of shear bands, in softening materials using standard plasticity formulations that are based on local continuum descriptions yields mesh dependent results, see e.g. [73]. Motivated by this problem we will analyse the regularising nature of the presented gradient plasticity formulation and compare the simulation results with those of a standard plasticity formulation. To this end, we focus on the boundary value problem sketched out in Figure 3.6 where the shear band formation is triggered by means of a geometric imperfection as the specimen is elongated, see also [42]. The load will be applied in terms of displacements at the right boundary while homogeneous Dirichlet boundary conditions are prescribed at the left boundary. Moreover, the material parameters which are used in the finite element simulations are provided in Table 3.2 and are chosen in accordance with Section 3.2.4.1.

The distribution of the hardening variable κ for an elongation of 2.5 mm is provided in Figures 3.7(a-c) for the reference formulation and in Figures 3.7(d-f) for the gradient plasticity formulation with $H_D = 0\,\mathrm{GPa\,mm^2}$. It can be observed that in both cases the plastic deformation localises in the vicinity of a few elements along the shear band and that the lateral width of the shear band decreases upon mesh-refinement. This significant mesh dependence is further underlined taking into account the corresponding
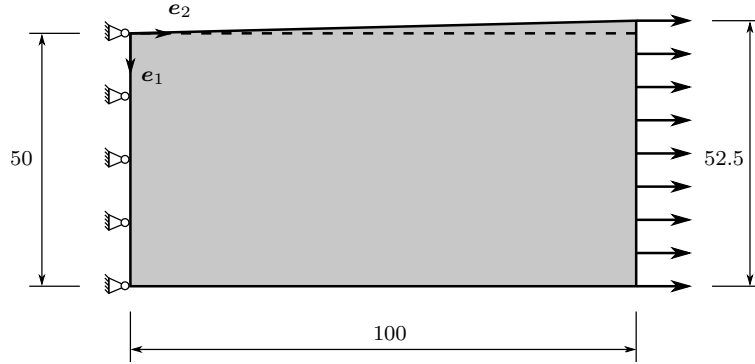
Figure 3.6: Sketch of the geometrically imperfect sample (in mm) subjected to tensile load.

Table 3.2: Material parameters for the simulation of the boundary value problem depicted in Figure 3.6.

λ	μ	q_0	H_κ	$H_{\boldsymbol{D}}$
100 GPa	69 GPa	200 MPa	-200 MPa	0-50 GPa mm^2

load-displacement curves provided in Figures 3.10(a,b) for discretisations with 10×20, 20×40 and 30×60 elements. Note, that the simulation results for the reference formulation and for the gradient plasticity formulation with $H_{\boldsymbol{D}} = 0\,\mathrm{GPa\,mm}^2$ are similar but not equal, in the sense that the plastic zone is slightly smeared in the gradient plasticity case even if $H_{\boldsymbol{D}} = 0\,\mathrm{GPa\,mm}^2$. This effect can be explained by taking into account (3.68) where $\boldsymbol{F}_\mathrm{p}$ is required to be equal to the $\mathcal{C}^0$-continuous field $\boldsymbol{\Theta}_\mathrm{p}$ in a weak sense, whereas $\boldsymbol{F}_\mathrm{p}$ is not constrained by such an equality in the reference formulation.

In contrast, the activation of the gradient energy contribution (3.59) regularises the plasticity formulation and results in shear bands of finite thickness as depicted in Figure 3.8 – the lateral width of the shear band is no longer determined by the finite element mesh but by the material parameter $H_{\boldsymbol{D}}$ which may take the interpretation of a (natural) material length scale parameter. These findings are underpinned by the load-displacement curves provided in Figures 3.10(c-f) which clearly indicate convergence upon mesh refinement in contrast to the load-displacement curves of the non-regularised formulations. We furthermore note that an increase of the value of $H_{\boldsymbol{D}}$ has a noteworthy influence on the deformation pattern as shown in Figure 3.8 and Figure 3.9 with the horizontal displacement of the upper boundary that results due to the shear band formation being significantly reduced. In fact, the formation of a shear band is suppressed for high values of $H_{\boldsymbol{D}}$, see Figure 3.9(f). Similar to the simulation results discussed in Section 3.2.4.1, the maximum accumulated plastic strain κ is found to decrease with increasing values of the material parameter $H_{\boldsymbol{D}}$, whereas the domain that shows plastic deformation is significantly widened.

(a) reference formulation,
    10×20 elements

(b) reference formulation,
    20×40 elements

(c) reference formulation,
    30×60 elements

(d) $H_D = 0.0\,\mathrm{GPa\,mm}^2$,
    10×20 elements

(e) $H_D = 0.0\,\mathrm{GPa\,mm}^2$,
    20×40 elements

(f) $H_D = 0.0\,\mathrm{GPa\,mm}^2$,
    30×60 elements

Figure 3.7: Shear band formation for the geometrically imperfect sample according to Figure 3.6 for an applied displacement of 2.5 mm. The simulation results of the reference formulation (a-c) and those of the novel formulation with an inactive gradient energy contribution (d-f) show a significant mesh dependence. To facilitate the evaluation of the deformation, the contour of the undeformed sample is depicted in light-grey colour.

(a) $H_{\boldsymbol{D}} = 5\,\mathrm{GPa\,mm^2}$, 10×20 elements

(b) $H_{\boldsymbol{D}} = 5\,\mathrm{GPa\,mm^2}$, 20×40 elements

(c) $H_{\boldsymbol{D}} = 5\,\mathrm{GPa\,mm^2}$, 30×60 elements

(d) $H_{\boldsymbol{D}} = 10\,\mathrm{GPa\,mm^2}$, 10×20 elements

(e) $H_{\boldsymbol{D}} = 10\,\mathrm{GPa\,mm^2}$, 20×40 elements

(f) $H_{\boldsymbol{D}} = 10\,\mathrm{GPa\,mm^2}$, 30×60 elements

Figure 3.8: Shear band formation for the geometrically imperfect sample according to Figure 3.6 for an applied displacement of 2.5 mm and moderate values of the material parameter $H_{\boldsymbol{D}}$. In contrast to the results depicted in Figure 3.7, the gradient plasticity formulation converges upon mesh refinement resulting in a shear band of finite thickness. The width of the shear band significantly increases with increasing values of $H_{\boldsymbol{D}}$. To facilitate the evaluation of the deformation, the contour of the undeformed sample is depicted in light-grey colour.

(a) $H_{\boldsymbol{D}} = 25\,\mathrm{GPa\,mm^2}$,
10 × 20 elements

(b) $H_{\boldsymbol{D}} = 25\,\mathrm{GPa\,mm^2}$,
20 × 40 elements

(c) $H_{\boldsymbol{D}} = 25\,\mathrm{GPa\,mm^2}$,
30 × 60 elements

(d) $H_{\boldsymbol{D}} = 50\,\mathrm{GPa\,mm^2}$,
10 × 20 elements

(e) $H_{\boldsymbol{D}} = 50\,\mathrm{GPa\,mm^2}$,
20 × 40 elements

(f) $H_{\boldsymbol{D}} = 50\,\mathrm{GPa\,mm^2}$,
30 × 60 elements

Figure 3.9: Shear band formation for the geometrically imperfect sample according to Figure 3.6 for an applied displacement of 2.5 mm and high values of the material parameter $H_{\boldsymbol{D}}$. A significant reduction in the horizontal displacement ($\boldsymbol{e}_1$-direction) for increasing values of $H_{\boldsymbol{D}}$ is observed. To facilitate the evaluation of the deformation, the contour of the undeformed sample is depicted in light-grey colour.

(a) reference formulation

(b) grad. plast. form. with $H_D = 0.0\,\mathrm{GPa\,mm}^2$

(c) grad. plast. form. with $H_D = 5\,\mathrm{GPa\,mm}^2$

(d) grad. plast. form. with $H_D = 10\,\mathrm{GPa\,mm}^2$

(e) grad. plast. form. with $H_D = 25\,\mathrm{GPa\,mm}^2$

(f) grad. plast. form. with $H_D = 50\,\mathrm{GPa\,mm}^2$
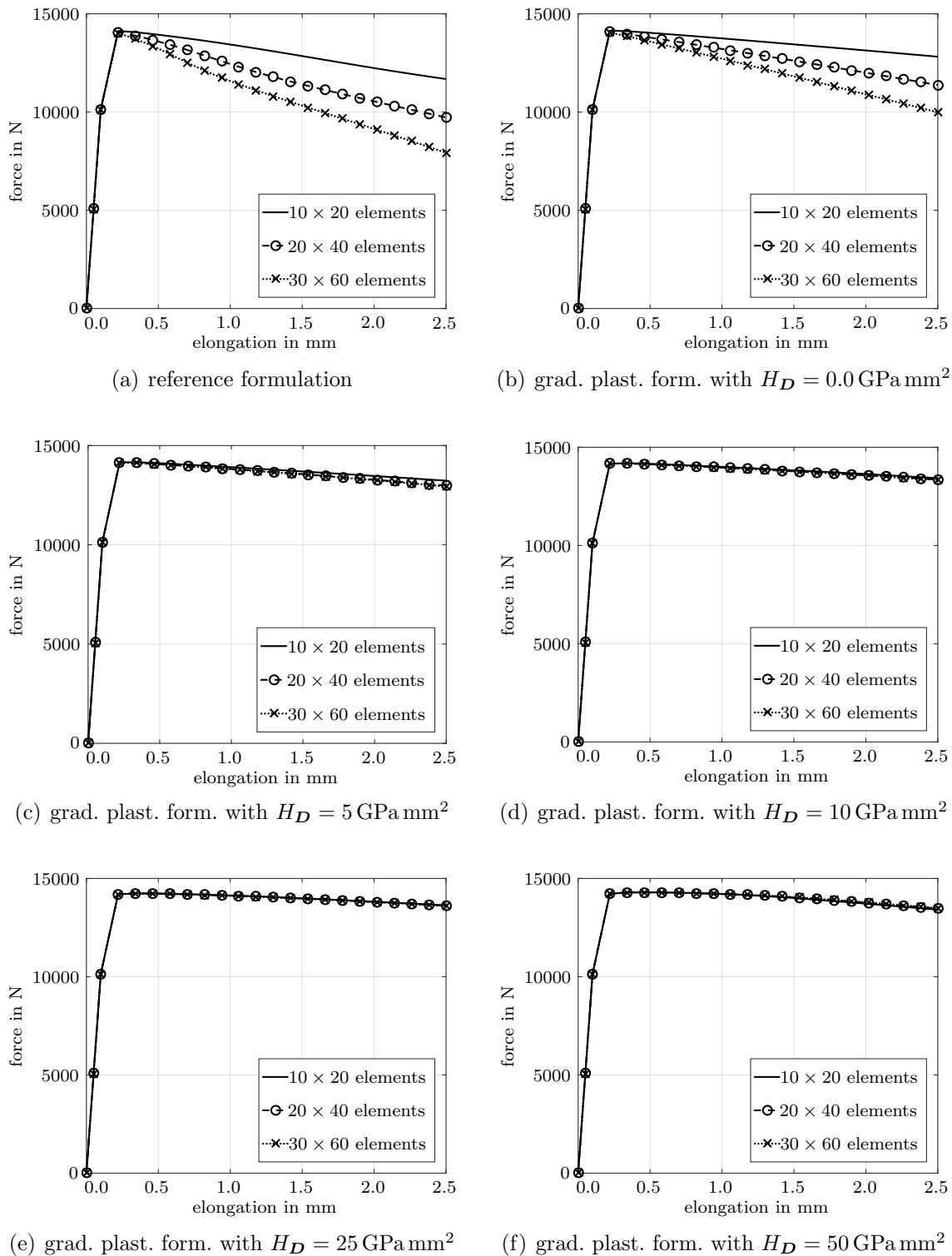
Figure 3.10: Mesh convergence study for the reference plasticity formulation and the multi-field gradient plasticity formulation in softening for a shear band formation that is induced by geometric imperfections. The calculation of the total longitudinal reaction forces is based on a sample thickness of 1 mm.
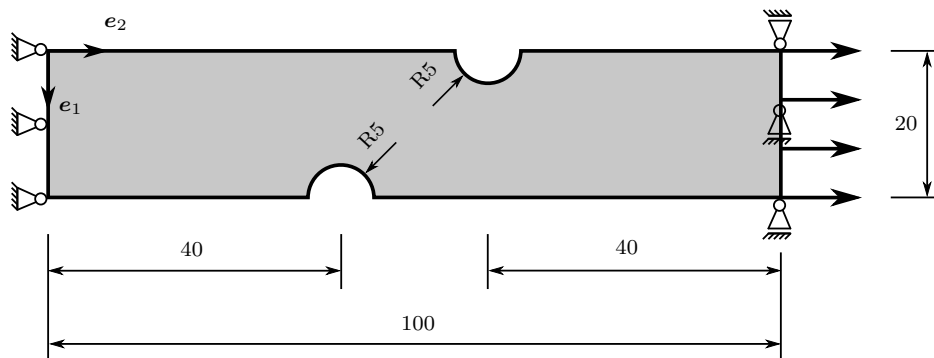
Figure 3.11: Sketch of a plate with two round notches (in mm) subjected to tensile loading.

Table 3.3: Material parameters for the simulation of the boundary value problem depicted in Figure 3.11.

λ	μ	q_0	H_κ (softening)	H_κ (hardening)	$H_{\boldsymbol{D}}$
100 GPa	69 GPa	200 MPa	-50 MPa	2000 MPa	$10 \, \mathrm{GPa\,mm^2}$

3.2.4.3 Finite deformation of a plate with two round notches

To study the model's properties in a finite deformation regime we consider the finite plastic deformation of a plate with two round notches as depicted in Figure 3.11 for both softening and hardening, using the gradient plasticity approach introduced in this contribution. As indicated in Figure 3.11, homogeneous Dirichlet boundary conditions in both spatial directions are enforced at the left boundary and in $\boldsymbol{e}_1$-direction at the right boundary, while displacements in $\boldsymbol{e}_2$-direction are prescribed at the right boundary. The material parameters are chosen in accordance with the simulations presented in Section 3.2.4.1 and Section 3.2.4.2, see Table 3.3.

The accumulated plastic strain-like variable κ which serves as a measure of the local accumulated plastic deformation is provided in Figure 3.12 for an applied displacement of 8 mm. Taking this information into account and comparing the deformed configurations depicted in Figure 3.12 against the undeformed configuration of the sample, the contour of which is given in light-grey colour, a significant deformation of the area in between the two round notches is revealed. In contrast and as expected, a notably smaller deformation takes place in the vicinity of the left and right boundaries. Comparing the resulting deformation in the case of softening Figures 3.12(a,b) with the one in the case of hardening Figures 3.12(c,d) we first find that κ takes significantly higher values in the case of softening. This is due to the existence of a plastic localisation zone between the two round notches as shown in Figures 3.12(a,b) which, moreover, results in notable necking in this area. In contrast, the plastic deformation is smeared over a larger area of the body in the case of hardening which results in a more accentuated lateral contraction near the left and right boundaries. We note that the transition area between the (left

(a) softening with $H_\kappa = -50\,\mathrm{MPa}$, 576 elements

(b) softening with $H_\kappa = -50\,\mathrm{MPa}$, 1600 elements

(c) hardening with $H_\kappa = 2000\,\mathrm{MPa}$, 576 elements

(d) hardening with $H_\kappa = 2000\,\mathrm{MPa}$, 1600 elements
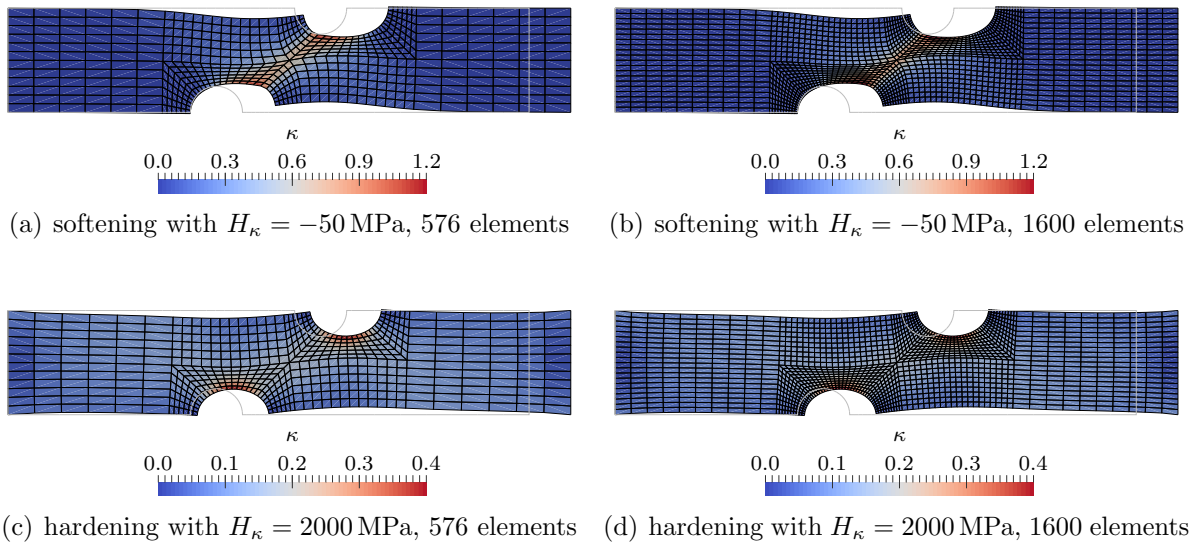
Figure 3.12: Deformation pattern and distribution of the accumulated plastic strain-like variable κ for the finite plastic deformation of a plate with two round notches according to Figure 3.11 and an applied displacement of 8 mm. The plate is analysed for softening ($H_\kappa = -50\,\mathrm{MPa}$, $H_D = 10\,\mathrm{GPa\,mm^2}$) and hardening ($H_\kappa = 2000\,\mathrm{MPa}$, $H_D = 10\,\mathrm{GPa\,mm^2}$) and two different discretisations are studied. To facilitate the evaluation of the deformation, the contour of the undeformed sample is depicted in light-grey colour.

(a) softening with $H_\kappa = -50\,\mathrm{MPa}$

(b) hardening with $H_\kappa = 2000\,\mathrm{MPa}$
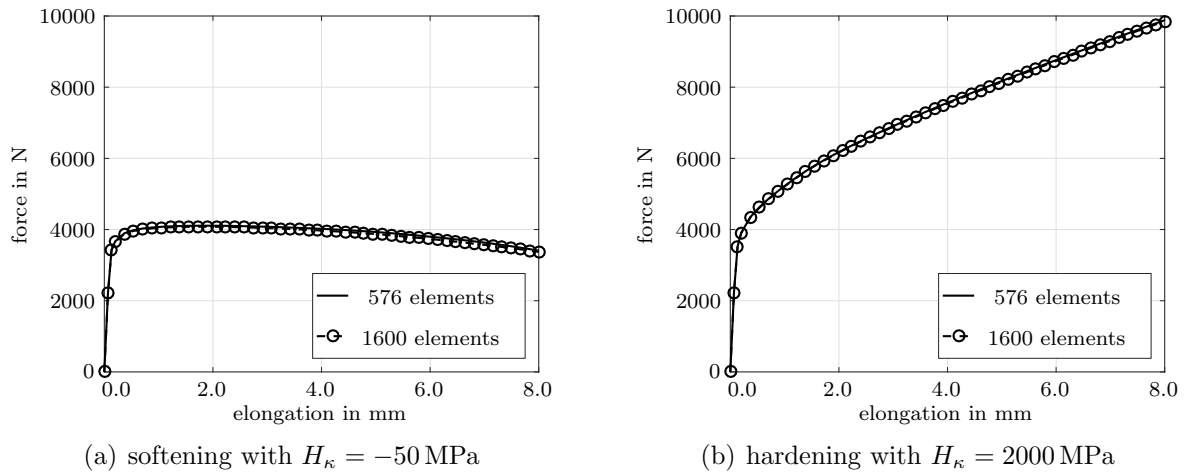
Figure 3.13: Total longitudinal reaction force as a function of the elongation for the boundary value problem sketched in Figure 3.11. The reaction force is calculated based on an assumed sample thickness of 1 mm and focus is on the analysis of the gradient plasticity formulation ($H_D = 10\,\mathrm{GPa\,mm^2}$) in softening ($H_\kappa = -50$ MPa) as well as in hardening ($H_\kappa = 2000$ MPa).

Table 3.4: Material parameters for the simulation of the boundary value problem depicted in Figure 3.14.

λ	μ	q_0	H_κ	$H_{\boldsymbol{D}}$
100 GPa	69 GPa	200 MPa	-200 MPa	0-25 GPa mm^2

and right) boundaries and the geometrically perturbed area may need to be larger in order to reduce the possible influence of boundary effects, especially when a comparison with experiments is envisaged.

Note that the formation of the shear band in the case of softening is not determined by the mesh size as revealed in Figures 3.12(a,b) when comparing the simulation results which are achieved with a 576-element discretisation to those resulting from a discretisation with 1600 elements, see also Section 3.2.4.2 for a more detailed analysis of the formulation's mesh objectivity. Thus, convergence upon mesh refinement of the load-displacement curves, additionally provided in Figure 3.13, is observed in both hardening as well as in softening.

3.2.4.4 Shear band formation in a three-dimensional setting

Extending the two-dimensional boundary value problems discussed in Section 3.2.4.2 to a three-dimensional setting, this section focuses again on the shear-band formation induced by geometric imperfections. The geometrically imperfect sample is visualised in Figure 3.14 and material parameters according to Table 3.4 are chosen. As indicated in Figure 3.14, the displacement in all three dimensions is suppressed at the left boundary. At the right boundary, the displacement in $\boldsymbol{e}_2$-direction is prescribed while the displacement in $\boldsymbol{e}_3$-direction is suppressed. The geometry, the placement field $\boldsymbol{\varphi}$ and the $\boldsymbol{\Theta}_{\mathrm{p}}$-field are discretised by means of 20-node serendipity elements, whereas eight-node Lagrangian elements are chosen for the discretisation of the generalised stress field $\widetilde{\overline{\boldsymbol{M}}}$ and of the κ-field for the novel formulation introduced in this contribution. Similar to Section 3.2.4.2, a standard von Mises plasticity model is taken into account as a reference which utilises a discretisation of the geometry and of the placement field in terms of 20-node serendipity elements. Occurring integrals are evaluated numerically in both formulations by means of a Gaussian quadrature scheme with 27 sampling points.

Analysing the shear band formation, four different models will be taken into account. These are: the novel gradient plasticity model with $H_{\boldsymbol{D}} = 25$ GPa mm^2 and $H_{\boldsymbol{D}} = 10$ GPa mm^2, a model which uses the same element formulation as the gradient plasticity model but neglects the gradient effect such that $H_{\boldsymbol{D}} = 0$ GPa mm^2, and a standard von Mises plasticity model as described above. The distribution of the accumulated plastic strain-like variable κ is provided in Figure 3.15 for a longitudinal elongation of 2.5 mm and for two different discretisations featuring 800, respectively 3200 elements. As expected on the basis of the two-dimensional simulation results dis-
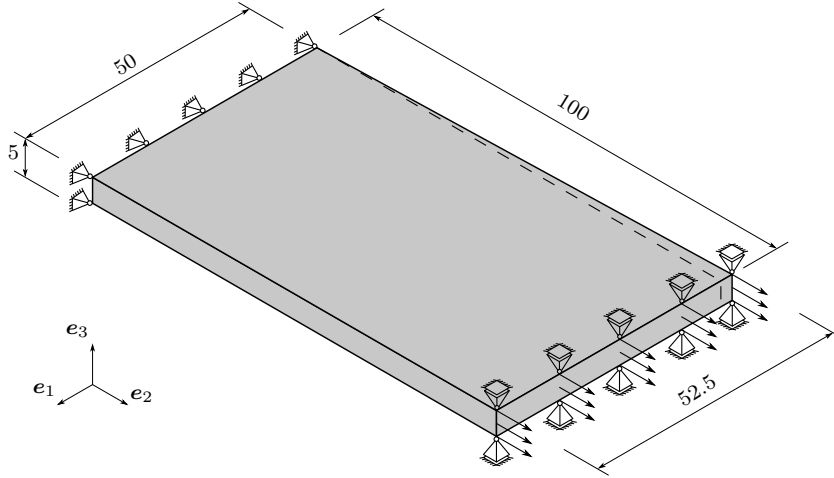
Figure 3.14: Sketch of a geometrically imperfect sample (in mm) in a three-dimensional setting subjected to tensile load.

cussed in Section 3.2.4.2, the κ-distribution indicates a strong mesh dependence of the reference formulation and of the novel formulation when the gradient term is not activated, i.e. when $H_{\boldsymbol{D}} = 0\,\mathrm{GPa\,mm}^2$. This mesh dependence is further underlined by the corresponding load-displacement curves provided in Figure 3.16. On the other hand, the formation of a shear band of finite thickness is observed in the gradient-enhanced formulation with $H_{\boldsymbol{D}} = 10\,\mathrm{GPa\,mm}^2$, respectively $H_{\boldsymbol{D}} = 25\,\mathrm{GPa\,mm}^2$, Figures 3.15(e,f) and Figures 3.15(g,h). Furthermore, the respective load-displacement curves suggest convergence upon mesh refinement, see Figure 3.16(c) and Figure 3.16(d).

3.2.5 Summary

In this section, a thermodynamically consistent gradient plasticity theory has been discussed which relies on the nonlocal extension of the Clausius-Duhem inequality proposed in [106]. Making use of these theoretical fundamentals, higher gradients of the plastic part of the deformation gradient tensor were introduced as additional arguments of the free energy function. In contrast to purely phenomenological approaches, these gradient terms could be interpreted as measures of the dislocation density and gave rise to the occurrence of back stress-type tensors in the respective yield functions based on thermodynamic considerations. We showed that assuming a specific quadratic energy contribution in the dislocation density tensor results in a well-interpretable form of the back stress-type tensor and analysed the model properties for this particular form of the free energy function. To be more specific, a multi-field finite element framework was established for the solution of the coupled system of (partial) differential equations, with the Karush-Kuhn-Tucker conditions being enforced on a global level by means of Fischer-Burmeister complementarity functions, and boundary value problems in two- and three-dimensional settings were analysed. Specifically speaking, the smoothing be-
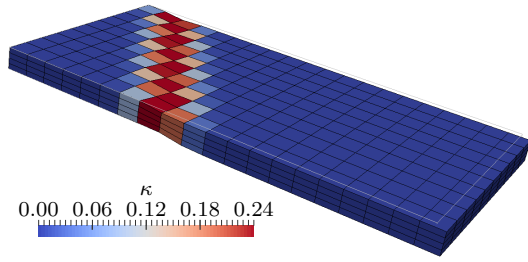
(a) reference formulation, $10 \times 20 \times 4$ elements
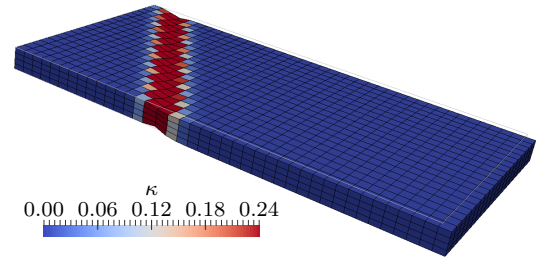
(b) reference formulation, $20 \times 40 \times 4$ elements
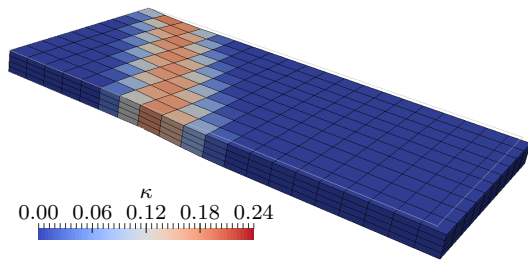
(c) $H_{\boldsymbol{D}} = 0\,\mathrm{GPa\,mm^2}$, $10 \times 20 \times 4$ elements
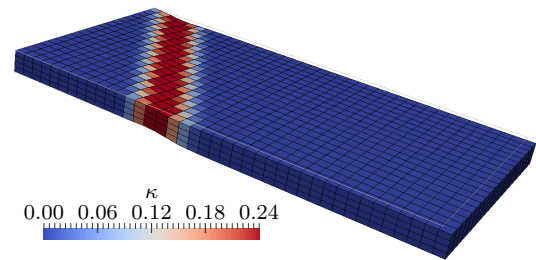
(d) $H_{\boldsymbol{D}} = 0\,\mathrm{GPa\,mm^2}$, $20 \times 40 \times 4$ elements
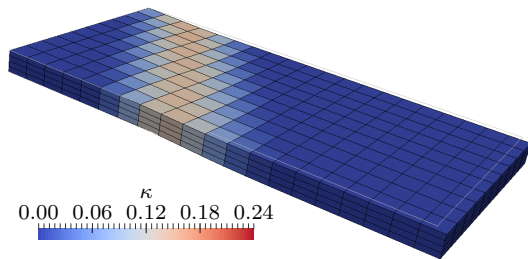
(e) $H_{\boldsymbol{D}} = 10\,\mathrm{GPa\,mm^2}$, $10 \times 20 \times 4$ elements
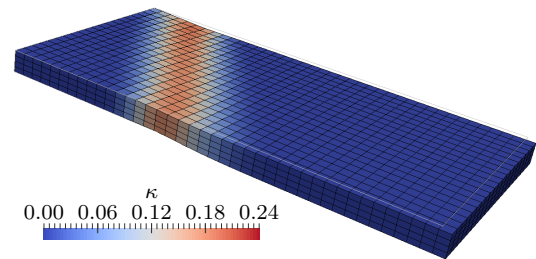
(f) $H_{\boldsymbol{D}} = 10\,\mathrm{GPa\,mm^2}$, $20 \times 40 \times 4$ elements
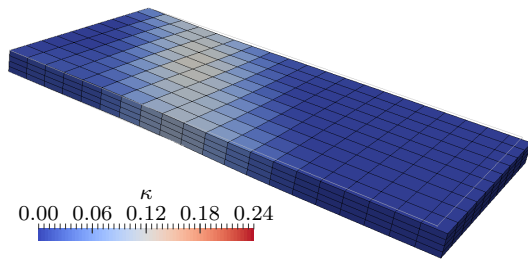
(g) $H_{\boldsymbol{D}} = 25\,\mathrm{GPa\,mm^2}$, $10 \times 20 \times 4$ elements

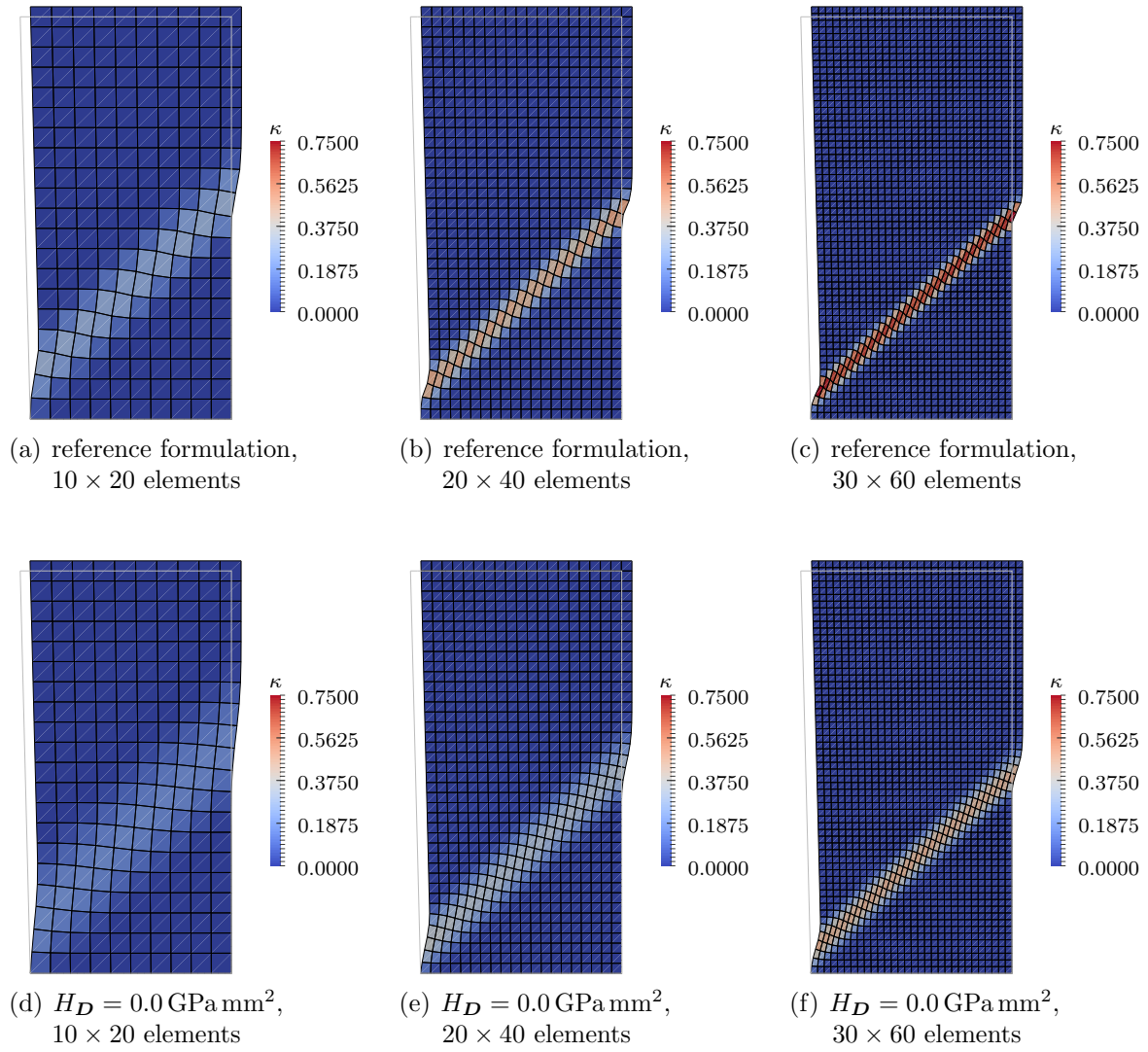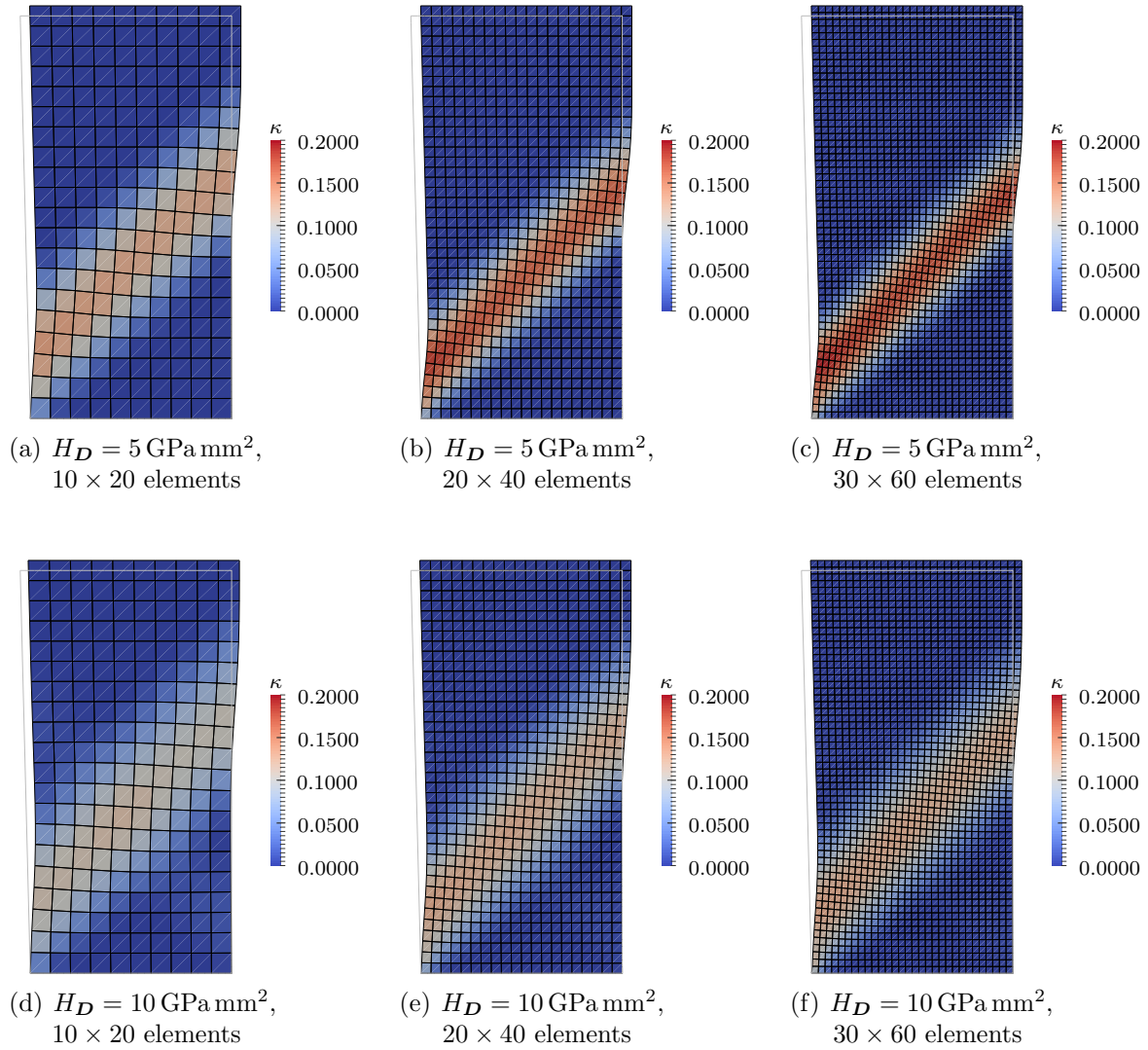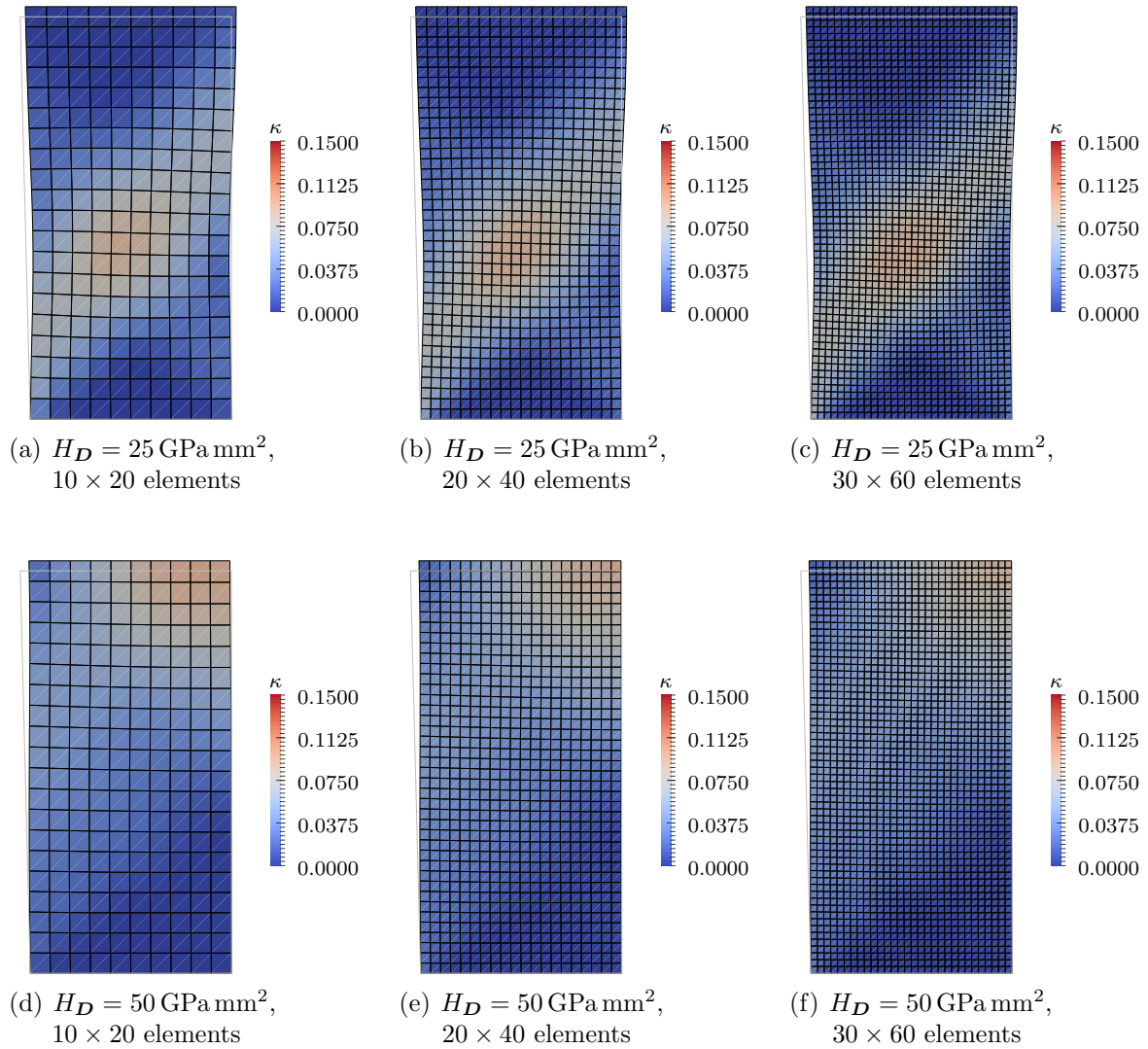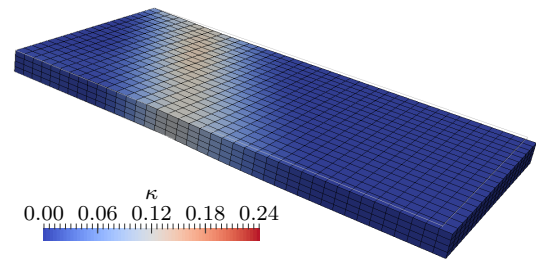(h) $H_{\boldsymbol{D}} = 25\,\mathrm{GPa\,mm^2}$, $20 \times 40 \times 4$ elements

Figure 3.15: Shear band formation for the geometrically imperfect sample according to Figure 3.14 for an applied displacement of 2.5 mm. To facilitate the evaluation of the deformation, the contour of the undeformed sample is depicted in light-grey colour.

(a) reference formulation

(b) grad. plast. form. ($H_{\boldsymbol{D}} = 0.0\,\mathrm{GPa\,mm}^2$)

(c) grad. plast. form. ($H_{\boldsymbol{D}} = 10\,\mathrm{GPa\,mm}^2$)

(d) grad. plast. form. ($H_{\boldsymbol{D}} = 25\,\mathrm{GPa\,mm}^2$)
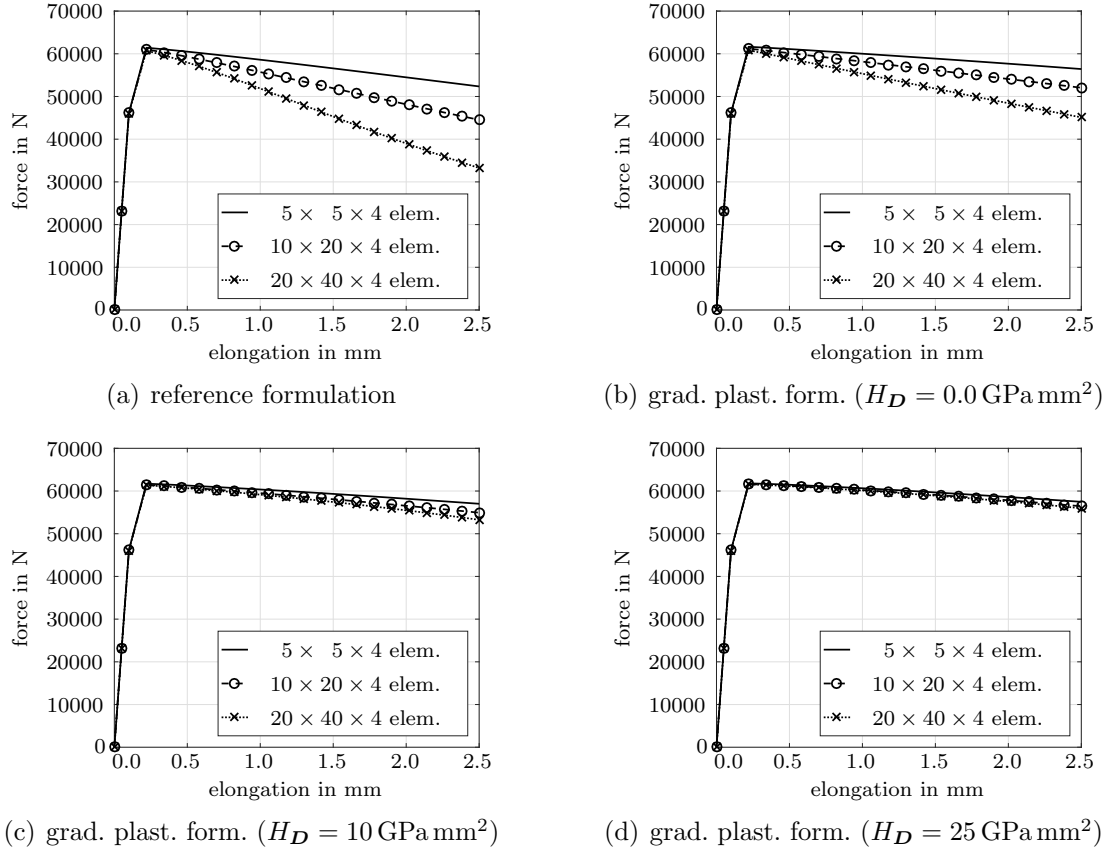
Figure 3.16: Mesh convergence study for the reference plasticity formulation and the multi-field gradient plasticity formulation in softening for a shear band formation that is induced by geometric imperfections in a three-dimensional setting.

haviour of the formulation at a material interface where the yield limit exhibits a jump discontinuity, the formation of shear bands in softening materials and the experimentally motivated, inhomogeneous, finite plastic deformation of tensile test samples were studied in detail in a two-dimensional setting. Extending the formulation to a three-dimensional setting, the focus was laid on the formation of shear bands that were induced by geometric imperfections. In summary, the presented results suggest that the regularised modelling framework can be used to simulate finite plastic deformation processes both in hardening as well as in softening, providing a physically well-motivated approach towards gradient plasticity.

Especially the replacement of the phenomenological associated-type flow rule by a crystal plasticity formulation seems a natural extension of the present formulation in terms of plastic anisotropies and will be discussed in detail in Section 3.3.
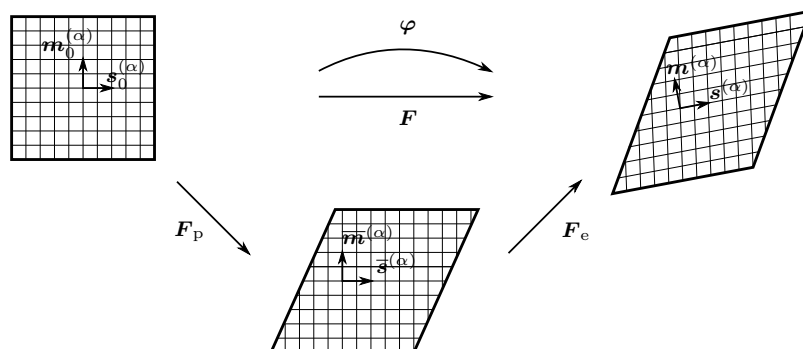
Figure 3.17: Representation of slip systems in the reference, intermediate and spatial configuration.

3.3 A gradient crystal plasticity formulation

This section focuses on the extension of the gradient plasticity framework developed in Section 3.2 to gradient crystal plasticity. To this end, the fundamentals of crystal plasticity are briefly summarised and the resulting form of the dissipation inequality is studied in detail in Section 3.3.1. Based on these theoretical foundations, a specific model is elaborated in Section 3.3.2, and the implementation with a focus on stabilisation algorithms and a multi-field finite element formulation are elaborated in Section 3.3.3. Section 3.3.4 eventually focuses on the simulation of representative boundary value problems. In particular, the constitutive response at material point level is studied first before the model is applied to the simulation of tension tests in a two-dimensional setting and to the experimentally motivated simulation of micro torsion tests in a three-dimensional setting.

3.3.1 Extension to crystal plasticity

This section focuses on the extension of the gradient plasticity theory introduced in Section 3.1 to crystal plasticity. Taking into account the definition of the spatial velocity gradient and inserting the multiplicative split (3.3) yields

$$\boldsymbol{l} = \dot{\boldsymbol{F}} \cdot \boldsymbol{F}^{-1} = \dot{\boldsymbol{F}}_{\mathrm{e}} \cdot \boldsymbol{F}_{\mathrm{e}}^{-1} + \boldsymbol{F}_{\mathrm{e}} \cdot \dot{\boldsymbol{F}}_{\mathrm{p}} \cdot \boldsymbol{F}_{\mathrm{p}}^{-1} \cdot \boldsymbol{F}_{\mathrm{e}}^{-1} \quad . \tag{3.82}$$

The second summand on the right-hand side is identified as the plastic part of the (spatial) velocity gradient. In crystal plasticity, this part can be well-motivated based on kinematic considerations, i.e. it is assumed that plastic slip occurs on distinct slip planes, identified by their normal vectors $\boldsymbol{m}^{(\alpha)}$, in certain slip directions $\boldsymbol{s}^{(\alpha)}$. A slip system is then defined by the pair $\{\boldsymbol{m}^{(\alpha)}, \boldsymbol{s}^{(\alpha)}\}$, see Figure 3.17. Since atomic bonds have to be broken and re-established in the sliding process, and since the atomic bonds weaken with increasing distance of the atoms, plastic slip tends to occur between crystallographic planes of greatest atomic density. Likewise, closest-packed directions in the slip planes

are identified with slip directions, see e.g. [33] for a detailed presentation. Based on these kinematic considerations, the plastic part of the spatial velocity gradient $\boldsymbol{l}_{\mathrm{p}}$ is assumed to take the form

$$\boldsymbol{l}_{\mathrm{p}} = \boldsymbol{F}_{\mathrm{e}} \cdot \dot{\boldsymbol{F}}_{\mathrm{p}} \cdot \boldsymbol{F}_{\mathrm{p}}^{-1} \cdot \boldsymbol{F}_{\mathrm{e}}^{-1} = \sum_{\alpha=1}^{\mathrm{n}_{\alpha}} \boldsymbol{s}^{(\alpha)} \otimes \boldsymbol{m}^{(\alpha)} \, \dot{\gamma}^{(\alpha)} \quad , \tag{3.83}$$

with $\dot{\gamma}^{(\alpha)}$ denoting the slip rate on the respective slip system and with the total number of slip systems n_{α}. In the case of face-centred cubic crystals one finds for example that $\mathrm{n}_{\alpha} = 12$. Note, that we do not restrict the slip rates $\dot{\gamma}^{(\alpha)}$ to be positive and thus do not need to distinguish between positive and negative slip directions as done in [27, 115]. The pull-back of (3.83) to the intermediate configuration yields

$$\overline{\boldsymbol{L}}_{\mathrm{p}} = \boldsymbol{F}_{\mathrm{e}}^{-1} \cdot \boldsymbol{l}_{\mathrm{p}} \cdot \boldsymbol{F}_{\mathrm{e}} = \sum_{\alpha=1}^{\mathrm{n}_{\alpha}} \overline{\boldsymbol{s}}^{(\alpha)} \otimes \overline{\boldsymbol{m}}^{(\alpha)} \, \dot{\gamma}^{(\alpha)} = \sum_{\alpha=1}^{\mathrm{n}_{\alpha}} \overline{\boldsymbol{Z}}^{(\alpha)} \, \dot{\gamma}^{(\alpha)} \quad , \tag{3.84}$$

with the representation of the slip direction and of the slip plane normal in the intermediate configuration

$$\overline{\boldsymbol{s}}^{(\alpha)} = \boldsymbol{F}_{\mathrm{e}}^{-1} \cdot \boldsymbol{s}^{(\alpha)} \quad , \tag{3.85} \qquad \overline{\boldsymbol{m}}^{(\alpha)} = \boldsymbol{F}_{\mathrm{e}}^{\mathrm{t}} \cdot \boldsymbol{m}^{(\alpha)} \quad , \tag{3.86}$$

and the associated projection tensor

$$\overline{\boldsymbol{Z}}^{(\alpha)} = \overline{\boldsymbol{s}}^{(\alpha)} \otimes \overline{\boldsymbol{m}}^{(\alpha)} \quad . \tag{3.87}$$

The slip directions and the slip plane normals are assumed to be convected with the elastic deformation and assumed to be left unaltered by the plastic deformation which resembles the assumption of an isoclinic intermediate configuration, see [29, 43]. Furthermore, $\overline{\boldsymbol{s}}^{(\alpha)}$ and $\overline{\boldsymbol{m}}^{(\alpha)}$ are introduced as normalised vectors and are clearly orthogonal such that

$$\overline{\boldsymbol{s}}^{(\alpha)} \cdot \overline{\boldsymbol{s}}^{(\alpha)} = 1 \quad (3.88) \qquad \overline{\boldsymbol{m}}^{(\alpha)} \cdot \overline{\boldsymbol{m}}^{(\alpha)} = 1 \quad (3.89) \qquad \overline{\boldsymbol{s}}^{(\alpha)} \cdot \overline{\boldsymbol{m}}^{(\alpha)} = 0 \quad (3.90)$$

hold (no summation over α). The orthogonality of $\overline{\boldsymbol{s}}^{(\alpha)}$ and $\overline{\boldsymbol{m}}^{(\alpha)}$ results in $\mathrm{tr}\left(\overline{\boldsymbol{Z}}^{(\alpha)}\right) = 0$ which with regard to (3.84) essentially implies that the plastic flow is volume preserving (at least in the continuous setting). As an example, the twelve slip systems of a face-centred cubic atomic arrangement are provided in Table 3.5 and sketched in Figure 3.18.
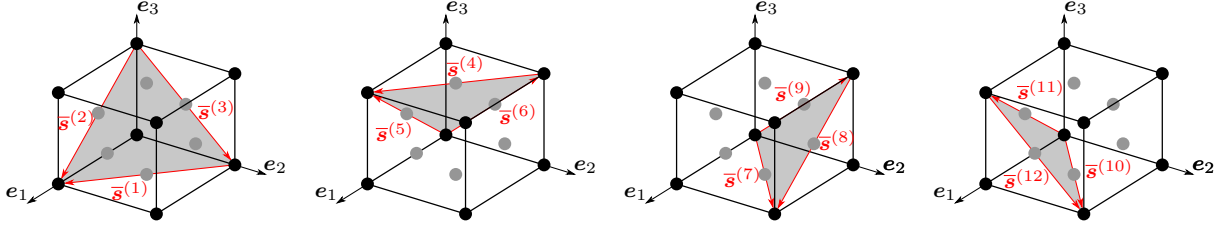
Figure 3.18: Slip systems in fcc-crystals according to Table 3.5.

Inserting (3.84) into (3.20) results in the specific form of the reduced dissipation inequality

$$\widetilde{\mathcal{D}}^{\text{red}} = \sum_{\alpha=1}^{n_\alpha} \widetilde{\overline{M}}^{(\alpha)} \dot{\widetilde{\gamma}}^{(\alpha)} + q\,\dot{\kappa} \geq 0 \tag{3.91}$$

where the definition of the projected generalised Mandel-type stress tensor

$$\widetilde{\overline{M}}^{(\alpha)} = \widetilde{\overline{\boldsymbol{M}}} : \overline{\boldsymbol{Z}}^{(\alpha)} \tag{3.92}$$

was used and where a tilde was added in the notation to underline the energetic duality between $\dot{\widetilde{\gamma}}^{(\alpha)}$ and $\widetilde{\overline{M}}^{(\alpha)}$. In the case that the gradient effects are neglected, $\widetilde{\overline{\boldsymbol{M}}}$ reduces to $\overline{\boldsymbol{M}}$, cf. (3.24), such that making use of the identity

$$\overline{M}^{(\alpha)} = \overline{\boldsymbol{M}} : \overline{\boldsymbol{Z}}^{(\alpha)} = \overline{\boldsymbol{M}} : \left[\overline{\boldsymbol{s}}^{(\alpha)} \otimes \overline{\boldsymbol{m}}^{(\alpha)}\right] = \boldsymbol{\tau} : \left[\boldsymbol{s}^{(\alpha)} \otimes \boldsymbol{m}^{(\alpha)}\right] = \tau^{(\alpha)} \tag{3.93}$$

with $\boldsymbol{\tau} = \boldsymbol{F}_{\text{e}}^{-\text{t}} \cdot \overline{\boldsymbol{M}} \cdot \boldsymbol{F}_{\text{e}}^{\text{t}}$ denoting the (mixed-variant) Kirchhoff stress tensor, gives rise to the classic form of the (reduced) dissipation inequality

$$\mathcal{D}^{\text{red}} = \sum_{\alpha=1}^{n_\alpha} \overline{M}^{(\alpha)} \dot{\gamma}^{(\alpha)} + q\,\dot{\kappa} \tag{3.94a}$$

$$= \sum_{\alpha=1}^{n_\alpha} \tau^{(\alpha)} \dot{\gamma}^{(\alpha)} + q\,\dot{\kappa} \geq 0 \quad, \tag{3.94b}$$

which implies the well-established energetic duality between the Schmid stress $\tau^{(\alpha)}$ and the plastic slip rate $\dot{\gamma}^{(\alpha)}$.

3.3.2 Specification of the constitutive model

The activity of slip systems in rate-independent crystal plasticity cannot generally be uniquely determined, see e.g. [6, 33, 54, 93, 115]. In the (time-)continuous case, this issue manifests itself in the singularity of matrices which need to be inverted in order

Table 3.5: Miller indices, slip plane normals $\overline{\boldsymbol{m}}^{(\alpha)}$ and slip directions $\overline{\boldsymbol{s}}^{(\alpha)}$ in an fcc-crystal, see e.g. [93, 115], with $[\bullet]_i$ denoting the coefficient matrix of a vector $\bullet$ with respect to an orthonormal basis that is aligned with the lattice vectors defining the unit cell, see Figure 3.18.

slip system α	Miller index	slip plane normal $\overline{\boldsymbol{m}}^{(\alpha)}$	slip direction $\overline{\boldsymbol{s}}^{(\alpha)}$
1	$(1,1,1)[1,\bar{1},0]$	$\left[\overline{\boldsymbol{m}}^{(1)}\right]_i = \frac{1}{\sqrt{3}}[1,1,1]$	$\left[\overline{\boldsymbol{s}}^{(1)}\right]_i = \frac{1}{\sqrt{2}}[1,-1,0]$
2	$(1,1,1)[1,0,\bar{1}]$	$\left[\overline{\boldsymbol{m}}^{(2)}\right]_i = \frac{1}{\sqrt{3}}[1,1,1]$	$\left[\overline{\boldsymbol{s}}^{(2)}\right]_i = \frac{1}{\sqrt{2}}[1,0,-1]$
3	$(1,1,1)[0,1,\bar{1}]$	$\left[\overline{\boldsymbol{m}}^{(3)}\right]_i = \frac{1}{\sqrt{3}}[1,1,1]$	$\left[\overline{\boldsymbol{s}}^{(3)}\right]_i = \frac{1}{\sqrt{2}}[0,1,-1]$
4	$(1,1,\bar{1})[1,\bar{1},0]$	$\left[\overline{\boldsymbol{m}}^{(4)}\right]_i = \frac{1}{\sqrt{3}}[1,1,-1]$	$\left[\overline{\boldsymbol{s}}^{(4)}\right]_i = \frac{1}{\sqrt{2}}[1,-1,0]$
5	$(1,1,\bar{1})[1,0,1]$	$\left[\overline{\boldsymbol{m}}^{(5)}\right]_i = \frac{1}{\sqrt{3}}[1,1,-1]$	$\left[\overline{\boldsymbol{s}}^{(5)}\right]_i = \frac{1}{\sqrt{2}}[1,0,1]$
6	$(1,1,\bar{1})[0,1,1]$	$\left[\overline{\boldsymbol{m}}^{(6)}\right]_i = \frac{1}{\sqrt{3}}[1,1,-1]$	$\left[\overline{\boldsymbol{s}}^{(6)}\right]_i = \frac{1}{\sqrt{2}}[0,1,1]$
7	$(1,\bar{1},1)[1,1,0]$	$\left[\overline{\boldsymbol{m}}^{(7)}\right]_i = \frac{1}{\sqrt{3}}[1,-1,1]$	$\left[\overline{\boldsymbol{s}}^{(7)}\right]_i = \frac{1}{\sqrt{2}}[1,1,0]$
8	$(1,\bar{1},1)[1,0,\bar{1}]$	$\left[\overline{\boldsymbol{m}}^{(8)}\right]_i = \frac{1}{\sqrt{3}}[1,-1,1]$	$\left[\overline{\boldsymbol{s}}^{(8)}\right]_i = \frac{1}{\sqrt{2}}[1,0,-1]$
9	$(1,\bar{1},1)[0,1,1]$	$\left[\overline{\boldsymbol{m}}^{(9)}\right]_i = \frac{1}{\sqrt{3}}[1,-1,1]$	$\left[\overline{\boldsymbol{s}}^{(9)}\right]_i = \frac{1}{\sqrt{2}}[0,1,1]$
10	$(\bar{1},1,1)[1,1,0]$	$\left[\overline{\boldsymbol{m}}^{(10)}\right]_i = \frac{1}{\sqrt{3}}[-1,1,1]$	$\left[\overline{\boldsymbol{s}}^{(10)}\right]_i = \frac{1}{\sqrt{2}}[1,1,0]$
11	$(\bar{1},1,1)[1,0,1]$	$\left[\overline{\boldsymbol{m}}^{(11)}\right]_i = \frac{1}{\sqrt{3}}[-1,1,1]$	$\left[\overline{\boldsymbol{s}}^{(11)}\right]_i = \frac{1}{\sqrt{2}}[1,0,1]$
12	$(\bar{1},1,1)[0,1,\bar{1}]$	$\left[\overline{\boldsymbol{m}}^{(12)}\right]_i = \frac{1}{\sqrt{3}}[-1,1,1]$	$\left[\overline{\boldsymbol{s}}^{(12)}\right]_i = \frac{1}{\sqrt{2}}[0,1,-1]$

to determine the plastic slip rates based on a prescribed stress or strain rate, i.e. slip mode uniqueness is generally not guaranteed, see [6, 54, 93]. In the (time-)discrete case, this shortcoming results in two main problems. Firstly, the active set search for the determination of the set of active slip systems does, in general, not result in a unique solution – i.e. different active sets which fulfil the discrete plastic consistency conditions may exist. Secondly, even if an active set has been determined, many different combinations of the plastic multipliers which represent the time discrete equivalent of the slip-rates may constitute a solution, see e.g. [33, 115]. Several numerical tools have been developed to deal with the latter problems such as the construction of generalised or pseudo inverses of the Jacobian, perturbation techniques or diagonal shift methods, e.g. [4, 21, 93]. However, by using these methods to generate a solution, there is no clear distinction between constitutive modelling and the algorithmic treatment of the resulting system of equations because the chosen algorithm influences the activity of the slip systems.

Against this background we will resort to rate-dependent viscoplasticity where the slip rates are uniquely determined by the stress state and possibly by some internal

variables, [115]. As argued in [134] it is always possible to regard the rate-independent theory as the limit case of the rate-dependent theory. However, by approaching this limit the system to be solved becomes considerably stiff and requires special numerical treatment. In what follows, we will take into account an extended version of the crystal (visco-)plasticity framework proposed in [134] and enhance the formulation in terms of a gradient energy contribution.

3.3.2.1 A specific crystal (visco-)plasticity model

The crystal (visco-)plasticity model to be used in this contribution is a modified version of the model proposed in [134]. At the outset, the free-energy density function is assumed to be additively composed of an elastic part $\widetilde{W}^{\text{cp,e}}$ and of a hardening part $\widetilde{W}^{\text{cp,p}}$ according to

$$\widetilde{W}^{\text{cp,ref}}\left(\boldsymbol{F}, \boldsymbol{F}_{\text{p}}, \kappa_{\text{cp}}\right) = \widetilde{W}^{\text{cp,e}}\left(\boldsymbol{F}, \boldsymbol{F}_{\text{p}}\right) + \widetilde{W}^{\text{cp,p}}\left(\kappa_{\text{cp}}\right) \qquad . \tag{3.95}$$

The elastic part is chosen identical to the one used in Section 3.2.2.1, i.e. (3.39), such that the specific forms of the Piola stress tensor (3.44), and of the (local) Mandel stress tensor (3.45), are recovered. The hardening part is chosen to be of the form

$$\widetilde{W}^{\text{cp,p}} = \tau_0\, \kappa_{\text{cp}} + \frac{[\tau_\infty - \tau_0]^2}{h_0}\, \ln\left(\cosh\left(\frac{h_0\, \kappa_{\text{cp}}}{\tau_\infty - \tau_0}\right)\right) \quad , \tag{3.96}$$

with the material constants τ_0, τ_∞ and with h_0 representing the initial shear yield stress, the saturation strength and the initial hardening rate. Evaluating (3.19) for the specific form of the free energy function yields

$$q_{\text{cp}} = -\left[\tau_0 + [\tau_\infty - \tau_0]\tanh\left(\frac{h_0\, \kappa_{\text{cp}}}{\tau_\infty - \tau_0}\right)\right] < 0 \quad . \tag{3.97}$$

Furthermore, the existence of a plastic potential which is additively composed of slip system contributions $\Phi^{(\alpha)}$ according to

$$\Phi^{\text{cp}} = \sum_{\alpha=1}^{n_\alpha} \Phi^{(\alpha)} \tag{3.98}$$

is assumed from which the slip rates $\dot{\gamma}^{(\alpha)}$ and the rate of the internal variable κ_{cp} are derivable via

$$\dot{\gamma}^{(\alpha)} = \frac{\partial \Phi^{\text{cp}}}{\partial \overline{M}^{(\alpha)}} \quad , \tag{3.99} \qquad \dot{\kappa}_{\text{cp}} = \frac{\partial \Phi^{\text{cp}}}{\partial q_{\text{cp}}} \quad . \tag{3.100}$$

Note, that this format also allows for an interpretation in terms of constrained optimisa-

tion conditions as shown in [134]. For the specific form of the slip system contributions to the plastic potential that is adopted in this contribution,

$$
\Phi^{(\alpha)} = -\dot{\gamma}_0 \frac{q_{\text{cp}}}{h_e + 1} \left| \frac{\overline{M}^{(\alpha)}}{q_{\text{cp}}} \right|^{h_e+1} \quad , \tag{3.101}
$$

with $\dot{\gamma}_0$ denoting the reference shear strain rate and with the rate sensitivity parameter h_e, one finally arrives at

$$
\dot{\gamma}^{(\alpha)} = \dot{\gamma}_0 \, \text{sgn}\left(\overline{M}^{(\alpha)}\right) \left| \frac{\overline{M}^{(\alpha)}}{q_{\text{cp}}} \right|^{h_e} \tag{3.102}
$$

and

$$
\dot{\kappa}_{\text{cp}} = -\frac{h_e}{h_e + 1} \sum_{\alpha=1}^{n_\alpha} \frac{\dot{\gamma}^{(\alpha)} \, \overline{M}^{(\alpha)}}{q_{\text{cp}}} \quad . \tag{3.103}
$$

Inserting (3.102) and (3.103) in (3.94a) in order to evaluate the dissipation inequality we find

$$
\mathcal{D}^{\text{red}} = \sum_{\alpha=1}^{n_\alpha} \overline{M}^{(\alpha)} \, \dot{\gamma}^{(\alpha)} + q_{\text{cp}} \, \dot{\kappa}_{\text{cp}} \tag{3.104a}
$$

$$
= \sum_{\alpha=1}^{n_\alpha} \left[1 - \frac{h_e}{h_e + 1} \right] \overline{M}^{(\alpha)} \, \dot{\gamma}^{(\alpha)} \tag{3.104b}
$$

$$
= \sum_{\alpha=1}^{n_\alpha} \left[1 - \frac{h_e}{h_e + 1} \right] \dot{\gamma}_0 \left| \overline{M}^{(\alpha)} \right| \left| \frac{\overline{M}^{(\alpha)}}{q_{\text{cp}}} \right|^{h_e} \geq 0 \tag{3.104c}
$$

since $\dot{\gamma}_0 > 0$ and $h_e > 0$, hold.

Remark 3.5 (Simplified rate equation for the plastic slip) *The simplified version of the rate equation* (3.103)

$$
\dot{\kappa}_{\text{cp}} = \sum_{\alpha=1}^{n_\alpha} \left| \dot{\gamma}^{(\alpha)} \right| \tag{3.105}
$$

that was proposed in [134], may violate the dissipation inequality (3.94a), *as*

$$
\mathcal{D}^{\text{red}} = \sum_{\alpha=1}^{n_\alpha} \overline{M}^{(\alpha)} \, \dot{\gamma}^{(\alpha)} + q_{\text{cp}} \, \dot{\kappa}_{\text{cp}} = \sum_{\alpha=1}^{n_\alpha} \overline{M}^{(\alpha)} \, \dot{\gamma}^{(\alpha)} + \sum_{\alpha=1}^{n_\alpha} q_{\text{cp}} \left| \dot{\gamma}^{(\alpha)} \right| \gtreqless 0 \quad , \tag{3.106}
$$

holds. To see this, assume a load state with $\overline{M}^{(\alpha)} > 0 \,\forall\, \alpha$ and accordingly $\dot{\gamma}^{(\alpha)} > 0 \,\forall\, \alpha$ but with $\overline{M}^{(\alpha)}$ being sufficiently small such that $\overline{M}^{(\alpha)} < |q_{\mathrm{cp}}| \,\forall\, \alpha$. In this case the dissipation is found to be negative and the dissipation inequality is violated. Note that it is always possible to generate a load state with $\overline{M}^{(\alpha)} > 0 \,\forall\, \alpha$ by changing the definition of the positive slip direction in the definition of the slip systems.

3.3.2.2 A specific gradient crystal (visco-)plasticity model

For the gradient crystal (visco-)plasticity model, the gradient energy contribution (3.59) that was proposed in Section 3.2.2.3 is added to (3.95) so that the gradient-enhanced free energy density function reads

$$\widetilde{W}^{\mathrm{cp}}\left(\boldsymbol{F}, \boldsymbol{F}_{\mathrm{p}}, \boldsymbol{D}, \widetilde{\kappa}_{\mathrm{cp}}\right) = \widetilde{W}^{\mathrm{cp,e}}\left(\boldsymbol{F}, \boldsymbol{F}_{\mathrm{p}}\right) + \widetilde{W}^{\mathrm{cp,p}}\left(\widetilde{\kappa}_{\mathrm{cp}}\right) + \widetilde{W}^{\mathrm{g}}\left(\boldsymbol{D}\right) \quad . \tag{3.107}$$

With the exception of renaming parameter κ_{cp} to $\widetilde{\kappa}_{\mathrm{cp}}$, the energy contributions $\widetilde{W}^{\mathrm{cp,e}}$ and $\widetilde{W}^{\mathrm{cp,p}}$ remain identical with their counterparts of the reference formulation, see (3.39) and (3.96), such that the stresses (3.44)-(3.45) remain unchanged and (3.97) results in

$$\widetilde{q}_{\mathrm{cp}} = -\left[\tau_0 + [\tau_\infty - \tau_0]\tanh\left(\frac{h_0\,\widetilde{\kappa}_{\mathrm{cp}}}{\tau_\infty - \tau_0}\right)\right] < 0 \quad . \tag{3.108}$$

Moreover, evaluation of (3.18) for the energy function (3.107) yields the specific form of the energetic dual to the dislocation density tensor (3.60) that was discussed in detail in Section 3.2.2.3.

In Section 3.3.1, the energetic duality between the projected generalised Mandel stress $\widetilde{\overline{M}}^{(\alpha)}$ and the slip rates $\dot{\widetilde{\gamma}}^{(\alpha)}$ was shown. Based on this observation, we propose to formulate the plastic potential

$$\widetilde{\Phi}^{\mathrm{cp}} = \sum_{\alpha=1}^{\mathrm{n}_\alpha} \widetilde{\Phi}^{(\alpha)} \quad , \tag{3.109}$$

or rather the contribution of each slip system to the latter, based on the projected generalised Mandel stress $\widetilde{\overline{M}}^{(\alpha)}$, i.e.

$$\widetilde{\Phi}^{(\alpha)} = -\dot{\gamma}_0 \frac{\widetilde{q}_{\mathrm{cp}}}{h_e + 1} \left|\frac{\widetilde{\overline{M}}^{(\alpha)}}{\widetilde{q}_{\mathrm{cp}}}\right|^{h_e + 1} \tag{3.110}$$

and define the energetic duals as

$$\dot{\widetilde{\gamma}}^{(\alpha)} = \frac{\partial \widetilde{\Phi}^{cp}}{\partial \widetilde{\overline{M}}^{(\alpha)}} \quad , \qquad (3.111) \qquad \dot{\widetilde{\kappa}}_{cp} = \frac{\partial \widetilde{\Phi}^{cp}}{\partial \widetilde{q}_{cp}} \quad , \qquad (3.112)$$

in accordance with (3.98)-(3.101). Evaluating (3.111) and (3.112) for the plastic potential (3.110) eventually yields the specific rate equations

$$\dot{\widetilde{\gamma}}^{(\alpha)} = \dot{\gamma}_0 \, \mathrm{sgn}\left(\widetilde{\overline{M}}^{(\alpha)}\right) \left|\frac{\widetilde{\overline{M}}^{(\alpha)}}{q_{cp}}\right|^{h_e} \qquad (3.113)$$

and

$$\dot{\widetilde{\kappa}}_{cp} = -\frac{h_e}{h_e + 1} \sum_{\alpha=1}^{n_\alpha} \frac{\dot{\widetilde{\gamma}}^{(\alpha)} \, \widetilde{\overline{M}}^{(\alpha)}}{\widetilde{q}_{cp}} \quad , \qquad (3.114)$$

similar to (3.102) and (3.103). Following the same procedure as for the reference formulation, inserting (3.113) and (3.114) in (3.91) yields the specific reduced form of the dissipation power

$$\widetilde{\mathcal{D}}^{red} = \sum_{\alpha=1}^{n_\alpha} \widetilde{\overline{M}}^{(\alpha)} \, \dot{\widetilde{\gamma}}^{(\alpha)} + \widetilde{q}_{cp} \, \dot{\widetilde{\kappa}}_{cp} \qquad (3.115a)$$

$$= \sum_{\alpha=1}^{n_\alpha} \left[1 - \frac{h_e}{h_e + 1} \right] \dot{\gamma}_0 \left|\widetilde{\overline{M}}^{(\alpha)}\right| \left|\frac{\widetilde{\overline{M}}^{(\alpha)}}{\widetilde{q}_{cp}}\right|^{h_e} \geq 0 \quad , \qquad (3.115b)$$

where, $\dot{\gamma}_0 > 0$ and $h_e > 0$ has once more been assumed.

Overall two main differences between the reference crystal plasticity formulation and the gradient crystal plasticity formulation exist: firstly, the introduction of the energy contribution (3.59) manifests itself in the action of the energetic dual to the dislocation density tensor $\boldsymbol{\Xi}$ in the balance equation (3.24). Secondly, the rate equations for the plastic slip (3.113) and for the accumulated plastic strain-like variable (3.114) are formulated with respect to the generalised Mandel stress tensor $\widetilde{\overline{\boldsymbol{M}}}$ motivated by energetic dualities. In fact, the gradient formulation reduces to the reference formulation for an inactive gradient energy contribution.

3.3.3 Numerics and finite element formulation

This section focuses on the finite element implementation of the gradient crystal (visco-) plasticity theory presented in Section 3.3.2.2 and on the system of evolution equations which needs to be solved at integration point level.

3.3.3.1 Field equations

The system of balance equations which describes the motion of the body under consideration consists of the balance equation of linear momentum

$$\nabla_{\boldsymbol{X}} \cdot \boldsymbol{P} = \boldsymbol{0} \quad \text{in } \mathcal{B}_0, \tag{3.116}$$

which is complemented by suitable boundary conditions in terms of placements $\bar{\boldsymbol{\varphi}}$ and tractions $\bar{\boldsymbol{t}}$ on mutually disjoint parts of the boundary such that

$$\boldsymbol{P} \cdot \boldsymbol{N} = \bar{\boldsymbol{t}} \quad \text{on } \partial\mathcal{B}_0^t, \quad \boldsymbol{\varphi} = \bar{\boldsymbol{\varphi}} \quad \text{on } \partial\mathcal{B}_0^\varphi, \quad \partial\mathcal{B}_0^t \cup \partial\mathcal{B}_0^\varphi = \partial\mathcal{B}_0, \quad \partial\mathcal{B}_0^t \cap \partial\mathcal{B}_0^\varphi = \emptyset \tag{3.117}$$

hold in the classic sense. In addition, by introducing the relative Mandel stress tensor

$$\widetilde{\overline{\boldsymbol{M}}}^{\text{rel}} = \widetilde{\overline{\boldsymbol{M}}} - \overline{\boldsymbol{M}} \tag{3.118}$$

the balance equation (3.24) will be taken into account in a modified form, namely

$$\widetilde{\overline{\boldsymbol{M}}}^{\text{rel}} - \text{Curl}^{\text{t}}\left(\boldsymbol{\Xi}\right) \cdot \boldsymbol{F}_{\text{p}}^{\text{t}} = \boldsymbol{0} \quad \text{in} \quad \mathcal{B}_0 \tag{3.119}$$

subject to the non-ambiguous constitutive boundary condition

$$\boldsymbol{\Xi} \cdot \text{Spn}\left(\boldsymbol{N}\right) \cdot \boldsymbol{F}_{\text{p}}^{\text{t}} = \boldsymbol{0} \quad \text{on } \partial\mathcal{B}_0 \quad , \tag{3.120}$$

derived in Section 3.1.2. The introduction of $\widetilde{\overline{\boldsymbol{M}}}^{\text{rel}}$ has the advantage that the principle structure of the numerical scheme at the quadrature point level can be maintained. Moreover, $\widetilde{\overline{\boldsymbol{M}}}^{\text{rel}}$ will be regarded as a primary field variable and discretised by means of C^0-continuous functions such that $\widetilde{\overline{\boldsymbol{M}}}$ is composed of a continuous part given by $\widetilde{\overline{\boldsymbol{M}}}^{\text{rel}}$ and of a part which may exhibit discontinuities, i.e. $\overline{\boldsymbol{M}}$, if a standard C^0-continuous approximation is chosen for the placement field.

3.3.3.2 Weak form of field equations

Multiplication of (3.116) and (3.119) with test functions $\boldsymbol{\eta}^{\varphi}$ and $\boldsymbol{\eta}^{\widetilde{\overline{\boldsymbol{M}}}^{\text{rel}}}$, integration over the domain $\mathcal{B}_0$ and application of Gauss's theorem results in the weak form of the balance equation of linear momentum

$$0 = \int_{\mathcal{B}_0} \nabla_{\boldsymbol{X}} \boldsymbol{\eta}^{\varphi} : \boldsymbol{P} \, \mathrm{d}V - \int_{\partial\mathcal{B}_0} \boldsymbol{\eta}^{\varphi} \cdot \boldsymbol{P} \cdot \boldsymbol{N} \, \mathrm{d}A \tag{3.121}$$

and in the weak form of the balance equation for the relative stress

$$0 = \int_{\mathcal{B}_0} \boldsymbol{\eta}^{\widetilde{\overline{\boldsymbol{M}}}^{\mathrm{rel}}} : \widetilde{\overline{\boldsymbol{M}}}^{\mathrm{rel}} - \boldsymbol{\Xi} : \mathrm{Curl}^{\mathrm{t}} \left(\boldsymbol{\eta}^{\widetilde{\overline{\boldsymbol{M}}}^{\mathrm{rel}}} \cdot \boldsymbol{F}_{\mathrm{p}} \right) \mathrm{d}V$$
$$+ \int_{\partial \mathcal{B}_0} \left[\boldsymbol{\Xi} \cdot \mathrm{Spn}\left(\boldsymbol{N}\right) \cdot \boldsymbol{F}_{\mathrm{p}}^{\mathrm{t}} \right] : \boldsymbol{\eta}^{\widetilde{\overline{\boldsymbol{M}}}^{\mathrm{rel}}} \mathrm{d}A \quad . \tag{3.122}$$

For the approximation of the spatial derivative of $\boldsymbol{F}_{\mathrm{p}}$ we additionally introduce the field variable $\boldsymbol{\Theta}_{\mathrm{p}}$ that is coupled to $\boldsymbol{F}_{\mathrm{p}}$ in terms of an L_2-projection, namely

$$0 = \int_{\mathcal{B}_0} \boldsymbol{\eta}^{\boldsymbol{\Theta}_{\mathrm{p}}} : [\boldsymbol{F}_{\mathrm{p}} - \boldsymbol{\Theta}_{\mathrm{p}}] \mathrm{d}V \quad , \tag{3.123}$$

with $\boldsymbol{\eta}^{\boldsymbol{\Theta}_{\mathrm{p}}}$ denoting the corresponding test function.

In the following, $\boldsymbol{\varphi}$, $\widetilde{\overline{\boldsymbol{M}}}^{\mathrm{rel}}$ and $\boldsymbol{\Theta}_{\mathrm{p}}$ will be regarded as the primary fields to be solved for and discretised using polynomial approximations according to

$$\boldsymbol{\varphi}^{\mathrm{h}} = \sum_{A=1}^{\mathrm{n}_{\mathrm{en},\boldsymbol{\varphi}}} N_A^{\boldsymbol{\varphi}} \, \boldsymbol{\varphi}_A \tag{3.124a} \qquad \boldsymbol{\eta}^{\boldsymbol{\varphi}\,\mathrm{h}} = \sum_{D=1}^{\mathrm{n}_{\mathrm{en},\boldsymbol{\varphi}}} N_D^{\boldsymbol{\varphi}} \, \boldsymbol{\eta}_D^{\boldsymbol{\varphi}} \tag{3.124b}$$

$$\widetilde{\overline{\boldsymbol{M}}}^{\mathrm{rel}\,\mathrm{h}} = \sum_{B=1}^{\mathrm{n}_{\mathrm{en},\widetilde{\overline{\boldsymbol{M}}}^{\mathrm{rel}}}} N_B^{\widetilde{\overline{\boldsymbol{M}}}^{\mathrm{rel}}} \, \widetilde{\overline{\boldsymbol{M}}}_B^{\mathrm{rel}} \tag{3.124c} \qquad \boldsymbol{\eta}^{\widetilde{\overline{\boldsymbol{M}}}^{\mathrm{rel}}\,\mathrm{h}} = \sum_{E=1}^{\mathrm{n}_{\mathrm{en},\widetilde{\overline{\boldsymbol{M}}}^{\mathrm{rel}}}} N_E^{\widetilde{\overline{\boldsymbol{M}}}^{\mathrm{rel}}} \, \boldsymbol{\eta}_E^{\widetilde{\overline{\boldsymbol{M}}}^{\mathrm{rel}}} \tag{3.124d}$$

$$\boldsymbol{\Theta}_{\mathrm{p}}^{\mathrm{h}} = \sum_{C=1}^{\mathrm{n}_{\mathrm{en},\boldsymbol{\Theta}_{\mathrm{p}}}} N_C^{\boldsymbol{\Theta}_{\mathrm{p}}} \, \boldsymbol{\Theta}_{\mathrm{p}C} \tag{3.124e} \qquad \boldsymbol{\eta}^{\widetilde{\overline{\boldsymbol{M}}}\,\mathrm{h}} = \sum_{F=1}^{\mathrm{n}_{\mathrm{en},\boldsymbol{\Theta}_{\mathrm{p}}}} N_F^{\boldsymbol{\Theta}_{\mathrm{p}}} \, \boldsymbol{\eta}_F^{\boldsymbol{\Theta}_{\mathrm{p}}} \tag{3.124f}$$

In analogy with the derivations presented in Section 3.2.3.3 the vector of internal forces that corresponds to the balance equation of linear momentum, (3.121), is defined as

$$\boldsymbol{f}_{\mathrm{int}}^{\boldsymbol{\varphi}\mathrm{h}} = \mathop{\mathbf{A}}_{e=1}^{\mathrm{n}_{\mathrm{el}}} \int_{\mathcal{B}_0^e} \boldsymbol{P} \cdot \nabla_{\boldsymbol{X}} N_D^{\boldsymbol{\varphi}} \, \mathrm{d}V_e \quad , \tag{3.125}$$

the generalised vector of internal forces corresponding to the balance equation of the relative Mandel stress, (3.122), as

$$\boldsymbol{f}_{\mathrm{int}}^{\widetilde{\overline{\boldsymbol{M}}}^{\mathrm{rel}}\,\mathrm{h}} = \mathop{\mathbf{A}}_{e=1}^{\mathrm{n}_{\mathrm{el}}} \int_{\mathcal{B}_0^e} N_E^{\widetilde{\overline{\boldsymbol{M}}}^{\mathrm{rel}}} \, \widetilde{\overline{\boldsymbol{M}}}^{\mathrm{rel}} + \boldsymbol{\Xi} \cdot \left[N_E^{\widetilde{\overline{\boldsymbol{M}}}^{\mathrm{rel}}} \, \nabla_{\boldsymbol{X}} \boldsymbol{\Theta}_{\mathrm{p}} : \boldsymbol{\epsilon}_0 - \boldsymbol{F}_{\mathrm{p}} \cdot \boldsymbol{\epsilon}_0 \cdot \nabla_{\boldsymbol{X}} N_E^{\widetilde{\overline{\boldsymbol{M}}}^{\mathrm{rel}}} \right]^{\mathrm{t}} \mathrm{d}V_e \quad , \tag{3.126}$$

and the one corresponding to (3.123) as

$$
\boldsymbol{f}_{\text{int}}^{\boldsymbol{\Theta}_\mathrm{p}\mathrm{h}} = \overset{n_{\text{el}}}{\underset{e=1}{\mathbf{A}}} \int_{\mathcal{B}_0^e} N_F^{\boldsymbol{\Theta}_\mathrm{p}} \left[\boldsymbol{F}_\mathrm{p} - \boldsymbol{\Theta}_\mathrm{p} \right] \mathrm{d}V_e \quad .
\tag{3.127}
$$

The consistent algorithmic tangent stiffness matrix that is required for a gradient-based solution of the discrete system (3.125)-(3.127) is provided in Appendix B.2.

3.3.3.3 Discrete system of evolution equations

Strategies to deal with the stiff systems that occur when the rate-independent limit is approached in crystal (visco-)plasticity will be presented in this section with reference to [134]. At each quadrature point, an update needs to be carried out of the stress state in terms of $\boldsymbol{P}$, respectively of $\overline{\boldsymbol{M}}$, of the energetic dual to the dislocation density tensor $\boldsymbol{\Xi}$ and of the internal variables that characterise the plastic deformation, i.e. of $\boldsymbol{F}_\mathrm{p}$ and of the accumulated plastic slip κ_{cp}. To this end, the material state at time t_n is assumed to be known and characterised by the internal variables $\boldsymbol{F}_\mathrm{p}^n$, $\widetilde{\kappa}_{\text{cp}}^n$. Advancing a time increment Δt to the next discrete point in time, t_{n+1}, the set of evolution equations (3.84), (3.113), (3.114) is discretised and evaluated by making use of the constitutive relations (3.44), (3.45), (3.60), (3.108). Although the derivations to be presented in the following will focus on the gradient crystal (visco-)plasticity formulation, the outlined algorithmic structure remains the same for the reference formulation with $\widetilde{\overline{\boldsymbol{M}}}^{\text{rel}}$ being zero in this case. Moreover, superscripts referring to time t_{n+1} are omitted in the derivations for the sake of clarity.

In the spirit of an incremental description, the rate equation for the plastic slip on each slip system, (3.113), is discretised by means of an implicit Euler scheme, resulting in

$$
\Delta\widetilde{\gamma}^{(\alpha)} = \Delta\gamma_0 \, \mathrm{sgn}\left(\widetilde{\overline{M}}^{(\alpha)} \right) \left| \frac{\widetilde{\overline{M}}^{(\alpha)}}{\widetilde{q}_{\text{cp}}} \right|^{h_e} \quad ,
\tag{3.128}
$$

with $\Delta\gamma_0 = \dot{\gamma}_0 \, \Delta t$ and the increments in plastic slip variables $\Delta\widetilde{\gamma}^{(\alpha)}$. By once more applying an implicit Euler scheme to discretise (3.114), by inserting (3.113) and using (3.128) one arrives at

$$
\Delta\widetilde{\kappa}_{\text{cp}} = -\frac{h_e}{h_e + 1} \sum_{\alpha=1}^{n_\alpha} \frac{\Delta\widetilde{\gamma}^{(\alpha)} \, \widetilde{\overline{M}}^{(\alpha)}}{\widetilde{q}_{\text{cp}}} \quad .
\tag{3.129}
$$

To evaluate the stresses on the right-hand side of (3.128) and (3.129), with $\boldsymbol{F}$ assumed to be given, the plastic part of the deformation gradient is updated by means of the generalised midpoint rule

$$\boldsymbol{F}_{\mathrm{p}} = [\boldsymbol{I} - \Theta\,\boldsymbol{\Lambda}_{\mathrm{p}}]^{-1} \cdot [\boldsymbol{I} + [1-\Theta]\,\boldsymbol{\Lambda}_{\mathrm{p}}] \cdot \boldsymbol{F}_{\mathrm{p}}^{n} \tag{3.130}$$

that results from the approximation of the exponential map discretisation of (3.84), as proposed in [134], with the incremental projection tensor

$$\boldsymbol{\Lambda}_{\mathrm{p}} = \sum_{\alpha=1}^{\mathrm{n}_{\alpha}} \Delta\widetilde{\gamma}^{(\alpha)}\,\overline{\boldsymbol{Z}}^{(\alpha)} \tag{3.131}$$

and the parameter Θ that controls the integrator. In this contribution $\Theta = 1/2$ will be used which yields the second-order accurate midpoint rule. The update in $\boldsymbol{F}_{\mathrm{p}}$ can hence be parametrised in terms of the increments in the plastic slip variables $\Delta\widetilde{\gamma}^{(\alpha)}$, while the discrete update of the energetic dual to $\widetilde{\kappa}_{\mathrm{cp}}$, cf. (3.108),

$$\widetilde{q}_{\mathrm{cp}} = -\left[\tau_0 + [\tau_\infty - \tau_0]\tanh\left(\frac{h_0\,[\widetilde{\kappa}_{\mathrm{cp}}^{n} + \Delta\widetilde{\kappa}_{\mathrm{cp}}]}{\tau_\infty - \tau_0}\right)\right] \tag{3.132}$$

is defined in terms of the increment in the accumulated plastic slip-like variable $\Delta\widetilde{\kappa}_{\mathrm{cp}}$.

Based on this observation, the discrete system of evolution equations is formulated in and solved for $\Delta\widetilde{\gamma}^{(\alpha)}$ and $\Delta\widetilde{\kappa}_{\mathrm{cp}}$. As elaborated in detail in [134] for a simplified, non-gradient-enhanced case, approaching the rate-independent limit by increasing h_e, the slightest overshoot in $\widetilde{\overline{M}}^{(\alpha)}$ compared with $\widetilde{q}_{\mathrm{cp}}$ prevents (3.128) from being evaluated. To deal with this difficulty it is proposed to reformulate the residual if $\widetilde{\overline{M}}^{(\alpha)} > \widetilde{q}_{\mathrm{cp}}$ as

$$R_{\Delta\widetilde{\gamma}^{(\alpha)}}^{>}\left(\Delta\widetilde{\gamma}^{(1)},\ldots,\Delta\widetilde{\gamma}^{(\mathrm{n}_\alpha)},\Delta\widetilde{\kappa}_{\mathrm{cp}};\boldsymbol{F},\boldsymbol{F}_{\mathrm{p}}^{n},\widetilde{\kappa}_{\mathrm{cp}}^{n}\right) = -\sqrt[h_e]{\frac{\Delta\widetilde{\gamma}^{(\alpha)}}{\Delta\gamma_0\,\mathrm{sgn}\left(\widetilde{\overline{M}}^{(\alpha)}\right)}} + \left|\frac{\widetilde{\overline{M}}^{(\alpha)}}{\widetilde{q}_{\mathrm{cp}}}\right|. \tag{3.133}$$

However, for $\Delta\widetilde{\gamma}^{(\alpha)} \to 0$ the derivative of $R_{\Delta\widetilde{\gamma}^{(\alpha)}}^{>}$ with respect to $\Delta\widetilde{\gamma}^{(\alpha)}$ that needs to be evaluated if a gradient-based solver is used, becomes infinite and requires the residual to be reformulated, again, with

$$R_{\Delta\widetilde{\gamma}^{(\alpha)}}^{<}\left(\Delta\widetilde{\gamma}^{(1)},\ldots,\Delta\widetilde{\gamma}^{(\mathrm{n}_\alpha)},\Delta\widetilde{\kappa}_{\mathrm{cp}};\boldsymbol{F},\boldsymbol{F}_{\mathrm{p}}^{n},\widetilde{\kappa}_{\mathrm{cp}}^{n}\right) = -\Delta\widetilde{\gamma}^{(\alpha)} + \Delta\gamma_0\,\mathrm{sgn}\left(\widetilde{\overline{M}}^{(\alpha)}\right)\left|\frac{\widetilde{\overline{M}}^{(\alpha)}}{\widetilde{q}_{\mathrm{cp}}}\right|^{h_e} \tag{3.134}$$

representing a natural choice. Moreover, the residual which corresponds to the discrete evolution equation (3.129) is given by

$$R_{\Delta\widetilde{\kappa}_{\mathrm{cp}}}\left(\Delta\widetilde{\gamma}^{(1)},\ldots,\Delta\widetilde{\gamma}^{(\mathrm{n}_\alpha)},\Delta\widetilde{\kappa}_{\mathrm{cp}};\boldsymbol{F},\boldsymbol{F}_{\mathrm{p}}^{n},\widetilde{\kappa}_{\mathrm{cp}}^{n}\right) = -\Delta\widetilde{\kappa}_{\mathrm{cp}} - \frac{h_e}{h_e+1}\sum_{\alpha=1}^{\mathrm{n}_\alpha}\frac{\Delta\widetilde{\gamma}^{(\alpha)}\,\widetilde{\overline{M}}^{(\alpha)}}{\widetilde{q}_{\mathrm{cp}}}\;. \quad (3.135)$$

The initial values of the plastic slip increments $\Delta\widetilde{\gamma}_{\mathrm{init}}^{(\alpha)}$ are calculated on the basis of a trial stress state $\widetilde{\overline{M}}_{\mathrm{trial}}^{(\alpha)} = \widetilde{\overline{M}}^{(\alpha)}\left(\boldsymbol{F},\boldsymbol{F}_{\mathrm{p}}^{n}\right)$ as $\Delta\widetilde{\gamma}_{\mathrm{init}}^{(\alpha)} = \Delta\gamma_0\,\mathrm{sgn}\left(\widetilde{\overline{M}}_{\mathrm{trial}}^{(\alpha)}\right)$ and a line-search is used on the set of iteration variables $\left\{\Delta\widetilde{\gamma}^{(1)},\ldots,\Delta\widetilde{\gamma}^{(\mathrm{n}_\alpha)},\Delta\widetilde{\kappa}_{\mathrm{cp}}\right\}$ if the constraint $\mathrm{sgn}\left(\Delta\widetilde{\gamma}^{(\alpha)}\right) = \mathrm{sgn}\left(\widetilde{\overline{M}}^{(\alpha)}\right)\forall\alpha$ is violated. If no convergence is achieved with this procedure, an augmented Lagrangian-type method is invoked, where the rate sensitivity parameter is slowly increased to its maximum value, analogous to the simplified model presented in [134]. Since $\boldsymbol{\Theta}_{\mathrm{p}}$ was introduced as a primary field variable, $\mathrm{Curl}^{\mathrm{t}}\left(\boldsymbol{\Theta}_{\mathrm{p}}\right)$ is known at quadrature point level so that the update of $\boldsymbol{\Xi}$ reduces to the evaluation of (3.60). The derivatives of the residual functions $R_{\Delta\widetilde{\gamma}^{(\alpha)}}^{>}$, $R_{\Delta\widetilde{\gamma}^{(\alpha)}}^{<}$ and $R_{\Delta\widetilde{\kappa}_{\mathrm{cp}}}$ with respect to the primary variables $\Delta\widetilde{\gamma}^{(\alpha)}$ and $\Delta\widetilde{\kappa}_{\mathrm{cp}}$ which are required for a gradient-based solution scheme are finally provided in Appendix B.3.

3.3.4 Representative simulation results

This section focuses on the analysis of representative boundary value problems in two- and three-dimensional settings. In order to validate the model, homogeneous simple shear deformation tests on a fictitious single crystal with two slip systems according to the planar double slip problem discussed in [134] are presented first, and extended to the case of an fcc crystal structure in a second step in Section 3.3.4.1. Focusing on finite element-based simulation results in a two-dimensional setting, the localised finite plastic deformation of a notched plate will be analysed in detail in Section 3.3.4.2. Proceeding to the three-dimensional case, experimentally motivated torsion tests on micro wires are presented in Section 3.3.4.3 and compared with the experimental findings documented in [48].

3.3.4.1 Simple shear deformation test

This section deals with the simulation of (homogeneous) simple shear deformation tests in order to 1) validate the model via a brief comparison with the results presented in [134] and to 2) show that the constitutive response is to a good approximation rate-independent for the chosen set of material parameters. Since the deformation state to be analysed is homogeneous, no finite element simulations are required and the problem reduces to the evaluation of constitutive relations at the material point level. The
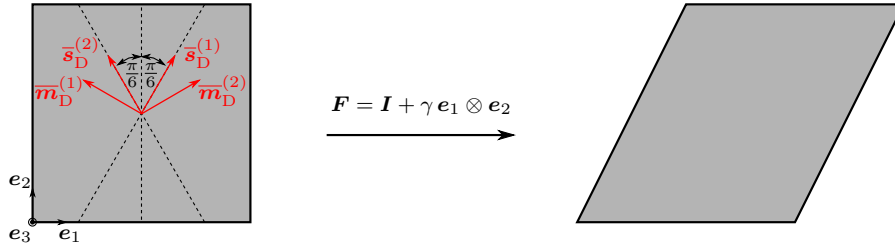
Figure 3.19: Fictitious crystal featuring two slip systems in simple shear deformation.

material parameters used in the simulations are summarised in Table 3.6 and are chosen in accordance with [134].

We first focus on the planar double slip problem sketched in Figure 3.19. This problem studies the simple shear deformation of a fictitious crystal featuring two slip systems with the slip planes being oriented at $\pm 30°$ relative to the $\boldsymbol{e}_2$-axis. The (single) crystal is subjected to a simple shear deformation state, namely,

$$\boldsymbol{F} = \boldsymbol{I} + \gamma\,\boldsymbol{e}_1 \otimes \boldsymbol{e}_2 \quad , \tag{3.136}$$

with the parameter γ that controls the shear deformation being linearly increased from 0.0 to 5.0. The deformation is applied within the course of $t_{\mathrm{L}} = 10\,\mathrm{s}$, respectively $t_{\mathrm{L}} = 100\,\mathrm{s}$, and $n_{\mathrm{L}} = 10$, $n_{\mathrm{L}} = 100$ or $n_{\mathrm{L}} = 1000$ loadsteps are used for the discretisation in time. The 11-, 12- and the 22-coefficients of the Kirchhoff stress tensor as a function of the applied deformation are provided in Figure 3.20. It can be seen that a discretisation with only $n_{\mathrm{L}} = 10$ time steps is too coarse to accurately reproduce the stress-strain curves. On the other hand, the difference between a discretisation with $n_{\mathrm{L}} = 100$ and $n_{\mathrm{L}} = 1000$ time steps is nearly negligible. Moreover, comparing the constitutive responses for $t_{\mathrm{L}} = 10\,\mathrm{s}$, Figures 3.20(a,c,e), with those corresponding to $t_{\mathrm{L}} = 100\,\mathrm{s}$, Figures 3.20(b,d,f), one observes that the material response is, to a good approximation, rate-independent. At this point, we do not further focus in more detail on the interpretation of the stress-strain curves. Rather, we would like to point out that the stress-strain curves shown in Figure 3.20 compare well with those provided in [134], especially when taking into account that the models are based on different (elastic) free energy density functions, which to some extent validates the implementation.

Extending the model, the crystallographic structure of face-centred cubic metals is taken into account. The respective slip systems are sketched in Figure 3.18 and detailed information on each slip system is provided in Table 3.5. For the simple shear test to be simulated, it is assumed that the crystallographic axes in Figure 3.18 are aligned with the coordinate system in Figure 3.19. In accordance with the planar double slip simulations, the influence of the duration of the experiment and of the time discretisation on the stress-strain curves is studied. Regarding Figure 3.21, a more complex stress-strain response compared with the double slip problem is revealed. However, the same tendencies are observable in the sense that a time discretisation with $n_{\mathrm{L}} = 10$ time steps

Table 3.6: Material parameters for the gradient crystal plasticity model in accordance with [134].

λ	μ	τ_0	τ_∞	$\dot{\gamma}_0$	h_0	h_e	$H_{\boldsymbol{D}}$
35.1 GPa	23.4 GPa	60 MPa	110 MPa	0.001 s^{-1}	540	200	$1.0 - 5.0\,\mathrm{GPa\,mm}^2$

is too coarse to accurately reproduce the stress-strain curves and that the constitutive response is, to a good approximation, rate-independent for the chosen set of material parameters.

3.3.4.2 Notched plate in a two-dimensional setting

In order to study the gradient energy contribution (3.59), inhomogeneous boundary value problems in a two-dimensional setting are analysed in this section. Being more specific, the focus lies on the plate with two round notches as depicted in Figure 3.22. The displacements of the centre nodes on the left and on the right boundary are fixed in vertical direction. In horizontal direction, homogeneous Dirichlet boundary conditions are assumed at the left boundary, and the displacement of the right boundary nodes is linearly increased to 6 mm within the course of $t_{\mathrm{L}} = 120\,\mathrm{s}$. An adaptive time-stepping scheme was used with a maximum allowed time step of 1 s for the reference and of 0.5 s for the gradient crystal (visco-)plasticity formulation. Moreover, the set of material parameters provided in Table 3.6 is used and an fcc crystallografic structure as defined in Table 3.5 is assumed, with the crystallographic axes being aligned with the $\boldsymbol{e}_1$-, $\boldsymbol{e}_2$- and $\boldsymbol{e}_3$-direction in the simulations as defined in Figure 3.22.

The model problem will be analysed by means of the reference crystal (visco-)plasticity formulation which is based on standard eight-node serendipity-type elements for the discretisation of the placement field, and by means of the gradient crystal (visco-)plasticity formulation for which a mixed-type element formulation is used. Specifically speaking, eight-node serendipity-type elements are used for the discretisation of the placement field and linear Lagrangian elements are used for the discretisation of the $\boldsymbol{\Theta}_{\mathrm{p}}$- and of the $\widetilde{\overline{\boldsymbol{M}}}^{\mathrm{rel}}$-field. For these element formulations, discretisations with 1200, 2352 and 4800 elements will be taken into account.

Focusing on the load-displacement curves depicted in Figure 3.23, one first finds that the reference formulation and a gradient crystal (visco-)plasticity formulation with $H_{\boldsymbol{D}} = 0.0\,\mathrm{GPa\,mm}^2$ both yield, within numerical tolerances, identical results. Activating the gradient contribution one observes an increase in the overall stiffness with increasing values of $H_{\boldsymbol{D}}$. The influence of the discretisation on the load displacement curves is small for all formulations.

Figure 3.24 and Figure 3.25 show the deformation of the plate and the distribution of the accumulated plastic strain-like variable κ_{cp}, respectively of $\widetilde{\kappa}_{\mathrm{cp}}$, for an applied displacement of 6 mm. For both the reference as well as for the gradient
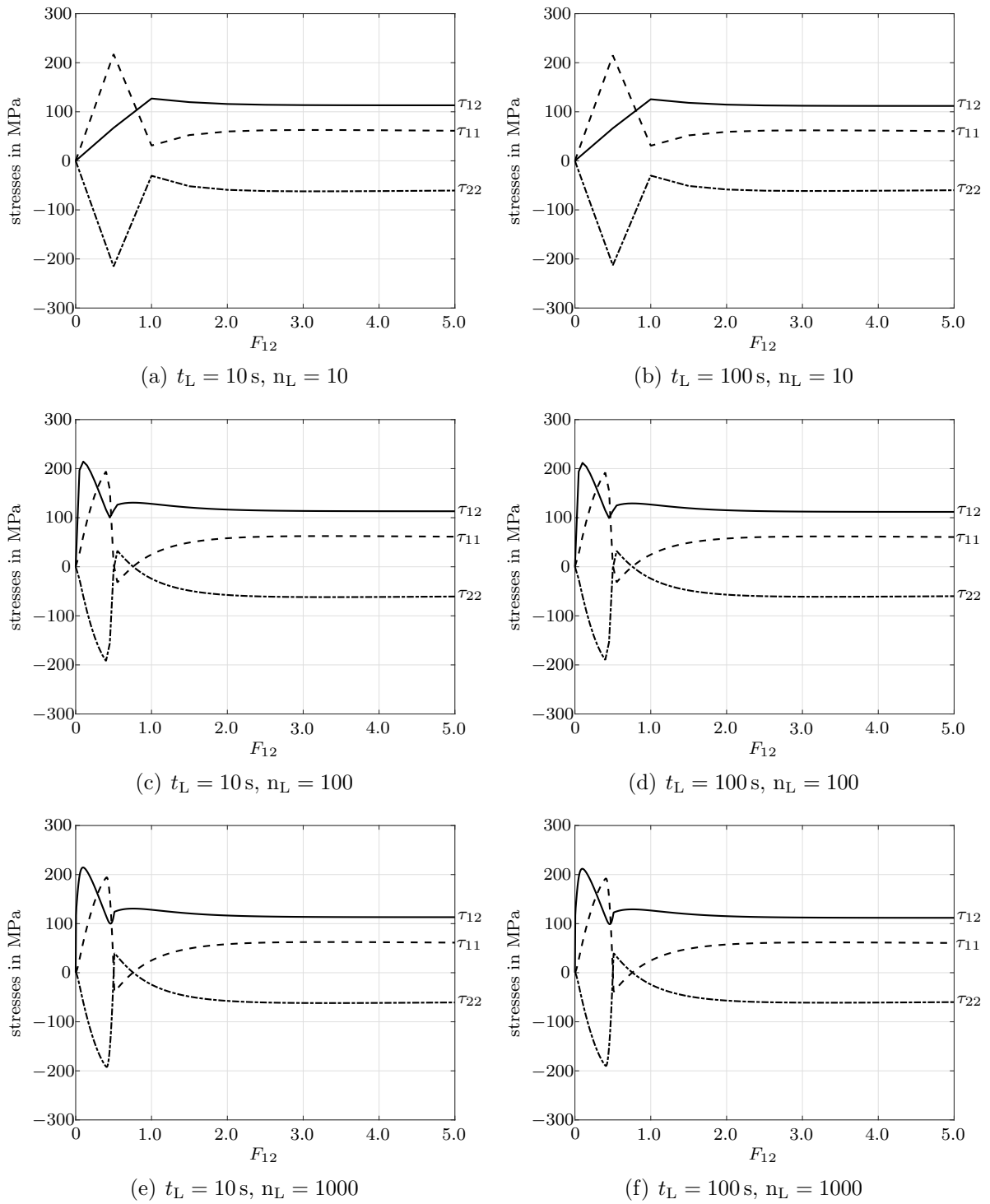
Figure 3.20: Simple shear deformation tests for planar double slip. Depicted are the coefficients of the Kirchhoff stress tensor as a function of the load which is applied in n_L equal time steps over a time interval t_L.

(a) $t_{\mathrm{L}} = 10\,\mathrm{s}$, $n_{\mathrm{L}} = 10$

(b) $t_{\mathrm{L}} = 100\,\mathrm{s}$, $n_{\mathrm{L}} = 10$

(c) $t_{\mathrm{L}} = 10\,\mathrm{s}$, $n_{\mathrm{L}} = 100$

(d) $t_{\mathrm{L}} = 100\,\mathrm{s}$, $n_{\mathrm{L}} = 100$

(e) $t_{\mathrm{L}} = 10\,\mathrm{s}$, $n_{\mathrm{L}} = 1000$

(f) $t_{\mathrm{L}} = 100\,\mathrm{s}$, $n_{\mathrm{L}} = 1000$
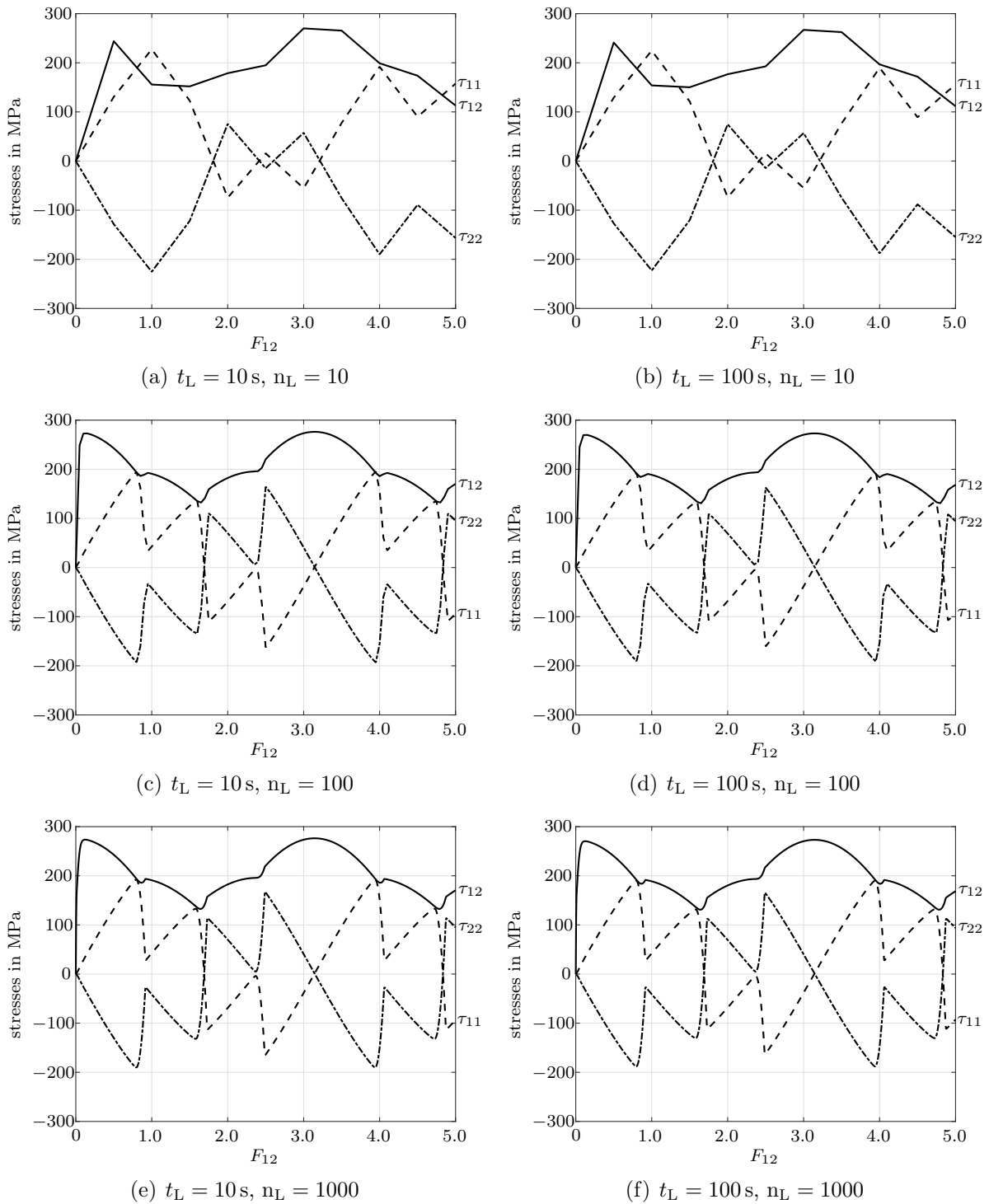
Figure 3.21: Simple shear deformation tests for fcc-single crystals with slip systems according to Table 3.5. Depicted are the coefficients of the Kirchhoff stress tensor as a function of the load which is applied in n_{L} equal time steps over a time interval t_{L}.
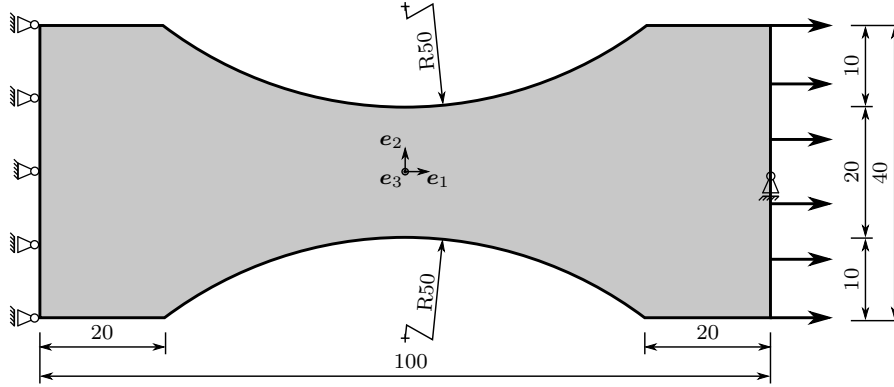
Figure 3.22: Sketch of a symmetric plate with two round notches (in mm) subjected to tensile loading.

crystal (visco-)plasticity formulation, the formation of a cross-like plastic deformation zone is observable which results in pronounced necking. We observe once more that the reference formulation and the gradient crystal (visco-)plasticity formulation with $H_{\boldsymbol{D}} = 0.0\,\mathrm{GPa\,mm}^2$ show practically identical results with a striking change in the curvature of the outer boundary near the centre of the plate, Figure 3.24. Activating the gradient energy contribution significantly influences the deformation pattern and results, for instance, in a significant reduction of the observed change in curvature near the centre of the plate, Figure 3.25. Focusing in more detail on the distribution of κ_{cp}, respectively of $\widetilde{\kappa}_{\mathrm{cp}}$, one finds that, although the principle cross-like structure is maintained in the gradient crystal (visco-)plasticity formulations, the plastic deformation zone seems to be smeared with increasing values of $H_{\boldsymbol{D}}$. This effect is in good agreement with the findings of Section 3.2. Again, we do not observe significant differences between the different discretisations.

It is important to note that the problem geometry and the boundary conditions on the placement field allow for a symmetric deformation with regard to the $\boldsymbol{e}_1$- and $\boldsymbol{e}_2$-axes. In addition, the initial orientation of the crystallographic unit cell has been chosen such that the crystallographic axes align with the $\boldsymbol{e}_1$- and $\boldsymbol{e}_2$-directions in Figure 3.22, which does not disturb the overall symmetry. Thus, symmetries with respect to both axes are observable in the deformation pattern and in the accumulated plastic strain-like variable. However, focusing on the individual slip systems, these symmetries are not maintained when the gradient energy contribution is activated as shown in Figure 3.26 and Figure 3.27. Regarding the coefficients of the projection operators $\overline{\boldsymbol{Z}}^{(1)}$, $\overline{\boldsymbol{Z}}^{(4)}$, $\overline{\boldsymbol{Z}}^{(7)}$ and $\overline{\boldsymbol{Z}}^{(10)}$, which represent the dominant slip systems, with respect to the Cartesian base vectors $\{\boldsymbol{e}_1, \boldsymbol{e}_2, \boldsymbol{e}_3\}$, namely

$$\left[\overline{\boldsymbol{Z}}^{(1)}\right]_{ij} = \begin{bmatrix} 1 & 1 & 1 \\ -1 & -1 & -1 \\ 0 & 0 & 0 \end{bmatrix} \quad (3.137\text{a}) \qquad \left[\overline{\boldsymbol{Z}}^{(4)}\right]_{ij} = \begin{bmatrix} 1 & 1 & -1 \\ -1 & -1 & 1 \\ 0 & 0 & 0 \end{bmatrix} \quad (3.137\text{b})$$

$$\left[\overline{\boldsymbol{Z}}^{(7)}\right]_{ij} = \begin{bmatrix} 1 & -1 & 1 \\ 1 & -1 & 1 \\ 0 & 0 & 0 \end{bmatrix} \quad (3.137\text{c}) \qquad \left[-\overline{\boldsymbol{Z}}^{(10)}\right]_{ij} = \begin{bmatrix} 1 & -1 & -1 \\ 1 & -1 & -1 \\ 0 & 0 & 0 \end{bmatrix} \quad (3.137\text{d})$$

one would expect all four slip systems to show the same activity, if no shear stresses in the third spatial direction occurred and if the driving force for the plastic slip, i.e. $\overline{\boldsymbol{M}}$, respectively $\widetilde{\overline{\boldsymbol{M}}}$, was symmetric. This is indeed the case for the reference formulation where $\overline{\boldsymbol{M}}$ is found to be symmetric due to the assumed elastic isotropy, cf. (3.45), and where the shear strains in $\boldsymbol{e}_3$-direction of the dominant slip systems, i.e. for $\alpha \in \{1, 4, 7, 10\}$, cancel each other out pair-wise, see also (3.137) together with (3.45) and (3.84). Thus, as is revealed in Figures 3.26(a-d) and Figures 3.27(a-d), the cross-like shape of the plastic deformation zone which has previously been observed for the accumulated plastic strain-like variable is recovered for each of the four slip systems.

In contrast, activating the gradient energy contribution the cross-like structure reduces to individual bands which are practically identical for the slip systems 1 and 4, Figures 3.26(e-h), and for the slip systems 7 and 10, Figures 3.27(e-h). Accordingly, the individual shear strain contributions in $\boldsymbol{e}_3$-direction cancel each other out, once again. However, taking a closer look at the generalised stress tensor $\widetilde{\overline{\boldsymbol{M}}}$ in (3.118), one finds that contribution $\widetilde{\overline{\boldsymbol{M}}}^{\text{rel}}$ is, in general, not symmetric for the specific form of the gradient energy contribution (3.59). Inserting (3.60) in (3.119) yields the specific (point-wise) definition of the relative stress field

$$\widetilde{\overline{\boldsymbol{M}}}^{\text{rel}} = -2\,H_{\boldsymbol{D}}\,\text{Curl}^{\text{t}}\left(\text{Curl}^{\text{t}}\left(\boldsymbol{F}_{\text{p}}\right)\right) \cdot \boldsymbol{F}_{\text{p}}^{\text{t}} \quad , \tag{3.138}$$

where $H_{\boldsymbol{D}}$ has been assumed to be constant and with the coefficient matrix of the Curl-Curl term on the right-hand side given by (3.62).

Thus, the unsymmetry in the $\widetilde{\overline{\boldsymbol{M}}}$-stress field that is induced by the gradient energy contribution seems to give rise to a different activity of the slip systems. Keeping these observations in mind, it is useful to take a closer look at the shear-coefficients of the plastic deformation gradient field which are presented in Figure 3.28. Whereas the shear activities in the $\boldsymbol{e}_1$-$\boldsymbol{e}_2$-plane (nearly) cancel each other out in the non-gradient-enhanced formulations, Figures 3.28(a-d), significant shear deformations are observable for the gradient crystal (visco-)plasticity formulations, Figures 3.28(e-h), which result from the different activity of the slip systems 1 and 7, respectively 4 and 10.
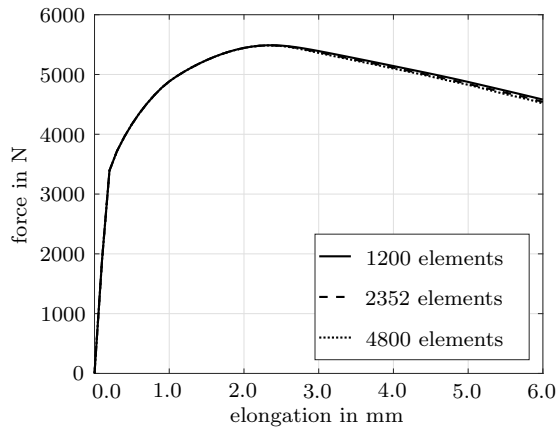
(a) reference formulation
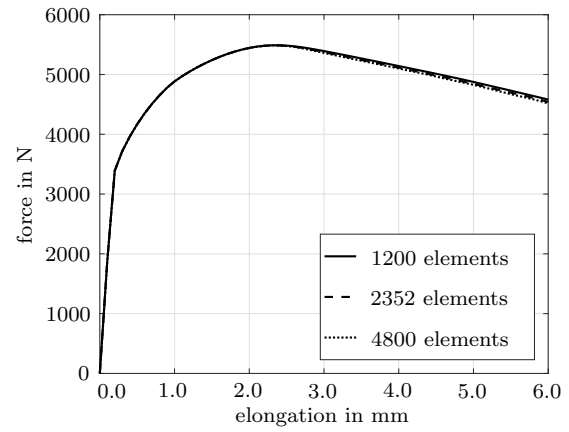
(b) gradient plasticity formulation with $H_{\boldsymbol{D}} = 0.0\,\mathrm{GPa\,mm^2}$
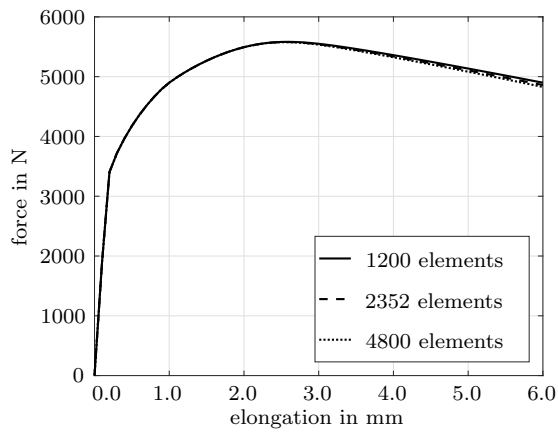
(c) gradient plasticity formulation with $H_{\boldsymbol{D}} = 1.0\,\mathrm{GPa\,mm^2}$
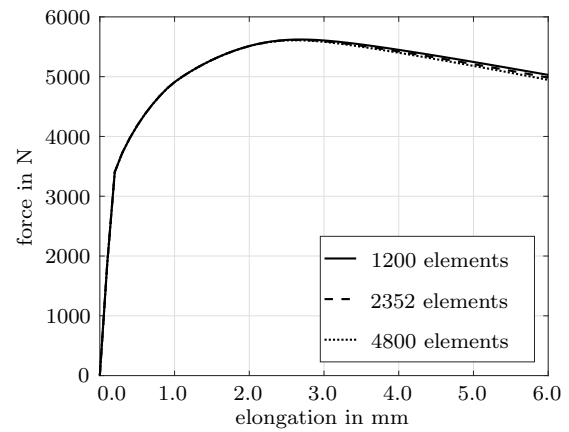
(d) gradient plasticity formulation with $H_{\boldsymbol{D}} = 5.0\,\mathrm{GPa\,mm^2}$

Figure 3.23: Load-displacement curves for the reference plasticity formulation and the multi-field gradient crystal (visco-)plasticity formulation for the plate with two round notches. The calculation of the total longitudinal reaction forces is based on a sample thickness of 1 mm.

(a) reference formulation, 1200 elements

(b) $H_D = 0.0\,\mathrm{GPa\,mm^2}$, 1200 elements

(c) reference formulation, 2352 elements

(d) $H_D = 0.0\,\mathrm{GPa\,mm^2}$, 2352 elements

(e) reference formulation, 4800 elements

(f) $H_D = 0.0\,\mathrm{GPa\,mm^2}$, 4800 elements
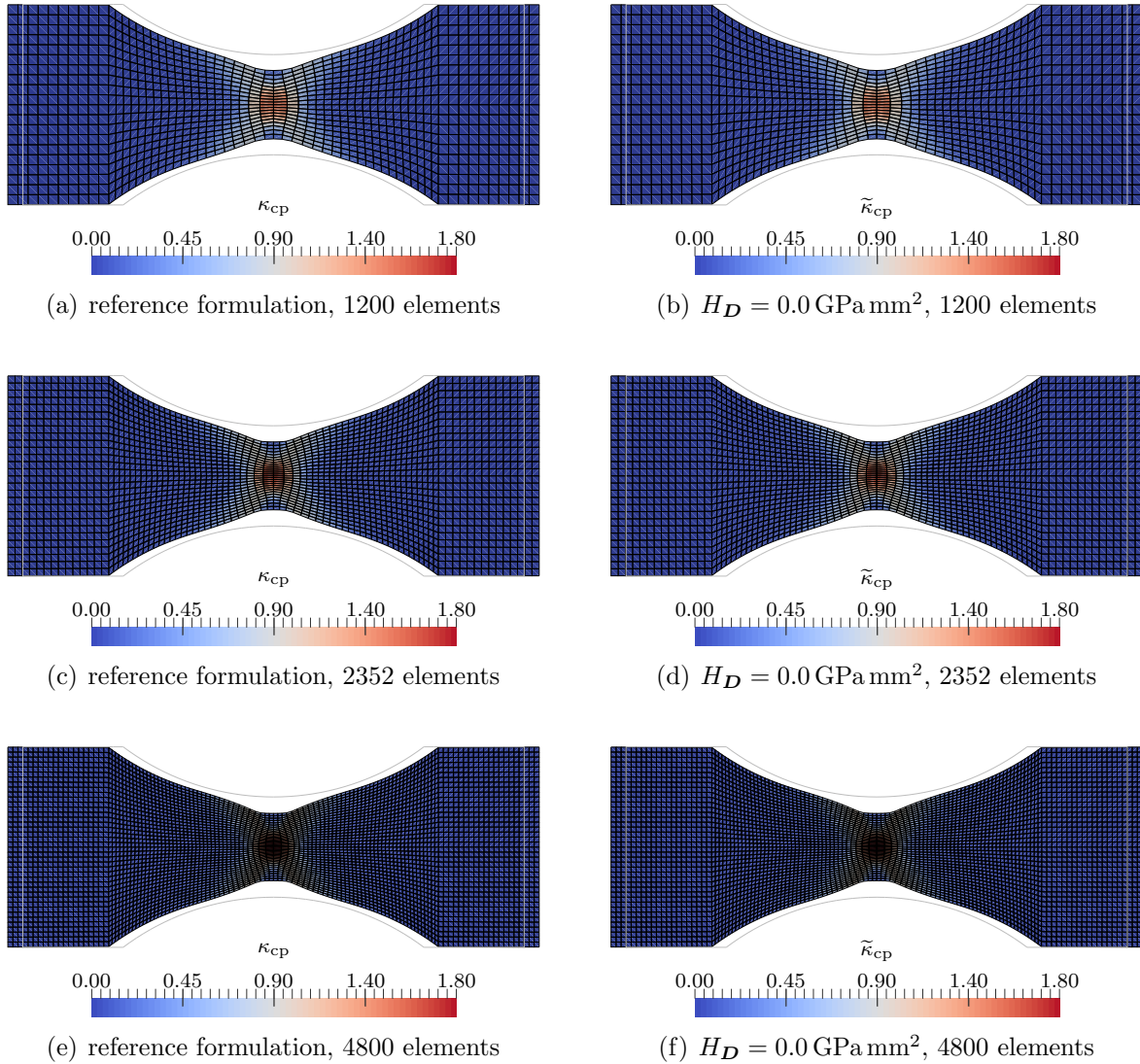
Figure 3.24: Deformation pattern and accumulated plastic strain-like variable κ_{cp}, respectively $\widetilde{\kappa}_{\mathrm{cp}}$, for the plate with two round notches according to Figure 3.22 and an applied displacement of $6\,\mathrm{mm}$. To facilitate the evaluation of the deformation, the contour of the undeformed sample, re-centred with respect to the centre of the deformed plate, is depicted in light-grey colour.

(a) $H_{\boldsymbol{D}} = 1.0\,\mathrm{GPa\,mm^2}$, 1200 elements

(b) $H_{\boldsymbol{D}} = 5.0\,\mathrm{GPa\,mm^2}$, 1200 elements

(c) $H_{\boldsymbol{D}} = 1.0\,\mathrm{GPa\,mm^2}$, 2352 elements

(d) $H_{\boldsymbol{D}} = 5.0\,\mathrm{GPa\,mm^2}$, 2352 elements

(e) $H_{\boldsymbol{D}} = 1.0\,\mathrm{GPa\,mm^2}$, 4800 elements

(f) $H_{\boldsymbol{D}} = 5.0\,\mathrm{GPa\,mm^2}$, 4800 elements
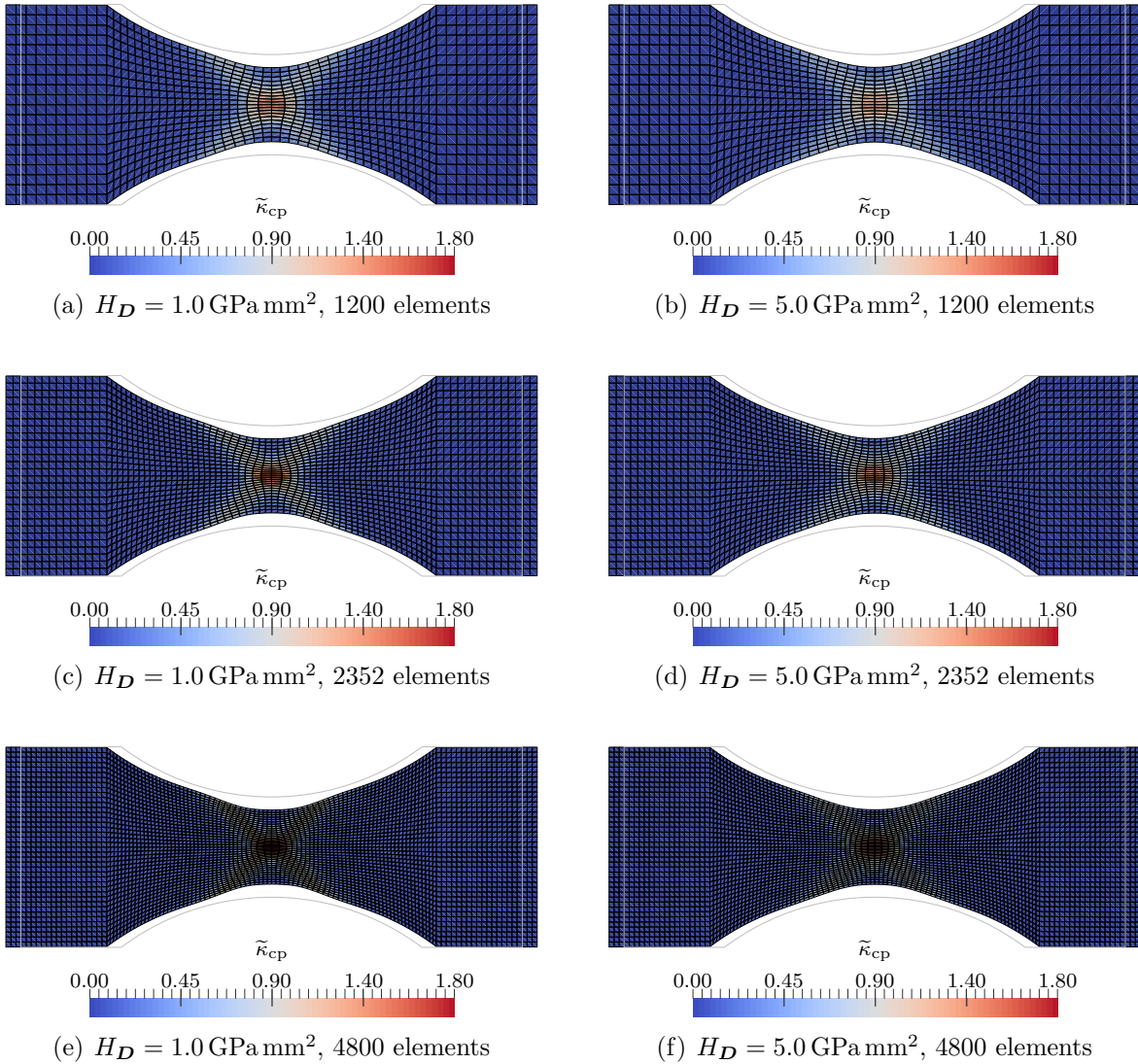
Figure 3.25: Deformation pattern and accumulated plastic strain-like variable $\widetilde{\kappa}_{\mathrm{cp}}$ for the plate with two round notches according to Figure 3.22 and an applied displacement of $6\,\mathrm{mm}$. To facilitate the evaluation of the deformation, the contour of the undeformed sample, re-centred with respect to the centre of the deformed plate, is depicted in light-grey colour.
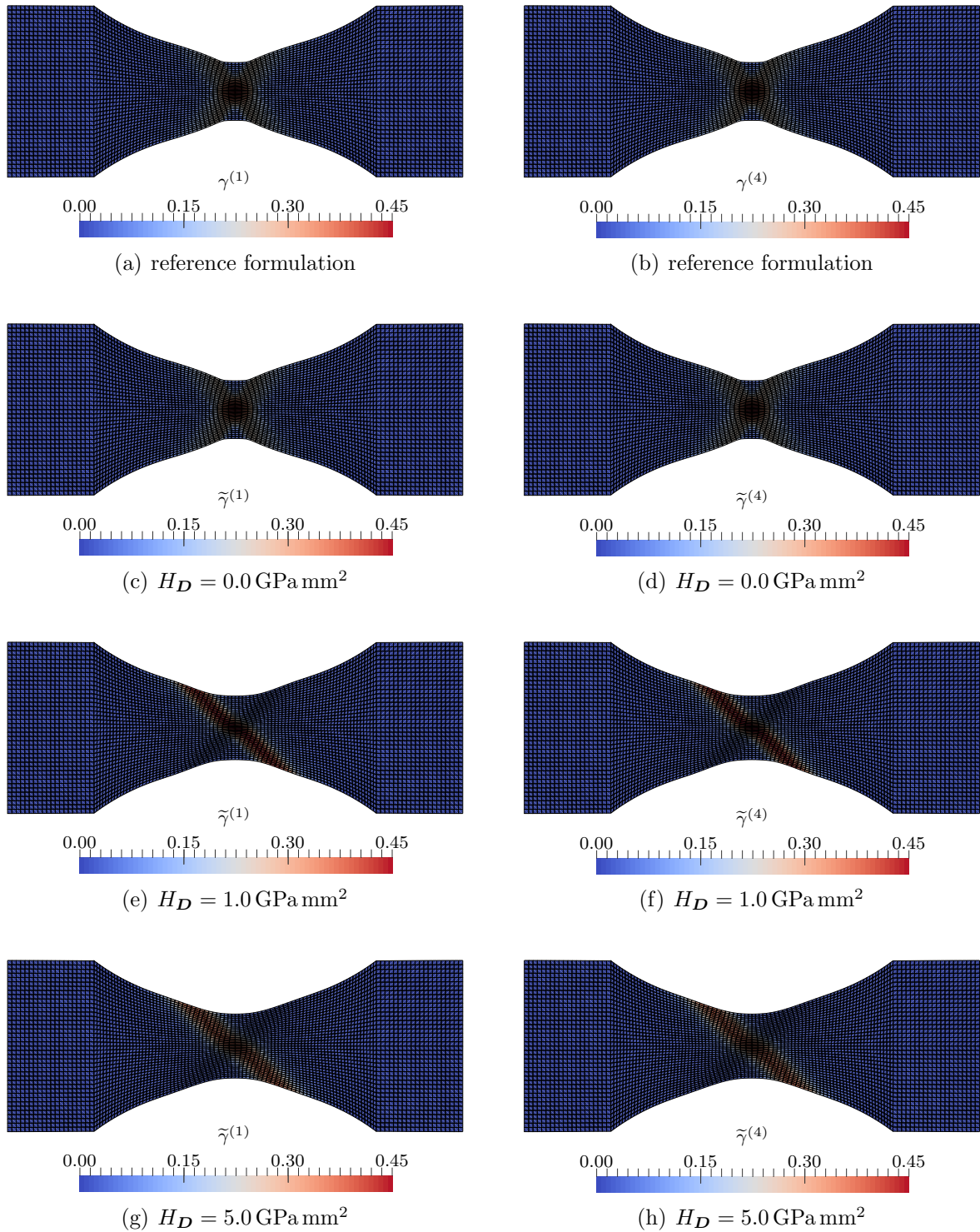
Figure 3.26: Activity of slip systems 1 and 4, for the plate with two round notches according to Figure 3.22 and an applied displacement of 6 mm. Depicted are the results of finite element simulations with 4800 elements for the reference formulation and for the gradient crystal (visco-)plasticity formulation with various values of the material parameter $H_{\boldsymbol{D}}$.

$\gamma^{(7)}$

0.00   0.15   0.30   0.45

(a) reference formulation

$-\gamma^{(10)}$

0.00   0.15   0.30   0.45

(b) reference formulation

$\widetilde{\gamma}^{(7)}$

0.00   0.15   0.30   0.45

(c) $H_{\boldsymbol{D}} = 0.0\,\mathrm{GPa\,mm}^2$

$-\widetilde{\gamma}^{(10)}$

0.00   0.15   0.30   0.45

(d) $H_{\boldsymbol{D}} = 0.0\,\mathrm{GPa\,mm}^2$

$\widetilde{\gamma}^{(7)}$

0.00   0.15   0.30   0.45

(e) $H_{\boldsymbol{D}} = 1.0\,\mathrm{GPa\,mm}^2$

$-\widetilde{\gamma}^{(10)}$

0.00   0.15   0.30   0.45

(f) $H_{\boldsymbol{D}} = 1.0\,\mathrm{GPa\,mm}^2$

$\widetilde{\gamma}^{(7)}$

0.00   0.15   0.30   0.45

(g) $H_{\boldsymbol{D}} = 5.0\,\mathrm{GPa\,mm}^2$

$-\widetilde{\gamma}^{(10)}$

0.00   0.15   0.30   0.45

(h) $H_{\boldsymbol{D}} = 5.0\,\mathrm{GPa\,mm}^2$
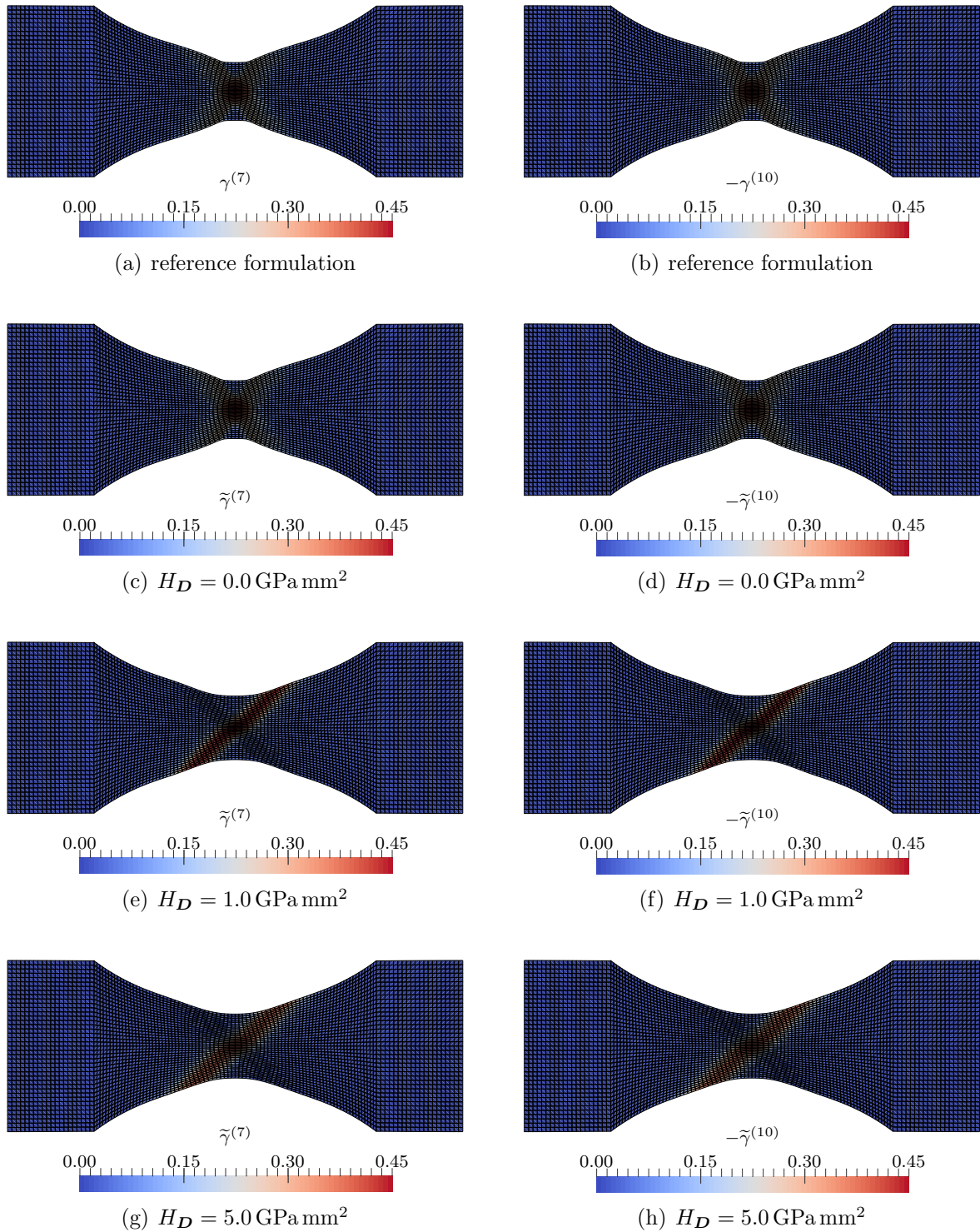
Figure 3.27: Activity of slip systems 7 and 10, for the plate with two round notches according to Figure 3.22 and an applied displacement of 6 mm. Depicted are the results of finite element simulations with 4800 elements for the reference formulation and for the gradient crystal (visco-)plasticity formulation with various values of the material parameter $H_{\boldsymbol{D}}$.
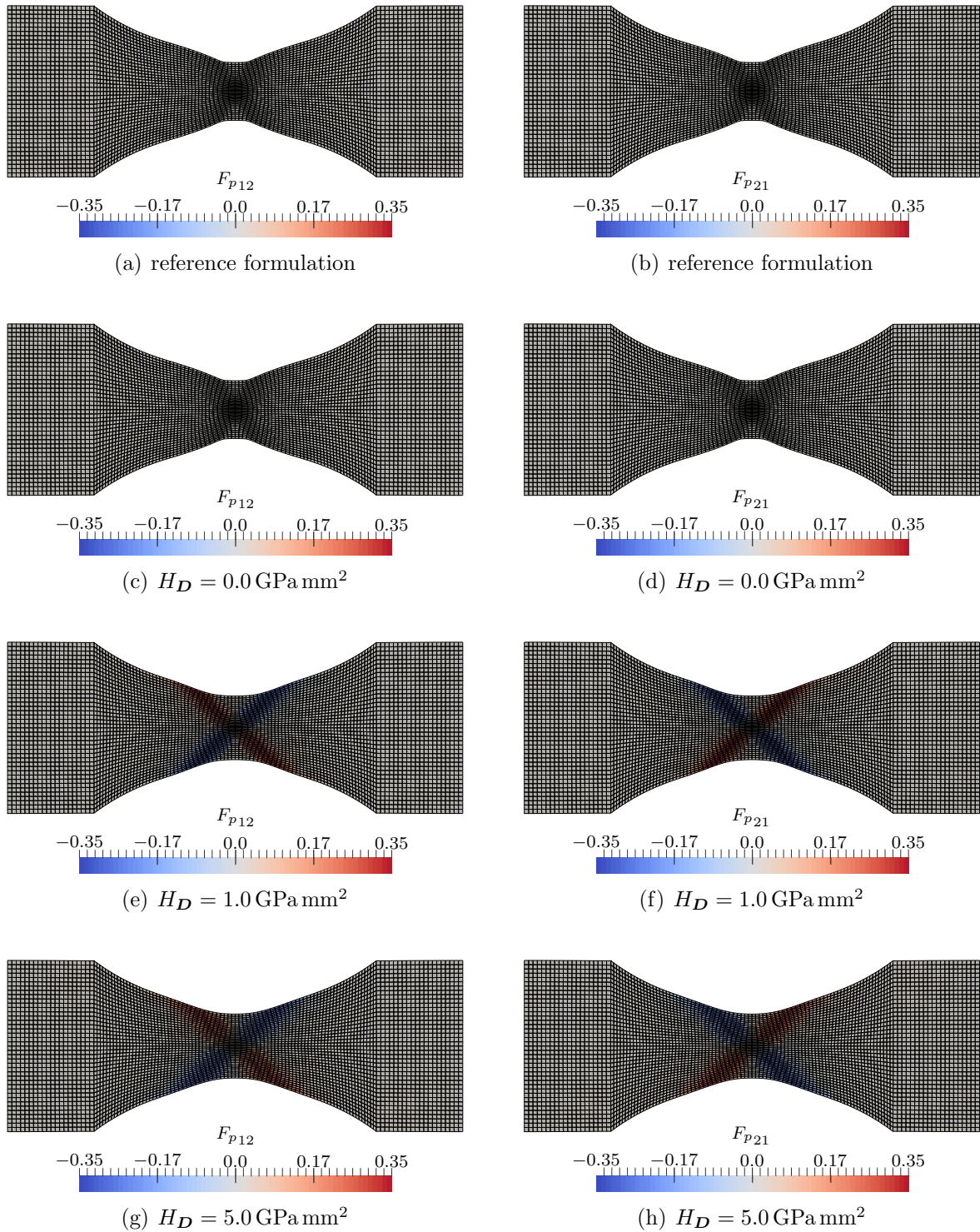
Figure 3.28: Distribution of the plastic deformation gradient coefficients F_{p12} and F_{p21}, for the plate with two round notches according to Figure 3.22 and an applied displacement of 6 mm. Depicted are the results of finite element simulations with 4800 elements for the reference formulation and for the gradient crystal (visco-)plasticity formulation with various values of the material parameter H_D.
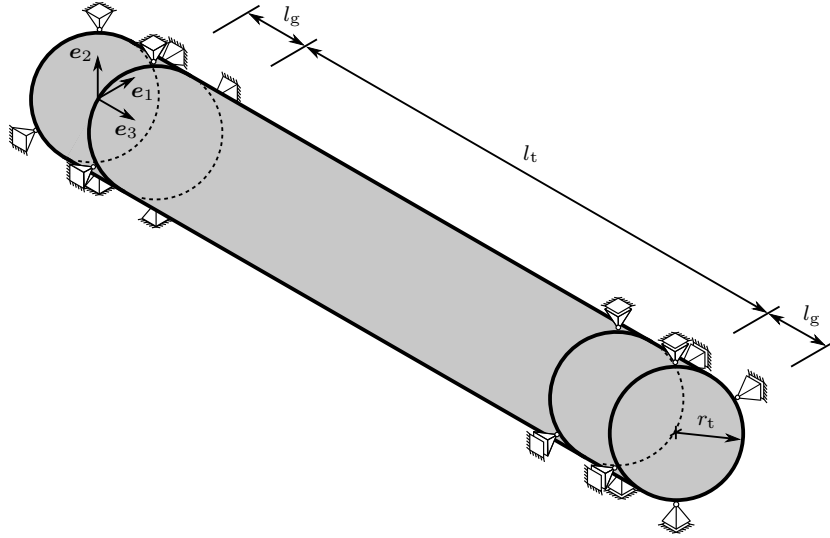
Figure 3.29: Sketch of a micro wire subjected to torsion load.

3.3.4.3 Torsion tests on (micro) wires

Motivated by the experimental findings on polycrystalline copper micro wires presented in [48] and summarised in Section 1.1.2, this section focuses on the size dependent response and, accordingly, on the internal length scale that is induced by higher-gradient contributions in terms of the dislocation density tensor.

Before analysing the torsion tests in detail it should be noted that this work does not intend to exactly reproduce the constitutive response of polycrystalline copper micro wires – it shall rather be shown that the proposed formulation is, in principle, capable of reproducing the observed size effect, while the reference formulation fails to do so. To this end, the focus will lie on the boundary value problem sketched out in Figure 3.29, and wires of three different radii, namely $r_\mathrm{t} \in \{5\,\mathrm{mm}, 10\,\mathrm{mm}, 20\,\mathrm{mm}\}$ will be analysed. The wires have a total length of $100\,\mathrm{mm}$ with the grip sections at both ends having a length of $l_\mathrm{g} = 10\,\mathrm{mm}$ and, accordingly, $l_\mathrm{t} = 80\,\mathrm{mm}$ holds. The displacement is assumed to be fixed in all three spatial dimensions at the lower grip section. At the upper grip section, a rotation $\Delta\varphi_\mathrm{t}$ with respect to the $\boldsymbol{e}_3$-axis is prescribed at the outer boundary nodes. The radial displacement is suppressed while an elongation or contraction in axial direction is not hindered, see Figure 3.29. Furthermore, the set of material parameters provided in Table 3.6 will be used for both the reference formulation and the gradient crystal (visco-)plasticity formulation with $H_{\boldsymbol{D}} = 10\,\mathrm{GPa}\,\mathrm{mm}^2$. From a numerical point of view, 20-node serendipity elements are used for the discretisation of the placement field, while both the $\boldsymbol{\Theta}_\mathrm{p}$- and the $\widetilde{\overline{\boldsymbol{M}}}^{\mathrm{rel}}$-field in the gradient crystal (visco-)plasticity formulation are discretised by means of linear Lagrangian elements. Occurring integrals are evaluated using a standard Gaussian quadrature scheme with 27 quadrature points.

In the simulations, the relative rotation between the upper and lower support is linearly increased within $100\,\mathrm{s}$ to $\Delta\varphi_\mathrm{t}^\mathrm{max} = \pi/4$ and the overall torque M_t at the (upper or lower) support is calculated. To allow for a good comparison with the experimental results of Figure 1.4(b) and in analogy with the presentation therein, the moment-rotation curves are provided in terms of the normalised torque $M_\mathrm{t}/r_\mathrm{t}^3$ and of the scaled twist per unit length $\Delta\varphi_\mathrm{t}\,r_\mathrm{t}/l_\mathrm{t}$, which can be interpreted in terms of the shear strain at the wire's surface, see [48]. Focusing on the reference formulation first, the normalised moment-rotation curves for the different radii presented in Figure 3.30(a) in fact coincide, as is theoretically expected since the reference formulation does not feature an internal length scale. In contrast, the simulation results of the gradient crystal (visco-)plasticity formulation depicted in Figure 3.30(b) clearly do not coincide but show the same tendency as was observed in the experiments, i.e. the overall hardening rate significantly increases with a decreasing wire diameter.

In addition, the distribution of the accumulated plastic slip-like variable κ_cp for the reference formulation, respectively $\widetilde{\kappa}_\mathrm{cp}$ for a gradient crystal (visco-)plasticity formulation with $H_{\boldsymbol{D}} = 10\,\mathrm{GPa\,mm^2}$, is provided in Figure 3.31. To give an example, the results for an applied twist of $\Delta\varphi_\mathrm{t} = \pi/4$ and for wires with radii $r_\mathrm{t} = 5\,\mathrm{mm}$ and $r_\mathrm{t} = 10\,\mathrm{mm}$ are depicted. In the case of the reference formulation, the anisotropic features that are naturally induced by the crystal (visco-)plasticity framework are revealed. A comparison of the results of the reference formulation with those of the gradient crystal (visco-)plasticity formulation reveals that the plastic zone is smeared in the gradient formulation. Moreover, one observes that the gradient effect becomes more dominant with a decreasing wire diameter.

Equation (3.24) together with the specific gradient energy contribution (3.59) and, accordingly, the specific form of the energetic dual to the dislocation density tensor (3.60) gives rise to a back stress-type stress contribution with regard to the plastic evolution, see (3.61), (3.92) and (3.113). Against this background, the constitutive response for cyclic loading is exemplarily analysed for wires with radius $r_\mathrm{t} = 10\,\mathrm{mm}$ and for three different material models, respectively sets of material parameters. Specifically, the reference crystal (visco-)plasticity formulation and gradient crystal (visco-)plasticity formulations with $H_{\boldsymbol{D}} = 5\,\mathrm{GPa\,mm^2}$ and $H_{\boldsymbol{D}} = 10\,\mathrm{GPa\,mm^2}$ are taken into account. The finite element simulations are based on the element formulations proposed at the beginning of this section and a discretisation with 450 elements is used. In analogy with the simulations presented before, the relative rotation between the upper and lower support is linearly increased within $100\,\mathrm{s}$ to $\Delta\varphi_\mathrm{t} = \pi/4$, first. Next, the relative rotation is linearly decreased to $\Delta\varphi_\mathrm{t} = -\pi/4$ within $200\,\mathrm{s}$. Upon reaching the minimal value, the loading is again reversed and the simulation is stopped $200\,\mathrm{s}$ later when a final relative rotation of $\Delta\varphi_\mathrm{t} = \pi/4$ is reached. The corresponding moment-rotation curves are given in terms of the normalised torque $M_\mathrm{t}/r_\mathrm{t}^3$ and of the scaled twist per unit length $\Delta\varphi_\mathrm{t}\,r_\mathrm{t}/l_\mathrm{t}$, with a significant influence of the gradient energy contribution being revealed, see Figure 3.32.

(a) reference formulation

(b) gradient plasticity formulation with $H_{\boldsymbol{D}} = 10.0\,\mathrm{GPa\,mm^2}$
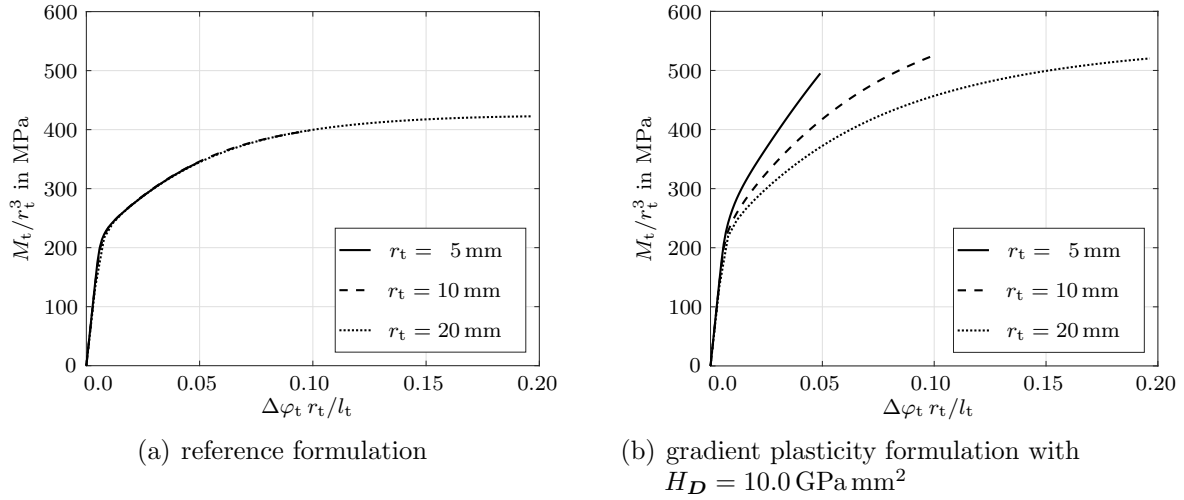
Figure 3.30: Simulation results of torsion tests according to Figure 3.29 for the reference formulation and for a gradient crystal (visco-)plasticity formulation with $H_{\boldsymbol{D}} = 10.0\,\mathrm{GPa\,mm^2}$. The simulation results are presented in terms of the normalised torque $M_{\mathrm{t}}/r_{\mathrm{t}}^3$ and of the scaled twist per unit length $\Delta\varphi_{\mathrm{t}}\,r_{\mathrm{t}}/l_{\mathrm{t}}$ in analogy with the experimental findings of Figure 1.4(b). The normalised simulation results of the reference formulation in fact coincide for the different radii. In contrast, a size dependent response is revealed for the gradient crystal (visco-)plasticity formulation.

3.3.5 Summary

This section dealt with a thermodynamic consistent gradient crystal (visco-)plasticity formulation which accounts for hardening effects that can be attributed to the presence of geometrically necessary dislocations by incorporating dislocation density tensors as additional arguments of the free energy density function. On the basis of the constitutive framework presented in Section 3.1, it was shown how the phenomenological gradient plasticity framework that was proposed in Section 3.2 can be extended to gradient crystal (visco-)plasticity. In particular, a numerical framework was developed on the basis of a different interpretation of the balance equation for the generalised stress field which allowed us to use the same stabilisation algorithms that were used for the reference crystal (visco-)plasticity formulation to approach the rate-independent limit.

For a specific model featuring twelve slip systems, the constitutive response at material point level was then studied first. In a second step, the focus was laid on the necking of a tension test specimen. It was observed that accounting for the presence of geometrically necessary dislocations in the present crystal (visco-)plasticity framework, significantly influenced the activity of the slip systems and the deformation pattern. Motivated by experimental findings on copper micro wires, the focus was finally laid on three-dimensional torsion tests, and it was shown that the reference formulation which does not feature an internal length scale failed to reproduce the experimentally observed size effect, whereas the gradient crystal (visco-)plasticity formulation was capable of doing so.

(a) reference formulation, $r_\mathrm{t} = 5\,\mathrm{mm}$

(b) gradient plasticity formulation, $H_{\boldsymbol{D}} = 10\,\mathrm{GPa\,mm}^2$, $r_\mathrm{t} = 5\,\mathrm{mm}$

(c) reference formulation, $r_\mathrm{t} = 10\,\mathrm{mm}$

(d) gradient plasticity formulation, $H_{\boldsymbol{D}} = 10\,\mathrm{GPa\,mm}^2$, $r_\mathrm{t} = 10\,\mathrm{mm}$
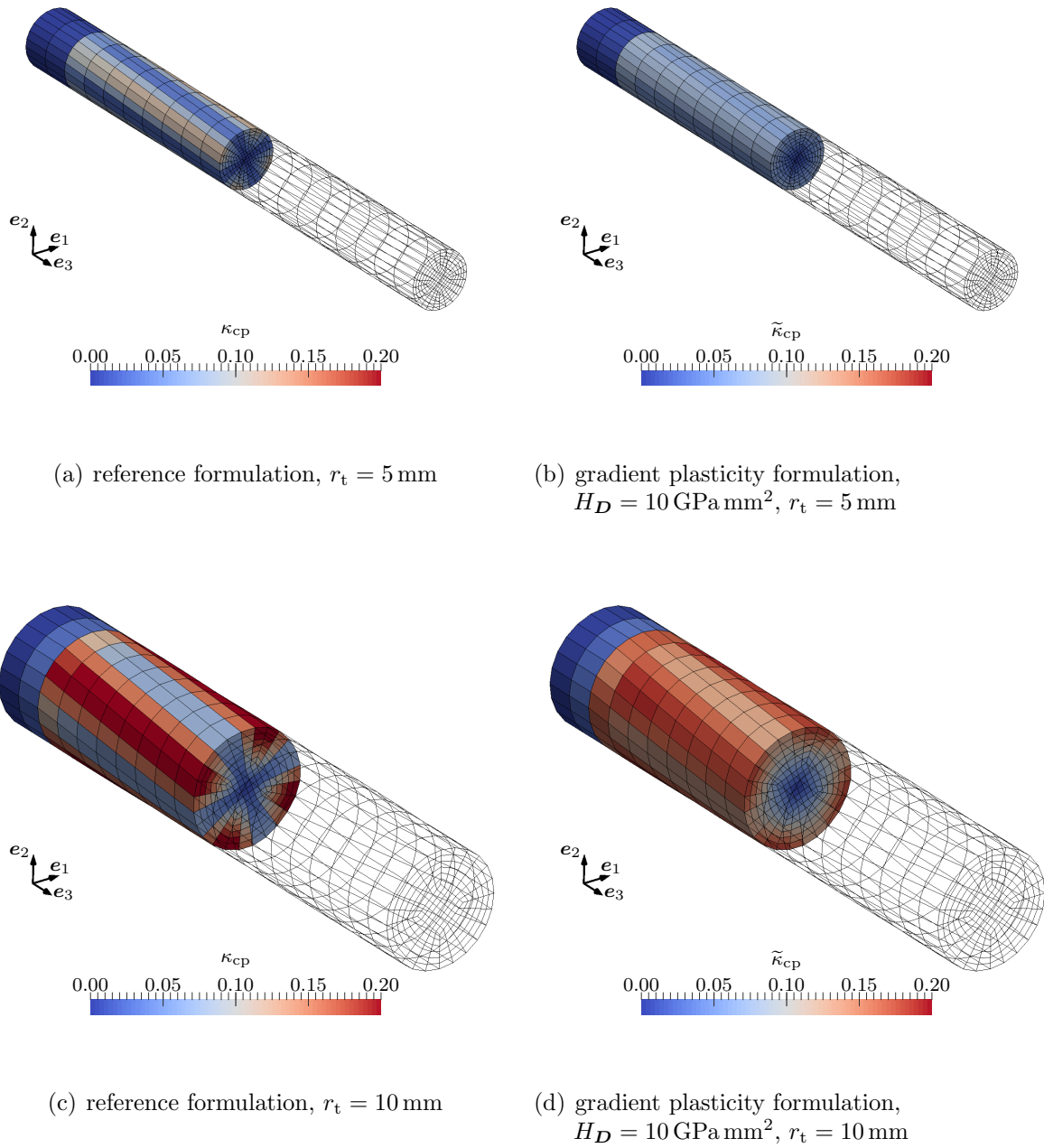
Figure 3.31: Simulation results for torsion tests according to Figure 3.29 and an applied twist of $\Delta\varphi_\mathrm{t} = \pi/4$. Depicted is the distribution of the accumulated plastic slip-like variable κ_cp for the reference formulation, respectively $\widetilde{\kappa}_\mathrm{cp}$ for the gradient crystal (visco-)plasticity formulation with $H_{\boldsymbol{D}} = 10\,\mathrm{GPa\,mm}^2$. For both formulations, the simulation results of wires with radii $r_\mathrm{t} = 5\,\mathrm{mm}$ and $r_\mathrm{t} = 10\,\mathrm{mm}$ are presented and discretisations with 3600 elements are used. Clearly, the plastic zone is smeared in the gradient-enhanced case in comparison with the reference simulations.
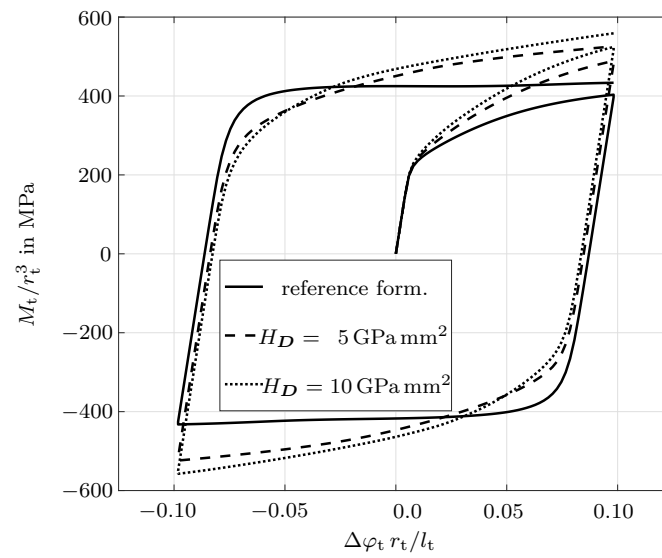
Figure 3.32: Simulation results of cyclic torsion tests according to Figure 3.29 with $r_t = 10\,\text{mm}$, for the reference formulation and for gradient crystal (visco-)plasticity formulations with $H_D = 5.0\,\text{GPa}\,\text{mm}^2$ and $H_D = 10.0\,\text{GPa}\,\text{mm}^2$. The simulation results are presented in terms of the normalised torque M_t/r_t^3 and the scaled twist per unit length $\Delta\varphi_t\,r_t/l_t$.

B Appendix

B.1 Derivation of the algorithmic tangent stiffness

In this section, the contributions to the consistent algorithmic tangent stiffness matrix, required for an iterative gradient-based solution of the non-linear system of equations (3.79), are derived subject to the assumption of the following functional dependencies

$$\boldsymbol{F}_{\mathrm{p}}\left(\widetilde{\overline{\boldsymbol{M}}},\, \kappa;\, \boldsymbol{F}_{\mathrm{p_n}},\, \kappa_{\mathrm{n}}\right) \tag{3.139a}$$

$$\overline{\boldsymbol{M}}\left(\boldsymbol{F}\left(\boldsymbol{\varphi}\right),\, \boldsymbol{F}_{\mathrm{p}}\left(\widetilde{\overline{\boldsymbol{M}}},\, \kappa;\, \boldsymbol{F}_{\mathrm{p_n}},\, \kappa_{\mathrm{n}}\right)\right) \tag{3.139b}$$

$$\boldsymbol{P}\left(\boldsymbol{F}\left(\boldsymbol{\varphi}\right),\, \boldsymbol{F}_{\mathrm{p}}\left(\widetilde{\overline{\boldsymbol{M}}},\, \kappa;\, \boldsymbol{F}_{\mathrm{p_n}},\, \kappa_{\mathrm{n}}\right)\right) \tag{3.139c}$$

$$\boldsymbol{\Xi}\left(\mathrm{Curl}^{\mathrm{t}}\left(\boldsymbol{\Theta}_{\mathrm{p}}\right),\, \boldsymbol{F}_{\mathrm{p}}\left(\widetilde{\overline{\boldsymbol{M}}},\, \kappa;\, \boldsymbol{F}_{\mathrm{p_n}},\, \kappa_{\mathrm{n}}\right)\right) \tag{3.139d}$$

$$\widetilde{f}\left(\widetilde{\overline{\boldsymbol{M}}},\, \kappa\right) \tag{3.139e}$$

An update step i in the global iteration procedure is then given by

$$\begin{bmatrix}\mathbf{0}\\ \mathbf{0}\\ \mathbf{0}\\ \mathbf{0}\end{bmatrix} = \begin{bmatrix}\boldsymbol{f}_{\mathrm{int}}^{\boldsymbol{\varphi}\mathrm{h}} - \boldsymbol{f}_{\mathrm{ext}}^{\boldsymbol{\varphi}\mathrm{h}}\\ \boldsymbol{f}_{\mathrm{int}}^{\widetilde{\overline{\boldsymbol{M}}}\mathrm{h}}\\ \boldsymbol{f}_{\mathrm{int}}^{\boldsymbol{\Theta}_{\mathrm{p}}\mathrm{h}}\\ \boldsymbol{f}_{\mathrm{int}}^{\kappa\mathrm{h}}\end{bmatrix}_{i} + \begin{bmatrix}\mathbf{K}^{\boldsymbol{\varphi}\boldsymbol{\varphi}} & \mathbf{K}^{\boldsymbol{\varphi}\widetilde{\overline{\boldsymbol{M}}}} & \mathbf{K}^{\boldsymbol{\varphi}\boldsymbol{\Theta}_{\mathrm{p}}} & \mathbf{K}^{\boldsymbol{\varphi}\kappa}\\ \mathbf{K}^{\widetilde{\overline{\boldsymbol{M}}}\boldsymbol{\varphi}} & \mathbf{K}^{\widetilde{\overline{\boldsymbol{M}}}\widetilde{\overline{\boldsymbol{M}}}} & \mathbf{K}^{\widetilde{\overline{\boldsymbol{M}}}\boldsymbol{\Theta}_{\mathrm{p}}} & \mathbf{K}^{\widetilde{\overline{\boldsymbol{M}}}\kappa}\\ \mathbf{K}^{\boldsymbol{\Theta}_{\mathrm{p}}\boldsymbol{\varphi}} & \mathbf{K}^{\boldsymbol{\Theta}_{\mathrm{p}}\widetilde{\overline{\boldsymbol{M}}}} & \mathbf{K}^{\boldsymbol{\Theta}_{\mathrm{p}}\boldsymbol{\Theta}_{\mathrm{p}}} & \mathbf{K}^{\boldsymbol{\Theta}_{\mathrm{p}}\kappa}\\ \mathbf{K}^{\kappa\boldsymbol{\varphi}} & \mathbf{K}^{\kappa\widetilde{\overline{\boldsymbol{M}}}} & \mathbf{K}^{\kappa\boldsymbol{\Theta}_{\mathrm{p}}} & \mathbf{K}^{\kappa\kappa}\end{bmatrix}_{i} \cdot \begin{bmatrix}\Delta\widehat{\boldsymbol{\varphi}}\\ \Delta\widehat{\widetilde{\overline{\boldsymbol{M}}}}\\ \Delta\widehat{\boldsymbol{\Theta}}_{\mathrm{p}}\\ \Delta\widehat{\kappa}\end{bmatrix}_{i} \tag{3.140}$$

with $\Delta\bullet$ denoting the update in the field variable $\bullet$ to be solved for. Note, that here and in the following, superscripts referring to the time step $\mathrm{n}+1$ are omitted for the sake of brevity.

Balance of linear momentum

$$\mathbf{K}^{\boldsymbol{\varphi}\boldsymbol{\varphi}} = \overset{n_{\mathrm{el}}}{\underset{e=1}{\mathbf{A}}} \int_{\mathcal{B}_0^e} \nabla_{\boldsymbol{X}} N_E^{\boldsymbol{\varphi}} \cdot \frac{\partial \boldsymbol{P}^{\mathrm{t}}}{\partial \boldsymbol{F}} \cdot \nabla_{\boldsymbol{X}} N_A^{\boldsymbol{\varphi}} \, \mathrm{d}V_e \tag{3.141a}$$

$$\mathbf{K}^{\boldsymbol{\varphi}\widetilde{\overline{\boldsymbol{M}}}} = \overset{n_{\mathrm{el}}}{\underset{e=1}{\mathbf{A}}} \int_{\mathcal{B}_0^e} \nabla_{\boldsymbol{X}} N_E^{\boldsymbol{\varphi}} \cdot \frac{\partial \boldsymbol{P}^{\mathrm{t}}}{\partial \widetilde{\overline{\boldsymbol{M}}}} \, N_B^{\widetilde{\overline{\boldsymbol{M}}}} \, \mathrm{d}V_e \tag{3.141b}$$

$$\mathbf{K}^{\boldsymbol{\varphi}\boldsymbol{\Theta}_{\mathrm{p}}} = \overset{n_{\mathrm{el}}}{\underset{e=1}{\mathbf{A}}} \quad \mathbf{0} \tag{3.141c}$$

$$\mathbf{K}^{\boldsymbol{\varphi}\kappa} = \overset{n_{\mathrm{el}}}{\underset{e=1}{\mathbf{A}}} \int_{\mathcal{B}_0^e} \nabla_{\boldsymbol{X}} N_E^{\boldsymbol{\varphi}} \cdot \frac{\partial \boldsymbol{P}^{\mathrm{t}}}{\partial \kappa} \, N_D^{\kappa} \, \mathrm{d}V_e \tag{3.141d}$$

Balance equation of the generalised Mandel stress tensor

$$\mathbf{K}^{\widetilde{\overline{M}}\varphi} = \mathop{\mathbf{A}}_{e=1}^{\mathrm{n_{el}}} \int_{\mathcal{B}_0^e} -N_F^{\widetilde{\overline{M}}} \frac{\partial \overline{M}}{\partial F} \cdot \nabla_X N_A^{\varphi} \, \mathrm{d}V_e \tag{3.142a}$$

$$\mathbf{K}^{\widetilde{\overline{M}}\widetilde{\overline{M}}} = \mathop{\mathbf{A}}_{e=1}^{\mathrm{n_{el}}} \int_{\mathcal{B}_0^e} \quad N_F^{\widetilde{\overline{M}}} \left[I \,\overline{\otimes}\, I - \frac{\partial \overline{M}}{\partial \widetilde{\overline{M}}} \right] N_B^{\widetilde{\overline{M}}} - \boldsymbol{\Xi} \cdot \boldsymbol{\epsilon}_0 : \left[\nabla_X N_F^{\widetilde{\overline{M}}} \otimes \frac{\partial F_{\mathrm{p}}^{\mathrm{t}}}{\partial \widetilde{\overline{M}}} N_B^{\widetilde{\overline{M}}} \right]$$

$$+ N_F^{\widetilde{\overline{M}}} \left[I \,\overline{\otimes}\, [F_{\mathrm{p}} : \boldsymbol{\epsilon}_0] \right] \qquad : \frac{\partial \boldsymbol{\Xi}}{\partial \widetilde{\overline{M}}} N_B^{\widetilde{\overline{M}}}$$

$$- \left[I \,\overline{\otimes}\, \left[F_{\mathrm{p}} \cdot \boldsymbol{\epsilon}_0 \cdot \nabla_X N_F^{\widetilde{\overline{M}}} \right] \right] : \frac{\partial \boldsymbol{\Xi}}{\partial \widetilde{\overline{M}}} N_B^{\widetilde{\overline{M}}} \, \mathrm{d}V_e \tag{3.142b}$$

$$\mathbf{K}^{\widetilde{\overline{M}}\Theta_{\mathrm{p}}} = \mathop{\mathbf{A}}_{e=1}^{\mathrm{n_{el}}} \int_{\mathcal{B}_0^e} - \left[I \,\overline{\otimes}\, \left[F_{\mathrm{p}} \cdot \boldsymbol{\epsilon}_0 \cdot \nabla_X N_F^{\widetilde{\overline{M}}} \right] \right] : \frac{\partial \boldsymbol{\Xi}}{\partial \nabla_X \boldsymbol{\Theta}_{\mathrm{p}}} \cdot \nabla_X N_C^{\boldsymbol{\Theta}_{\mathrm{p}}}$$

$$+ \left[I \,\overline{\otimes}\, \left[\nabla_X \boldsymbol{\Theta}_{\mathrm{p}} : \boldsymbol{\epsilon}_0 \, N_F^{\widetilde{\overline{M}}} \right] \right] : \frac{\partial \boldsymbol{\Xi}}{\partial \nabla_X \boldsymbol{\Theta}_{\mathrm{p}}} \cdot \nabla_X N_C^{\boldsymbol{\Theta}_{\mathrm{p}}}$$

$$+ N_F^{\widetilde{\overline{M}}} \left[\boldsymbol{\Xi} \cdot \boldsymbol{\epsilon}_0 \cdot \nabla_X N_C^{\boldsymbol{\Theta}_{\mathrm{p}}} \right] \,\underline{\otimes}\, I \, \mathrm{d}V_e \tag{3.142c}$$

$$\mathbf{K}^{\widetilde{\overline{M}}\kappa} = \mathop{\mathbf{A}}_{e=1}^{\mathrm{n_{el}}} \int_{\mathcal{B}_0^e} -\frac{\partial \boldsymbol{\Xi}}{\partial \kappa} \cdot \boldsymbol{\epsilon}_0 : \left[\nabla_X N_F^{\widetilde{\overline{M}}} \otimes F_{\mathrm{p}}^{\mathrm{t}} \right] N_D^{\kappa} - N_F^{\widetilde{\overline{M}}} \frac{\partial \overline{M}}{\partial \kappa} N_D^{\kappa}$$

$$- \boldsymbol{\Xi} \cdot \boldsymbol{\epsilon}_0 : \left[\nabla_X N_F^{\widetilde{\overline{M}}} \otimes \frac{\partial F_{\mathrm{p}}^{\mathrm{t}}}{\partial \kappa} \right] N_D^{\kappa} + N_F^{\widetilde{\overline{M}}} \frac{\partial \boldsymbol{\Xi}}{\partial \kappa} \cdot [\nabla_X \boldsymbol{\Theta}_{\mathrm{p}} : \boldsymbol{\epsilon}_0]^{\mathrm{t}} \, N_D^{\kappa} \, \mathrm{d}V_e \tag{3.142d}$$

L_2-projection of the plastic deformation gradient

$$\mathbf{K}^{\boldsymbol{\Theta}_{\mathrm{p}}\varphi} = \mathop{\mathbf{A}}_{e=1}^{\mathrm{n_{el}}} \mathbf{0} \tag{3.143a}$$

$$\mathbf{K}^{\boldsymbol{\Theta}_{\mathrm{p}}\widetilde{\overline{M}}} = \mathop{\mathbf{A}}_{e=1}^{\mathrm{n_{el}}} \int_{\mathcal{B}_0^e} N_G^{\boldsymbol{\Theta}_{\mathrm{p}}} \frac{\partial F_{\mathrm{p}}}{\partial \widetilde{\overline{M}}} N_B^{\widetilde{\overline{M}}} \, \mathrm{d}V_e \tag{3.143b}$$

$$\mathbf{K}^{\boldsymbol{\Theta}_{\mathrm{p}}\boldsymbol{\Theta}_{\mathrm{p}}} = \mathop{\mathbf{A}}_{e=1}^{\mathrm{n_{el}}} \int_{\mathcal{B}_0^e} -N_G^{\boldsymbol{\Theta}_{\mathrm{p}}} I \,\overline{\otimes}\, I \, N_C^{\boldsymbol{\Theta}_{\mathrm{p}}} \, \mathrm{d}V_e \tag{3.143c}$$

$$\mathbf{K}^{\boldsymbol{\Theta}_{\mathrm{p}}\kappa} = \mathop{\mathbf{A}}_{e=1}^{\mathrm{n_{el}}} \int_{\mathcal{B}_0^e} N_G^{\boldsymbol{\Theta}_{\mathrm{p}}} \frac{\partial F_{\mathrm{p}}}{\partial \kappa} N_D^{\kappa} \, \mathrm{d}V_e \tag{3.143d}$$

Karush-Kuhn-Tucker condition   To calculate the derivative of the Fischer-Burmeister function (3.78) with respect to the field variables we first note that

$$\frac{\partial \boldsymbol{f}_{\mathrm{int}}^{\kappa\mathrm{h}}}{\partial \boldsymbol{f}_{\mathrm{int}}^{\widetilde{f}\,\mathrm{h}}} = \mathrm{diag}\left(\upsilon_1, \ldots, \upsilon_{\mathrm{n}_{\mathrm{np},\kappa}}\right) \quad , \quad \upsilon_i = \frac{\left[\boldsymbol{f}_{\mathrm{int}}^{\widetilde{f}\,\mathrm{h}}\right]_i}{\sqrt{\left[\boldsymbol{f}_{\mathrm{int}}^{\widetilde{f}\,\mathrm{h}}\right]_i^2 + \left[\boldsymbol{f}_{\mathrm{int}}^{\lambda_{\mathrm{p}}\mathrm{h}}\right]_i^2}} + 1 \tag{3.144}$$

and

$$\frac{\partial \boldsymbol{f}_{\mathrm{int}}^{\kappa\mathrm{h}}}{\partial \boldsymbol{f}_{\mathrm{int}}^{\lambda_{\mathrm{p}}\mathrm{h}}} = \mathrm{diag}\left(\Upsilon_1, \ldots, \Upsilon_{\mathrm{n}_{\mathrm{np},\kappa}}\right) \quad , \quad \Upsilon_i = \frac{\left[\boldsymbol{f}_{\mathrm{int}}^{\lambda_{\mathrm{p}}\mathrm{h}}\right]_i}{\sqrt{\left[\boldsymbol{f}_{\mathrm{int}}^{\widetilde{f}\,\mathrm{h}}\right]_i^2 + \left[\boldsymbol{f}_{\mathrm{int}}^{\lambda_{\mathrm{p}}\mathrm{h}}\right]_i^2}} - 1 \quad . \tag{3.145}$$

Using (3.144) and (3.145), the contributions to the consistent algorithmic stiffness matrix can be specified as

$$\mathbf{K}^{\kappa\boldsymbol{\varphi}} = \frac{\partial \boldsymbol{f}_{\mathrm{int}}^{\kappa\mathrm{h}}}{\partial \boldsymbol{f}_{\mathrm{int}}^{\widetilde{f}\,\mathrm{h}}} \cdot \mathbf{K}^{\widetilde{f}\boldsymbol{\varphi}} + \frac{\partial \boldsymbol{f}_{\mathrm{int}}^{\kappa\mathrm{h}}}{\partial \boldsymbol{f}_{\mathrm{int}}^{\lambda_{\mathrm{p}}\mathrm{h}}} \cdot \mathbf{K}^{\lambda_{\mathrm{p}}\boldsymbol{\varphi}} \tag{3.146a}$$

$$\mathbf{K}^{\kappa\widetilde{\boldsymbol{M}}} = \frac{\partial \boldsymbol{f}_{\mathrm{int}}^{\kappa\mathrm{h}}}{\partial \boldsymbol{f}_{\mathrm{int}}^{\widetilde{f}\,\mathrm{h}}} \cdot \mathbf{K}^{\widetilde{f}\widetilde{\boldsymbol{M}}} + \frac{\partial \boldsymbol{f}_{\mathrm{int}}^{\kappa\mathrm{h}}}{\partial \boldsymbol{f}_{\mathrm{int}}^{\lambda_{\mathrm{p}}\mathrm{h}}} \cdot \mathbf{K}^{\lambda_{\mathrm{p}}\widetilde{\boldsymbol{M}}} \tag{3.146b}$$

$$\mathbf{K}^{\kappa\boldsymbol{\Theta}_{\mathrm{p}}} = \frac{\partial \boldsymbol{f}_{\mathrm{int}}^{\kappa\mathrm{h}}}{\partial \boldsymbol{f}_{\mathrm{int}}^{\widetilde{f}\,\mathrm{h}}} \cdot \mathbf{K}^{\widetilde{f}\boldsymbol{\Theta}_{\mathrm{p}}} + \frac{\partial \boldsymbol{f}_{\mathrm{int}}^{\kappa\mathrm{h}}}{\partial \boldsymbol{f}_{\mathrm{int}}^{\lambda_{\mathrm{p}}\mathrm{h}}} \cdot \mathbf{K}^{\lambda_{\mathrm{p}}\boldsymbol{\Theta}_{\mathrm{p}}} \tag{3.146c}$$

$$\mathbf{K}^{\kappa\kappa} = \frac{\partial \boldsymbol{f}_{\mathrm{int}}^{\kappa\mathrm{h}}}{\partial \boldsymbol{f}_{\mathrm{int}}^{\widetilde{f}\,\mathrm{h}}} \cdot \mathbf{K}^{\widetilde{f}\kappa} + \frac{\partial \boldsymbol{f}_{\mathrm{int}}^{\kappa\mathrm{h}}}{\partial \boldsymbol{f}_{\mathrm{int}}^{\lambda_{\mathrm{p}}\mathrm{h}}} \cdot \mathbf{K}^{\lambda_{\mathrm{p}}\kappa} \tag{3.146d}$$

with

$$\mathbf{K}^{\widetilde{f}\boldsymbol{\varphi}} = \underset{e=1}{\overset{\mathrm{n_{el}}}{\mathbf{A}}} \mathbf{0} \tag{3.147a} \qquad\qquad \mathbf{K}^{\widetilde{f}\widetilde{\boldsymbol{M}}} = \underset{e=1}{\overset{\mathrm{n_{el}}}{\mathbf{A}}} \int_{\mathcal{B}_0^e} N_H^\kappa \frac{\partial \widetilde{f}}{\partial \widetilde{\boldsymbol{M}}} N_B^{\widetilde{\boldsymbol{M}}} \, \mathrm{d}V_e \tag{3.147b}$$

$$\mathbf{K}^{\widetilde{f}\boldsymbol{\Theta}_{\mathrm{p}}} = \underset{e=1}{\overset{\mathrm{n_{el}}}{\mathbf{A}}} \mathbf{0} \tag{3.147c} \qquad\qquad \mathbf{K}^{\widetilde{f}\kappa} = \underset{e=1}{\overset{\mathrm{n_{el}}}{\mathbf{A}}} \int_{\mathcal{B}_0^e} N_H^\kappa \frac{\partial \widetilde{f}}{\partial \kappa} N_D^\kappa \, \mathrm{d}V_e \tag{3.147d}$$

and

$$\mathbf{K}^{\lambda_{\mathrm{p}}\boldsymbol{\varphi}} = \underset{e=1}{\overset{\mathrm{n_{el}}}{\mathbf{A}}} \mathbf{0} \tag{3.148a} \qquad\qquad \mathbf{K}^{\lambda_{\mathrm{p}}\widetilde{\boldsymbol{M}}} = \underset{e=1}{\overset{\mathrm{n_{el}}}{\mathbf{A}}} \mathbf{0} \tag{3.148b}$$

$$\mathbf{K}^{\lambda_{\mathrm{p}}\boldsymbol{\Theta}_{\mathrm{p}}} = \underset{e=1}{\overset{\mathrm{n_{el}}}{\mathbf{A}}} \mathbf{0} \tag{3.148c} \qquad\qquad \mathbf{K}^{\lambda_{\mathrm{p}}\kappa} = \underset{e=1}{\overset{\mathrm{n_{el}}}{\mathbf{A}}} \int_{\mathcal{B}_0^e} N_I^\kappa N_D^\kappa \, \mathrm{d}V_e \tag{3.148d}$$

Supplementary derivatives   In this paragraph, the derivatives of the functions $\boldsymbol{F}_\mathrm{p}$, $\boldsymbol{P}$, $\overline{\boldsymbol{M}}$, $\boldsymbol{\Xi}$ and $\widetilde{f}$ with respect to $\boldsymbol{F}$, $\nabla_{\boldsymbol{X}}\boldsymbol{\Theta}_\mathrm{p}$, $\widetilde{\overline{\boldsymbol{M}}}$ and κ that are required for the finite element implementation will be specified for the material model proposed in Section 3.2.2.

Focusing first on the derivatives of the plastic part of the deformation gradient, which is defined in (3.58), we find

$$
\frac{\partial \boldsymbol{F}_\mathrm{p}}{\partial \widetilde{\overline{\boldsymbol{M}}}} = -\frac{\partial \boldsymbol{F}_\mathrm{p}}{\partial \left[\boldsymbol{I} - \frac{\widetilde{\overline{\boldsymbol{M}}}_\mathrm{dev}}{\left\| \widetilde{\overline{\boldsymbol{M}}}_\mathrm{dev} \right\|} \left[\kappa - \kappa^n \right] \right]} : \left[\boldsymbol{I} \,\overline{\otimes}\, \boldsymbol{I} - \frac{1}{3} \boldsymbol{I} \otimes \boldsymbol{I} - \frac{\widetilde{\overline{\boldsymbol{M}}}_\mathrm{dev}}{\left\| \widetilde{\overline{\boldsymbol{M}}}_\mathrm{dev} \right\|} \otimes \frac{\widetilde{\overline{\boldsymbol{M}}}_\mathrm{dev}}{\left\| \widetilde{\overline{\boldsymbol{M}}}_\mathrm{dev} \right\|} \right] \frac{\kappa - \kappa^\mathrm{n}}{\left\| \widetilde{\overline{\boldsymbol{M}}}_\mathrm{dev} \right\|}
$$
(3.149a)

and

$$
\frac{\partial \boldsymbol{F}_\mathrm{p}}{\partial \kappa} = -\frac{\partial \boldsymbol{F}_\mathrm{p}}{\partial \left[\boldsymbol{I} - \frac{\widetilde{\overline{\boldsymbol{M}}}_\mathrm{dev}}{\left\| \widetilde{\overline{\boldsymbol{M}}}_\mathrm{dev} \right\|} \left[\kappa - \kappa^n \right] \right]} : \frac{\widetilde{\overline{\boldsymbol{M}}}_\mathrm{dev}}{\left\| \widetilde{\overline{\boldsymbol{M}}}_\mathrm{dev} \right\|} \quad ,
$$
(3.149b)

with

$$
\frac{\partial \boldsymbol{F}_\mathrm{p}}{\partial \left[\boldsymbol{I} - \frac{\widetilde{\overline{\boldsymbol{M}}}_\mathrm{dev}}{\left\| \widetilde{\overline{\boldsymbol{M}}}_\mathrm{dev} \right\|} \left[\kappa - \kappa^n \right] \right]} = -\left[\boldsymbol{I} - \frac{\widetilde{\overline{\boldsymbol{M}}}_\mathrm{dev}}{\left\| \widetilde{\overline{\boldsymbol{M}}}_\mathrm{dev} \right\|} \left[\kappa - \kappa^n \right] \right]^{-1} \overline{\otimes} \left[\left[\boldsymbol{I} - \frac{\widetilde{\overline{\boldsymbol{M}}}_\mathrm{dev}}{\left\| \widetilde{\overline{\boldsymbol{M}}}_\mathrm{dev} \right\|} \left[\kappa - \kappa^n \right] \right]^{-1} \cdot \boldsymbol{F}_\mathrm{p}^\mathrm{n} \right]^\mathrm{t}.
$$
(3.150)

Taking into account (3.149a) and (3.149b), the derivatives of the Piola stress tensor, see (3.44), can be specified as

$$
\frac{\partial \boldsymbol{P}}{\partial \boldsymbol{F}} = \lambda\, J_\mathrm{e}^2\, \boldsymbol{F}^{-\mathrm{t}} \otimes \boldsymbol{F}^{-\mathrm{t}} - \left[\frac{\lambda}{2} \left[J_\mathrm{e}^2 - 1 \right] - \mu \right] \boldsymbol{F}^{-1} \,\overline{\otimes}\, \boldsymbol{F}^{-\mathrm{t}} + \mu\, \boldsymbol{I} \,\overline{\otimes}\, \boldsymbol{C}_\mathrm{p}^{-1}
$$
(3.151a)

and

$$
\frac{\partial \boldsymbol{P}}{\partial \widetilde{\overline{\boldsymbol{M}}}} = -\left[\lambda\, J_\mathrm{e}^2\, \boldsymbol{F}^{-\mathrm{t}} \otimes \boldsymbol{F}_\mathrm{p}^{-\mathrm{t}} + \mu \left[\boldsymbol{F} \cdot \boldsymbol{C}_\mathrm{p}^{-1} \right] \,\underline{\otimes}\, \boldsymbol{F}_\mathrm{p}^{-1} + \mu\, \boldsymbol{F}_\mathrm{e} \,\overline{\otimes}\, \boldsymbol{C}_\mathrm{p}^{-1} \right] : \frac{\partial \boldsymbol{F}_\mathrm{p}}{\partial \widetilde{\overline{\boldsymbol{M}}}} \quad , \quad (3.151\mathrm{b})
$$

$$
\frac{\partial \boldsymbol{P}}{\partial \kappa} = -\left[\lambda\, J_\mathrm{e}^2\, \boldsymbol{F}^{-\mathrm{t}} \otimes \boldsymbol{F}_\mathrm{p}^{-\mathrm{t}} + \mu \left[\boldsymbol{F} \cdot \boldsymbol{C}_\mathrm{p}^{-1} \right] \,\underline{\otimes}\, \boldsymbol{F}_\mathrm{p}^{-1} + \mu\, \boldsymbol{F}_\mathrm{e} \,\overline{\otimes}\, \boldsymbol{C}_\mathrm{p}^{-1} \right] : \frac{\partial \boldsymbol{F}_\mathrm{p}}{\partial \kappa} \quad . \quad (3.151\mathrm{c})
$$

Analogously, the derivatives of the Mandel stress tensor of the intermediate configuration are given by

$$
\frac{\partial \overline{\boldsymbol{M}}}{\partial \boldsymbol{F}} = \lambda\, J_\mathrm{e}^2\, \boldsymbol{I} \otimes \boldsymbol{F}^{-\mathrm{t}} + \mu\, \boldsymbol{F}_\mathrm{p}^{-\mathrm{t}} \,\underline{\otimes}\, \boldsymbol{F}_\mathrm{e}^\mathrm{t} + \mu\, \boldsymbol{F}_\mathrm{e}^\mathrm{t} \,\overline{\otimes}\, \boldsymbol{F}_\mathrm{p}^{-\mathrm{t}}
$$
(3.152a)

and

$$\frac{\partial \overline{\boldsymbol{M}}}{\partial \widetilde{\overline{\boldsymbol{M}}}} = -\left[\lambda J_{\mathrm{e}}^2 \, \boldsymbol{I} \otimes \boldsymbol{F}_{\mathrm{p}}^{-\mathrm{t}} + \mu \, \boldsymbol{F}_{\mathrm{p}}^{-\mathrm{t}} \, \underline{\otimes} \, \boldsymbol{C}_{\mathrm{e}} + \mu \, \boldsymbol{C}_{\mathrm{e}} \, \overline{\otimes} \, \boldsymbol{F}_{\mathrm{p}}^{-\mathrm{t}} \right] : \frac{\partial \boldsymbol{F}_{\mathrm{p}}}{\partial \widetilde{\overline{\boldsymbol{M}}}} \quad , \tag{3.152b}$$

$$\frac{\partial \overline{\boldsymbol{M}}}{\partial \kappa} = -\left[\lambda J_{\mathrm{e}}^2 \, \boldsymbol{I} \otimes \boldsymbol{F}_{\mathrm{p}}^{-\mathrm{t}} + \mu \, \boldsymbol{F}_{\mathrm{p}}^{-\mathrm{t}} \, \underline{\otimes} \, \boldsymbol{C}_{\mathrm{e}} + \mu \, \boldsymbol{C}_{\mathrm{e}} \, \overline{\otimes} \, \boldsymbol{F}_{\mathrm{p}}^{-\mathrm{t}} \right] : \frac{\partial \boldsymbol{F}_{\mathrm{p}}}{\partial \kappa} \quad . \tag{3.152c}$$

Finally, the derivatives of the yield function are given by

$$\frac{\partial f}{\partial \widetilde{\overline{\boldsymbol{M}}}} = \frac{\widetilde{\overline{\boldsymbol{M}}}_{\mathrm{dev}}}{\left\| \widetilde{\overline{\boldsymbol{M}}}_{\mathrm{dev}} \right\|} \tag{3.153} \qquad\qquad \frac{\partial f}{\partial \kappa} = -H_{\boldsymbol{D}} \tag{3.154}$$

and those of the energetic dual to the dislocation density tensor (3.60) by

$$\frac{\partial \boldsymbol{\Xi}}{\partial \nabla_{\boldsymbol{X}} \boldsymbol{\Theta}_{\mathrm{p}}} = 2 \, H_{\boldsymbol{D}} \, \boldsymbol{I} \, \overline{\otimes} \, \boldsymbol{\epsilon}_0 \tag{3.155a} \qquad\qquad \frac{\partial \boldsymbol{\Xi}}{\partial \kappa} = \boldsymbol{0} \tag{3.155b}$$

and

$$\frac{\partial \boldsymbol{\Xi}}{\partial \widetilde{\overline{\boldsymbol{M}}}} = \boldsymbol{0} \quad . \tag{3.155c}$$

B.2 Derivation of the algorithmic tangent stiffness – crystal plasticity

In this appendix, the contributions to the consistent algorithmic tangent stiffness matrix that is required for a gradient-based solution of the non-linear system of equations (3.125)-(3.127) with corresponding boundary conditions, are presented. A standard Newton update step i in the global iteration procedure is of the form

$$\begin{bmatrix} \boldsymbol{0} \\ \boldsymbol{0} \\ \boldsymbol{0} \end{bmatrix} = \begin{bmatrix} \boldsymbol{f}_{\mathrm{int}}^{\boldsymbol{\varphi}\mathrm{h}} - \boldsymbol{f}_{\mathrm{ext}}^{\boldsymbol{\varphi}\mathrm{h}} \\ \boldsymbol{f}_{\mathrm{int}}^{\widetilde{\overline{\boldsymbol{M}}}^{\mathrm{rel}}\mathrm{h}} \\ \boldsymbol{f}_{\mathrm{int}}^{\boldsymbol{\Theta}_{\mathrm{p}}\mathrm{h}} \end{bmatrix}_i + \begin{bmatrix} \mathbf{K}^{\boldsymbol{\varphi}\boldsymbol{\varphi}} & \mathbf{K}^{\boldsymbol{\varphi}\widetilde{\overline{\boldsymbol{M}}}^{\mathrm{rel}}} & \mathbf{K}^{\boldsymbol{\varphi}\boldsymbol{\Theta}_{\mathrm{p}}} \\ \mathbf{K}^{\widetilde{\overline{\boldsymbol{M}}}^{\mathrm{rel}}\boldsymbol{\varphi}} & \mathbf{K}^{\widetilde{\overline{\boldsymbol{M}}}^{\mathrm{rel}}\widetilde{\overline{\boldsymbol{M}}}^{\mathrm{rel}}} & \mathbf{K}^{\widetilde{\overline{\boldsymbol{M}}}^{\mathrm{rel}}\boldsymbol{\Theta}_{\mathrm{p}}} \\ \mathbf{K}^{\boldsymbol{\Theta}_{\mathrm{p}}\boldsymbol{\varphi}} & \mathbf{K}^{\boldsymbol{\Theta}_{\mathrm{p}}\widetilde{\overline{\boldsymbol{M}}}^{\mathrm{rel}}} & \mathbf{K}^{\boldsymbol{\Theta}_{\mathrm{p}}\boldsymbol{\Theta}_{\mathrm{p}}} \end{bmatrix}_i \cdot \begin{bmatrix} \Delta \widehat{\boldsymbol{\varphi}} \\ \Delta \widehat{\widetilde{\overline{\boldsymbol{M}}}}^{\mathrm{rel}} \\ \Delta \widehat{\boldsymbol{\Theta}}_{\mathrm{p}} \end{bmatrix}_i \tag{3.156}$$

with $\Delta \widehat{\bullet}$ denoting the update in the global list of degrees of freedom $\widehat{\bullet}$, corresponding to the field variable $\bullet$, to be solved for. Here and in the following, the superscripts referring to the time step $\mathrm{n} + 1$ are omitted for the sake of brevity and frequently occurring derivatives are not inserted but summarised at the end of this appendix.

Balance of linear momentum

$$\mathbf{K}^{\boldsymbol{\varphi}\boldsymbol{\varphi}} \quad = \overset{n_{el}}{\underset{e=1}{\mathbf{A}}} \int_{\mathcal{B}_0^e} \nabla_{\boldsymbol{x}} N_D^{\boldsymbol{\varphi}} \cdot \frac{\mathrm{d}\boldsymbol{P}^{\mathrm{t}}}{\mathrm{d}\boldsymbol{F}} \cdot \nabla_{\boldsymbol{x}} N_A^{\boldsymbol{\varphi}} \, \mathrm{d}V_e \tag{3.157a}$$

$$\mathbf{K}^{\boldsymbol{\varphi}\widetilde{\overline{\boldsymbol{M}}}^{\mathrm{rel}}} = \overset{n_{el}}{\underset{e=1}{\mathbf{A}}} \int_{\mathcal{B}_0^e} \nabla_{\boldsymbol{x}} N_D^{\boldsymbol{\varphi}} \cdot \frac{\mathrm{d}\boldsymbol{P}^{\mathrm{t}}}{\mathrm{d}\widetilde{\overline{\boldsymbol{M}}}^{\mathrm{rel}}} N_B^{\widetilde{\overline{\boldsymbol{M}}}^{\mathrm{rel}}} \, \mathrm{d}V_e \tag{3.157b}$$

$$\mathbf{K}^{\boldsymbol{\varphi}\boldsymbol{\Theta}_{\mathrm{p}}} = \overset{n_{el}}{\underset{e=1}{\mathbf{A}}} \quad \mathbf{0} \tag{3.157c}$$

Balance equation of the generalised Mandel stress tensor

$$\mathbf{K}^{\widetilde{\overline{\boldsymbol{M}}}^{\mathrm{rel}}\boldsymbol{\varphi}} \quad = \overset{n_{el}}{\underset{e=1}{\mathbf{A}}} \int_{\mathcal{B}_0^e} \quad \boldsymbol{\Xi} \cdot \left[\boldsymbol{\epsilon}_0 \cdot \nabla_{\boldsymbol{X}} N_E^{\widetilde{\overline{\boldsymbol{M}}}^{\mathrm{rel}}} \right] \cdot \frac{\mathrm{d}\boldsymbol{F}_{\mathrm{p}}^{\mathrm{t}}}{\mathrm{d}\boldsymbol{F}} \cdot \nabla_{\boldsymbol{X}} N_A^{\boldsymbol{\varphi}} \, \mathrm{d}V_e \tag{3.158a}$$

$$\mathbf{K}^{\widetilde{\overline{\boldsymbol{M}}}^{\mathrm{rel}}\widetilde{\overline{\boldsymbol{M}}}^{\mathrm{rel}}} = \overset{n_{el}}{\underset{e=1}{\mathbf{A}}} \int_{\mathcal{B}_0^e} \quad N_E^{\widetilde{\overline{\boldsymbol{M}}}^{\mathrm{rel}}} \, \boldsymbol{I} \,\overline{\otimes}\, \boldsymbol{I} \, N_B^{\widetilde{\overline{\boldsymbol{M}}}^{\mathrm{rel}}}$$

$$+ \boldsymbol{\Xi} \cdot \left[\boldsymbol{\epsilon}_0 \cdot \nabla_{\boldsymbol{X}} N_E^{\widetilde{\overline{\boldsymbol{M}}}^{\mathrm{rel}}} \right] \cdot \frac{\mathrm{d}\boldsymbol{F}_{\mathrm{p}}^{\mathrm{t}}}{\mathrm{d}\widetilde{\overline{\boldsymbol{M}}}^{\mathrm{rel}}} N_B^{\widetilde{\overline{\boldsymbol{M}}}^{\mathrm{rel}}} \, \mathrm{d}V_e \tag{3.158b}$$

$$\mathbf{K}^{\widetilde{\overline{\boldsymbol{M}}}^{\mathrm{rel}}\boldsymbol{\Theta}_{\mathrm{p}}} \quad = \overset{n_{el}}{\underset{e=1}{\mathbf{A}}} \int_{\mathcal{B}_0^e} \quad \left[\boldsymbol{I} \,\overline{\otimes}\, \left[\boldsymbol{F}_{\mathrm{p}} \cdot \boldsymbol{\epsilon}_0 \cdot \nabla_{\boldsymbol{X}} N_E^{\widetilde{\overline{\boldsymbol{M}}}^{\mathrm{rel}}} \right] \right] : \frac{\partial \boldsymbol{\Xi}}{\partial \nabla_{\boldsymbol{X}} \boldsymbol{\Theta}_{\mathrm{p}}} \cdot \nabla_{\boldsymbol{X}} N_C^{\boldsymbol{\Theta}_{\mathrm{p}}}$$

$$+ \left[\boldsymbol{I} \,\overline{\otimes}\, \left[\nabla_{\boldsymbol{X}} \boldsymbol{\Theta}_{\mathrm{p}} : \boldsymbol{\epsilon}_0 \, N_E^{\widetilde{\overline{\boldsymbol{M}}}^{\mathrm{rel}}} \right] \right] : \frac{\partial \boldsymbol{\Xi}}{\partial \nabla_{\boldsymbol{X}} \boldsymbol{\Theta}_{\mathrm{p}}} \cdot \nabla_{\boldsymbol{X}} N_C^{\boldsymbol{\Theta}_{\mathrm{p}}}$$

$$+ N_E^{\widetilde{\overline{\boldsymbol{M}}}^{\mathrm{rel}}} \left[\boldsymbol{\Xi} \cdot \boldsymbol{\epsilon}_0 \cdot \nabla_{\boldsymbol{X}} N_C^{\boldsymbol{\Theta}_{\mathrm{p}}} \right] \,\underline{\otimes}\, \boldsymbol{I} \, \mathrm{d}V_e \tag{3.158c}$$

L_2-projection of the plastic deformation gradient

$$\mathbf{K}^{\boldsymbol{\Theta}_{\mathrm{p}}\boldsymbol{\varphi}} \quad = \overset{n_{el}}{\underset{e=1}{\mathbf{A}}} \int_{\mathcal{B}_0^e} \quad N_F^{\boldsymbol{\Theta}_{\mathrm{p}}} \frac{\mathrm{d}\boldsymbol{F}_{\mathrm{p}}}{\mathrm{d}\boldsymbol{F}} N_A^{\boldsymbol{\varphi}} \, \mathrm{d}V_e \tag{3.159a}$$

$$\mathbf{K}^{\boldsymbol{\Theta}_{\mathrm{p}}\widetilde{\overline{\boldsymbol{M}}}^{\mathrm{rel}}} = \overset{n_{el}}{\underset{e=1}{\mathbf{A}}} \int_{\mathcal{B}_0^e} \quad N_F^{\boldsymbol{\Theta}_{\mathrm{p}}} \frac{\mathrm{d}\boldsymbol{F}_{\mathrm{p}}}{\mathrm{d}\widetilde{\overline{\boldsymbol{M}}}^{\mathrm{rel}}} N_B^{\widetilde{\overline{\boldsymbol{M}}}^{\mathrm{rel}}} \, \mathrm{d}V_e \tag{3.159b}$$

$$\mathbf{K}^{\boldsymbol{\Theta}_{\mathrm{p}}\boldsymbol{\Theta}_{\mathrm{p}}} \quad = \overset{n_{el}}{\underset{e=1}{\mathbf{A}}} \int_{\mathcal{B}_0^e} -N_F^{\boldsymbol{\Theta}_{\mathrm{p}}} \, \boldsymbol{I} \,\overline{\otimes}\, \boldsymbol{I} \, N_C^{\boldsymbol{\Theta}_{\mathrm{p}}} \, \mathrm{d}V_e \tag{3.159c}$$

Supplementary derivatives   This paragraph focuses on (the derivation of) the derivatives $\mathrm{d}\boldsymbol{P}/\mathrm{d}\boldsymbol{F}$, $\mathrm{d}\boldsymbol{P}/\mathrm{d}\widetilde{\overline{\boldsymbol{M}}}^{\mathrm{rel}}$, $\mathrm{d}\boldsymbol{F}_{\mathrm{p}}/\mathrm{d}\boldsymbol{F}$, $\mathrm{d}\boldsymbol{F}_{\mathrm{p}}/\mathrm{d}\widetilde{\overline{\boldsymbol{M}}}^{\mathrm{rel}}$ and $\partial \boldsymbol{\Xi}/\partial \nabla_{\boldsymbol{X}} \boldsymbol{\Theta}_{\mathrm{p}}$, which are required to set up the consistent algorithmic tangent stiffness. Noting that the Piola stress tensor $\boldsymbol{P}$

in (3.44) can be regarded as a function of $\boldsymbol{F}$ and $\boldsymbol{F}_\mathrm{p}$, with $\boldsymbol{F}_\mathrm{p}$ being an implicit function of $\boldsymbol{F}$ and $\widetilde{\overline{\boldsymbol{M}}}^{\mathrm{rel}}$, the total differential of $\boldsymbol{P}$ results in

$$\mathrm{d}\boldsymbol{P} = \left[\frac{\partial \boldsymbol{P}}{\partial \boldsymbol{F}} + \frac{\partial \boldsymbol{P}}{\partial \boldsymbol{F}_\mathrm{p}} : \frac{\mathrm{d}\boldsymbol{F}_\mathrm{p}}{\mathrm{d}\boldsymbol{F}}\right] : \mathrm{d}\boldsymbol{F} + \left[\frac{\partial \boldsymbol{P}}{\partial \boldsymbol{F}_\mathrm{p}} : \frac{\mathrm{d}\boldsymbol{F}_\mathrm{p}}{\mathrm{d}\widetilde{\overline{\boldsymbol{M}}}^{\mathrm{rel}}}\right] : \mathrm{d}\widetilde{\overline{\boldsymbol{M}}}^{\mathrm{rel}} \quad , \tag{3.160}$$

with

$$\frac{\partial \boldsymbol{P}}{\partial \boldsymbol{F}} = \lambda\, J_\mathrm{e}^2\, \boldsymbol{F}^{-\mathrm{t}} \otimes \boldsymbol{F}^{-\mathrm{t}} - \left[\frac{\lambda}{2}\left[J_\mathrm{e}^2 - 1\right] - \mu\right]\boldsymbol{F}^{-1}\,\overline{\otimes}\,\boldsymbol{F}^{-\mathrm{t}} + \mu\,\boldsymbol{I}\,\overline{\otimes}\,\boldsymbol{C}_\mathrm{p}^{-1} \quad , \tag{3.161a}$$

$$\frac{\partial \boldsymbol{P}}{\partial \boldsymbol{F}_\mathrm{p}} = -\left[\lambda\, J_\mathrm{e}^2\, \boldsymbol{F}^{-\mathrm{t}} \otimes \boldsymbol{F}_\mathrm{p}^{-\mathrm{t}} + \mu\left[\boldsymbol{F}\cdot\boldsymbol{C}_\mathrm{p}^{-1}\right]\,\underline{\otimes}\,\boldsymbol{F}_\mathrm{p}^{-1} + \mu\,\boldsymbol{F}_\mathrm{e}\,\overline{\otimes}\,\boldsymbol{C}_\mathrm{p}^{-1}\right] \quad , \tag{3.161b}$$

and

$$\mathrm{d}\boldsymbol{F}_\mathrm{p} = \left[\sum_{\alpha=1}^{n_\alpha}\left[\boldsymbol{I} - \Theta\,\boldsymbol{\Lambda}_\mathrm{p}\right]^{-1}\cdot\overline{\boldsymbol{Z}}^{(\alpha)}\cdot\left[\boldsymbol{I} + \Theta\left[\boldsymbol{I} - \Theta\,\boldsymbol{\Lambda}_\mathrm{p}\right]^{-1}\cdot\boldsymbol{\Lambda}_\mathrm{p}\right]\cdot\boldsymbol{F}_\mathrm{p}^n \otimes \frac{\mathrm{d}\Delta\widetilde{\gamma}^{(\alpha)}}{\mathrm{d}\boldsymbol{F}}\right] : \mathrm{d}\boldsymbol{F}$$

$$+ \left[\sum_{\alpha=1}^{n_\alpha}\left[\boldsymbol{I} - \Theta\,\boldsymbol{\Lambda}_\mathrm{p}\right]^{-1}\cdot\overline{\boldsymbol{Z}}^{(\alpha)}\cdot\left[\boldsymbol{I} + \Theta\left[\boldsymbol{I} - \Theta\,\boldsymbol{\Lambda}_\mathrm{p}\right]^{-1}\cdot\boldsymbol{\Lambda}_\mathrm{p}\right]\cdot\boldsymbol{F}_\mathrm{p}^n \otimes \frac{\mathrm{d}\Delta\widetilde{\gamma}^{(\alpha)}}{\mathrm{d}\widetilde{\overline{\boldsymbol{M}}}^{\mathrm{rel}}}\right] : \mathrm{d}\widetilde{\overline{\boldsymbol{M}}}^{\mathrm{rel}} \tag{3.162}$$

To derive the derivatives $\mathrm{d}\Delta\widetilde{\gamma}^{(\alpha)}/\mathrm{d}\boldsymbol{F}$ and $\mathrm{d}\Delta\widetilde{\gamma}^{(\alpha)}/\mathrm{d}\widetilde{\overline{\boldsymbol{M}}}^{\mathrm{rel}}$ use will be made of the implicit function theorem. Denoting the generalised residual of a slip system at integration point level by $R_{\Delta\widetilde{\gamma}^{(\alpha)}}$, with $R_{\Delta\widetilde{\gamma}^{(\alpha)}}$ being either $R_{\Delta\widetilde{\gamma}^{(\alpha)}}^{<}$ or $R_{\Delta\widetilde{\gamma}^{(\alpha)}}^{>}$, depending on the current state as outlined in Section 3.3.3.3, and following standard procedure one arrives at

$$\begin{bmatrix} \mathrm{d}\Delta\widetilde{\gamma}^{(1)} \\ \vdots \\ \mathrm{d}\Delta\widetilde{\gamma}^{(n_\alpha)} \\ \mathrm{d}\Delta\widetilde{\kappa}_\mathrm{cp} \end{bmatrix} = - \begin{bmatrix} \frac{\partial R_{\Delta\widetilde{\gamma}^{(1)}}}{\partial\Delta\widetilde{\gamma}^{(1)}} & \cdots & \frac{\partial R_{\Delta\widetilde{\gamma}^{(1)}}}{\partial\Delta\widetilde{\gamma}^{(n_\alpha)}} & \frac{\partial R_{\Delta\widetilde{\gamma}^{(1)}}}{\partial\Delta\widetilde{\kappa}_\mathrm{cp}} \\ \vdots & \ddots & \vdots & \vdots \\ \frac{\partial R_{\Delta\widetilde{\gamma}^{(n_\alpha)}}}{\partial\Delta\widetilde{\gamma}^{(1)}} & \cdots & \frac{\partial R_{\Delta\widetilde{\gamma}^{(n_\alpha)}}}{\partial\Delta\widetilde{\gamma}^{(n_\alpha)}} & \frac{\partial R_{\Delta\widetilde{\gamma}^{(n_\alpha)}}}{\partial\Delta\widetilde{\kappa}_\mathrm{cp}} \\ \frac{\partial R_{\Delta\widetilde{\kappa}_\mathrm{cp}}}{\partial\Delta\widetilde{\gamma}^{(1)}} & \cdots & \frac{\partial R_{\Delta\widetilde{\kappa}_\mathrm{cp}}}{\partial\Delta\widetilde{\gamma}^{(n_\alpha)}} & \frac{\partial R_{\Delta\widetilde{\kappa}_\mathrm{cp}}}{\partial\Delta\widetilde{\kappa}_\mathrm{cp}} \end{bmatrix}^{-1} \cdot \begin{bmatrix} \frac{\partial R_{\Delta\widetilde{\gamma}^{(1)}}}{\partial\boldsymbol{F}} \\ \vdots \\ \frac{\partial R_{\Delta\widetilde{\gamma}^{(n_\alpha)}}}{\partial\boldsymbol{F}} \\ \frac{\partial R_{\Delta\widetilde{\kappa}_\mathrm{cp}}}{\partial\boldsymbol{F}} \end{bmatrix} : \mathrm{d}\boldsymbol{F}$$

$$- \begin{bmatrix} \frac{\partial R_{\Delta\widetilde{\gamma}^{(1)}}}{\partial\Delta\widetilde{\gamma}^{(1)}} & \cdots & \frac{\partial R_{\Delta\widetilde{\gamma}^{(1)}}}{\partial\Delta\widetilde{\gamma}^{(n_\alpha)}} & \frac{\partial R_{\Delta\widetilde{\gamma}^{(1)}}}{\partial\Delta\widetilde{\kappa}_\mathrm{cp}} \\ \vdots & \ddots & \vdots & \vdots \\ \frac{\partial R_{\Delta\widetilde{\gamma}^{(n_\alpha)}}}{\partial\Delta\widetilde{\gamma}^{(1)}} & \cdots & \frac{\partial R_{\Delta\widetilde{\gamma}^{(n_\alpha)}}}{\partial\Delta\widetilde{\gamma}^{(n_\alpha)}} & \frac{\partial R_{\Delta\widetilde{\gamma}^{(n_\alpha)}}}{\partial\Delta\widetilde{\kappa}_\mathrm{cp}} \\ \frac{\partial R_{\Delta\widetilde{\kappa}_\mathrm{cp}}}{\partial\Delta\widetilde{\gamma}^{(1)}} & \cdots & \frac{\partial R_{\Delta\widetilde{\kappa}_\mathrm{cp}}}{\partial\Delta\widetilde{\gamma}^{(n_\alpha)}} & \frac{\partial R_{\Delta\widetilde{\kappa}_\mathrm{cp}}}{\partial\Delta\widetilde{\kappa}_\mathrm{cp}} \end{bmatrix}^{-1} \cdot \begin{bmatrix} \frac{\partial R_{\Delta\widetilde{\gamma}^{(1)}}}{\partial\widetilde{\overline{\boldsymbol{M}}}^{\mathrm{rel}}} \\ \vdots \\ \frac{\partial R_{\Delta\widetilde{\gamma}^{(n_\alpha)}}}{\partial\widetilde{\overline{\boldsymbol{M}}}^{\mathrm{rel}}} \\ \frac{\partial R_{\Delta\widetilde{\kappa}_\mathrm{cp}}}{\partial\widetilde{\overline{\boldsymbol{M}}}^{\mathrm{rel}}} \end{bmatrix} : \mathrm{d}\widetilde{\overline{\boldsymbol{M}}}^{\mathrm{rel}}$$

$$\tag{3.163}$$

The derivatives of the residual functions with respect to the increments in the plastic slips $\Delta\widetilde{\gamma}^{(\alpha)}$ and with respect to the increment in the accumulated plastic strain-like variable $\Delta\widetilde{\kappa}_{\mathrm{cp}}$ are provided in Appendix B.3. The derivatives of the residual functions with respect to $\boldsymbol{F}$ read

$$\frac{\partial R_{\Delta\widetilde{\gamma}^{(\alpha)}}^{<}}{\partial \boldsymbol{F}} = \Delta\gamma_0\, h_e\, \frac{2\,\mu}{\left|\widetilde{\overline{M}}^{(\alpha)}\right|}\, \left|\frac{\widetilde{\overline{M}}^{(\alpha)}}{\widetilde{q}_{\mathrm{cp}}}\right|^{h_e}\, \boldsymbol{F}_{\mathrm{e}} \cdot \overline{\boldsymbol{Z}}^{(\alpha)} \cdot \boldsymbol{F}_{\mathrm{p}}^{-\mathrm{t}} \quad , \tag{3.164a}$$

$$\frac{\partial R_{\Delta\widetilde{\gamma}^{(\alpha)}}^{>}}{\partial \boldsymbol{F}} = \frac{2\,\mu}{\left|\widetilde{q}_{\mathrm{cp}}\right|}\, \mathrm{sgn}\left(\widetilde{\overline{M}}^{(\alpha)}\right)\, \boldsymbol{F}_{\mathrm{e}} \cdot \overline{\boldsymbol{Z}}^{(\alpha)} \cdot \boldsymbol{F}_{\mathrm{p}}^{-\mathrm{t}} \quad , \tag{3.164b}$$

$$\frac{\partial R_{\Delta\widetilde{\kappa}_{\mathrm{cp}}}}{\partial \boldsymbol{F}} = \sum_{\alpha=1}^{\mathrm{n}_\alpha} -\frac{h_e}{h_e+1}\, \frac{2\,\mu}{\widetilde{q}_{\mathrm{cp}}}\, \Delta\widetilde{\gamma}^{(\alpha)}\, \boldsymbol{F}_{\mathrm{e}} \cdot \overline{\boldsymbol{Z}}^{(\alpha)} \cdot \boldsymbol{F}_{\mathrm{p}}^{-\mathrm{t}} \quad , \tag{3.164c}$$

and those with respect to $\widetilde{\overline{\boldsymbol{M}}}^{\mathrm{rel}}$ are given by

$$\frac{\partial R_{\Delta\widetilde{\gamma}^{(\alpha)}}^{<}}{\partial \widetilde{\overline{\boldsymbol{M}}}^{\mathrm{rel}}} = \Delta\gamma_0\, h_e\, \frac{1}{\left|\widetilde{\overline{M}}^{(\alpha)}\right|}\, \left|\frac{\widetilde{\overline{M}}^{(\alpha)}}{\widetilde{q}_{\mathrm{cp}}}\right|^{h_e}\, \overline{\boldsymbol{Z}}^{(\alpha)} \quad , \tag{3.165a}$$

$$\frac{\partial R_{\Delta\widetilde{\gamma}^{(\alpha)}}^{>}}{\partial \widetilde{\overline{\boldsymbol{M}}}^{\mathrm{rel}}} = \frac{1}{\left|\widetilde{q}_{\mathrm{cp}}\right|}\, \mathrm{sgn}\left(\widetilde{\overline{M}}^{(\alpha)}\right)\, \overline{\boldsymbol{Z}}^{(\alpha)} \quad , \tag{3.165b}$$

$$\frac{\partial R_{\Delta\widetilde{\kappa}_{\mathrm{cp}}}}{\partial \widetilde{\overline{\boldsymbol{M}}}^{\mathrm{rel}}} = \sum_{\alpha=1}^{\mathrm{n}_\alpha} -\frac{h_e}{h_e+1}\, \frac{1}{\widetilde{q}_{\mathrm{cp}}}\, \Delta\widetilde{\gamma}^{(\alpha)}\, \overline{\boldsymbol{Z}}^{(\alpha)} \quad . \tag{3.165c}$$

Finally, the derivative of the energetic dual to the dislocation density tensor $\boldsymbol{\Xi}$ with respect to $\nabla_{\boldsymbol{X}}\boldsymbol{\Theta}_{\mathrm{p}}$ can be specified as

$$\frac{\partial \boldsymbol{\Xi}}{\partial \nabla_{\boldsymbol{X}}\boldsymbol{\Theta}_{\mathrm{p}}} = 2\, H_{\boldsymbol{D}}\, \boldsymbol{I}\, \overline{\otimes}\, \boldsymbol{\epsilon}_0 \quad . \tag{3.166}$$

B.3 Iteration scheme at quadrature point level

In this appendix, the derivatives of the residual functions (3.133)-(3.135) with respect to the primary variables $\Delta\widetilde{\gamma}^{(1)}, \ldots, \Delta\widetilde{\gamma}^{(\mathrm{n}_\alpha)}$ and $\Delta\widetilde{\kappa}_{\mathrm{cp}}$ will briefly be summarised, assuming the functional dependencies

$$R_{\Delta\widetilde{\gamma}^{(\alpha)}}^{<}\left(\Delta\widetilde{\gamma}^{(1)},\ldots,\Delta\widetilde{\gamma}^{(\mathrm{n}_\alpha)},\Delta\widetilde{\kappa}_{\mathrm{cp}};\boldsymbol{F},\boldsymbol{F}_{\mathrm{p}}^{n},\widetilde{\kappa}_{\mathrm{cp}}^{n}\right)\quad,\tag{3.167a}$$

$$R_{\Delta\widetilde{\gamma}^{(\alpha)}}^{>}\left(\Delta\widetilde{\gamma}^{(1)},\ldots,\Delta\widetilde{\gamma}^{(\mathrm{n}_\alpha)},\Delta\widetilde{\kappa}_{\mathrm{cp}};\boldsymbol{F},\boldsymbol{F}_{\mathrm{p}}^{n},\widetilde{\kappa}_{\mathrm{cp}}^{n}\right)\quad,\tag{3.167b}$$

$$R_{\Delta\widetilde{\kappa}_{\mathrm{cp}}}\left(\Delta\widetilde{\gamma}^{(1)},\ldots,\Delta\widetilde{\gamma}^{(\mathrm{n}_\alpha)},\Delta\widetilde{\kappa}_{\mathrm{cp}};\boldsymbol{F},\boldsymbol{F}_{\mathrm{p}}^{n},\widetilde{\kappa}_{\mathrm{cp}}^{n}\right)\quad.\tag{3.167c}$$

The derivatives of the residual function (3.133) with respect to the increments in the plastic slips and with respect to the accumulated plastic strain-like variable are given by

$$\frac{\partial R_{\Delta\widetilde{\gamma}^{(\alpha)}}^{<}}{\partial\Delta\widetilde{\gamma}^{(\beta)}}=\quad-\delta^{\alpha\beta}+\Delta\gamma_0\,h_e\,\frac{1}{\left|\widetilde{\overline{M}}^{(\alpha)}\right|}\left|\frac{\widetilde{\overline{M}}^{(\alpha)}}{\widetilde{q}_{\mathrm{cp}}}\right|^{h_e}\frac{\partial\widetilde{\overline{M}}^{(\alpha)}}{\partial\Delta\widetilde{\gamma}^{(\beta)}}\quad,\tag{3.168a}$$

$$\frac{\partial R_{\Delta\widetilde{\gamma}^{(\alpha)}}^{<}}{\partial\Delta\widetilde{\kappa}_{\mathrm{cp}}}=\mathrm{sgn}\left(\widetilde{\overline{M}}^{(\alpha)}\right)\Delta\gamma_0\,h_e\,\frac{1}{\left|\widetilde{q}_{\mathrm{cp}}\right|}\left|\frac{\widetilde{\overline{M}}^{(\alpha)}}{\widetilde{q}_{\mathrm{cp}}}\right|^{h_e}\frac{\partial\widetilde{q}_{\mathrm{cp}}}{\partial\Delta\widetilde{\kappa}_{\mathrm{cp}}}\quad.\tag{3.168b}$$

The derivatives of the reformulated residual function, (3.134), read

$$\frac{\partial R_{\Delta\widetilde{\gamma}^{(\alpha)}}^{>}}{\partial\Delta\widetilde{\gamma}^{(\beta)}}=-\frac{1}{h_e}\left[\frac{\Delta\widetilde{\gamma}^{(\alpha)}}{\Delta\gamma_0\,\mathrm{sgn}\left(\widetilde{\overline{M}}^{(\alpha)}\right)}\right]^{\frac{1}{h_e}-1}\frac{\delta^{\alpha\beta}}{\Delta\gamma_0\,\mathrm{sgn}\left(\widetilde{\overline{M}}^{(\alpha)}\right)}$$
$$+\frac{1}{\left|\widetilde{q}_{\mathrm{cp}}\right|}\,\mathrm{sgn}\left(\widetilde{\overline{M}}^{(\alpha)}\right)\frac{\partial\widetilde{\overline{M}}^{(\alpha)}}{\partial\Delta\widetilde{\gamma}^{(\beta)}}\quad,\tag{3.169a}$$

$$\frac{\partial R_{\Delta\widetilde{\gamma}^{(\alpha)}}^{>}}{\partial\Delta\widetilde{\kappa}_{\mathrm{cp}}}=\frac{\left|\widetilde{\overline{M}}^{(\alpha)}\right|}{\widetilde{q}_{\mathrm{cp}}^{2}}\frac{\partial\widetilde{q}_{\mathrm{cp}}}{\partial\Delta\widetilde{\kappa}_{\mathrm{cp}}}\quad,\tag{3.169b}$$

and the ones corresponding to (3.135) can be specified as

$$\frac{\partial R_{\Delta\widetilde{\kappa}_{\mathrm{cp}}}}{\partial\Delta\widetilde{\gamma}^{(\beta)}}=-\frac{1}{\widetilde{q}_{\mathrm{cp}}}\frac{h_e}{h_e+1}\left[\widetilde{\overline{M}}^{(\beta)}+\sum_{\alpha=1}^{\mathrm{n}_\alpha}\Delta\widetilde{\gamma}^{(\alpha)}\frac{\partial\widetilde{\overline{M}}^{(\alpha)}}{\partial\Delta\widetilde{\gamma}^{(\beta)}}\right]\quad,\tag{3.170a}$$

$$\frac{\partial R_{\Delta\widetilde{\kappa}_{\mathrm{cp}}}}{\partial\Delta\widetilde{\kappa}_{\mathrm{cp}}}=-1+\frac{h_e}{h_e+1}\left[\sum_{\alpha=1}^{\mathrm{n}_\alpha}\Delta\widetilde{\gamma}^{(\alpha)}\,\widetilde{\overline{M}}^{(\alpha)}\right]\frac{1}{\widetilde{q}_{\mathrm{cp}}^{2}}\frac{\partial\widetilde{q}_{\mathrm{cp}}}{\partial\Delta\widetilde{\kappa}_{\mathrm{cp}}}\quad.\tag{3.170b}$$

The derivative of $\widetilde{\overline{M}}^{(\alpha)}$ with respect to $\Delta\widetilde{\gamma}^{(\beta)}$, namely

$$\frac{\partial\widetilde{\overline{M}}^{(\alpha)}}{\partial\Delta\widetilde{\gamma}^{(\beta)}} = \left[2\,\mu\,\boldsymbol{F}_{\mathrm{e}}\cdot\overline{\boldsymbol{Z}}^{(\alpha)}\right] : \left[-\boldsymbol{F}_{\mathrm{e}}\,\overline{\otimes}\,\boldsymbol{F}_{\mathrm{p}}^{-\mathrm{t}}\right]$$
$$: \left[[\boldsymbol{I}-\Theta\,\boldsymbol{\varLambda}_{\mathrm{p}}]^{-1}\cdot\overline{\boldsymbol{Z}}^{(\alpha)}\cdot\left[\boldsymbol{I}+\Theta\,[\boldsymbol{I}-\Theta\,\boldsymbol{\varLambda}_{\mathrm{p}}]^{-1}\cdot\boldsymbol{\varLambda}_{\mathrm{p}}\right]\cdot\boldsymbol{F}_{\mathrm{p}}^{n}\right]$$
$$(3.171)$$

and the derivative of $\widetilde{q}_{\mathrm{cp}}$ with respect to $\Delta\widetilde{\kappa}_{\mathrm{cp}}$, i.e.

$$\frac{\partial\widetilde{q}_{\mathrm{cp}}}{\partial\Delta\widetilde{\kappa}_{\mathrm{cp}}} = -h_0\,\mathrm{sech}^2\left(\frac{h_0\,\left[\widetilde{\kappa}_{\mathrm{cp}}^{\,n}+\Delta\widetilde{\kappa}_{\mathrm{cp}}\right]}{\tau_\infty-\tau_0}\right) \tag{3.172}$$

have not been inserted in the previous equations for the sake of clarity.

4 Deformation-induced anisotropy evolution in finite plasticity

Motivated by the experimental findings on cold-rolled sheet metal by Kim and Yin, [65], which suggest an evolution of the (plastic) material symmetry group in finite plastic deformation processes, this chapter focuses on the modelling of evolving plastic anisotropies and is structured as follows:

Section 4.1 *(Constitutive framework)* sets the stage by briefly introducing the extended notation, and the covariant modelling framework which was proposed in [77]. In addition, general results with regard to the evaluation of the dissipation inequality are presented.

Section 4.2 *(Elasto-plastic prototype model)* focuses on the elaboration of a specific elasto-plastic prototype model. In particular, the dissipation inequality is analysed and the thermodynamic consistency of the proposed model is shown.

Section 4.3 *(Plastic spin prototype model)* first gives a brief summary of the experimental findings by Kim and Yin, [65]. Motivated by the latter, the evolution equation for the structural tensor is studied in detail in a second step and a specific, well-interpretable, form is proposed.

Section 4.4 *(Representative simulation results)* addresses the solution of the resulting coupled system of differential equations and presents finite element-based simulation results for tension tests in two- and three-dimensional settings which are compared with the experimental observations. In addition, simulation results for in-plane torsion tests are discussed to analyse the model's properties for shear dominated deformation states.

4.1 Constitutive framework

After introducing the extended notation to be used in this chapter in Section 4.1.1, the theoretical foundations of the modelling of evolving material symmetry groups as derived in [77] are briefly summarised in Section 4.1.2, and the implications on the dissipation inequality are studied in Section 4.1.3 based on the findings presented in [9].

4.1.1 Notation

Since the differential geometric nature of the various tensor valued quantities to be introduced in this section is of primary interest for the ensuing developments, a more rigorous notation than the one used in the previous chapters will be adopted. To this end let $\boldsymbol{\alpha}$ and $\boldsymbol{\beta}$ be elements of the tangent space $T_{\boldsymbol{X}}\mathcal{B}_0$ at point $\boldsymbol{X}$ and let $\boldsymbol{\gamma}$ be an element of the corresponding cotangent space $T_{\boldsymbol{X}}^{\star}\mathcal{B}_0$ which is defined by means of duality pairings according to $\langle \bullet, \bullet \rangle_{\mathcal{B}_0} : T_{\boldsymbol{X}}^{\star}\mathcal{B}_0 \times T_{\boldsymbol{X}}\mathcal{B}_0 \to \mathbb{R}$. Furthermore, let $\boldsymbol{G}^{\flat}$ denote the (covariant) metric tensor on $\mathcal{B}_0$, see e.g. [77, 83] for further details.

For a mixed-variant tensor $\boldsymbol{T} : T_{\boldsymbol{X}}\mathcal{B}_0 \to T_{\boldsymbol{X}}\mathcal{B}_0$ the adjoint $\boldsymbol{T}^{\star} : T_{\boldsymbol{X}}^{\star}\mathcal{B}_0 \to T_{\boldsymbol{X}}^{\star}\mathcal{B}_0$ is defined by the identity

$$\boldsymbol{\gamma} \cdot \boldsymbol{T} \cdot \boldsymbol{\alpha} = \boldsymbol{\alpha} \cdot \boldsymbol{T}^{\star} \cdot \boldsymbol{\gamma} \quad \forall \quad \boldsymbol{\alpha} \in T_{\boldsymbol{X}}\mathcal{B}_0, \; \boldsymbol{\gamma} \in T_{\boldsymbol{X}}^{\star}\mathcal{B}_0 \tag{4.1}$$

and the transpose $\boldsymbol{T}^{\mathrm{t}} : T_{\boldsymbol{X}}\mathcal{B}_0 \to T_{\boldsymbol{X}}\mathcal{B}_0$ is given by

$$\left[\boldsymbol{G}^{\flat} \cdot \boldsymbol{\alpha} \right] \cdot [\boldsymbol{T} \cdot \boldsymbol{\beta}] = \left[\boldsymbol{G}^{\flat} \cdot \boldsymbol{\beta} \right] \cdot \left[\boldsymbol{T}^{\mathrm{t}} \cdot \boldsymbol{\alpha} \right] \quad \forall \quad \boldsymbol{\alpha}, \boldsymbol{\beta} \in T_{\boldsymbol{X}}\mathcal{B}_0 \quad . \tag{4.2}$$

Taking into account (4.1) and (4.2) furthermore reveals the useful relation

$$\boldsymbol{T}^{\mathrm{t}} = \left[\boldsymbol{G}^{\flat} \right]^{-1} \cdot \boldsymbol{T}^{\star} \cdot \boldsymbol{G}^{\flat} \quad . \tag{4.3}$$

If the tensor $\boldsymbol{T} : T_{\boldsymbol{X}}\mathcal{B}_0 \to T_{\boldsymbol{X}}\mathcal{B}_0$ fulfils the property $\boldsymbol{T} = \boldsymbol{T}^{\mathrm{t}}$, respectively $\boldsymbol{T}^{\star} \cdot \boldsymbol{G}^{\flat} = \boldsymbol{G}^{\flat} \cdot \boldsymbol{T}$, it will be termed $\boldsymbol{G}^{\flat}$-symmetric. Likewise, the tensor $\boldsymbol{T}$ will be referred to as $\boldsymbol{G}^{\flat}$-skew if the relation $\boldsymbol{T} = -\boldsymbol{T}^{\mathrm{t}}$ or equivalently $\boldsymbol{T}^{\star} \cdot \boldsymbol{G}^{\flat} = -\boldsymbol{G}^{\flat} \cdot \boldsymbol{T}$, holds. The $\boldsymbol{G}^{\flat}$-symmetric part of a tensor will be denoted by $\boldsymbol{T}^{\boldsymbol{G}^{\flat}-\mathrm{sym}}$ and the $\boldsymbol{G}^{\flat}$-skew part by $\boldsymbol{T}^{\boldsymbol{G}^{\flat}-\mathrm{skw}}$. Moreover, we term a tensor $\boldsymbol{G}^{\flat}$-orthogonal if it fulfils the metric preservation property, that is if

$$\boldsymbol{\alpha} \cdot \boldsymbol{T}^{\star} \cdot \boldsymbol{G}^{\flat} \cdot \boldsymbol{T} \cdot \boldsymbol{\beta} = \boldsymbol{\alpha} \cdot \boldsymbol{G}^{\flat} \cdot \boldsymbol{\beta} \quad \forall \quad \boldsymbol{\alpha}, \boldsymbol{\beta} \in T_{\boldsymbol{X}}\mathcal{B}_0 \tag{4.4}$$

holds.

4.1.2 Modelling of evolving material symmetry groups

In [77] a continuum-mechanical theory for the modelling of anisotropic finite plasticity is proposed which is based on the principle of covariance. Although the proposed modelling approach tries to circumvent the explicit use of a local, unstressed intermediate configuration such that the classic multiplicative split does not need to be invoked explicitly and hence the (indeterminate) plastic rotation does not enter the associated constitutive functions, it is instructive to invoke the multiplicative split for the sake of motivation. To this end let $\mathcal{B}_0 \subset \mathbb{R}^3$ be the region occupied by the body under consideration at a certain reference time $t_0 \in \mathbb{R}$ and let $\mathcal{B}_t \subset \mathbb{R}^3$ be the region occupied at time $t \geq t_0$. The position vector of a material point at time t, i.e. $\boldsymbol{x} \in \mathcal{B}_t$, is related to the position vector in the reference configuration $\boldsymbol{X} \in \mathcal{B}_0$ via the deformation map $\boldsymbol{\varphi}\left(\boldsymbol{X}, t\right) : \mathcal{B}_0 \times \mathbb{R} \to \mathcal{B}_t \subset \mathbb{R}^3$. The deformation gradient $\boldsymbol{F} : T_{\boldsymbol{X}}\mathcal{B}_0 \to T_{\boldsymbol{x}}\mathcal{B}_t$ is defined as the associated tangent map, more specifically $\boldsymbol{F} = T_{\boldsymbol{X}}\boldsymbol{\varphi}$ with $J_{\boldsymbol{F}} = \det\left(\boldsymbol{F}\right) > 0$ and $T_{\boldsymbol{X}}\mathcal{B}_0$, respectively $T_{\boldsymbol{x}}\mathcal{B}_t$, designating the tangent spaces at $\boldsymbol{X}$ and $\boldsymbol{x}$. The corresponding cotangent spaces, denoted by $T_{\boldsymbol{X}}^{\star}\mathcal{B}_0$ and $T_{\boldsymbol{x}}^{\star}\mathcal{B}_t$, are related by the adjoint mapping $\boldsymbol{F}^{\star} : T_{\boldsymbol{x}}^{\star}\mathcal{B}_t \to T_{\boldsymbol{X}}^{\star}\mathcal{B}_0$ and the co- and contravariant metric tensors are given by $\boldsymbol{G}^{\flat} : T_{\boldsymbol{X}}\mathcal{B}_0 \to T_{\boldsymbol{X}}^{\star}\mathcal{B}_0$ and $\boldsymbol{g}^{\flat} : T_{\boldsymbol{x}}\mathcal{B}_t \to T_{\boldsymbol{x}}^{\star}\mathcal{B}_t$, respectively by $\boldsymbol{G}^{\sharp} : T_{\boldsymbol{X}}^{\star}\mathcal{B}_0 \to T_{\boldsymbol{X}}\mathcal{B}_0$ and $\boldsymbol{g}^{\sharp} : T_{\boldsymbol{x}}^{\star}\mathcal{B}_t \to T_{\boldsymbol{x}}\mathcal{B}_t$. In addition, the referential and spatial mixed-variant second order identity tensors will be indicated by $\boldsymbol{G}^{\natural} : T_{\boldsymbol{X}}\mathcal{B}_0 \to T_{\boldsymbol{X}}\mathcal{B}_0$ and $\boldsymbol{g}^{\natural} : T_{\boldsymbol{x}}\mathcal{B}_t \to T_{\boldsymbol{x}}\mathcal{B}_t$, as summarised in Figure 4.1. Based on the multiplicative split of the deformation gradient, see [71],

$$\boldsymbol{F} = \boldsymbol{F}_{\mathrm{e}} \cdot \boldsymbol{F}_{\mathrm{p}} \tag{4.5}$$

with $\boldsymbol{F}_{\mathrm{p}} : T_{\boldsymbol{X}}\mathcal{B}_0 \to T_{\overline{\boldsymbol{X}}}\overline{\mathcal{B}}$ and $\boldsymbol{F}_{\mathrm{e}} : T_{\overline{\boldsymbol{X}}}\overline{\mathcal{B}} \to T_{\boldsymbol{x}}\mathcal{B}_t$, the local incompatible intermediate configuration $\overline{\mathcal{B}}$ with tangent space $T_{\overline{\boldsymbol{X}}}\overline{\mathcal{B}}$ and cotangent space $T_{\overline{\boldsymbol{X}}}^{\star}\overline{\mathcal{B}}$ is introduced. In analogy with the reference and current configuration, the co- and contravariant metric tensors are denoted by $\overline{\boldsymbol{G}}^{\flat} : T_{\overline{\boldsymbol{X}}}\overline{\mathcal{B}} \to T_{\overline{\boldsymbol{X}}}^{\star}\overline{\mathcal{B}}$, respectively $\overline{\boldsymbol{G}}^{\sharp} : T_{\overline{\boldsymbol{X}}}^{\star}\overline{\mathcal{B}} \to T_{\overline{\boldsymbol{X}}}\overline{\mathcal{B}}$, and the second order mixed-variant identity tensor is given by $\overline{\boldsymbol{G}}^{\natural} : T_{\overline{\boldsymbol{X}}}\overline{\mathcal{B}} \to T_{\overline{\boldsymbol{X}}}\overline{\mathcal{B}}$. We take note of the fact that the multiplicative split and hence the intermediate configuration is defined except for a rotation. This rotational indeterminacy merits special attention with regard to anisotropic plasticity, see e.g. [29], and motivated the theoretical developments presented in [77] and the current work.

Assuming a stored energy function of the form

$$W = \widehat{W}\left(\boldsymbol{F} \cdot \boldsymbol{F}_{\mathrm{p}}^{-1}, \boldsymbol{g}^{\flat}, \overline{\boldsymbol{G}}^{\flat}, \kappa\right) \tag{4.6}$$

in a first step, with κ being a scalar valued internal variable that characterises the hardening, it is shown in [77, 78, 88, 89] that invoking the postulate of covariance yields, as a special case, the same constitutive reductions as invariance under superposed rigid
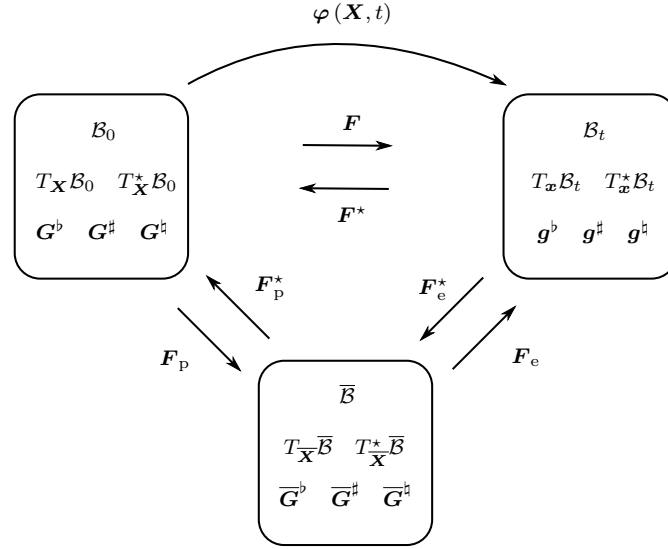
Figure 4.1: Referential, spatial and intermediate configuration with tangent spaces, cotangent spaces and the corresponding mappings.

body motions on the spatial and intermediate configuration. Specifically (4.6) may equivalently be written in terms of

$$W = \widetilde{W}\left(\boldsymbol{C}, \boldsymbol{C}_{\mathrm{p}}, \kappa\right) \quad, \tag{4.7}$$

with the right Cauchy-Green tensor $\boldsymbol{C}$ and the right Cauchy-Green plastic deformation tensor $\boldsymbol{C}_{\mathrm{p}}$ defined as

$$\boldsymbol{C} = \boldsymbol{F}^{\star} \cdot \boldsymbol{g}^{\flat} \cdot \boldsymbol{F} \quad, \tag{4.8a} \qquad \boldsymbol{C}_{\mathrm{p}} = \boldsymbol{F}_{\mathrm{p}}^{\star} \cdot \overline{\boldsymbol{G}}^{\flat} \cdot \boldsymbol{F}_{\mathrm{p}} \quad. \tag{4.8b}$$

We point out that referential covariance implies that a material characterised by (4.7) is (elastically) isotropic. Moreover, we should like to stress that the plastic metric $\boldsymbol{C}_{\mathrm{p}}$ will be regarded as a primitive variable such that the multiplicative split and the definition (4.8b) are only invoked for the sake of motivation. The evolution of the plastic deformation may then be defined in terms of rate-type equations for $\boldsymbol{C}_{\mathrm{p}}$ in the form

$$\dot{\boldsymbol{C}}_{\mathrm{p}} = \boldsymbol{C}_{\mathrm{p}} \cdot \boldsymbol{\Gamma}_{\mathrm{p}} + \boldsymbol{\Gamma}_{\mathrm{p}}^{\star} \cdot \boldsymbol{C}_{\mathrm{p}} \quad, \tag{4.9}$$

with $\boldsymbol{\Gamma}_{\mathrm{p}}$ representing a constitutive function which needs to be specified in accordance with the dissipation inequality and which may be motivated based on the multiplicative split, see Section 4.1.3, Section 4.2.3 and [77] for a detailed discussion. Furthermore, note that $\boldsymbol{\Gamma}_{\mathrm{p}}$ is assumed to be $\boldsymbol{C}_{\mathrm{p}}$-symmetric, as adding any $\boldsymbol{C}_{\mathrm{p}}$-skew tensor to $\boldsymbol{\Gamma}_{\mathrm{p}}$ would not alter the right-hand side of (4.9).

Both the elastic material response and the yielding behaviour may show a significant directional dependency. Based on the physical assumptions that the material symmetry group is induced by the crystalline structure and that the plastic deformation leaves the structure of the crystal lattice unaltered, it is proposed in [77] to characterise the symmetry group by means of Euclidean orthogonal transformations in the intermediate configuration. Referring to Noll's rule it is then argued that the representation of the symmetry group relative to the reference configuration $\mathscr{G}$ is a subgroup of the C_{p}-orthogonal group and hence characterised by (referential) tensors Q that satisfy the property

$$Q^{\star} \cdot C_{\mathrm{p}} \cdot Q = C_{\mathrm{p}} \quad . \tag{4.10}$$

The symmetry group of the elastic response may certainly be different from the one of the yield function. It may, for example, be assumed with regard to metal plasticity that the yielding behaviour exhibits appreciable directional dependence, while the elastic response may merely be treated as isotropic. In this case, the symmetry group of the yield function is a subgroup of the symmetry group of the elastic response, i.e. a subgroup of the symmetry group of the strain energy function. Essentially, this reflects the notion that the anisotropic features which are assumed to be induced by the crystalline structure manifest themselves in the yielding behaviour and, possibly, in the elastic response.

A natural approach to account for the anisotropic material response is given by the introduction of (referential) structural tensors A_i, which characterise the respective symmetry group, into the constitutive equations. The structural tensors are invariant with respect to transformations which belong to the respective symmetry group. In particular, for second order structural tensors

$$Q \cdot A_i \cdot Q^{\star} = A_i \quad \forall \quad Q \in \mathscr{G}_i \tag{4.11}$$

holds, and it is shown in [76, 89] for the case of non-linear elasticity that anisotropic tensor functions may be rewritten as covariant functions when suitable structural tensors are additionally included in the list of arguments. The latter approach has been extended to elastic-plastic materials in [77] and is the basis for the modelling of evolving plastic anisotropies in the present contribution. Since the structural tensors reflect the material anisotropy in the constitutive equations, the evolution of the material's symmetry group may equivalently be described in terms of appropriate rate-type equations for the structural tensors. It has specifically been shown in [77] that, in order to be consistent with (4.9), (4.10) and (4.11), the structural tensors must evolve according to

$$\dot{A}_i = \underbrace{\left[-\boldsymbol{\Gamma}_{\mathrm{p}} \cdot A_i - A_i \cdot \boldsymbol{\Gamma}_{\mathrm{p}}^{\star} \right]}_{\text{①}} + \underbrace{\left[-W_i \cdot A_i - A_i \cdot W_i^{\star} \right]}_{\text{②}} \quad , \tag{4.12}$$

with $\boldsymbol{W}_i$ denoting arbitrary $\boldsymbol{C}_{\mathrm{p}}$-skew tensors, i.e. tensors that satisfy the relation $\boldsymbol{W}_i^\star \cdot \boldsymbol{C}_{\mathrm{p}} + \boldsymbol{C}_{\mathrm{p}} \cdot \boldsymbol{W}_i = \boldsymbol{0}$. Equation (4.12) suggests that the rate of the structural tensor may additively be decomposed into two contributions. The first one, termed "convected evolution", is directly related to changes in the right Cauchy-Green plastic deformation tensor. The second contribution, which we will refer to as the "residual evolution", on the other hand, allows the structural tensor to evolve independently of the plastic deformation tensor $\boldsymbol{C}_{\mathrm{p}}$, reflecting a rotation of the preferred material axes which may be related to the notion of a plastic spin. For a deeper understanding of the convected and residual evolution, the multiplicative split may further be invoked as shown in Remark 4.1.

4.1.3 Dissipation inequality

In this section we focus on the constitutive restrictions which may be deduced from the dissipation inequality. To this end, assume a stored energy function of the form

$$W = \breve{W}\left(\boldsymbol{C}, \boldsymbol{C}_{\mathrm{p}}, \boldsymbol{A}_i, \kappa\right) \tag{4.13}$$

and evaluate the dissipation rate (in local referential form)

$$\mathcal{D} = \frac{1}{2}\,\boldsymbol{S} : \dot{\boldsymbol{C}} - \dot{\breve{W}} = \left[\frac{1}{2}\,\boldsymbol{S} - \frac{\partial \breve{W}}{\partial \boldsymbol{C}}\right] : \dot{\boldsymbol{C}} - \frac{\partial \breve{W}}{\partial \boldsymbol{C}_{\mathrm{p}}} : \dot{\boldsymbol{C}}_{\mathrm{p}} - \sum_i \frac{\partial \breve{W}}{\partial \boldsymbol{A}_i} : \dot{\boldsymbol{A}}_i - \frac{\partial \breve{W}}{\partial \kappa}\,\dot{\kappa} \quad . \tag{4.14}$$

Using standard argumentation yields the classic definition of the Piola-Kirchhoff stress tensor

$$\boldsymbol{S} = 2\,\frac{\partial \breve{W}}{\partial \boldsymbol{C}} \tag{4.15}$$

and the reduced dissipation rate according to

$$\mathcal{D}^{\mathrm{red}} = -\frac{\partial \breve{W}}{\partial \boldsymbol{C}_{\mathrm{p}}} : \dot{\boldsymbol{C}}_{\mathrm{p}} - \sum_i \frac{\partial \breve{W}}{\partial \boldsymbol{A}_i} : \dot{\boldsymbol{A}}_i + q\,\dot{\kappa} \quad , \tag{4.16}$$

with the energy-conjugate variable to κ introduced as

$$q = -\frac{\partial \breve{W}}{\partial \kappa} \quad . \tag{4.17}$$

Invoking the covariance condition, see [76, 77, 88, 89] for details,

$$\boldsymbol{C} \cdot \frac{\partial \breve{W}}{\partial \boldsymbol{C}} + \boldsymbol{C}_{\mathrm{p}} \cdot \frac{\partial \breve{W}}{\partial \boldsymbol{C}_{\mathrm{p}}} - \sum_i \frac{\partial \breve{W}}{\partial \boldsymbol{A}_i} \cdot \boldsymbol{A}_i = \boldsymbol{0} \tag{4.18}$$

and making use of the rate equations (4.9) and (4.12), (4.16) may further be rewritten as

$$\mathcal{D}^{\mathrm{red}} = [\boldsymbol{C} \cdot \boldsymbol{S}] : \boldsymbol{\Gamma}_{\mathrm{p}} + 2 \sum_i \left[\frac{\partial \breve{W}}{\partial \boldsymbol{A}_i} \cdot \boldsymbol{A}_i \right] : \boldsymbol{W}_i + q \, \dot{\kappa} \quad . \tag{4.19}$$

At this stage we observe the energy conjugacy between the referential Mandel stress tensor

$$\boldsymbol{M} = \boldsymbol{C} \cdot \boldsymbol{S} \tag{4.20}$$

and $\boldsymbol{\Gamma}_{\mathrm{p}}$.

To proceed, assume for now that all structural tensors spin with the same rate, i.e. $\boldsymbol{W}_i = \boldsymbol{W} \; \forall \; i$, and use again (4.18) such that

$$2 \sum_i \left[\frac{\partial \breve{W}}{\partial \boldsymbol{A}_i} \cdot \boldsymbol{A}_i \right] : \boldsymbol{W}_i = 2 \left[\sum_i \frac{\partial \breve{W}}{\partial \boldsymbol{A}_i} \cdot \boldsymbol{A}_i \right] : \boldsymbol{W} = 2 \left[\boldsymbol{C} \cdot \frac{\partial \breve{W}}{\partial \boldsymbol{C}} + \boldsymbol{C}_{\mathrm{p}} \cdot \frac{\partial \breve{W}}{\partial \boldsymbol{C}_{\mathrm{p}}} \right] : \boldsymbol{W} . \tag{4.21}$$

Noting that $\left[\boldsymbol{C}_{\mathrm{p}} \cdot \partial \breve{W} / \partial \boldsymbol{C}_{\mathrm{p}} \right] : \boldsymbol{W} = \partial \breve{W} / \partial \boldsymbol{C}_{\mathrm{p}} : [\boldsymbol{C}_{\mathrm{p}} \cdot \boldsymbol{W}] = 0$ due to the symmetry of $\partial \breve{W} / \partial \boldsymbol{C}_{\mathrm{p}}$ and the $\boldsymbol{C}_{\mathrm{p}}$-skew symmetry of $\boldsymbol{W}$ results in

$$\mathcal{D}^{\mathrm{red}} = \boldsymbol{M} : \boldsymbol{\Gamma}_{\mathrm{p}} + \boldsymbol{M} : \boldsymbol{W} + q \, \dot{\kappa} \quad , \tag{4.22}$$

where (4.15) and (4.20) were used again. Since $\boldsymbol{W}$ is $\boldsymbol{C}_{\mathrm{p}}$-skew, the $\boldsymbol{C}_{\mathrm{p}}$-symmetric part of $\boldsymbol{M}$ does not contribute to $\boldsymbol{M} : \boldsymbol{W}$. We hence find that the $\boldsymbol{C}_{\mathrm{p}}$-skew part of the Mandel stress tensor is the thermodynamic-conjugate force to the plastic spin tensor $\boldsymbol{W}$.

Consider now a material which is elastically isotropic. For this particular case, the referential Mandel stress tensor $\boldsymbol{M}$ can be shown to be $\boldsymbol{C}_{\mathrm{p}}$-symmetric such that $\boldsymbol{M} : \boldsymbol{W} = 0$ holds. Essentially, the latter observation means that the spin tensor $\boldsymbol{W}$ is not thermodynamically constrained in the case of elastic isotropy such that $\boldsymbol{W}$ may be chosen arbitrarily (within the group of $\boldsymbol{C}_{\mathrm{p}}$-skew tensors) without violating thermodynamic consistency. This result is of particular importance for the ensuing developments.

Remark 4.1 (Interpretation of the convected and residual evolution) *To provide a better understanding of the convected and residual evolution, the multiplicative split will be invoked in this remark. To this end we note that the referential representation of a structural tensor $\boldsymbol{A}$ may be related to its representation in the intermediate configuration via*

$$\overline{\boldsymbol{A}} = \boldsymbol{F}_{\mathrm{p}} \cdot \boldsymbol{A} \cdot \boldsymbol{F}_{\mathrm{p}}^{\star} \quad . \tag{4.23}$$

Furthermore, we take note of the fact that the purely referential tensor $\boldsymbol{\Gamma}_{\mathrm{p}}$ may be motivated based on the multiplicative split of the deformation gradient as shown in [77], resulting in relation

$$\boldsymbol{\Gamma}_{\mathrm{p}} = [\boldsymbol{L}_{\mathrm{p}}]^{C_{\mathrm{p}}-\mathrm{sym}} = \boldsymbol{L}_{\mathrm{p}} - [\boldsymbol{L}_{\mathrm{p}}]^{C_{\mathrm{p}}-\mathrm{skw}} \quad , \tag{4.24}$$

with

$$\boldsymbol{L}_{\mathrm{p}} = \boldsymbol{F}_{\mathrm{p}}^{-1} \cdot \dot{\boldsymbol{F}}_{\mathrm{p}} \tag{4.25}$$

denoting the referential representation of the plastic velocity gradient. By making use of (4.12) and (4.23)–(4.25), the rate of $\overline{\boldsymbol{A}}$ can be specified as

$$\dot{\overline{\boldsymbol{A}}} = \quad \dot{\boldsymbol{F}}_{\mathrm{p}} \cdot \boldsymbol{A} \cdot \boldsymbol{F}_{\mathrm{p}}^{\star} + \boldsymbol{F}_{\mathrm{p}} \cdot \boldsymbol{A} \cdot \dot{\boldsymbol{F}}_{\mathrm{p}}^{\star} + \boldsymbol{F}_{\mathrm{p}} \cdot \dot{\boldsymbol{A}} \cdot \boldsymbol{F}_{\mathrm{p}}^{\star} \tag{4.26a}$$

$$\begin{aligned} = \quad & \dot{\boldsymbol{F}}_{\mathrm{p}} \cdot \boldsymbol{A} \cdot \boldsymbol{F}_{\mathrm{p}}^{\star} + \boldsymbol{F}_{\mathrm{p}} \cdot \boldsymbol{A} \cdot \dot{\boldsymbol{F}}_{\mathrm{p}}^{\star} \\ & + \boldsymbol{F}_{\mathrm{p}} \cdot \left[\left[-\boldsymbol{\Gamma}_{\mathrm{p}} \cdot \boldsymbol{A} - \boldsymbol{A} \cdot \boldsymbol{\Gamma}_{\mathrm{p}}^{\star} \right] + \left[-\boldsymbol{W} \cdot \boldsymbol{A} - \boldsymbol{A} \cdot \boldsymbol{W}^{\star} \right] \right] \cdot \boldsymbol{F}_{\mathrm{p}}^{\star} \end{aligned} \tag{4.26b}$$

$$\begin{aligned} = \quad & \dot{\boldsymbol{F}}_{\mathrm{p}} \cdot \boldsymbol{A} \cdot \boldsymbol{F}_{\mathrm{p}}^{\star} + \boldsymbol{F}_{\mathrm{p}} \cdot \boldsymbol{A} \cdot \dot{\boldsymbol{F}}_{\mathrm{p}}^{\star} - \left[\dot{\boldsymbol{F}}_{\mathrm{p}} \cdot \boldsymbol{A} \cdot \boldsymbol{F}_{\mathrm{p}}^{\star} + \boldsymbol{F}_{\mathrm{p}} \cdot \boldsymbol{A} \cdot \dot{\boldsymbol{F}}_{\mathrm{p}}^{\star} \right] \\ & + \left[\boldsymbol{F}_{\mathrm{p}} \cdot [\boldsymbol{L}_{\mathrm{p}}]^{C_{\mathrm{p}}-\mathrm{skw}} \cdot \boldsymbol{A} \cdot \boldsymbol{F}_{\mathrm{p}}^{\star} \;+\; \boldsymbol{F}_{\mathrm{p}} \cdot \boldsymbol{A} \cdot \left[[\boldsymbol{L}_{\mathrm{p}}]^{C_{\mathrm{p}}-\mathrm{skw}} \right]^{\star} \cdot \boldsymbol{F}_{\mathrm{p}}^{\star} \right] \\ & - \left[\boldsymbol{F}_{\mathrm{p}} \cdot \boldsymbol{W} \cdot \qquad \boldsymbol{A} \cdot \boldsymbol{F}_{\mathrm{p}}^{\star} \;+\; \boldsymbol{F}_{\mathrm{p}} \cdot \boldsymbol{A} \cdot \boldsymbol{W}^{\star} \cdot \qquad \boldsymbol{F}_{\mathrm{p}}^{\star} \right] \end{aligned} \tag{4.26c}$$

$$= [\overline{\boldsymbol{L}}_{\mathrm{p}}]^{\overline{\boldsymbol{G}}^{\flat}-\mathrm{skw}} \cdot \overline{\boldsymbol{A}} + \overline{\boldsymbol{A}} \cdot \left[[\overline{\boldsymbol{L}}_{\mathrm{p}}]^{\overline{\boldsymbol{G}}^{\flat}-\mathrm{skw}} \right]^{\star} - \overline{\boldsymbol{W}} \cdot \overline{\boldsymbol{A}} - \overline{\boldsymbol{A}} \cdot \overline{\boldsymbol{W}}^{\star} \quad , \tag{4.26d}$$

with the classic plastic velocity gradient-type tensor

$$\overline{\boldsymbol{L}}_{\mathrm{p}} = \dot{\boldsymbol{F}}_{\mathrm{p}} \cdot \boldsymbol{F}_{\mathrm{p}}^{-1} \quad , \tag{4.27}$$

and the spin tensor

$$\overline{\boldsymbol{W}} = \boldsymbol{F}_{\mathrm{p}} \cdot \boldsymbol{W} \cdot \boldsymbol{F}_{\mathrm{p}}^{-1} \quad , \tag{4.28}$$

which resembles the push forward of $\boldsymbol{W}$ with respect to tangent map $\boldsymbol{F}_{\mathrm{p}}$. Since $\boldsymbol{W}$ is $\boldsymbol{C}_{\mathrm{p}}$-skew as argued in Section 4.1.2, $\overline{\boldsymbol{W}}$ turns out to be $\overline{\boldsymbol{G}}^{\flat}$-skew. It is thus revealed that an evolution equation of the form (4.12) results in a pure rotation of the structural tensor $\overline{\boldsymbol{A}}$. The corresponding rate equation (4.26d) consists of two additive parts: the first part which is governed by $\overline{\boldsymbol{L}}_{\mathrm{p}}$ renders the structural tensor spin at the same rate as the intermediate configuration while the second part which is defined by $\overline{\boldsymbol{W}}$ allows the structural tensor to spin at a rate different from that of the intermediate configuration. The second part is thus closely related to the notion of the plastic spin. We take note of the fact that (4.26d) can also be well interpreted in the context of co-rotational rates, see [80, 83].

4.2 Elasto-plastic prototype model

In this section, a specific prototype model will be proposed on the basis of [9]. We will especially focus on the stored energy function and on the form of the yield function which will be introduced in the intermediate configuration based on physical considerations. An equivalent referential form is then derived and the thermodynamic consistency of the model is shown.

4.2.1 Stored energy function and hardening potential

Following standard practise we assume that the material response may be characterised by the energy density function W which is additively decomposed into the stored energy function W^{e} and the hardening potential W^{p} according to

$$W = W^{\mathrm{e}}\left(\boldsymbol{C}, \boldsymbol{C}_{\mathrm{p}}\right) + W^{\mathrm{p}}\left(\kappa\right) \quad . \tag{4.29}$$

Although W^{e} may, in general, be an anisotropic function of $\boldsymbol{C}$ and $\boldsymbol{C}_{\mathrm{p}}$, we will assume the elastic material behaviour to be isotropic. Being more specific, the Neo-Hookean-type energy function

$$W^{\mathrm{e}}\left(\boldsymbol{C}, \boldsymbol{C}_{\mathrm{p}}\right) = \frac{\mu}{2}\left[J_{\mathrm{e}1} - 2\ln\left(J_{\mathrm{e}}\right) - 3\right] + \frac{\lambda}{2}\ln^2\left(J_{\mathrm{e}}\right) \quad , \tag{4.30}$$

with

$$J_{\mathrm{e}1} = \mathrm{tr}\left(\boldsymbol{C} \cdot \boldsymbol{C}_{\mathrm{p}}^{-1}\right) \ (4.31\mathrm{a}) \qquad J_{\mathrm{e}3} = \det\left(\boldsymbol{C} \cdot \boldsymbol{C}_{\mathrm{p}}^{-1}\right) \ (4.31\mathrm{b}) \qquad J_{\mathrm{e}} = \sqrt{J_{\mathrm{e}3}} \ (4.31\mathrm{c})$$

and the material parameters λ and μ which are akin to the Lamé constants of the small strain theory, will be adopted. Furthermore, we will use a hardening potential of the form

$$W^{\mathrm{p}}\left(\kappa\right) = R_{\mathrm{inf}}\left[\kappa + \varepsilon_0 \exp\left(-\frac{\kappa}{\varepsilon_0}\right)\right] \quad , \tag{4.32}$$

similar to [52], with the material parameter R_{inf} controlling the maximal yield stress and with ε_0 controlling the hardening speed. By making use of (4.15), (4.17) and (4.20), the Piola-Kirchhoff stress tensor

$$\boldsymbol{S} = \mu\left[\boldsymbol{C}_{\mathrm{p}}^{-1} - \boldsymbol{C}^{-1}\right] + \lambda\ln\left(J_{\mathrm{e}}\right)\boldsymbol{C}^{-1} \quad , \tag{4.33}$$

the Mandel stress tensor

$$\boldsymbol{M} = \mu\left[\boldsymbol{C} \cdot \boldsymbol{C}_{\mathrm{p}}^{-1} - \boldsymbol{G}^{\natural\star}\right] + \lambda\ln\left(J_{\mathrm{e}}\right)\boldsymbol{G}^{\natural\star} \tag{4.34}$$

and the energetic dual to κ

$$q = -R_{\text{inf}} \left[1 - \exp \left(-\frac{\kappa}{\varepsilon_0} \right) \right] \tag{4.35}$$

may be specified.

4.2.2 Yield function

In contrast to the elastic material behaviour it will be assumed that the yielding behaviour exhibits appreciable directional dependence. Being more specific, a yield function of orthotropic type will be chosen in accordance with the experimental findings to be discussed in Section 4.3.1. As stated before, it is assumed that the anisotropic material behaviour is thought to be induced by the crystallographic symmetry itself. Based on this motivation we propose to formulate the yield function as an orthotropic function of the Mandel stress tensor in the intermediate configuration. To this end, the contravariant second order structural tensor

$$\overline{\boldsymbol{A}} = \frac{1}{2} \left[\overline{\boldsymbol{N}}_{\overline{\boldsymbol{A}}1} \otimes \overline{\boldsymbol{N}}_{\overline{\boldsymbol{A}}1} - \overline{\boldsymbol{N}}_{\overline{\boldsymbol{A}}2} \otimes \overline{\boldsymbol{N}}_{\overline{\boldsymbol{A}}2} \right] \tag{4.36}$$

is introduced in accordance with [101, 153], with $\overline{\boldsymbol{N}}_{\overline{\boldsymbol{A}}1}$ and $\overline{\boldsymbol{N}}_{\overline{\boldsymbol{A}}2}$ denoting the normals of the two planes of reflectional symmetry. We take note of the fact that the two direction vectors $\overline{\boldsymbol{N}}_{\overline{\boldsymbol{A}}1}$ and $\overline{\boldsymbol{N}}_{\overline{\boldsymbol{A}}2}$ are normalised with respect to the metric of the intermediate configuration $\overline{\boldsymbol{G}}^\flat$, such that

$$\overline{\boldsymbol{N}}_{\overline{\boldsymbol{A}}1} \cdot \overline{\boldsymbol{G}}^\flat \cdot \overline{\boldsymbol{N}}_{\overline{\boldsymbol{A}}1} = 1 \ (4.37a) \quad \overline{\boldsymbol{N}}_{\overline{\boldsymbol{A}}2} \cdot \overline{\boldsymbol{G}}^\flat \cdot \overline{\boldsymbol{N}}_{\overline{\boldsymbol{A}}2} = 1 \ (4.37b) \quad \overline{\boldsymbol{N}}_{\overline{\boldsymbol{A}}1} \cdot \overline{\boldsymbol{G}}^\flat \cdot \overline{\boldsymbol{N}}_{\overline{\boldsymbol{A}}2} = 0 \ (4.37c)$$

hold. With the appropriate structural tensor at hand, the anisotropic yield function can be rewritten as an isotropic function of the structural tensor and of the Mandel stress tensor of the intermediate configuration $\overline{\boldsymbol{M}}$, enabling an invariant-based representation. Specifically the set of invariants

$$\left\{ \text{tr} \left(\overline{\boldsymbol{M}} \right), \text{tr} \left(\overline{\boldsymbol{M}}^2 \right), \text{tr} \left(\overline{\boldsymbol{M}}^3 \right), \text{tr} \left(\overline{\boldsymbol{M}} \cdot \overline{\boldsymbol{G}}^\flat \cdot \overline{\boldsymbol{A}} \right), \right.$$
$$\left. \text{tr} \left(\overline{\boldsymbol{M}}^2 \cdot \overline{\boldsymbol{G}}^\flat \cdot \overline{\boldsymbol{A}} \right), \text{tr} \left(\overline{\boldsymbol{M}} \cdot \left[\overline{\boldsymbol{G}}^\flat \cdot \overline{\boldsymbol{A}} \right]^2 \right), \text{tr} \left(\overline{\boldsymbol{M}}^2 \cdot \left[\overline{\boldsymbol{G}}^\flat \cdot \overline{\boldsymbol{A}} \right]^2 \right) \right\} \tag{4.38}$$

forms an integrity basis, since $\overline{\boldsymbol{M}}$ is symmetric due to the assumed elastic isotropy. If we restrict the yield function to be quadratic in $\overline{\boldsymbol{M}}$, we find that it may be composed as a linear combination of the invariants

$$\left\{ \operatorname{tr}\left(\overline{\boldsymbol{M}}\right)\operatorname{tr}\left(\overline{\boldsymbol{M}}\right),\ \operatorname{tr}\left(\overline{\boldsymbol{M}}^{2}\right),\ \operatorname{tr}\left(\overline{\boldsymbol{M}}\cdot\overline{\boldsymbol{A}}_{\mathrm{p}}\right)\operatorname{tr}\left(\overline{\boldsymbol{M}}\cdot\overline{\boldsymbol{A}}_{\mathrm{p}}\right),\ \operatorname{tr}\left(\overline{\boldsymbol{M}}\cdot\overline{\boldsymbol{A}}_{\mathrm{p}}^{2}\right)\operatorname{tr}\left(\overline{\boldsymbol{M}}\cdot\overline{\boldsymbol{A}}_{\mathrm{p}}^{2}\right),\right.$$

$$\operatorname{tr}\left(\overline{\boldsymbol{M}}\right)\operatorname{tr}\left(\overline{\boldsymbol{M}}\cdot\overline{\boldsymbol{A}}_{\mathrm{p}}\right),\ \operatorname{tr}\left(\overline{\boldsymbol{M}}\right)\operatorname{tr}\left(\overline{\boldsymbol{M}}\cdot\overline{\boldsymbol{A}}_{\mathrm{p}}^{2}\right),\ \operatorname{tr}\left(\overline{\boldsymbol{M}}\cdot\overline{\boldsymbol{A}}_{\mathrm{p}}\right)\operatorname{tr}\left(\overline{\boldsymbol{M}}\cdot\overline{\boldsymbol{A}}_{\mathrm{p}}^{2}\right),$$

$$\left.\operatorname{tr}\left(\overline{\boldsymbol{M}}^{2}\cdot\overline{\boldsymbol{A}}_{\mathrm{p}}\right),\ \operatorname{tr}\left(\overline{\boldsymbol{M}}^{2}\cdot\overline{\boldsymbol{A}}_{\mathrm{p}}^{2}\right)\right\},\tag{4.39}$$

with the mixed variant structural tensor being introduced according to

$$\overline{\boldsymbol{A}}_{\mathrm{p}}=\overline{\boldsymbol{G}}^{\flat}\cdot\overline{\boldsymbol{A}}\tag{4.40}$$

for the sake of brevity. If we further assume the yielding behaviour to be independent of the hydrostatic pressure, the Mandel stress tensor should only enter the yield function in terms of its deviatoric component which is given by

$$\overline{\boldsymbol{M}}_{\mathrm{dev}}=\overline{\boldsymbol{M}}-\frac{1}{3}\operatorname{tr}\left(\overline{\boldsymbol{M}}\right)\overline{\boldsymbol{G}}^{\natural\star},\tag{4.41}$$

resulting in a possible yield function of the form

$$f=\left[a_{1}\operatorname{tr}\left(\overline{\boldsymbol{M}}_{\mathrm{dev}}^{2}\right)+a_{2}\operatorname{tr}\left(\overline{\boldsymbol{M}}_{\mathrm{dev}}\cdot\overline{\boldsymbol{A}}_{\mathrm{p}}\right)\operatorname{tr}\left(\overline{\boldsymbol{M}}_{\mathrm{dev}}\cdot\overline{\boldsymbol{A}}_{\mathrm{p}}\right)+a_{3}\operatorname{tr}\left(\overline{\boldsymbol{M}}_{\mathrm{dev}}\cdot\overline{\boldsymbol{A}}_{\mathrm{p}}^{2}\right)\operatorname{tr}\left(\overline{\boldsymbol{M}}_{\mathrm{dev}}\cdot\overline{\boldsymbol{A}}_{\mathrm{p}}^{2}\right)\right.$$

$$\left.+a_{4}\operatorname{tr}\left(\overline{\boldsymbol{M}}_{\mathrm{dev}}\cdot\overline{\boldsymbol{A}}_{\mathrm{p}}\right)\operatorname{tr}\left(\overline{\boldsymbol{M}}_{\mathrm{dev}}\cdot\overline{\boldsymbol{A}}_{\mathrm{p}}^{2}\right)+a_{5}\operatorname{tr}\left(\overline{\boldsymbol{M}}_{\mathrm{dev}}^{2}\cdot\overline{\boldsymbol{A}}_{\mathrm{p}}\right)+a_{6}\operatorname{tr}\left(\overline{\boldsymbol{M}}_{\mathrm{dev}}^{2}\cdot\overline{\boldsymbol{A}}_{\mathrm{p}}^{2}\right)\right]-M_{\mathrm{y}}.$$

$$\tag{4.42}$$

In (4.42), the constants a_1 - a_6 denote material parameters which control the shape of the yield surface and which need to be adjusted based on experiments as will be discussed in Appendix C.1. On the other hand, the current yield limit M_{y} is assumed to be of the form

$$M_{\mathrm{y}}=1-q\tag{4.43}$$

which, in conjunction with the specific form of the hardening potential (4.32) and the associated-type evolution equation (4.51b) that will be assumed as this work proceeds, results in an exponential-type hardening behaviour.

Since the intermediate configuration and, accordingly, the multiplicative split are only introduced for the sake of motivation, a representation of the yield function in terms of

purely referential quantities is aspired. To this end, performing the pull-back operation with respect to the tangent map $\boldsymbol{F}_\mathrm{p}$ results in

$$
\begin{aligned}
f = &\Bigg[a_1 \operatorname{tr}\left(\boldsymbol{M}_\mathrm{dev}^2\right) + a_2 \operatorname{tr}\left(\boldsymbol{M}_\mathrm{dev} \cdot \boldsymbol{A}_\mathrm{p}\right) \operatorname{tr}\left(\boldsymbol{M}_\mathrm{dev} \cdot \boldsymbol{A}_\mathrm{p}\right) + a_3 \operatorname{tr}\left(\boldsymbol{M}_\mathrm{dev} \cdot \boldsymbol{A}_\mathrm{p}^2\right) \operatorname{tr}\left(\boldsymbol{M}_\mathrm{dev} \cdot \boldsymbol{A}_\mathrm{p}^2\right) \\
&+ a_4 \operatorname{tr}\left(\boldsymbol{M}_\mathrm{dev} \cdot \boldsymbol{A}_\mathrm{p}\right) \operatorname{tr}\left(\boldsymbol{M}_\mathrm{dev} \cdot \boldsymbol{A}_\mathrm{p}^2\right) + a_5 \operatorname{tr}\left(\boldsymbol{M}_\mathrm{dev}^2 \cdot \boldsymbol{A}_\mathrm{p}\right) + a_6 \operatorname{tr}\left(\boldsymbol{M}_\mathrm{dev}^2 \cdot \boldsymbol{A}_\mathrm{p}^2\right) \Bigg] - M_\mathrm{y} ,
\end{aligned}
\tag{4.44}
$$

with the deviatoric part of the referential Mandel stress tensor defined as

$$
\boldsymbol{M}_\mathrm{dev} = \boldsymbol{M} - \frac{1}{3} \operatorname{tr}\left(\boldsymbol{M}\right) \boldsymbol{G}^{\natural\star}
\tag{4.45}
$$

and the mixed-variant referential structural tensor as

$$
\boldsymbol{A}_\mathrm{p} = \boldsymbol{C}_\mathrm{p} \cdot \boldsymbol{A} = \frac{1}{2} \boldsymbol{C}_\mathrm{p} \cdot [\boldsymbol{N}_{\overline{\boldsymbol{A}}1} \otimes \boldsymbol{N}_{\overline{\boldsymbol{A}}1} - \boldsymbol{N}_{\overline{\boldsymbol{A}}2} \otimes \boldsymbol{N}_{\overline{\boldsymbol{A}}2}] \quad .
\tag{4.46}
$$

We note that the direction vectors

$$
\boldsymbol{N}_{\overline{\boldsymbol{A}}1} = \boldsymbol{F}_\mathrm{p}^{-1} \cdot \overline{\boldsymbol{N}}_{\overline{\boldsymbol{A}}1} \tag{4.47a} \qquad\qquad \boldsymbol{N}_{\overline{\boldsymbol{A}}2} = \boldsymbol{F}_\mathrm{p}^{-1} \cdot \overline{\boldsymbol{N}}_{\overline{\boldsymbol{A}}2} \tag{4.47b}
$$

are $\boldsymbol{C}_\mathrm{p}$-orthonormal, i.e.,

$$
\boldsymbol{N}_{\overline{\boldsymbol{A}}1} \cdot \boldsymbol{C}_\mathrm{p} \cdot \boldsymbol{N}_{\overline{\boldsymbol{A}}1} = 1 \ \ (4.48a) \quad \boldsymbol{N}_{\overline{\boldsymbol{A}}2} \cdot \boldsymbol{C}_\mathrm{p} \cdot \boldsymbol{N}_{\overline{\boldsymbol{A}}2} = 1 \ \ (4.48b) \quad \boldsymbol{N}_{\overline{\boldsymbol{A}}1} \cdot \boldsymbol{C}_\mathrm{p} \cdot \boldsymbol{N}_{\overline{\boldsymbol{A}}2} = 0 \ \ (4.48c)
$$

which allows for a simple representation of higher-order powers of the mixed-variant structural tensor, e.g.,

$$
\boldsymbol{A}_\mathrm{p}^2 = \frac{1}{4} \boldsymbol{C}_\mathrm{p} \cdot [\boldsymbol{N}_{\overline{\boldsymbol{A}}1} \otimes \boldsymbol{N}_{\overline{\boldsymbol{A}}1} + \boldsymbol{N}_{\overline{\boldsymbol{A}}2} \otimes \boldsymbol{N}_{\overline{\boldsymbol{A}}2}] \quad .
\tag{4.49}
$$

4.2.3 Evaluation of the dissipation inequality

For an elastically isotropic material it was shown in Section 4.1.3 that the reduced dissipation inequality takes the form

$$
D^\mathrm{red} = \boldsymbol{M} : \boldsymbol{\Gamma}_\mathrm{p} + q\,\dot{\kappa} \geq 0 \quad .
\tag{4.50}
$$

In order to fulfil (4.50) a priori for every possible load path we will assume the existence of a convex plastic potential in the spirit of generalised standard materials, [51]. More specifically speaking, an associated-type flow rule is used such that the plastic potential coincides with the yield function. Following a standard procedure, the corresponding rate

equations for the plastic velocity gradient-type tensor $\boldsymbol{\Gamma}_{\mathrm{p}}$ and for the internal variable κ are then given by

$$\boldsymbol{\Gamma}_{\mathrm{p}} = \lambda_{\mathrm{p}} \frac{\partial f}{\partial \boldsymbol{M}} = \lambda_{\mathrm{p}} \boldsymbol{\Lambda}_{\mathrm{p}} \qquad (4.51\mathrm{a}) \qquad \dot{\kappa} = \lambda_{\mathrm{p}} \frac{\partial f}{\partial q} \qquad (4.51\mathrm{b})$$

with the plastic multiplier $\lambda_{\mathrm{p}} \geq 0$. We take note of the fact that $\lambda_{\mathrm{p}} > 0$ in the case of plastic loading, while the identity $\lambda_{\mathrm{p}} = 0$ holds if the material deforms only elastically. Moreover, evaluating (4.51a) and (4.51b) for the specific yield function (4.44) yields

$$
\begin{aligned}
\boldsymbol{\Gamma}_{\mathrm{p}} = \lambda_{\mathrm{p}} \Bigg[\ & 2\,a_1\,\boldsymbol{M}_{\mathrm{dev}}^{\star} + 2\,a_2\,\mathrm{tr}\left(\boldsymbol{M}_{\mathrm{dev}} \cdot \boldsymbol{A}_{\mathrm{p}}\right)\,\boldsymbol{A}_{\mathrm{p}}^{\star} + 2\,a_3\,\mathrm{tr}\left(\boldsymbol{M}_{\mathrm{dev}} \cdot \boldsymbol{A}_{\mathrm{p}}^2\right)\left[\boldsymbol{A}_{\mathrm{p}}^2\right]^{\star} \\
& + \ a_4\left[\mathrm{tr}\left(\boldsymbol{M}_{\mathrm{dev}} \cdot \boldsymbol{A}_{\mathrm{p}}^2\right)\,\boldsymbol{A}_{\mathrm{p}}^{\star} + \mathrm{tr}\left(\boldsymbol{M}_{\mathrm{dev}} \cdot \boldsymbol{A}_{\mathrm{p}}\right)\left[\boldsymbol{A}_{\mathrm{p}}^2\right]^{\star}\right] \\
& + \ a_5\left[\boldsymbol{M} \cdot \boldsymbol{A}_{\mathrm{p}} + \boldsymbol{A}_{\mathrm{p}} \cdot \boldsymbol{M}\right]^{\star} + a_6\left[\boldsymbol{M} \cdot \boldsymbol{A}_{\mathrm{p}}^2 + \boldsymbol{A}_{\mathrm{p}}^2 \cdot \boldsymbol{M}\right]^{\star} \Bigg] : \mathsf{I}_{\mathrm{dev}}^{\natural\star}
\end{aligned} \qquad (4.52)
$$

and

$$\dot{\kappa} = \lambda_{\mathrm{p}} \quad , \qquad\qquad\qquad\qquad\qquad\qquad\qquad\qquad\qquad (4.53)$$

with the fourth order deviatoric projection operator defined as

$$\mathsf{I}_{\mathrm{dev}}^{\natural\star} = \boldsymbol{G}^{\natural\star} \,\overline{\otimes}\, \boldsymbol{G}^{\natural} - \frac{1}{3}\,\boldsymbol{G}^{\natural\star} \otimes \boldsymbol{G}^{\natural} \quad . \qquad\qquad\qquad\qquad (4.54)$$

Note that the specific form of $\boldsymbol{\Gamma}_{\mathrm{p}}$ proposed in (4.52) can be shown to be $\boldsymbol{C}_{\mathrm{p}}$-symmetric by appealing to the $\boldsymbol{C}_{\mathrm{p}}$-symmetry of $\boldsymbol{M}_{\mathrm{dev}}$ and $\boldsymbol{A}_{\mathrm{p}}$. Since the yield function is chosen to be a function of the deviatoric referential Mandel stress tensor, $\boldsymbol{\Gamma}_{\mathrm{p}}$ is likewise found to be deviatoric. By making use of (4.9) this observation furthermore implies $\mathrm{tr}\left(\dot{\boldsymbol{C}}_{\mathrm{p}} \cdot \boldsymbol{C}_{\mathrm{p}}^{-1}\right) = 0$ and, accordingly, $\mathrm{d}\left(\det\left(\boldsymbol{C}_{\mathrm{p}}\right)\right)/\mathrm{dt} = 0$, i.e. the plastic flow is volume preserving.

For a convex yield function of the form

$$f = M_{\mathrm{eq}} - [1 - q] \quad , \qquad\qquad\qquad\qquad\qquad\qquad\qquad (4.55)$$

which will be employed in this contribution with M_{eq} being given by the quadratic form in (4.44), the dissipation inequality can be estimated for the case that plastic deformation occurs according to

$$\mathcal{D}^{\mathrm{red}} = \boldsymbol{M} : \lambda_{\mathrm{p}} \frac{\partial f}{\partial \boldsymbol{M}} + q\,\lambda_{\mathrm{p}} \frac{\partial f}{\partial q} = \lambda_{\mathrm{p}}\left[\frac{\partial f}{\partial \boldsymbol{M}} : \boldsymbol{M} + q\right] \geq \lambda_{\mathrm{p}}\left[1 - q + q\right] = \lambda_{\mathrm{p}} > 0 \,. \quad (4.56)$$

On the other hand, if the material only deforms elastically, the plastic multiplier is zero, such that the dissipation inequality is trivially fulfilled.

4.2.4 On the convexity of the yield function

In Section 4.2.3 it is shown that the dissipation inequality is fulfilled if the yield function which serves as the plastic potential is a convex function of the referential Mandel stress tensor. In this contribution we focus on an orthotropic yield function of the deviatoric part of the referential Mandel stress tensor $\boldsymbol{M}_{\mathrm{dev}}$ which is given in its general form by (4.44). For the yield function to be convex in $\boldsymbol{M}$, the condition

$$\mathrm{d}\boldsymbol{M} : \frac{\partial^2 f}{\partial \boldsymbol{M} \partial \boldsymbol{M}} : \mathrm{d}\boldsymbol{M} \geq 0 \tag{4.57}$$

has to hold for every possible load state. By inserting the second derivatives with respect to the Mandel stresses, we arrive at

$$\mathrm{d}\boldsymbol{M} : \frac{\partial^2 f}{\partial \boldsymbol{M} \partial \boldsymbol{M}} : \mathrm{d}\boldsymbol{M} = \left[\mathbf{I}_{\mathrm{dev}}^{\natural\star} : \mathrm{d}\boldsymbol{M} \right] : \frac{\partial^2 f}{\partial \boldsymbol{M}_{\mathrm{dev}} \partial \boldsymbol{M}_{\mathrm{dev}}} : \left[\mathbf{I}_{\mathrm{dev}}^{\natural\star} : \mathrm{d}\boldsymbol{M} \right] \tag{4.58}$$

with

$$\begin{aligned}
\frac{\partial^2 f}{\partial \boldsymbol{M}_{\mathrm{dev}} \partial \boldsymbol{M}_{\mathrm{dev}}} = {}& 2\,a_1\,\boldsymbol{G}^{\natural} \underline{\otimes} \boldsymbol{G}^{\natural\star} \\
& + 2\,a_2\,\boldsymbol{A}_{\mathrm{p}}^{\star} \otimes \boldsymbol{A}_{\mathrm{p}}^{\star} + 2\,a_3\,\left[\boldsymbol{A}_{\mathrm{p}}^2 \right]^{\star} \otimes \left[\boldsymbol{A}_{\mathrm{p}}^2 \right]^{\star} + a_4\,\left[\boldsymbol{A}_{\mathrm{p}}^{\star} \otimes \left[\boldsymbol{A}_{\mathrm{p}}^2 \right]^{\star} + \left[\boldsymbol{A}_{\mathrm{p}}^2 \right]^{\star} \otimes \boldsymbol{A}_{\mathrm{p}}^{\star} \right] \\
& + \quad a_5 \left[\boldsymbol{A}_{\mathrm{p}}^{\star} \,\overline{\otimes}\, \boldsymbol{G}^{\natural\star} + \boldsymbol{G}^{\natural} \underline{\otimes} \boldsymbol{A}_{\mathrm{p}} \right] \qquad + a_6 \left[\left[\boldsymbol{A}_{\mathrm{p}}^2 \right]^{\star} \,\overline{\otimes}\, \boldsymbol{G}^{\natural\star} + \boldsymbol{G}^{\natural} \underline{\otimes} \boldsymbol{A}_{\mathrm{p}}^2 \right].
\end{aligned} \tag{4.59}$$

Since the material parameters a_5 and a_6 are chosen to be zero for the specific prototype model to be employed in this contribution, see Appendix C.1, we will focus on the remaining four summands. First, we find that

$$\left[\mathbf{I}_{\mathrm{dev}}^{\natural\star} : \mathrm{d}\boldsymbol{M} \right] : \left[2\,\boldsymbol{G}^{\natural} \underline{\otimes} \boldsymbol{G}^{\natural\star} \right] : \left[\mathbf{I}_{\mathrm{dev}}^{\natural\star} : \mathrm{d}\boldsymbol{M} \right] = 2\,\mathrm{tr}\left(\mathrm{d}\boldsymbol{M}_{\mathrm{dev}} \cdot \mathrm{d}\boldsymbol{M}_{\mathrm{dev}} \right) \geq 0 \tag{4.60}$$

holds. Note, that all eigenvalues of $\boldsymbol{M}$ are real-valued since $\boldsymbol{M}$ is defined as the product of the two symmetric tensors $\boldsymbol{C}$ and $\boldsymbol{S}$, cf. (4.20), with $\boldsymbol{C}$ being positive definite. By using (4.60), introducing the abbreviations

$$\mathrm{d}M_- = \boldsymbol{A}_{\mathrm{p}}^{\star} \quad : \left[\mathbf{I}_{\mathrm{dev}}^{\natural\star} : \mathrm{d}\boldsymbol{M} \right] \tag{4.61a}$$

$$\mathrm{d}M_+ = \left[\boldsymbol{A}_{\mathrm{p}}^2 \right]^{\star} : \left[\mathbf{I}_{\mathrm{dev}}^{\natural\star} : \mathrm{d}\boldsymbol{M} \right] \tag{4.61b}$$

and with the requirement

$$a_1 \geq 0 \qquad (4.62\text{a}) \qquad a_2 \geq 0 \qquad (4.62\text{b}) \qquad a_3 \geq 0 \qquad (4.62\text{c})$$

one finally arrives at

$$\mathrm{d}\boldsymbol{M} : \frac{\partial^2 f}{\partial \boldsymbol{M} \partial \boldsymbol{M}} : \mathrm{d}\boldsymbol{M} \geq 2\,a_2\,\mathrm{d}M_-^2 \;+ 2\,a_3\,\mathrm{d}M_+^2 \;+ 2\,a_4\,\mathrm{d}M_-\,\mathrm{d}M_+ \qquad (4.63\text{a})$$

$$\geq 4\,|\sqrt{a_2}\,\mathrm{d}M_-|\,|\sqrt{a_3}\,\mathrm{d}M_+| + 2\,a_4\,\mathrm{d}M_-\,\mathrm{d}M_+ \qquad (4.63\text{b})$$

where the inequality

$$\left[\,|\sqrt{a_2}\,\mathrm{d}M_-| - |\sqrt{a_3}\,\mathrm{d}M_+|\,\right]^2 = |\sqrt{a_2}\,\mathrm{d}M_-|^2 + |\sqrt{a_3}\,\mathrm{d}M_+|^2 - 2\,|\sqrt{a_2}\,\mathrm{d}M_-|\,|\sqrt{a_3}\,\mathrm{d}M_+| \geq 0$$
$$(4.64)$$

has been invoked. For the dissipation inequality to be fulfilled we thus require relation

$$2\,\sqrt{a_2}\,\sqrt{a_3} \geq |a_4| \qquad (4.65)$$

between the material parameters to hold.

4.3 Plastic spin prototype model

After a brief summary of the experimental findings presented in [65] and motivated by the latter, this section focuses on the development of a specific form of the plastic spin tensor $\boldsymbol{W}$.

4.3.1 Experimental findings

Kim and Yin experimentally analysed the yielding behaviour of cold-rolled steel sheet metal made of low-carbon steel by means of tension tests with the focus of the investigations being on the directional dependency of the uni-axial yield limit, i.e. on the symmetry group of the yield function, and its evolution due to finite plastic deformation processes. Their experimental results published in [65] suggest that the symmetry group is maintained throughout the deformation process, but that the principal material axes of the initially (plastically) orthotropic material align with the principal loading directions of the tension tests.

In a first experimental step, full size metal sheets were stretched along the rolling direction (RD) to increase the initially mild plastic anisotropy which was induced by the rolling process. From these sheets, medium size tensile specimens were prepared at various angles ϕ_{L} relative to the rolling direction in a second step, as schematically indicated by the light grey surface in Figure 4.2. The medium size specimens were
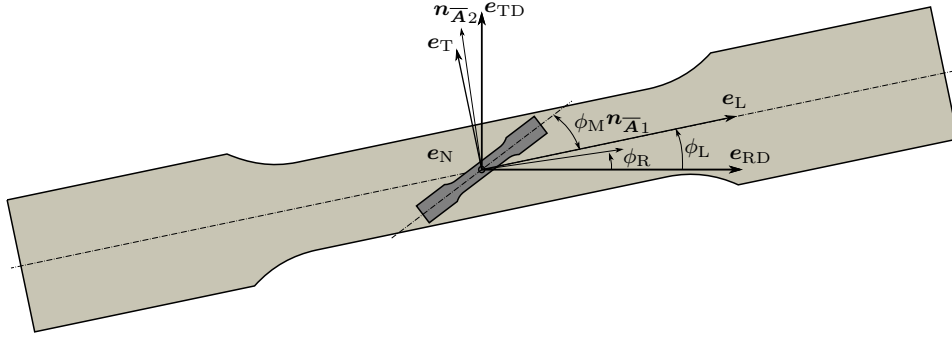
Figure 4.2: Experimental setup and definitions of various angles.

then subjected to various amounts of strain, given in terms of the respective coefficient of the Hencky strain tensor in loading direction, H_{L}. For each load level, i.e. $H_{\mathrm{L}} \in \{0\%, 1\%, 2\%, 5\%, 10\%\}$, the distribution of the uni-axial yield limit relative to the tensile axis was determined in a final step. To this end, miniature tensile specimens were prepared from the gauge section of the medium size tensile specimens at angles ϕ_{M} as indicated in Figure 4.2, and tension tests were carried out. The experimental results are summarised in Figures 4.3(a-c) with the solid lines indicating the quadratic yield function of Hill [55] which Kim and Yin fitted to the experimental data. Based on these experiments, Kim and Yin argued that the initial orthotropic symmetry is maintained but that the orientations of the orthotropy axes change continuously with the deformation, meaning that they align with the loading direction. The observed rotation of the preferred material axes was furthermore quantified in terms of the angle ϕ_{R} between the rolling direction (RD) and the first preferred material direction $\boldsymbol{n}_{\overline{\boldsymbol{A}}1}$, respectively, between the transverse direction (TD) and the second preferred material direction $\boldsymbol{n}_{\overline{\boldsymbol{A}}2}$, and is provided in Figure 4.10. It is noted that the rolling direction and the preferred material direction $\boldsymbol{n}_{\overline{\boldsymbol{A}}1}$ coincide after the rolling process and hence also after the first pre-stretching such that ϕ_{R} resembles the rotation of the material axes.

Focusing in more detail on the experimental findings, Figure 4.3 suggests that an anticlockwise rotation of the symmetry group is observable for $\phi_{\mathrm{L}} = 30°$, while a clockwise rotation is seen for $\phi_{\mathrm{L}} = 60°$, with nearly the same qualitative evolution being observable. This observation might be explained based on the, to a good approximation, 90° symmetry of the yielding behaviour such that the load case $\phi_{\mathrm{L}} = 60°$ is approximately equal with a loading at an angle $\phi_{\mathrm{L}} = -30°$. If we suppose, based on this observation, that the spin of the symmetry group is a function of the angle between the loading direction and the closest preferred material direction, and if this function is supposed to be continuous, this essentially means that the spin of the symmetry group needs to be zero for an angle of $30° < \phi_{\mathrm{L}}^0 < 60°$. Moreover, due to symmetry considerations, it seems reasonable to expect the root to be close to $\phi_{\mathrm{L}} = 45°$.

Interestingly, the experimental results for $\phi_{\mathrm{L}} = 45°$ do not show the same qualitative pattern as those for $\phi_{\mathrm{L}} = 30°$ and $\phi_{\mathrm{L}} = 60°$. Specifically speaking, we do observe an
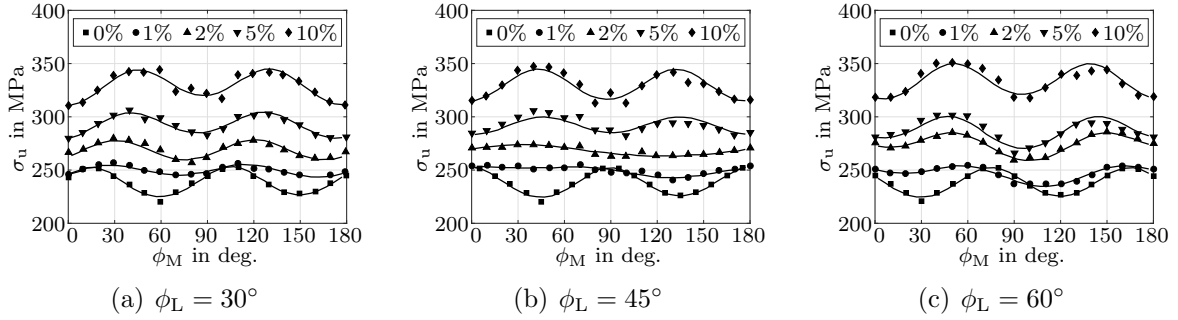
Figure 4.3: Experimental findings by Kim and Yin, reproduced from [65]. Depicted is the uni-axial yield limit in terms of the Cauchy stresses σ_{u} for various angles ϕ_{M} relative to the loading direction ϕ_{L} and various (uni-axial) elongations in terms of the Hencky strain in loading direction H_{L}. The solid lines represent Hill's quadratic yield function which is fitted against the experimental data in [65].

alignment of the preferred material axes with the loading direction, cf. the experimental results for $H_{\mathrm{L}} = 5\%$ and $H_{\mathrm{L}} = 10\%$ in Figure 4.3(b). However, a closer look at the experimental results for $H_{\mathrm{L}} = 1\%$ and $H_{\mathrm{L}} = 2\%$ reveals an isotropic yielding behaviour rather than an orthotropic one such that, although the final results suggest a rotation of the symmetry group, the path does not. We suppose that this observation can be explained if we think of the material being a polycrystalline metal and taking into account the observations for $\phi_{\mathrm{L}} = 30°$ and $\phi_{\mathrm{L}} = 60°$ discussed before. Due to the rolling process, a preferred material axis at each material point is nearly aligned with the rolling direction. However, this alignment is not perfect – nor is the loading direction $\phi_{\mathrm{L}} = 45°$. Thus, an anticlockwise rotation of the symmetry group should be observable at some material points, while a clockwise rotation might be observed in others. Hence, we expect a (macroscopically) quasi-isotropic material behaviour for a rotation of approximately $\pm 22.5°$ (at each material point) due to the almost $90°$ symmetry of the yielding behaviour. Appealing to the same notion we furthermore expect a (macroscopically) anisotropic response for rotations $|\phi_{\mathrm{R}}| > 22.5°$, again, which is in good accordance with the experimental results shown in Figure 4.3(b).

The latter observations have important implications on the development of the specific form of the spin tensor $\boldsymbol{W}$ to be discussed in Section 4.3.2 and will be subject to a detailed analysis with regard to the finite element-based simulations to be presented in Section 4.4.2.

4.3.2 A specific evolution equation for the structural tensor

In the following we attempt to simulate the experimentally observed rotation of the preferred material axes based on the constitutive framework summarised in Section 4.1 and on the specific model presented in Section 4.2. However, to complete the model description, a suitable form of the residual-type evolution equation still needs to be

developed, since a model which is solely based on a convected-type evolution of the structural tensor cannot capture the experimental findings, as will be shown as this work proceeds.

As the elastic material response is assumed to be isotropic, the plastic spin tensor $\boldsymbol{W}$, governing the residual-type evolution of the material symmetry group, may be chosen arbitrarily without violating thermodynamic consistency, see Section 4.1.3. By again invoking the multiplicative split for the sake of motivation, it is observed that the (referential) $\boldsymbol{C}_\mathrm{p}$-skew tensor $\boldsymbol{W}$ can be related to the $\overline{\boldsymbol{G}}^\flat$-skew tensor $\overline{\boldsymbol{W}}$ of the intermediate configuration. Following the same lines as for the yield function we will derive a well-interpretable form of the plastic spin tensor in the intermediate configuration first, and in a second step define $\boldsymbol{W}$ based on the pull-back operation to the reference configuration. To this end, we first assume that the evolution of the symmetry group takes place during plastic deformation only and that it is inactive for purely elastic loadings. In accordance with the experimental findings presented in Section 4.3.1 we further require that the preferred material axes undergo a rotation such that they align with the principal loading direction, in terms of the stresses or strains as will be discussed in the ensuing developments. This additionally implies that no rotation of the preferred material axes occurs if the principal loading direction is aligned with a preferred material direction, i.e. if the loading direction coincides with the rolling direction or the direction perpendicular to it, and that a saturation-kind behaviour is to be expected. According to the experimental findings presented in Section 4.3.1, the sense of rotation should moreover depend on the direction of the principal loading relative to the preferred material axes.

Since the elastic material response is assumed to be isotropic, it is observed that the elastic right Cauchy-Green tensor $\boldsymbol{C}_\mathrm{e} = \boldsymbol{F}_\mathrm{e}^\star \cdot \boldsymbol{g}^\flat \cdot \boldsymbol{F}_\mathrm{e}$ and the elastic Piola-Kirchhoff stress tensor $\boldsymbol{S}_\mathrm{e} = 2\,\partial W/\partial \boldsymbol{C}_\mathrm{e}$ commute. Accordingly, the Mandel stress tensor of the intermediate configuration $\overline{\boldsymbol{M}} = \boldsymbol{C}_\mathrm{e} \cdot \boldsymbol{S}_\mathrm{e}$ is symmetric and features the same principal directions as $\boldsymbol{C}_\mathrm{e}$ and $\boldsymbol{S}_\mathrm{e}$. We thus note that by aligning any of the latter tensors with the preferred material directions, i.e. with the eigenvectors of $\overline{\boldsymbol{A}}$, the other tensors considered are aligned likewise. To motivate a suitable form of the plastic spin tensor $\overline{\boldsymbol{W}}$ we will make use of the spectral decompositions of the tensors $\overline{\boldsymbol{A}}$ and $\boldsymbol{C}_\mathrm{e}$, specifically,

$$\overline{\boldsymbol{A}} = \sum_{i=1}^{3} \lambda_{\overline{\boldsymbol{A}}i}\,\overline{\boldsymbol{N}}_{\overline{\boldsymbol{A}}i} \otimes \overline{\boldsymbol{N}}_{\overline{\boldsymbol{A}}i} \quad = \quad \frac{1}{2}\,\overline{\boldsymbol{N}}_{\overline{\boldsymbol{A}}1} \otimes \overline{\boldsymbol{N}}_{\overline{\boldsymbol{A}}1} \quad - \quad \frac{1}{2}\,\overline{\boldsymbol{N}}_{\overline{\boldsymbol{A}}2} \otimes \overline{\boldsymbol{N}}_{\overline{\boldsymbol{A}}2} \quad (4.66\mathrm{a})$$

$$\boldsymbol{C}_\mathrm{e} = \sum_{i=1}^{3} \lambda_{\boldsymbol{C}_\mathrm{e}i}\,\overline{\boldsymbol{N}}_{\boldsymbol{C}_\mathrm{e}i} \otimes \overline{\boldsymbol{N}}_{\boldsymbol{C}_\mathrm{e}i} = \lambda_{\boldsymbol{C}_\mathrm{e}1}\,\overline{\boldsymbol{N}}_{\boldsymbol{C}_\mathrm{e}1} \otimes \overline{\boldsymbol{N}}_{\boldsymbol{C}_\mathrm{e}1} + \lambda_{\boldsymbol{C}_\mathrm{e}2}\,\overline{\boldsymbol{N}}_{\boldsymbol{C}_\mathrm{e}2} \otimes \overline{\boldsymbol{N}}_{\boldsymbol{C}_\mathrm{e}2}$$
$$+ \lambda_{\boldsymbol{C}_\mathrm{e}3}\,\overline{\boldsymbol{N}}_{\boldsymbol{C}_\mathrm{e}3} \otimes \overline{\boldsymbol{N}}_{\boldsymbol{C}_\mathrm{e}3} \qquad (4.66\mathrm{b})$$

with eigenvalues $\lambda_\bullet$ and eigenvectors $\overline{\boldsymbol{N}}_\bullet$ as well as $\lambda_{\boldsymbol{C}_\mathrm{e}1} \geq \lambda_{\boldsymbol{C}_\mathrm{e}2} \geq \lambda_{\boldsymbol{C}_\mathrm{e}3} > 0$. In the experiments discussed in Section 4.3.1, the principal material axes are initially aligned with the rolling direction (RD) and the transverse direction (TD). The prepared samples

are then subjected to a load acting in the plane which is spanned by the latter two directions, and an in-plane rotation of the preferred material axes is observed. Motivated by the latter observations let us assume for now that the first two eigenvectors of $\boldsymbol{C}_{\mathrm{e}}$ lie in the RD-TD-plane and denote the angle between $\overline{\boldsymbol{N}}_{\overline{\boldsymbol{A}}1}$ and $\overline{\boldsymbol{N}}_{\boldsymbol{C}_{\mathrm{e}}1}$ by χ, Figure 4.4(a). The non-zero coefficients of the $\overline{\boldsymbol{G}}^{\flat}$-skew part of $\overline{\boldsymbol{A}} \cdot \boldsymbol{C}_{\mathrm{e}}$ with respect to an orthonormal basis with two base vectors in the RD-TD-plane, e.g. $\overline{\boldsymbol{N}}_{\overline{\boldsymbol{A}}1}$ and $\overline{\boldsymbol{N}}_{\overline{\boldsymbol{A}}2}$, read

$$\overline{\boldsymbol{N}}_{\overline{\boldsymbol{A}}1} \cdot \overline{\boldsymbol{G}}^{\flat} \cdot \frac{1}{2} \left[\overline{\boldsymbol{A}} \cdot \boldsymbol{C}_{\mathrm{e}} - \left[\overline{\boldsymbol{A}} \cdot \boldsymbol{C}_{\mathrm{e}} \right]^{\mathrm{t}} \right] \cdot \overline{\boldsymbol{N}}_{\overline{\boldsymbol{A}}2} = \frac{1}{2} \left[\lambda_{\boldsymbol{C}_{\mathrm{e}}1} - \lambda_{\boldsymbol{C}_{\mathrm{e}}2} \right] \cos\left(\chi \right) \sin\left(\chi \right), \quad (4.67\mathrm{a})$$

$$\overline{\boldsymbol{N}}_{\overline{\boldsymbol{A}}2} \cdot \overline{\boldsymbol{G}}^{\flat} \cdot \frac{1}{2} \left[\overline{\boldsymbol{A}} \cdot \boldsymbol{C}_{\mathrm{e}} - \left[\overline{\boldsymbol{A}} \cdot \boldsymbol{C}_{\mathrm{e}} \right]^{\mathrm{t}} \right] \cdot \overline{\boldsymbol{N}}_{\overline{\boldsymbol{A}}1} = -\frac{1}{2} \left[\lambda_{\boldsymbol{C}_{\mathrm{e}}1} - \lambda_{\boldsymbol{C}_{\mathrm{e}}2} \right] \cos\left(\chi \right) \sin\left(\chi \right). \quad (4.67\mathrm{b})$$

In addition, we observe that

$$\overline{\boldsymbol{A}} : \boldsymbol{C}_{\mathrm{e}} = \frac{1}{2} \left[\lambda_{\boldsymbol{C}_{\mathrm{e}}1} - \lambda_{\boldsymbol{C}_{\mathrm{e}}2} \right] \left[\cos^{2}\left(\chi \right) - \sin^{2}\left(\chi \right) \right]. \quad (4.68)$$

Based on (4.67) and (4.68) we thus propose $\overline{\boldsymbol{W}}$ to be of the form

$$\overline{\boldsymbol{W}} = \lambda_{\mathrm{p}}\, c_{\boldsymbol{W}} \frac{1}{2} \left[\overline{\boldsymbol{A}} \cdot \boldsymbol{C}_{\mathrm{e}} - \left[\overline{\boldsymbol{A}} \cdot \boldsymbol{C}_{\mathrm{e}} \right]^{\mathrm{t}} \right] \overline{\boldsymbol{A}} : \boldsymbol{C}_{\mathrm{e}} \quad (4.69\mathrm{a})$$

$$= \lambda_{\mathrm{p}}\, c_{\boldsymbol{W}} \frac{1}{2} \left[\overline{\boldsymbol{A}} \cdot \boldsymbol{C}_{\mathrm{e}} - \overline{\boldsymbol{G}}^{\sharp} \cdot \boldsymbol{C}_{\mathrm{e}} \cdot \overline{\boldsymbol{A}} \cdot \overline{\boldsymbol{G}}^{\flat} \right] \overline{\boldsymbol{A}} : \boldsymbol{C}_{\mathrm{e}} \quad (4.69\mathrm{b})$$

such that

$$\overline{\boldsymbol{N}}_{\overline{\boldsymbol{A}}1} \cdot \overline{\boldsymbol{G}}^{\flat} \cdot \overline{\boldsymbol{W}} \cdot \overline{\boldsymbol{N}}_{\overline{\boldsymbol{A}}2} = \frac{1}{16} \lambda_{\mathrm{p}}\, c_{\boldsymbol{W}} \left[\lambda_{\boldsymbol{C}_{\mathrm{e}}1} - \lambda_{\boldsymbol{C}_{\mathrm{e}}2} \right]^{2} \sin\left(4\,\chi \right), \quad (4.70\mathrm{a})$$

$$\overline{\boldsymbol{N}}_{\overline{\boldsymbol{A}}2} \cdot \overline{\boldsymbol{G}}^{\flat} \cdot \overline{\boldsymbol{W}} \cdot \overline{\boldsymbol{N}}_{\overline{\boldsymbol{A}}1} = -\frac{1}{16} \lambda_{\mathrm{p}}\, c_{\boldsymbol{W}} \left[\lambda_{\boldsymbol{C}_{\mathrm{e}}1} - \lambda_{\boldsymbol{C}_{\mathrm{e}}2} \right]^{2} \sin\left(4\,\chi \right), \quad (4.70\mathrm{b})$$

with the material parameter $c_{\boldsymbol{W}} \geq 0$ controlling the speed of the residual-type evolution. By construction, the operator $\overline{\boldsymbol{W}}$ is scaled by the plastic multiplier λ_{p} such that the plastic spin is inactive for purely elastic loading, and increases with the rate of plastic deformation. Furthermore, we observe that the residual-type evolution increases with the difference of the eigenvalues of $\boldsymbol{C}_{\mathrm{e}}$. Essentially this means that no rotation will occur in the limiting case when the two (in-plane) eigenvalues of $\boldsymbol{C}_{\mathrm{e}}$ coincide. In this case, every vector in the RD-TD-plane would be an eigenvector so that there is no distinct orthonormal set of vectors which the preferred material directions could align with. On the other hand, if the difference between the two in-plane eigenvalues is significant, two distinct principal directions of deformation exist. Whereas the other factors were restricted to being positive, the last factor in (4.70) may take a negative or positive sign, thus controlling the plastic spin direction. Specifically speaking, as illustrated in Figure 4.4(a) and Figure 4.4(b), the sign depends on the relative orientation between the preferred material axes and the principal loading direction, and thus allows
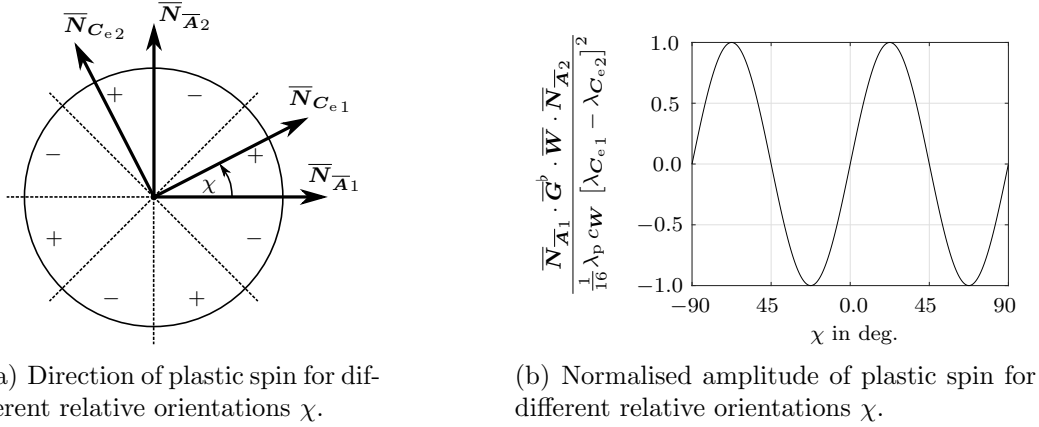
(a) Direction of plastic spin for different relative orientations χ.

(b) Normalised amplitude of plastic spin for different relative orientations χ.

Figure 4.4: Direction and normalised amplitude of $\overline{W}$ as a function of the relative orientation χ between the principal loading direction and the preferred material axes.

us to account for the experimentally observed clockwise or anticlockwise rotation of the preferred material axes.

Since the multiplicative split is only invoked for the sake of motivation and since a purely referential representation is sought, the $\overline{G}^{\flat}$-skew tensor $\overline{W}$ needs to be related to the C_p-skew tensor W, which determines the residual-type evolution of the structural tensor, cf. (4.12). Performing the pull-back operation with respect to the tangent map F_p according to (4.28) results in

$$W = \lambda_\mathrm{p}\, c_W\, \frac{1}{2}\left[A \cdot C - C_\mathrm{p}^{-1} \cdot C \cdot A \cdot C_\mathrm{p}\right]\ A : C = \lambda_\mathrm{p}\, \Omega \quad . \tag{4.71}$$

4.4 Representative simulation results

In this section we will focus on the application of the specific model proposed in Section 4.2 and Section 4.3 to the modelling of evolving anisotropies of rolled sheet metal as experimentally observed in [65]. To this end, we will investigate as to whether a convected evolution-based model is capable of reproducing the experimentally observed rotation of the preferred material axes or whether a residual-type evolution additionally needs to be taken into account. In addition to tension tests, we will furthermore focus on the simulation of in-plane torsion tests to analyse the principal model properties for shear-dominated boundary value problems.

Focusing on the calculation of the symmetry group's rotation we face the conceptual difficulty that the symmetry group is defined in the intermediate configuration based on the notion of the multiplicative split. However, the multiplicative split is only used for motivation purposes and not invoked in the calculations for its rotational indeterminacy, which is a key advantage of the modelling approach summarised in Section 4.1, so that the quantities which are defined in the fictitious intermediate configuration are not

accessible. The primary and the referential form of the yield function (4.42) and (4.44) give rise to the spatial representation

$$
\begin{aligned}
f = \Big[\quad & a_1 \operatorname{tr}\left(\left[\boldsymbol{\tau}_{\mathrm{dev}}^{\natural\star}\right]^2\right) + a_2 \operatorname{tr}\left(\boldsymbol{\tau}_{\mathrm{dev}}^{\natural\star} \cdot \boldsymbol{c}_{\mathrm{e}} \cdot \boldsymbol{a}\right) \operatorname{tr}\left(\boldsymbol{\tau}_{\mathrm{dev}}^{\natural\star} \cdot \boldsymbol{c}_{\mathrm{e}} \cdot \boldsymbol{a}\right) \\
& + a_3 \operatorname{tr}\left(\boldsymbol{\tau}_{\mathrm{dev}}^{\natural\star} \cdot [\boldsymbol{c}_{\mathrm{e}} \cdot \boldsymbol{a}]^2\right) \operatorname{tr}\left(\boldsymbol{\tau}_{\mathrm{dev}}^{\natural\star} \cdot [\boldsymbol{c}_{\mathrm{e}} \cdot \boldsymbol{a}]^2\right) + a_4 \operatorname{tr}\left(\boldsymbol{\tau}_{\mathrm{dev}}^{\natural\star} \cdot \boldsymbol{c}_{\mathrm{e}} \cdot \boldsymbol{a}\right) \operatorname{tr}\left(\boldsymbol{\tau}_{\mathrm{dev}}^{\natural\star} \cdot [\boldsymbol{c}_{\mathrm{e}} \cdot \boldsymbol{a}]^2\right) \\
& + a_5 \operatorname{tr}\left(\left[\boldsymbol{\tau}_{\mathrm{dev}}^{\natural\star}\right]^2 \cdot \boldsymbol{c}_{\mathrm{e}} \cdot \boldsymbol{a}\right) + a_6 \operatorname{tr}\left(\left[\boldsymbol{\tau}_{\mathrm{dev}}^{\natural\star}\right]^2 \cdot [\boldsymbol{c}_{\mathrm{e}} \cdot \boldsymbol{a}]^2\right) \Big] - M_{\mathrm{y}}
\end{aligned}
\tag{4.72}
$$

with the deviatoric mixed-variant Kirchhoff stress tensor

$$
\boldsymbol{\tau}_{\mathrm{dev}}^{\natural\star} = \boldsymbol{F}^{-\star} \cdot \boldsymbol{M}_{\mathrm{dev}} \cdot \boldsymbol{F}^{\star} = \boldsymbol{F}_{\mathrm{e}}^{-\star} \cdot \overline{\boldsymbol{M}}_{\mathrm{dev}} \cdot \boldsymbol{F}_{\mathrm{e}}^{\star} \quad,
\tag{4.73}
$$

respectively the spatial Mandel-type stress tensor, the (contravariant) spatial structural tensor

$$
\boldsymbol{a} = \boldsymbol{F} \cdot \boldsymbol{A} \cdot \boldsymbol{F}^{\star} = \boldsymbol{F}_{\mathrm{e}} \cdot \overline{\boldsymbol{A}} \cdot \boldsymbol{F}_{\mathrm{e}}^{\star}
\tag{4.74}
$$

and the spatial representation of the intermediate configuration's metric

$$
\boldsymbol{c}_{\mathrm{e}} = \boldsymbol{F}^{-\star} \cdot \boldsymbol{C}_{\mathrm{p}} \cdot \boldsymbol{F}^{-1} = \boldsymbol{F}_{\mathrm{e}}^{-\star} \cdot \overline{\boldsymbol{G}}^{\flat} \cdot \boldsymbol{F}_{\mathrm{e}}^{-1} \quad.
\tag{4.75}
$$

Regarding metal plasticity, the elastic strain is usually assumed to be small so that $\boldsymbol{c}_{\mathrm{e}}$ is expected to be close to the identity. Since $\boldsymbol{C}_{\mathrm{p}}$ is a primary variable, this condition can easily be verified for the particular implementation at hand by invoking (4.75). Keeping the latter observation in mind and taking into account (4.72) we propose to carry out the spectral decomposition on the spatial structural tensor according to

$$
\boldsymbol{a} = \sum_{i=1}^{3} \lambda_{\boldsymbol{a}i}\, \boldsymbol{n}_{\boldsymbol{a}i} \otimes \boldsymbol{n}_{\boldsymbol{a}i} \quad,
\tag{4.76}
$$

with $\lambda_{\boldsymbol{a}1} \geq \lambda_{\boldsymbol{a}2} \geq \lambda_{\boldsymbol{a}3}$, to approximate the eigen-directions $\overline{\boldsymbol{N}}_{\overline{\boldsymbol{A}}i}$ of the structural tensor $\overline{\boldsymbol{A}}$ which was defined in the intermediate configuration, see also (4.66a), respectively to approximate their spatial representations $\boldsymbol{n}_{\overline{\boldsymbol{A}}i} = \boldsymbol{F}_{\mathrm{e}} \cdot \overline{\boldsymbol{N}}_{\overline{\boldsymbol{A}}i}$. Expressed differently, if $\boldsymbol{c}_{\mathrm{e}}$ is close to the identity, $\boldsymbol{F}_{\mathrm{e}}$ reduces to a pure rotation such that carrying out the spectral decomposition on $\overline{\boldsymbol{A}}$ and pushing the eigen-directions to the spatial configuration is identical with carrying out the spectral decomposition on $\boldsymbol{a}$. Note that $\boldsymbol{a}$ is symmetric so that the left and right eigenvectors are identical. As this work proceeds, the rotation of the material symmetry group will be calculated based on the rotation of the (first) eigenvector $\boldsymbol{n}_{\boldsymbol{a}1}$ at a selected quadrature point of each element. To quantify an effective value of the rotation ϕ_{R} which can be compared with the experiments [65], we will finally

take the mean value of the rotations which are observed at the elements of the gauge section.

4.4.1 Algorithmic formulation

The system of differential equations which governs the evolution of the internal variables in the case of plastic loading is given by the rate equations for the plastic right-Cauchy-Green tensor (4.9), the (contravariant) structural tensor (4.12) and the accumulated plastic strain (4.53), and is complemented by the yield condition $f = 0$. Applying standard Adams-Moulton-type time integration in terms of the trapezoidal rule, see also Remark 4.2, and making use of the symmetry properties of $\boldsymbol{C}_{\mathrm{p}}$ and $\boldsymbol{A}$ results in the discrete system of 14 unknowns

$$
\begin{aligned}
\boldsymbol{0} = {}& -\boldsymbol{C}_{\mathrm{p}}{}^{n+1} + \boldsymbol{C}_{\mathrm{p}}{}^{n} + \lambda_{\mathrm{p}}\frac{\Delta t}{2}\left[\boldsymbol{C}_{\mathrm{p}}{}^{n+1}\cdot\boldsymbol{\Lambda}_{\mathrm{p}}{}^{n+1} + \boldsymbol{\Lambda}_{\mathrm{p}}^{\star n+1}\cdot\boldsymbol{C}_{\mathrm{p}}{}^{n+1}\right] \\
& + \lambda_{\mathrm{p}}\frac{\Delta t}{2}\left[\boldsymbol{C}_{\mathrm{p}}{}^{n}\cdot\boldsymbol{\Lambda}_{\mathrm{p}}{}^{n} \quad + \boldsymbol{\Lambda}_{\mathrm{p}}^{\star n}\cdot\boldsymbol{C}_{\mathrm{p}}{}^{n}\right] \qquad =: \boldsymbol{R}_{\boldsymbol{C}_{\mathrm{p}}}
\end{aligned}
\tag{4.77a}
$$

$$
\begin{aligned}
\boldsymbol{0} = {}& -\boldsymbol{A}^{n+1} + \boldsymbol{A}^{n} - \lambda_{\mathrm{p}}\frac{\Delta t}{2}\left[\boldsymbol{\Lambda}_{\mathrm{p}}{}^{n+1}\cdot\boldsymbol{A}^{n+1} + \boldsymbol{A}^{n+1}\cdot\boldsymbol{\Lambda}_{\mathrm{p}}^{\star n+1}\right] \\
& - \lambda_{\mathrm{p}}\frac{\Delta t}{2}\left[\boldsymbol{\Omega}^{n+1}\cdot\boldsymbol{A}^{n+1} + \boldsymbol{A}^{n+1}\cdot\boldsymbol{\Omega}^{\star n+1}\right] \\
& - \lambda_{\mathrm{p}}\frac{\Delta t}{2}\left[\boldsymbol{\Lambda}_{\mathrm{p}}{}^{n}\cdot\boldsymbol{A}^{n} \quad + \boldsymbol{A}^{n}\cdot\boldsymbol{\Lambda}_{\mathrm{p}}^{\star n}\right] \\
& - \lambda_{\mathrm{p}}\frac{\Delta t}{2}\left[\boldsymbol{\Omega}^{n}\cdot\boldsymbol{A}^{n} \quad + \boldsymbol{A}^{n}\cdot\boldsymbol{\Omega}^{\star n}\right] \qquad =: \boldsymbol{R}_{\boldsymbol{A}}
\end{aligned}
\tag{4.77b}
$$

$$
0 = -\kappa^{n+1} + \kappa^{n} + \lambda_{\mathrm{p}}\Delta t \qquad\qquad\qquad\qquad =: R_{\kappa} \tag{4.77c}
$$

$$
0 = f^{n+1} \qquad\qquad\qquad\qquad\qquad\qquad\qquad =: R_{f} \tag{4.77d}
$$

which is to be solved on integration point level, see Appendix C.2 for details on the sensitivities . In (4.77), $\bullet^{n+1}$ designates the unknown value of an internal variable or function $\bullet$ after the application of a load increment in (fictitious) time $\Delta t = t^{n+1} - t^{n} \geq 0$, while $\bullet^{n}$ refers to the known value of the state variable or the known value of the function from the previous load step.

For a finite element-based implementation in terms of the Piola stress tensor $\boldsymbol{P}$, the (consistent) algorithmic tangent stiffness

$$
\begin{aligned}
\frac{\mathrm{d}\boldsymbol{P}^{n+1}}{\mathrm{d}\boldsymbol{F}^{n+1}} = {}& \boldsymbol{g}^{\natural}\,\overline{\otimes}\,\boldsymbol{S}^{n+1} + \boldsymbol{F}^{n+1}\cdot\left[\frac{\partial\boldsymbol{S}^{n+1}}{\partial\boldsymbol{F}^{n+1}} + \frac{\partial\boldsymbol{S}^{n+1}}{\partial\boldsymbol{C}_{\mathrm{p}}{}^{n+1}}:\frac{\mathrm{d}\boldsymbol{C}_{\mathrm{p}}{}^{n+1}}{\mathrm{d}\boldsymbol{F}^{n+1}} + \frac{\partial\boldsymbol{S}^{n+1}}{\partial\boldsymbol{A}^{n+1}}:\frac{\mathrm{d}\boldsymbol{A}^{n+1}}{\mathrm{d}\boldsymbol{F}^{n+1}}\right. \\
& \left. + \frac{\partial\boldsymbol{S}^{n+1}}{\partial\kappa^{n+1}}\otimes\frac{\mathrm{d}\kappa^{n+1}}{\mathrm{d}\boldsymbol{F}^{n+1}} + \frac{\partial\boldsymbol{S}^{n+1}}{\partial\lambda_{\mathrm{p}}}\otimes\frac{\mathrm{d}\lambda_{\mathrm{p}}}{\mathrm{d}\boldsymbol{F}^{n+1}}\right]
\end{aligned}
\tag{4.78}
$$

is required. The respective sensitivities of the internal variables with respect to the deformation gradient can be calculated following standard procedure as

$$
\begin{bmatrix} \mathrm{d}\boldsymbol{C}_{\mathrm{p}}^{n+1} \\[2mm] \mathrm{d}\boldsymbol{A}^{n+1} \\[2mm] \mathrm{d}\kappa^{n+1} \\[2mm] \mathrm{d}\lambda_{\mathrm{p}} \end{bmatrix} = - \begin{bmatrix} \frac{\partial \boldsymbol{R}_{C_{\mathrm{p}}}}{\partial \boldsymbol{C}_{\mathrm{p}}^{n+1}} & \frac{\partial \boldsymbol{R}_{C_{\mathrm{p}}}}{\partial \boldsymbol{A}^{n+1}} & \frac{\partial \boldsymbol{R}_{C_{\mathrm{p}}}}{\partial \kappa^{n+1}} & \frac{\partial \boldsymbol{R}_{C_{\mathrm{p}}}}{\partial \lambda_{\mathrm{p}}} \\[2mm] \frac{\partial \boldsymbol{R}_{A}}{\partial \boldsymbol{C}_{\mathrm{p}}^{n+1}} & \frac{\partial \boldsymbol{R}_{A}}{\partial \boldsymbol{A}^{n+1}} & \frac{\partial \boldsymbol{R}_{A}}{\partial \kappa^{n+1}} & \frac{\partial \boldsymbol{R}_{A}}{\partial \lambda_{\mathrm{p}}} \\[2mm] \frac{\partial R_{\kappa}}{\partial \boldsymbol{C}_{\mathrm{p}}^{n+1}} & \frac{\partial R_{\kappa}}{\partial \boldsymbol{A}^{n+1}} & \frac{\partial R_{\kappa}}{\partial \kappa^{n+1}} & \frac{\partial R_{\kappa}}{\partial \lambda_{\mathrm{p}}} \\[2mm] \frac{\partial R_{f}}{\partial \boldsymbol{C}_{\mathrm{p}}^{n+1}} & \frac{\partial R_{f}}{\partial \boldsymbol{A}^{n+1}} & \frac{\partial R_{f}}{\partial \kappa^{n+1}} & \frac{\partial R_{f}}{\partial \lambda_{\mathrm{p}}} \end{bmatrix}^{-1} \begin{bmatrix} \frac{\partial \boldsymbol{R}_{C_{\mathrm{p}}}}{\partial \boldsymbol{F}^{n+1}} \\[2mm] \frac{\partial \boldsymbol{R}_{A}}{\partial \boldsymbol{F}^{n+1}} \\[2mm] \frac{\partial R_{\kappa}}{\partial \boldsymbol{F}^{n+1}} \\[2mm] \frac{\partial R_{f}}{\partial \boldsymbol{F}^{n+1}} \end{bmatrix} : \mathrm{d}\boldsymbol{F}^{n+1} \quad , \tag{4.79}
$$

by making use of an appropriate matrix notation and of the derivatives of the residual terms $\boldsymbol{R}_{\bullet}$ with respect to the internal variables as specified in Appendix C.2.

Remark 4.2 (Numerical time integrator) *The simulation results to be presented in this contribution use the trapezoidal rule as a numerical time integration scheme. Sample calculations suggest that this integration scheme is more suitable for the problem at hand than the classic implicit Euler method would be. We furthermore point out that the integration scheme preserves the symmetry of the tensors $\boldsymbol{A}$ and $\boldsymbol{C}_{\mathrm{p}}$ in the discrete setting, cf. (4.77). The plastic incompressibility constraint is not explicitly enforced but could be accounted for as a side condition in the Newton-Raphson scheme as proposed in e.g. [34].*

Remark 4.3 (Evolution equation in terms of $\boldsymbol{A}_{\mathrm{p}}$) *The structural tensor $\boldsymbol{A}$ enters the yield function only in terms of its associated mixed-variant tensor $\boldsymbol{A}_{\mathrm{p}}$ so that it is alternatively possible to describe the evolution of the symmetry group directly in terms of the evolution of $\boldsymbol{A}_{\mathrm{p}}$. To this end, taking the time derivative of (4.46), inserting (4.9) and (4.12) in the ensuing equation and making use of the $\boldsymbol{C}_{\mathrm{p}}$-skew property of $\boldsymbol{W}$ one arrives at*

$$
\dot{\boldsymbol{A}}_{\mathrm{p}} = \left[\boldsymbol{\Gamma}_{\mathrm{p}}^{\star} \cdot \boldsymbol{A}_{\mathrm{p}} - \boldsymbol{A}_{\mathrm{p}} \cdot \boldsymbol{\Gamma}_{\mathrm{p}}^{\star} \right] + \left[\boldsymbol{W}^{\star} \cdot \boldsymbol{A}_{\mathrm{p}} - \boldsymbol{A}_{\mathrm{p}} \cdot \boldsymbol{W}^{\star} \right] \quad , \tag{4.80}
$$

which is similar in structure to (4.12). However, since $\boldsymbol{A}_{\mathrm{p}}$ is $\boldsymbol{C}_{\mathrm{p}}$-symmetric it features, in general, nine independent coefficients. Moreover, formulating the evolution equations directly in $\boldsymbol{A}$ allows us to conveniently enforce the symmetry condition (in Euclidean sense) on $\boldsymbol{A}$ in the discrete setting.

4.4.2 Tension tests

Motivated by the experimental findings on uni-axial tension tests by Kim and Yin presented in Section 4.3.1, we will focus on finite element-based simulations of tension tests in a two- and three-dimensional setting. The ensuing simulations are based on the specific model presented in Section 4.2 which is complemented by the specific form of the

Table 4.1: Material parameters used in the finite element simulations in accordance with [52] and with $a_1 - a_6$ given in GPa^{-2}.

λ	μ	R_{inf}	ε_0	a_1	a_2	a_3	a_4	a_5	a_6
121.2 GPa	80.7 GPa	0.5	2 MPa	19.6	21.1	296.4	-21.6	0.0	0.0

spin tensor $\boldsymbol{W}$ derived in Section 4.3.2 so that a local system of evolution equations of the form (4.77) is to be solved at integration point level.

The material parameters are chosen in accordance with [52] and are summarised in Table 4.1. With regard to the parameters $\{a_1, \ldots, a_6\}$ we would like to point out that an orthotropic quadratic yield function in terms of the Kirchhoff stress tensor is used in [52]. This yield function can be taken into account to calibrate the material parameters of the yield function (4.44) used in this contribution via a structural comparison as shown in Appendix C.1. However, we note that the orthotropic quadratic yield function in terms of the Mandel stress tensor of the intermediate configuration and the one in terms of the Kirchhoff stress tensor used in [52] are not equal.

Regarding the specific boundary value problem we will focus on a tensile-test specimen of type E as standardised according to DIN 50125, [1]. The specific dimensions of the specimen used in the simulations are provided in Figure 4.5. With regard to the experimental findings we are primarily interested in the rotation of the material symmetry group and in the component of the Hencky strain tensor $H_{\text{L}} = \boldsymbol{H} : [\boldsymbol{e}_{\text{L}} \otimes \boldsymbol{e}_{\text{L}}]$, with $\boldsymbol{H} = 1/2 \ln(\boldsymbol{C})$ and with $\boldsymbol{e}_{\text{L}}$ denoting the unit vector in loading direction. The longitudinal stretch of the specimen H_{L} will be approximated based on the displacement of the surface nodes which are positioned at the boundary of the gauge section according to

$$H_{\text{L}} = \ln\left(1 + \frac{\Delta u_{\text{G}}}{l_{\text{G}}}\right) \tag{4.81}$$

with the mean change of the gauge length Δu_{G} and the initial gauge length $l_{\text{G}} = 60\text{mm}$. Regarding the three-dimensional case, only the nodes at the top and bottom surface (at the boundaries of the gauge section) will be taken into account, resembling the use of an extensometer in an experiment.

4.4.2.1 Two-dimensional simulations

This section focuses on the finite element-based simulation of tension tests in a two-dimensional setting subject to the assumption of a plane strain state, negligible body forces and to quasi-statics. The simulations are based on the specific tension test specimen of type E depicted in Figure 4.5 and standardised in DIN 50125. From a numeric point of view, (standard) four-node quadrilateral elements are used for the discretisation
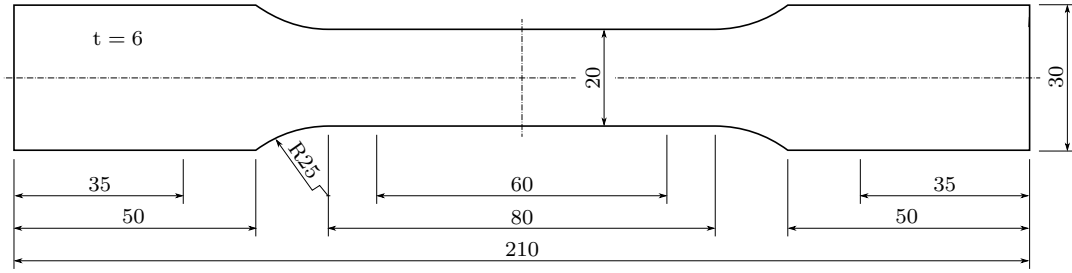
Figure 4.5: Dimensions (in mm) of tension test specimen of type E according to DIN 50125, see [1], used in the finite element-based simulations.

of both the geometry and the placement field, resulting e.g. in the finite element meshes depicted in Figure 4.6 to Figure 4.9. The boundary conditions at the grip sections of the specimen, specifically at the last 35mm of each end, are of special interest. Assuming that no slip between the grips and the specimen occurs in the experiments, homogeneous Dirichlet boundary conditions in both spatial dimensions are applied at the left boundary. At the right boundary, the displacement in e_{T}-direction is fixed, while the displacement in e_{L}-direction is prescribed, resulting in displacement-controlled simulations. We take note of the fact that this type of boundary condition is equivalent to the prescription of the displacement at the inner boundaries of the grip sections, since the displacement of the grip sections is completely controlled – this, however, will be different regarding the three-dimensional setting in Section 4.4.2.2.

With regard to the experimental findings summarised in Section 4.3.1 the analysis will especially focus on load states which are characterised by specific Hencky strain values in loading direction, i.e. $H_{\mathrm{L}} \in \{0\%, 1\%, 2\%, 5\%, 10\%\}$. Taking into account (4.76), (4.81) and Appendix C.3, the rotation of the material symmetry group is depicted as a function of H_{L} in Figure 4.10, with lines indicating the simulation results for various values of material parameter $c_{\boldsymbol{W}}$ and with circles representing the experimental results reproduced from [65]. Regarding the results for a loading direction $\phi_{\mathrm{L}} = 30°$ we find that the experiments, as well as the finite element simulations, predict an asymptotic behaviour with limit value $30°$, see Figure 4.10(a). As expected based on the observations of Section 4.3.1 and Section 4.3.2, an asymptotic behaviour with limit value $-30°$ is also predicted by the finite element-based simulations for $\phi_{\mathrm{L}} = 60°$, however, the absolute value of the limit observed in the experiments is slightly smaller, see Figure 4.10(b). In order to assess the experimental results better with regard to e.g. the scattering of the data, more experimental data is desirable but to the author's best knowledge currently not available. Furthermore, we note that load-rotation curves for the loading direction $\phi_{\mathrm{L}} = 45°$ will not be discussed for the reasons stated in Section 4.3.1.

Focusing in more detail on the evolution of the material symmetry group and on the evolution of the plasticity itself, the first eigen-direction of the spatial structural tensor, i.e. $\boldsymbol{n}_{\boldsymbol{a}1}$, calculated at a selected quadrature point of each element is depicted on the spatial configuration of the specimen alongside the element-wise mean value of

the accumulated plastic strain κ in Figure 4.6 to Figure 4.9. In addition to the loading directions $\phi_L \in \{30°, 45°, 60°\}$ we will take into account an element-wise-perturbed loading direction defined by a Gaussian distribution with expected value $E_{\phi_L} = 45°$ and standard deviation $\sigma_{\phi_L} = 2.5°$. The latter distribution may account for the non-perfect initial alignment of the individual crystals with the rolling direction as discussed in Section 4.3.1. Furthermore, it is noted that the grip sections of the samples are not depicted in Figure 4.6 to Figure 4.9.

Due to the anisotropic nature of the yield function, the formation of a band-like structure for the loading directions $\phi_L = 30°$ and $\phi_L = 60°$ is observable in Figure 4.6 and Figure 4.7. Although the band is clearly visible at the beginning of the tension test, it vanishes with increasing (plastic) deformation which can be explained by the alignment of the material symmetry group with the principal loading directions. For the present setting with $c_W = 0.15 \, \text{Pa}^{-1}$ and a deformation of approximately $H_L \approx 5\%$ the material symmetry group and the loading direction are nearly aligned in the gauge section so that the plastic flow direction coincides with the principal loading direction. Moreover, the anticlockwise rotation of the symmetry group for $\phi_L = 30°$ and the clockwise rotation for $\phi_L = 60°$ is clearly revealed. Regarding the simulation results for $\phi_L = 45°$ we observe an anticlockwise rotation in the upper right and in the lower left part of the sample, while a clockwise rotation is observable in the lower right and in the upper left part. The rotation starts near the outer boundaries of the gauge section, Figure 4.8(d), and evolves in the direction of the sample's centre, Figure 4.8(e). On the other hand, if we take into account an element-wise perturbation of the symmetry group's initial orientation with a standard perturbation $\sigma_{\phi_L} = 2.5°$, the position where the plastic deformation starts to evolve (in the gauge section) is not deterministic. As shown in Figure 4.9 for one specific perturbed distribution of the symmetry group's initial orientation, plasticity starts to evolve close to the right boundary with adjacent elements showing significantly different values of the accumulated plastic strain, cf. Figure 4.9(b) and Figure 4.9(c) – interestingly, the observed evolution of the plastic deformation is quite different compared to the previously discussed load case $\phi_L = 45°$. To be specific, we find that the slight perturbation is sufficient to induce rotations with different senses in adjacent elements in the gauge section, see Figure 4.9(d). This observation is of particular importance since it might be related to the macroscopically quasi-isotropic yielding behaviour observed in the experiments, see Section 4.3.1. Due to the nearly 90°-symmetry of the yielding behaviour, elements which exhibited a $+45°$ rotation and those which exhibited a $-45°$ rotation show a similar response such that the macroscopically observable yielding behaviour for specimens prepared from the gauge section should again be orthotropic, cf. Figure 4.9(e).

Finally, the load-displacement curves which are predicted by the finite element simulations are provided in Figure 4.11. Essentially, these curves result from three main, partly opposing, effects. First, regarding the curves for $c_W = 0.00 \, \text{Pa}^{-1}$ which resemble models based on classic anisotropic plasticity with an exponential-type hardening behaviour, we observe an increase in the force required for a certain elongation after the onset of

plasticity due to the hardening behaviour. At a certain deformation stage, the necking effect dominates the hardening behaviour, so that the slope of the load-displacement curve becomes negative. Focusing on the simulation results with $c_{\boldsymbol{W}} \neq 0.00 \, \mathrm{Pa}^{-1}$, we observe a distinct decrease in the yield limit after a certain amount of plastic deformation which can be explained by the rotation of the material symmetry group or rather by the alignment of the preferred material axes with the loading direction such that the yield limit in loading direction decreases. Finally, we note that the initial yield limit of, e.g., about 295 MPa for $\phi_{\mathrm{L}} = 30°$ and 316 MPa for $\phi_{\mathrm{L}} = 45°$ is slightly higher than the one predicted by the experiments which may be attributed to the plane strain conditions as will be shown in Section 4.4.2.2.

4.4.2.2 Three-dimensional simulations

In accordance with the two-dimensional plane strain simulations presented in Section 4.4.2.1, this section focuses on the simulation of tension tests in a three-dimensional setting, again assuming a quasi static deformation process and negligible body forces. To this end, the three-dimensional tension test sample of type E depicted in Figure 4.5 is discretised by means of (standard) eight-node hexahedral elements, see e.g. Figure 4.12 to Figure 4.15. Regarding the boundary conditions which are applied at the grip sections, we will fix the displacement in $\boldsymbol{e}_{\mathrm{L}}$- and $\boldsymbol{e}_{\mathrm{T}}$-direction at the top and bottom on the left side of the sample. On the right side, the displacement in $\boldsymbol{e}_{\mathrm{T}}$-direction is assumed to be zero, while the displacement in $\boldsymbol{e}_{\mathrm{L}}$-direction is prescribed such that the boundary conditions in $\boldsymbol{e}_{\mathrm{L}}$- and $\boldsymbol{e}_{\mathrm{T}}$-direction are comparable to those used in the two-dimensional simulations. Regarding the $\boldsymbol{e}_{\mathrm{N}}$-direction we assume the same boundary conditions for the left and right grip section – specifically speaking, homogeneous Dirichlet boundary conditions are enforced at the bottom of the grip sections, while homogeneous Neumann boundary conditions are chosen at the top. Thus, we do not hinder a contraction of the grip sections in $\boldsymbol{e}_{\mathrm{N}}$-direction and we do not induce a certain symmetry pattern as would be the case if the $\boldsymbol{e}_{\mathrm{N}}$-displacement in the middle-plane was chosen to be zero.

The rotation-displacement curves for the loading directions $\phi_{\mathrm{L}} = 30°$ and $\phi_{\mathrm{L}} = 60°$ are provided in Figure 4.16 for various values of the material parameter $c_{\boldsymbol{W}}$ and by taking into account (4.76), (4.81) and Appendix C.3. As in the two-dimensional case we observe an asymptotic behaviour with limit value $\phi_{\mathrm{R}} = 30°$, respectively $\phi_{\mathrm{R}} = -30°$. Although, the two- and three-dimensional simulation results are qualitatively similar and in good agreement with the experimental findings, the three-dimensional simulations predict a slower saturation speed for the same values of the material parameter $c_{\boldsymbol{W}}$.

Focusing on the evolution of plasticity and on the specific spatial distribution of the symmetry group's orientation for certain deformation states, the eigenvector $\boldsymbol{n}_{\boldsymbol{a}1}$ of the spatial structural tensor (predicted at a selected quadrature point) and the element-wise mean value of the accumulated plastic strain κ are provided in Figure 4.12 to Figure 4.15, with the specimen's grip sections not being depicted. With regard to κ we once more observe the formation of band-like structures for the loading directions
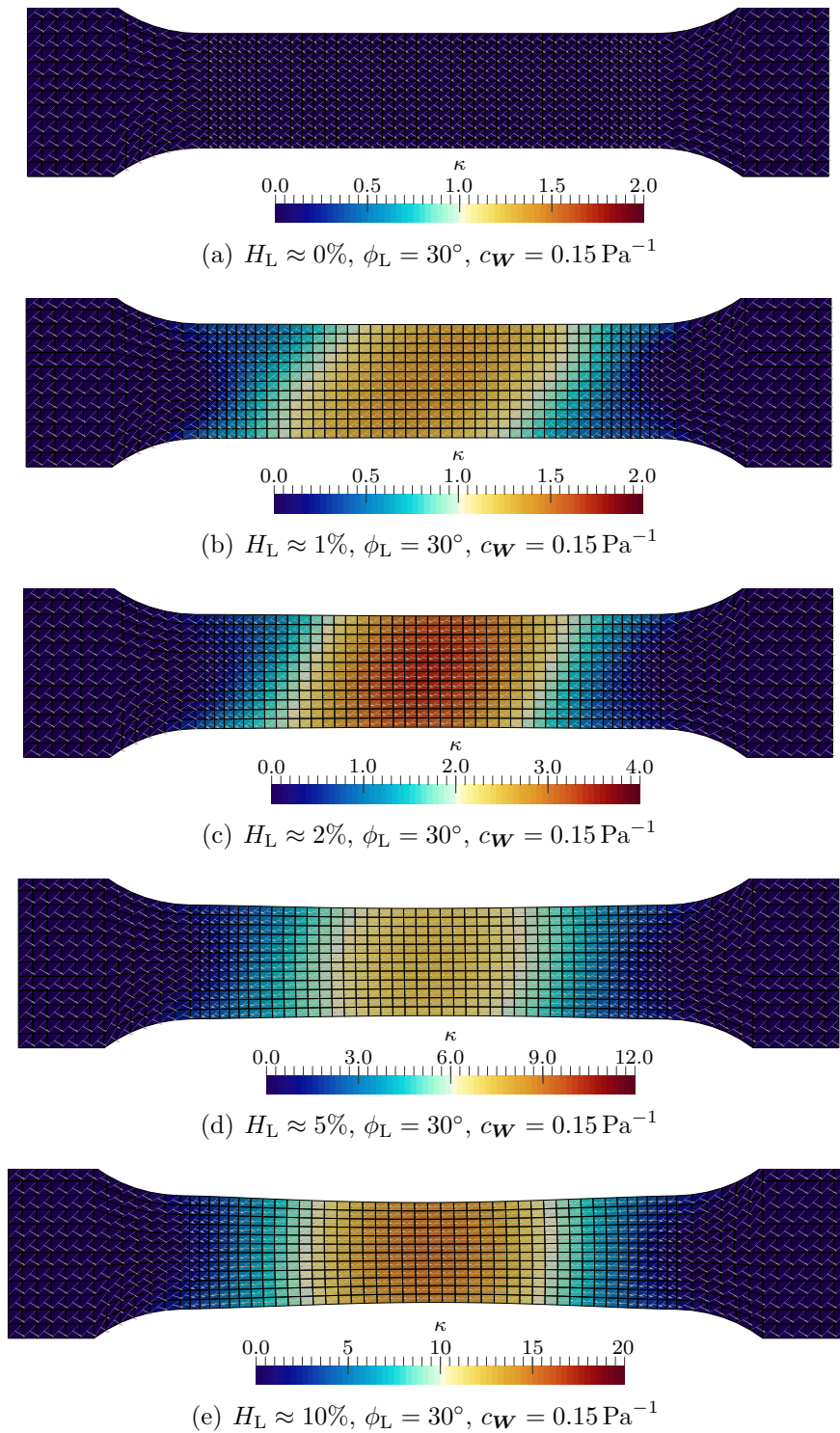
(a) $H_{\mathrm{L}} \approx 0\%$, $\phi_{\mathrm{L}} = 30°$, $c_{\boldsymbol{W}} = 0.15\,\mathrm{Pa}^{-1}$

(b) $H_{\mathrm{L}} \approx 1\%$, $\phi_{\mathrm{L}} = 30°$, $c_{\boldsymbol{W}} = 0.15\,\mathrm{Pa}^{-1}$

(c) $H_{\mathrm{L}} \approx 2\%$, $\phi_{\mathrm{L}} = 30°$, $c_{\boldsymbol{W}} = 0.15\,\mathrm{Pa}^{-1}$

(d) $H_{\mathrm{L}} \approx 5\%$, $\phi_{\mathrm{L}} = 30°$, $c_{\boldsymbol{W}} = 0.15\,\mathrm{Pa}^{-1}$

(e) $H_{\mathrm{L}} \approx 10\%$, $\phi_{\mathrm{L}} = 30°$, $c_{\boldsymbol{W}} = 0.15\,\mathrm{Pa}^{-1}$

Figure 4.6: Evolution of the plastic deformation in terms of the accumulated plastic strain κ and rotation of the (plastic) material symmetry group, predicted by (two-dimensional) plane strain finite element simulations. Depicted is the (first) eigenvector $\boldsymbol{n}_{\boldsymbol{a}1}$ of the spatial structural tensor $\boldsymbol{a}$ that is predicted at a selected quadrature point of each element for various loadings, $\phi_{\mathrm{L}} = 30°$ and $c_{\boldsymbol{W}} = 0.15\,\mathrm{Pa}^{-1}$.

(a) $H_{\mathrm{L}} \approx 0\%$, $\phi_{\mathrm{L}} = 60°$, $c_{\boldsymbol{W}} = 0.15\,\mathrm{Pa}^{-1}$

(b) $H_{\mathrm{L}} \approx 1\%$, $\phi_{\mathrm{L}} = 60°$, $c_{\boldsymbol{W}} = 0.15\,\mathrm{Pa}^{-1}$

(c) $H_{\mathrm{L}} \approx 2\%$, $\phi_{\mathrm{L}} = 60°$, $c_{\boldsymbol{W}} = 0.15\,\mathrm{Pa}^{-1}$

(d) $H_{\mathrm{L}} \approx 5\%$, $\phi_{\mathrm{L}} = 60°$, $c_{\boldsymbol{W}} = 0.15\,\mathrm{Pa}^{-1}$

(e) $H_{\mathrm{L}} \approx 10\%$, $\phi_{\mathrm{L}} = 60°$, $c_{\boldsymbol{W}} = 0.15\,\mathrm{Pa}^{-1}$
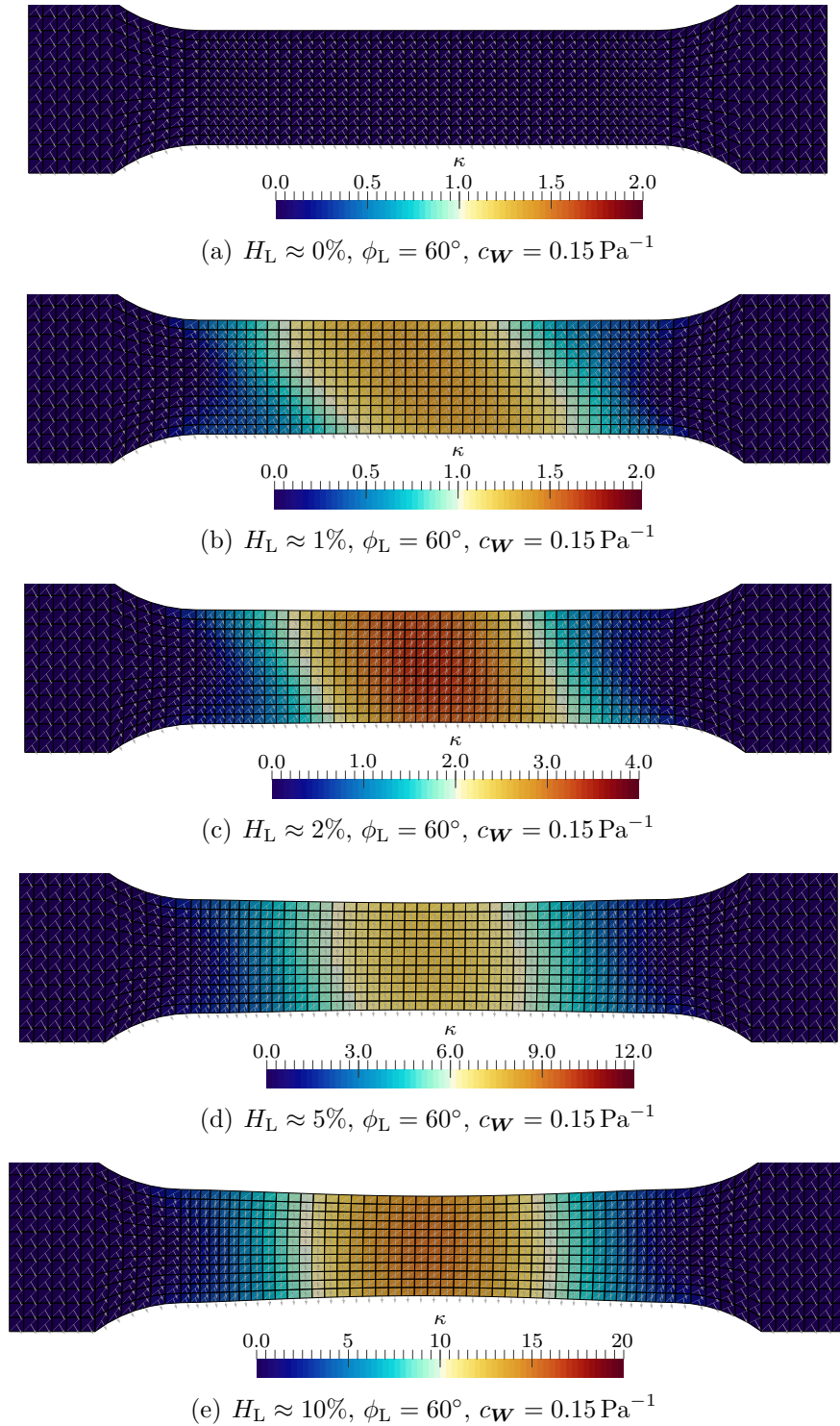
Figure 4.7: Evolution of the plastic deformation in terms of the accumulated plastic strain κ and rotation of the (plastic) material symmetry group, predicted by (two-dimensional) plane strain finite element simulations. Depicted is the (first) eigenvector $\boldsymbol{n}_{\boldsymbol{a}1}$ of the spatial structural tensor $\boldsymbol{a}$ that is predicted at a selected quadrature point of each element for various loadings, $\phi_{\mathrm{L}} = 60°$ and $c_{\boldsymbol{W}} = 0.15\,\mathrm{Pa}^{-1}$.

197

(a) $H_{\mathrm{L}} \approx 0\%$, $\phi_{\mathrm{L}} = 45°$, $c_{\boldsymbol{W}} = 0.15\,\mathrm{Pa}^{-1}$

(b) $H_{\mathrm{L}} \approx 1\%$, $\phi_{\mathrm{L}} = 45°$, $c_{\boldsymbol{W}} = 0.15\,\mathrm{Pa}^{-1}$

(c) $H_{\mathrm{L}} \approx 2\%$, $\phi_{\mathrm{L}} = 45°$, $c_{\boldsymbol{W}} = 0.15\,\mathrm{Pa}^{-1}$

(d) $H_{\mathrm{L}} \approx 5\%$, $\phi_{\mathrm{L}} = 45°$, $c_{\boldsymbol{W}} = 0.15\,\mathrm{Pa}^{-1}$

(e) $H_{\mathrm{L}} \approx 10\%$, $\phi_{\mathrm{L}} = 45°$, $c_{\boldsymbol{W}} = 0.15\,\mathrm{Pa}^{-1}$
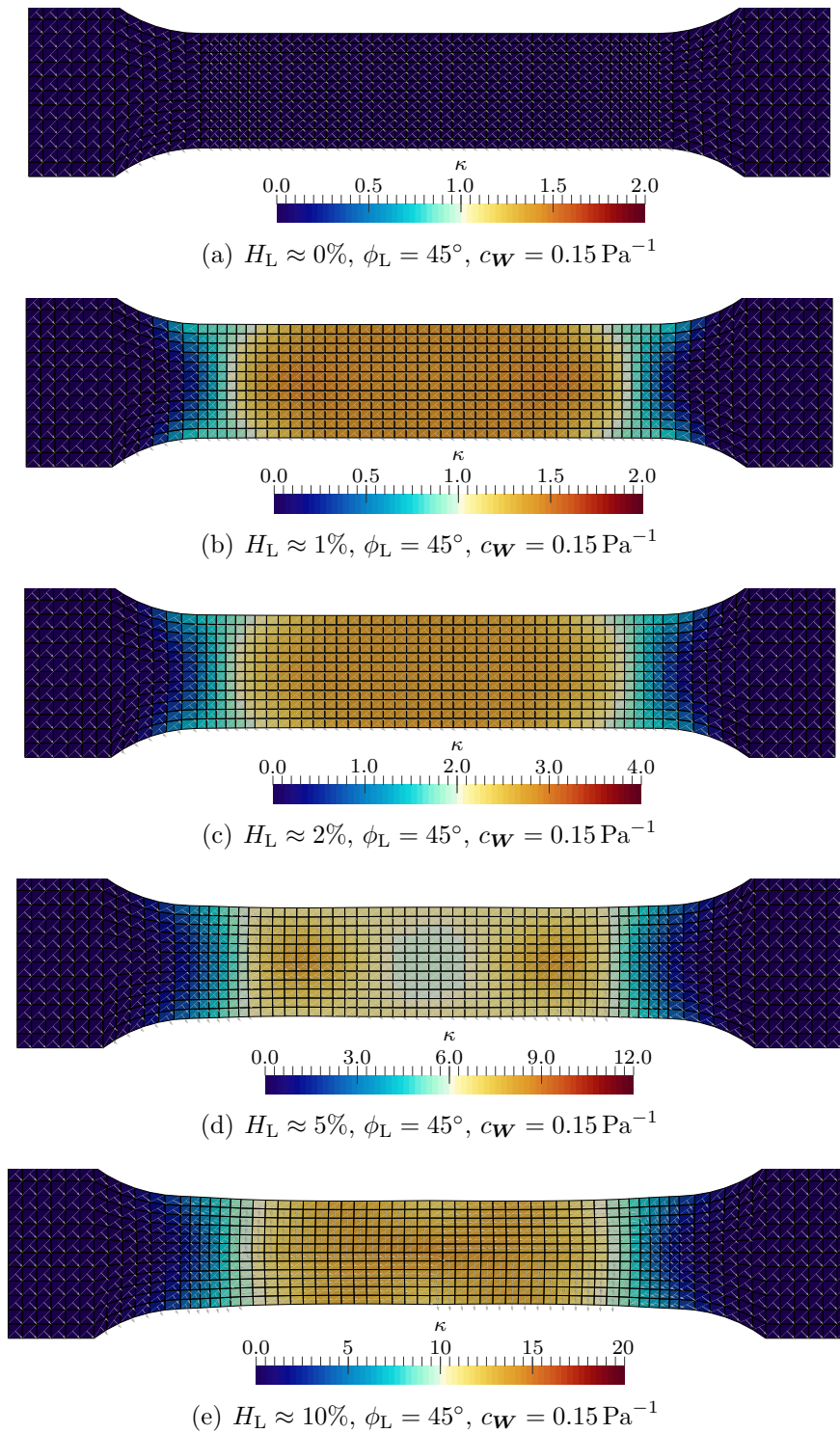
Figure 4.8: Evolution of the plastic deformation in terms of the accumulated plastic strain κ and rotation of the (plastic) material symmetry group, predicted by (two-dimensional) plane strain finite element simulations. Depicted is the (first) eigenvector $\boldsymbol{n}_{\boldsymbol{a}1}$ of the spatial structural tensor $\boldsymbol{a}$ that is predicted at a selected quadrature point of each element for various loadings, $\phi_{\mathrm{L}} = 45°$ and $c_{\boldsymbol{W}} = 0.15\,\mathrm{Pa}^{-1}$.

(a) $H_{\mathrm{L}} \approx 0\%$, $\mathrm{E}_{\phi_{\mathrm{L}}} = 45°$ with $\sigma_{\phi_{\mathrm{L}}} = 2.5°$, $c_{\boldsymbol{W}} = 0.15\,\mathrm{Pa}^{-1}$

(b) $H_{\mathrm{L}} \approx 1\%$, $\mathrm{E}_{\phi_{\mathrm{L}}} = 45°$ with $\sigma_{\phi_{\mathrm{L}}} = 2.5°$, $c_{\boldsymbol{W}} = 0.15\,\mathrm{Pa}^{-1}$

(c) $H_{\mathrm{L}} \approx 2\%$, $\mathrm{E}_{\phi_{\mathrm{L}}} = 45°$ with $\sigma_{\phi_{\mathrm{L}}} = 2.5°$, $c_{\boldsymbol{W}} = 0.15\,\mathrm{Pa}^{-1}$

(d) $H_{\mathrm{L}} \approx 5\%$, $\mathrm{E}_{\phi_{\mathrm{L}}} = 45°$ with $\sigma_{\phi_{\mathrm{L}}} = 2.5°$, $c_{\boldsymbol{W}} = 0.15\,\mathrm{Pa}^{-1}$

(e) $H_{\mathrm{L}} \approx 10\%$, $\mathrm{E}_{\phi_{\mathrm{L}}} = 45°$ with $\sigma_{\phi_{\mathrm{L}}} = 2.5°$, $c_{\boldsymbol{W}} = 0.15\,\mathrm{Pa}^{-1}$

Figure 4.9: Evolution of the plastic deformation in terms of the accumulated plastic strain κ and rotation of the (plastic) material symmetry group, predicted by (two-dimensional) plane strain finite element simulations. Depicted is the (first) eigenvector $\boldsymbol{n}_{\boldsymbol{a}1}$ of the spatial structural tensor $\boldsymbol{a}$ that is predicted at a selected quadrature point of each element for various loadings, $\mathrm{E}_{\phi_{\mathrm{L}}} = 45°$ with $\sigma_{\phi_{\mathrm{L}}} = 2.5°$ and $c_{\boldsymbol{W}} = 0.15\,\mathrm{Pa}^{-1}$.
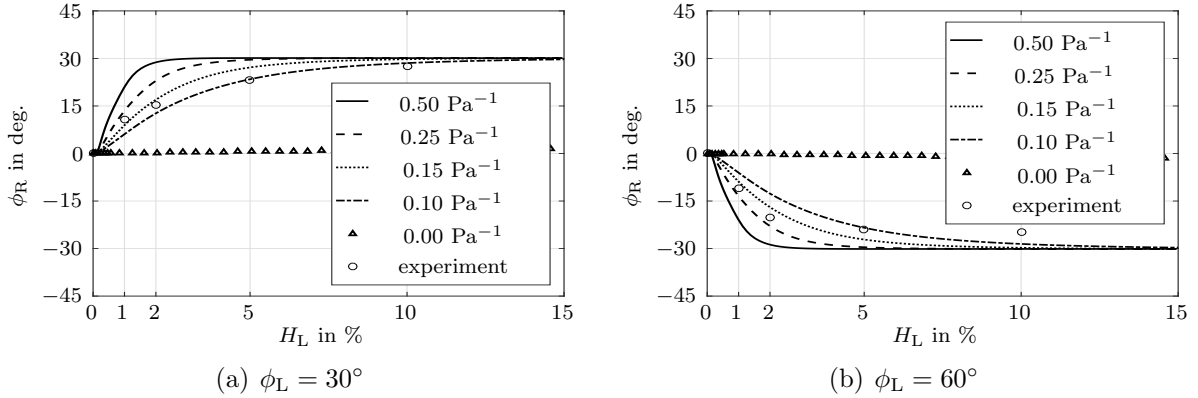
Figure 4.10: Comparison of experimentally observed rotations of the preferred material axes against the two-dimensional plane strain finite element simulation results for various deformation states in terms of the Hencky strain H_{L} in loading direction $\boldsymbol{e}_{\mathrm{L}}$ and various values of the material parameter $c_{\boldsymbol{W}}$. The experimental results are reproduced from [65].
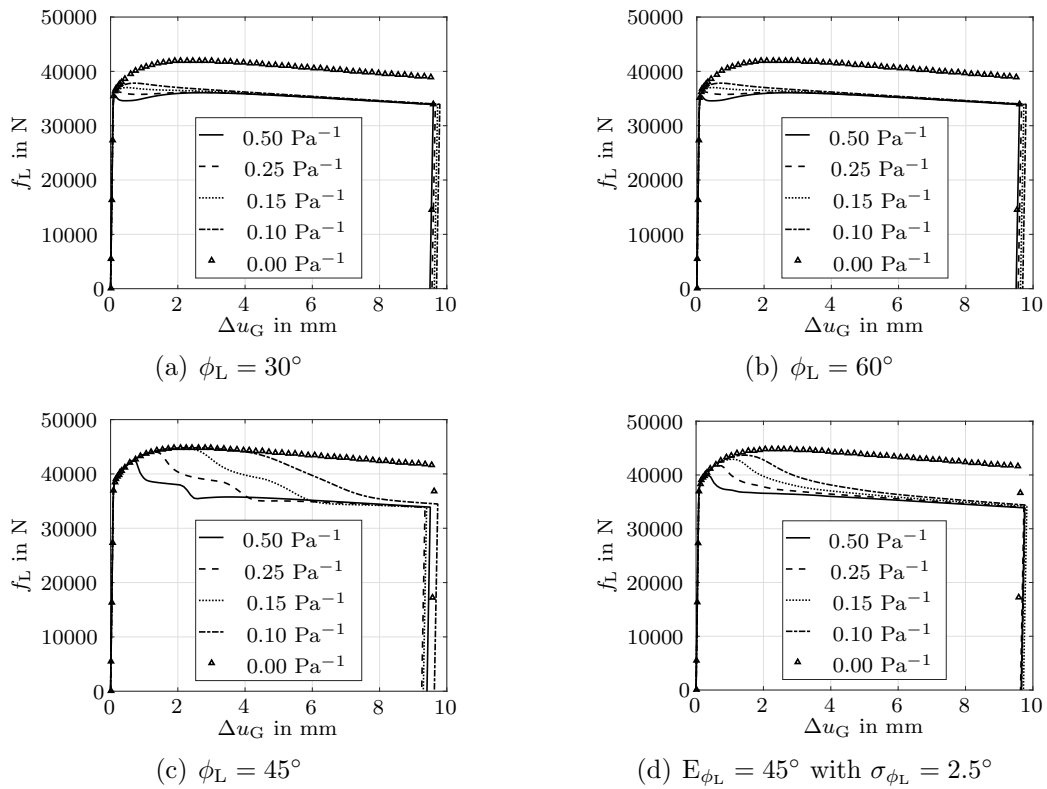
Figure 4.11: Reaction force f_{L} in loading direction $\boldsymbol{e}_{\mathrm{L}}$ as a function of the change of the gauge length Δu_{G} for various values of the material parameter $c_{\boldsymbol{W}}$ and various loading directions ϕ_{L}, relative to the rolling direction. The calculations are based on a two-dimensional plane strain setting and the simulation results for the displacement-controlled loading and unloading of the sample are shown.

$\phi_{\mathrm{L}} = 30°$ and $\phi_{\mathrm{L}} = 60°$ which disappear with increasing plastic deformation for the same reasons discussed in Section 4.4.2.1, see Figure 4.12 and Figure 4.13. Whereas the results for the (element-wise) perturbed loading direction $\mathrm{E}_{\phi_{\mathrm{L}}} = 45°$ with $\sigma_{\phi_{\mathrm{L}}} = 2.5°$ depicted in Figure 4.15 are similar to their two-dimensional counterparts presented in Section 4.4.2.1, with the position where the plasticity starts to evolve being non-deterministic and rotations of different senses being observed in adjacent elements, the two- and three-dimensional simulation results for the loading direction $\phi_{\mathrm{L}} = 45°$ are noticeably different. In particular we observed in the two-dimensional simulations that the symmetry group started to evolve simultaneously near the left and right boundary of the gauge section with the symmetry group's rotation direction being different in the upper and lower parts of the specimen, Figure 4.8. In contrast to the latter results, regarding the three-dimensional simulation results for $c_{\boldsymbol{W}} = 0.15\,\mathrm{Pa}^{-1}$ presented in Figure 4.14, we find that the evolution of plasticity focuses on the centre of the specimen where the rotation of the symmetry group also starts. Furthermore, a clockwise rotation of the structural tensor is revealed in every element of the gauge section. However, we take note of the fact that we still observe results similar to those of the two-dimensional setting for significantly higher values of the material parameter $c_{\boldsymbol{W}}$, e.g. $c_{\boldsymbol{W}} = 0.50\,\mathrm{Pa}^{-1}$.

Although the load-displacement curves which are predicted by the three-dimensional simulations, see Figure 4.17, are found to be similar to their plane strain counterparts depicted in Figure 4.11 with, principally, the same effects being observable, there are two main differences which we should like to point out. First, the initial yield limit predicted by the three-dimensional simulations is smaller compared to the one observed under plane strain conditions. Specifically speaking, we observe an initial yield limit of approximately 250 MPa for $\phi_{\mathrm{L}} = 30°$, respectively 261 MPa for $\phi_{\mathrm{L}} = 45°$. Secondly, we find that the onset of the softening-type behaviour which is due to the alignment of the symmetry group with the principal loading directions is delayed and that the softening rate itself is reduced, e.g. Figure 4.17(c) and Figure 4.17(d). The latter effect can be explained by the previously observed slower rotation of the structural tensors, see also Figure 4.10 and Figure 4.11.
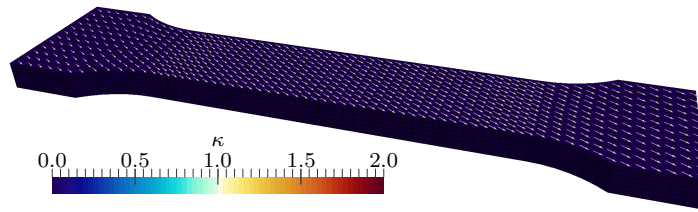
(a) $H_\mathrm{L} \approx 0\%$, $\phi_\mathrm{L} = 30°$, $c_{\boldsymbol{W}} = 0.15\,\mathrm{Pa}^{-1}$
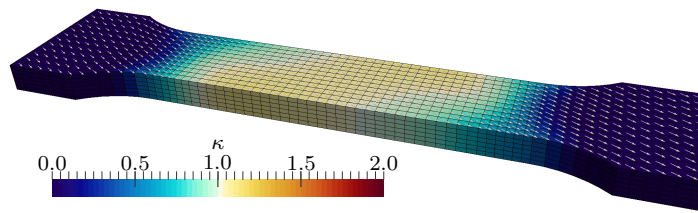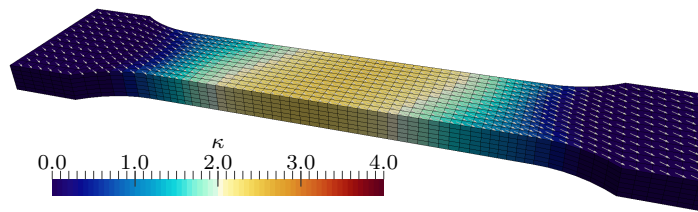
(b) $H_\mathrm{L} \approx 1\%$, $\phi_\mathrm{L} = 30°$, $c_{\boldsymbol{W}} = 0.15\,\mathrm{Pa}^{-1}$
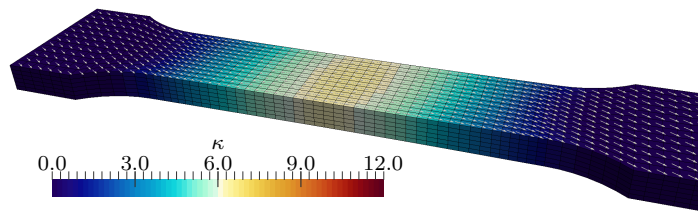
(c) $H_\mathrm{L} \approx 2\%$, $\phi_\mathrm{L} = 30°$, $c_{\boldsymbol{W}} = 0.15\,\mathrm{Pa}^{-1}$
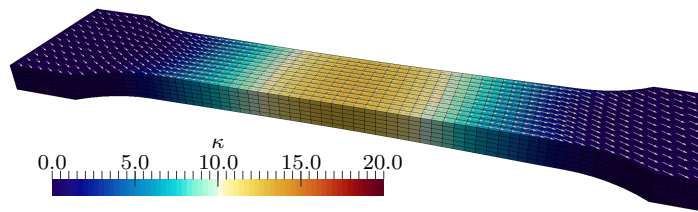
(d) $H_\mathrm{L} \approx 5\%$, $\phi_\mathrm{L} = 30°$, $c_{\boldsymbol{W}} = 0.15\,\mathrm{Pa}^{-1}$

(e) $H_\mathrm{L} \approx 10\%$, $\phi_\mathrm{L} = 30°$, $c_{\boldsymbol{W}} = 0.15\,\mathrm{Pa}^{-1}$

Figure 4.12: Evolution of the plastic deformation in terms of the accumulated plastic strain κ and rotation of the (plastic) material symmetry group, predicted by three-dimensional finite element simulations. Depicted is the (first) eigenvector $\boldsymbol{n}_{\boldsymbol{a}1}$ of the spatial structural tensor $\boldsymbol{a}$ that is predicted at a selected quadrature point of each element for various loadings, $\phi_\mathrm{L} = 30°$ and $c_{\boldsymbol{W}} = 0.15\,\mathrm{Pa}^{-1}$.
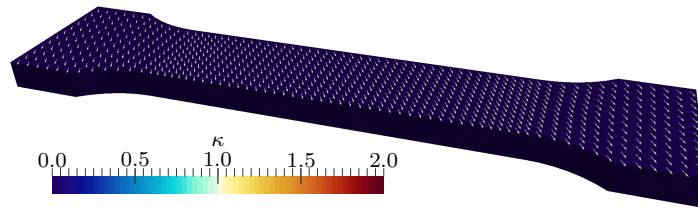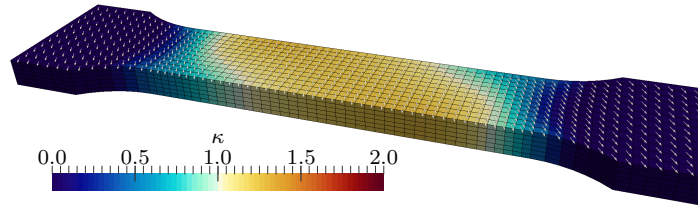
(a) $H_{\mathrm{L}} \approx 0\%$, $\phi_{\mathrm{L}} = 60°$, $c_{\boldsymbol{W}} = 0.15\,\mathrm{Pa}^{-1}$
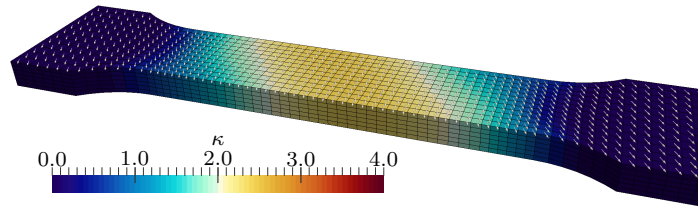
(b) $H_{\mathrm{L}} \approx 1\%$, $\phi_{\mathrm{L}} = 60°$, $c_{\boldsymbol{W}} = 0.15\,\mathrm{Pa}^{-1}$

(c) $H_{\mathrm{L}} \approx 2\%$, $\phi_{\mathrm{L}} = 60°$, $c_{\boldsymbol{W}} = 0.15\,\mathrm{Pa}^{-1}$

(d) $H_{\mathrm{L}} \approx 5\%$, $\phi_{\mathrm{L}} = 60°$, $c_{\boldsymbol{W}} = 0.15\,\mathrm{Pa}^{-1}$

(e) $H_{\mathrm{L}} \approx 10\%$, $\phi_{\mathrm{L}} = 60°$, $c_{\boldsymbol{W}} = 0.15\,\mathrm{Pa}^{-1}$

Figure 4.13: Evolution of the plastic deformation in terms of the accumulated plastic strain κ and rotation of the (plastic) material symmetry group, predicted by three-dimensional finite element simulations. Depicted is the (first) eigenvector $\boldsymbol{n}_{\boldsymbol{a}1}$ of the spatial structural tensor $\boldsymbol{a}$ that is predicted at a selected quadrature point of each element for various loadings, $\phi_{\mathrm{L}} = 60°$ and $c_{\boldsymbol{W}} = 0.15\,\mathrm{Pa}^{-1}$.
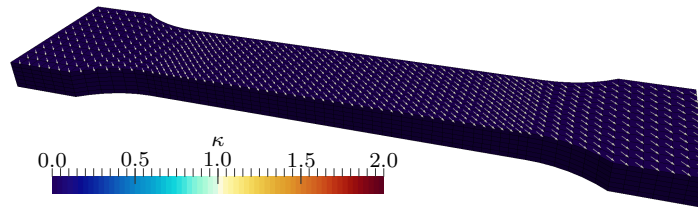
(a) $H_{\mathrm{L}} \approx 0\%$, $\phi_{\mathrm{L}} = 45°$, $c_{\boldsymbol{W}} = 0.15\,\mathrm{Pa}^{-1}$
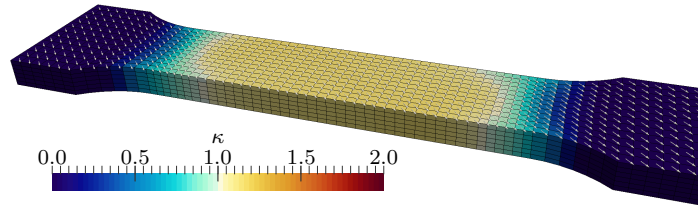
(b) $H_{\mathrm{L}} \approx 1\%$, $\phi_{\mathrm{L}} = 45°$, $c_{\boldsymbol{W}} = 0.15\,\mathrm{Pa}^{-1}$
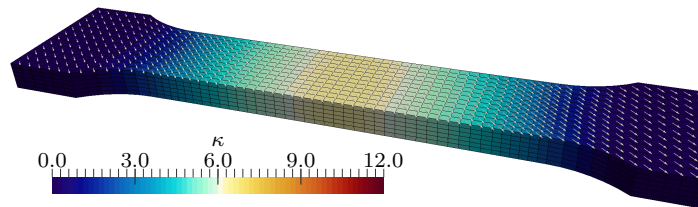
(c) $H_{\mathrm{L}} \approx 2\%$, $\phi_{\mathrm{L}} = 45°$, $c_{\boldsymbol{W}} = 0.15\,\mathrm{Pa}^{-1}$
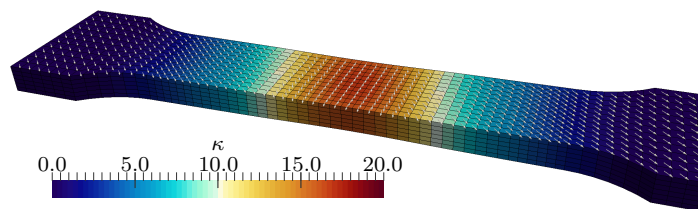
(d) $H_{\mathrm{L}} \approx 5\%$, $\phi_{\mathrm{L}} = 45°$, $c_{\boldsymbol{W}} = 0.15\,\mathrm{Pa}^{-1}$

(e) $H_{\mathrm{L}} \approx 10\%$, $\phi_{\mathrm{L}} = 45°$, $c_{\boldsymbol{W}} = 0.15\,\mathrm{Pa}^{-1}$

Figure 4.14: Evolution of the plastic deformation in terms of the accumulated plastic strain κ and rotation of the (plastic) material symmetry group, predicted by three-dimensional finite element simulations. Depicted is the (first) eigenvector $\boldsymbol{n}_{\boldsymbol{a}1}$ of the spatial structural tensor $\boldsymbol{a}$ that is predicted at a selected quadrature point of each element for various loadings, $\phi_{\mathrm{L}} = 45°$ and $c_{\boldsymbol{W}} = 0.15\,\mathrm{Pa}^{-1}$.

(a) $H_\mathrm{L} \approx 0\%$, $\mathrm{E}_{\phi_\mathrm{L}} = 45°$ with $\sigma_{\phi_\mathrm{L}} = 2.5°$, $c_{\boldsymbol{W}} = 0.15\,\mathrm{Pa}^{-1}$

(b) $H_\mathrm{L} \approx 1\%$, $\mathrm{E}_{\phi_\mathrm{L}} = 45°$ with $\sigma_{\phi_\mathrm{L}} = 2.5°$, $c_{\boldsymbol{W}} = 0.15\,\mathrm{Pa}^{-1}$

(c) $H_\mathrm{L} \approx 2\%$, $\mathrm{E}_{\phi_\mathrm{L}} = 45°$ with $\sigma_{\phi_\mathrm{L}} = 2.5°$, $c_{\boldsymbol{W}} = 0.15\,\mathrm{Pa}^{-1}$

(d) $H_\mathrm{L} \approx 5\%$, $\mathrm{E}_{\phi_\mathrm{L}} = 45°$ with $\sigma_{\phi_\mathrm{L}} = 2.5°$, $c_{\boldsymbol{W}} = 0.15\,\mathrm{Pa}^{-1}$

(e) $H_\mathrm{L} \approx 10\%$, $\mathrm{E}_{\phi_\mathrm{L}} = 45°$ with $\sigma_{\phi_\mathrm{L}} = 2.5°$, $c_{\boldsymbol{W}} = 0.15\,\mathrm{Pa}^{-1}$
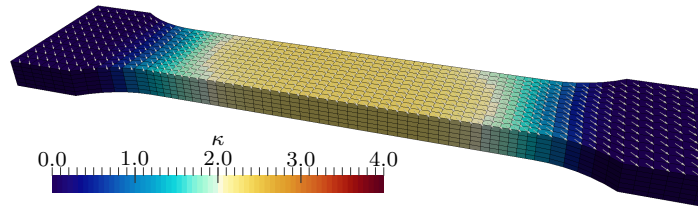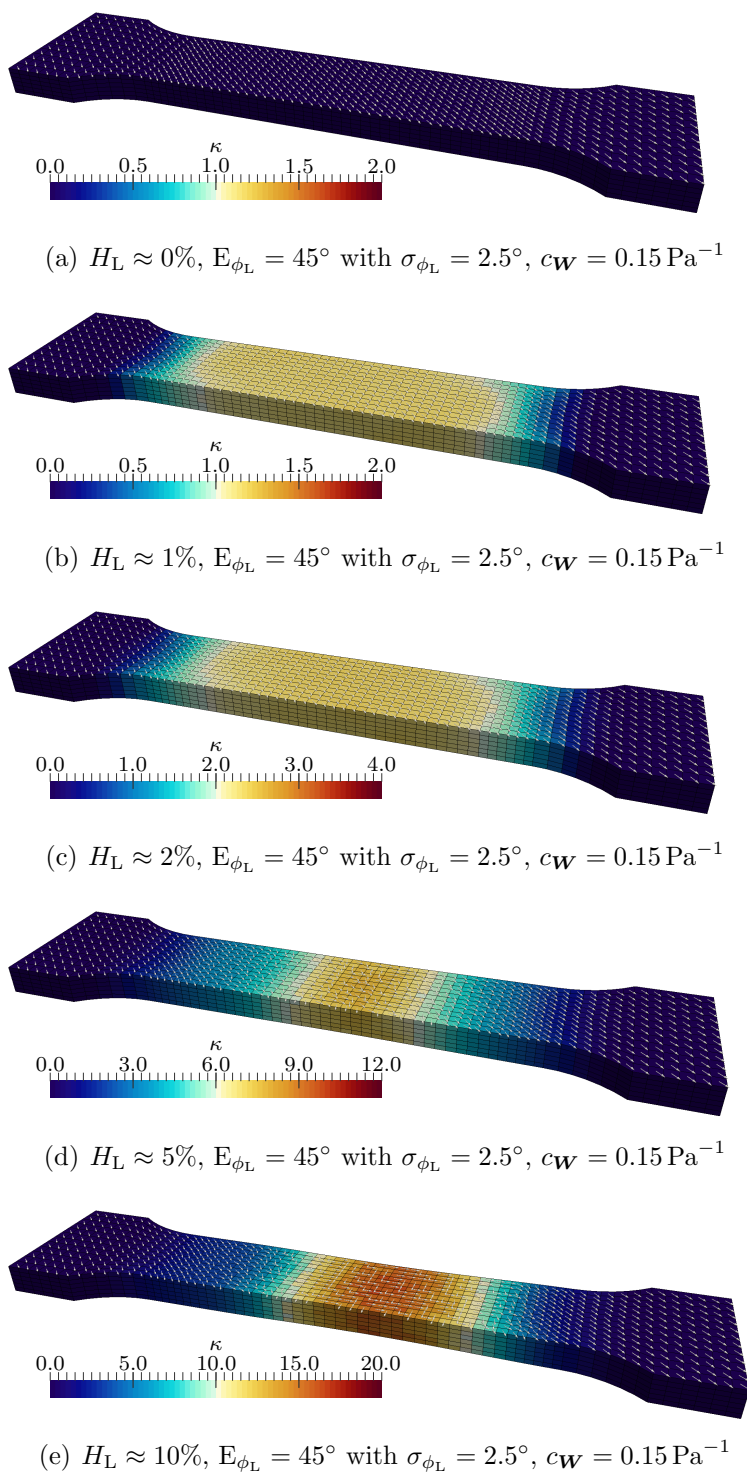
Figure 4.15: Evolution of the plastic deformation in terms of the accumulated plastic strain κ and rotation of the (plastic) material symmetry group, predicted by three-dimensional finite element simulations. Depicted is the (first) eigenvector $\boldsymbol{n}_{\boldsymbol{a}1}$ of the spatial structural tensor $\boldsymbol{a}$ that is predicted at a selected quadrature point of each element for various loadings, $\mathrm{E}_{\phi_\mathrm{L}} = 45°$ with $\sigma_{\phi_\mathrm{L}} = 2.5°$ and $c_{\boldsymbol{W}} = 0.15\,\mathrm{Pa}^{-1}$.
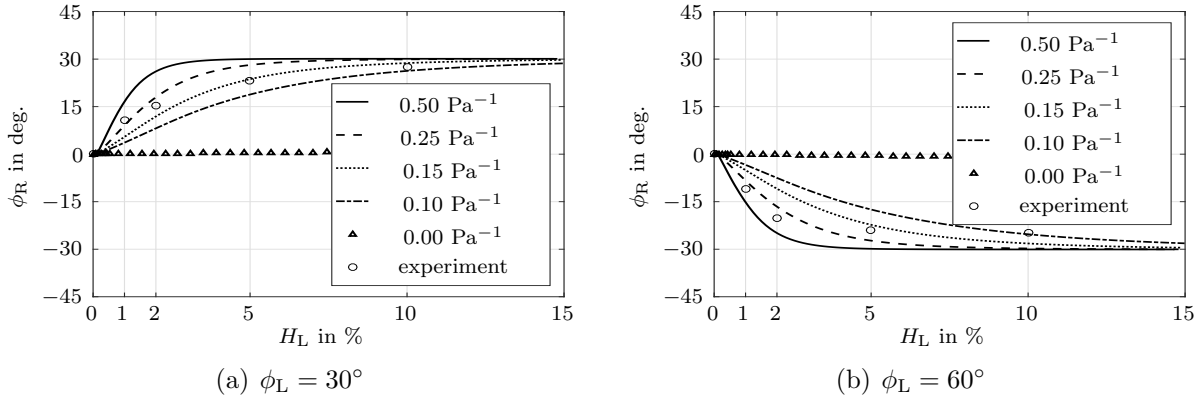
Figure 4.16: Comparison of experimentally observed rotations of the preferred material axes against the three-dimensional finite element simulation results for various deformation states in terms of the Hencky strain H_L in loading direction $\boldsymbol{e}_\mathrm{L}$ and various values of the material parameter $c_{\boldsymbol{W}}$. The experimental results are reproduced from [65].
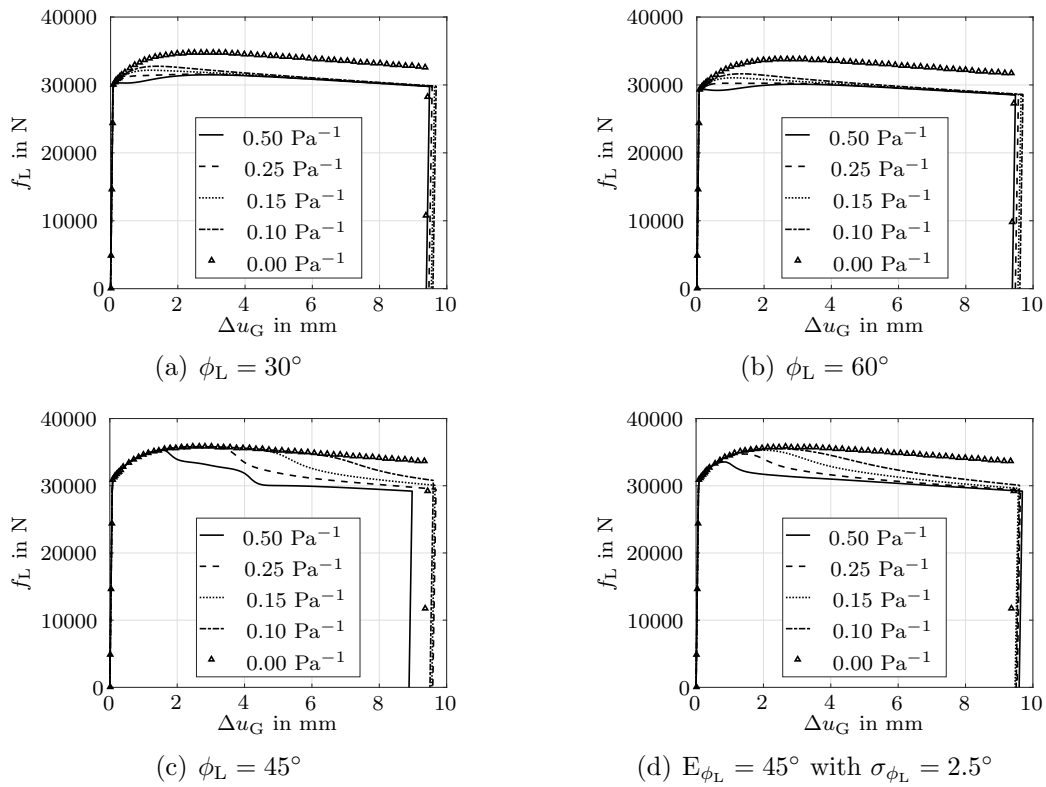
Figure 4.17: Reaction force f_L in loading direction $\boldsymbol{e}_\mathrm{L}$ as a function of the change of the gauge length Δu_G for various values of the material parameter $c_{\boldsymbol{W}}$ and various loading directions ϕ_L, relative to the rolling direction. The calculations are based on a three-dimensional setting and the simulation results for the displacement-controlled loading and unloading of the sample are shown.
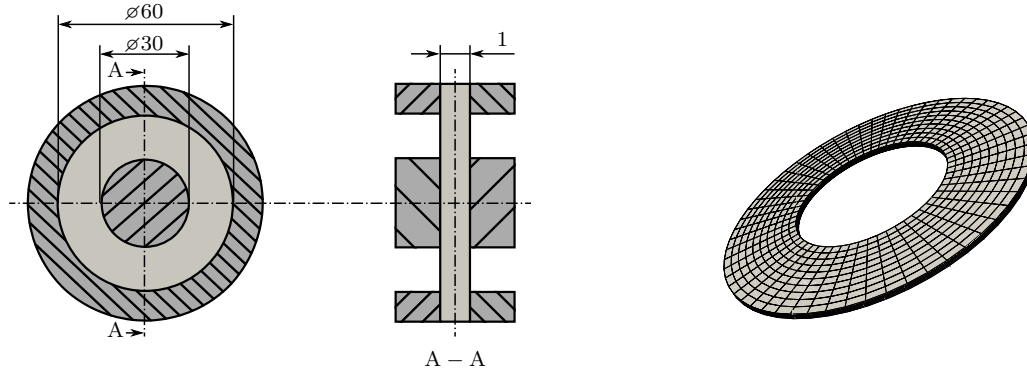
(a) Schematic design of in-plane torsion tests based on [150].

(b) Finite element mesh used for the simulation of in-plane torsion tests.

Figure 4.18: Schematic design, dimensions (in mm) and finite element mesh of in-plane torsion tests. a) Depicted is the specimen (light-grey colour) which is clamped between the inner and outer clamps (dark-grey colour) that rotate relative to each other. b) Finite element mesh that was used for the simulations of in-plane torsion tests in a three-dimensional setting.

4.4.3 In-plane torsion tests

The proper characterisation of materials and the assessment of the applicability of a certain material model in general requires the analysis of the material response for different load states and different loading paths. This can for example be done by taking into account experimental data based on tension-, compression-, shear- or bending tests. In this section we will focus on the simulation of shear-dominated deformation states as they are observed in the in-plane torsion test, see for example [82, 150]. In this test, a round sheet metal sample is clamped between the outer and inner clamps of the testing machine as schematically shown in Figure 4.18(a). By applying a relative rotation between the outer and the inner clamps, a shear-type deformation is induced in the free circular area between the clamps, and (cyclic) stress-strain curves are determined, see e.g. [150]. The objective of the present contribution is not the precise reproduction of experimentally obtained stress-strain curves. Rather, we focus on the general influence of the residual-type part of the evolution equation and on the evolution of the yield function's symmetry axes for shear-dominated deformation states.

To this end, the in-plane torsion test is simulated based on three different material models, respectively based on three different sets of material parameters. In particular, we will take into account the prototype model presented in Section 4.2 with the set of material parameters given in Table 4.1 and an active ($c_{\boldsymbol{W}} = 0.15$ Pa^{-1}) and non-active ($c_{\boldsymbol{W}} = 0.00$ Pa^{-1}) residual-type evolution. For the sake of comparison we will furthermore consider a plastically isotropic material model which results as a special case of (4.44) for $a_2 = 0.00 \frac{1}{\text{GPa}^2}$, $a_3 = 0.00 \frac{1}{\text{GPa}^2}$, $a_4 = 0.00 \frac{1}{\text{GPa}^2}$, $a_5 = 0.00 \frac{1}{\text{GPa}^2}$ and $a_6 = 0.00 \frac{1}{\text{GPa}^2}$. To allow for a good comparability of the results the material parameter a_1 will be scaled such that the isotropic yield function results in approximately the

207

same yield limit as the anisotropic one in the three-dimensional tension test presented in Section 4.4.2.2. Specifically speaking, $a_1 = 23.9\,\frac{1}{\text{GPa}^2}$ will be chosen (for the isotropic yield function) which results in a necessary force for yielding $f_\text{L} \approx 30150\,\text{N}$, respectively a yield limit of approximately $251\,\text{MPa}$.

The finite element simulations are based on the discrete geometry model depicted in Figure 4.18(b) with an inner radius of $15\,\text{mm}$, an outer radius of $30\,\text{mm}$ and a height of $1\,\text{mm}$. The displacement at the inner boundary will be fixed in radial-, azimuthal- and height direction. At the outer boundary we will enforce homogeneous Dirichlet boundary conditions in both the radial- and the height direction, however, a displacement φ_T in azimuthal direction will be prescribed. More precisely speaking, the azimuthal displacement will be linearly increased to $\varphi_\text{T} = 30°$ and afterwards reduced to $\varphi_\text{T} = 0°$, again. Although a more accurate simulation e.g. by means of contact elements would be possible, this set of boundary conditions is sufficient for the present purpose. Dealing with (rolled) sheet metal we will assume a spatially uniform distribution of the initial axes of plastic material symmetry, as indicated in Figure 4.19(a) and Figure 4.19(b). Together with the (initial) rotation symmetry of the geometry and taking into account that the material will respond elastically isotropic, we find that every relative orientation (measured in the plane spanned by the radial and azimuthal direction) between the (first) principal stress direction and the axes of plastic material symmetry is observable as long as no plastic deformation has taken place.

For the evaluation of the in-plane torsion tests we will focus on the accumulated plastic strain κ as a measure of the plastic deformation and on the first eigenvector $\boldsymbol{n_{a1}}$ of the spatial structural tensor as a measure of the symmetry group's rotation, see also the discussion at the beginning of Section 4.4. Focusing on the simulation results for a plastically anisotropic material with an active residual-type evolution, first, we observe a spatially non-homogeneous rotation of the vectors $\boldsymbol{n_{a1}}$ with increasing plastic deformation. Depending on the spatial position, or rather on the angle that is enclosed by the radial direction and the eigen-direction in the reference state, see Figure 4.19(a), a clockwise rotation of the symmetry group is induced in some of the elements while an anticlockwise rotation is observed in others. For the shear dominated boundary value problem at hand and with regard to the elastic isotropy we expect that the principal stress directions enclose an angle of approx. $45°$ with the radial direction, at least in the small strain limit. According to the derivations presented in Section 4.3.2 the material symmetry group undergoes an evolution such that the principal axes of plastic material symmetry align with the principal loading directions. We thus expect a reorientation of the vectors $\boldsymbol{n_{a1}}$ in the direction of approx. $\pm 45°$ relative to the radial direction with increasing plastic deformation, as observed in Figure 4.19. Moreover, we note that the anisotropic features of the yield function do not significantly manifest themselves in the spatial distribution of κ due to the local alignment of the structural tensor with the stress tensor. Before proceeding it is instructive to note that the direction vectors $\boldsymbol{n_{a1}}$ which correspond to elements that deformed only elastically up to the respective

(a) $c_{\boldsymbol{W}} = 0.15 \text{ Pa}^{-1}$, $\varphi_{\text{T}} = 0°$

(b) $c_{\boldsymbol{W}} = 0.00 \text{ Pa}^{-1}$, $\varphi_{\text{T}} = 0°$

(c) $c_{\boldsymbol{W}} = 0.15 \text{ Pa}^{-1}$, $\varphi_{\text{T}} = 15°$

(d) $c_{\boldsymbol{W}} = 0.00 \text{ Pa}^{-1}$, $\varphi_{\text{T}} = 15°$

(e) $c_{\boldsymbol{W}} = 0.15 \text{ Pa}^{-1}$, $\varphi_{\text{T}} = 30°$

(f) $c_{\boldsymbol{W}} = 0.00 \text{ Pa}^{-1}$, $\varphi_{\text{T}} = 30°$

(g) $c_{\boldsymbol{W}} = 0.15 \text{ Pa}^{-1}$, $\varphi_{\text{T}} = 0°$
(after deformation)

(h) $c_{\boldsymbol{W}} = 0.00 \text{ Pa}^{-1}$, $\varphi_{\text{T}} = 0°$
(after deformation)
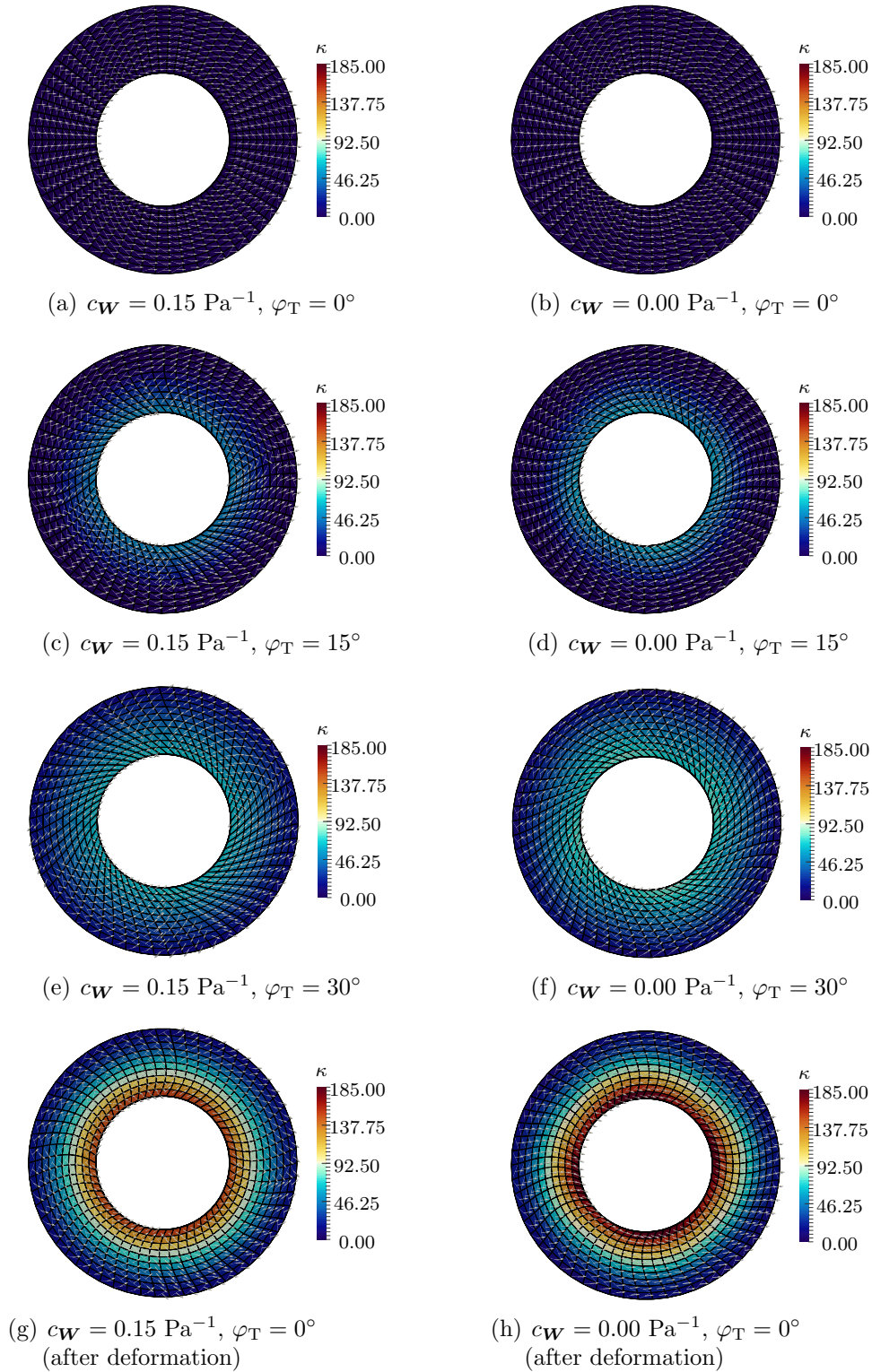
Figure 4.19: Evolution of the plastic deformation and of the material symmetry group for the in-plane torsion test for a plastically anisotropic material with and without a residual-type evolution of the symmetry group. Depicted is the element-wise mean value of the accumulated plastic strain κ and the first eigenvector $\boldsymbol{n}_{\boldsymbol{a}1}$ of the spatial structural tensor $\boldsymbol{a}$ at a selected quadrature point of each element.

209
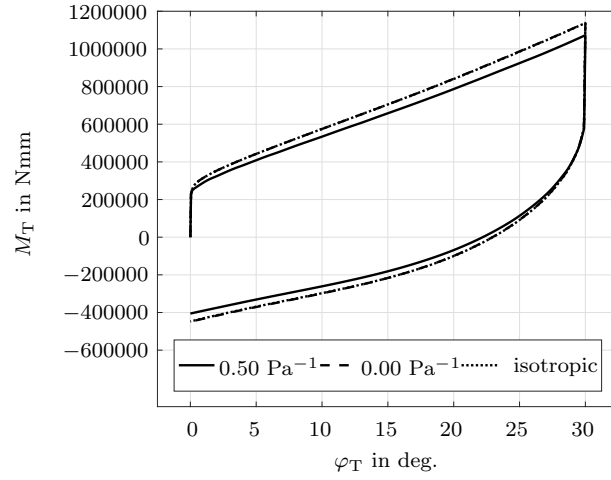
Figure 4.20: Depicted is the moment against the applied relative rotation between the outer and inner boundary for three different sets of material parameters. We specifically focus on a plastically anisotropic material with evolving preferred material directions ($c_{\boldsymbol{W}} = 0.15$ Pa^{-1}), on a plastically anisotropic material without a residual-type evolution of the preferred material directions ($c_{\boldsymbol{W}} = 0.00$ Pa^{-1}) and on a plastically isotropic material ($a_1 = 23.9 \frac{1}{\text{GPa}^2}$, $a_2 = 0.00 \frac{1}{\text{GPa}^2}$, $a_3 = 0.00 \frac{1}{\text{GPa}^2}$, $a_4 = 0.00 \frac{1}{\text{GPa}^2}$, $a_5 = 0.00 \frac{1}{\text{GPa}^2}$, $a_6 = 0.00 \frac{1}{\text{GPa}^2}$).

deformation state also exhibit a certain rotation which, however, is not (directly) related to the principal loading direction, see e.g. Figure 4.19(c).

This effect is due to the convected-type evolution and becomes more apparent when regarding the simulation results for a material which does not show a residual-type evolution of the symmetry group as depicted in Figures 4.19(b,d,f,h). Being more precise, the directors $\boldsymbol{n_{a1}}$ exhibit the (local) continuum rotation, except for errors due to the elastic strain, see the discussion at the beginning of Section 4.4, and inaccuracies related to the numerical time integration. Neglecting the residual-type evolution for now, equation (4.26d) shows that the structural tensor in the intermediate configuration spins at the same (indeterminate) rate as the intermediate configuration. Regardless of the chosen split of the rotation part of $\boldsymbol{F}$ into an elastic and plastic part in the spirit of the multiplicative split, the elastic and plastic rotation must add up to the continuum rotation. If the elastic strain is small the spatial structural tensor is thus found to rotate with the continuum. In contrast to the previously discussed material with an active residual-type evolution we furthermore find that the plastic material anisotropy significantly manifests itself in the spatial distribution of the accumulated plastic strain κ, see Figure 4.19(h).

Finally, load-displacement curves in terms of the relative rotation φ_{T} between the inner and outer clamps and the applied moment with respect to the centre of the circular sample M_{T} are provided in Figure 4.20. We observe, in principle, the same load-displacement response for the plastically isotropic material with a modified material parameter $a_1 = 23.9 \frac{1}{\text{GPa}^2}$ and a plastically anisotropic material with a purely convected-

type evolution of the structural tensor. Furthermore it is revealed that activating the residual-type evolution results in a smaller necessary moment after the onset of yielding due to the alignment of the structural tensors with the principal loading directions.

4.5 Summary

The experiments on cold-rolled sheet metal by Kim and Yin, [65], suggest that the experimentally observed, initially orthotropic yielding behaviour is maintained throughout a finite plastic deformation process. Moreover, the symmetry group of the yield function is found to evolve in such a way that the symmetry axes align with the principal loading directions, i.e. a rotation of the (plastic) symmetry group is observed.

Inspired by these experiments, this chapter focused on the development of a specific, thermodynamically consistent model which allows us to capture the experimentally observed evolution of the plastic anisotropy. The presented developments were substantially based on the principal theoretical developments by Lu and Papadopoulos, [77], with respect to a covariant formulation of anisotropic finite plasticity. For motivational purposes we relied on the physical interpretation of the intermediate configuration, although the multiplicative split was never invoked explicitly due to its rotational indeterminacy. Being more specific, an orthotropic yield function in terms of the Mandel stress tensor of the intermediate configuration was assumed. The respective symmetry group of this yield function could be characterised by a structural tensor which itself was defined in the intermediate configuration. Focusing on the modelling of evolving material symmetries, a well-interpretable evolution equation for the structural tensor was proposed. Taking the latter into account, we derived a purely referential representation of the yield function and of the evolution equations for the internal variables, thus circumventing the use of the multiplicative split.

The rate equations for the structural tensor, for the right Cauchy-Green plastic deformation tensor and for the accumulated plastic strain formed a non-linear system of differential equations which was solved (locally) at each integration point of the employed finite element scheme. Focusing on the comparison with experimental findings, tension tests in a two-dimensional plane strain setting and in a general three-dimensional setting were simulated. Specifically speaking, we observed that a convected-type evolution equation for the structural tensor was not sufficient in order to capture the experimentally observed rotation of the material symmetry group. However, by additionally invoking the specific residual-type evolution equation developed in this chapter, the simulation results closely matched the experimental findings and gave rise to some new possibilities of interpreting the experimental findings. In a next step in-plane torsion tests were simulated to analyse the principal model properties for shear-dominated boundary value problems, revealing once again the alignment of the axes of plastic material symmetry with the principal loading directions.

C Appendix

C.1 Specification of material parameters

The experimental findings by Kim and Yin suggest that the initial yield function can be well approximated by Hill's yield function, [55], and that the orthotropic yielding behaviour is maintained during the experiments, while a rotation of the preferred material axes is observed, see Section 4.3.1 and [65]. In [52], an orthotropic yield function in terms of the Kirchhoff stress tensor was fitted based on the experimental data by Kim and Yin, [65]. This yield function will be taken into account to calibrate the initial yield function in terms of the Mandel stress tensor used in this contribution, similar to the derivations presented in [9]. To this end, the equivalence of (4.42) with a yield function of the form

$$\tilde{f} = A_1 \, \tilde{I}_{y1} + A_2 \, \tilde{I}_{y2} + A_3 \, \tilde{I}_{y3} + A_4 \left[\tilde{I}_{y4}\right]^2 + A_5 \left[\tilde{I}_{y5}\right]^2 + A_6 \, \tilde{I}_{y4} \, \tilde{I}_{y5} - \tilde{M}_{\mathrm{y}} \qquad (4.82)$$

with invariants

$$\tilde{I}_{y1} = \mathrm{tr}\left(\overline{\boldsymbol{M}}_{\mathrm{dev}}^2\right) \tag{4.83a}$$

$$\tilde{I}_{y2} = \mathrm{tr}\left(\overline{\boldsymbol{M}}_{\mathrm{dev}}^2 \cdot \overline{\boldsymbol{G}}^{\flat} \cdot \left[\overline{\boldsymbol{N}}_{\overline{\boldsymbol{A}}_1} \otimes \overline{\boldsymbol{N}}_{\overline{\boldsymbol{A}}_1}\right]\right) \tag{4.83b}$$

$$\tilde{I}_{y3} = \mathrm{tr}\left(\overline{\boldsymbol{M}}_{\mathrm{dev}}^2 \cdot \overline{\boldsymbol{G}}^{\flat} \cdot \left[\overline{\boldsymbol{N}}_{\overline{\boldsymbol{A}}_2} \otimes \overline{\boldsymbol{N}}_{\overline{\boldsymbol{A}}_2}\right]\right) \tag{4.83c}$$

$$\tilde{I}_{y4} = \mathrm{tr}\left(\overline{\boldsymbol{M}}_{\mathrm{dev}} \cdot \overline{\boldsymbol{G}}^{\flat} \cdot \left[\overline{\boldsymbol{N}}_{\overline{\boldsymbol{A}}_1} \otimes \overline{\boldsymbol{N}}_{\overline{\boldsymbol{A}}_1}\right]\right) \tag{4.83d}$$

$$\tilde{I}_{y5} = \mathrm{tr}\left(\overline{\boldsymbol{M}}_{\mathrm{dev}} \cdot \overline{\boldsymbol{G}}^{\flat} \cdot \left[\overline{\boldsymbol{N}}_{\overline{\boldsymbol{A}}_2} \otimes \overline{\boldsymbol{N}}_{\overline{\boldsymbol{A}}_2}\right]\right) \tag{4.83e}$$

which itself can be related to Hill's yield function, cf. [28], will be shown. Introducing the notation

$$I_{y1} = \mathrm{tr}\left(\overline{\boldsymbol{M}}_{\mathrm{dev}}^2\right) \;\; (4.84a) \quad I_{y2} = \mathrm{tr}\left(\overline{\boldsymbol{M}}_{\mathrm{dev}} \cdot \overline{\boldsymbol{A}}_{\mathrm{p}}\right) \;\; (4.84b) \quad I_{y3} = \mathrm{tr}\left(\overline{\boldsymbol{M}}_{\mathrm{dev}} \cdot \overline{\boldsymbol{A}}_{\mathrm{p}}^2\right) \;\; (4.84c)$$

$$I_{y4} = \mathrm{tr}\left(\overline{\boldsymbol{M}}_{\mathrm{dev}}^2 \cdot \overline{\boldsymbol{A}}_{\mathrm{p}}\right) \;\; (4.84d) \quad I_{y5} = \mathrm{tr}\left(\overline{\boldsymbol{M}}_{\mathrm{dev}}^2 \cdot \overline{\boldsymbol{A}}_{\mathrm{p}}^2\right) \;\; (4.84e)$$

and inserting the relations

$$\tilde{I}_{y1} = I_{y1} \quad (4.85a) \qquad \tilde{I}_{y2} = I_{y4} + 2\,I_{y5} \;\; (4.85b) \qquad \tilde{I}_{y3} = -I_{y4} + 2\,I_{y5} \;\; (4.85c)$$

$$\tilde{I}_{y4} = I_{y2} + 2\,I_{y3} \;\; (4.85d) \qquad \tilde{I}_{y5} = -I_{y1} + 2\,I_{y3} \;\; (4.85e)$$

into (4.82) one ends up with

$$\tilde{f} = A_1\,I_{y1} + [A_4 + A_5 - A_6]\,[I_{y2}]^2 \quad + [4\,A_4 + 4\,A_5 + 4\,A_6]\,[I_{y3}]^2 \quad + [4\,A_4 - 4\,A_5]\,I_{y2}\,I_{y3}$$
$$+ [A_2 - A_3]\,I_{y4} \qquad\qquad + [2\,A_2 + 2\,A_3]\,I_{y5} \qquad\qquad - \tilde{M}_{\mathrm{y}} \quad .$$
(4.86)

Comparing (4.42) with (4.86) finally yields the conditions

$$a_1 = A_1 \qquad (4.87\mathrm{a}) \qquad a_2 = A_4 + A_5 - A_6 \quad (4.87\mathrm{b}) \qquad a_3 = 4\,A_4 + 4\,A_5 + 4\,A_6 \quad (4.87\mathrm{c})$$

$$a_4 = 4\,A_4 - 4\,A_5 \quad (4.87\mathrm{d}) \qquad a_5 = A_2 - A_3 \qquad (4.87\mathrm{e}) \qquad a_6 = 2\,A_2 + 2\,A_3 \qquad (4.87\mathrm{f})$$

C.2 Derivation of the algorithmic tangent stiffness

In this appendix, the sensitivities with respect to the internal variables and to the deformation gradient tensor which are required for a gradient-based iterative solution of the local system of differential equations (4.77) and for the specification of the (consistent) algorithmic tangent stiffness operator (4.78) are summarised for the prototype model presented in Section 4.2 and Section 4.3.2. For the sake of brevity, superscripts $n + 1$ will be omitted in the following.

To start with, the derivative of the Piola-Kirchhoff stresses with respect to the deformation gradient reads

$$\frac{\partial \boldsymbol{S}}{\partial \boldsymbol{F}} = \frac{1}{2}\left[[\mu - \lambda \ln{(J_{\mathrm{e}})}]\left[\boldsymbol{C}^{-1}\,\overline{\otimes}\,\boldsymbol{C}^{-1} + \boldsymbol{C}^{-1}\,\underline{\otimes}\,\boldsymbol{C}^{-1}\right] + \lambda\,\boldsymbol{C}^{-1}\otimes\boldsymbol{C}^{-1}\right]$$
$$: \left[\boldsymbol{G}^{\natural\star}\,\underline{\otimes}\,\left[\boldsymbol{F}^{\star}\cdot\boldsymbol{g}^{\flat}\right] + \left[\boldsymbol{F}^{\star}\cdot\boldsymbol{g}^{\flat}\right]\,\overline{\otimes}\,\boldsymbol{G}^{\natural\star}\right]$$
(4.88)

and the derivative with respect to the plastic right Cauchy-Green tensor is given by

$$\frac{\partial \boldsymbol{S}}{\partial \boldsymbol{C}_{\mathrm{p}}} = -\frac{1}{2}\,\mu\left[\boldsymbol{C}_{\mathrm{p}}^{-1}\,\overline{\otimes}\,\boldsymbol{C}_{\mathrm{p}}^{-1} + \boldsymbol{C}_{\mathrm{p}}^{-1}\,\underline{\otimes}\,\boldsymbol{C}_{\mathrm{p}}^{-1}\right] - \frac{1}{2}\,\lambda\,\boldsymbol{C}^{-1}\otimes\boldsymbol{C}_{\mathrm{p}}^{-1}$$
(4.89)

while the derivatives with respect to the remaining internal variables vanish identically, i.e.

$$\frac{\partial \boldsymbol{S}}{\partial \boldsymbol{A}} = \boldsymbol{0} \qquad (4.90) \qquad\qquad \frac{\partial \boldsymbol{S}}{\partial \kappa} = \boldsymbol{0} \qquad (4.91) \qquad\qquad \frac{\partial \boldsymbol{S}}{\partial \lambda_{\mathrm{p}}} = \boldsymbol{0} \qquad (4.92)$$

In addition, the sensitivities of the residual terms of the local iteration scheme with

respect to the internal variables as well as with respect to the deformation gradient are required. For the sake of brevity, the derivatives of the trace-terms

$$\frac{\partial \operatorname{tr} (\boldsymbol{M}_{\mathrm{dev}} \cdot \boldsymbol{A}_{\mathrm{p}})}{\partial \boldsymbol{A}_{\mathrm{p}}} : \frac{\partial \boldsymbol{A}_{\mathrm{p}}}{\partial \boldsymbol{C}_{\mathrm{p}}} = \frac{1}{2} \left[[\boldsymbol{A} \cdot \boldsymbol{M}_{\mathrm{dev}}]^{\star} + \boldsymbol{A} \cdot \boldsymbol{M}_{\mathrm{dev}} \right] \tag{4.93}$$

$$\frac{\partial \operatorname{tr} (\boldsymbol{M}_{\mathrm{dev}} \cdot \boldsymbol{A}_{\mathrm{p}})}{\partial \boldsymbol{A}} = \frac{1}{2} \left[[\boldsymbol{M}_{\mathrm{dev}} \cdot \boldsymbol{C}_{\mathrm{p}}]^{\star} + \boldsymbol{M}_{\mathrm{dev}} \cdot \boldsymbol{C}_{\mathrm{p}} \right] \tag{4.94}$$

$$\frac{\partial \operatorname{tr} \left(\boldsymbol{M}_{\mathrm{dev}} \cdot \boldsymbol{A}_{\mathrm{p}}{}^2 \right)}{\partial \boldsymbol{A}_{\mathrm{p}}} : \frac{\partial \boldsymbol{A}_{\mathrm{p}}}{\partial \boldsymbol{C}_{\mathrm{p}}} = \frac{1}{2} \left[\begin{array}{l} [\boldsymbol{A} \cdot \boldsymbol{A}_{\mathrm{p}} \cdot \boldsymbol{M}_{\mathrm{dev}}]^{\star} + \boldsymbol{A} \cdot \boldsymbol{A}_{\mathrm{p}} \cdot \boldsymbol{M}_{\mathrm{dev}} \\ + [\boldsymbol{A} \cdot \boldsymbol{M}_{\mathrm{dev}} \cdot \boldsymbol{A}_{\mathrm{p}}]^{\star} + \boldsymbol{A} \cdot \boldsymbol{M}_{\mathrm{dev}} \cdot \boldsymbol{A}_{\mathrm{p}} \end{array} \right] \tag{4.95}$$

$$\frac{\partial \operatorname{tr} \left(\boldsymbol{M}_{\mathrm{dev}} \cdot \boldsymbol{A}_{\mathrm{p}}{}^2 \right)}{\partial \boldsymbol{A}} = \frac{1}{2} \left[\begin{array}{l} [\boldsymbol{A}_{\mathrm{p}} \cdot \boldsymbol{M}_{\mathrm{dev}} \cdot \boldsymbol{C}_{\mathrm{p}}]^{\star} + \boldsymbol{A}_{\mathrm{p}} \cdot \boldsymbol{M}_{\mathrm{dev}} \cdot \boldsymbol{C}_{\mathrm{p}} \\ + [\boldsymbol{M}_{\mathrm{dev}} \cdot \boldsymbol{A}_{\mathrm{p}} \cdot \boldsymbol{C}_{\mathrm{p}}]^{\star} + \boldsymbol{M}_{\mathrm{dev}} \cdot \boldsymbol{A}_{\mathrm{p}} \cdot \boldsymbol{C}_{\mathrm{p}} \end{array} \right] \tag{4.96}$$

and the derivatives of the mixed-variant structural tensor $\boldsymbol{A}_{\mathrm{p}} = \boldsymbol{C}_{\mathrm{p}} \cdot \boldsymbol{A}$, see (4.46),

$$\frac{\partial \boldsymbol{A}_{\mathrm{p}}}{\partial \boldsymbol{C}_{\mathrm{p}}} = \frac{1}{2} \left[\boldsymbol{G}^{\natural\star} \, \overline{\otimes} \, \boldsymbol{A} + \boldsymbol{G}^{\natural\star} \, \underline{\otimes} \, \boldsymbol{A} \right] \tag{4.97}$$

$$\frac{\partial \boldsymbol{A}_{\mathrm{p}}}{\partial \boldsymbol{A}} = \frac{1}{2} \left[\boldsymbol{C}_{\mathrm{p}} \, \overline{\otimes} \, \boldsymbol{G}^{\natural} + \boldsymbol{C}_{\mathrm{p}} \, \underline{\otimes} \, \boldsymbol{G}^{\natural} \right] \tag{4.98}$$

$$\frac{\partial \boldsymbol{A}_{\mathrm{p}}^2}{\partial \boldsymbol{C}_{\mathrm{p}}} = \frac{1}{2} \left[\boldsymbol{G}^{\natural\star} \, \overline{\otimes} \, \left[\boldsymbol{A}_{\mathrm{p}}^{\star} \cdot \boldsymbol{A} \right] + \boldsymbol{G}^{\natural\star} \, \underline{\otimes} \, \left[\boldsymbol{A}_{\mathrm{p}}^{\star} \cdot \boldsymbol{A} \right] + \boldsymbol{A}_{\mathrm{p}} \, \overline{\otimes} \, \boldsymbol{A} + \boldsymbol{A}_{\mathrm{p}} \, \underline{\otimes} \, \boldsymbol{A} \right] \tag{4.99}$$

$$\frac{\partial \boldsymbol{A}_{\mathrm{p}}^2}{\partial \boldsymbol{A}} = \frac{1}{2} \left[\boldsymbol{C}_{\mathrm{p}} \, \overline{\otimes} \, \boldsymbol{A}_{\mathrm{p}}^{\star} + \boldsymbol{C}_{\mathrm{p}} \, \underline{\otimes} \, \boldsymbol{A}_{\mathrm{p}}^{\star} + [\boldsymbol{A}_{\mathrm{p}} \cdot \boldsymbol{C}_{\mathrm{p}}] \, \overline{\otimes} \, \boldsymbol{G}^{\natural} + [\boldsymbol{A}_{\mathrm{p}} \cdot \boldsymbol{C}_{\mathrm{p}}] \, \underline{\otimes} \, \boldsymbol{G}^{\natural} \right] \tag{4.100}$$

with respect to the plastic right Cauchy-Green tensor and with respect to the structural tensor $\boldsymbol{A}$ will not be inserted in the ensuing equations. The same holds for the derivatives of $\boldsymbol{\Lambda}_{\mathrm{p}}$, which are given by

$$\begin{aligned}
\frac{\partial \boldsymbol{\Lambda}_{\mathrm{p}}}{\partial \boldsymbol{A}_{\mathrm{p}}} : \frac{\partial \boldsymbol{A}_{\mathrm{p}}}{\partial \boldsymbol{C}_{\mathrm{p}}} = \mathsf{I}_{\mathrm{dev}}^{\natural} : \Bigg[& 2 \, a_2 \left[\boldsymbol{A}_{\mathrm{p}}^{\star} \otimes \frac{\partial \operatorname{tr} (\boldsymbol{M}_{\mathrm{dev}} \cdot \boldsymbol{A}_{\mathrm{p}})}{\partial \boldsymbol{A}_{\mathrm{p}}} : \frac{\partial \boldsymbol{A}_{\mathrm{p}}}{\partial \boldsymbol{C}_{\mathrm{p}}} + \operatorname{tr} (\boldsymbol{M}_{\mathrm{dev}} \cdot \boldsymbol{A}_{\mathrm{p}}) \frac{\partial \boldsymbol{A}_{\mathrm{p}}^{\star}}{\partial \boldsymbol{C}_{\mathrm{p}}} \right] \\
& + 2 \, a_3 \left[[\boldsymbol{A}_{\mathrm{p}}^2]^{\star} \otimes \frac{\partial \operatorname{tr} \left(\boldsymbol{M}_{\mathrm{dev}} \cdot \boldsymbol{A}_{\mathrm{p}}^2 \right)}{\partial \boldsymbol{A}_{\mathrm{p}}} : \frac{\partial \boldsymbol{A}_{\mathrm{p}}}{\partial \boldsymbol{C}_{\mathrm{p}}} + \operatorname{tr} \left(\boldsymbol{M}_{\mathrm{dev}} \cdot \boldsymbol{A}_{\mathrm{p}}^2 \right) \frac{\partial \left[\boldsymbol{A}_{\mathrm{p}}^2 \right]^{\star}}{\partial \boldsymbol{C}_{\mathrm{p}}} \right] \\
& + a_4 \left[\boldsymbol{A}_{\mathrm{p}}^{\star} \otimes \frac{\partial \operatorname{tr} \left(\boldsymbol{M}_{\mathrm{dev}} \cdot \boldsymbol{A}_{\mathrm{p}}^2 \right)}{\partial \boldsymbol{A}_{\mathrm{p}}} : \frac{\partial \boldsymbol{A}_{\mathrm{p}}}{\partial \boldsymbol{C}_{\mathrm{p}}} + \operatorname{tr} \left(\boldsymbol{M}_{\mathrm{dev}} \cdot \boldsymbol{A}_{\mathrm{p}}{}^2 \right) \frac{\partial \boldsymbol{A}_{\mathrm{p}}^{\star}}{\partial \boldsymbol{C}_{\mathrm{p}}} \right. \\
& \left. \quad + [\boldsymbol{A}_{\mathrm{p}}^2]^{\star} \otimes \frac{\partial \operatorname{tr} (\boldsymbol{M}_{\mathrm{dev}} \cdot \boldsymbol{A}_{\mathrm{p}})}{\partial \boldsymbol{A}_{\mathrm{p}}} : \frac{\partial \boldsymbol{A}_{\mathrm{p}}}{\partial \boldsymbol{C}_{\mathrm{p}}} + \operatorname{tr} (\boldsymbol{M}_{\mathrm{dev}} \cdot \boldsymbol{A}_{\mathrm{p}}) \frac{\partial \left[\boldsymbol{A}_{\mathrm{p}}^2 \right]^{\star}}{\partial \boldsymbol{C}_{\mathrm{p}}} \right]
\end{aligned}$$

$$+ a_5 \left[\left[\boldsymbol{G}^\natural \mathbin{\underline{\otimes}} \boldsymbol{G}^{\natural\star} \right] : \left[\boldsymbol{M}_{\mathrm{dev}} \cdot \frac{\partial \boldsymbol{A}_{\mathrm{p}}}{\partial \boldsymbol{C}_{\mathrm{p}}} \right] + \boldsymbol{M}_{\mathrm{dev}}^\star \cdot \frac{\partial \boldsymbol{A}_{\mathrm{p}}^\star}{\partial \boldsymbol{C}_{\mathrm{p}}} \right]$$

$$+ a_6 \left[\left[\boldsymbol{G}^\natural \mathbin{\underline{\otimes}} \boldsymbol{G}^{\natural\star} \right] : \left[\boldsymbol{M}_{\mathrm{dev}} \cdot \frac{\partial \boldsymbol{A}_{\mathrm{p}}^2}{\partial \boldsymbol{C}_{\mathrm{p}}} \right] + \boldsymbol{M}_{\mathrm{dev}}^\star \cdot \frac{\partial \left[\boldsymbol{A}_{\mathrm{p}}^2 \right]^\star}{\partial \boldsymbol{C}_{\mathrm{p}}} \right] \right] \quad (4.101)$$

and

$$\frac{\partial \boldsymbol{\Lambda}_{\mathrm{p}}}{\partial \boldsymbol{A}} = \mathbf{I}_{\mathrm{dev}}^\natural : \left[2\,a_2 \left[\boldsymbol{A}_{\mathrm{p}}^\star \otimes \frac{\partial \operatorname{tr}\left(\boldsymbol{M}_{\mathrm{dev}} \cdot \boldsymbol{A}_{\mathrm{p}} \right)}{\partial \boldsymbol{A}} + \operatorname{tr}\left(\boldsymbol{M}_{\mathrm{dev}} \cdot \boldsymbol{A}_{\mathrm{p}} \right) \frac{\partial \boldsymbol{A}_{\mathrm{p}}^\star}{\partial \boldsymbol{A}} \right] \right.$$

$$+ 2\,a_3 \left[\left[\boldsymbol{A}_{\mathrm{p}}^2 \right]^\star \otimes \frac{\partial \operatorname{tr}\left(\boldsymbol{M}_{\mathrm{dev}} \cdot \boldsymbol{A}_{\mathrm{p}}^2 \right)}{\partial \boldsymbol{A}} + \operatorname{tr}\left(\boldsymbol{M}_{\mathrm{dev}} \cdot \boldsymbol{A}_{\mathrm{p}}^2 \right) \frac{\partial \left[\boldsymbol{A}_{\mathrm{p}}^2 \right]^\star}{\partial \boldsymbol{A}} \right]$$

$$+ a_4 \left[\boldsymbol{A}_{\mathrm{p}}^\star \otimes \frac{\partial \operatorname{tr}\left(\boldsymbol{M}_{\mathrm{dev}} \cdot \boldsymbol{A}_{\mathrm{p}}^2 \right)}{\partial \boldsymbol{A}} + \operatorname{tr}\left(\boldsymbol{M}_{\mathrm{dev}} \cdot \boldsymbol{A}_{\mathrm{p}}^2 \right) \frac{\partial \boldsymbol{A}_{\mathrm{p}}^\star}{\partial \boldsymbol{C}_{\mathrm{p}}} \right.$$

$$\left. + \left[\boldsymbol{A}_{\mathrm{p}}^2 \right]^\star \otimes \frac{\partial \operatorname{tr}\left(\boldsymbol{M}_{\mathrm{dev}} \cdot \boldsymbol{A}_{\mathrm{p}} \right)}{\partial \boldsymbol{A}} + \operatorname{tr}\left(\boldsymbol{M}_{\mathrm{dev}} \cdot \boldsymbol{A}_{\mathrm{p}} \right) \frac{\partial \left[\boldsymbol{A}_{\mathrm{p}}^2 \right]^\star}{\partial \boldsymbol{A}} \right]$$

$$+ a_5 \left[\left[\boldsymbol{G}^\natural \mathbin{\underline{\otimes}} \boldsymbol{G}^{\natural\star} \right] : \left[\boldsymbol{M}_{\mathrm{dev}} \cdot \frac{\partial \boldsymbol{A}_{\mathrm{p}}}{\partial \boldsymbol{A}} \right] + \boldsymbol{M}_{\mathrm{dev}}^\star \cdot \frac{\partial \boldsymbol{A}_{\mathrm{p}}^\star}{\partial \boldsymbol{A}} \right]$$

$$+ a_6 \left[\left[\boldsymbol{G}^\natural \mathbin{\underline{\otimes}} \boldsymbol{G}^{\natural\star} \right] : \left[\boldsymbol{M}_{\mathrm{dev}} \cdot \frac{\partial \boldsymbol{A}_{\mathrm{p}}^2}{\partial \boldsymbol{A}} \right] + \boldsymbol{M}_{\mathrm{dev}}^\star \cdot \frac{\partial \left[\boldsymbol{A}_{\mathrm{p}}^2 \right]^\star}{\partial \boldsymbol{A}} \right] \right] \quad,$$

$$(4.102)$$

with $\mathbf{I}_{\mathrm{dev}}^\natural$ denoting the fourth-order deviatoric projection tensor

$$\mathbf{I}_{\mathrm{dev}}^\natural = \boldsymbol{G}^\natural \mathbin{\overline{\otimes}} \boldsymbol{G}^{\natural\star} - \frac{1}{3} \boldsymbol{G}^\natural \otimes \boldsymbol{G}^{\natural\star} \quad . \quad (4.103)$$

With these derivatives at hand and by making use of (4.52), (4.58), (4.59) and (4.71) the derivatives of the residual terms which are related to the evolution of $\boldsymbol{C}_{\mathrm{p}}$ are given by

$$\frac{\partial \boldsymbol{R}_{\boldsymbol{C}_{\mathrm{p}}}}{\partial \boldsymbol{C}_{\mathrm{p}}} = -\frac{1}{2} \left[\boldsymbol{G}^{\natural\star} \mathbin{\overline{\otimes}} \boldsymbol{G}^{\natural\star} + \boldsymbol{G}^{\natural\star} \mathbin{\underline{\otimes}} \boldsymbol{G}^{\natural\star} \right]$$

$$+ \frac{1}{4} \Delta t\, \lambda_{\mathrm{p}} \left[\boldsymbol{G}^{\natural\star} \mathbin{\overline{\otimes}} \boldsymbol{\Lambda}_{\mathrm{p}}^\star + \boldsymbol{G}^{\natural\star} \mathbin{\underline{\otimes}} \boldsymbol{\Lambda}_{\mathrm{p}}^\star \right]$$

$$+ \frac{1}{4} \Delta t\, \lambda_{\mathrm{p}} \left[\boldsymbol{\Lambda}_{\mathrm{p}}^\star \mathbin{\overline{\otimes}} \boldsymbol{G}^{\natural\star} + \boldsymbol{\Lambda}_{\mathrm{p}}^\star \mathbin{\underline{\otimes}} \boldsymbol{G}^{\natural\star} \right]$$

$$- \frac{1}{4} \Delta t\, \lambda_{\mathrm{p}} \left[\boldsymbol{G}^{\natural\star} \mathbin{\overline{\otimes}} \boldsymbol{G}^{\natural\star} + \boldsymbol{G}^{\natural\star} \mathbin{\underline{\otimes}} \boldsymbol{G}^{\natural\star} \right] : \left[\boldsymbol{C}_{\mathrm{p}} \cdot \frac{\partial^2 f}{\partial \boldsymbol{M} \partial \boldsymbol{M}} \right]$$

$$: \left[\mu\, \boldsymbol{C} \cdot \left[\boldsymbol{C}_{\mathrm{p}}^{-1} \,\overline{\otimes}\, \boldsymbol{C}_{\mathrm{p}}^{-1} + \boldsymbol{C}_{\mathrm{p}}^{-1} \,\underline{\otimes}\, \boldsymbol{C}_{\mathrm{p}}^{-1} \right] + \lambda\, \boldsymbol{G}^{\natural\star} \otimes \boldsymbol{C}_{\mathrm{p}}^{-1} \right]$$

$$+ \frac{1}{2}\, \Delta t\, \lambda_{\mathrm{p}} \left[\boldsymbol{G}^{\natural\star} \,\overline{\otimes}\, \boldsymbol{G}^{\natural\star} + \boldsymbol{G}^{\natural\star} \,\underline{\otimes}\, \boldsymbol{G}^{\natural\star} \right] : \left[\boldsymbol{C}_{\mathrm{p}} \cdot \frac{\partial \boldsymbol{\Lambda}_{\mathrm{p}}}{\partial \boldsymbol{A}_{\mathrm{p}}} : \frac{\partial \boldsymbol{A}_{\mathrm{p}}}{\partial \boldsymbol{C}_{\mathrm{p}}} \right] \tag{4.104}$$

$$\frac{\partial \boldsymbol{R}_{C_{\mathrm{p}}}}{\partial \boldsymbol{A}} = \frac{1}{2}\, \Delta t\, \lambda_{\mathrm{p}} \left[\boldsymbol{G}^{\natural\star} \,\overline{\otimes}\, \boldsymbol{G}^{\natural\star} + \boldsymbol{G}^{\natural\star} \,\underline{\otimes}\, \boldsymbol{G}^{\natural\star} \right] : \left[\boldsymbol{C}_{\mathrm{p}} \cdot \frac{\partial \boldsymbol{\Lambda}_{\mathrm{p}}}{\partial \boldsymbol{A}} \right] \tag{4.105}$$

$$\frac{\partial \boldsymbol{R}_{C_{\mathrm{p}}}}{\partial \kappa} = \boldsymbol{0} \tag{4.106}$$

$$\frac{\partial \boldsymbol{R}_{C_{\mathrm{p}}}}{\partial \lambda_{\mathrm{p}}} = \frac{1}{2}\, \Delta t \left[\left[\boldsymbol{C}_{\mathrm{p}} \cdot \boldsymbol{\Lambda}_{\mathrm{p}} + \boldsymbol{\Lambda}_{\mathrm{p}}^{\star} \cdot \boldsymbol{C}_{\mathrm{p}} \right] + \left[\boldsymbol{C}_{\mathrm{p}}{}^{n} \cdot \boldsymbol{\Lambda}_{\mathrm{p}}{}^{n} + \boldsymbol{\Lambda}_{\mathrm{p}}^{\star n} \cdot \boldsymbol{C}_{\mathrm{p}}{}^{n} \right] \right] \tag{4.107}$$

and those of the residual terms which are related to the evolution of the structural tensor read

$$\frac{\partial \boldsymbol{R}_{A}}{\partial \boldsymbol{C}_{\mathrm{p}}} = \frac{1}{4}\, \Delta t\, \lambda_{\mathrm{p}} \left[\boldsymbol{G}^{\natural} \,\overline{\otimes}\, \boldsymbol{A} + \boldsymbol{A} \,\underline{\otimes}\, \boldsymbol{G}^{\natural} \right] : \frac{\partial^{2} f}{\partial \boldsymbol{M} \partial \boldsymbol{M}}$$

$$: \left[\mu\, \boldsymbol{C} \cdot \left[\boldsymbol{C}_{\mathrm{p}}^{-1} \,\overline{\otimes}\, \boldsymbol{C}_{\mathrm{p}}^{-1} + \boldsymbol{C}_{\mathrm{p}}^{-1} \,\underline{\otimes}\, \boldsymbol{C}_{\mathrm{p}}^{-1} \right] + \lambda\, \boldsymbol{G}^{\natural\star} \otimes \boldsymbol{C}_{\mathrm{p}}^{-1} \right]$$

$$- \frac{1}{2}\, \Delta t\, \lambda_{\mathrm{p}} \left[\boldsymbol{G}^{\natural} \,\overline{\otimes}\, \boldsymbol{A} + \boldsymbol{A} \,\underline{\otimes}\, \boldsymbol{G}^{\natural} \right] : \frac{\partial \boldsymbol{\Lambda}_{\mathrm{p}}}{\partial \boldsymbol{A}_{\mathrm{p}}} : \frac{\partial \boldsymbol{A}_{\mathrm{p}}}{\partial \boldsymbol{C}_{\mathrm{p}}}$$

$$- \frac{1}{8}\, \Delta t\, \lambda_{\mathrm{p}} \left[\boldsymbol{G}^{\natural} \,\overline{\otimes}\, \boldsymbol{A} + \boldsymbol{A} \,\underline{\otimes}\, \boldsymbol{G}^{\natural} \right] c_{\boldsymbol{W}}$$

$$: \left[\left[\boldsymbol{G}^{\natural} \,\overline{\otimes}\, \left[\boldsymbol{C}_{\mathrm{p}} \cdot \boldsymbol{A} \cdot \boldsymbol{C} \right] \right] : \left[\boldsymbol{C}_{\mathrm{p}}^{-1} \,\overline{\otimes}\, \boldsymbol{C}_{\mathrm{p}}^{-1} + \boldsymbol{C}_{\mathrm{p}}^{-1} \,\underline{\otimes}\, \boldsymbol{C}_{\mathrm{p}}^{-1} \right] \boldsymbol{A} : \boldsymbol{C} \right.$$

$$\left. - \left[\left[\boldsymbol{C}_{\mathrm{p}}^{-1} \cdot \boldsymbol{C} \cdot \boldsymbol{A} \right] \,\overline{\otimes}\, \boldsymbol{G}^{\natural\star} + \left[\boldsymbol{C}_{\mathrm{p}}^{-1} \cdot \boldsymbol{C} \cdot \boldsymbol{A} \right] \,\underline{\otimes}\, \boldsymbol{G}^{\natural\star} \right] \boldsymbol{A} : \boldsymbol{C} \right] \tag{4.108}$$

$$\frac{\partial \boldsymbol{R}_{A}}{\partial \boldsymbol{A}} = -\frac{1}{2} \left[\boldsymbol{G}^{\natural} \,\overline{\otimes}\, \boldsymbol{G}^{\natural} + \boldsymbol{G}^{\natural} \,\underline{\otimes}\, \boldsymbol{G}^{\natural} \right]$$

$$- \frac{1}{4}\, \Delta t\, \lambda_{\mathrm{p}} \left[\boldsymbol{\Lambda}_{\mathrm{p}} \,\overline{\otimes}\, \boldsymbol{G}^{\natural} + \boldsymbol{\Lambda}_{\mathrm{p}} \,\underline{\otimes}\, \boldsymbol{G}^{\natural} \right] - \frac{1}{4}\, \Delta t\, \lambda_{\mathrm{p}} \left[\boldsymbol{G}^{\natural} \,\overline{\otimes}\, \boldsymbol{\Lambda}_{\mathrm{p}} + \boldsymbol{G}^{\natural} \,\underline{\otimes}\, \boldsymbol{\Lambda}_{\mathrm{p}} \right]$$

$$- \frac{1}{4}\, \Delta t\, \lambda_{\mathrm{p}} \left[\boldsymbol{\Omega} \,\overline{\otimes}\, \boldsymbol{G}^{\natural} + \boldsymbol{\Omega} \,\underline{\otimes}\, \boldsymbol{G}^{\natural} \right] - \frac{1}{4}\, \Delta t\, \lambda_{\mathrm{p}} \left[\boldsymbol{G}^{\natural} \,\overline{\otimes}\, \boldsymbol{\Omega} + \boldsymbol{G}^{\natural} \,\underline{\otimes}\, \boldsymbol{\Omega} \right]$$

$$- \frac{1}{2}\, \Delta t\, \lambda_{\mathrm{p}} \left[\boldsymbol{G}^{\natural} \,\overline{\otimes}\, \boldsymbol{A} + \boldsymbol{A} \,\underline{\otimes}\, \boldsymbol{G}^{\natural} \right] : \frac{\partial \boldsymbol{\Lambda}_{\mathrm{p}}}{\partial \boldsymbol{A}} \tag{4.109}$$

$$- \frac{1}{8}\, \Delta t\, \lambda_{\mathrm{p}} \left[\boldsymbol{G}^{\natural} \,\overline{\otimes}\, \boldsymbol{A} + \boldsymbol{A} \,\underline{\otimes}\, \boldsymbol{G}^{\natural} \right] c_{\boldsymbol{W}} \left[\boldsymbol{A} : \boldsymbol{C} \right]$$

$$: \left[\boldsymbol{G}^{\natural} \,\overline{\otimes}\, \boldsymbol{C} + \boldsymbol{G}^{\natural} \,\underline{\otimes}\, \boldsymbol{C} - \left[\boldsymbol{C}_{\mathrm{p}}^{-1} \cdot \boldsymbol{C} \right] \,\overline{\otimes}\, \boldsymbol{C}_{\mathrm{p}} - \left[\boldsymbol{C}_{\mathrm{p}}^{-1} \cdot \boldsymbol{C} \right] \,\underline{\otimes}\, \boldsymbol{C}_{\mathrm{p}} \right]$$

$$- \frac{1}{4}\, \Delta t\, \lambda_{\mathrm{p}} \left[\boldsymbol{G}^{\natural} \,\overline{\otimes}\, \boldsymbol{A} + \boldsymbol{A} \,\underline{\otimes}\, \boldsymbol{G}^{\natural} \right] : c_{\boldsymbol{W}} \left[\boldsymbol{A} \cdot \boldsymbol{C} - \boldsymbol{C}_{\mathrm{p}}^{-1} \cdot \boldsymbol{C} \cdot \boldsymbol{A} \cdot \boldsymbol{C}_{\mathrm{p}} \right] \otimes \boldsymbol{C}$$

$$\frac{\partial \boldsymbol{R}_{A}}{\partial \kappa} = \boldsymbol{0} \tag{4.110}$$

$$\frac{\partial \boldsymbol{R_A}}{\partial \lambda_{\mathrm{p}}} = \quad \left[-\boldsymbol{\Lambda}_{\mathrm{p}} \cdot \boldsymbol{A} - \boldsymbol{A} \cdot \boldsymbol{\Lambda}_{\mathrm{p}}^{\star}\right] \frac{1}{2} \Delta t + \quad \left[-\boldsymbol{\Omega} \cdot \boldsymbol{A} - \boldsymbol{A} \cdot \boldsymbol{\Omega}^{\star}\right] \frac{1}{2} \Delta t$$
$$+ \left[-\boldsymbol{\Lambda}_{\mathrm{p}}{}^{n} \cdot \boldsymbol{A}^{n} - \boldsymbol{A}^{n} \cdot \boldsymbol{\Lambda}_{\mathrm{p}}^{\star n}\right] \frac{1}{2} \Delta t + \left[-\boldsymbol{\Omega}^{n} \cdot \boldsymbol{A}^{n} - \boldsymbol{A}^{n} \cdot \boldsymbol{\Omega}^{\star n}\right] \frac{1}{2} \Delta t \tag{4.111}$$

Furthermore, the sensitivities of the scalar valued evolution equation which characterises the evolution of κ can be specified as

$$\frac{\partial R_{\kappa}}{\partial \boldsymbol{C}_{\mathrm{p}}} = \boldsymbol{0} \ (4.112) \qquad \frac{\partial R_{\kappa}}{\partial \boldsymbol{A}} = \boldsymbol{0} \ (4.113) \quad \frac{\partial R_{\kappa}}{\partial \kappa} = -1 \ (4.114) \quad \frac{\partial R_{\kappa}}{\partial \lambda_{\mathrm{p}}} = \Delta t \ (4.115)$$

and those of the yield function are given by

$$\frac{\partial R_f}{\partial \boldsymbol{C}_{\mathrm{p}}} = - \frac{1}{2} \boldsymbol{\Lambda}_{\mathrm{p}} : \left[\mu \boldsymbol{C} \cdot \left[\boldsymbol{C}_{\mathrm{p}}^{-1} \overline{\otimes} \boldsymbol{C}_{\mathrm{p}}^{-1} + \boldsymbol{C}_{\mathrm{p}}^{-1} \underline{\otimes} \boldsymbol{C}_{\mathrm{p}}^{-1}\right] + \lambda \boldsymbol{G}^{\natural\star} \otimes \boldsymbol{C}_{\mathrm{p}}^{-1}\right]$$
$$+ 2\, a_2 \operatorname{tr}\left(\boldsymbol{M}_{\mathrm{dev}} \cdot \boldsymbol{A}_{\mathrm{p}}\right) \ \frac{\partial \operatorname{tr}\left(\boldsymbol{M}_{\mathrm{dev}} \cdot \boldsymbol{A}_{\mathrm{p}}\right)}{\partial \boldsymbol{A}_{\mathrm{p}}} : \frac{\partial \boldsymbol{A}_{\mathrm{p}}}{\partial \boldsymbol{C}_{\mathrm{p}}}$$
$$+ 2\, a_3 \operatorname{tr}\left(\boldsymbol{M}_{\mathrm{dev}} \cdot \boldsymbol{A}_{\mathrm{p}}^{2}\right) \ \frac{\partial \operatorname{tr}\left(\boldsymbol{M}_{\mathrm{dev}} \cdot \boldsymbol{A}_{\mathrm{p}}^{2}\right)}{\partial \boldsymbol{A}_{\mathrm{p}}} : \frac{\partial \boldsymbol{A}_{\mathrm{p}}}{\partial \boldsymbol{C}_{\mathrm{p}}}$$
$$+ \quad a_4 \left[\operatorname{tr}\left(\boldsymbol{M}_{\mathrm{dev}} \cdot \boldsymbol{A}_{\mathrm{p}}^{2}\right) \frac{\partial \operatorname{tr}\left(\boldsymbol{M}_{\mathrm{dev}} \cdot \boldsymbol{A}_{\mathrm{p}}\right)}{\partial \boldsymbol{A}_{\mathrm{p}}} : \frac{\partial \boldsymbol{A}_{\mathrm{p}}}{\partial \boldsymbol{C}_{\mathrm{p}}}\right.$$
$$\left. + \operatorname{tr}\left(\boldsymbol{M}_{\mathrm{dev}} \cdot \boldsymbol{A}_{\mathrm{p}}\right) \frac{\partial \operatorname{tr}\left(\boldsymbol{M}_{\mathrm{dev}} \cdot \boldsymbol{A}_{\mathrm{p}}^{2}\right)}{\partial \boldsymbol{A}_{\mathrm{p}}} : \frac{\partial \boldsymbol{A}_{\mathrm{p}}}{\partial \boldsymbol{C}_{\mathrm{p}}}\right] \tag{4.116}$$
$$+ \quad a_5 \frac{\partial \operatorname{tr}\left(\boldsymbol{M}_{\mathrm{dev}}^{2} \cdot \boldsymbol{A}_{\mathrm{p}}\right)}{\partial \boldsymbol{A}_{\mathrm{p}}} : \frac{\partial \boldsymbol{A}_{\mathrm{p}}}{\partial \boldsymbol{C}_{\mathrm{p}}} + \quad a_6 \frac{\partial \operatorname{tr}\left(\boldsymbol{M}_{\mathrm{dev}}^{2} \cdot \boldsymbol{A}_{\mathrm{p}}^{2}\right)}{\partial \boldsymbol{A}_{\mathrm{p}}} : \frac{\partial \boldsymbol{A}_{\mathrm{p}}}{\partial \boldsymbol{C}_{\mathrm{p}}}$$

$$\frac{\partial R_f}{\partial \boldsymbol{A}} = \quad 2\, a_2 \quad \operatorname{tr}\left(\boldsymbol{M}_{\mathrm{dev}} \cdot \boldsymbol{A}_{\mathrm{p}}\right) \frac{\partial \operatorname{tr}\left(\boldsymbol{M}_{\mathrm{dev}} \cdot \boldsymbol{A}_{\mathrm{p}}\right)}{\partial \boldsymbol{A}} + 2\, a_3 \operatorname{tr}\left(\boldsymbol{M}_{\mathrm{dev}} \cdot \boldsymbol{A}_{\mathrm{p}}^{2}\right) \frac{\partial \operatorname{tr}\left(\boldsymbol{M}_{\mathrm{dev}} \cdot \boldsymbol{A}_{\mathrm{p}}^{2}\right)}{\partial \boldsymbol{A}}$$
$$+ \quad a_4 \left[\operatorname{tr}\left(\boldsymbol{M}_{\mathrm{dev}} \cdot \boldsymbol{A}_{\mathrm{p}}^{2}\right) \frac{\partial \operatorname{tr}\left(\boldsymbol{M}_{\mathrm{dev}} \cdot \boldsymbol{A}_{\mathrm{p}}\right)}{\partial \boldsymbol{A}} + \quad \operatorname{tr}\left(\boldsymbol{M}_{\mathrm{dev}} \cdot \boldsymbol{A}_{\mathrm{p}}\right) \frac{\partial \operatorname{tr}\left(\boldsymbol{M}_{\mathrm{dev}} \cdot \boldsymbol{A}_{\mathrm{p}}^{2}\right)}{\partial \boldsymbol{A}}\right]$$
$$+ \quad a_5 \frac{\partial \operatorname{tr}\left(\boldsymbol{M}_{\mathrm{dev}}^{2} \cdot \boldsymbol{A}_{\mathrm{p}}\right)}{\partial \boldsymbol{A}} + \quad a_6 \frac{\partial \operatorname{tr}\left(\boldsymbol{M}_{\mathrm{dev}}^{2} \cdot \boldsymbol{A}_{\mathrm{p}}^{2}\right)}{\partial \boldsymbol{A}} \tag{4.117}$$

$$\frac{\partial R_f}{\partial \kappa} = -\frac{R_{\mathrm{inf}}}{\varepsilon_0} \exp\left(-\frac{\kappa}{\varepsilon_0}\right) \qquad (4.118) \qquad \frac{\partial R_f}{\partial \lambda_{\mathrm{p}}} = 0 \qquad (4.119)$$

217

Finally, the (partial) derivatives of the residual terms with respect to the deformation gradient need to be specified to evaluate (4.79). For the sake of brevity, the frequently occurring derivatives

$$
\frac{\partial \boldsymbol{\Lambda}_{\mathrm{p}}}{\partial \boldsymbol{F}} = \frac{\partial^2 f}{\partial \boldsymbol{M} \partial \boldsymbol{M}} : \left[\left[\boldsymbol{G}^{\natural\star} \,\overline{\otimes}\, \boldsymbol{S} \right] : \left[\boldsymbol{G}^{\natural\star} \,\underline{\otimes}\, \left[\boldsymbol{F}^{\star} \cdot \boldsymbol{g}^{\flat} \right] + \left[\boldsymbol{F}^{\star} \cdot \boldsymbol{g}^{\flat} \right] \,\overline{\otimes}\, \boldsymbol{G}^{\natural\star} \right] + \boldsymbol{C} \cdot \frac{\partial \boldsymbol{S}}{\partial \boldsymbol{F}} \right]
$$

(4.120)

and

$$
\begin{aligned}
\frac{\partial \boldsymbol{\Omega}}{\partial \boldsymbol{F}} =& \frac{1}{2} c_{\boldsymbol{W}} \left[\boldsymbol{A} \,\overline{\otimes}\, \boldsymbol{G}^{\natural\star} - \boldsymbol{C}_{\mathrm{p}}^{-1} \,\overline{\otimes}\, [\boldsymbol{C}_{\mathrm{p}} \cdot \boldsymbol{A}] \right] : \left[\boldsymbol{G}^{\natural\star} \,\underline{\otimes}\, \left[\boldsymbol{F}^{\star} \cdot \boldsymbol{g}^{\flat} \right] + \left[\boldsymbol{F}^{\star} \cdot \boldsymbol{g}^{\flat} \right] \,\overline{\otimes}\, \boldsymbol{G}^{\natural\star} \right] \boldsymbol{A} : \boldsymbol{C}_{\mathrm{p}} \\
&+ \frac{1}{2} c_{\boldsymbol{W}} \left[\boldsymbol{A} \cdot \boldsymbol{C} - \boldsymbol{C}_{\mathrm{p}}^{-1} \cdot \boldsymbol{C} \cdot \boldsymbol{A} \cdot \boldsymbol{C}_{\mathrm{p}} \right] \otimes \boldsymbol{A} : \left[\boldsymbol{G}^{\natural\star} \,\underline{\otimes}\, \left[\boldsymbol{F}^{\star} \cdot \boldsymbol{g}^{\flat} \right] + \left[\boldsymbol{F}^{\star} \cdot \boldsymbol{g}^{\flat} \right] \,\overline{\otimes}\, \boldsymbol{G}^{\natural\star} \right]
\end{aligned}
$$

(4.121)

are not inserted into the derivatives

$$
\frac{\partial \boldsymbol{R}_{\boldsymbol{C}_{\mathrm{p}}}}{\partial \boldsymbol{F}} = \Delta t \, \lambda_{\mathrm{p}} \left[\boldsymbol{G}^{\natural\star} \,\overline{\otimes}\, \boldsymbol{G}^{\natural\star} + \boldsymbol{G}^{\natural\star} \,\underline{\otimes}\, \boldsymbol{G}^{\natural\star} \right] : \left[\boldsymbol{C}_{\mathrm{p}} \cdot \frac{\partial \boldsymbol{\Lambda}_{\mathrm{p}}}{\partial \boldsymbol{F}} \right]
$$

(4.122)

$$
\frac{\partial \boldsymbol{R}_{\boldsymbol{A}}}{\partial \boldsymbol{F}} = -\Delta t \, \lambda_{\mathrm{p}} \left[\boldsymbol{G}^{\natural} \,\overline{\otimes}\, \boldsymbol{A} + \boldsymbol{A} \,\underline{\otimes}\, \boldsymbol{G}^{\natural} \right] : \left[\frac{\partial \boldsymbol{\Lambda}_{\mathrm{p}}}{\partial \boldsymbol{F}} + \frac{\partial \boldsymbol{\Omega}}{\partial \boldsymbol{F}} \right]
$$

(4.123)

$$
\frac{\partial R_{\kappa}}{\partial \boldsymbol{F}} = \boldsymbol{0}
$$

(4.124)

$$
\frac{\partial R_f}{\partial \boldsymbol{F}} = \boldsymbol{\Lambda}_{\mathrm{p}} : \left[\left[\boldsymbol{G}^{\natural\star} \,\overline{\otimes}\, \boldsymbol{S} \right] : \left[\boldsymbol{G}^{\natural\star} \,\underline{\otimes}\, \left[\boldsymbol{F}^{\star} \cdot \boldsymbol{g}^{\flat} \right] + \left[\boldsymbol{F}^{\star} \cdot \boldsymbol{g}^{\flat} \right] \,\overline{\otimes}\, \boldsymbol{G}^{\natural\star} \right] + \boldsymbol{C} \cdot \frac{\partial \boldsymbol{S}}{\partial \boldsymbol{F}} \right]
$$

(4.125)

C.3 Analysis of the elastic deformation

In this appendix we will briefly present the evolution of the tensor $\boldsymbol{c}_{\mathrm{e}}$ and show that, as expected in metal plasticity, $\boldsymbol{c}_{\mathrm{e}}$ remains close to the identity. To this end we will focus on the quantities

$$
\Delta c_{\mathrm{e}\nabla\triangle} = \max_{e \in e_{\mathrm{g}}} \left| \boldsymbol{e}_{\nabla} \cdot \left[{}^{e}\boldsymbol{c}_{\mathrm{e}} - \boldsymbol{g}^{\flat} \right] \cdot \boldsymbol{e}_{\triangle} \right| \quad ,
$$

(4.126)

with the volumetric average of $\boldsymbol{c}_{\mathrm{e}}$, see (4.75), for the specific element denoted as ${}^{e}\boldsymbol{c}_{\mathrm{e}}$ and the maximum operation being carried out with respect to all elements e_{g} of the gauge section. In what follows, we will take into account the projections of ${}^{e}\boldsymbol{c}_{\mathrm{e}} - \boldsymbol{g}^{\flat}$ into the loading direction $\boldsymbol{e}_{\mathrm{L}}$, the transverse direction $\boldsymbol{e}_{\mathrm{T}}$ and the normal direction $\boldsymbol{e}_{\mathrm{N}}$, see Figure 4.2 for the definition of the respective base vectors. With these definitions at hand, the evolution of $\boldsymbol{c}_{\mathrm{e}}$ is provided in Figure 4.21 for the two-dimensional simulations presented in Section 4.4.2.1 and in Figure 4.22 for the three-dimensional setting presented in Section 4.4.2.2.
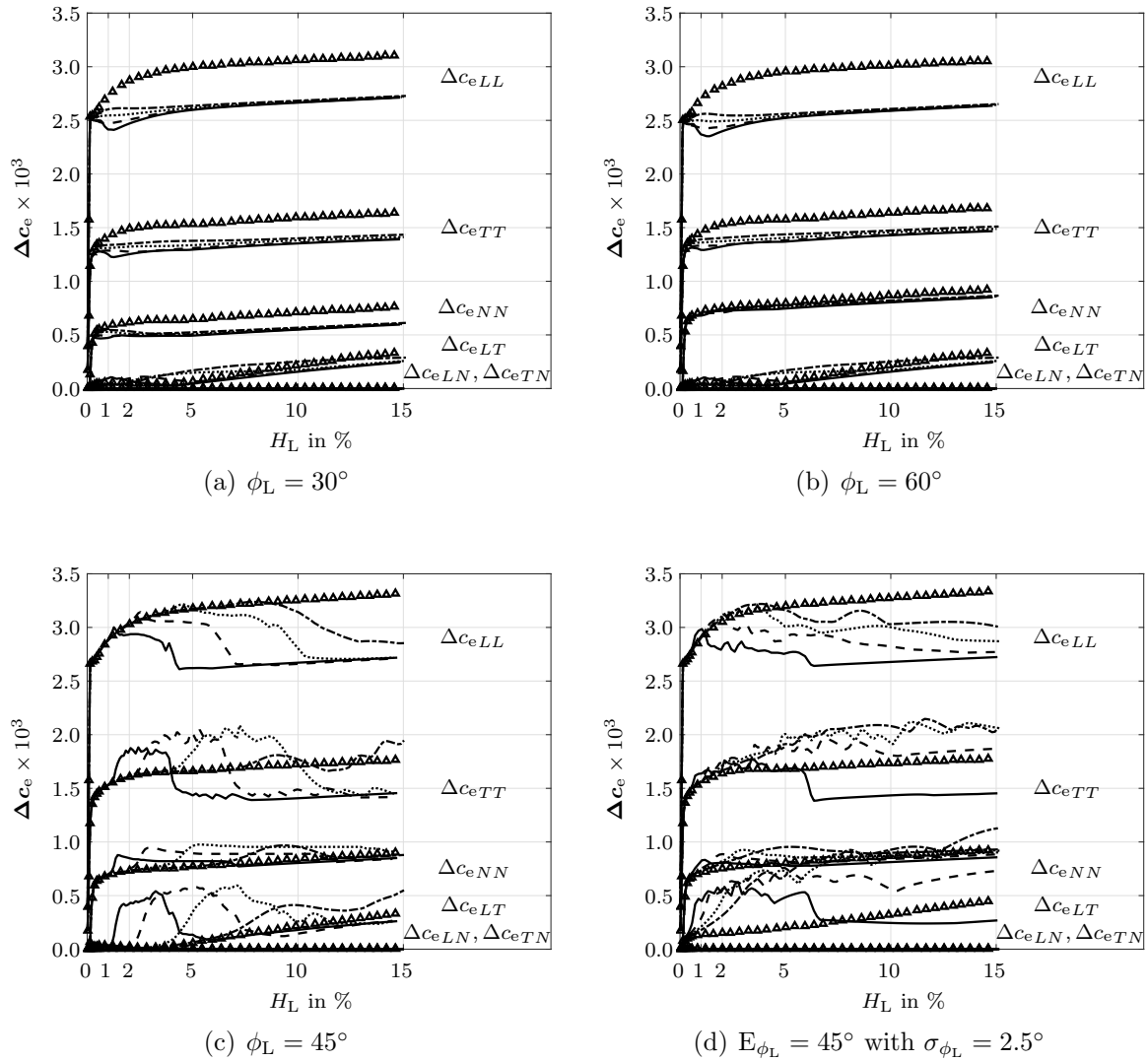
(a) $\phi_{\mathrm{L}} = 30°$

(b) $\phi_{\mathrm{L}} = 60°$

(c) $\phi_{\mathrm{L}} = 45°$

(d) $\mathrm{E}_{\phi_{\mathrm{L}}} = 45°$ with $\sigma_{\phi_{\mathrm{L}}} = 2.5°$

Figure 4.21: Coefficients of $\mathbf{\Delta c}_{\mathrm{e}}$ as a function of the load-state in terms of H_{L} for various values of the angle ϕ_{L} and the (two-dimensional) simulations discussed in Section 4.4.2.1. The different curves represent different values of the material parameter $c_{\boldsymbol{W}}$, specifically speaking: $-0.50\ \mathrm{Pa}^{-1}$, -- $0.25\ \mathrm{Pa}^{-1}$, $\cdots$ $0.15\ \mathrm{Pa}^{-1}$, -· $0.10\mathrm{Pa}^{-1}$, $\triangle$ $0.00\ \mathrm{Pa}^{-1}$.
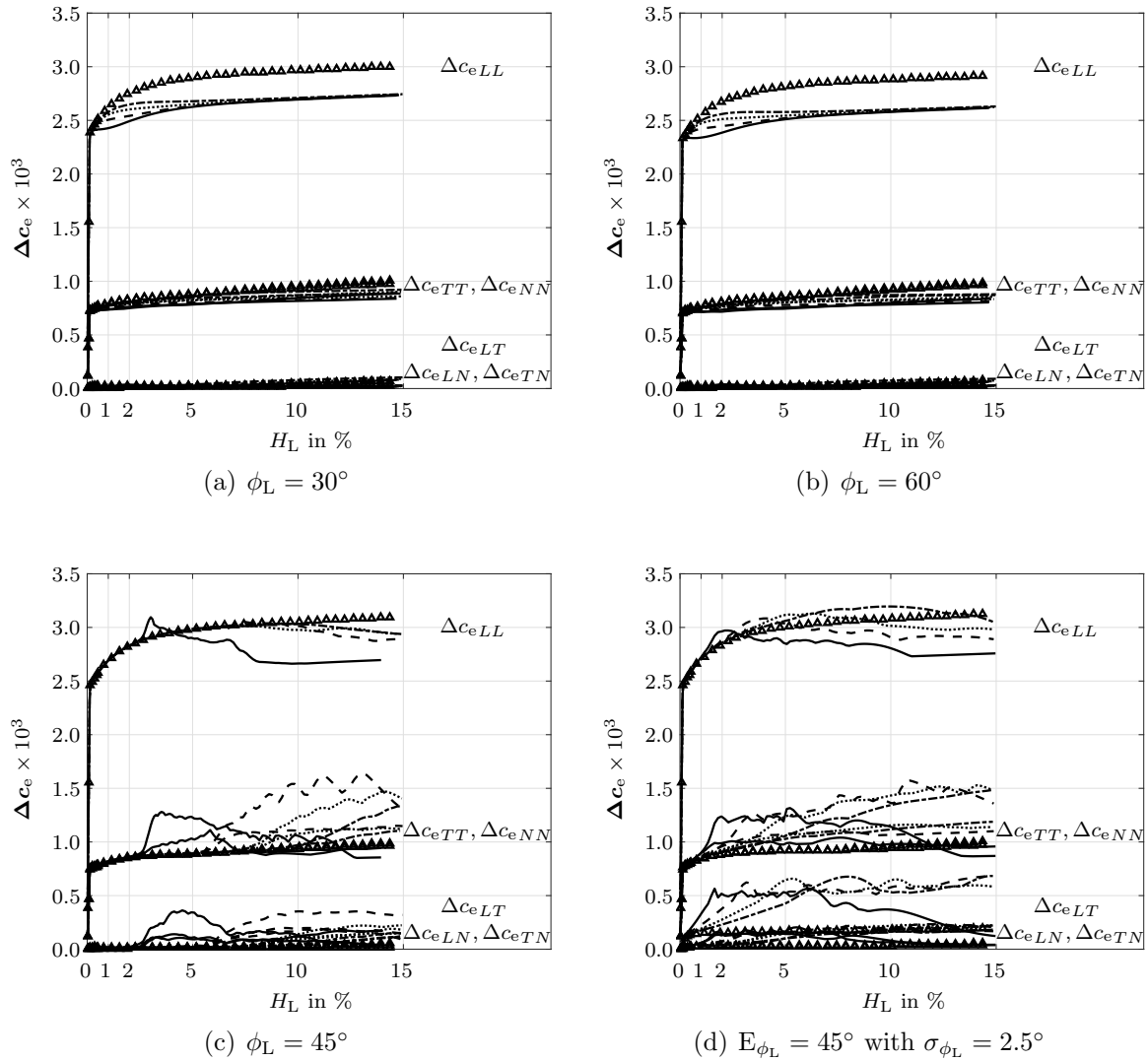
Figure 4.22: Coefficients of $\boldsymbol{\Delta c}_{\mathrm{e}}$ as a function of the load-state in terms of H_{L} for various values of the angle ϕ_{L} and the (three-dimensional) simulations discussed in Section 4.4.2.2. The different curves represent different values of the material parameter $c_{\boldsymbol{W}}$, specifically speaking: -0.50 Pa^{-1}, -- 0.25 Pa^{-1}, $\cdot\cdot$ 0.15 Pa^{-1}, $-\cdot$ 0.10 Pa^{-1}, $\triangle$ 0.00 Pa^{-1}.

5 Concluding remarks

The present work dealt with the modelling and simulation of non-simple and anisotropic materials and was structured into three primary parts covering various aspects of gradient elasticity, gradient plasticity and of anisotropic materials. In particular:

Chapter 2 *(Fibre-reinforced composites with fibre-bending stiffness)* focused on the development of a gradient elasticity-based modelling approach for fibre-reinforced composites which takes into account the possible influence of fibre-bending stiffness in addition to the anisotropic features that are accounted for by the classic structural tensor approach. To this end, the gradient of the spatial fibre direction field was additionally included as an argument of the stored energy function and it was shown that by doing so, higher gradients of the deformation map enter the formulation.

The solution of the underlying system of coupled partial differential equations was addressed by means of a multi-field finite element formulation which was validated in a first step. To this end, the azimuthal shear deformation of a tube-like structure for which an analytical solution is available was analysed in detail, and the finite element-based simulation results were found to compare well with the analytical solution. Having validated the finite element formulation, the focus was eventually on the development of a well-interpretable form of the gradient energy contribution. In particular we showed that a fibre-curvature measure can be extracted from the generalised list of invariants, in which the stored energy function is parametrised. The analysis of the specific proposed form of the stored energy function in terms of the curvature measure was particularly revealing as it could be shown to give rise to physically well-interpretable contributions to the stress and couple stress tensor. Regarding possible areas of application of the proposed formulation, experimental findings on the micro- and nanoscale were taken into consideration which suggest the occurrence of size effects. Accounting for contributions to the stored energy function which depend on higher gradients of the deformation map, the presented formulation intrinsically includes a natural length scale and thus allows, in principle, the capturing of these effects. Motivated by the experimental findings, a detailed analysis of the size dependent response of the presented formulation was finally carried out.

Chapter 3 *(Dislocation density tensor-based gradient plasticity)* addressed physically well-motivated gradient plasticity formulations which include gradients of internal variables that characterise the plastic deformation as additional arguments of the energy function. Being more specific, incompatibilities in the plastic deformations were taken into account which can be interpreted in terms of dislocation density tensors and thus allow for a physical interpretation of the gradient contributions.

The gradient-enhanced form of the energy function, together with an extended form of the Clausius-Duhem inequality gave rise to the balance equation of a generalised stress field (together with its constitutive boundary conditions) which was shown to be energetically conjugated to the plastic deformation. Moreover, the occurrence of a back stress-type tensor in the respective yield function, respectively in the evolution equation for the plastic flow was revealed, which was found to be closely related to the (geometrically necessary) dislocation density. Within the framework of the presented theory, the focus was then first on the development of a specific dislocation density-based gradient plasticity model that represents an extension of classic associated-type plasticity models. The solution of the resulting system of coupled partial differential equations was addressed by means of a multi-field finite element formulation with the plastic consistency conditions being accounted for on a global level by means of Fischer-Burmeister complementarity functions. Various boundary value problems that focused, for example, on the plastic evolution at material interfaces or on the shear band formation that is induced by geometric imperfections were eventually studied to show the applicability of the presented formulation. In a next step, an extension of the formulation to gradient crystal plasticity was pursued. To this end, the balance equation of the generalised stress field was re-interpreted and a different set of primary field variables was chosen in the finite element formulation. This modification allowed us to use the same stabilisation algorithms as in the underlying classic crystal (visco-)plasticity model to approach the rate-independent limit. For a specific model featuring twelve slip systems, the finite plastic deformation of a plate with two-round notches was studied with a different activity of the slip systems in the reference and in the gradient crystal plasticity formulation being revealed. Motivated by experimental findings on copper micro wires, micro torsion tests for wires with different diameters were finally simulated. The observed size effect was found to be in good accordance with the experimental findings.

Chapter 4 *(Deformation-induced anisotropy evolution in finite plasticity)* focused on the deformation-induced evolution of material symmetry groups in finite plasticity. Specifically speaking, an invariant-based formulation was pursued and a specific (thermodynamically consistent) evolution equation for the structural tensor that characterised the respective material symmetry group was proposed.

At the outset of the theory it was assumed that the evolution equation for the structural tensor which reflects the anisotropic material properties in the constitutive equations is composed of two parts which were denoted convected- and residual-type evo-

lution. Whereas the convected-type evolution could be shown to link the evolution of the structural tensor to that of the plastic metric, the residual-type evolution allowed the structural tensor to evolve (to a certain extent) independently from the latter and was observed to be closely related to the notion of the plastic spin. After analysing the implications of the evolution equation for the structural tensor on the dissipation inequality in detail, the focus was eventually on the development of a well-interpretable form of the residual-type evolution equation which allowed us to capture the experimentally observed evolution of the plastic anisotropy. For this specific form of the evolution equation, finite element-based simulations of tension tests were carried out and the evolution of the (plastic) material symmetry group was studied in detail. Finally, in-plane torsion tests were simulated in order to analyse the predicted evolution of the material symmetry group in shear-dominated deformation processes.

Bibliography

[1] DIN 50125:2016-12, Prüfung metallischer Werkstoffe – Zugprobe.

[2] A. Acharya and J. Bassani. Lattice incompatibility and a gradient theory of crystal plasticity. *Journal of the Mechanics and Physics of Solids*, 48(8):1565–1595, 2000. doi:10.1016/s0022-5096(99)00075-7.

[3] B. Akgöz and Ö. Civalek. Bending analysis of embedded carbon nanotubes resting on an elastic foundation using strain gradient theory. *Acta Astronautica*, 119:1–12, 2016. doi:10.1016/j.actaastro.2015.10.021.

[4] L. Anand and M. Kothari. A computational procedure for rate-independent crystal plasticity. *Journal of the Mechanics and Physics of Solids*, 44(4):525–558, 1996. doi:10.1016/0022-5096(96)00001-4.

[5] A. Anthoine. Effect of couple-stresses on the elastic bending of beams. *International Journal of Solids and Structures*, 37(7):1003–1018, 2000. doi:10.1016/S0020-7683(98)00283-2.

[6] R. J. Asaro. Crystal plasticity. *Journal of Applied Mechanics*, 50(4b):921–934, 1983. doi:10.1115/1.3167205.

[7] B. Ashrafi, P. Hubert, and S. Vengallatore. Carbon nanotube-reinforced composites as structural materials for microactuators in microelectromechanical systems. *Nanotechnology*, 17(19):4895–4903, 2006. doi:10.1088/0957-4484/17/19/019.

[8] H. Askes and E. C. Aifantis. Gradient elasticity in statics and dynamics: an overview of formulations, length scale identification procedures, finite element implementations and new results. *International Journal of Solids and Structures*, 48 (13):1962–1990, 2011. doi:10.1016/j.ijsolstr.2011.03.006.

[9] T. Asmanoglo. Constitutive Modeling of Evolving Anisotropies in Finite Plasticity. Bachelor's thesis, Institute of Mechanics, TU Dortmund University, Germany, 2014.

[10] T. Asmanoglo. Fibre-Reinforced Composites – Finite Deformation Higher-Gradient Theory and Mixed Finite Element Formulation. Master's thesis, Institute of Mechanics, TU Dortmund University, Germany, 2015.

[11] T. Asmanoglo and A. Menzel. A finite deformation continuum modelling framework for curvature effects in fibre-reinforced nanocomposites. *Journal of the Mechanics and Physics of Solids*, 107:411–432, 2017. doi:10.1016/j.jmps.2017.06.012.

[12] T. Asmanoglo and A. Menzel. Fibre-reinforced composites with fibre-bending stiffness under azimuthal shear – Comparison of simulation results with analytical solutions. *International Journal of Non-Linear Mechanics*, 91:128–139, 2017. doi:10.1016/j.ijnonlinmec.2017.01.001.

[13] T. Asmanoglo and A. Menzel. A multi-field finite element approach for the modelling of fibre-reinforced composites with fibre-bending stiffness. *Computer Methods in Applied Mechanics and Engineering*, 317:1037–1067, 2017. doi:10.1016/j.cma.2017.01.003.

[14] M. Aydogdu. Axial vibration analysis of nanorods (carbon nanotubes) embedded in an elastic medium using nonlocal elasticity. *Mechanics Research Communications*, 43:34–40, 2012. doi:10.1016/j.mechrescom.2012.02.001.

[15] C. E. Bakis, L. C. Bank, V. L. Brown, E. Cosenza, J. F. Davalos, J. J. Lesko, A. Machida, S. H. Rizkalla, and T. C. Triantafillou. Fiber-reinforced polymer composites for construction – State-of-the-art review. *Journal of Composites for Construction*, 6(2):73–87, 2002. doi:10.1061/(asce)1090-0268(2002)6:2(73).

[16] D. Balzani, P. Neff, J. Schröder, and G. A. Holzapfel. A polyconvex framework for soft biological tissues. Adjustment to experimental data. *International Journal of Solids and Structures*, 43(20):6052–6070, 2006. doi:10.1016/j.ijsolstr.2005.07.048.

[17] T. Bartel and K. Hackl. Multiscale modeling of martensitic phase transformations: On the numerical determination of heterogeneous mesostructures within shape-memory alloys induced by precipitates. *Technische Mechanik*, 30(4):324–342, 2010.

[18] A. Bertram and S. Forest. The thermodynamics of gradient elastoplasticity. *Continuum Mechanics and Thermodynamics*, 26(3):269–286, 2014. doi:10.1007/s00161-013-0300-2.

[19] B. A. Bilby, R. Bullough, and E. Smith. Continuous distributions of dislocations: A new application of the methods of non-Riemannian geometry. *Proceedings of the Royal Society of London. Series A, Mathematical and Physical Sciences*, 231 (1185):263–273, 1955. doi:10.1098/rspa.1955.0171.

[20] J.-P. Boehler. A simple derivation of representations for non-polynomial constitutive equations in some cases of anisotropy. *ZAMM-Journal of Applied Mathematics and Mechanics/Zeitschrift für Angewandte Mathematik und Mechanik*, 59(4):157–167, 1979. doi:10.1002/zamm.19790590403.

[21] R. I. Borja and J. R. Wren. Discrete micromechanics of elastoplastic crystals. *International Journal for Numerical Methods in Engineering*, 36(22):3815–3840, 1993. doi:10.1002/nme.1620362205.

[22] K. Carlsson, K. Runesson, F. Larsson, and M. Ekh. A comparison of the primal and semi-dual variational formats of gradient-extended crystal inelasticity. *Computational Mechanics*, 60(4):531–548, 2017. doi:10.1007/s00466-017-1419-y.

[23] C. Q. Chen, Y. Shi, Y. S. Zhang, J. Zhu, and Y. J. Yan. Size dependence of Young's modulus in ZnO nanowires. *Physical review letters*, 96(7):075505, 2006. doi:10.1103/PhysRevLett.96.075505.

[24] Y. Chen, B. L. Dorgan Jr., D. N. McIlroy, and D. E. Aston. On the importance of boundary conditions on nanomechanical bending behavior and elastic modulus determination of silver nanowires. *Journal of Applied Physics*, 100(10):104301, 2006. doi:10.1063/1.2382265.

[25] H. Y. Cheung, M. P. Ho, K. T. Lau, F. Cardona, and D. Hui. Natural fibre-reinforced composites for bioengineering and environmental engineering applications. *Composites Part B: Engineering*, 40(7):655–663, 2009. doi:10.1016/j.compositesb.2009.04.014.

[26] S. Cuenot, C. Frétigny, S. Demoustier-Champagne, and B. Nysten. Surface tension effect on the mechanical properties of nanomaterials measured by atomic force microscopy. *Physical Review B*, 69:165410, 2004. doi:10.1103/PhysRevB.69.165410.

[27] A. M. Cuitino and M. Ortiz. Computational modelling of single crystals. *Modelling and Simulation in Materials Science and Engineering*, 1(3):225–263, 1993. doi:10.1088/0965-0393/1/3/001.

[28] Y. F. Dafalias. The plastic spin in viscoplasticity. *International Journal of Solids and Structures*, 26(2):149–163, 1990. doi:10.1016/0020-7683(90)90048-Z.

[29] Y. F. Dafalias. Plastic spin: necessity or redundancy? *International Journal of Plasticity*, 14(9):909–931, 1998. doi:10.1016/S0749-6419(98)00036-9.

[30] M. A. Dagher and K. P. Soldatos. On small azimuthal shear deformation of fibre-reinforced cylindrical tubes. *Journal of Mechanics of Materials and Structures*, 6 (1):141–168, 2011. doi:10.2140/jomms.2011.6.141.

[31] M. A. Dagher and K. P. Soldatos. Pure azimuthal shear deformation of an incompressible tube reinforced by radial fibres resistant in bending. *IMA Journal of Applied Mathematics*, 79(5):848–868, 2014. doi:10.1093/imamat/hxu013.

[32] R. de Borst, L. Sluys, H. Muhlhaus, and J. Pamin. Fundamental issues in finte element analysis of localization deformation. *Engineering Computations*, 10(2): 99–121, 1993. doi:10.1108/eb023897.

[33] E. A. de Souza Neto, D. Peric, and D. R. J. Owen. *Computational Methods for Plasticity: Theory and Applications*. John Wiley & Sons, Chichester, United Kingdom, 2008. doi:10.1002/9780470694626.

[34] R. Denzer and A. Menzel. Configurational forces for quasi-incompressible large strain electro-viscoelasticity – Application to fracture mechanics. *European Journal of Mechanics - A/Solids*, 48:3–15, 2014. doi:10.1016/j.euromechsol.2014.05.012.

[35] D. G. B. Edelen and N. Laws. On the thermodynamics of systems with nonlocality. *Archive for Rational Mechanics and Analysis*, 43(1):24–35, 1971. doi:10.1007/bf00251543.

[36] M. Ekh, M. Grymer, K. Runesson, and T. Svedberg. Gradient crystal plasticity as part of the computational modelling of polycrystals. *International Journal for Numerical Methods in Engineering*, 72(2):197–220, 2007. doi:10.1002/nme.2015.

[37] A. C. Eringen. On nonlocal plasticity. *International Journal of Engineering Science*, 19(12):1461–1474, 1981. doi:10.1016/0020-7225(81)90072-0.

[38] A. C. Eringen. Theories of nonlocal plasticity. *International Journal of Engineering Science*, 21(7):741–751, 1983. doi:10.1016/0020-7225(83)90058-7.

[39] A. C. Eringen. On differential equations of nonlocal elasticity and solutions of screw dislocation and surface waves. *Journal of Applied Physics*, 54(9):4703–4710, 1983. doi:10.1063/1.332803.

[40] A. C. Eringen. *Nonlocal Continuum Field Theories*. Springer-Verlag, New York, 2002. doi:10.1007/b97697.

[41] A. C. Eringen and H. Liebowitz. Theory of micropolar elsticity. In H. Liebowitz, editor, *Fracture, Volume VII*, pages 621–629. Academic Press, Inc., New York, 1968. doi:10.1007/978-1-4612-0555-5_5.

[42] M. Ettehad and R. K. A. Al-Rub. On the numerical implementation of the higher-order strain gradient-dependent plasticity theory and its non-classical boundary conditions. *Finite Elements in Analysis and Design*, 93:50–69, 2015. doi:10.1016/j.finel.2014.08.005.

[43] L. Evers, D. Parks, W. Brekelmans, and M. Geers. Crystal plasticity model with enhanced hardening by geometrically necessary dislocation accumulation. *Journal of the Mechanics and Physics of Solids*, 50(11):2403–2424, 2002. doi:10.1016/s0022-5096(02)00032-7.

[44] W. Fang, H.-Y. Chu, W.-K. Hsu, T.-W. Cheng, and N.-H. Tai. Polymer-reinforced, aligned multiwalled carbon nanotube composites for microelectromechanical systems applications. *Advanced Materials*, 17(24):2987–2992, 2005. doi:10.1002/adma.200501305.

[45] A. Fischer. A special Newton-type optimization method. *Optimization*, 24(3-4):269–284, 1992. doi:10.1080/02331939208843795.

[46] P. Fischer, M. Klassen, J. Mergheim, P. Steinmann, and R. Müller. Isogeometric analysis of 2D gradient elasticity. *Computational Mechanics*, 47(3):325–334, 2011. doi:10.1007/s00466-010-0543-8.

[47] J. Fish and T. Belytschko. *A First Course in Finite Elements*. John Wiley & Sons, 2007. doi:10.1002/9780470510858.

[48] N. A. Fleck, G. M. Muller, M. F. Ashby, and J. W. Hutchinson. Strain gradient plasticity: Theory and experiment. *Acta Metallurgica et Materialia*, 42(2):475–487, 1994. doi:10.1016/0956-7151(94)90502-9.

[49] F. Frank. Crystal dislocations-Elementary concepts and definitions. *The London, Edinburgh, and Dublin Philosophical Magazine and Journal of Science*, 42(331):809–819, 1951. doi:10.1080/14786445108561310.

[50] N. Graupner, A. S. Herrmann, and J. Müssig. Natural and man-made cellulose fibre-reinforced poly (lactic acid)(PLA) composites: An overview about mechanical characteristics and application areas. *Composites Part A: Applied Science and Manufacturing*, 40(6):810–821, 2009. doi:10.1016/j.compositesa.2009.04.003.

[51] B. Halphen and Q. Son Nguyen. Sur les matériaux standard généralisés. *Journal de Mécanique*, 14:39–63, 1975.

[52] M. Harrysson and M. Ristinmaa. Description of evolving anisotropy at large strains. *Mechanics of Materials*, 39(3):267–282, 2007. doi:10.1016/j.mechmat.2006.05.005.

[53] J. He and C. M. Lilley. Surface effect on the elastic behavior of static bending nanowires. *Nano Letters*, 8(7):1798–1802, 2008. doi:10.1021/nl0733233.

[54] R. Hill and J. Rice. Constitutive analysis of elastic-plastic crystals at arbitrary strain. *Journal of the Mechanics and Physics of Solids*, 20(6):401–413, 1972. doi:10.1016/0022-5096(72)90017-8.

[55] R. Hill. *The Mathematical Theory of Plasticity*. Oxford University Press, 1950.

[56] E. Hinton and J. S. Campbell. Local and global smoothing of discontinuous finite element functions using a least squares method. *International Journal for Numerical Methods in Engineering*, 8(3):461–480, 1974. doi:10.1002/nme.1620080303.

[57] F. Y. Huang, B. H. Yan, J. L. Yan, and D. U. Yang. Bending analysis of micropolar elastic beam using a 3-D finite element method. *International Journal of Engineering Science*, 38(3):275–286, 2000. doi:10.1016/S0020-7225(99)00041-5.

[58] T. J. R. Hughes, J. A. Cottrell, and Y. Bazilevs. Isogeometric analysis: CAD, finite elements, NURBS, exact geometry and mesh refinement. *Computer Methods in Applied Mechanics and Engineering*, 194(39):4135–4195, 2005. doi:10.1016/j.cma.2004.10.008.

[59] G. Y. Jing, H. L. Duan, X. M. Sun, Z. S. Zhang, J. Xu, Y. D. Li, J. X. Wang, and D. P. Yu. Surface effects on elastic properties of silver nanowires: Contact atomic-force microscopy. *Physical Review B*, 73(23):235409, 2006. doi:10.1103/PhysRevB.73.235409.

[60] G. Johansson, A. Menzel, and K. Runesson. Modeling of anisotropic inelasticity in pearlitic steel at large strains due to deformation induced substructure evolution. *European Journal of Mechanics - A/Solids*, 24(6):899–918, 2005.

doi:10.1016/j.euromechsol.2005.06.006.

[61] G. Johansson and M. Ekh. On the modeling of evolving anisotropy and large strains in pearlitic steel. *European Journal of Mechanics - A/Solids*, 25(6):1041–1060, 2006. doi:10.1016/j.euromechsol.2006.02.003.

[62] T. Kaiser and A. Menzel. A dislocation density tensor-based crystal plasticity framework. *Journal of the Mechanics and Physics of Solids*, 131:276–302, 2019. doi:https://doi.org/10.1016/j.jmps.2019.05.019.

[63] T. Kaiser and A. Menzel. An incompatibility tensor-based gradient plasticity formulation – Theory and numerics. *Computer Methods in Applied Mechanics and Engineering*, 345:671–700, 2019. doi:https://doi.org/10.1016/j.cma.2018.11.013.

[64] T. Kaiser, J. Lu, A. Menzel, and P. Papadopoulos. A covariant formulation of finite plasticity with plasticity-induced evolution of anisotropy: Modeling, algorithmics, simulation, and comparison to experiments. *International Journal of Solids and Structures*, 2019. doi:https://doi.org/10.1016/j.ijsolstr.2019.08.005.

[65] K. H. Kim and J. J. Yin. Evolution of anisotropy under plane stress. *Journal of the Mechanics and Physics of Solids*, 45(5):841–851, 1997. doi:10.1016/S0022-5096(96)00085-3.

[66] K. Kondo. On the geometrical and physical foundations of the theory of yielding. In *Proceedings of the Second Japanese National Congress on Applied Mechanics*, pages 41–47, 1952.

[67] A. Krishnan, E. Dujardin, T. W. Ebbesen, P. N. Yianilos, and M. M. J. Treacy. Young's modulus of single-walled nanotubes. *Physical Review B*, 58(20):14013, 1998. doi:10.1103/PhysRevB.58.14013.

[68] E. Kröner. *Kontinuumstheorie der Versetzungen und Eigenspannungen*, volume 5. Springer Verlag, Berlin, Göttingen, Heidelberg, 1958. doi:10.1007/978-3-642-94719-3.

[69] E. Kröner. Allgemeine Kontinuumstheorie der Versetzungen und Eigenspannungen. *Archive for Rational Mechanics and Analysis*, 4(1):273–334, 1959. doi:10.1007/BF00281393.

[70] D. C. C. Lam, F. Yang, A. C. M. Chong, J. Wang, and P. Tong. Experiments and theory in strain gradient elasticity. *Journal of the Mechanics and Physics of Solids*, 51(8):1477–1508, 2003. doi:10.1016/S0022-5096(03)00053-X.

[71] E. H. Lee. Elastic-plastic deformation at finite strains. *Journal of Applied Mechanics*, 36(1):1–6, 1969. doi:10.1115/1.3564580.

[72] J. Lee, D. Bhattacharyya, M. Q. Zhang, and Y. C. Yuan. Mechanical properties of a self-healing fibre reinforced epoxy composites. *Composites Part B: Engineering*, 78:515–519, 2015. doi:10.1016/j.compositesb.2015.04.014.

[73] T. Liebe, P. Steinmann, and A. Benallal. Theoretical and computational aspects of a thermodynamically consistent framework for geometrically linear gradient damage. *Computer Methods in Applied Mechanics and Engineering*, 190(49):6555–6576, 2001. doi:10.1016/s0045-7825(01)00250-x.

[74] T. Liebe and P. Steinmann. Theory and numerics of a thermodynamically consistent framework for geometrically linear gradient plasticity. *International Journal for Numerical Methods in Engineering*, 51(12):1437–1467, 2001. doi:10.1002/nme.195.

[75] T. Liebe, A. Menzel, and P. Steinmann. Theory and numerics of geometrically non-linear gradient plasticity. *International Journal of Engineering Science*, 41 (13):1603–1629, 2003. doi:10.1016/s0020-7225(03)00030-2.

[76] J. Lu and P. Papadopoulos. A covariant constitutive description of anisotropic non-linear elasticity. *Zeitschrift für angewandte Mathematik und Physik ZAMP*, 51(2):204–217, 2000. doi:10.1007/s000330050195.

[77] J. Lu and P. Papadopoulos. A covariant formulation of anisotropic finite plasticity: Theoretical developments. *Computer Methods in Applied Mechanics and Engineering*, 193(48-51):5339–5358, 2004. doi:10.1016/j.cma.2004.01.040.

[78] J. Lu. A covariant condition and related constitutive results in finite plasticity. *Journal of Applied Mathematics and Physics*, 57:313–323, 2006. doi:10.1007/s00033-005-0010-0.

[79] P. Lu, H. P. Lee, C. Lu, and P. Q. Zhang. Application of nonlocal beam models for carbon nanotubes. *International Journal of Solids and Structures*, 44(16):5289–5300, 2007. doi:10.1016/j.ijsolstr.2006.12.034.

[80] V. A. Lubarda. *Elastoplasticity Theory*. CRC Press, Boca Raton, 2001. doi:10.1201/9781420040784.

[81] H. M. Ma, X. L. Gao, and J. N. Reddy. A microstructure-dependent Timoshenko beam model based on a modified couple stress theory. *Journal of the Mechanics and Physics of Solids*, 56(12):3379–3391, 2008. doi:10.1016/j.jmps.2008.09.007.

[82] Z. Marciniak. Influence of the sign change of the load on the strain hardening curve of a copper test subject to torsion. *Archiwum Mechaniki Stosowanej*, 13: 743–751, 1961.

[83] J. E. Marsden and T. J. Hughes. *Mathematical Foundations of Elasticity*. Dover Publications, Inc., New York, 1994.

[84] G. Maugin. Internal variables and dissipative structures. *Journal of Non-Equilibrium Thermodynamics*, 15:173–192, 1990. doi:10.1515/jnet.1990.15.2.173.

[85] G. Maugin and W. Muschik. Thermodynamics with internal variables. Part I. general concepts. *Journal of Non-Equilibrium Thermodynamics*, 19:217–249, 1994. doi:10.1515/jnet.1994.19.3.217.

[86] M. Mazière and S. Forest. Strain gradient plasticity modeling and finite element simulation of Lüders band formation and propagation. *Continuum Mechanics and Thermodynamics*, 27(1):83–104, 2015. doi:10.1007/s00161-013-0331-8.

[87] A. Menzel and P. Steinmann. On the continuum formulation of higher gradient plasticity for single and polycrystals. *Journal of the Mechanics and Physics of Solids*, 48(8):1777–1796, 2000. doi:10.1016/s0022-5096(99)00024-1.

[88] A. Menzel and P. Steinmann. On the spatial formulation of anisotropic multiplicative elasto-plasticity. *Computer Methods in Applied Mechanics and Engineering*, 192(31-32):3431–3470, 2003. doi:10.1016/S0045-7825(03)00353-0.

[89] A. Menzel and P. Steinmann. A view on anisotropic finite hyper-elasticity. *European Journal of Mechanics-A/Solids*, 22(1):71–87, 2003. doi:10.1016/S0997-7538(02)01253-6.

[90] A. Menzel and P. Steinmann. On configurational forces in multiplicative elasto-plasticity. *International Journal of Solids and Structures*, 44(13):4442–4471, 2007. doi:10.1016/j.ijsolstr.2006.11.032.

[91] A. Menzel, R. Denzer, and P. Steinmann. On the comparison of two approaches to compute material forces for inelastic materials. Application to single-slip crystal-plasticity. *Computer Methods in Applied Mechanics and Engineering*, 193(48): 5411–5428, 2004. doi:10.1016/j.cma.2003.12.070.

[92] A. Menzel and P. Steinmann. On the comparison of two strategies to formulate orthotropic hyperelasticity. *Journal of Elasticity*, 62(3):171–201, 2001. doi:10.1023/A:1012937501411.

[93] C. Miehe and J. Schröder. A comparative study of stress update algorithms for rate-independent and rate-dependent crystal plasticity. *International Journal for Numerical Methods in Engineering*, 50(2):273–298, 2001. doi:10.1002/1097-0207(20010120)50:2<273::aid-nme17>3.0.co;2-q.

[94] R. D. Mindlin and H. F. Tiersten. Effects of couple-stresses in linear elasticity. *Archive for Rational Mechanics and Analysis*, 11(1):415–448, 1962. doi:10.1007/BF00253946.

[95] A. P. Mouritz, M. K. Bannister, P. J. Falzon, and K. H. Leong. Review of applications for advanced three-dimensional fibre textile composites. *Composites Part A: Applied Science and Manufacturing*, 30(12):1445–1461, 1999. doi:10.1016/S1359-835X(99)00034-2.

[96] S. G. Nilsson, X. Borrisé, and L. Montelius. Size effect on Young's modulus of thin chromium cantilevers. *Applied Physics Letters*, 85(16):3555–3557, 2004. doi:10.1063/1.1807945.

[97] W. Noll. A mathematical theory of the mechanical behavior of continuous media. *Archive for Rational Mechanics and Analysis*, 2(1):197–226, 1958. doi:10.1007/978-

3-642-85992-2_3.

[98] W. Noll. A new mathematical theory of simple materials. *Archive for Rational Mechanics and Analysis*, 48(1):1–50, 1972. doi:10.1007/BF00253367.

[99] J. Nye. Some geometrical relations in dislocated crystals. *Acta Metallurgica*, 1(2): 153–162, 1953. doi:10.1016/0001-6160(53)90054-6.

[100] J. Pamin, H. Askes, and R. de Borst. Two gradient plasticity theories discretized with the element-free Galerkin method. *Computer Methods in Applied Mechanics and Engineering*, 192(20):2377–2403, 2003. doi:10.1016/s0045-7825(03)00263-9.

[101] P. Papadopoulos and J. Lu. On the formulation and numerical solution of problems in anisotropic finite plasticity. *Computer Methods in Applied Mechanics and Engineering*, 190(37):4889–4910, 2001. doi:10.1016/S0045-7825(00)00355-8.

[102] S. A. Papanicolopulos, A. Zervos, and I. Vardoulakis. A three-dimensional C^1 finite element for gradient elasticity. *International Journal for Numerical Methods in Engineering*, 77(10):1396–1415, 2009. doi:10.1002/nme.2449.

[103] S. K. Park and X. L. Gao. Bernoulli–Euler beam model based on a modified couple stress theory. *Journal of Micromechanics and Microengineering*, 16(11): 2355, 2006. doi:10.1088/0960-1317/16/11/015.

[104] J. Peddieson, G. R. Buchanan, and R. P. McNitt. Application of nonlocal continuum models to nanotechnology. *International Journal of Engineering Science*, 41 (3):305–312, 2003. doi:10.1016/S0020-7225(02)00210-0.

[105] J. Petera and J. F. T. Pittman. Isoparametric hermite elements. *International Journal for Numerical Methods in Engineering*, 37(20):3489–3519, 1994. doi:10.1002/nme.1620372006.

[106] C. Polizzotto and G. Borino. A thermodynamics-based formulation of gradient-dependent plasticity. *European Journal of Mechanics – A/Solids*, 17(5):741–761, 1998. doi:10.1016/s0997-7538(98)80003-x.

[107] P. Poncharal, Z. L. Wang, D. Ugarte, and W. A. de Heer. Electrostatic deflections and electromechanical resonances of carbon nanotubes. *Science*, 283(5407):1513–1516, 1999. doi:10.1126/science.283.5407.1513.

[108] S. Ramezani, R. Naghdabadi, and S. Sohrabpour. Analysis of micropolar elastic beams. *European Journal of Mechanics A/Solids*, 28(2):202–208, 2009. doi:10.1016/j.euromechsol.2008.06.006.

[109] M. Ristinmaa and M. Vecchi. Use of couple-stress theory in elasto-plasticity. *Computer Methods in Applied Mechanics and Engineering*, 136(3):205–224, 1996. doi:10.1016/0045-7825(96)00996-6.

[110] S. Rudraraju, A. Van der Ven, and K. Garikipati. Three-dimensional isogeometric solutions to general boundary value problems of Toupin's gradient elasticity theory at finite strains. *Computer Methods in Applied Mechanics and Engineering*, 278:

705–728, 2014. doi:10.1016/j.cma.2014.06.015.

[111] J. P. Salvetat, J. M. Bonard, N. H. Thomson, A. J. Kulik, L. Forro, W. Benoit, and L. Zuppiroli. Mechanical properties of carbon nanotubes. *Applied Physics A*, 69(3):255–260, 1999. doi:10.1007/s003390050999.

[112] J. P. Salvetat, G. A. D. Briggs, J. M. Bonard, R. R. Bacsa, A. J. Kulik, T. Stöckli, N. A. Burnham, and L. Forró. Elastic and shear moduli of single-walled carbon nanotube ropes. *Physical Review Letters*, 82(5):944–947, 1999. doi:doi.org/10.1103/PhysRevLett.82.944.

[113] J. P. Salvetat, A. J. Kulik, J. M. Bonard, G. A. D. Briggs, T. Stöckli, K. Méténier, S. Bonnamy, F. Béguin, N. A. Burnham, and L. Forró. Elastic modulus of ordered and disordered multiwalled carbon nanotubes. *Advanced Materials*, 11(2):161–165, 1999. doi:10.1002/(SICI)1521-4095(199902)11:2<161::AID-ADMA161>3.0.CO;2-J.

[114] J. Sandler, S. Pegel, M. Cadek, F. Gojny, M. van Es, J. Lohmar, W. Blau, K. Schulte, A. Windle, and M. Shaffer. A comparative study of melt spun polyamide-12 fibres reinforced with carbon nanotubes and nanofibres. *Polymer*, 45(6):2001–2015, 2004. doi:10.1016/j.polymer.2004.01.023.

[115] M. Schmidt-Baldassari. Numerical concepts for rate-independent single crystal plasticity. *Computer Methods in Applied Mechanics and Engineering*, 192(11): 1261–1280, 2003. doi:10.1016/s0045-7825(02)00563-7.

[116] J. Schröder, P. Neff, and D. Balzani. A variational approach for materially stable anisotropic hyperelasticity. *International Journal of Solids and Structures*, 42(15): 4352–4371, 2005. doi:10.1016/j.ijsolstr.2004.11.021.

[117] J. Schröder and P. Neff. Invariant formulation of hyperelastic transverse isotropy based on polyconvex free energy functions. *International Journal of Solids and Structures*, 40(2):401–445, 2003. doi:10.1016/S0020-7683(02)00458-4.

[118] M. J. Sewell. On configuration-dependent loading. *Archive for Rational Mechanics and Analysis*, 23(5):327–351, 1967. doi:10.1007/BF00276777.

[119] L. Shen and J. Li. Transversely isotropic elastic properties of multiwalled carbon nanotubes. *Physical Review B*, 71(3):035412, 2005. doi:10.1103/PhysRevB.71.035412.

[120] J. Y. Shu, W. E. King, and N. A. Fleck. Finite elements for materials with strain gradient effects. *International Journal for Numerical Methods in Engineering*, 44(3):373–391, 1999. doi:10.1002/(SICI)1097-0207(19990130)44:3<373::AID-NME508>3.0.CO;2-7.

[121] J. C. Simo and L. Vu-Quoc. A three-dimensional finite-strain rod model. Part II: computational aspects. *Computer Methods in Applied Mechanics and Engineering*, 58(1):79–116, 1986. doi:10.1016/0045-7825(86)90079-4.

[122] V. I. Smirnov. *A Course of Higher Mathematics: Adiwes International Series in Mathematics*, volume 2. Elsevier, 2014. doi:10.1016/C2013-0-01755-0.

[123] K. P. Soldatos and V. P. Hadjigeorgiou. Three-dimensional solution of the free vibration problem of homogeneous isotropic cylindrical shells and panels. *Journal of Sound and Vibration*, 137(3):369–384, 1990. doi:10.1016/0022-460X(90)90805-A.

[124] K. P. Soldatos. Towards a new generation of 2D mathematical models in the mechanics of thin-walled fibre-reinforced structural components. *International Journal of Engineering Science*, 47(11):1346–1356, 2009. doi:10.1016/j.ijengsci.2008.07.004.

[125] K. P. Soldatos. Second-gradient plane deformations of ideal fibre-reinforced materials: implications of hyper-elasticity theory. *Journal of Engineering Mathematics*, 68(1):99–127, 2010. doi:10.1007/s10665-009-9353-4.

[126] K. P. Soldatos. On loss of ellipticity in second-gradient hyper-elasticity of fibre-reinforced materials. *International Journal of Non-Linear Mechanics*, 47(2):117–127, 2012. doi:10.1016/j.ijnonlinmec.2011.03.012.

[127] Y. S. Song and J. R. Youn. Modeling of effective elastic properties for polymer based carbon nanotube composites. *Polymer*, 47(5):1741–1748, 2006. doi:10.1016/j.polymer.2006.01.013.

[128] C. Soutis. Fibre reinforced composites in aircraft construction. *Progress in Aerospace Sciences*, 41(2):143–151, 2005. doi:10.1016/j.paerosci.2005.02.004.

[129] A. J. M. Spencer. *Deformations of Fibre-Reinforced Materials*. Oxford Univ. Press. New York, 1972.

[130] A. J. M. Spencer and K. P. Soldatos. Finite deformations of fibre-reinforced elastic solids with fibre bending stiffness. *International Journal of Non-Linear Mechanics*, 42(2):355–368, 2007. doi:10.1016/j.ijnonlinmec.2007.02.015.

[131] D. J. Steigmann. Frame-invariant polyconvex strain-energy functions for some anisotropic solids. *Mathematics and Mechanics of Solids*, 8(5):497–506, 2003. doi:10.1177/10812865030085004.

[132] P. Steinmann and E. Stein. A unifying treatise of variational principles for two types of micropolar continua. *Acta Mechanica*, 121(1-4):215–232, 1997. doi:10.1007/BF01262533.

[133] P. Steinmann. *Geometrical Foundations of Continuum Mechanics: An Application to First- and Second-Order Elasticity and Elasto-Plasticity*. Springer-Verlag Berlin Heidelberg, 2015. doi:10.1007/978-3-662-46460-1.

[134] P. Steinmann and E. Stein. On the numerical treatment and analysis of finite deformation ductile single crystal plasticity. *Computer Methods in Applied Mechanics and Engineering*, 129(3):235–254, 1996. doi:10.1016/0045-7825(95)00913-2.

[135] L. Strömberg and M. Ristinmaa. FE-formulation of a nonlocal plasticity theory. *Computer Methods in Applied Mechanics and Engineering*, 136(1):127–144, 1996. doi:10.1016/0045-7825(96)00997-8.

[136] H. Suemasu, A. Kondo, K. Itatani, and A. Nozue. A probabilistic approach to the toughening mechanism in short-fiber-reinforced ceramic-matrix composites. *Composites Science and Technology*, 61(2):281–288, 2001. doi:10.1016/S0266-3538(00)00211-6.

[137] R. L. Taylor, O. C. Zienkiewicz, and J. Z. Zhu. *The Finite Element Method: Its Basis and Fundamentals*. Butterworth-Heinemann, 7 edition, 2005. doi:10.1016/C2009-0-24909-9.

[138] E. T. Thostenson and T.-W. Chou. On the elastic properties of carbon nanotube-based composites: Modelling and characterization. *Journal of Physics D: Applied Physics*, 36(5):573–582, 2003. doi:10.1088/0022-3727/36/5/323.

[139] M. M. J. Treacy, T. W. Ebbesen, and J. M. Gibson. Exceptionally high Young's modulus observed for individual carbon nanotubes. *Nature*, 381:678–680, 1996. doi:10.1038/381678a0.

[140] C. L. Tucker III and E. Liang. Stiffness predictions for unidirectional short-fiber composites: Review and evaluation. *Composites Science and Technology*, 59(5): 655–671, 1999. doi:10.1016/S0266-3538(98)00120-1.

[141] T. Waffenschmidt, C. Polindara, A. Menzel, and S. Blanco. A gradient-enhanced large-deformation continuum damage model for fibre-reinforced materials. *Computer Methods in Applied Mechanics and Engineering*, 268:801–842, 2014. doi:10.1016/j.cma.2013.10.013.

[142] B. Wang, J. Zhao, and S. Zhou. A micro scale Timoshenko beam model based on strain gradient elasticity theory. *European Journal of Mechanics A/Solids*, 29(4): 591–599, 2010. doi:10.1016/j.euromechsol.2009.12.005.

[143] G. Williams, R. Trask, and I. Bond. A self-healing carbon fibre reinforced polymer for aerospace applications. *Composites Part A: Applied Science and Manufacturing*, 38(6):1525–1532, 2007. doi:10.1016/j.compositesa.2007.01.013.

[144] E. W. Wong, P. E. Sheehan, and C. M. Lieber. Nanobeam mechanics: elasticity, strength, and toughness of nanorods and nanotubes. *Science*, 277(5334):1971–1975, 1997. doi:10.1126/science.277.5334.197.

[145] P. Wriggers. *Nonlinear Finite Element Methods*. Springer, 2008. doi:10.1007/978-3-540-71001-1.

[146] S. Wulfinghoff and T. Böhlke. Gradient crystal plasticity including dislocation-based work-hardening and dislocation transport. *International Journal of Plasticity*, 69:152–169, 2015. doi:10.1016/j.ijplas.2014.12.003.

[147] T. Yalçinkaya, W. A. M. Brekelmans, and M. G. D. Geers. Non-convex rate dependent strain gradient crystal plasticity and deformation patterning. *International Journal of Solids and Structures*, 49(18):2625–2636, 2012. doi:10.1016/j.ijsolstr.2012.05.029.

[148] T. Yalçinkaya. *Strain Gradient Crystal Plasticity: Thermodynamics and Implementation, In: Handbook of Nonlocal Continuum Mechanics for Materials and Structures*, pages 1–32. Springer International Publishing, 2017. doi:10.1007/978-3-319-22977-5_2-1.

[149] F. Yang, A. C. M. Chong, D. C. C. Lam, and P. Tong. Couple stress based strain gradient theory for elasticity. *International Journal of Solids and Structures*, 39 (10):2731–2743, 2002. doi:10.1016/S0020-7683(02)00152-X.

[150] Q. Yin, A. E. Tekkaya, and H. Traphöner. Determining cyclic flow curves using the in-plane torsion test. *CIRP Annals - Manufacturing Technology*, 64(1):261–264, 2015. doi:10.1016/j.cirp.2015.04.087.

[151] H. M. Zbib, M. Rhee, and J. P. Hirth. On plastic deformation and the dynamics of 3D dislocations. *International Journal of Mechanical Sciences*, 40(2):113–127, 1998. doi:10.1016/S0020-7403(97)00043-X.

[152] H. M. Zbib, T. Diaz de la Rubia, and V. Bulatov. A multiscale model of plasticity based on discrete dislocation dynamics. *Journal of Engineering Materials and Technology*, 124(1):78–87, 2001. doi:10.1115/1.1421351.

[153] Q. S. Zheng. Theory of representations for tensor functions– a unified invariant approach for constitutive equations. *Applied Mechanics Reviews*, 47(11):545–587, 1994. doi:10.1115/1.3111066.

[154] O. C. Zienkiewicz and R. L. Taylor. *The Finite Element Method for Solid and Structural Mechanics*. Elsevier Butterworth-Heinemann, 6 edition, 2005. doi:10.1016/C2009-0-26332-X.

[155] L. Zybell, U. Mühlich, M. Kuna, and Z. Zhang. A three-dimensional finite element for gradient elasticity based on a mixed-type formulation. *Computational Materials Science*, 52(1):268–273, 2012. doi:10.1016/j.commatsci.2011.02.026.

Curriculum Vitae

Personal Data

Name	Tobias Kaiser, né Asmanoglo
Date of Birth	September 23, 1990
Place of Birth	Castrop-Rauxel, Germany
Nationality	German

Professional Occupation

since 12/2015	Scientific Assistant, Institute of Mechanics, TU Dortmund University
04/2014 – 11/2015	Student Assistant, Institute of Mechanics, TU Dortmund University
10/2013 – 03/2014	Internship, MAN Bus & Truck AG, Germany, Division: Simulation Chassis
10/2011 – 09/2013	Student Assistant, Institute of Mechanics, TU Dortmund University

University Education

10/2015	Academic Degree: Master of Science (M.Sc.) in Mechanical Engineering
11/2014 – 10/2015	Master Studies of Mechanical Engineering, TU Dortmund University
11/2014	Academic Degree: Bachelor of Science (B.Sc.) in Mechanical Engineering
10/2010 – 11/2014	Bachelor Studies of Mechanical Engineering, TU Dortmund University

School Education

06/2010	Abitur (University-entrance Diploma), Heinrich-Heine-Gymnasium, Dortmund

Publication series of the Institute of Mechanics

published to date:

2010/01   Palnau, V.: Implementierung eines netzfreien Diskretisierungsverfahrens und seine Anwendung auf die Scherbandanalyse. ISBN 978-3-921823-51-4

2010/02   Klusemann, B.: Application of homogenization methods and crystal plasticity to the modeling of heterogeneous materials of technological interest. ISBN 978-3-921823-53-8

2011/01   Hortig, C.: Local and non-local thermomechanical modeling and finite-element simulation of high-speed cutting. ISBN 978-3-921823-54-5

2011/02   Parvizian, F.: Modeling of microstructure evolution in aluminum alloys during hot extrusion. ISBN 978-3-921823-56-9

2011/03   Noman, M.: Characterization and model identification for the simulation of the forming behavior of ferritic steels. ISBN: 978-3-921823-55-2

2011/04   Kayser, T.: Characterization of microstructure in aluminum alloys based on electron backscatter diffraction. ISBN: 978-3-921823-57-6

2011/05   Bargmann, S.: Computational modeling of material behavior on different scales based on continuum mechanics. ISBN: 978-3-921823-58-3

2013/01   Waffenschmidt, T.: Modelling and simulation of adaptation and degradation in anisotropic biological tissues. ISBN: 978-3-921823-61-3

2015/01   Ostwald, R.: Modelling and simulation of phase-transformations in elastoplastic polycrystals. ISBN: 978-3-921823-66-8

2016/01   Subramanian, M.: Phenomenological modelling and simulation of ferroelectric ceramics. ISBN: 978-3-921823-74-3

2016/02   Clausmeyer, T.: Evolution of plastic anisotropy in metals.
ISBN: 978-3-921823-76-7

2016/03   Holtermann, R.: Computational multiscale modelling of grinding processes.
ISBN: 978-3-921823-86-6

2017/01   Bartels, A.: Modelling of evolving microstructures at different scales.
ISBN: 978-3-921823-93-4

2017/03   Dusthakar Kumar Rao, D. K.: Computational modelling of single and poly-crystalline ferroelectric materials. ISBN 978-3-921823-94-1

2019/01   Buckmann, K.: Microstructure evolution in functional magnetic materials. ISBN 978-3-947323-09-8

2019/02   Kaiser, T.: Computational modelling of non-simple and anisotropic materials. ISBN 978-3-947323-14-2